PLASMA DIAGNOSTICS PACKAGE

FINAL SCIENCE REPORT

Volume 2

SPACELAB 2 SECTION

Part B

THESIS PROJECTS

Department of Physics and Astronomy

THE UNIVERSITY OF IOWA

Iowa City, Iowa 52242

630

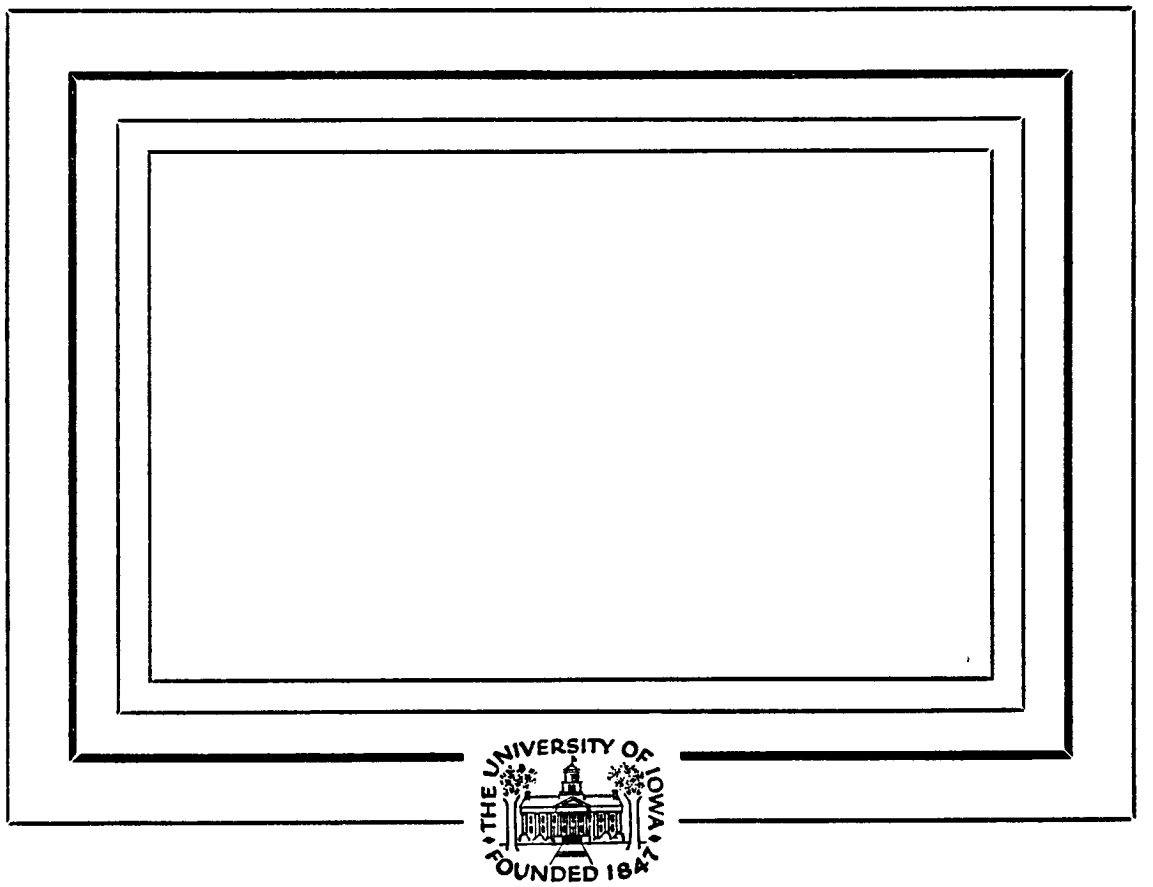

Department of Physics and Astronomy

THE UNIVERSITY OF IOWA

Iowa City, Iowa 52242

630

PLASMA DIAGNOSTICS PACKAGE

FINAL SCIENCE REPORT

Volume 2

SPACELAB 2 SECTION

Part B

THESIS PROJECTS

NASA/MSFC Contract No. NAS8-32807

Compiled By

J. S. Pickett
L. A. Frank
W. S. Kurth

Department of Physics and Astronomy
University of Iowa
Iowa City, Iowa 52242

June, 1988

THESIS PROJECTS

Design and Development of an Instrument for the Precise Measurement of S-Band and KU-Band Electric Fields Aboard Orbiter OV-099, G. B. Murphy, M.S.E.E. Thesis, University of Iowa, Iowa City, Iowa, March, 1985.

Plasma Parameters in the Vicinity of the Shuttle Orbiter, A. C. Tribble, Master's Thesis, University of Iowa, Iowa City, Iowa, May, 1986.

An Analysis of Whistler Mode Radiation from the Spacelab 2 Electron Beam, W. M. Farrell, Doctoral Thesis, University of Iowa, Iowa City, Iowa, July, 1987.

Ion Plasmas in the Vicinity of the Orbiter: Observations and Modeling, W. R. Paterson, Master's Thesis, University of Iowa, Iowa City, Iowa, July, 1987.

The Large Scale Wake Structure of the Shuttle Orbiter: Plasma Density, Temperature, and Turbulence, A. C. Tribble, Doctoral Thesis, University of Iowa, Iowa City, Iowa, May, 1988.

Quasi-Static Electric Field Measurements Made with the Plasma Diagnostics Package in Free Flight During Spacelab-2, J. T. Steinberg, Doctoral Thesis, University of Iowa, Iowa City, Iowa, May, 1988.

DESIGN AND DEVELOPMENT OF AN INSTRUMENT FOR THE PRECISE MEASUREMENT OF S-BAND AND KU-BAND ELECTRIC FIELDS ABOARD ORBITER OV-099

Gerald B. Murphy

A project submitted to the Dept. of Electrical and Computer Engineering, University of Iowa, in partial fulfillment of the requirements for M.S.E.E.

March 21, 1985

Project Committee: Prof. Karl E. Lonngren
Prof. Donald C. Enemark
Prof. Dong H. Chyung

TABLE OF CONTENTS

LIST OF FIGURES

LIST OF FIGURES (Continued)

LIST OF TABLES

INTRODUCTION AND SCOPE

The purpose of this report is to describe the definition, electrical and operational design, and calibration of an instrument which was built specifically to measure the electric fields generated by the Ku-band and S-band transmitters on board the shuttle orbiter. The Ku-band/S-band Receiver (KUSR) actually consists of two separate detector systems, one which is engineered specifically for the task of measuring S-band electric fields, and the other which is designed to measure peak fields generated by a pulsed Ku-band radar.

The scope of this paper will be such that the most emphasis will be placed on the Ku-band component of the receiver, since it is entirely a new design whereas the S-band receiver is a modification of an older instrument.

Section 1 will describe the background leading to the development and funding of the instrument. The requirements placed on the instrument and characteristics of the shuttle rendezvous radar and S-band communication link.

Section 2 details the design and development of the instrument. In particular the detector/antenna selection, pulse detector, self-calibration circuit, and spacecraft interface are described in detail.

Section 3 discusses the calibration of the instrument and the degree to which the measurement accuracy requirements are satisfied.

In order to accurately measure the Ku and S-band fields, considerable thought must be given to the methods of measurement while on orbit. Section 4 describes the operational scenario that will be used to fulfill the measurement objectives and some of the problems considered in the operation.

Section 5 presents a summary of the data flow during the mission as well as the data processing and analysis afterwards.

Section 6, the summary, compares the final instrument sensitivity and measurement objectives to design goals and summarizes the financial status of the contract.

The instrument proposal, measurements made on the previous mission, and the detailed schematics, are all referenced several times in the text, but are too bulky to include in the main body of material. Therefore, these data are included as appendices for the sake of completeness.

1.0 BACKGROUND

Since the shuttle orbiters were designed to haul cargo into orbit and retrieve it from orbit, and since that cargo can be extremely varied in its application, a great effort has been made to define the environment in and near the orbiter in all launch/recovery phases. By knowing precisely what environment to expect, engineers can appropriately design the payloads to operate safely and reliably within that environment.

The Plasma Diagnostics Package (PDP) is a cluster of 14 instruments designed primary to define the way in which the orbiter perturbs the natural plasma environment. These data are needed for the sake of future space plasma experimentation. Since plasma wave instruments were part of the cluster in the PDP, measuring electric and magnetic fields to approximately 200 kHz, it was logical to use the PDP to measure orbiter induced EMI as well. The wave measurements were therefore extended in frequency range to measure fields generated by the orbiter's transmitters. An S-band receiver was added specifically to measure field magnitudes due to the PM and FM communication link. Appendix A consists of two papers which summarize the EMI results obtained from the PDP wave instruments on the third test flight of the orbiter Columbia.

Soon after the data of the first mission were analyzed, it became evident that a more precise measurement of S-band fields as well as a measurement of Ku-band fields generated by the soon to be operational rendezvous radar were needed. The Air Force asked the PDP team to conduct a feasibility study on the engineering problems and costs associated with making these measurements. Several systems were considered and the one which emphasized simplicity, redundancy and accuracy of measurement was accepted.

At this point in time, a proposal was submitted to the Marshall Space Flight Center offering to include an instrument on the PDP which could accomplish these goals during a reflight opportunity aboard the Spacelab-2 mission (then scheduled for late 1984). This proposal (Appendix B) defined the capabilities of such an instrument and costed its design, development, fabrication, calibration and data analysis. The instrument was to be funded by the Air Force Space Test Program.

After negotiation and acceptance of this proposaal for Ku-band measurements, we were asked to submit costing for a modification and reflight of the S-band receiver system as well. Since the original design was a compromise between an HF and S-band system, it was decided to eliminate the HF measurement and try to improve the S-band system alone. An engineering cost proposal was prepared and negotiated (Appendix C) for this system. This constitutes the other half of the KUSR system.

1.1 Need for On-Orbit Measurements

Despite extensive developmental and ground test programs with the rendezvous radar, there were certain gaps which needed to be filled by measurements made on the flight system once installed in the orbiter.

These measurements could have been made in an anechoic chamber (if large enough) and to the extent possible they were, however, certain parameters were just not cost effective to measure in the laboratory.

Let us examine the parameters that are important from the point of view of the payload, crew safety, and Verification Flight Test (VFT) of the radar system.

For the deployable payload, which may have engineering systems that are susceptable to S-band or Ku-band fields, it is important to know: 1) The maximum field strength they may expect to see while secured in the payload bay; 2) The maximum expected field strength while being deployed near the orbiter; 3) The expected fields due to the radar while they are being tracked.

For the orbiter communication and radar subsystems, it is necessary to access the performance by: 1) Knowing that the output power is within specified range; and 2) Knowing that the antenna pattern is what is expected (for the S-band link the phased array can produce 8 beams).

Certainly ground measurements can provide most of the above information and in fact has, but verification of all 8 beams of the S-band link has not been done nor has there been measurements of E-fields in the vicinity of the orbiter in flight configuration. (See Appendix B.) As mentioned before, the problems associated with putting the full-up orbiter system in an anechoic chamber were prohibitive from a cost and programmatical standpoint.

It is with the above needs that the following design goals of the KUSR were set:

1. The maximum electric field obtainable in the near field of the Ku-band radar antenna is expected to be 240 V/m. The minimum field of concern is 1 to 2 V/m.

2. The instrument should have the sensitivity to probe the near field and scattered fields in and around the payload bay by having the Remote Manipulator System (RMS) arm move the PDP to the appropriate position.

3. The instrument should have dynamic range enough to measure the Ku and S-band fields at distances to several hundred meters when the PDP has been released from the orbiter.

4. The expected range for the S-band receiver should be ~ .1 V/m to 75 V/m.

5. An absolute accuracy of ±1 dB is desired for all field measurements.

Some of the above goals are more easily obtainable than others. Section 2 will describe the engineering trade-offs necessary to accomplish the above goals within the constraints given.

1.2 The Shuttle Radar

Since the orbiter uses the same amplifier and parabolic antenna for operation of its TDRS data link (15.0034 GHz CW) and its radar link (5 frequencies between 13.987 GHz and 13.987 GHz pulsed) and their peak output is essentially the same, it is sufficient to measure one or the other. The radar is linear polarization where as the communication mode is circular. Because of the flexibility of the radar system and the fact that it will be tracking the PDP while it is a free-flyer, it was decided to make all measurements in radar mode. All details of the radar system may be obtained from Reference 1, but are given below in a summary form.

The Ku-band radar and communications system is folded inside the payload bay for ascent and entry and deployed over the sill next to the forward bulkhead when in use. Details of the antenna pattern and circular polarization feed will be discussed in Sections 3 and 4. The antenna has a 2-axis positioner and is pointed by rotation around these two axes when tracking satellites, but employs a "mask" to prevent its pointing at certain elements of the orbiter and payload.

The radar system (in passive mode) is designed to track a standard Swerling target from approximately 100 ft. to 20 nm. Since this is a range gated radar, both the pulse width (PW) and pulse repetition frequency (prf) are variable depending on the target distance. Table 1.1 lists the various pulse widths and prf's available depending on target distance and whether the radar is in its search or track mode. Although the radar has an active mode, it will be of little concern to us. It is not likely to ever be used since a workable and affordable transponder design has not been carried to completion.

In order to minimize scintillation effects, the radar frequency is varied over the band indicated above in steps 52 MHz apart giving the following operational frequencies: 13.779, 13.831, 13.883, 13.935, 13.987 GHz. This frequency switching happens rapidly compared to our KUSR measurement cycle and will be important only in the design of the wave guide and antenna (see Section 2).

Since there is a wide range in the possible return power, (depending on target size and distance), it would be difficult to design the front end of the radar receiver section to handle such a dynamic range, thus several output power levels are available. The power levels of these modes and the predicted field strength in the main beam at a distance of 100m are contained in Table 1.2. The output power depends not only on the distance to the target, but the radar mode selected. By choosing the proper mode, the PDP can make measurements of the radar beam even when it is not being tracked by the radar.

TABLE 1.1
SIGNAL PARAMETERS FOR RR RADAR

Mode	Range (nmi)	prf	pw (μsec)
Passive Track	> 9.5	2987	33.2
	3.8 - 9.5	6970	16.6
	1.9 - 3.8	6970	8.3
	.95 - 1.9	6970	4.15
	.42 - .95	6970	2.07
	< .42	6970	.122
Passive Manual Search	> .42	2987	66.4
	> .42	6970	.122

TABLE 1.2
RADAR POWER OUTPUT

Mode (Radar)	Output Power Level	Maximum Near Field (V/m)*	Far Field+
Hi Power	70 watts	225**	2985/R
12 dB Pad	4.4 watts	57	746/R
24 dB Pad	.3 watts	14	188/R
TWT Bypass	~ 4 mwatts	1.4	19/R

**In Fresnel Zone extending to ~ 10m

*Maximum in Communication Mode is 240 V/m

+Begins at ~ 70m from dish

From the above description, we can further specify some desirable characteristics for the KUSR which must measure these fields.

1. It should have a relatively flat frequency response over the bandwidth including all radar frequencies.

2. It should have good response down to ~ 100 nsec pw and ~ 10 kHz prf. (If sensitive to pulse width or prf, this sensitivity must be accounted for in calibration.)

3. Sensitivity at high end (240 V/m) dynamic range can be traded operationally against measurement in an attenuated mode with extrapolation to the expected fields at full power. This will relax the system dynamic range requirement from 1 to 240 V/m to 1 to 60 V/m (the 12 dB attenuation mode). This results in a dynamic range of 36 dB instead of 48 dB. (See Section 3 for details on how this is accomplished.)

4 It should either measure circular polarization or have dual linear capability so that the incident linear polarization may be detected regardless of orientation.

1.3 Orbiter S-Band Communication Link

This link is similar to the one on Columbia on which measurements were made during the STS-3 mission (See Appendix A). There are several communication systems in the S-band frequency range, but only the one with highest power output is of concern for our measurements. This system, the CW phase modulated link, operates through the so called S-band "Quad" antennas located above and below the cabin area. Since the configuration of the antenna beams has changed from that which was measured on the previous mission (there were 4 beams then instead of the present 8), the information obtained by the KUSR both on the RMS arm and as a free-flyer, will be particularly useful.

The high frequency mode (2287.5 MHz) has the highest output power and will be selected when the KUSR makes its measurements. Ground based measurements of this system were confined to scale models and 1/4 section models. At no time was the whole system (with 8 beams) or a model of the whole system tested in an anechoic chamber. The measured fields were on the high side of predictions on the previous system (Appendix A), but the error was large. A brief description of the S-band part of the KUSR in Section 2 will detail what was done to improve the accuracy of this system. Apart from this discussion and a description of the S-band calibration scheme, most of the attention in the rest of this report will be confined to the Ku-band section of the system.

After this brief introduction to the orbiter systems, the KUSR must measure, and the needs for the measurements, Table 1.3 presents a summary of the design specifications as negotiated in the KUSR proposals and delineated in the preliminary design review.

TABLE 1.3
DESIGN CRITERIA FOR KUSR SYSTEM

	Ku-band Specification	S-band Specification
Frequency Range	13 - 15 GHz	1900 - 2500 MHz
Amplitude Response	< 1 - 60 V/m	.1 - 70 V/m
Minimum PW Response	.1 μsec	---
Polarization	Circular or 2 Linear	Linear
Sensitivity	< ±.5 dB	< ±.5 dB
Absolute Accuracy	±1 dB	±1 dB

2.0 INSTRUMENT DESIGN AND DEVELOPMENT

Overall instrument development involved many tasks some which were unrelated to the experiment itself, but associated with solving problems such as the susceptibility of other PDP hardware to high field strength of the radar. For completeness, the following list summarizes some of the design, logistic, or planning problems which were dealt with, and which had a direct or indirect influence on the KUSR design.

Most of these tasks had to either proceed in parallel with the hardware design or preceed it in order to provide necessary design criteria. With exception of the first item, these will be described in detail in either this or later sections of the report and the location of this additional information is noted where applicable.

- No measurement instrumentation for design work in the 10-18 GHz range existed. A set of appropriate equipment had to be procured, rented and borrowed.
- Ground Support Equipment (GSE) to simulate the PDP interface was developed. This had to be used during all bench test and design stages (Section 2.5).
- A method to access the susceptability of the PDP to high radar fields and adequately shield it from those fields was devised (Section 2.1.3).

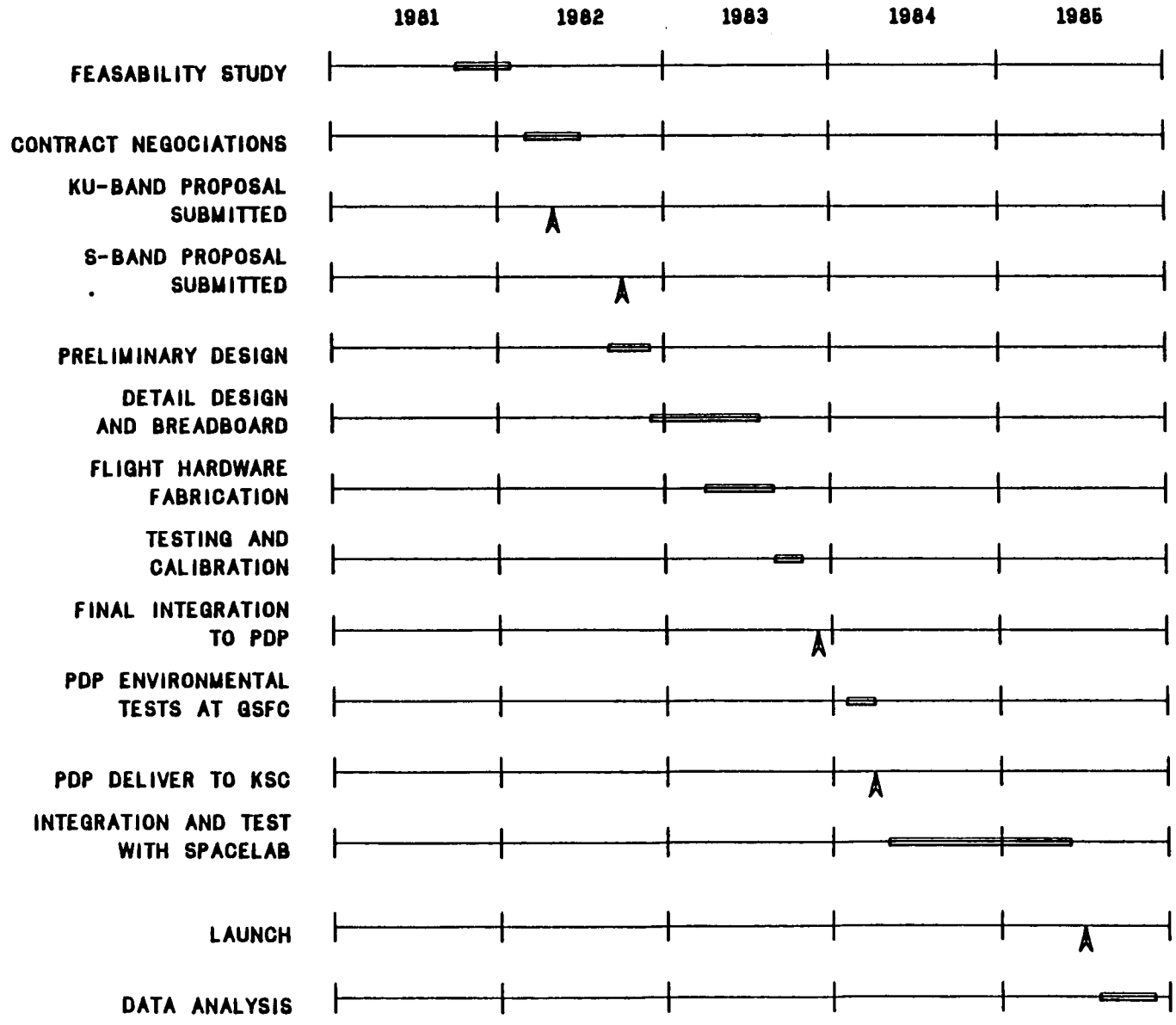
KUSR DEVELOPMENT AND FLIGHT SCHEDULE
1981
1982
1983
1984
1985
FEASABILITY STUDY
CONTRACT NEGOCIATIONS
KU-BAND PROPOSAL SUBMITTED
S-BAND PROPOSAL SUBMITTED
PRELIMINARY DESIGN
DETAIL DESIGN AND BREADBOARD
FLIGHT HARDWARE FABRICATION
TESTING AND CALIBRATION
FINAL INTEGRATION TO PDP
PDP ENVIRONMENTAL TESTS AT GSFC
PDP DELIVER TO KSC
INTEGRATION AND TEST WITH SPACELAB
LAUNCH
DATA ANALYSIS

Figure 2.1

- A calibration procedure as well as instrument design which could approach the ±1 dB absolute accuracy requirement was implemented (Section 3).

- The test and procurement program had to be consistent with and meet the specifications in NASA requirements (Section 2.4).

- It was necessary to define and/or develop data analysis software and assure that all data necessary for interpretation of KUSR measurements was to be contained in the data delivered post mission (Section 5.2).

- Work with Johnson Space Center (JSC) personnel was needed to develop an experiment plan consistent with operational limitations of the radar, RMS and orbiter (Section 4).

Figure 2.1 shows the design and development timeline for the instrument from the initial feasibility study through integration and test. This schedule assumed an April 17, 1985, launch date which has now slipped due to orbiter problems. All of the work indicated here is finished except that which falls under the data analysis and program development. (See Section 5.)

The detailed hardware definition and design phase can be broken into two major parts: the design of the system interface to the PDP (both electrical and mechanical) and the detailed design of the detector system itself.

A highly detailed description of the design process at the individual circuit level would be lengthy and uninteresting. Instead the requirements placed on each piece of the system and an outline of the final solution which gives the most significant design trade-offs necessary along the way is presented. The presentation of design material will be in a logical rather than chronological order since most tasks had to proceed in parallel to some degree or another.

2.1 Electrical and Mechanical Interface

The overall KUSR design was driven by the measurement requirements already described in Table 1.3, but also needed to meet another set of criteria in order to interface to the PDP and meet certain reliability standards. These requirements are listed below:

- Instrument must have its own power supply.
- Total power consumption should be $\lesssim$ 5 watts (including modified S-band).
- Conducted emission on power lines must meet specification.
- Redundancy should be used wherever reasonable.
- Use the clock interface presently available from the standard PDP encoder.
- Two to three kilograms total weight is a useful mass guideline.
- Total footprint available for mounting is very limited and special hardware may be required (The original guideline was 4" x 7").
- The Ku-band antenna must be small enough to not interfere with other instrument fields of view.
- The new S-band antenna should meet these same minimum interference requirements.
- Output will be 2 data lines each sampled 10 times per second by the PDP encoder (0-5v range).
- The PDP encoder will provide at least 2 sets of thermistor lines (voltage already on line) and the instrument needs only to select the best place for mounting.

Figure 2.2 is a functional block diagram of the KUSR. Each of the basic blocks will be discussed in turn and the S-band system as a whole treated in Section 2.3.

The electrical interface to the PDP was fixed very early in the design phase and will be discussed first.

2.1.1 Timing and Interface Assembly

Figure 2.3 is the detailed KUSR assembly block diagram. This section will describe the design of what is called the "PDP Spacecraft Interface" on Figure 2.2 and "Ku Board Assembly 85-3826" on Figure 2.3. The purpose of the interface is to:

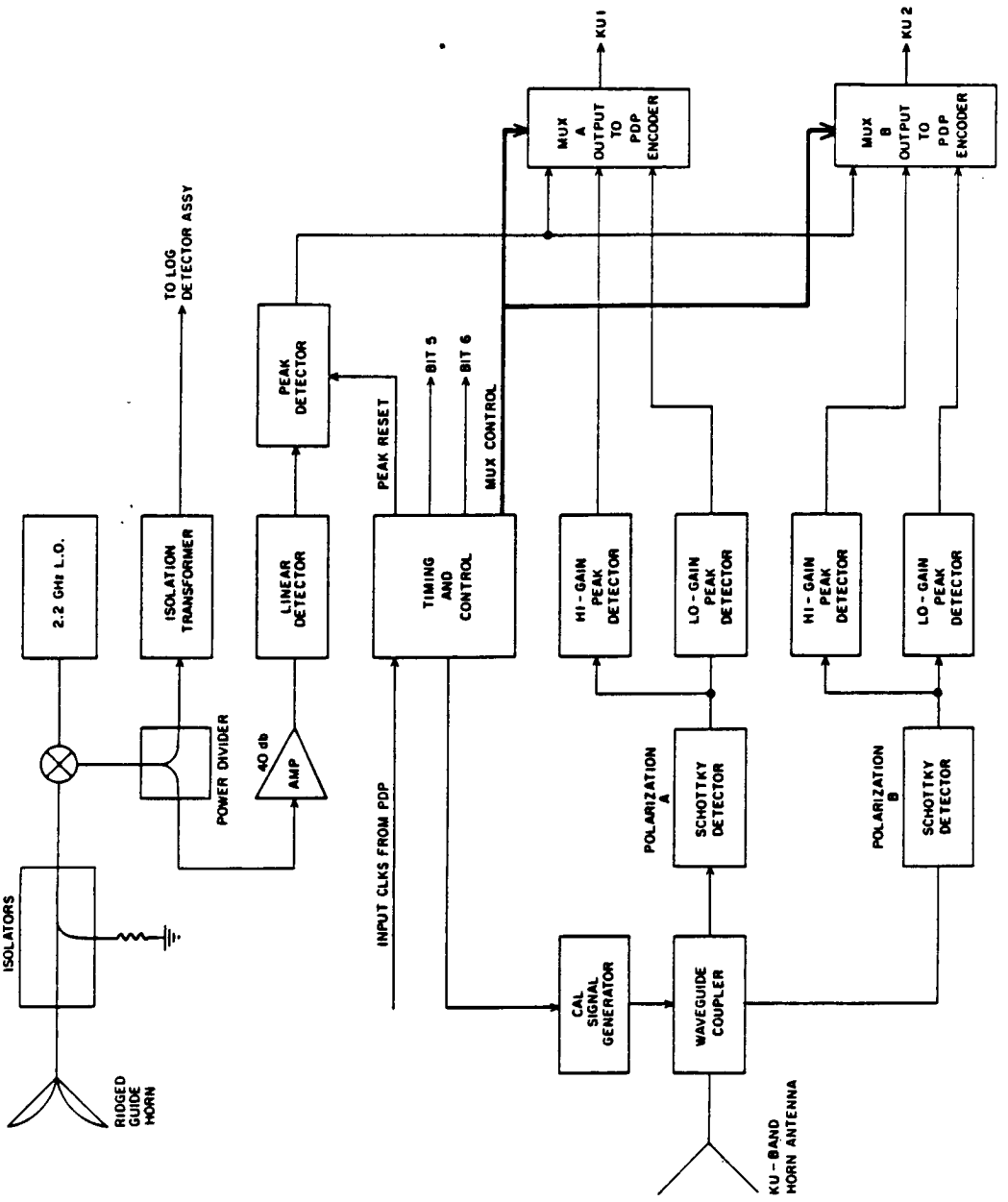

KUSR FUNCTIONAL BLOCK DIAGRAM

Figure 2.2

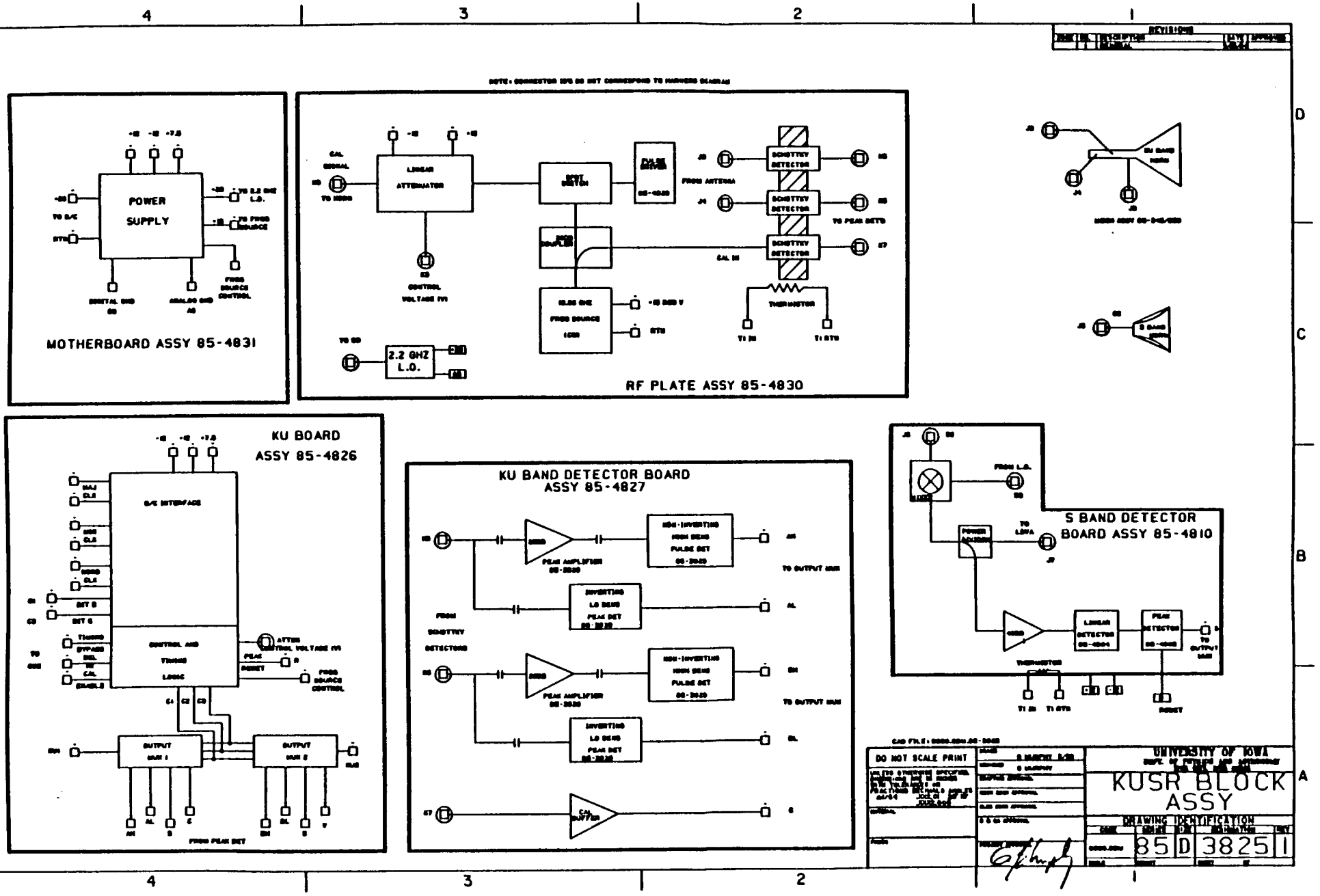

Figure 2.3

1. collect peak detector data from the 2 redundant Ku-band detector systems and the single channel S-band linear detector system;

2. using a differential buffer interface, take 3 timing signals from the PDP encoder and create the clocks necessary to MUX the detector outputs as well as self-calibration data and instrument status over the 2 redundant analog channels;

3. generate peak reset and calibration control signals;

4. serve as the interface to the instrument and spacecraft ground support equipment (GSE) during instrument checkout.

Figure 2.4 indicates the three timing signals generated by the PDP encoder. Each major frame of PDP data consists of 16 minor frames each containing 144 8-bit words. Since the major frame has a period of 1.6 seconds, the data rate from the entire sytem is 11.52 kbits. Two specific words in each minor frame are assigned to the KUSR and sampled once each minor frame or at a rate of 10 Hz (Figure 2.4).

Since only two output lines were available, the output multiplexers were designed to provide as complete a set of data as possible even if one channel failed. Table 2.1a lists the inputs to the multiplexer and Table 2.1b shows the output of each channel as a function of minor frame number. Since the Ku-band part of the instrument has a self-calibration cycle (Section 2.2.3), the output of the mux is different for this cycle which is also indicated in Table 2.1b.

As an aid toward knowing the status of the instrument, two clock outputs are provided (these are combined by the encoder with one bit data from other instruments into engineering status words contained in each minor frame and are referred to as bit 5 and bit 6 in the detailed block assembly diagram Figure 2.3). Bit 5 toggles with a period of 8 minor frames which is the major MUX cycle as noted in Table 2.1b (it indicates hi or lo gain selection). Bit 6 indicates the status of the calibration cycle which happens once every 386 major frames (10 minutes 18 seconds).

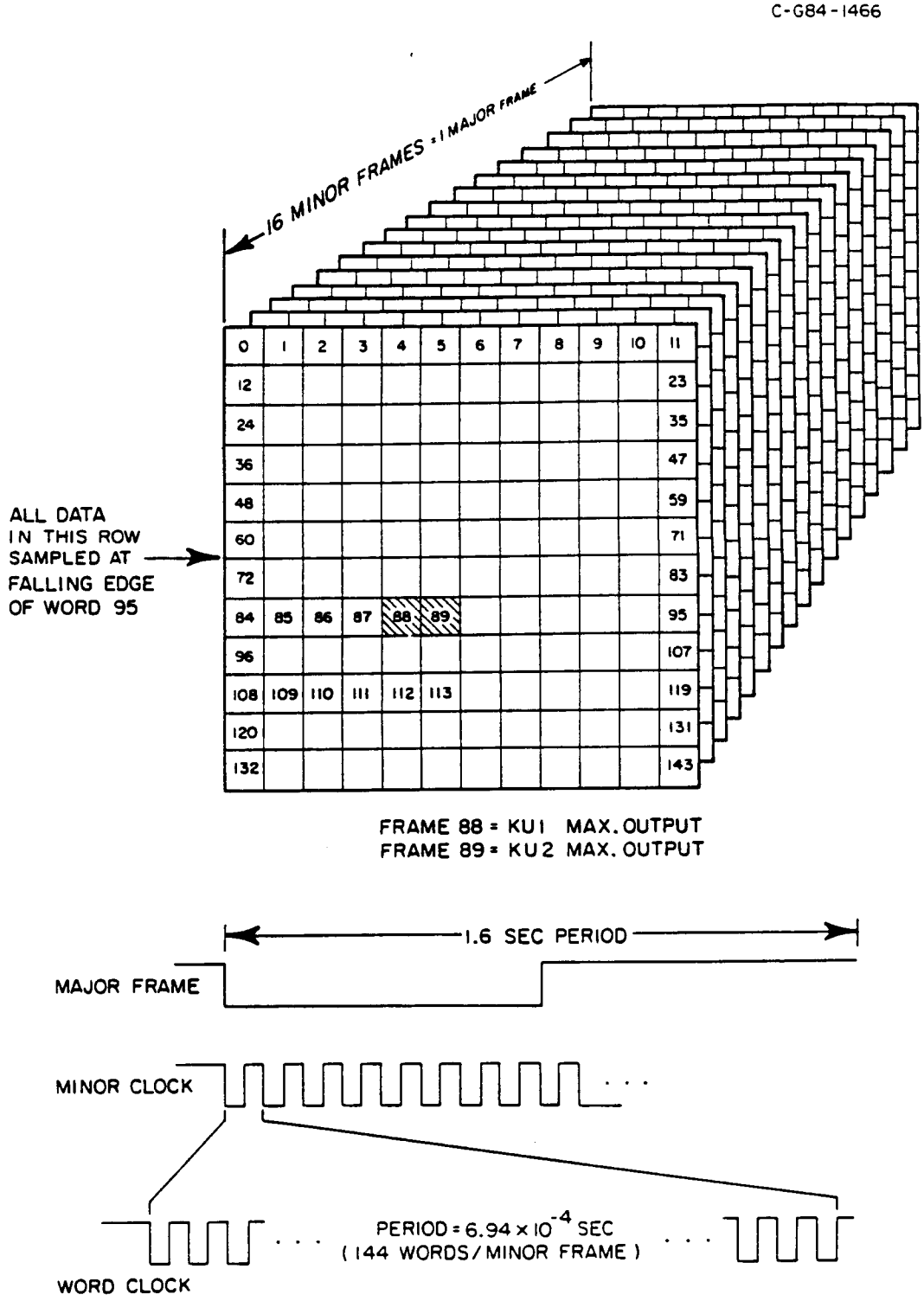

Figure 2.4 Data Sampling and Input Clocks

TABLE 2.1A
MULTIPLEXER INPUTS

MUX A (KU 1)*	MUX B (KU 2)
KAL (Detector "A", "Lo" Gain)	KBL (Detector "B")
KAH ("Hi" Gain)	KBH
Cal Detector (C)	Cal Control Voltage (CV)
S-band Linear	S-band Linear

TABLE 2.1B
MULTIPLEXER OUTPUTS

Cal Status	Timing Cycle	Minor Frame	Bits 5	Bits 6	MUX A (KU 1)	MUX B (KU 2)
Off	1	0-3	0	0	KAL	KBL
Off	2	4-7	1	0	KAH	KBH
Off	3	8-11	0	0	S	KBL
Off	4	12-15	1	0	KAH	S
On	1	0-3	0	1	KAL	KBL
On	2	4-7	1	1	KAH	KBH
On	3	8-11	0	1	C	CV
On	4	12-15	1	1	C	CV

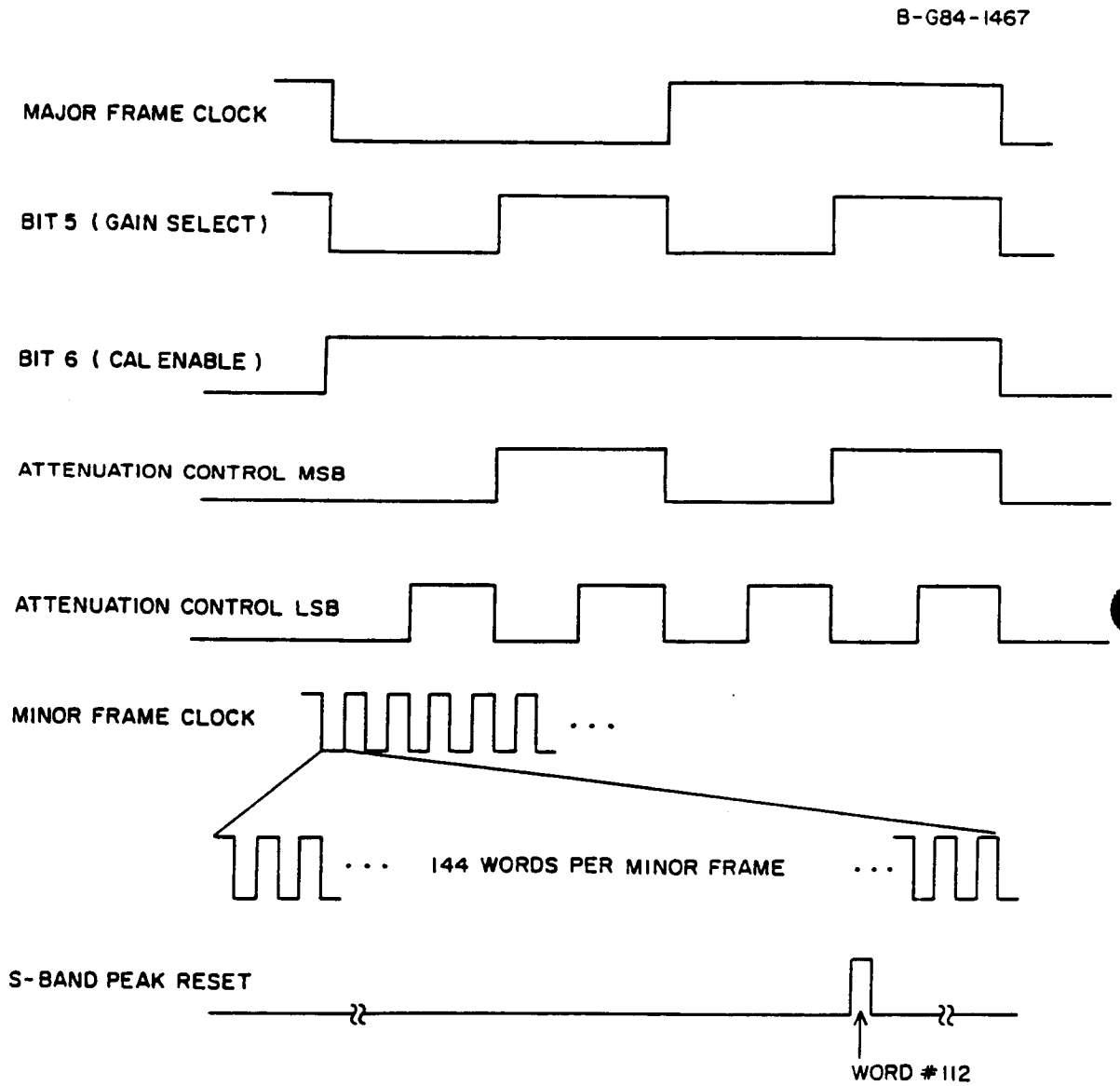

OUTPUT CLOCK SIGNALS

Figure 2.5

Another function of the interface system is that of generating a peak reset for the S-band detector. This is done shortly after the S-band signal is sampled and its timing is illustrated in Figure 2.5.

In summary, the interface board takes in 3 timing signals, synchronizes with the falling edge of the major clock, generates C_1, C_2, and C_3 (Figure 2.5) to control the multiplexors, generates control signals for CAL circuit, and produces bit 5 and bit 6 for status monitoring. A summary of the output clocks from this board is presented in Figure 2.5.

Since it is desirable to control the mode of the instrument manually during development and calibration, the ability to bypass the normal cycling of the MUX fixing either the HI gain or LO gain signals at the output, or manually enabling the calibration signal is also provided by this board. (See "TIMING BYPASS", "SEL HI", or "CAL ENABLE" on Figure 2.3). These are simply external switch closures.

Detailed schematics of this timing and control interface are in Appendix D.

2.1.2 Power Supply Requirements and Design

In the early stages of KUSR development, it was necessary to scope the power converter requirements. The power converter design would be patterned from DC-DC converters used in other instruments on the PDP. The number and polarity of voltages determine the number of modules needed for regulators, and the transformer size. The total power required determines the size of inductors and capacitors as well as the capacity of the chopper transistors. Thus, once the total power and number of voltages has been determined, it is fairly straightforward to guess the size of the motherboard required. Figure 2.6 shows the block diagram for the KUSR power supply. Initial estimates of the voltages and currents required of the power supply are in Table 2.2 as well as the final power consumption of the instrument. Several special characteristics of the power supply should be noted:

1. The relatively high current draw for this instrument size requires large hand wound inductors, wide traces, and hefty chopper transistors. These can be noted in Figure 2.7 which is the assembly diagram of the power supply.

2. Since the S-Band local oscillator required 100 ma at 28v, it was decided, because of problems associated with adding that additional power and regulation capability, that the PDP spacecraft 28v would simply be filtered and delivered to the oscillator directly (Figure 2.6).

3. For purposes of heat dissipation, the transistors Q_1 through Q_6 were mounted in heat sinks to the inside wall of the housing above the power supply board.

4. The 15v supply is used solely for the Ku-band self-calibration circuit and is enabled through transistor Q_7, (Figure 2.6) by a signal from the timing and control electronics. This minimizes power consumption since the cal circuit is used only once every 386 major clock cycles.

All other power supply schematics as well as pictures of the finished board can be found in Appendix D.

TABLE 2.2
POWER SUPPLY REQUIREMENTS

Voltage	Use	Current
+ 7.5	CMOS (Timing Board)	25 ma
± 12	S-band Linear Detector	180 ma
	Ku-band Peak Detector	65 ma
	Linear Attenuator	50 ma
+ 15	Ku-band Frequency Source	100 ma
+ 24*	S-band L. O.*	60 ma

Total Estimated Power	10.2 watts
Total Actual Power (Ku-CAL enabled)	7.7 watts

*This voltage, taken directly from PDP power bus, does not come from KUSR power supply.

2.1.3 EMI Minimization

An important factor in the integration of any instrument into a system is the control of EMI. In the case of the KUSR, that primarily meant control of conducted and radiated emissions. Radiated emissions in this case are principly due to the S-band Local Oscillator

ORIGINAL PAGE IS
OF POOR QUALITY

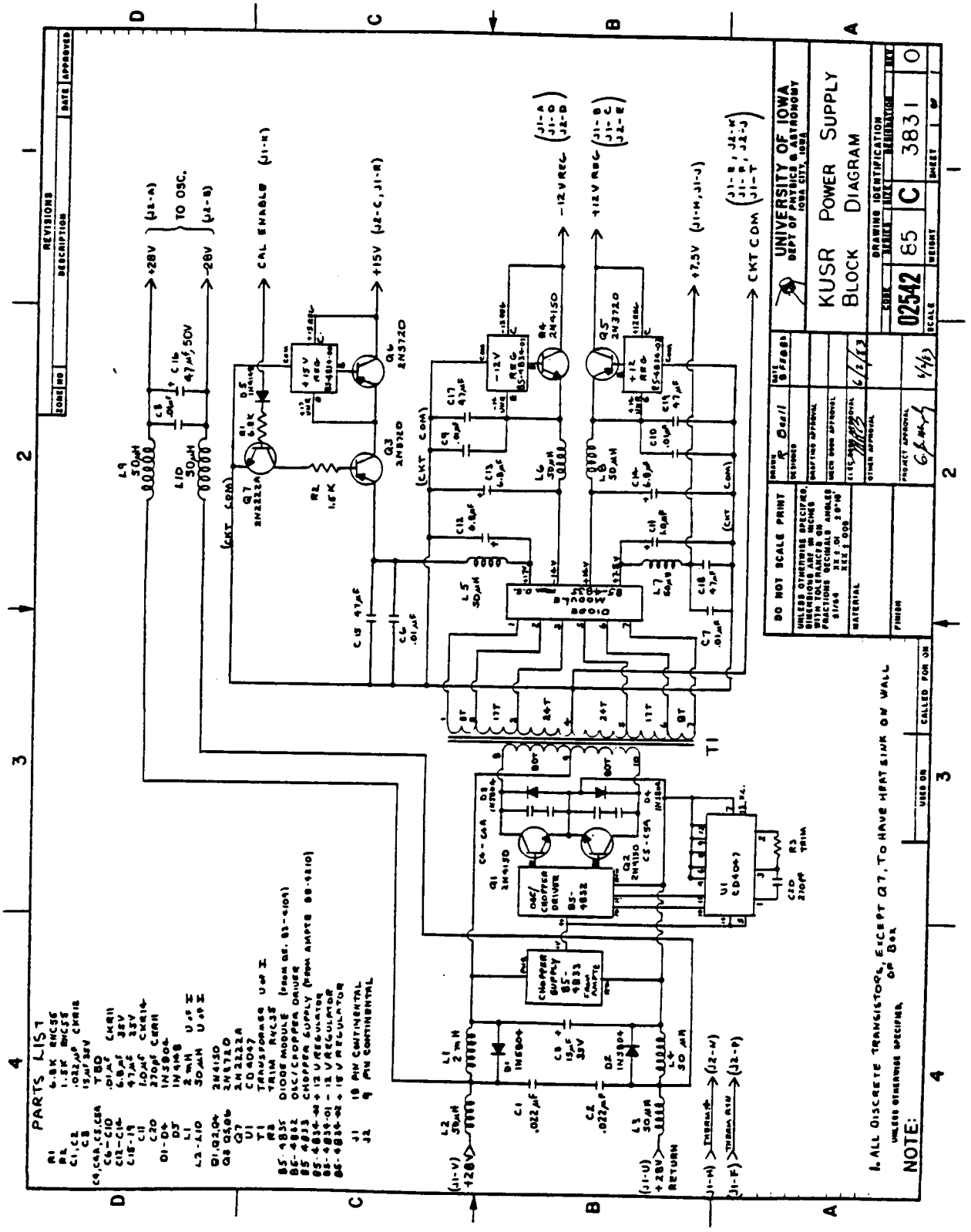

Figure 2.6 Power Supply Block Diagram

(2.2 GHz) and Ku-band calibration source (13.9 GHz) since these signals radiate from the receiving antennas. Since the KUSR is a completely contained in a metal housing, the only other possible sources of radiated emissions are the cables connecting the KUSR to the rest of the PDP. The problem then reduces to one of controlling radiated emissions to the world external to the PDP and controlling the conducted emissions on all wires on the internal harness which connects to the KUSR.

Radiated emissions are a problem at 2.2 GHz and 13.9 GHz, simply because they fall close to or within the receiving frequencies of the shuttle systems we are trying to measure. Two isolators in series with the input antenna of the S-band system are used to prevent "leakage" of the 2.2 GHz L.O. signal out through the antenna. As can be seen in the block diagram Figure 2.3, the only device between the local oscillator and the antenna is the mixer which is specified to have an local oscillator port to RF port rejection of 20-25 dB. Measurement confirms that without isolators, the 2.2 GHz power coming out to the horn is at -8 dbm (See Table 2.3). Considering the antenna gain this gives an E field at a distance of 1m from the PDP of approximately .5 V/m. Each isolator provides an attenutation of this signal of ~ 30 dB bringing the radiated emission within a range which is acceptable.

TABLE 2.3
S-BAND EMI MINIMIZATION

	Power to Horn at 2.2 GHz	Equivalent E-field Due to Radiated Power (V/m)
Before Isolator Installation	-8 dBm	.5/r V/m
After Isolator Installation	-76 dBm*	2×10^{-4}/r V/m

*Loss in Forward Direction .3 ±.1 dB

Emission of 13.9 GHz results because the calibration source injects a pulsed 13.9 GHz signal directly into the waveguide of the Ku-band horn assembly (See Section 2.2.3). Calculations have shown that in this special case the emissions will not result in a problem. Had the emission been for a duration significantly longer than 1.6 seconds or occurred much more frequently, it could cause the shuttle radar to become "confused" while tracking the PDP. Since the PDP spins at a rate of ~ 30°/second and the cal signal lasts for 1.6

TABLE 2.4
SUMMARY EMI CALCULATION

Problem: Calculate probability that the 7 khz 4.15 μs pulses generated by the KUSR will interfere with the return signal to the rendevous radar and cause loss of track.

RUSR: 13.9 Ghz, 7 khz prf, 4.15 sec pw, 1.6 sec duration, max radiated power P_t = 0 dbm (other levels 10, 20, and 30 db lower)

Radar: Will use 5 of 16 doppler filters, range gate .122 μsec

Distance: 100 meters (typ)

1. Probability that KUSR signal will enter tracking spectram

$$Pd = \frac{5}{16} = .31$$

2. Probability 4.15 μsec pulse will overlap range gate (4.15μs pulse is followed by 142.8 μsec gap)

$$Pr = \frac{4.15}{142.8} = .029$$

3. What is probability that the interference signal is stronger than the reflected signal we are trying to detect.

consider gain of KUSR antenna (G = 17 db)
power density at the radar dish (100 meters away) is:

$$P = \frac{P_t G}{4\pi R^2} = 0 + 17 - 11 - 40 = -34 \text{dbm/m}^2$$

reflected power: (assuming worst case radar transmit power of 5.7 dbm)

$$P_r = \frac{P_t' G' \sigma}{(4\pi)^2 R^4}$$

P_t' = 5.7 dbm
G' = gain of radar dish = 37.7 db
σ = radar cross section (assume σ = 1 m^2)

$$P_r = 5.7 + 37.7 + 0 - 22 - 80 = -58.6 \text{ dbm/m}^2$$

this implies probability of interference is

$$P_i = 1$$

TABLE 2.4 (Continued)
SUMMARY EMI CALCULATION

4. Since the PDP rotates what is the probability that the KUSR is pointing at the radar while the CAL signal is present?
   Spin rate = 5 rpm = 30°/sec x 1.6 sec = 48°
   BWFN ≈75° (worst case)
   Total angle of interference 123°

$$P_s = \frac{123}{360} .342$$

5. Guidance and navigation computer samples radar data once every four seconds. The probability of getting a bad data point is

$$P_g = \frac{1.6}{4} = .4$$

Total probability of a given CAL cycle causing a problem is

$$P = P_d \cdot P_r \cdot P_i \cdot P_s \cdot P_g = 1.2 \times 10^{-3}$$

seconds, there is only a 34% probability that during any given calibration cycle the PDP KUSR horn will be facing the radar antenna. The E-field due to this emission steps through 4 levels during a cycle producing 4 levels of electric fields. Table 2.4 summarizes the problem of calculating the possible interference with the radar and concludes that it will not present a problem.

Conducted emission onto the KUSR harness as well as the susceptibility of the KUSR to noise generated by other instruments is controlled primary by the use of judiciously placed filters on the power lines as well as all other signal lines. These filters are all contained on a "feedthrough" plate inside the housing. The power converter in the KUSR runs at 20 kHz and the power line filters have been chosen to block this frequency and its harmonic as much as possible. The feedthrough filters on all other lines are chosen so as not to interfere with the rise times necessary for the digitial signals. The circuit model for the power supply filter is shown in Figure 2.7. The KUSR circuit common on the secondary side is tied to chassis at one point on the power supply board. The primary power return is isolated from chassis. Appendix D contains photographs of the finished filter plate and attached harness.

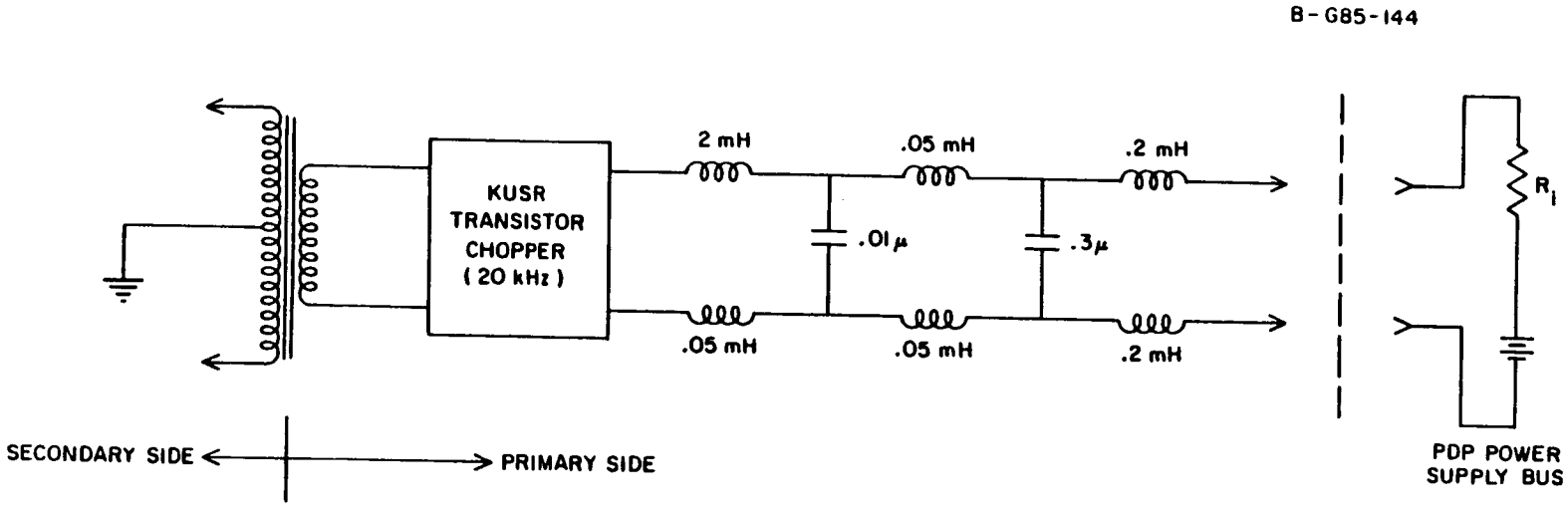

FILTER CHARACTERISTICS

FREQUENCY (kHz)	ATTENUATION (db)
20	44
40	69
60	80
80	87
100	92

Figure 2.7 EMI Conducted Emission Filter

Aside from the conducted and radiated emission problems discussed above, the issue of the radiated susceptibility of the PDP aluded to in Section 2.0 had to be dealt with. The PDP was not designed to be EMI "hard" and an assessment had to be made a) whether significant RF power could be coupled inside the PDP and b) if a large enough portion of this power could be picked up by the unshielded cables and cause logic upsets or component failures.

The PDP was constructed with a 50 mil aluminum skin bolted to a framework which supports the instruments. There were many apertures through which cables run or instruments protruded. The combination of these apertures and the poor contact between the skin and structure which created efficient slot radiators resulted in very poor shielding. At Ku-band frequencies test results from experiments in the anechoic chamber proved that any opening $>\sim$ 1/4" was efficient at reradiating RF energy into the PDP (Figure 2.8 illustrates this fact)[2]. There were numerous gaps of this size and greater in the PDP skin. Other tests proved that for slot radiators several wavelengths long and as narrow as a few thousandths of an inch, the attenuation was extremely poor. Depending on the spacing between the metal to metal contact and size of the gap, the attenuation varied from $\sim$ 20-50 dB. Experimentation proved that covering apertures with a find mesh screen and using copper tape with silver impregnated conductive adhesive to cover the "slots" created by the metal seams, the attenuation could be brought to $>$ 75 dB in all test cases.

Although the PDP could be made reasonably RF tight for a relatively minimal cost, it was still necessary to investigate Part B of the problem--how much power could unshielded cables pick up and could this cause logic upsets or component failures.

The maximum power that can be coupled into an unshielded wire with a perfectly matched load[3] is $.13\ P\lambda^2$ where P is the incident power density. Experiments done by R. Coronel et al.[4], at TRW have substantiated these results. This will serve as an upper limit for the analysis since in reality loads will not be matched and the resistive losses are high in cable bundles at this frequency.

Considerable study has been done to understand the susceptibility of various circuit components as a function of frequency. Most of this work has been funded by DOD and much is classified, however, Figure 2.9 summarizes many sets of data and is a useful guideline[5]. The data can be summarized by saying that in general, devices which cannot operate well at high frequencies are also less susceptable. Capacitance to substrate material and in IC leads makes it very difficult to couple enough power into the device to cause problems. As a guideline from Figure 2.9, we take 20 mW or +13 dBm as an allowable upper limit to the total power coupled to the device.

Assuming a 75 dB attenuation of the incident signal (70 watts maximum radar power into $\sim$ $3m^2$ at close distances ($\cong$ 25 watts/m^2 power density) there could be a power density of .8mw/m^2 inside the PDP. Considering the wire coupling this results in a maximum possible power into the electronic device of -43 dBm. This is well below the determined problem level.

A-G85-192

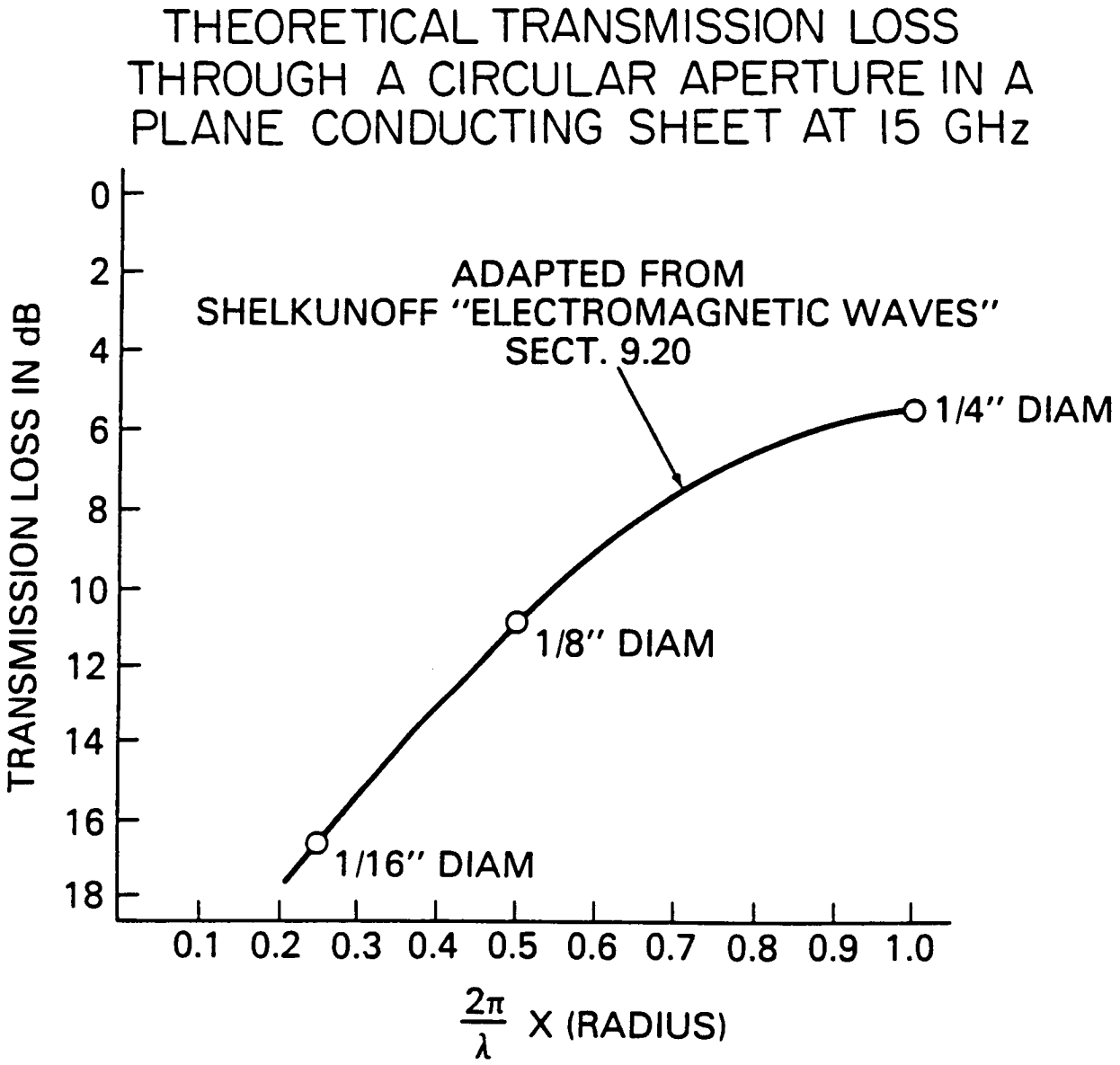

Figure 2.8

INTEGRATED CIRCUITS RFI SUSCEPTIBILITY

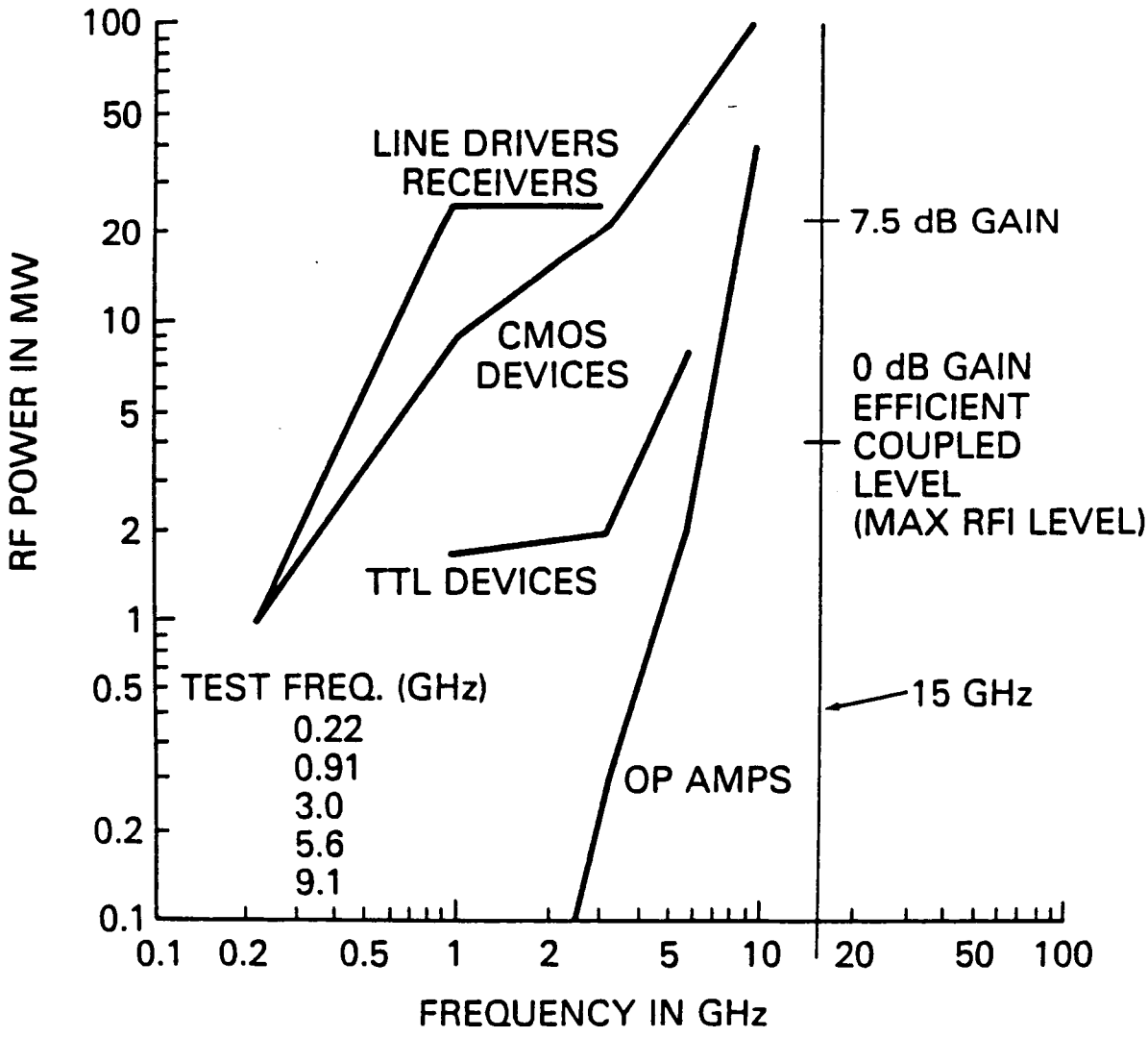

Figure 2.9

Based on the above findings, the following approach was taken.

1. Cover all openings >~ 1/4 inch or slots longer than ~ 1/2 inch with copper tape or mesh as appropriate.

2. Install feedthrough filters on all external lines coming into the PDP (these lines are used while the PDP is on the RMS arm).

3. Avoid operating the PDP in the near field of the radar beam while the radar is in Hi power mode (primarily this will protect the other payload elements and the radar itself from reflected fields).

4. Test the PDP after assembly in the anechoic chamber to as high a field level as is possible with available equipment.

During instrument calibration (Section 3.0), the PDP was tested to >70 V/m with no observed problems.

2.1.4 Mechanical Integration and Housing Design

Mechanical integration presented few problems once a housing design was chosen. The power supply board (the largest of all circuit boards in the assembly) placed a lower limit on the dimensions of the housing. Initial estimates of the size of the circuit boards were:

1. Power Supply = 5" x 7"
2. Ku-band Detector Board = 3" x 6"
3. Timing and Control Board = 4" x 6"
4. Modified S-band linear detector board = 4" x 6"

Also needed was a section of the housing to mount the oscillators, power dividers, attenuators, etc. needed for the RF end of the system. It was decided to build a housing in two sections, the first would house the power supply board on one side and the Ku-band, S-band, and timing boards on the other. This section would also contain the wiring harness and feedthrough filters. The second section would be made to accommodate all the RF components. The housing had to meet the following criteria:

1. The power supply must be accessable simply by removing the lid.

2. Adequate space needed to be allowed for heat sinks (6) to mount to the side of the power supply section of the housing.

3. The section which held the feedthrough filters had to electrically isolate the "inside" from "outside".

4. The depth of the sections were determined by the need to accommodate the cordwood modules of the S-band and power supply board, and the Ku-band detector and timing boards when stacked together.

5. All boards must be easily removable with the harness connectors accessable.

6. The semirigid coax which connects the RF section to the detectors must be easily installed after the box is assembled.

7. The housing should be mounted by one end with extension "feet" necessary to straddle a cable and filter already installed on the PDP instrument deck.

8. Vibration specifies as per Section 14 of the Integrated Payload Requirements Document (MSFC #JA0017) must be met.

Appendix D has pictures showing the sections of the housing in various stages of assembly.

In addition to the housing, mounts for the two antennas had to be designed for the PDP. These mounts needed to be relatively close to the KUSR to minimize cable loss. These constraints were easily met and Appendix D shows the two antennas in their final configurations.

The only elements of the KUSR system, other than antennas, not contained within the KUSR housing are the two S-band isolators referred to in Section 2.1.3 and low-pass and band-pass filters associated with the log detector used as part of the S-band system (See Section 2.2.4).

2.2 Detector and Antenna Selection and Design

In the preliminary study phase it was determined that various types of diode detectors in conjunction with either a linear or log peak detector could (if the receiving antenna had gain >~ 10 dB) give the required sensitivity without the need for amplifiers. Since the design needed to be simple and reliable, the fewer active components the better. Considerations of reliability, frequency response, and sensitivity led me to look into three basic detector types 1. Schottky, 2. Zero Bias Schottky, and 3. Tunnel Diodes.

Several parameters characterize the diodes and guide choosing which to use for the detector:

1. The open circuit output voltage sensitivity "K" (the "transfer function" of the device in mV/mW) should be as large as possible for the ±1 dB accuracy goal.

2. The Tangential Signal Sensitivity "TSS" (the input signal required to raise the output 6 dB above the noise level) should be minimized.

3. Bias: Since a bias circuit gives another opportunity for failure a diode without bias is preferred.

4. Power Rating: The ability to withstand the possible high continuous power from the communication link as well as the pulsed radar is important.

5. Video Resistance: Since the output of the diode will be fed to a high input impedance op-amp circuit for peak detection, this parameter is not important in this case.

6. Temperature stability and rating: The instrument should operate over a relatively narrow range, however, qualification testing runs from -40° to +80°C or possibly +125°. As long as the device is calibrated over the expected temperature range (0° to +40°C) it must simply survive all other testing.

Table 2.5 lists typical characteristics of the diodes mentioned and a summary of their performance under the above criteria[6].

A zero bias Schottky was chosen because of its excellent power rating, high K, and low TSS. It was felt that temperature variation could be calibrated out and would not be a problem. The actual characteristics as well as the measured calibration curve (±1/2 dB) are shown in Figure 2.10.

TABLE 2.5
DIODE PERFORMANCE SUMMARY

Performance	Biased Schottky	Zero-Bias Schottky	Ga As Tunnel
Bias	Yes	No	No
T.S.S. Typ. (NF = 3 dB)	-50 to -52 dBm (Excellent)	-52 dBm (Excellent)	-49 dBm (Good)
K (Voltage Sensitivity)	1200 - 2000 (Medium)	2000 (High)	300 - 700 (Low)
Video Resistance Ω (Square Law Range)	200 - 400	400 - 600	100 - 150
Input VSWR	2:1 to 4:1 (Fair)	6:1 (Poor)	3:1 (Fair)
Temperature Stability	± 1 dB (Fair)	±2 dB (Poor)	±.5 dB (Excellent)
Typical CW Power Rating	+23 dBm (Excellent)	+23 dBm (Excellent)	+17 dBm (Good)

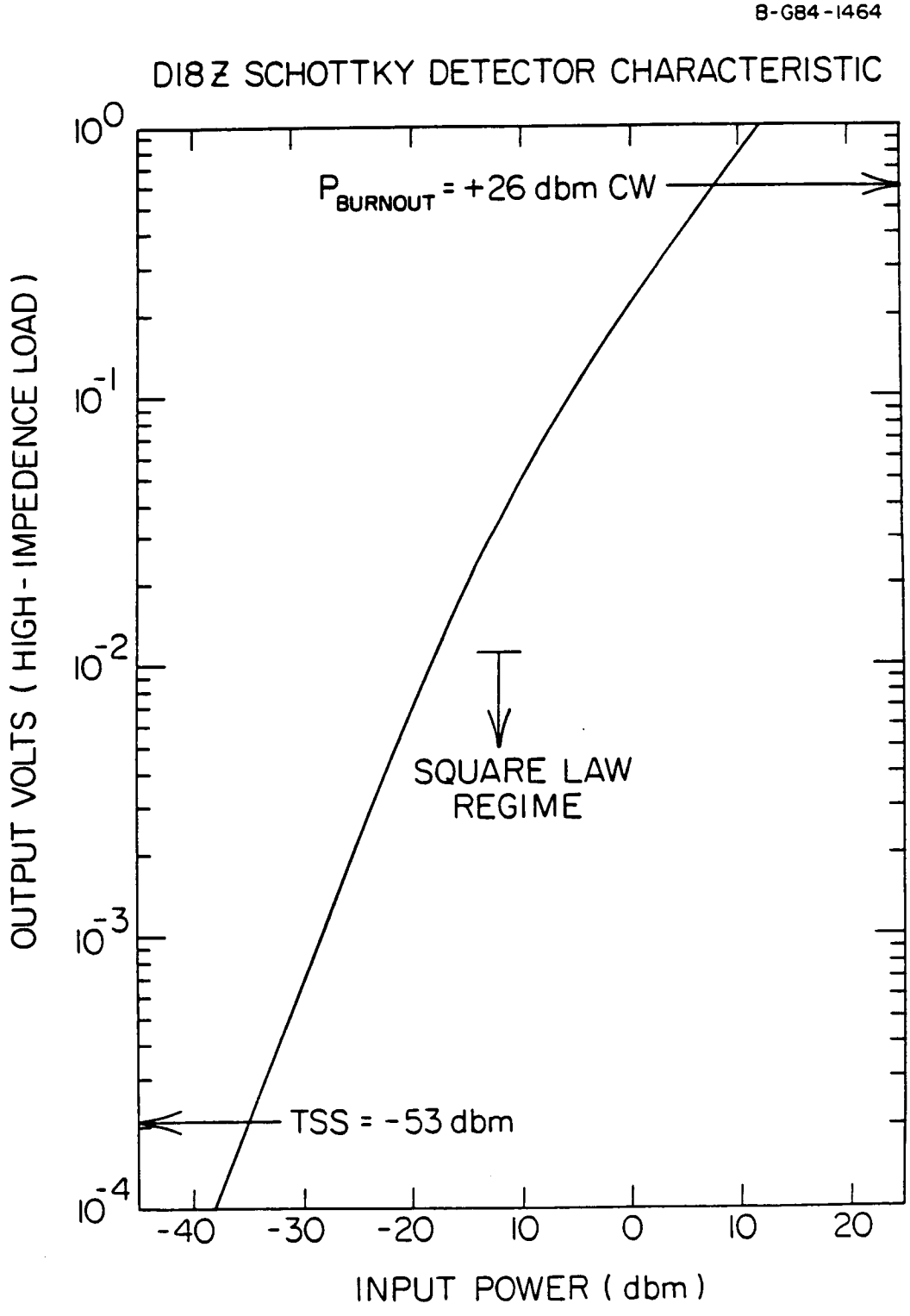

Figure 2.10 Calibration Curve for Typical Zero Bias Schottky Detector

The next most important factor in determining the sensitivity of the KUSR is its antenna which will be discussed in the next section.

2.2.1 Horn Waveguide Assembly

Selection of the horn waveguide assembly was driven by the following specifications:

1. The gain of the horn and loss in the waveguide must be adjusted so that a) 1 V/m E fields produce an output voltage on the detector of at least 1 mV and b) the highest possible E-field (240 V/m) does not yield an input power to the detector greater than 26 dbm (the burnout rating is 26 dbm cw).

2. The system should be dual polarization to provide 2 parallel and redundant measurement systems (recall that the radar is linearly polarized). With both polarizations working the total E-field can easily be reconstructed.

3. The system should be of minimal weight and size.

4. Waveguide cutoffs should be adjusted so that ideally pure TE_{11} waves exist at the probes. This is to minimize VSWR of the dual orthoganal probes and minimize cross coupling effects.

5. The PDP will be spinning when it makes some of its measurements at ~30° per second. Since the time resolution will be .1 second, the pattern should be smooth with a beam width > 3°. (This could potentially conflict with #1 requirements.)

6. The system should be easy to fabricate and tune.

With the above considerations in mind, many antenna types were researched, but is soon became evident that a simple conical horn with appropriate flare angle and length to meet criteria #1 and #5 (and suitable modifications to minimize diffraction effects) could also be joined to a simple pipe with plunge tuner and provide the needed dual polarization system. This system looked to be simple to fabricate as well, enabling a certain trial and error in the antenna design within the time alloted.

First let us bound the gain of the horn. Assuming no waveguide loss and probe mismatch, the power received by the antenna is:

2.1) $$P = A_e S$$

A_e = effective area of antenna aperture

S = incident power density

For a plane electromagnetic wave in free space

2.2) $$S = E^2/Z_o$$

E = electric field intensity in volts/meter
Z_o = impedance of free space = 337Ω

for E = 1 V/m => S = 2.7 mW/m^2
for E = 240 V/m => S = 153 watts/m^2

A_e the effective area of an antenna is by definition related to the gain by:

2.3) $$A_e = \frac{G\lambda^2}{4\pi}$$

λ = free space wavelength

From Figure 2.12, we see that a 1 mV output of the Shottky detector implies an input of -28 dbm (1.6×10^{-3} mW) so we bound the gain by saying that an input field of 1 V/m should produce a power to the detector of > -28 dbm and an input field of 240 V/m should result in < +26 dBm (400 mw).

Assuming a perfect match and using, eqn., 2.3:

$$12 \text{ dB} < G < 18.5 \text{ dB}$$

This is easily within the achievable range for conical horns.

The gain and the half power beam width (HPBW) are tradeoffs in the design of any antenna. Since the far field power pattern is the Fourier transform of the aperture distribution of the electric field at the horn, the HPBW can be related to the aperture by:

2.4) $$HPBW = 2 \sin^{-1} \left(\frac{.51\lambda}{D}\right)$$

D = Aperture Diameter

for a uniform aperture distribution. In real cases the aperture distributions are not uniform making the gain less than expected and the pattern broader. If our criteria that HPBW be >12° (one high gain-low gain measurement cycle is .4 sec long so the PDP rotates 12° during this time) then the above relation implies a maximum aperture size of 4.87λ.

The length and aperture diameter of a horn determines the beam shape since the flare angle determines the modes that propagate within the horn and thus its aperture distribution. For a given aperture diameter the gain will be optimized at a given horn length

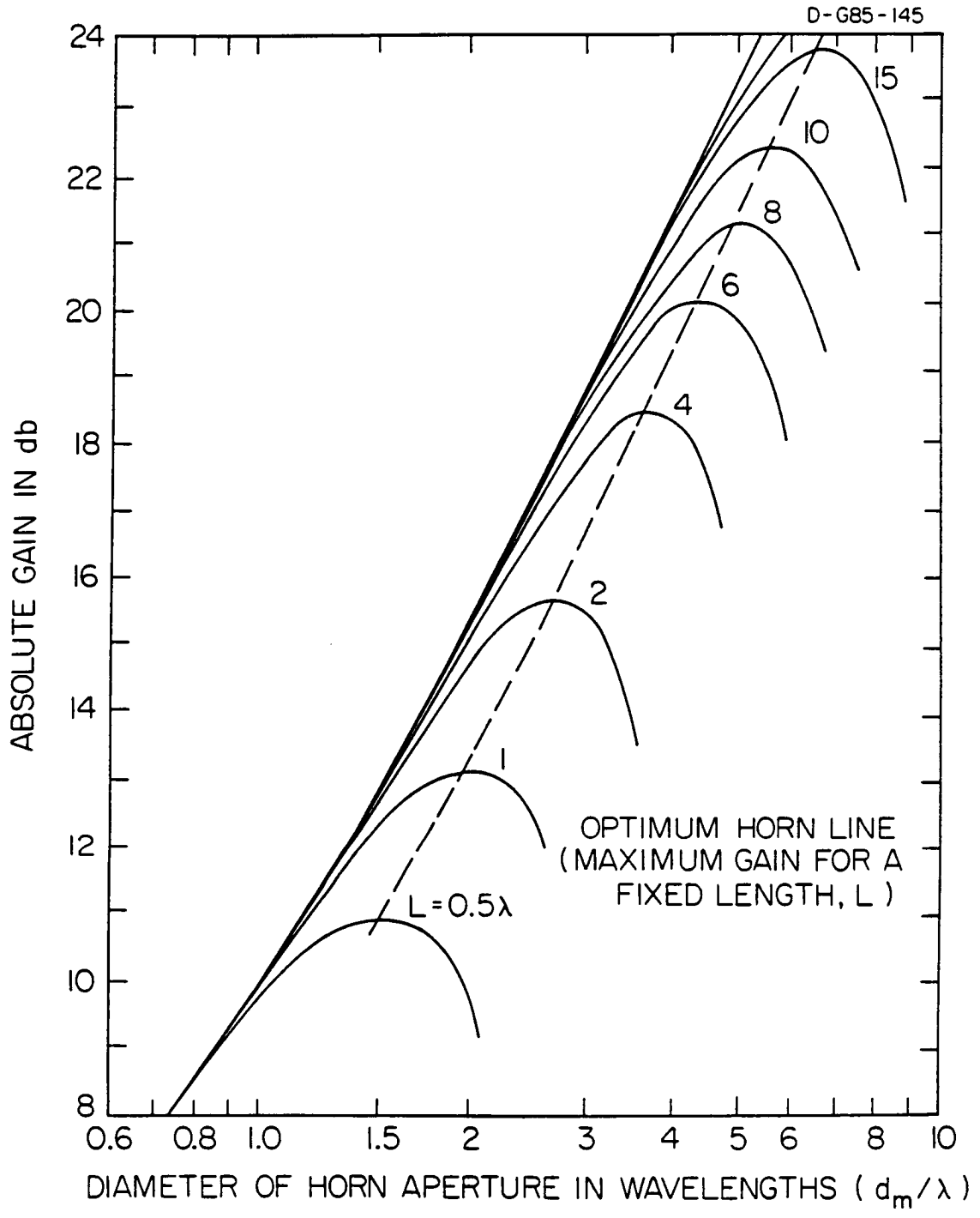

Figure 2.11 Gain of an Electromagnetic Horn as Function of Length and Aperture Diameter Assuming Uniform Aperture Distribution

and degraded at other lengths because of beam shape distortions due to multiple and higher order electromagnetic modes. Figure 2.11 illustrates the variation in the gain as a function of length and aperture.[7] Note that after a certain optimum aperture size is reached, the gain starts to decrease.

By plotting the length and diameter of the optimal design, we obtain Figure 2.12. Note that above a gain of about 17.5 dB, a horn needs to be longer for a given diameter, that is the flair angle has to decrease.[8] From Figure 2.12, it can be seen that a so called optimum gain horn of approximately 4 wavelengths long with a 4 wavelength aperture meets roughly the gain criteria. Next, we must worry in detail if the beam width criteria can be met as well. Experimentally optimal gain horns with apertures in the range of 1.5λ to 15λ have been shown to have HPBW in the E and H planes of the following:

2.5) $$HPBW_H^\circ \sim \frac{70\lambda}{D}$$

2.6) $$HPBW_E^\circ \sim \frac{60\lambda}{D}$$

This is slightly broader than that predicted by eqn. 2.4. Eqns. 2.5 and 2.6 are plotted in Figure 2.13.

A horn was constructed (Figure in Appendix D) with the 4λ by 4λ dimensions and its measured characteristics which are described in detail in Section 3 are summarized in Table 2.6.

TABLE 2.6
KU-BAND ANTENNA CHARACTERISTICS

Size	Flair Angle	Maximum Gain	Gain Flatness
3.37" x 3.37"	26.5°	17.1 dB	13.7 - 14 GHz=.5dB

A_e (at 13.9 GHz)	$HPBW_E$	$HPBW_H$	BWFN*
1.5×10^{-3} m^2	18 ±2°	18 ±2°	±75°

*Total beam width to first nulls

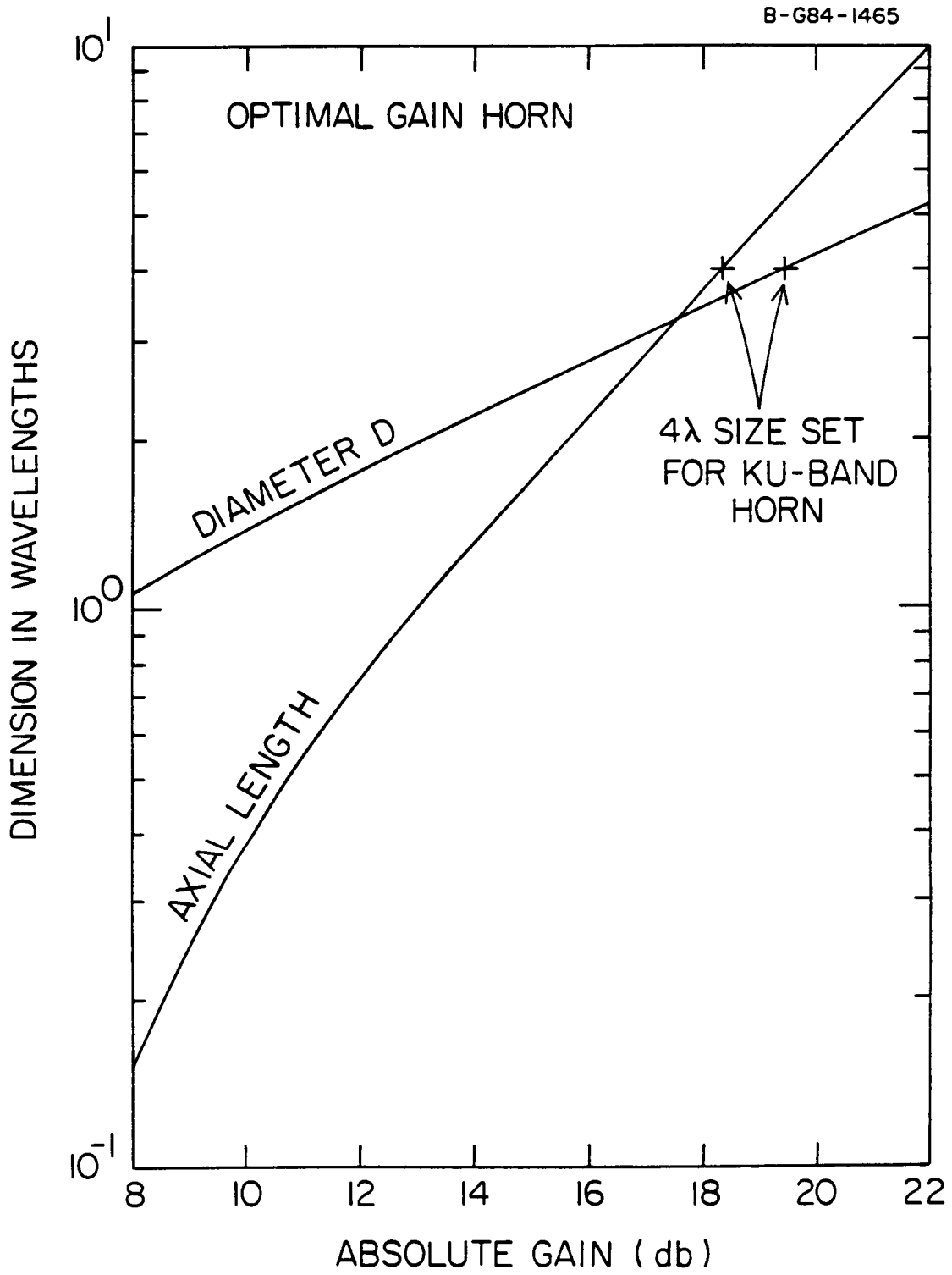

Figure 2.12 Dimensions for Optimal Gain Horn

The next task was to design a waveguide to properly feed the horn. Recall that the solutions to Maxwell's equations in a circular waveguide are given by the following sets of equations (in cylindrical coordinates).[11]

For TM waves:

2.7) $$E_z = AJ_n (k_c r) \begin{matrix} \cos (n\ \phi) \\ \sin (n\ \phi) \end{matrix}$$

For TE waves:

2.8) $$H_z = BJ_n (k_c r) \begin{matrix} \cos (n\ \phi) \\ \sin (n\ \phi) \end{matrix}$$

where $J_n (k_c r)$ is the n^{th} order Bessel function

Other components follow from the solutions of Maxwell's equations, but it is the Tangential component of the electric field (E_z) and Tangential component of the derivative of H (H'_Z) that determines the boundary conditions and thus the mode cutoffs.

For TM waves, the boundary conditions that tangential component of the electric field vanish at the walls of the conductor ($E_z = 0$ at $r = a$) leads to:

2.9) $$J_n (k_c a) = 0$$

If p_{nl} is the ℓth root of the nth order Bessel function:

2.10) $$k_c = \frac{p_{n\ell}}{a}$$

$$\text{where } k_c = \frac{2\pi}{\lambda_c}$$

λ_c becomes the cutoff wavelength meaning longer wavelenths cannot propagate in the guide in this mode ($TM_{n\ell}$). The lowest value of $p_{n\ell}$ is the first root of the zero order Bessel function ($p_{01} = 2.4$) and thus has the longest cutoff wavelength (lowest cutoff frequency) of any TM mode.

The TE mode boundary condition is just that the normal derivative of H_z be zero at $r = a$.

This implies:

2.11) $$J_n' (k_c a) = o$$

Likewise, cutoff frequencies can be defined for these modes and the lowest non zero values of P_{nl} is $P_{11} = 1.84$ implying the lowest cutoff frequency of all modes is for TE_{11}. Thus, it is the TE_{11} mode that is the fundamental one is a circular guide. Figure 2.14[10]

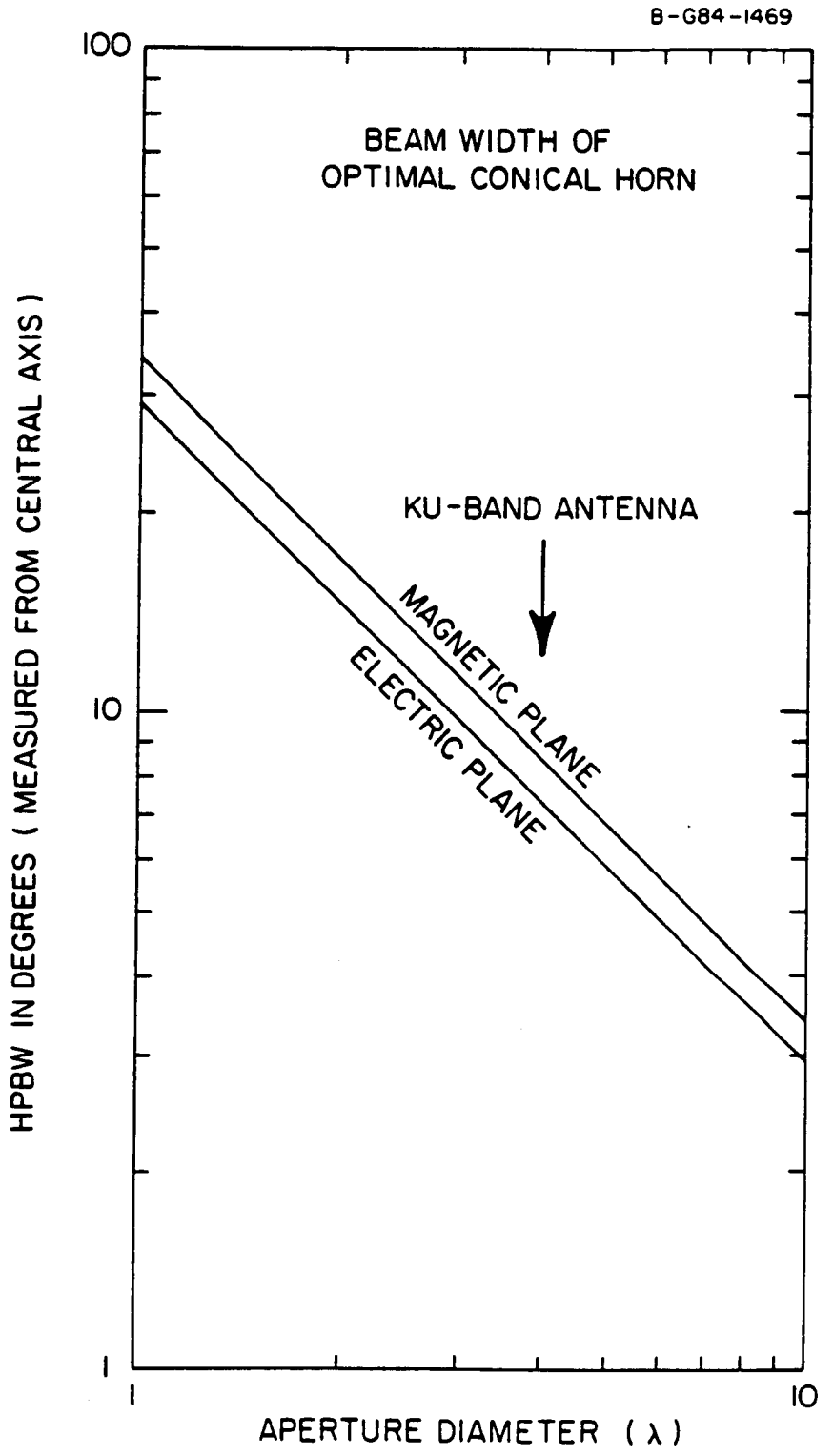
B-G84-1469
100
BEAM WIDTH OF
OPTIMAL CONICAL HORN
KU-BAND ANTENNA
MAGNETIC PLANE
ELECTRIC PLANE
10
1
1
10
HPBW IN DEGREES (MEASURED FROM CENTRAL AXIS)
APERTURE DIAMETER (λ)

Figure 2.13

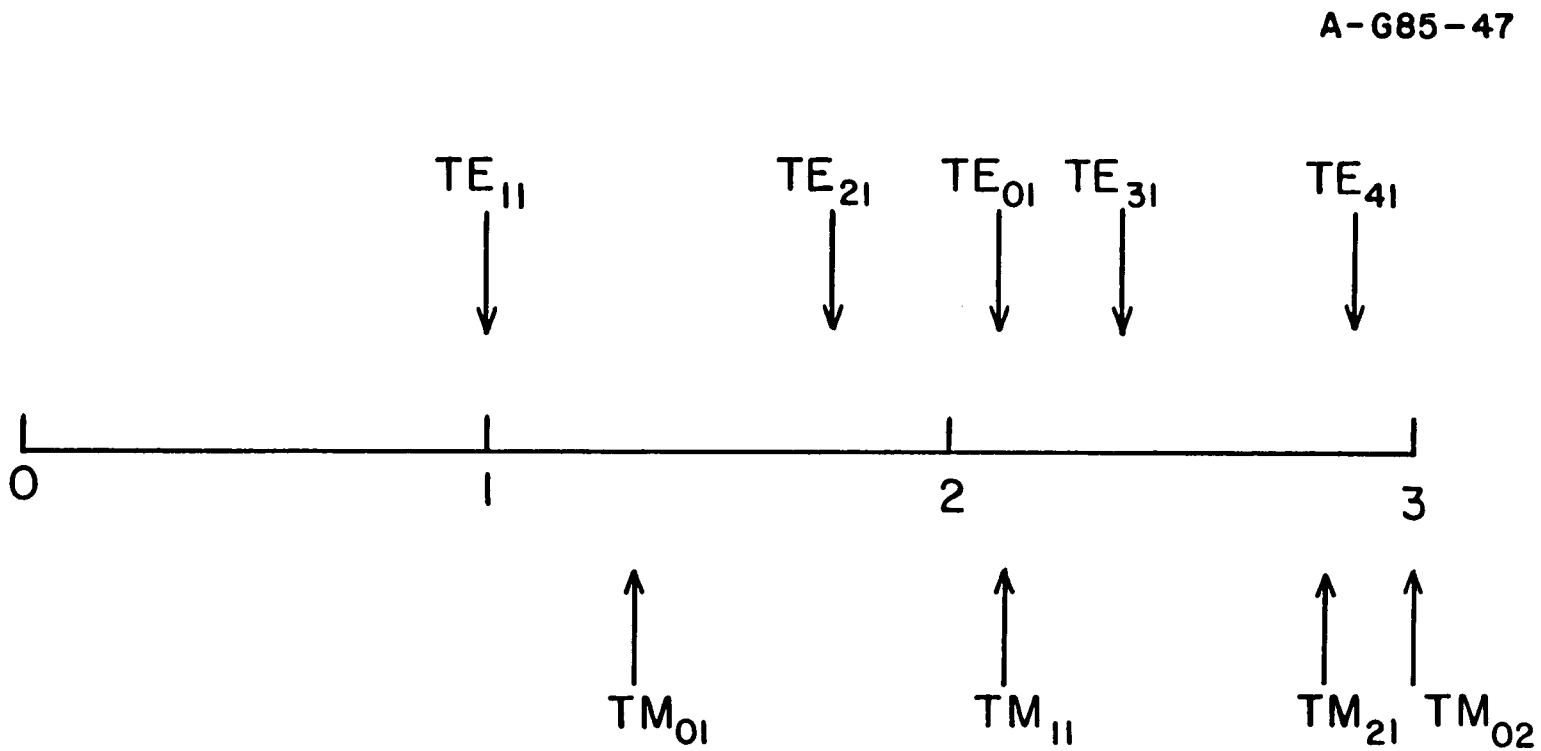

Figure 2.14 Cylindrical Waveguide Mode Cutoffs Normalized to the TE_{11} Mode

illustrates the mode cutoffs as normalized to the TE_{11} cutoff. The goal is to design a waveguide that propagates only the TE_{11} mode since the radiation pattern of the horn depends on this and the matching and cross coupling of the probes depend on this as well.

Calculations show that a waveguide made of pipe .75" inside diameter (easily available) will produce a cutoff frequency for TE_{11} of 9.22 GHz and for TM_{01} of 12.03 GHz. This is not ideal, but acceptable as long as there are several wavelengths between the probe and the horn. It should also be noted that a probe (wire) inserted radially in the guide will naturally excite the TE_{11} mode. (See Figure 2.15.)[11]

In order to determine the placement of the probes, it is necessary to first install one. Next, find the lengths between successive tunes and install the next probe orthogonal to the first at that distance. Theoretically, the two probes should be an integral or half integral number of guide wavelengths from the back wall and from each other. At 13.9 GHz the guide wavelength is:

2.12) $$\frac{1}{\lambda_g^2} = \frac{1}{\lambda^2} - \frac{1}{\lambda_c^2}$$

where λ_c = 3.25 cm (the cutoff wavelength for TE_{11}). The result is λ_g = 2.88 cm at 13.9 GHz

The actual distance between the 2 probes was chosen to be 2.83 cm. The distance between the calibration probe (closest to the horn) and the first signal probe was chosen to be two wavelengths to minimize interference.

The VSWR of each probe is affected by the other because of their proximity in the waveguide and the impurity of the TE_{11} mode. Thus, careful tuning by adjusting the length and diameter of each probe as well as the position of the tuning short at the end of the waveguide was required. Figure 2.16 shows the return loss of each of the three probes in their final configuration. Note that for a return loss of greater than 20 dB, less than 10% of the incident power is being reflected.

In order to insure that the probe/waveguide configuration does not lose its optimal tune through vibration, thermal cycles etc., it is encased in a Teflon shell which is anchored to both sides of the waveguide wall, and the tuning stub is permanently secured in its proper position. (See Figure in Appendix D.)

2.2.2 Ku-band Peak Detectors

Since the front end sensitivity is now established, the approximate extremes of the Schottky detector outputs can be determined.

Wave Type	TM_{01}	TM_{02}	TM_{11}	TE_{01}	TE_{11}
Field distributions in cross-sectional plane, at plane of maximum transverse fields	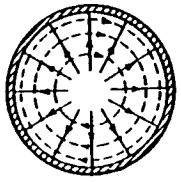	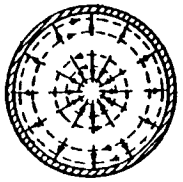	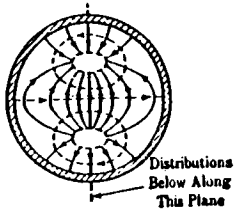	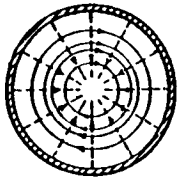	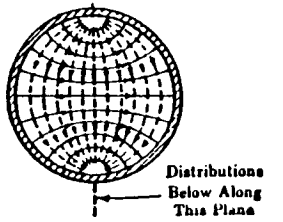
Field distributions along guide	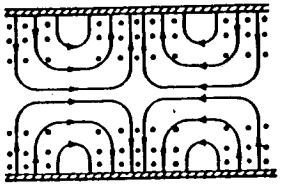	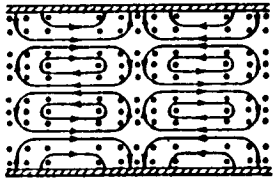	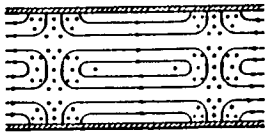	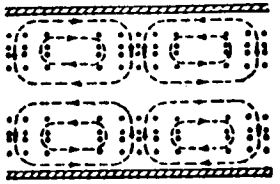	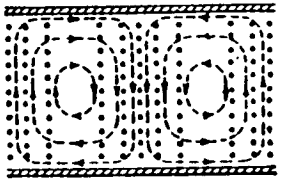
Field components present	E_z, E_r, H_ϕ	E_z, E_r, H_ϕ	$E_z, E_r, E_\phi, H_r, H_\phi$	H_z, H_r, E_ϕ	$H_z, H_r, H_\phi, E_r, E_\phi$
p_{nl} or p'_{nl}	2.405	5.52	3.83	3.83	1.84
$(k_c)_{nl}$	$\frac{2.405}{a}$	$\frac{5.52}{a}$	$\frac{3.83}{a}$	$\frac{3.83}{a}$	$\frac{1.84}{a}$
$(\lambda_c)_{nl}$	$2.61a$	$1.14a$	$1.64a$	$1.64a$	$3.41a$
$(f_c)_{nl}$	$\frac{0.383}{a\sqrt{\mu\epsilon}}$	$\frac{0.877}{a\sqrt{\mu\epsilon}}$	$\frac{0.609}{a\sqrt{\mu\epsilon}}$	$\frac{0.609}{a\sqrt{\mu\epsilon}}$	$\frac{0.293}{a\sqrt{\mu\epsilon}}$
Attenuation due to imperfect conductors	$\frac{R_s}{a\eta}\frac{1}{\sqrt{1-(f_c/f)^2}}$	$\frac{R_s}{a\eta}\frac{1}{\sqrt{1-(f_c/f)^2}}$	$\frac{R_s}{a\eta}\frac{1}{\sqrt{1-(f_c/f)^2}}$	$\frac{R_s}{a\eta}\frac{(f_c/f)^2}{\sqrt{1-(f_c/f)^2}}$	$\frac{R_s}{a\eta}\frac{1}{\sqrt{1-(f_c/f)^2}}\left[\left(\frac{f_c}{f}\right)^2+0.420\right]$

Figure 2.15 An Illustration of the Various Low Order Modes in a Cylindrical Waveguide

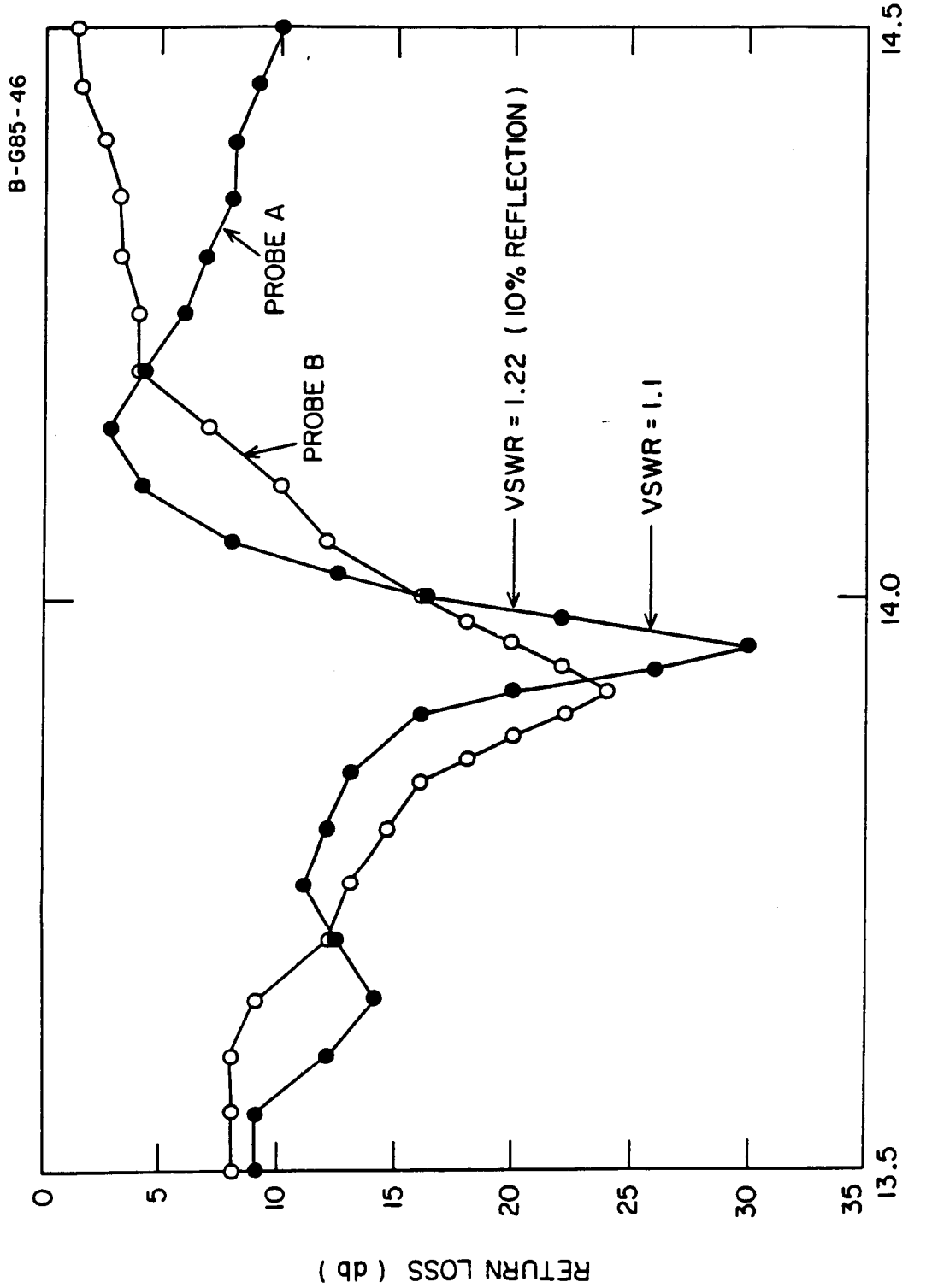

Figure 2.16 Return Loss Characteristics of the Ku-band Radar Probes over the Frequency Interval of Interest

An input electric field will result in power to the Schottky detector given by equation 2.1. For a 17 dB gain horn (assuming no loss) the 1 V/m field produces -24 dBm at the input to the Shottky detector and at the other measurement extreme of 60 V/m produces an input of +12 dBm. (We have already determined that a gain of < 18.5 dB could not cause burn out.)

From the detector curve in Figure 2.10, we see that the resulting output voltage varies from approximately 2 mV to 1 volt, a 54 dB variation. Since we only have an 8 bit data system, (maximum range for 1 dB accuracy is 42 dB) it is necessary, in order to preserve the desired accuracy of ±1dB and the dynamic range, to use a dual range detector system.

The peak detector system consists of two identicial peak detectors (differing only in their input polarity) in parallel with the output of the Schottky detectors. One of the peak detectors has an amplifier with a gain of approximately 40 dB in front of it. The minimum cutting level of the A/D converter in the PDP encoder is 20 mv. If one considers the LSB to be unreliable, the 1 mv output of the Schottky detector must be amplified to approximately 40 mv. The result is a system which provides an area of overlap but has the necessary dynamic range and accuracy. (See Section 3.2.3 for details.)

A brief summary of the peak detector design should include these design constraints:

1. The detector must respond to the ~ 100 nsec pw of the radar. That is, the system should reach a suitable fraction of the peak level before the end of the pulse. This requires a wide bandwidth system at low input levels and a fast slew rate for higher inputs. It is the prime reason the HA2520 and LF156 are used in the design (see drawing #85-3827 Appendix D.)

2. The system must hold the pulse for the relatively long period of time between pulses, but bleed the charge off at a rate fast compared to the 10 Hz instrument sample rate (the bleed rate is an alternative to having a "resetable" peak detector). These are the prime reasons for the LF156 in the feedback loop, the special glass capacitor, and the .25 x $10^9\Omega$ resistor in the detector.

3. It should respond only to pulses not cw and be immune to effects of input bias currents. This leads to the capacitive coupling of the input.

The amplifier needed plenty of gain (> 36 dB) and a bandwidth wide enough to reach the peak level of a 100 nsec pulse quickly (but not so high a bandwidth as to promote noise and stability problems.) The cascode amplifier was chosen and trimmed to provide ~ 40 dB gain

up to about 10 MHz. This is quite a low frequency compared to the > 100 MHz capability of the 2N918 but stability (especially over temperature) was of prime concern. In this case the limits in the response are due to the slew rate of the HA 2520 anyway so the amplifier was tuned to be slightly overdamped in its response to a step input with a rise time of approximately 50 nsec.

Careful layout and attention to grounding yielded a single board system which showed excellent stability over temperature and an acceptable response at the 100 nsec pw (See Section 3.2.1.)

Appendix D contains all circuit diagrams and a photo of the completed board.

2.2.3 Ku-band Self Calibration

Since it is important to know both after the delivery of the PDP to NASA and on-orbit that the KUSR is performing nominally, a self-calibration scheme was conceived. Figure 2.17 is a block diagram of that system. The purpose of the system is to inject a 4μsec 7 kHz prf pulse (identical to one of the normal radar modes) at a 45° angle to both sensor probes into the waveguide of the antenna.

As discussed in 2.1.1, the control logic generates a calibration command once each 386 major frames. This command simultaneously turns on transistor Q_7 on the power supply board supplying voltage to the 13.9 GHz source oscillator, and starts a voltage step generator on the timing and control board which provides the control of the linear attentuator. The linear attenuator provides four power levels of the output signal, two are within the dynamic range of the low gain and two within the dynamic range of the high gain detectors. In order to assure that the system is operating properly, the power level of the oscillator as well as the voltage level of the linear attenuator are monitored. These are referred to as "Cal" and "Cal Voltage" in Table 2.1a. The detector in Figure 2.17 which monitors the RF power output is identical to the two Schottky detectors which serve as the detectors for the two orthogonal polarizations of the antenna. All three detectors are mounted in the same vespel block and have their temperature monitored. Most engineering effort was spent in impedance matching the cal probe in the waveguide and choosing appropriate components to get the right power level to the detectors. Although original plans called for use of a power splitter isolator, and couplers, to put the "fake radar pulses" directly into the KU1 and KU2 detectors it was impossible to accommodate the RF components and necessary semirigid coax into the KUSR housing without adding another section thus, the use of the waveguide itself as a coupler.

Figure 2.18 shows the assembled RF section and all of the calibration components. Table 2.7 lists the output levels of the cal signal as seen by the KU1 and KU2 detectors.

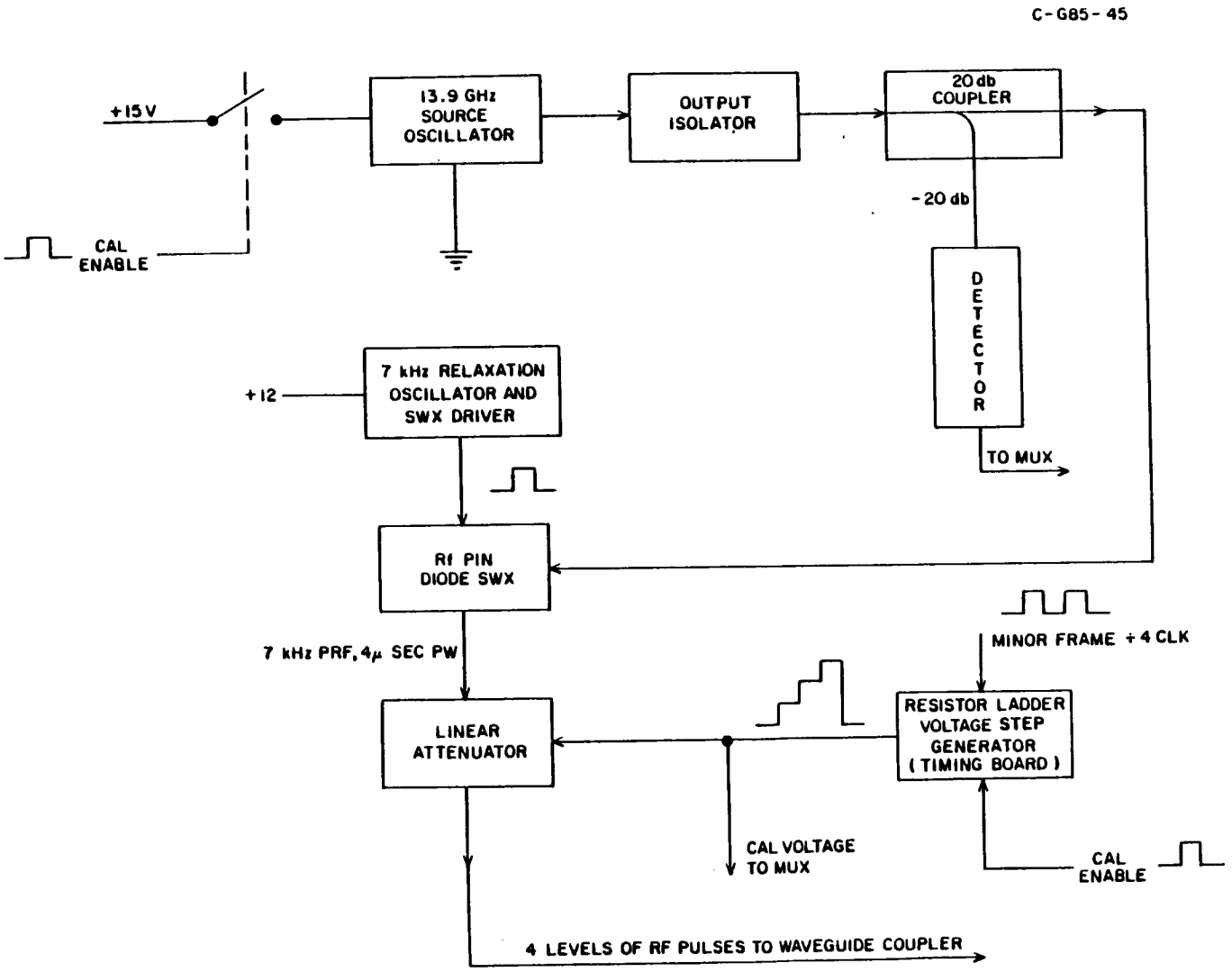

SELF-CALIBRATION BLOCK DIAGRAM

ure 2.17

ORIGINAL PAGE
BLACK AND WHITE PHOTOGRAPH

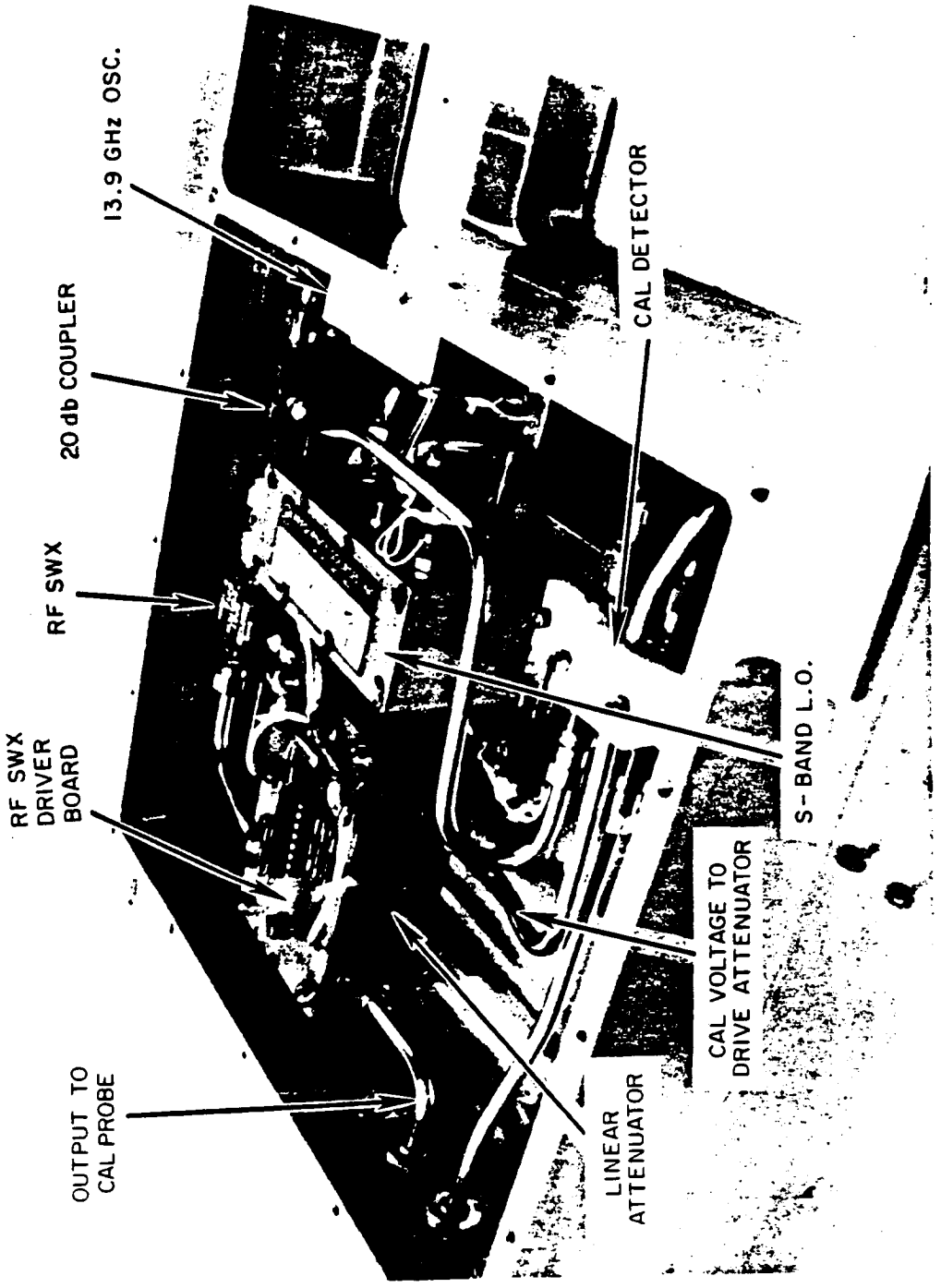

Figure 2.18 Assembled Rf Section

This page intentionally blank

TABLE 2.7
OUTPUT OF CALIBRATION CIRCUIT

Output Power of Source	Equivalent Field Seen by Detector (Hi Gain) dB V/m	Equivalent Field Seen by Detector (Low Gain) dB V/m
+ 8 dBm	-------	+13
- 3 dBm	-------	+4
-12 dBm	-4	-------
-20 dBm	-10	-------

2.3 Modification of the S-band Receiver System

The S-band system as previously flown is shown in block diagram form in Appendix C. There were several problems with the system (see Appendix A) aside from the fact that a relay failed to operate properly disabling the log detector part of the system.

1. The system used an HF antenna (meant only to respond up to 800 MHz) which was multilobed and had a pattern so complicated that only slow rotations which reproduced the ground measured pattern on-orbit produced useful data. The linear detector part of the system was not sensitive enough owing in part to losses in the system and low antenna gain.

2. The RF relays proved prone to failure and have a short life.

3. The log detector was shared with the HF system giving S-band data only a fraction of the time.

4. Calibration was inadequate due to short delivery time and underfunding.

Each of these shortcomings was addressed in the proposal to modify and refly. (Appendix C)

A new antenna selected for its relatively low cost and uniform E and H plane response replaced the old HF antenna. (See Section 3.1.1 for antenna patterns.) The HF system was dropped (i.e. there is always a 2.2 GHz L.O. and mixer ahead of the video part of the system). The relays were replaced with passive devices and, lastly, a thorough calibration scheme was designed and executed (See Section 3.1.)

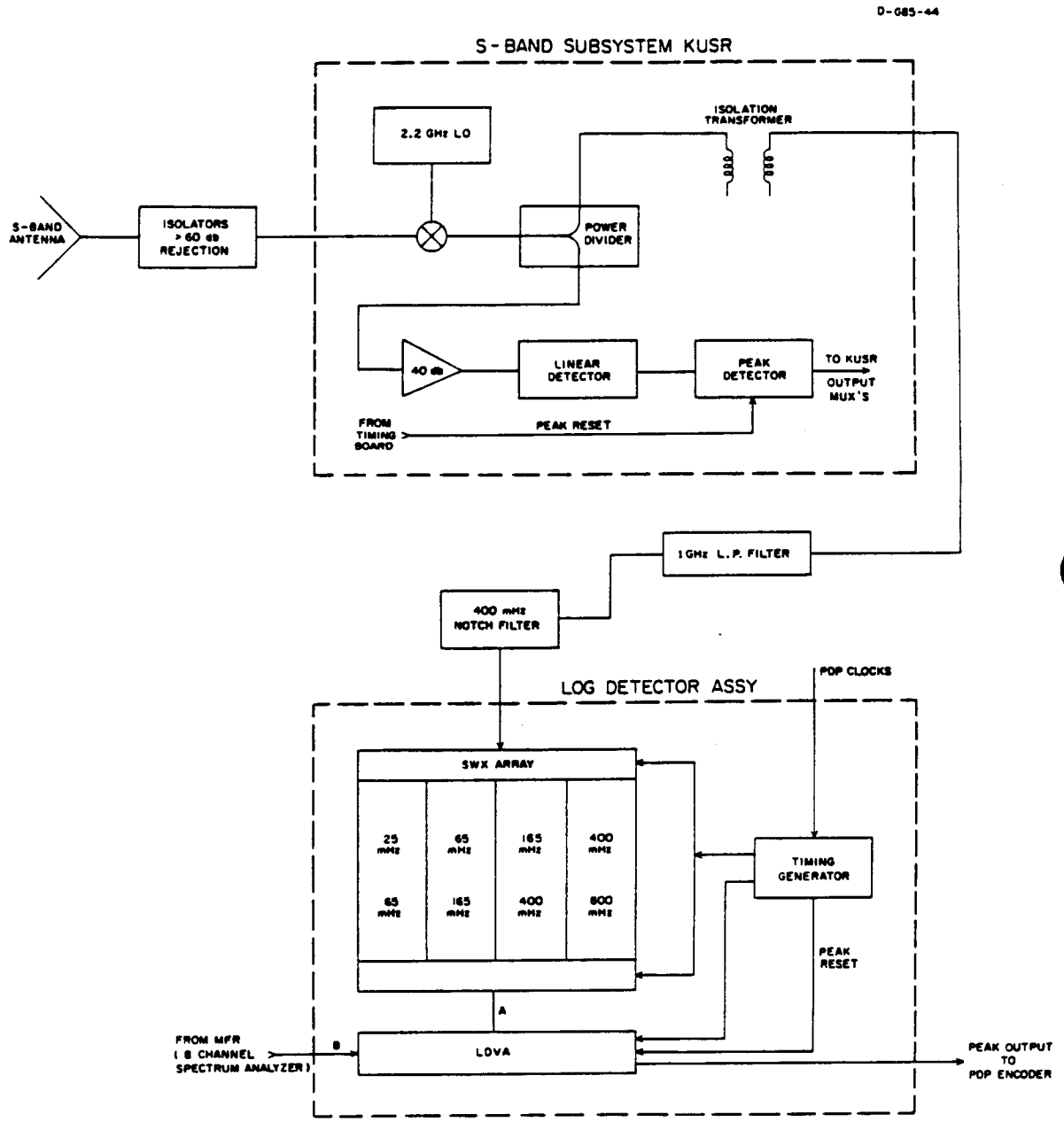

Figure 2.19 KUSR S-Band Subsystem Block Diagram

Although the modifications are simple in principle, a number of hurdles had to be overcome to integrate the S-band linear detector into the KUSR. On Figure 2.19 the parts within the dotted line are contained within the KUSR housing. The two biggest problems were 1) a new circuit board had to be laid out and adequate grounding and component placement chosen to provide unconditional stability over temperature, and 2) the package had to be small enough to fit into the alloted space in the KUSR. Appendix D contains the circuit diagram of the linear detector system carried over from the previous design and also pictures of the assembled product.

2.4 Procurement and Test Program

As with all space hardware, rigorous demands are placed on an instrument and its components due to the stress of launch and thermal extremes of the space environment. From experience with a previous flight, it is however ironically true that the required qualification test program in this case is far worse than the actual environment encountered during the mission!

To ensure that the instrument quality control meets the required standards procurement of parts met standars given in Table 2.8. A log of all parts as well as their status was kept by the Q.A. Engineer and assembly at all stages was monitored by Q.A. as well. Several anomalies and part failures which occurred after assembly were also logged as well as reasons for the failures and the corrective action taken. A sample of the Q.A. assembly control card is included as Figure 2.20.

TABLE 2.
KUSR PARTS PROCUREMENT SPECIFICATION

Part	Applicable Spec
Connectors	Cannon: GSFC-311-P409-3P-B-15 Continental: Manufacturers Spec, UI Inspect Continental Coaxial: MIL-C-39012B
Inductors	Hand Wound (U of I Inspection)
Capacitors	Ceramic: MIL-C-39014/5 Glass: MIL-C-23269/1 Tantulum: GR500/A (Kemet Hi-rel)
Transformer	Hand Wound (U of I Inspect)
Transistors/Diodes	MIL-5-19500/XXX
Integrated Circuits	Manufacturers Spec, Screened to MIL-883B-5004-6 Class B
Oscillators	S-BAND: U of I Spec #100-0101 Ku-band: U of I Spec #100-0108
Couplers	MIL-C-15370
Detectors	Manufacturers Spec (OMNI) Tested to MIL-3-5400, MIL-E-16400
Isolators	U of I Spec (Hi-rel Connectors, Lefkoweld 46/LM52 Adhesive, Silver Solder Sealed, Tested to MIL-std-202 Method 107 Condition A)
Pin Diode Swx	Manufacturers Spec (Narda)
Feed-through Filters	GSFC 5-311-P-5(03) Rev 1 (Erie)
Linear Attenuator	Manufacturers Spec. (MIL-E-5400, MIL-3-16400 Environmental)
Internal Wiring	Ray-Chem-Spec 55 (55A0811-24-9)
Printed Circuit Boards	Material: Type GF MIL-P-13949/4 Manufacturing: UI Spec #85 A 6001 Rev 1 (calls out MIL-P-55110B) Soldering: NHB 5300.4 (3A-1)

All other materials (conformal coating, epoxy, etc.) are selected according to NASA Spacelab materials selection criteria MSFC-HDBK-527 Rev B.

The test program of the instrument is detailed in Table 2.9. This included 3 axis vibration, thermal shock, thermal cycling, and thermal vacuum testing.

TABLE 2.9
KUSR TEST PROGRAM

Vibration

1. Sinusoidal Resonance

5-2000hz	.5g	1 octave/min.	x,y,z axes

2. Random

Z axis	20 hz	$4 \times 10^{-4} g^2/Hz$
	20-92	+12db/oct
	92-250	$.18 g^2/Hz$
	250-2000	-6db/oct
	2000	$2.8 \times 10^{-3} g^2/Hz$
	Composite = 8.4g rms	
X, Y axis	20 hz	$1.7 \times 10^{-4} g^2/Hz$
	20-128 hz	+9db/oct
	128-400 hz	$4.4 \times 10^{-2} g^2/Hz$
	400-2000 hz	-8db/oct
	2000 hz	$6 \times 10^{-3} g^2/Hz$
	Composite = 4.8g rms	

Duration = 60 seconds each axis

Thermal Shock

+50°C → -40°C 100°/hr. with 1 hour soak at each end (2 cycles)

Thermal Vac

Profile: Hot soaks at 50°C, 40°C, 30°C (8 hrs)
Cold soaks at -10°, 0°, 0°C (8 hrs)
Transitions: ~10°/hour 'typ'

CONTROL CARD

ELECTRONIC ASSEMBLY
THE UNIVERSITY OF IOWA
DEPARTMENT OF PHYSICS AND ASTRONOMY

PROJECT PDP SL-II KUSR

ASSEMBLY DRAWING NO. 85-4831 REV. ____

NAME OF ASSEMBLY Power supply mother board

FOR ____ SERIAL NO. SB3100

OPERATION	PERF. BY	DATE	PASS	REJ.	NOTE
Attach Power Transistor Subassemblies	SK	6-21-83	—	—	
UI/ONR Inspection	SK	7/19/83			3
CONFORMAL COAT POWER TRANSISTOR SOLDER COVER. COLOR CODE 4			—	—	2
UI Inspection	SK	7-19-83	—	—	
Final Electrical	MB	7-20			

OPERATION	PERF. BY	DATE	PASS	REJ.	NOTE
prepare control card	GM	6/9	—	—	
approve card					
select M/B cut and drill	SK	6/9	—	—	
pull parts	[illegible]	6/8	—	—	
log in assy shop	SK	6/9/83	-	-	
attach components, ~~feedthrus, connectors~~	SK	6/9/83	-	-	
clean board and pot wires	DC/GM	6/9/83	-	-	1
UI inspection — coat top of board	C.W. / MC	6-9-83 / 6/10/83	—	—	2
attach {inductors, transformers, modules}	R.W.	6-14-83	-	-	
electrical check	MMB	6-15-83	OK		
UI inspection	ECK	6-16-83			3
coat bottom of board	KP	6-21	—	—	2
UI/ONR inspection	ECK / DQ	7-19-83 / 7-25-83			3

NOTE NO.	REMARKS; (Rework, MRB, etc.)
1	Use Scotchweld 2216 B/A for wire potting & bonding.
2	Use Solithane 113/113-300, Formula 1, per manufacturer's instructions.
—	
3	Need MIT No's for parts on Material Withdrawal Record (IN5804's, ~~etc.~~ capacitors, etc). ECK

ASSEMBLY STATUS: ☐ OK TO USE ☐ SCRAP

PROJECT MGMT./ENG. REPRESENTATIVE ____ DATE ____

R & QA REPRESENTATIVE ____ DATE ____

Figure 2.20 Sample Quality Control Traveler for KUSR Fabrication

2.5 Instrument Ground Support Equipment (IGSE)

The purpose of the IGSE is not only to provide a simulated PDP interface, but to support the instrument throughout the development and test cycle. Although the IGSE is a very important piece of equipment, little time is usually devoted to its development since the instrument itself always gets the priority engineering support. Unfortunately, the KUSR IGSE was no exception. Designed and fabricated in a piece-meal fashion, it served its minimally required role without any degree of sophistication.

A block diagram of the IGSE is included as Figure 2.21. The IGSE consists of a front panel control for the "timing bypass", "gain select", and "cal enable" functions as well as a choice of internal or external clocks (external was used to speed up or slow down the timing cycle). Inside the IGSE are 2 boards, one producing the 3 timing signals associated with the PDP clocks, and the other a demultiplexer and display driver board which drove the front panel DVM. Since the output was muxed, two thumb wheel switches on the front panel controlled which output was selected for the DVM. The IGSE also contained a 28v power supply which could power the KUSR when it was not mounted in the PDP. Two cables could connect the IGSE to the instrument (See Figure 2.21) J1, which was identical to the interface provided in the PDP, provided power and monitored instrument status. J2, which could be used in conjunction with J1 either on or off of the PDP, monitored additional functions (voltage and clocks) not included in the 2 analog outputs alloted the KUSR on the J1 interface.

The IGSE also provided an output to an A/D board and portable computer which were used for gathering data during thermal calibrations. (See Section 3.3.)

Circuit diagrams as well as pictures of the IGSE can be found in Appendix D.

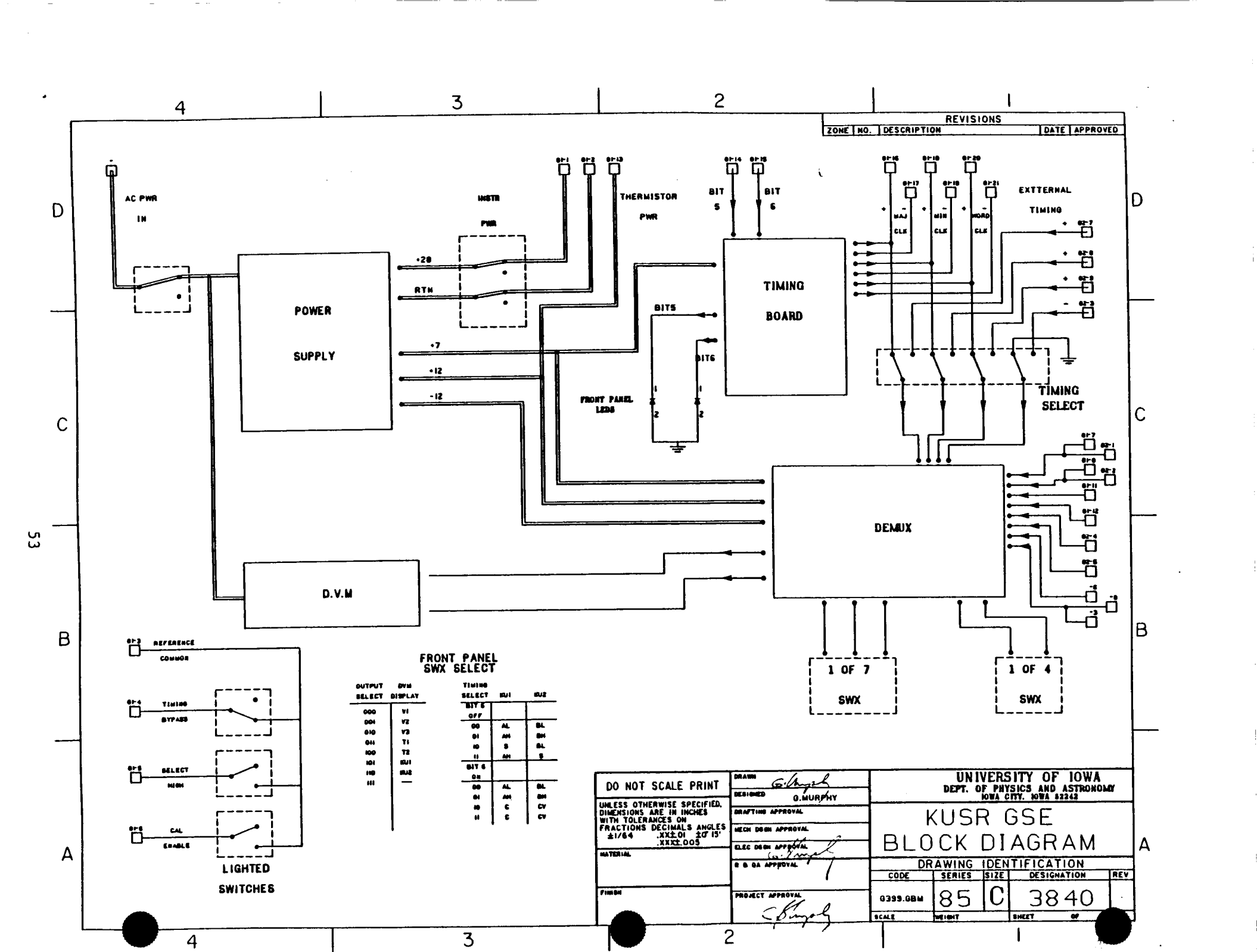
REVISIONS
ZONE | NO. | DESCRIPTION | DATE | APPROVED
AC PWR IN
POWER SUPPLY
INSTR PWR
+28
RTN
+7
+12
-12
THERMISTOR PWR
BIT 5
BIT 6
BIT5
BIT6
FRONT PANEL LEDS
TIMING BOARD
EXTTERNAL TIMING
MAJ CLK
MIN CLK
WORD CLK
TIMING SELECT
DEMUX
D.V.M
1 OF 7 SWX
1 OF 4 SWX
REFERENCE COMMON
TIMING BYPASS
SELECT HIGH
CAL ENABLE
LIGHTED SWITCHES
FRONT PANEL SWX SELECT
OUTPUT SELECT
DVM DISPLAY
TIMING SELECT
SU1
SU2
DO NOT SCALE PRINT
UNLESS OTHERWISE SPECIFIED, DIMENSIONS ARE IN INCHES WITH TOLERANCES ON FRACTIONS DECIMALS ANGLES
DRAWN
DESIGNED G.MURPHY
DRAFTING APPROVAL
MECH DSGN APPROVAL
ELEC DSGN APPROVAL
R & QA APPROVAL
PROJECT APPROVAL
MATERIAL
FINISH
UNIVERSITY OF IOWA
DEPT. OF PHYSICS AND ASTRONOMY
IOWA CITY, IOWA 52242
KUSR GSE
BLOCK DIAGRAM
DRAWING IDENTIFICATION
CODE | SERIES | SIZE | DESIGNATION | REV
0399.0BM | 85 | C | 3840
SCALE | WEIGHT | SHEET OF

3.0 INSTRUMENT CALIBRATION

Although it is fairly straightforward to measure quantities like voltage, current or frequency to accuracies far better than 1%, the precise measurement of an electric field presents a unique problem. Our only way of measuring the intensity of a high frequency electric field is by the relatively indirect method of measuring the current and voltage induced on a wire (antenna) and the power dissipated in a matched load. In the real world there are innumerable obstacles to prevent one from doing this accurately!

1. A "standard antenna" must be used--one whose gain is known accurately because it was measured against another accepted standard.

2. The load must be well matched (in this case a VSWR less than 1.2 would produce an error of $< 10\%$ or ~ 1 dB).

3. The load must itself be calibrated accurately (voltage out = K x power in).

4. The measurement must take place in an environment free of reflections or objects that can produce diffraction effects.

Assuming the above hurdles can be overtaken, the engineer must be aware of numerous practical problems associated with actually doing the measurement[7].

1. Mismatch in detectors, cables, antennas, etc., can induce errors of several dB unless VSWR is measured and the devices matched or, alternatively, pads are used to minimize the effects of mismatch.

2. Measurement in the near field of an antenna can lead to errors of several dB.

3. The use of a variety of cables with different lengths (and thus different losses) and possible high VSWR connectors can cause errors of several db.

4. The allowance of too little time to perform the test adequately and verify all data is a potential problem when precision is required.

5. Failure to monitor all test equipment and RF sources continually to verify proper operation results in errors because of drift in oscillations, etc.

6. Failure to allow adequate "warmup" time so that all equipment stabilizes--this is particularly important with bolometers, produces errors particularly in amplitude measurements.

B-G85-43

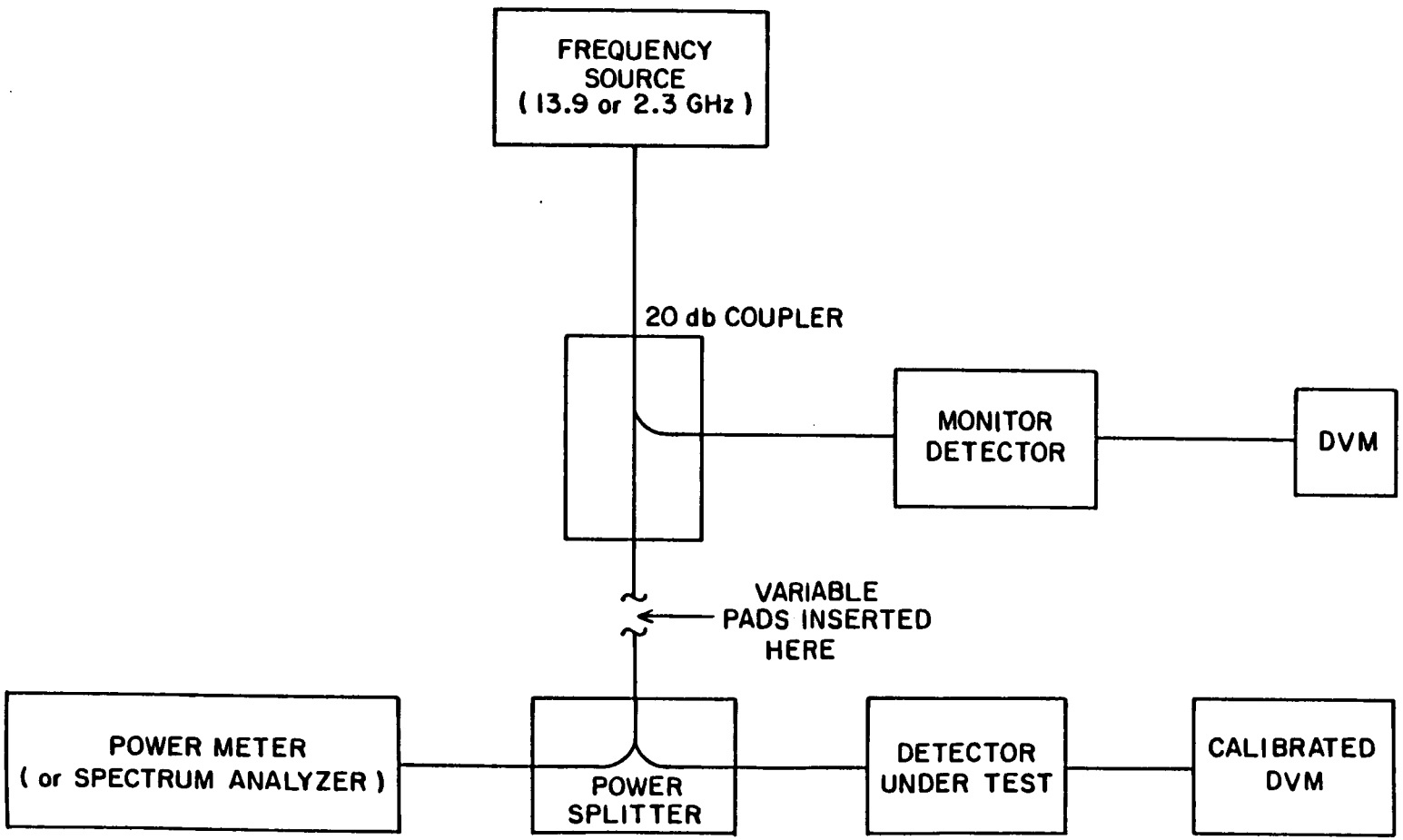

Figure 3.1 Calibration of Standard Detectors

Virtually all of the above problems can be dealt with if all involved in a test are cognizant of them. The test program for calibration of the KUSR was designed such that all absolute calibration ultimately depended only on the accuracy of three things:

1. The repeatability of a measurement setup.

2. The absolute calibration of a power meter.

3. The absolute accuracy of a standard gain horn.

The following sections describe the tests performed, their setup, methods and results, in calibration of both the Ku-band and S-band sections of the instrument.

A word about the measurement standards is in order. For most tests, which required measuring received power an Aertech Model D18Z detector was used. This detector (there were two which were matched) was calibrated against two separate instruments--first a HP model power meter and probe (which itself was calibrated the previous week by the Rockwell Collins Metrology Laboratory) and secondly against a Tex model 7L13 spectrum analyzer (independently calibrated). The setup is illustrated in Figure 3.1. It is satisfying to note that the results agree ±.5 dB which is approximately the margin of error in reading the amplitude on the spectrum analyzer.

After the calibration of these detectors, it was they, rather than the power meter itself, which were used in all testing. They are much more convenient to use and less prone to error because there is no scale to misread and no zero adjustment which requires careful attention.

3.1 S-band Calibration

Since not until the KUSR is installed in the PDP are both linear and log detectors active, all calibration data were acquired (except temperature tests on the linear detector) after integration with the PDP system. The PDP was mounted on a two-axis elevation over azimuth antenna positioner in the anechoic chamber and the following calibrations were performed.

1. Antenna pattern test (2-axis, multiple frequencies)

2. Three dB calibration of both linear and log detectors against the standard gain horn.

3. Frequency sensitivity at fixed amplitude.

After the PDP was removed from the chamber, measurements on the uniformity of the electric field as well as the reference points used in the 3 dB calibration were measured using the standard horn. The following three sections summarize the procedure and results of each test.

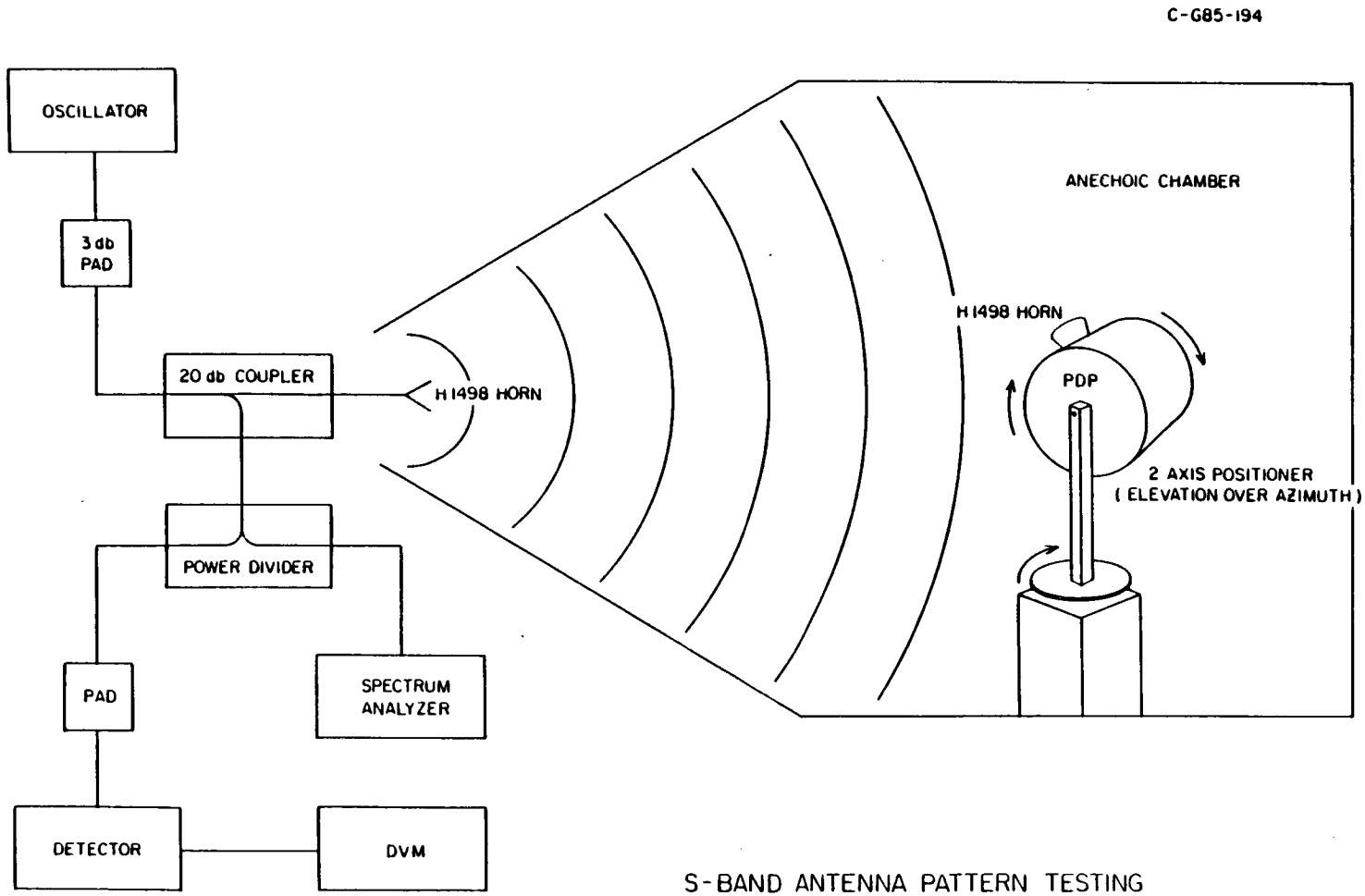
C-G85-194
OSCILLATOR
3 db PAD
20 db COUPLER
H 1498 HORN
POWER DIVIDER
PAD
SPECTRUM ANALYZER
DETECTOR
DVM
ANECHOIC CHAMBER
H 1498 HORN
PDP
2 AXIS POSITIONER
(ELEVATION OVER AZIMUTH)
S-BAND ANTENNA PATTERN TESTING

Figure 3.2

3.1.1 Antenna Power Patterns

Since a major headache in data reduction on the previous mission was the complex antenna pattern of the HF antenna, considerable effort went into the adequate definition of the pattern of the AEL model H1498 antenna used for the instrument. Figure 3.2 illustrates the setup in the anechoic chamber during these tests. Although 2287.5 MHz is the prime frequency of interest, the desire to calibrate at several frequencies was expressed by the contractor. The patterns in E and H planes were done at 1900, 2100, 2300, and 2500 MHz. Figures 3.3a and 3.3b are the results for 2100 and 2300 respectively. One of the prime reasons this antenna was chosen for the instrument was its broad bandwidth and relatively uniform E and H plane response. The AEL antenna is called a ridged guide antenna and is patterned from work done by Walton and Sandberg 1964[13] and Kerr 1973.[14] Its broadband characteristics are evident in the uniformity of these patterns.

In Section 4 when the on-orbit operations are discussed, it will become clear why a uniform, wide, and predictable response in both planes is important.

3.1.2 3 dB Calibration

Most other calibration tests are concerned only with relative power or relative field strength over the duration of the test. In contrast, while doing this absolute measurement, one must worry about all of the problems discussed in the introduction to this section. Figure 3.4 illustrates the configuration used for both this and the frequency response test. All cables were labeled, the VSWR of connectors checked, the power levels of the TWT amplifier monitored, pads were used at points where mismatch was a problem and the frequency of the source carefully monitored. The purpose here is to illuminate the PDP with a uniform electric field at 3 dB intensity intervals and at several frequencies both of which can be reproduced precisely when the PDP is removed and replaced with the S-band standard gain horn. For example, since TWT output power can be somewhat variable, the power actually sent to the transmitting horn is monitored and as variable pads are placed in the system. This power is adjusted to be repeatable over the duration of the testing. By comparing the output of the KUSR linear and log detectors as a function of field intensity and frequency to that of the standard gain horn with calibrated detectors, we can reduce the unknowns in the system to only three things:

1. The repeatability of the setup and test between the measurements taken with the PDP in the chamber and with the standard gain horn.

2. The gain of the standard horn.

3. The calibration of the detector used.

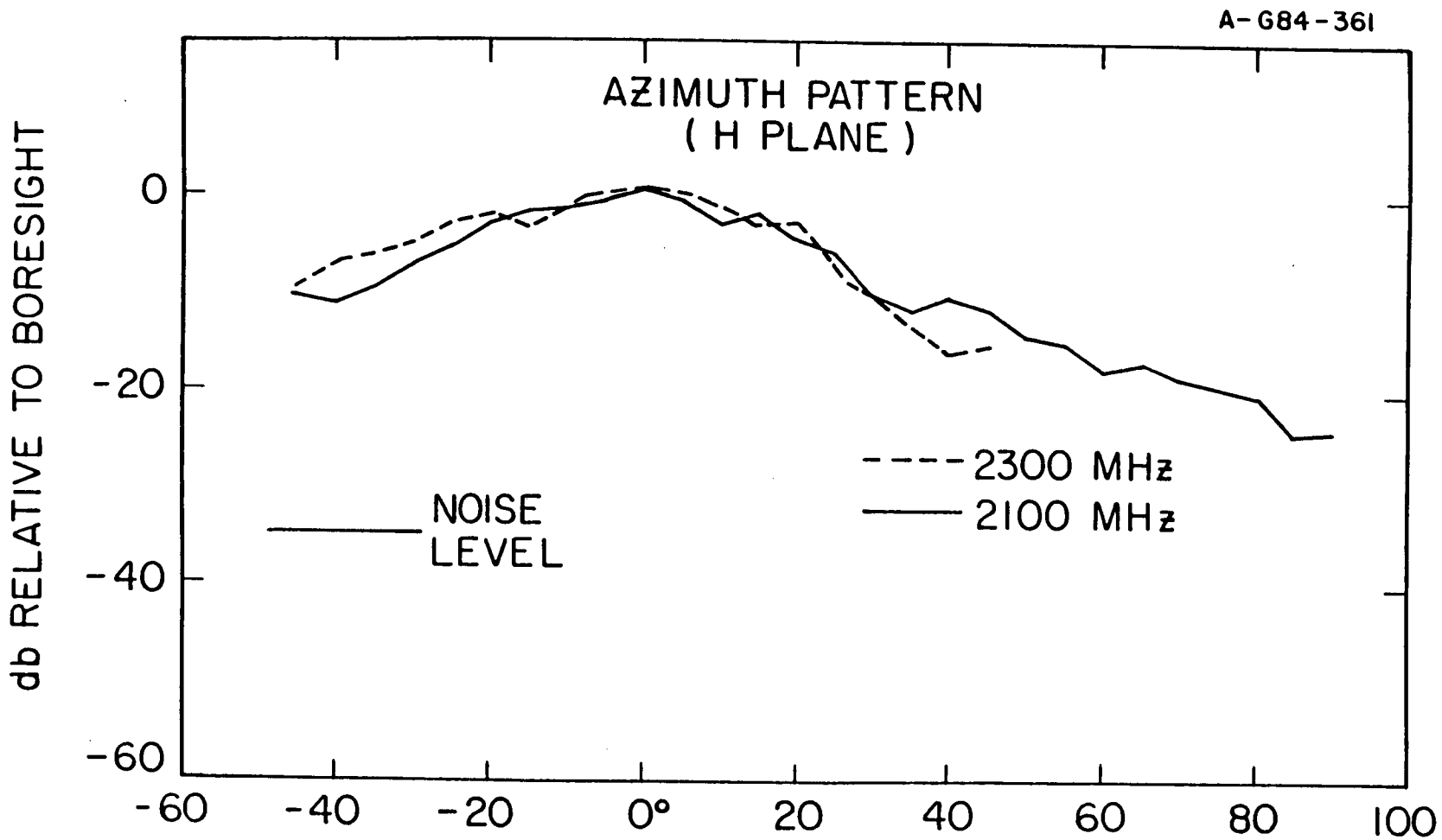

Figure 3.3a H-Plane Pattern of H1498 Antenna

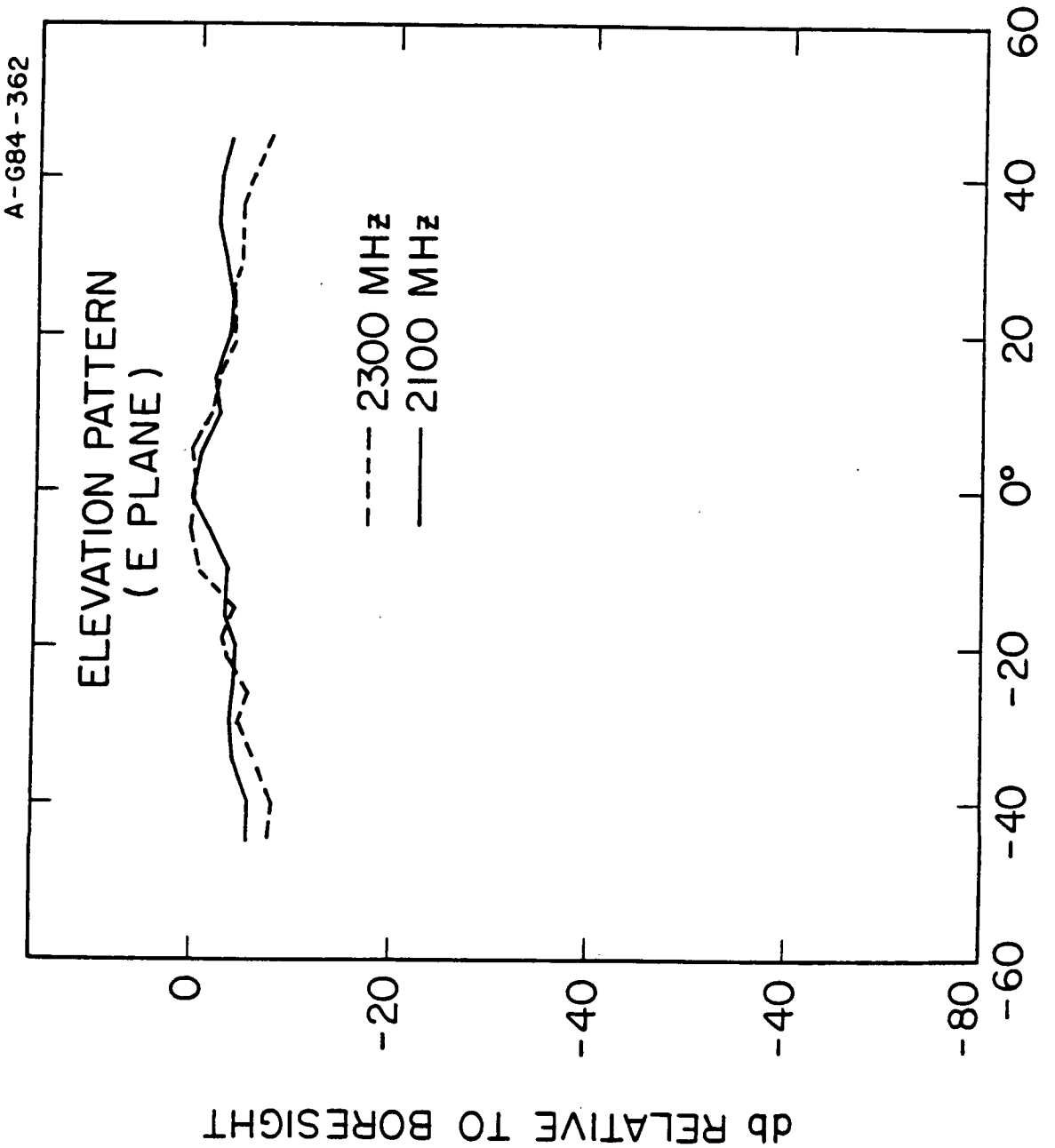

Figure 3.3b E-Plane Pattern of H1498 Antenna

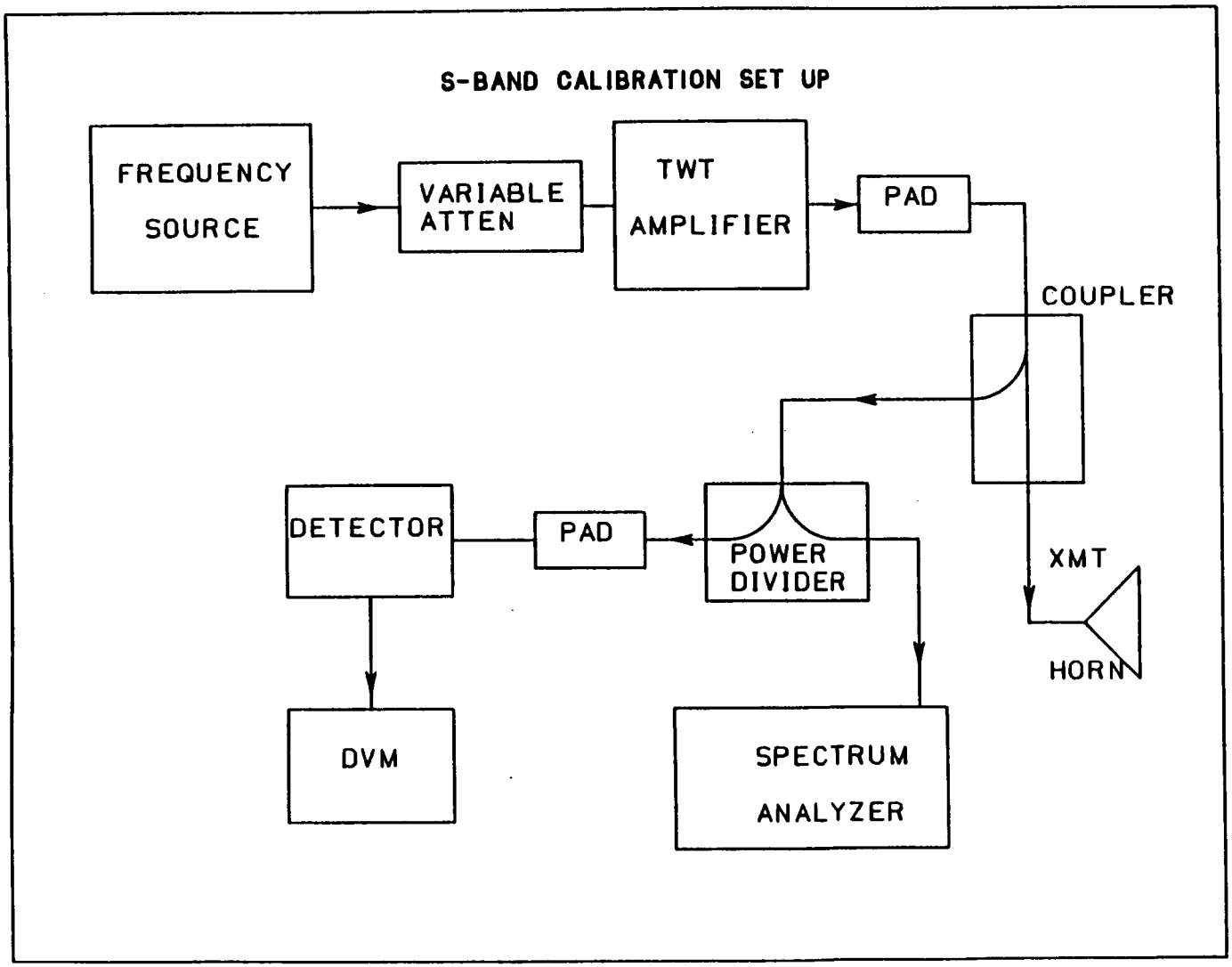
S-BAND CALIBRATION SET UP
FREQUENCY SOURCE
VARIABLE ATTEN
TWT AMPLIFIER
PAD
COUPLER
XMT
HORN
POWER DIVIDER
PAD
DETECTOR
DVM
SPECTRUM ANALYZER

Figure 3.4

The setup repeatability was tested by disassembling the apparatus and then reassembling it several times. By adjusting the output power to reproduce the same reading on the DVM (See Figure 3.4), the same electric field was reproduced in the chamber ±.5 dB. Both the gain of the standard horn and the uncertainty in calibration of the detector have already been discussed and are approximately ±1 dB each. As can be seen from the final calibration curve of the linear and log system (Figure 3.5), the slope of the log detector curve is ~ 16 dB/volt. Considering the PDP is an 8-bit system (the LSB must often be ignored) the resolution of the log detector would be approximately .6 dB. The linear detector has a constant voltage error of the transfer function x .02 volts which amounts to a constant error of about ±.25v/m. This is ±3db worst case but becomes better than the absolute calibration accuracy as the electric field increases. If we take .6 dB to be typical sensitivity (except at the extreme ends of the measurement range) then the total RMS error of the S-band system is $(.5^2 + 1^2 + 1^2 + .6^2)^{1/2} = \pm 1.6$ dB.

As can now be seen, it is very difficult to get the ±1 dB desired accuracy without improving the accuracy of calibration of the detector and horn.

There are several methods of measurement of the standard gain horn: the two antenna technique, the three antenna technique, mirror method etc.[10] and I have taken the 1 dB as a worst case error since I have no knowledge of the particular method used.

3.1.3 Frequency Response

Using the configuration depicted in Figure 3.4 the frequency sensitivity of both the log and linear detector was determined. Table 3.1 lists the frequencies at which calibrations were made, and the sensitivity of the linear and log detectors relative to that at 2287 MHz. In all cases, frequency sensitivity of the standard gain horn and variability in output power of the transmittining antenna were taken into account. Thus Table 3.1 is the sensitivity of the detectors at the noted frequencies assuming a constant E-field magnitude.

There are four filters in the log detector assembly (Figure 2.19) 25-65 MHz, 65-165 MHz, 165-400, and 400-800 MHz. Figure 3.6 is a graph of the response of all channels in the log detector at each of the frequencies in Table 3.1. The filter response can easily be seen.

3.2 Ku-band Calibrations

The Ku-band system calibration procedures were similar to those of the S-band system with the exception that two more variables were included in the problem--an additional antenna polarization, and the pulse width of the calibration signal. Variation of the system response

TABLE 3.1

S-BAND SYSTEM FREQUENCY SENSITIVITY
(Relative to 2287.5 MHz)*

Calibration Frequency	Linear+ Sensitivity	25-65 MHz	65-165 MHz	165-400 MHz	400-800 MHz
1720	-2.5	---	---	---	-4
1800	-3.5	---	---	---	-34
1900	-3.25	---	---	+.8	-16
2000	-2.0	---	---	+.5	-22
2100	-2.25	---	+1.6	---	---
2300	0	---	+0	---	---
2400	+.75	---	---	+1.6	-18
2500	-2.25	---	---	+1.2	---
2700	-7.5	---	---	---	-3
2205**	+1.8	---	---	---	---
2250	-2.4	+.5	---	---	---
2217	-.5	---	---	---	---

*Recall L. O. Frequency is 2200 MHz

+Note linear detectors most sensitive at ~ 2287.5 MHz with typical variation ±3 dB (BW is 300 MHz).

**2205, 2217 and 2250 are other lower power transponder frequencies also present in the orbiter system.

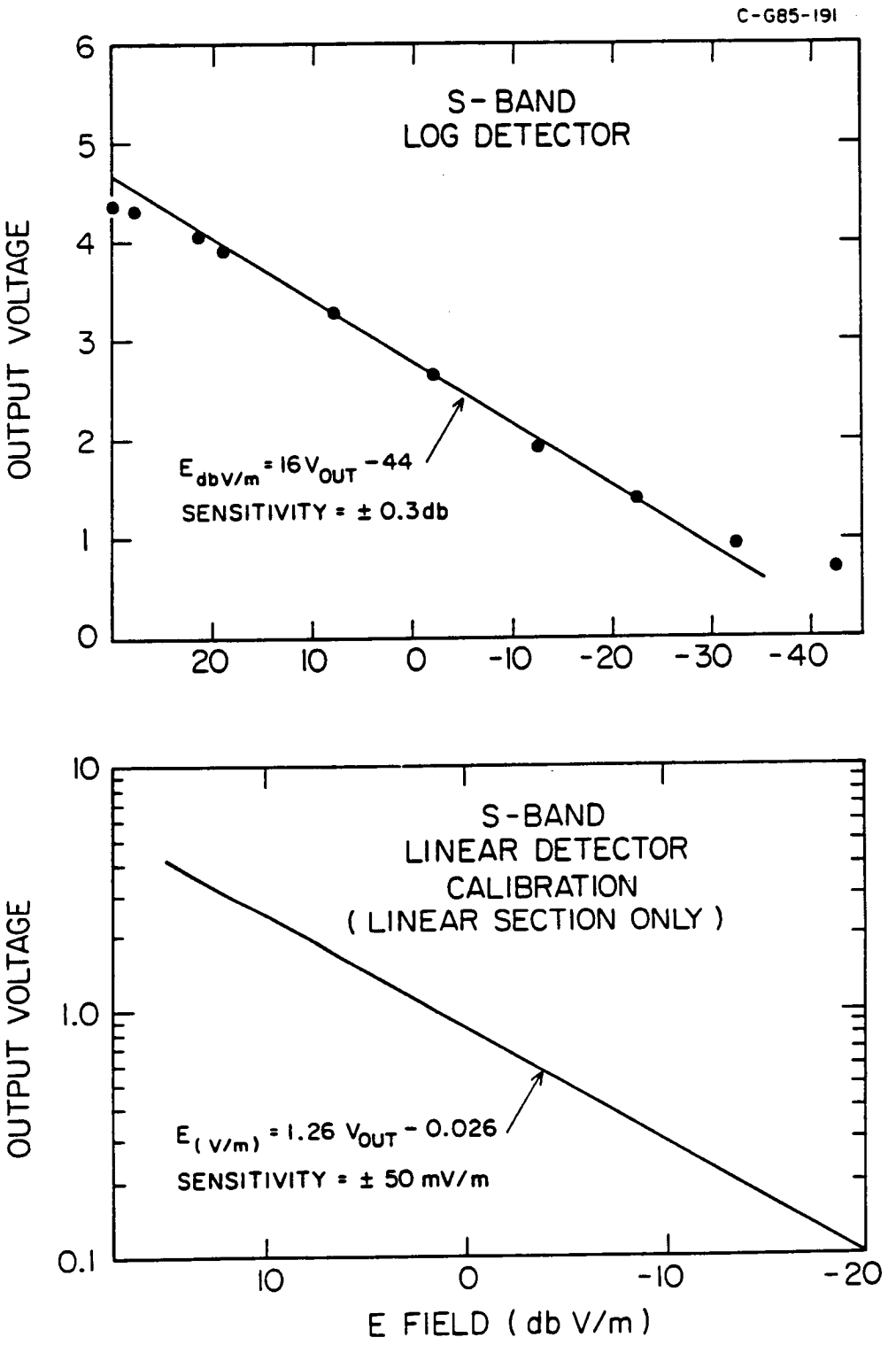

Figure 3.5 S-Band Detector Calibration Curves

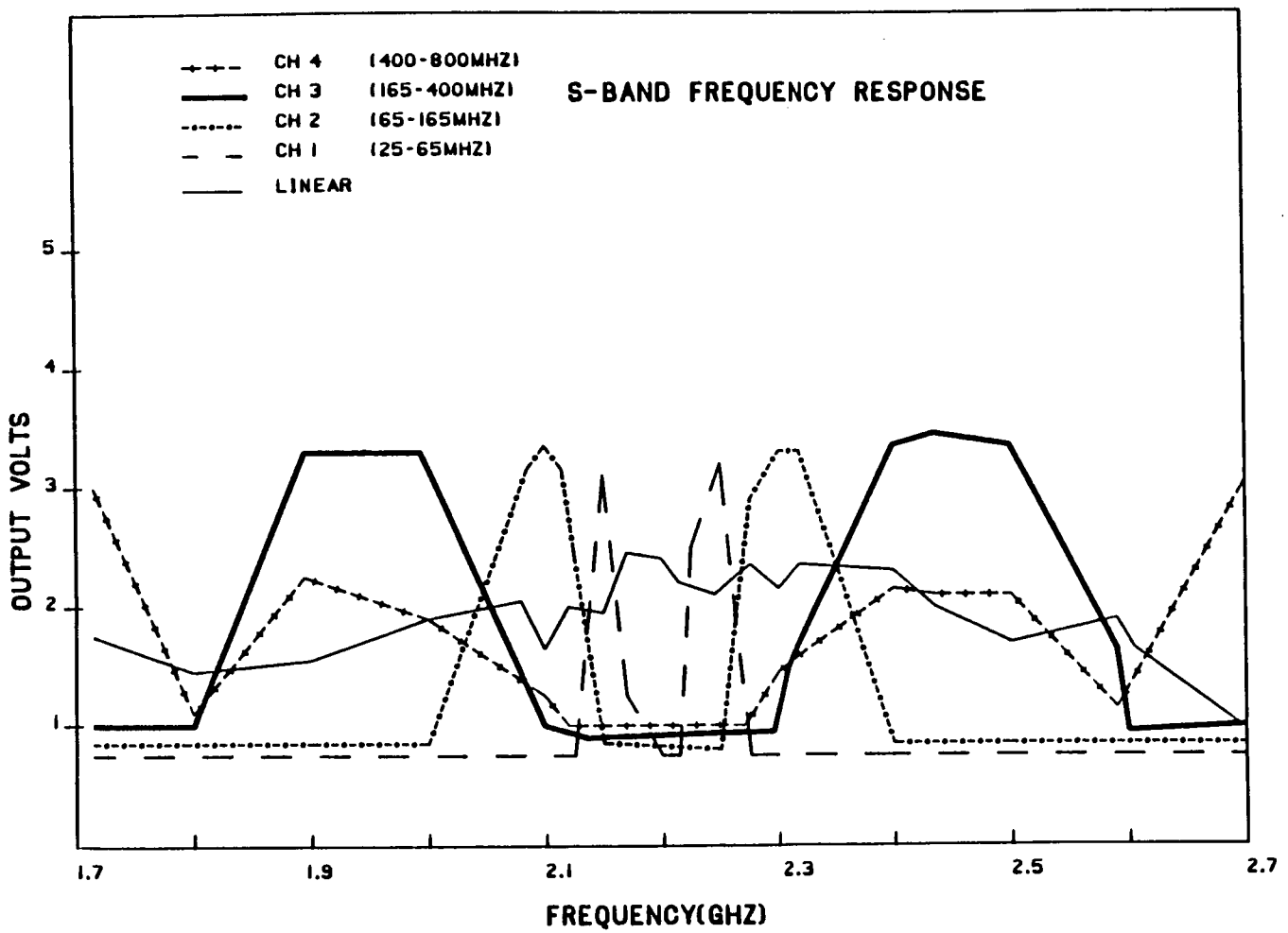
CH 4 (400-800MHZ)
CH 3 (165-400MHZ)
CH 2 (65-165MHZ)
CH 1 (25-65MHZ)
LINEAR
S-BAND FREQUENCY RESPONSE
OUTPUT VOLTS
5
4
3
2
1
1.7
1.9
2.1
2.3
2.5
2.7
FREQUENCY(GHZ)

Figure 3.6

A-G85-42

KU 2 FREQUENCY RESPONSE
(CONSTANT RF DETECTOR AMPLITUDE)

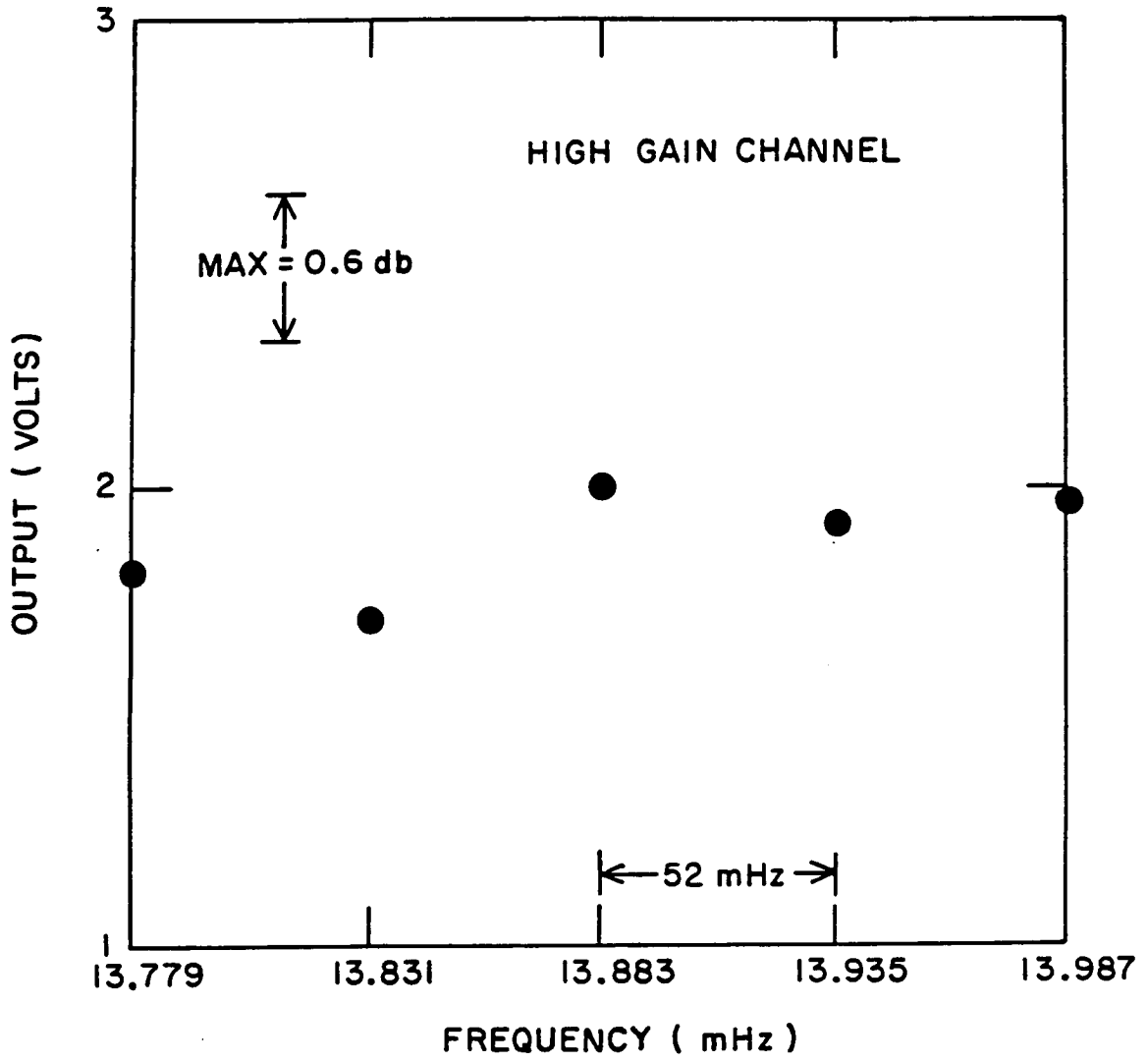

Figure 3.7

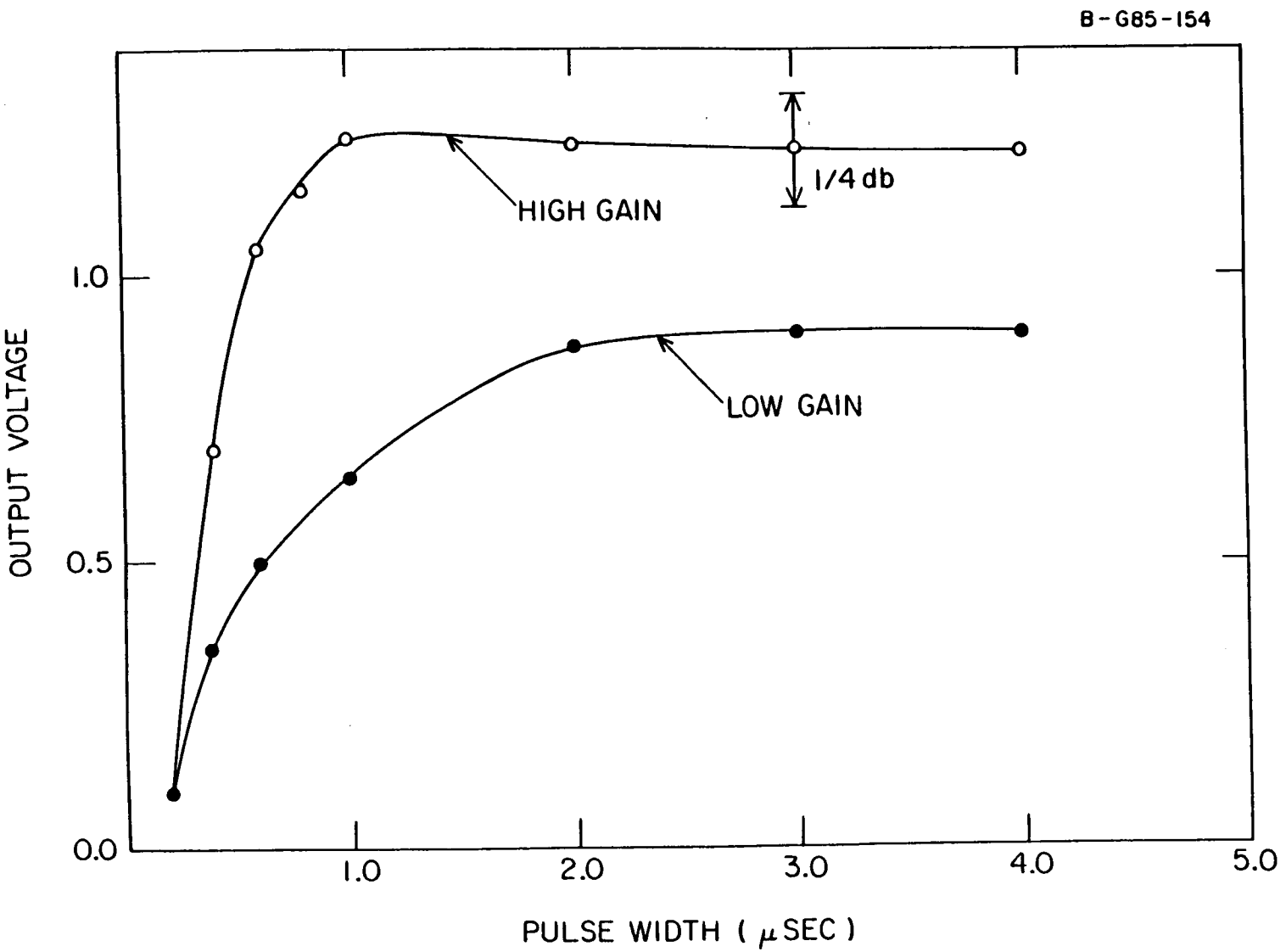

Figure 3.8 Ku-band Detector Pulse Width Sensitivity

to pulse width and μwave frequency were done as bench calibrations and the results are presented in Section 3.2.1. All measurements in the anechoic chamber were done at one standard PW (2.07 μsec) and PRF (6970 Hz). The subsequent sections discuss the results of calibration over frequency and pulse width, the antenna response for both polarizations, and the 3 dB calibration for all 4 peak detectors.

3.2.1 Pulse Width and Frequency Response

Although the radar steps through its frequencies on a time scale that is short compared to the .1 sec sampling period of the KUSR, it is important to understand the system frequency response since the peak output will be determined by the frequency at which the instrument is most sensitive. Figure 3.7 indicates that the peak sensitivity is at 13.883 GHz which is where all absolute sensitivity measurements discussed below were subsequently made.

The pulse width response is limited by the slew rate of the peak detector (Section 2.2.2) and thus pulse widths less than a certain value do not allow the detector to fully charge the capacitor and reach equilibriam. Figure 3.8 shows the results of bench measurements used to determine the relative pulse width sensitivity of the system. Note that the detector (detector A) which is plotted as an example indicates that 2 μsec and above shows little system sensitivity to pulse width. Note that the response of the hi gain detector is virtually the same as the low since we are being limited by bandwidth and slew rate of the HA 2520 op amp which is part of the peak detector in both hi and low gain system. The radar PW of 2.07 μsec (a nominal operational PW) was chosen for all the subsequent calibrations. A slightly longer PW (4.0 μsec) was designed into the self calibration circuit described in Section 2.2.3.

3.2.2 Ku-band Antenna Response

Final measurements of the antenna response with the assembled PDP in the anechoic chamber produced remarkably similar results to those of a test horn made much earlier (Section 2.2.1). The equipment configuration for this as well as the 3 dB calibration test is shown in Figure 3.9. Figure 3.10 indicates measurements taken on the uniformity of the electric field at the position of the PDP in the chamber. Considering the 21" radius of the PDP the greatest field strength variation was 2 dB which would be a correction only at antenna angles greater than approximately 50°. Just as in the S-band testing, careful control was exercised over the cables, power level, variable attenuators, pulse width and frequency. E and H plane measurements using the front probe (KU1) are shown in Figure 3.11. Note the symmetry and lack of sidelobes makes this antenna a good compromise for the measurements needed while on the RMS arm. Ideally of course a dipole would have been best for the RMS measurements, but would not be suitable for free flight objectives because of its low gain.

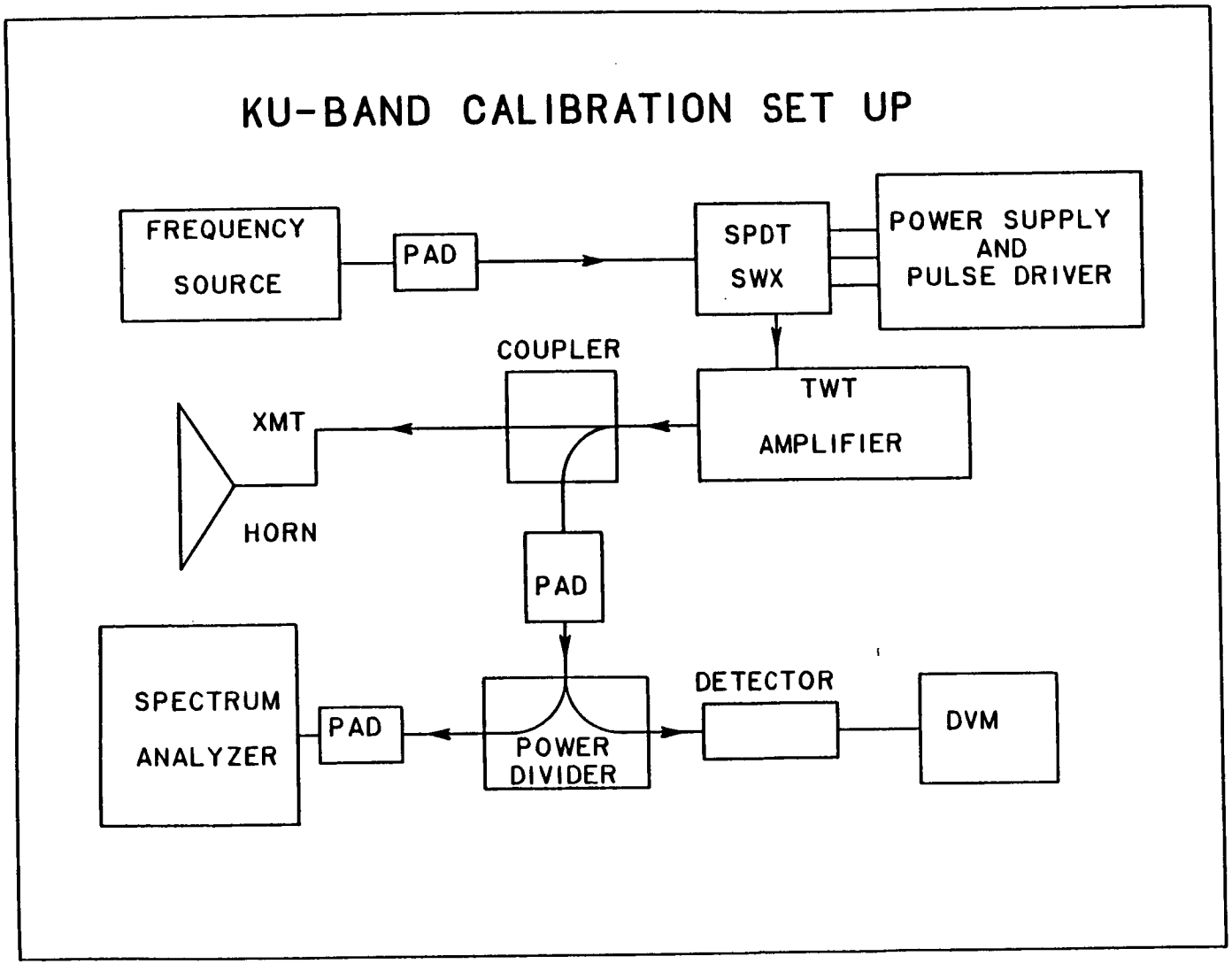
KU-BAND CALIBRATION SET UP
FREQUENCY SOURCE
PAD
SPDT SWX
POWER SUPPLY AND PULSE DRIVER
COUPLER
TWT AMPLIFIER
XMT
HORN
PAD
SPECTRUM ANALYZER
PAD
POWER DIVIDER
DETECTOR
DVM

Figure 3.9

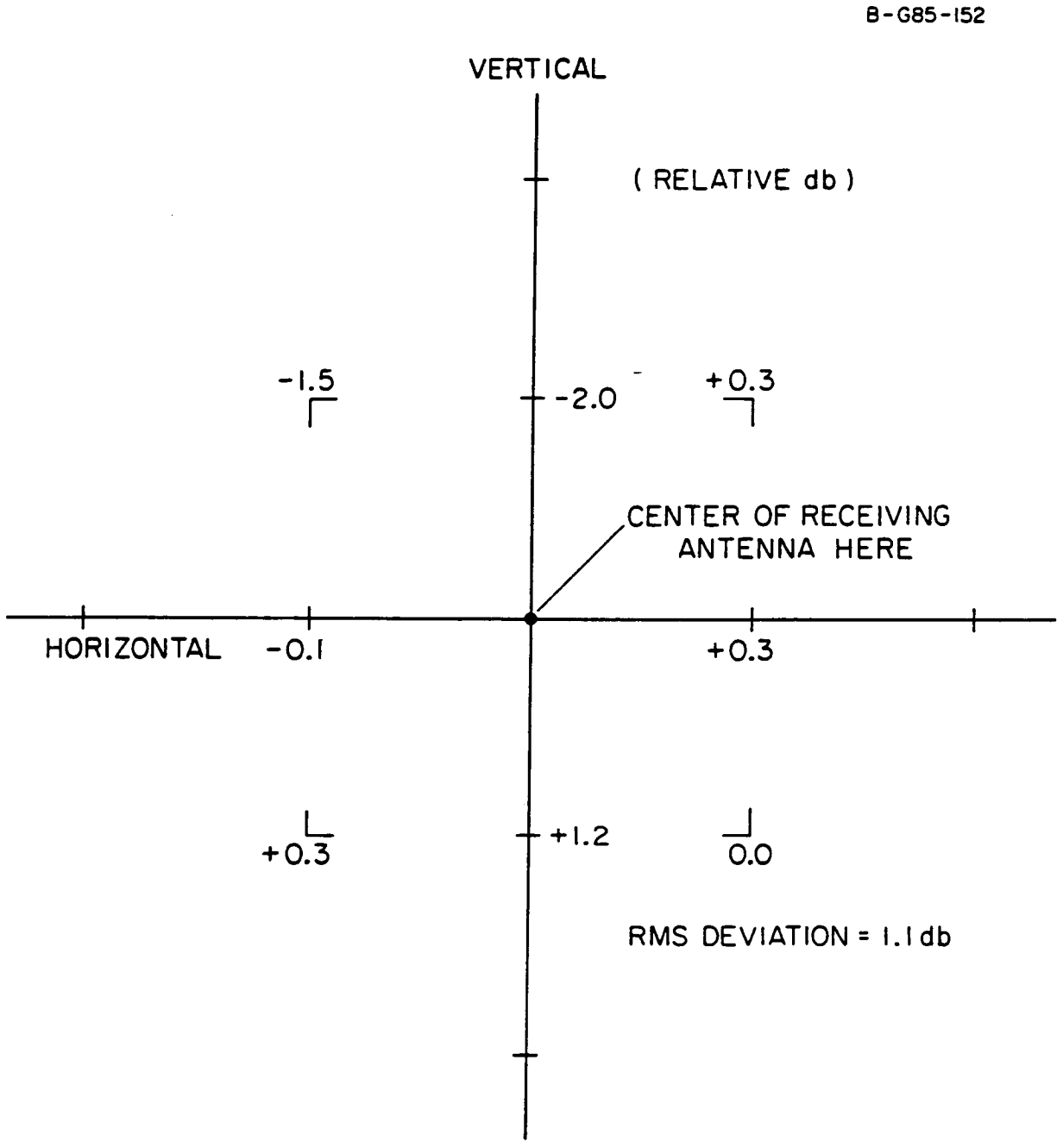

Figure 3.10 Field Uniformity in Anechoic Chamber. Tick Marks are in Feet.

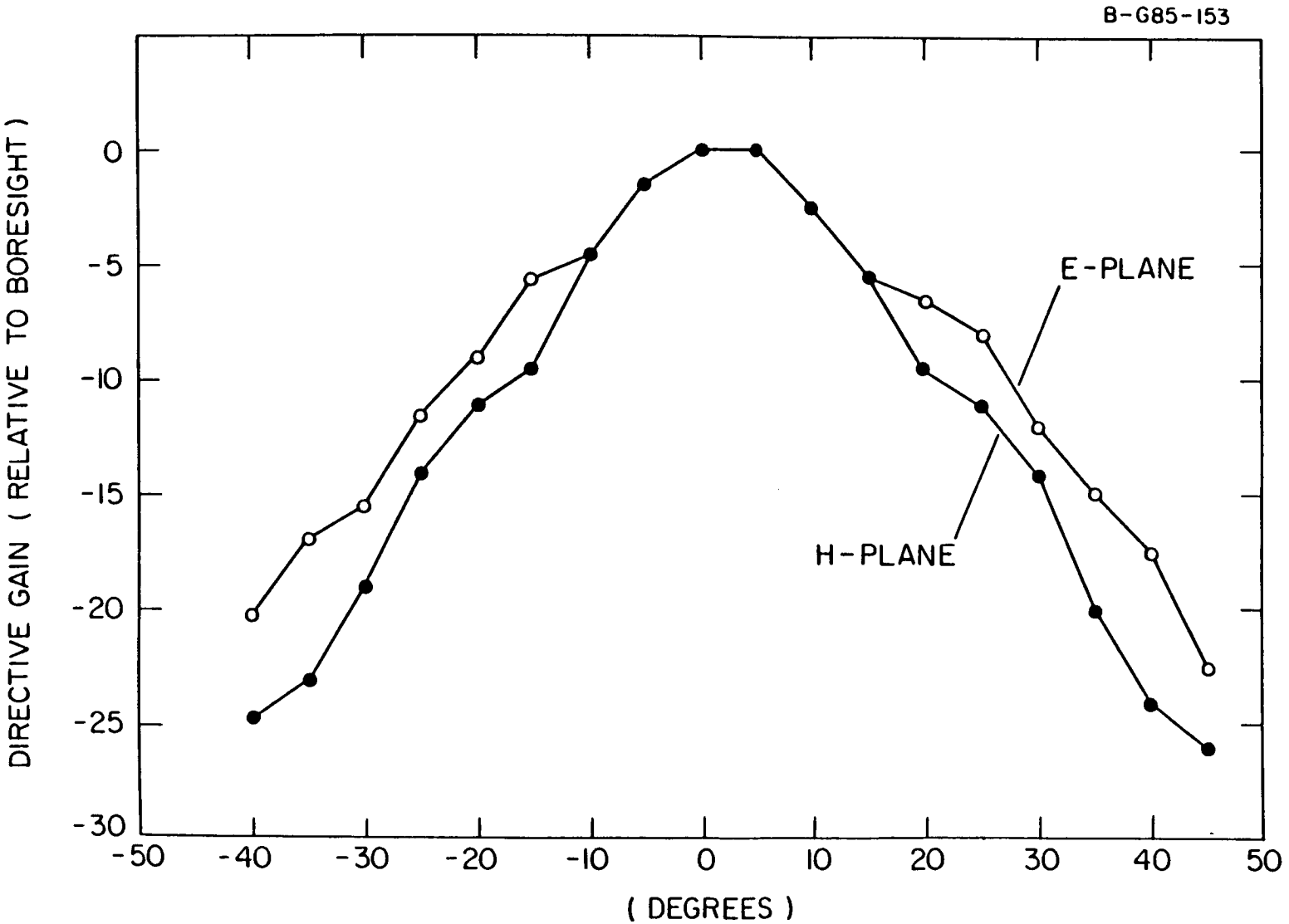

Figure 3.11 Antenna Patterns of Ku-band Horn

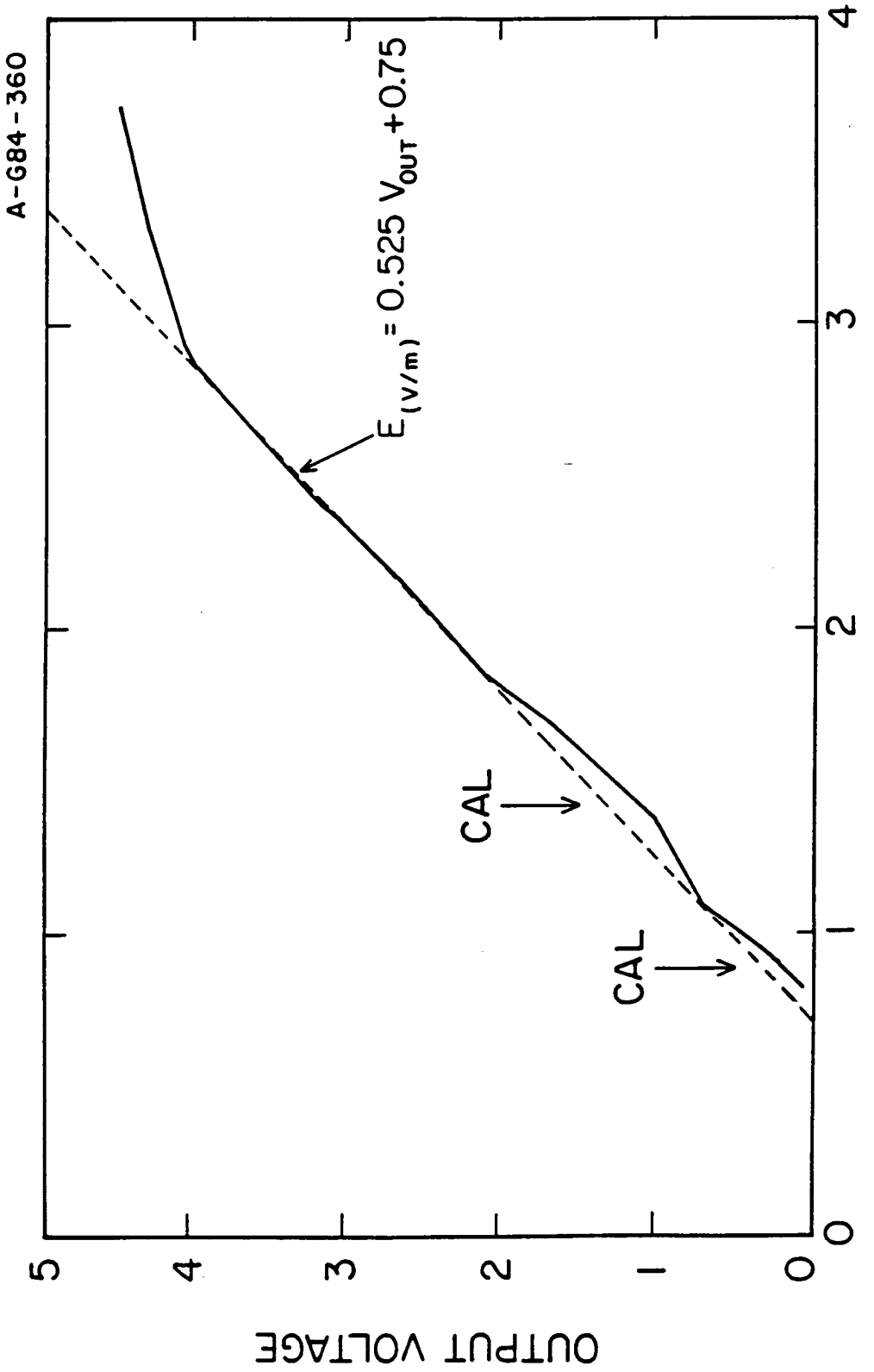

Figure 3.12a Calibration for High Gain Detector

ORIGINAL PAGE IS
OF POOR QUALITY

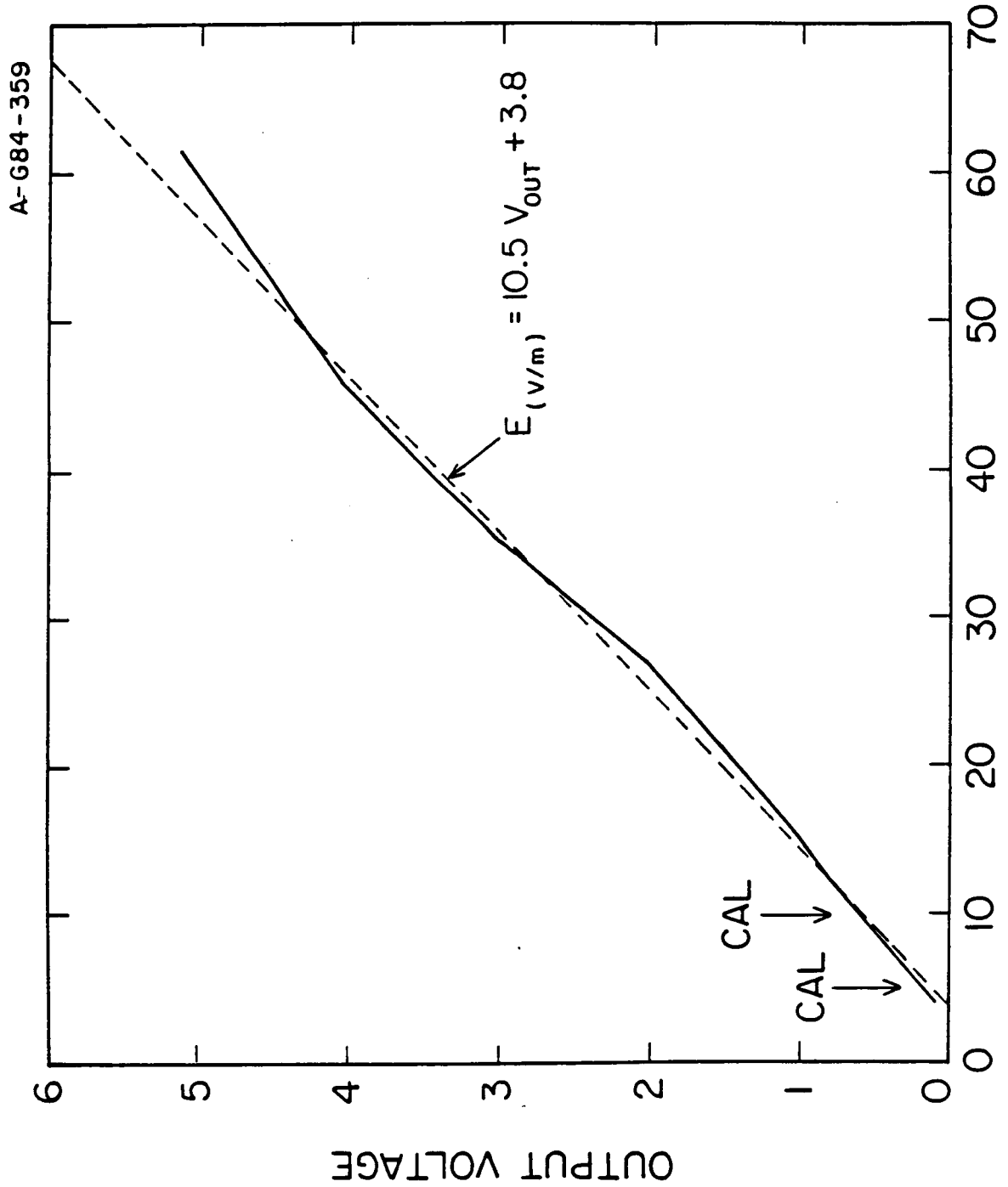

Figure 3.12b. Calibration Curve for Low Gain Port

As a point of comparison, the measurements taken on the prototype antenna fall within 1.5 db of those in Figure 3.11. Since the original points were measured by the use of only the antenna/waveguide and detector and the final sensitivity plot depends on the conversion of instrument output voltage to relative input electric fields, the fact that they agree so well is a testimonial in part to the accuracy of the absolute calibration discussed in the next subsection. (It means the transfer function must be approximately correct.)

3.2.3 Ku-band Amplitude Calibration

The amplitude calibration steps were essentially the same as those for the S-band receiver, but had to be made at two orthogonal polarizations and with a pulsed signal. When the PDP was replaced with the standard gain horn, the RF SWX (Figure 3.9) was held in a closed position instead of pulsed to facilitate accurate readings of the standard horn detector with the DVM. The results of the 3 dB amplitude calibrations for detector KU1 lo and hi gains are shown in Figures 3.12a and 3.12b. The results for KU2 are virtually identical and not shown. The total dynamic range of the system (at 2.07 μsec pw) is approximately 40 dB with an overlap of about 4.5 dB. The place where the calibration signal (Section 2.2.3) hits the two detectors is also indicated.

3.3 Temperature Calibration

In order to preserve the accuracies of the system, the last variable that must be considered is the response of the system over temperature. To cover thoroughly all variables as a function of temperature, a test matrix was devised which, for Ku-band, measured the response of both channels hi and lo gain detectors at varying pulse widths and amplitudes, and for S-band, measured the response of the linear detector at different amplitudes and frequencies. An arrangement utilizing a temperature chamber, the IGSE and a portable Radio Shack computer was devised to automate the task of gathering such a large data base. The configuration is shown in Figure 3.13. The data was gathered for each of 31 thermal cycles by the portable computer and then transferred to a database for sorting and calculation. Table 3.2 summarizes the test matrix.

Even though data was gathered from -25°C to +50°C, the expected operating regime of the instrument (based on previous flight data) is 0°C to +25°C. The data in this data base is being used to generate "correction factors" accurate to ±.1 dB which are tabular driven and added or subtracted from the data based on thermistor outputs. Although the temperature dependence is not extreme it can affect the result by several db especially for short pulse width of the radar.

TABLE 3.2
TEMPERATURE TEST SUMMARY

Channels A and B of Ku-band System*

PW (μsec)	Input Relative Amplitudes++(-dB)	Number of Cycles
.1	0, 6, 10, 16	8
2.1	0, 10, 16, 20, 26, 30, 36, 40	11
4.1	0, 6, 10, 16, 20, 26, 30	7
8.3	0, 6, 10, 20, 26	5

S-band Linear

Frequency	Input Relative Amplitudes++(-dB)	Number of Cycles
2287.5	0, 3, 6, 10, 20, 26, 30, 36	9
2250	0, 3, 10, 12, 16, 20, 26, 30, 36	10
2205	0, 6, 10, 16, 26	7
2435	6, 16, 26	3
2589	6, 26	2

*All cycles range from -25°C to +50°C at 13.883 GHz 6970 prf

++Relative to unattenuated signal (these were chosen to assure some response across the amplitude range of both hi and lo gain detectors, or across the entire linear detector range in the S-band system).

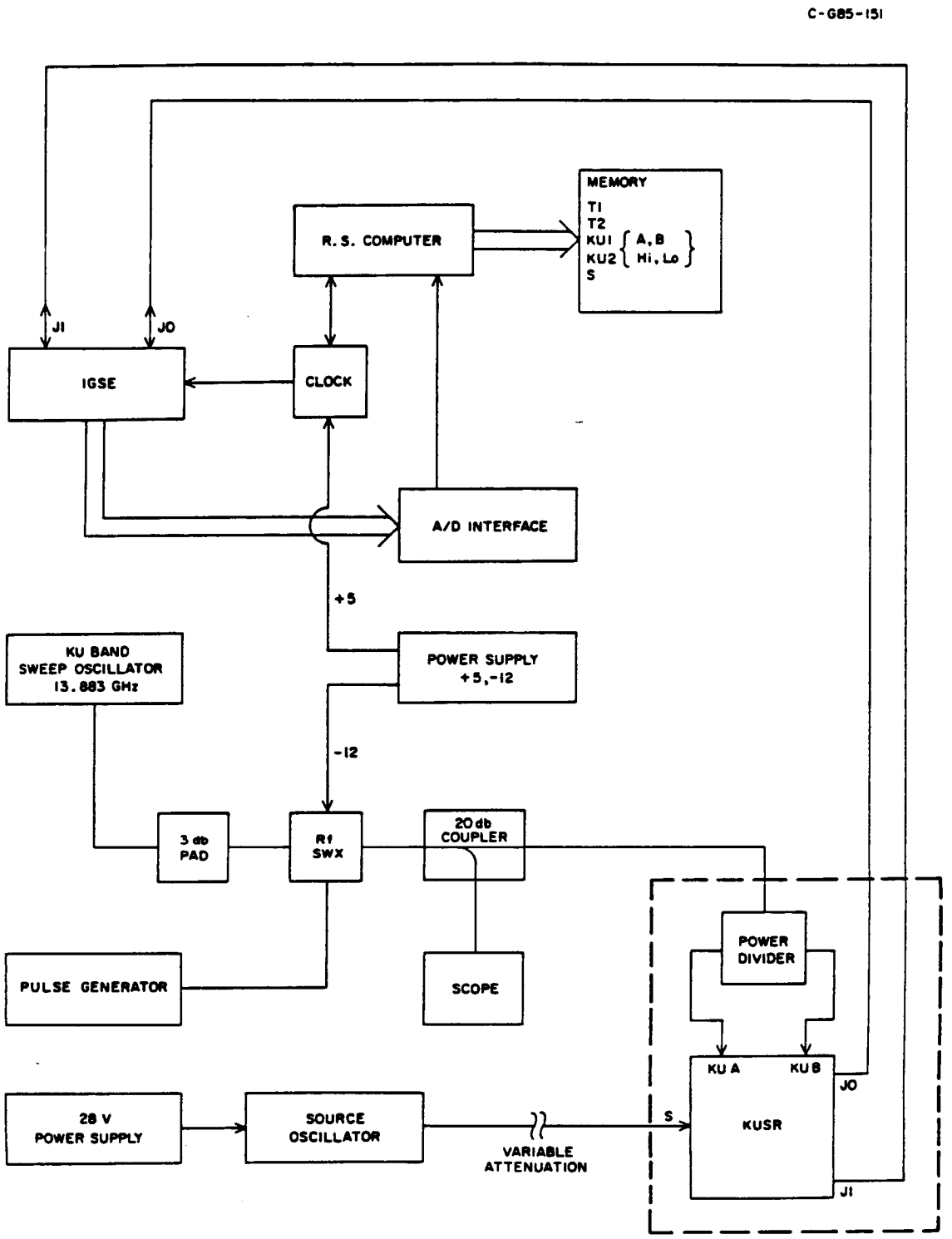

Figure 3.13 Temperature Test Configuration

4.0 ON-ORBIT OPERATIONAL DESIGN

Section 1.1 brought out the general need for on-orbit measurements of the radar and communication systems. Specifically, the data required involve the following:

1. Determine the worst case expected electric fields in and near the payload bay envelope due to the Ku-band radar or communication link.

2. Measure the electric fields in the Fresnel zone of the radar dish and compare to laboratory models.

3. In the far radar field, determine a value of K where $E = K/r$.

4. Measure the worst case E-field near the payload bay due to the 2287.5 MHz transmitter.

5. Measure the field strength of each of the eight beams of the S-band link and compare to those expected.

In order to achieve each of the above goals on the Spacelab-2 mission, detailed descriptions of configurations and procedures are required as well as time estimates for executing these objectives. The details are needed by mission planning and timeline engineers at NASA in order to adequately design the mission as a whole.

Problems in understanding the capabilities and limits of the orbiter systems and RMS arm had to be solved early so that a realizable scenario could be developed. Details of the capabilities of these systems or problems worked before the final procedure was developed are not within the scope of this paper. The following two sections describe some of the fundamental constraints that lead to the final operational design.

4.1 KUSR Measurements of Radar

Worst case E-fields in or near the cargo bay occur when the radar dish is pointed directly across the payload bay. The radar and communication links both employ a mask in the software which, when enabled, prevents the antenna from pointing at certain parts of the orbiter. Further protection can be provided by employing a variable limit on one of the gimble angles of the dish. Since we are interested in a worst case test, we will want to position the PDP over the payload bay and move the radar dish as close as possible to the edge of the software mask. Several safety constraints place limitation(s) of this operation:

1. Although in theory the mask could be disabled, concern for other instrumentation on Spacelab prevents this.

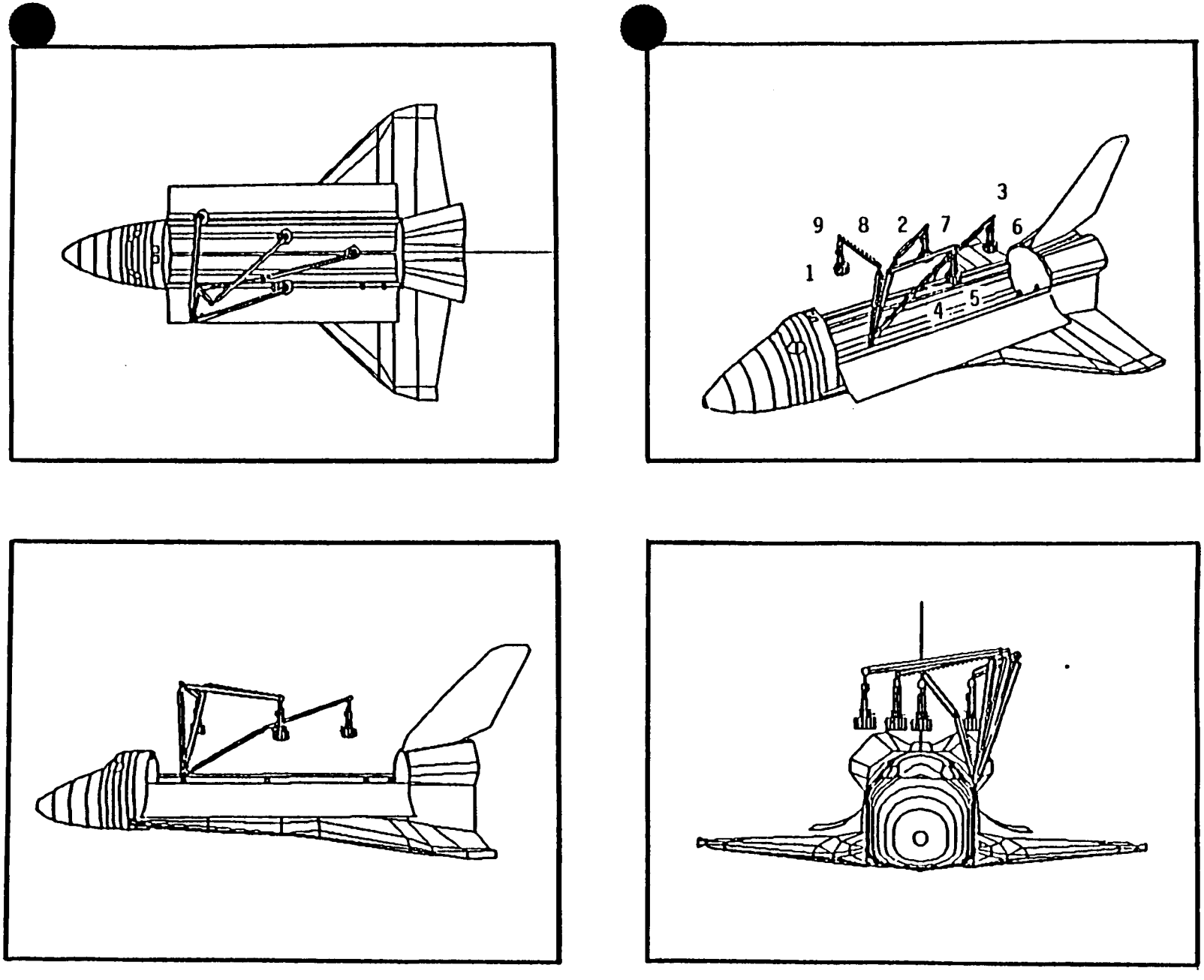

Figure 4.1 RMS Auto Sequence "K1"

2. The PDP (while on the RMS arm) cannot be allowed closer than 5 ft. to any other payload element. This is to prevent collisions in case of RMS joint "run-away" during computer controlled sequences.

3. Hi power radar should not be used with the PDP directly in the beam. Although the PDP has been EMI hardened to Ku-band fields, reflected power may be above operational limits of other elements of the payload.

Considering these constraints, an RMS sequence (K1) was designed which moved the PDP along the orbiter payload bay at the level of the cargo bay doors. (Figure 4.1) The radar antenna is then pointed in the direction of the starboard OMS pod (close to the vertical stabilizer) as close as possible to the mask and operated in low or medium power mode. The PDP is moved along the "V" shaped path illustrated in Figure 4.1 while keeping the KUSR receiving antenna pointed at the radar dish. At point 4/5 (Figure 4.1) the PDP is rotated, directing its receiving horn at the starboard OMS pod to measure reflected power, and the "V" pattern is then retraced. During the time between points 5 and 6, the radar may be operated in medium or high power mode to put the reflected signals above the receiver thresholds.

By using this sequence which takes approximately 6 1/2 minutes, a number of points in the vicinity of the payload envelope can be measured giving a better understanding of what E-fields can be expected and thus whether protection in the form of gimble angle restrictions above and beyond the nominal orbiter mask are required.

Fresnel zone measurements of the radar require a different configuration. Again, the same constraints regarding high power operation apply.

Figure 4.2 illustrates another RMS sequence (designated K2) which was designed to move the PDP along the axis of the radar dish while it is pointed parallel to the orbiter -Z axis (directly up out of the bay). The sequence has "pause points" where the RMS stops and allows the crewman to manually move the PDP transverse to the axis of the dish ±2 meters.

Considerable work was done in the laboratory on measurement and design of the beam shape for the Ku-band system. Figure 4.3 illustrates the predicted near field power pattern which is best fit to a 36 inch diameter dish with a 25 dB Taylor aperture distribution. The pause points on the RMS sequence K2 were designed to coincide with the predicted bifurcation points in the power pattern. Problems in using the PDP (a large cylindrical metal object) to make these measurements are principally those of reflections. Although precise agreement with the model depicted in Figure 4.3 is not expected, the data should be a true indication of what fields can be expected by objects immersed in the near beam.

In order to achieve the objective of determining an "K/r" model for the electric field in far field, measurements must be made at a distance $>\sim$ 70m which is the classic far field limit in this case.

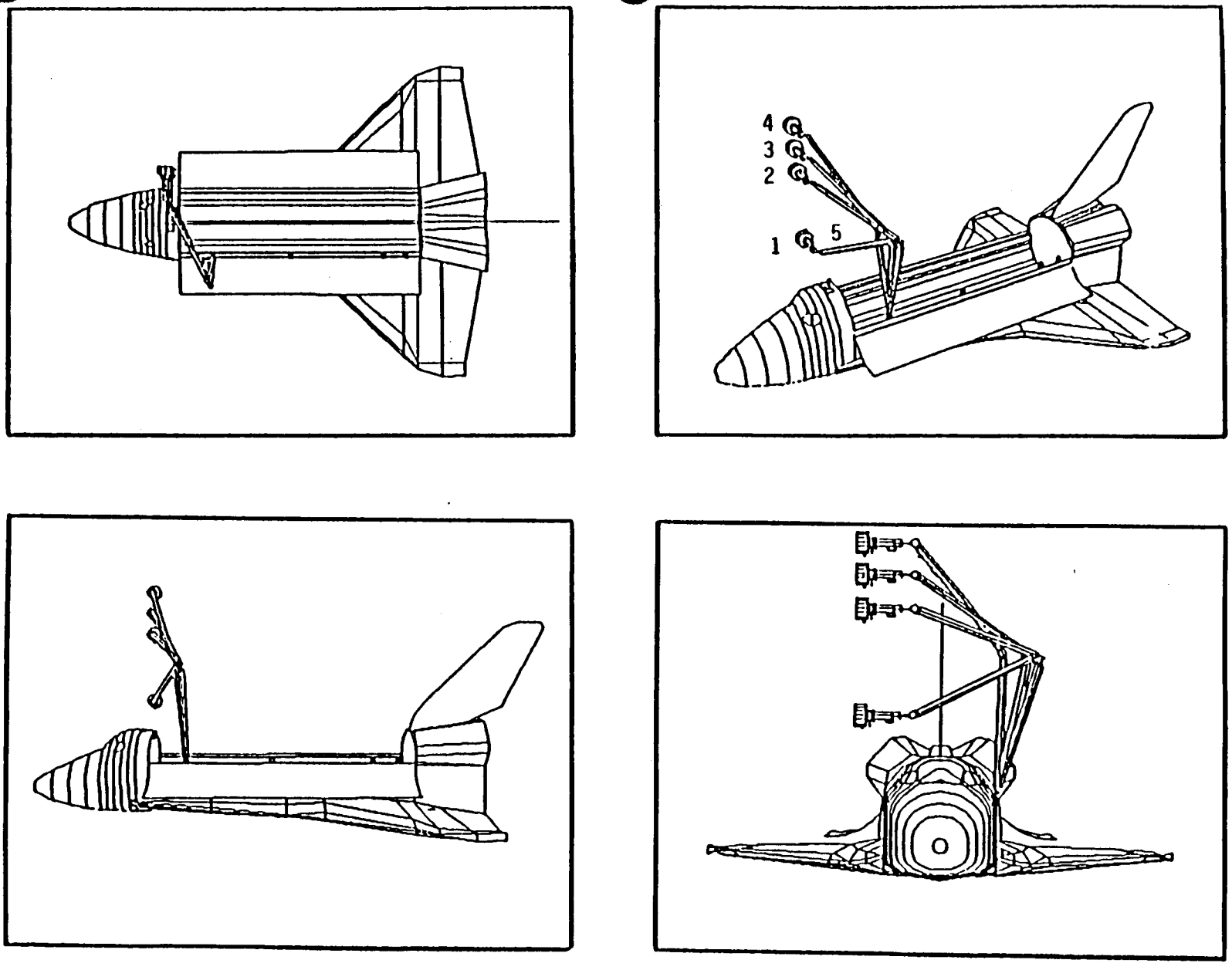

Figure 4.2 RMS Auto Sequence "K2"

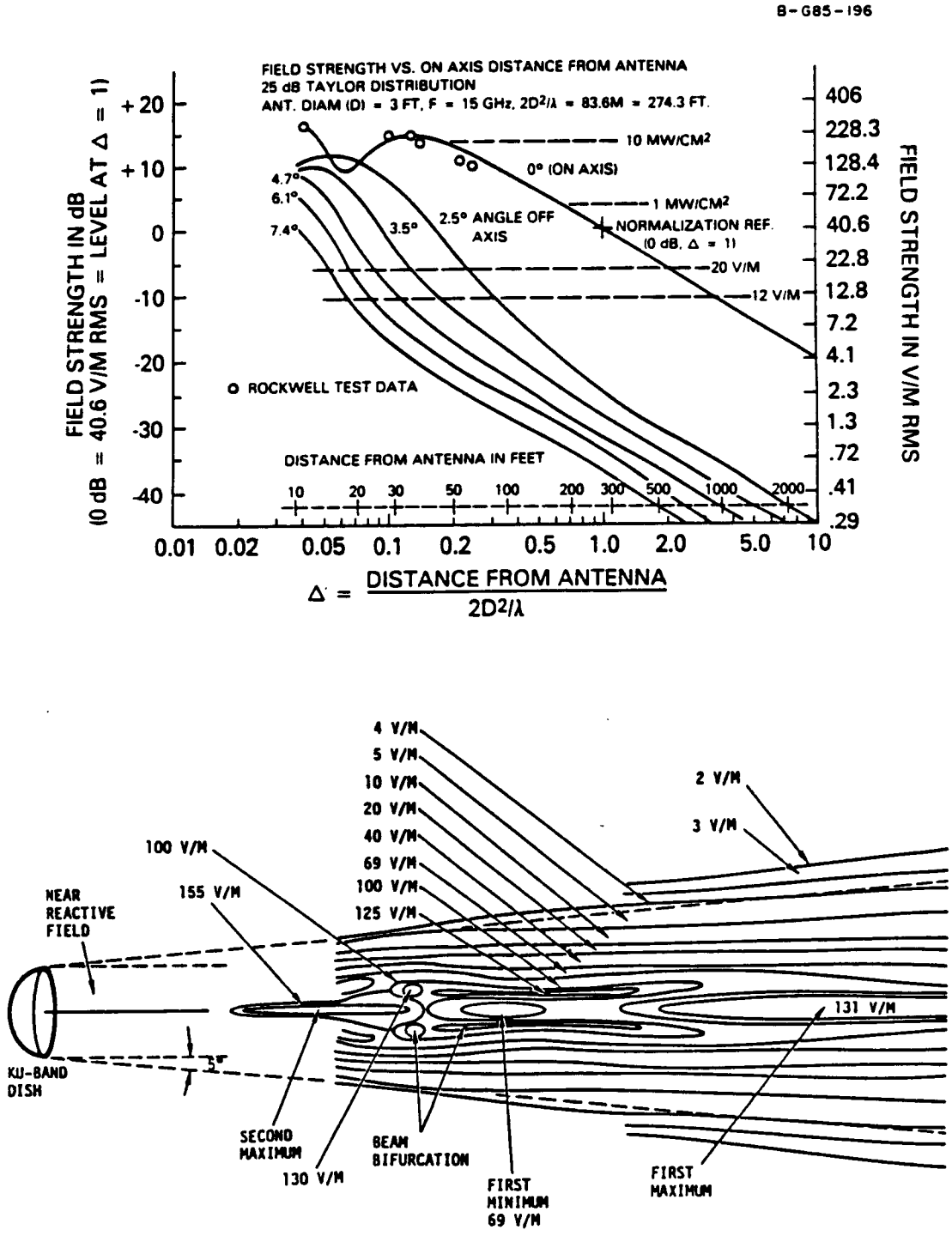

Figure 4.3 Near field electric field model for the radar dish. In top figure the data points are fit to a 24dB Taylor aperature distribution.[15] The bottom figure is constructed from data taken at Rockwell on an antenna prototype.[16]

C-G85-195

ORBITER S-BAND ANTENNA PROFILES
(TOP HEMISPHERE ONLY)

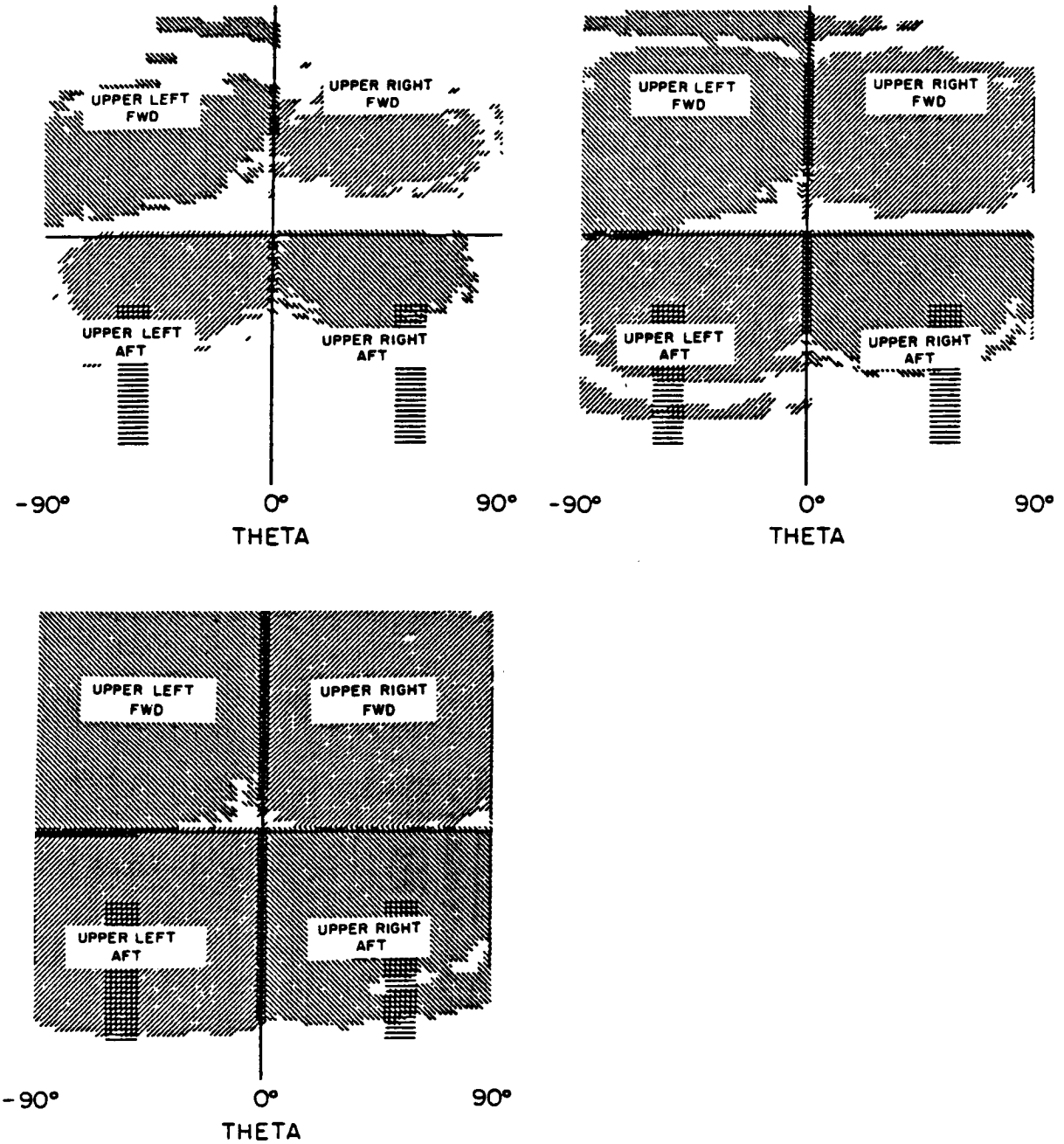

Figure 4.4 Antenna profiles (far field) are for upper hemisphere only. Theta = 0 corresponds to orbiter X axis. The top left is a +4dB contour, the top right a +2dB and the bottom left +0dB. Note that the coverage is quite uniform.[17] Doubly cross-hatched areas indicate blockage by the orbiter.

During the PDP free-flight, the orbiter first releases the PDP then backs off along the velocity vector to a distance of 300 feet. The radar acquisition is predicted to occur at a distance of 70 to 100 feet. After release, the PDP will begin to spin-up, over a period of approximately 20 minutes, to a final rate of ~ 30°/second (5 rpm). Since the PDP will be spinning at a rate of approximately 1 rpm, by the time radar acquistion takes place, it will be getting one radar field level measurement with each rotation or one "data point" at intervals of 6 ft. from the source, considering the separation rate of the orbiter and PDP. This spacial resolution improves as the PDP rotation rate increases to its maximum value. By fitting the electric field measurements to a curve proportional to 1/r, the proportionality constant may be determined. Table 1.2 illustrated the predicted field which was 2985/r V/m for the hi power operation.

During the remaining part of the PDP free-flight, the radar tracks the PDP at all times (with the exception of data dump intervals when the system is in communication mode) and the distance varies from 200 ft. to 900 ft. All of the data recorded by the KUSR during this time can be used to give further accuracy in the determination of this proportionality constant.

All of the above procedures, RMS sequences etc., have been simulated by NASA Johnson Space Center and its contractors and verified to be valid and workable scenarios.

4.2 S-band Measurements

Requirements 4 and 5 in Section 4.0 are somewhat easier to fulfill than the first 3. As discussed in Sections 1.0 and 1.1, measurements relating to requirement #4 were first made on STS-3 (Appendix A). All that is substantially needed is to repeat those measurements again under a similar configuration. Since OV99 (Challenger) does not have the same S-band antenna configuration that OV102 (Columbia) had during STS-3, direct comparison will not be possible. Figure 4.4 is a map of the measured E-field intensity of the S-band antenna system (upper hemisphere only). The worst case electric fields over and in the cargo bay will occur when either the upper aft starboard or upper aft port beams are selected. By using the same RMS sequences as before, we can choose the upper aft starboard beam at 2287.5 MHz (hi power) and have a good basis for comparisons. Figure 4.5 illustrates the RMS sequence that will be used. A rotation about the PDP spin axis is executed at each point and the peak field measured. Predicted field strengths are different than on the previous flight due to the higher directivity of the S-band beam, however, since this system has improved accuracy and calibration, much more reliable comparisons to predictions can be made.

The last objective requires that the PDP be a free-flyer since no measurements of antenna beams on the bottom of the orbiter are possible with the PDP on the RMS. Timelined to happen after the orbiter has

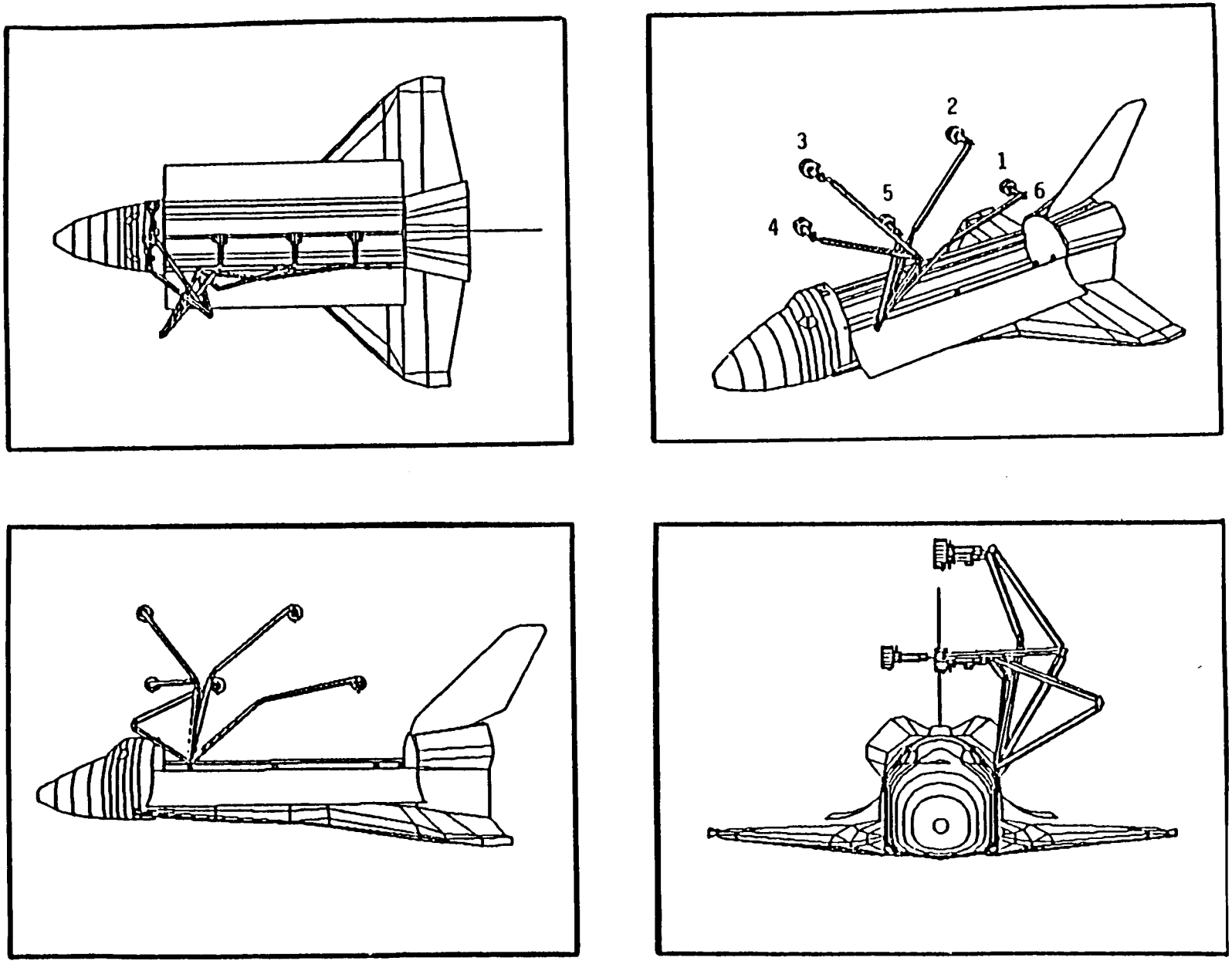

Figure 4.5 RMS Auto Sequence "S"

"backed away" to 100 meters, the S-band beam test consists of two consecutive orbiter rolls combined with a series of antenna beam selections. Again, several constraints apply.

1. The test should take less than ~20 minutes including configuration time.

2. Since the PDP is spinning approximately once each 13.5 seconds and the pattern of its receiving antenna has a beam width optimal for measurement over ~ 60°, there will be "dead zones" in the data. These zones should be < 9° (10% of the ~ 90° wide transmitting beam).

3. The orbiter attitude deadband should be .2° in this case.

By rolling the orbiter (about its x axis) at a .75°/second rate and switching antenna beams every 90°, it will take 16 minutes (not counting setup time) to do the experiment. The switching time is only a few seconds, but it takes about a minute to setup the roll and at least another minute to stop it and restore the original attitude. Thus, we see that much slower than a .75°/second roll rate would violate the time constraint.

Consider during the 90° (2 minutes) of orbiter rotation that a given antenna is selected, the PDP will revolve ~ 9 times obtaining data with gaps which comprise approximately 30-50% of the beam. These data must then be fit to a model to determine an accurate pattern (Section 5.2).

Uncertainty in orbiter attitude (±.2°) is not a factor in this case since the 2287.5 Mhz beam is very wide.

Knowing the distance of the PDP from radar tracking data, a value for the constant in the $E = K/r$ expression can then be determined and compared with predictions. Since data taken on the RMS is (for the most part) already in the far field, it too can be used in the determination of this constant.

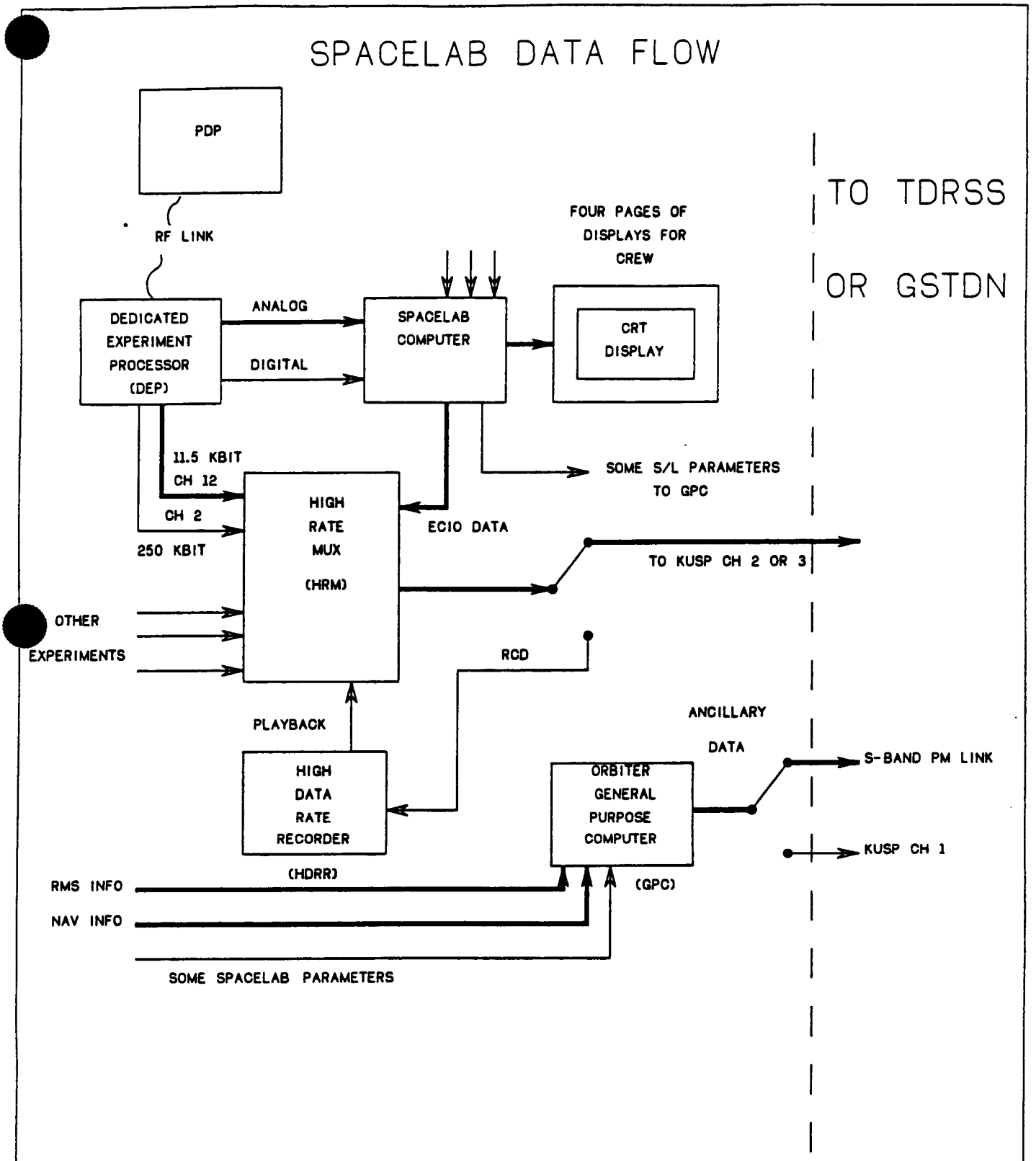

Figure 5.1 An illustration of data flow aboard the orbiter. KUSR data flow as well as ancillary data needed to process it are highlighted with black arrows. Note that the Instrument and ancillary data remain on separate channels.

5.0 DATA ACQUISITION AND ANALYSIS

Data analysis for the KUSR involves data not only from the instrument itself, but data from the orbiter and its systems as well. Objectives which use the RMS in sequences K1, K2, and S require position and attitude of the PDP on the arm. Those free-flight objectives need information about the relative position between the orbiter and the PDP as well as orbiter attitude and antenna pointing. The PDP attitude is also needed as well as its spin phase in order to properly account for the KU or S-band antenna gain function. All operations whether on the RMS or as a free-flyer, require information that verifies the operational mode chosen for the radar as well as TWT output power (when applicable). The antenna selection, frequency, and output power for the S-band system are also required.

None of this information is part of the PDP data stream itself and is available through various other ancillary data sources. Table 5.1 summarizes the ancillary data needs and their sources.

5.1 Operational Data Flow

A brief discussion of the data flow through the orbiter system as well as the origin of the data products referenced in Table 5.1 is in order. All PDP data flows through the High Rate Multiplexer (HRM) which handles data in a variable format from all of the Spacelab experiments. This data is either downlinked directly through the Ku-band return link (Figure 5.1) or recorded on the High Data Rate Recorder (HDRR) for downlink when the TDRSS satellite and Ku-band antenna are available. Note that because of this restriction, none of the Ku-band measurements can be available on the ground real time since the Ku-band antenna cannot be used for this data link during the measurement. In order to provide some feedback that the ongoing operation is a successful one, several outputs from the PDP, including one Ku-band hi and lo gain channel and one S-band output (the log detector channel sensitive to 2287.5 MHz), are made available to the crew via a digital display.

Once the data are downlinked to the White Sands ground station, it is turned around via a Domsat link and recorded both at Johnson Space Center (JSC) and Goddard Space Flight Center (GSFC).

The JSC data, is in turn made available to the various experimenters in the Payload Operations Control Center (POCC) where they are able to process their data as they please. Also available in the POCC, are most ancillary data of interest (orbiter attitude, trajectory etc). A data display has been designed for the PDP Ground Support Equipment which displays (in an uncalibrated format) the raw outputs of the KUSR and S-band log detector. By observing a playback of the data taken during our prime objectives and discussing the status of the experiment with the crew on orbit and NASA communications engineers, we will be able to determine whether or not the measurements are successful, confirm that all systems are configured properly and that the KUSR itself is operating nominally.

TABLE 5.1
ANCILLARY DATA SOURCES

Date Type Needed	Source File	Source Institution
RMS Position and Attitude (X Y Z) (P Y R)	OANC*	JSC
Orbiter State Vector X Y Z • • • X Y Z	SPMA+ OANC	GSFC JSC
Ku-band Antenna Angles Pointing (α, β)	OANC	JSC
S-band Antenna Select, Output Pwr	OANC	JSC
Relative Position (PDP - Orbiter)	RELBET++	JSC
PDP Attitude and Spin Rate (Free-Flight Mode)	PDP ANC	University of Iowa

*OANC "Orbiter Ancillary" is produced at Johnson Space Center for internal use and distributed to experimenters through Goddard Space Flight Center (GSFC).

+SPMA "Spacelab Mission Ancillary" data are produced at GSFC by merging certain spacelab exgineering and ancillary parameters along with Best Estimate Trajectory (BET) information.

++RELBET "Relative Best Estimate Trajectory" is produced post mission by JSC in a complex algorithm which Kalman filters the radar data and other sources of relative trajectory producing a best fit for the PDP free-flight profile.

At the GSFC Spacelab data processing facility the experiment data is demuxed, recorded and preprocessed. Instrumentation Data Tapes (IDT's) containing, analog bi-phase encoded data are produced and then shipped to Iowa within approximately 30 days of the mission. At GSFC, all of the ancillary data from the Spacelab Subsystems are captured and combined with trajectory and attitude data to produce the SPMA data product referenced in Table 5.1.

The origin of relative trajectory information (RELBET), is a special set of processing software at JSC designed for rendezvous operations. RELBET is a file of the relative distances and rates (6 dimensional vector) between the orbiter and the PDP produced once per second by a filtering and smoothing algorithm. It should be noted that samples of each of the above data products have been delivered to us well ahead of the mission so that processing software can be developed.

After the data has arrived at the University of Iowa, the real work on instrument data processing begins. Figure 5.2 illustrates the processing flow which is discussed in detail below.

5.2 Data Processing

The first step in the processing is to sort out the KUSR parameters from the PDP data frames, including S-band log detector data, encoder sampled temperatures, the bits 5 and 6 clocks, and Mission Elapsed Time. These data are then transferred to an indexed data file keyed by time and reside on the Vax 11-780 disk system. Table 5.2 summarizes the data and totals the number of records needed for storage. Note that this data file is small enough to be stored in the on-line system.

The next step (Figure 5.2) is to correct the raw data parameters for temperature making a new data file (also indexed by time). This data file KUSCORREC.DAT then becomes the principle data source for all further analysis.

Analysis now becomes dependent on the functional objective. Several programs are being developed for this final analysis, all of which use as input files KUSCORREC.DAT plus data from either SPMA, RELBET, or both. These various analysis steps will now be considered separately.

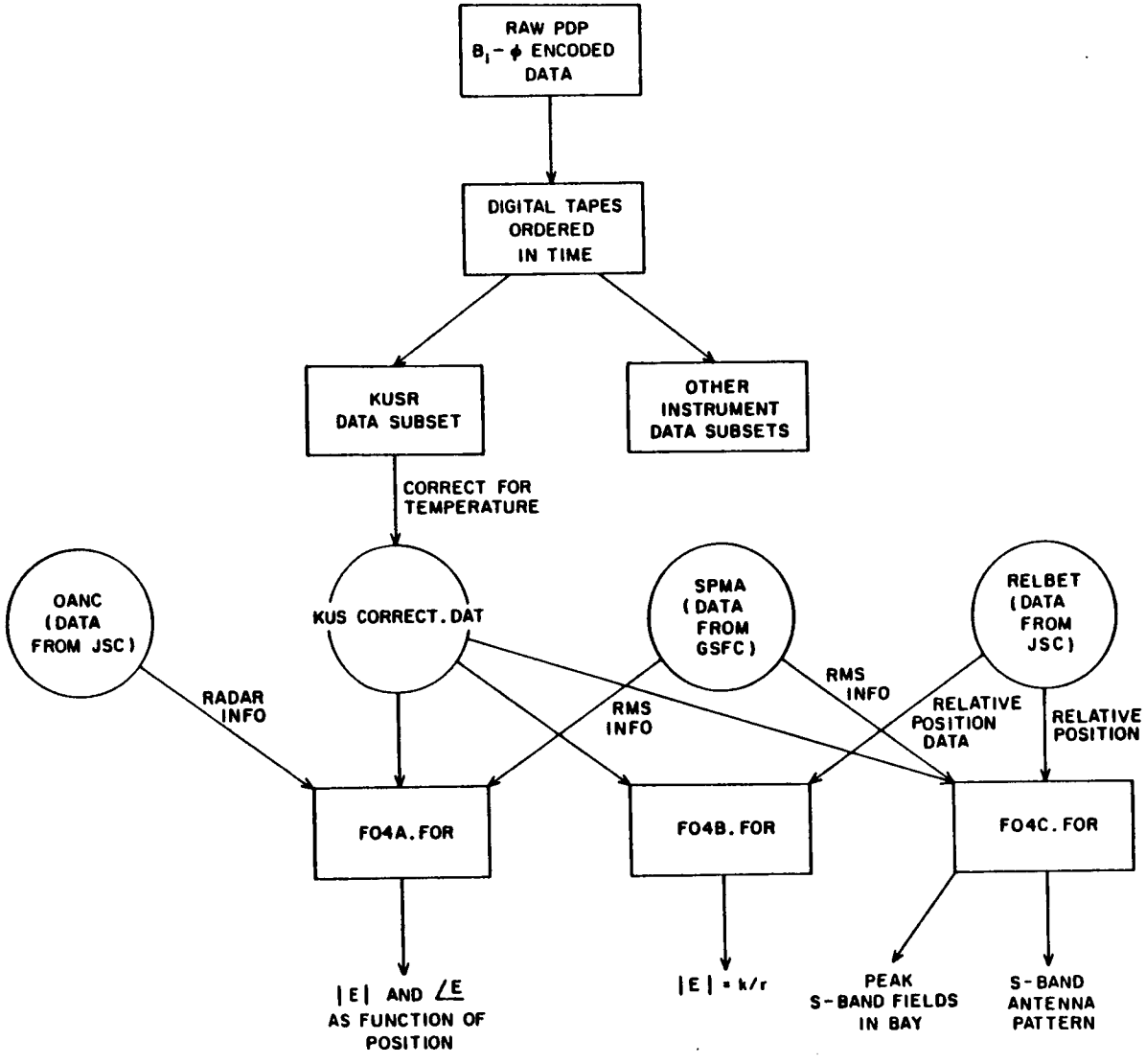

Figure 5.2 KUSR Data Analysis Software and Products. Note the need to obtain ancillary data (RMS, NAV, etc.) from separate sources.

TABLE 5.2
DATA STORAGE REQUIREMENTS

	Samples/Major Frame*	Bytes/Frame
S-band log detector (4 channels)	16	64
Clock bits	16	16
Temperatures (2)	1	2
Ku1	16	16
Ku2	16	16
MET	1	4
	Total	118 bytes
		= 4425 bytes/hour
		= ~9 blocks+/hour
Total RMS time for data	(1 hour)	
Total free flight time for data	(6.5 hours)	

*Major frame = 1.6 seconds

+Data is stored in byte instead of integer form (1 block = 512 bytes)

5.2.1 Measurement of Radar Fields in the Payload Bay

For this objective, the program F04A.FOR takes as input the radar mode (pw), the radar position angle, the RMS sequence positions (as a function of time) and the raw temperature corrected data from KUSCORREC.DAT. The raw data is then corrected for pulse width and an electric field calculated from:

$$E_{(P,G)} = \alpha(P,G)\ V_{OUT} + \beta(P,G)$$

where $E_{(P,G)}$ = calculated electric field from instrument calibration curve.

$\alpha(P,G)$, $\beta(P,G)$ = transfer function constants for the instrument

V_{OUT} = Output Voltage

P = Polarization (1 or 2)

G = Gain (Hi or Lo)

The hi gain or lo gain value is selected based on the criteria that the hi gain is used unless it is saturated (output greater than a given value dependent on which polarization we are using).

From these values, the magnitude and polarization of the electric field can then be determined from:

$$E_{mag} = \left(E_{(1,G)}^2 + E_{(2,G)}^2\right)^{1/2}$$

$$\Theta = \text{Arctangent}\left(\frac{E_{1G}}{E_{2G}}\right)$$

E_{mag} = total peak electric field magnitude

Θ = polarization angle (relative to the spin axis of the PDP)

The program will then output the file FO4A.DAT containing the electric field and polarization angle as a function of RMS position.

Since the RMS auto sequence consists of 2 parts, one with the Ku-band receiving antenna pointing at the radar transmitting antenna and one where the receiving antenna points at the RMS pod (reflected fields), the data will be likewise divided into two distinct parts.

A separate set of software (FO4PLT1.FOR) will plot these fields as a function of relative position in the payload bay.

It should be noted that if one KUSR channel fails, this particular objective would be affected. However, all other Ku-band measurements which have a predictable polarization because of lack of reflections etc., should be accurate. Only one additional variable is required and that is the polarization angle of the transmitting antenna.

5.2.2 Measurement of the Fresnel Zone of the Ku-band Antenna

The software designated FO4A.FOR can also be used for this objective. Since the KUSR receiving antenna is again directed at the radar dish, no adjustment for the antenna gain function $G(\Theta,\phi)$ is required. The electric field is calculated identically to the previous example. The output file which has electric field magnitude and polarization angle information together with RMS position is input into a different plot routine FO4APLT2.FOR which knowing the position of the center of the radar dish produces plots of electric

field magnitude and polarization as a function of distance from the dish for comparison to data and to the theoretical 25 dB Taylor aperture distribution (Figure 4.3).

5.2.3 Ku-band Antenna Far Field Measurements

A slightly different set of software is required for this and other objectives that are accomplished in the PDP free-flight mode. Instead of RMS data available from SPMA, the vector from the PDP to the Ku-band radar dish is required. Program 404B.FOR reads the appropriate RELBET data as a function of time and calculates the appropriate angles and distance vector. Assuming that the radar beam always points approximately at the PDP, the measured electric field is:

$$Em = [(E_{(1,G)}G_1(\Theta,\phi)^2 + (E_{(2,G)}G_2(\Theta,\phi))^2]^{1/2}$$

Because of the orbital trajectory and orientation of the PDP, the maximum deviation of the angle Θ from boresight during the free-flight is about 30° and thus a considerable gain correction is required. Since the PDP spins about an axis that varies ϕ in the gain function G, corresponding to an E plane correction for one polarization and an H plane correction for the other, it is sensible to calculate the equivalent E field at the peak measurement only. This eliminates the need for the two dimensional matrix correction and requires a consideration only of $G(\Theta)$. This is done by a polynominal fit to the data for low values of ϕ during each rotation of the PDP. The maximum value is then taken for the peak electric field.

This peak measurement is assumed to have taken place as the PDP rotates through $\phi = 0$ so this electric field value E_p is corrected by the gain function $G(\Theta)$ and E_m computed from:

$$E_m = [(E_{P,1}\ G_E(\Theta))^2 + (E_{P,2}\ G_H(\Theta))^2]^{1/2}$$

where $G_E(\Theta)$ is the E field power pattern for Detector 1 and

$G_H(\Theta)$ the H field power pattern for Detector 2

The output file of this routine can then be plotted as a function of distance from the source and a fit done to $E = K/r$.

5.2.4 Data Processing for S-band Objectives

Two similar sets of software are being developed for the S-band measurements. The program F04C.FOR has two sets of outputs. The first uses the information from RMS "S" scan and a similar method to that discussed above to compute a peak electric field during each

rotation of the PDP. This peak field is then plotted against its predicted value for the E-field at the corresponding point in the selected beam. The other output of FO4C.FOR is also a peak field for each rotation of the PDP, but this time that data is plotted as a function of distance from the orbiter in one case and as a function shuttle roll angle in the other to achieve a map of all of the S-band link beams.

It should now be obvious why a relatively uniform beam pattern which has similar E and H plane characteristics is very desirable. With too many sidelobes or a response which was too narrow it would be very difficult to give accurate field values for angles which were not close to boresight.

Another point about FO4C.FOR is that the software is being written so that it places priority on the linear detector measurement as long as they fall within the calibrated range of the detector. The linear detector system experienced extensive thermal testing in a laboratory environment. The log detector system did not undergo such testing (recall this was only integrated into the KUSR system after installation in the PDP). Its data although accurate at temperatures close to 25°C will be considered as backup only for these measurement objectives.

6.0 SUMMARY

In final analysis, it is significant to compare some of the original design criteria to the final product. Table 6.1 compares the engineering specification to final design and Table 6.2 summarizes the source of error in measurement for comparison to the ±1 dB goal set at the beginning of the project.

Since the project was given money through NASA/MSFC, as an add-on to an existing contract, it was necessary to submit monthly financial status reports and quarterly projections. Based on these forms, it is relatively easy to compare the rate at which contract money was spent to that which was predicted in the original proposal. At this point in the project, after delivery and integration of the experiment, all that remains is some software development and then data analysis. The original proposal allocated 24.8K (See Appendix B).

Figure 6.1 is a bar chart indicating the predicted vs. actual money spent for labor, parts, equipment etc., and indicates that the amount left for data analysis is ~ 20K which is quite close to that needed. Assuming no major problems develop requiring excess travel or labor expenses during this phase, the project should be completed by the end of NASA FY85 (October 1985) within the budget allocated.

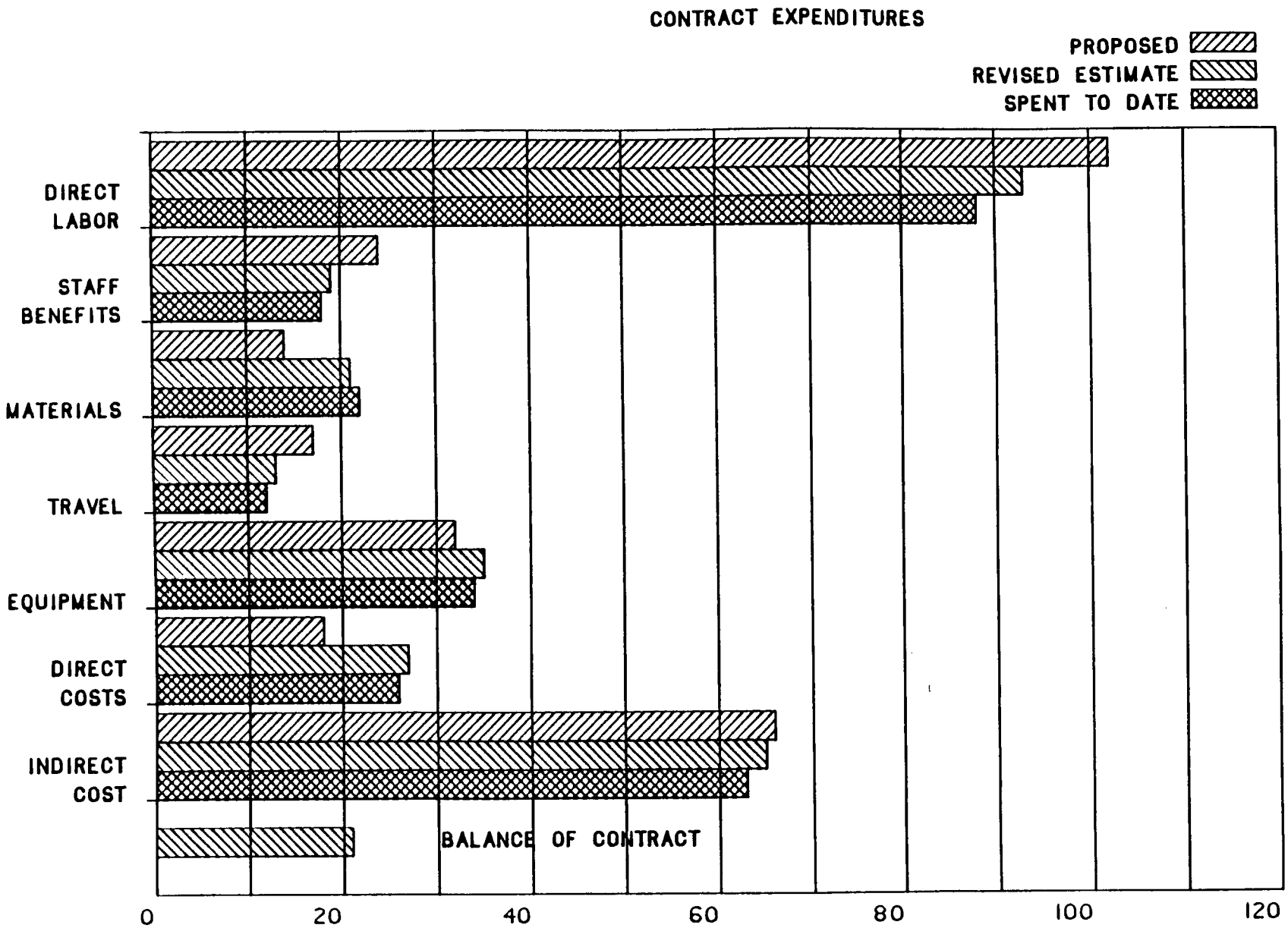

Figure 6.1 Comparison of Proposed vs. Actual on the Major Subdivisions of Project Money. The Balance of Contract is for Data Analysis and is Valid for Jan. 1, 1985.

TABLE 6.1
KUSR ENGINEERING SPECIFICATION

	Desired	Achieved
Power Consumption	$\lesssim$ 5	6.3 watts (Not including Ku-band cal source)
Weight	2-3 kg	3.416 kg
Footprint	4" x 7"	4.125" x 9.0"
Ku-band Measurement Range	< 1 - 50 V/m	.8 - 63 V/m (2.07 μsec Pw)
Ku-band Sensitivity	< ±.5 dB	±.25 dB worst case
S-band Range	-20 dB V/m to +37 dB V/m	-42 dB V/m to +29 dB V/m (-18 dB V/m to +13 dB V/m Linear Only)
S-band Sensitivity	< ±.5 dB	± 3 dB worst case ±.6 typ (log detector)
Angular Resolution (Assume 30°/Sec Spin Rate)	Not Specified Explicitly	6° (assuming either hi or lo gain output but not both)
Polarization	Not Specified	Ku-band Dual Linear S-band Linear

TABLE 6.2
MEASUREMENT ACCRUACY SUMMARY

Source of Error	Magnitude of Error (dB) Ku-band	S-band
Setup Repeatability+	± .5	±.5
Gain of Standard Horn	± 1	± 1
Calibration of Detector	± 1	± 1
Mismatch Detector/Antenna	± .5	±.5
Sensitivity	± .25 (typ)	±.6 (typ)
Temperature Correction	± .2	±.5*
Total RMS Error		
± 1 dB Desired	± 1.6 dB	± 1.76 dB

+See Section 3.1.2 for Explanation

*Log Detector was not Calibrated Over Temperature

ACKNOWLEDGMENTS

The author wishes to extend his appreciation to those who played a major role in the design, test, and assembly of the instrument:

Miles Bailey for his work with the power supply;
Martin Berry for his dedication to the S-band system and help with calibration;
Tim Clark for detailed housing design and help on the CAD;
Evan Clemmens for a professional job on the instrument housing;
Dave Cramer for his remarkable abiity to assemble semi-rigid coax;
Don Enemark for many fruitful discussions and much helpful advice;
Elwood Kruse for his lessons in quality control and patience with my impatience;
Rose Wenman, Sharon Kutcher and Rita McKenna for outstanding craftmanship in assembly of the instrument;
Howard Zimmon and Bob Beall for their assistance in drafting.

Thanks also to Professor Lonngren for his guidance in the preparation of this thesis and advice on my degree goals, and to Professor Enemark and Professor Chyung for evaluating such a weighty document. This manuscript was typed and brought to its present level of polish by Chris Joyner and Jean Hospodarsky. Last of all, thanks to Professor Stan Shawhan for giving me the room to learn and a chance to grow.

REFERENCES

1. Specification: Integrated Communication and Radar Equipment, Ku-band, Rockwell International, DOC #MC409-0025.

2. Hockensmith, R. P., R. W. Moss, Information and Concerns Relating to Payload Susceptability to Ku-band Radiated Fields, ISEE/AIAA Conference on Payload Susceptability to Space Shuttle Ku-band Radiated Fields, May 30, 1984.

3. Kraus, J. D., Antennas, p. 51, McGraw Hill, 1950.

4. Coronel, R., Wire Coupling at Ku-band Frequencies, IEEE/AIAA Conference on Payload Susceptability to Space Shuttle Ku-band Radiated Fields, May 30, 1984.

5. Hockensmith, R. P., R. W. Moss, Information and Concerns Relating to Payload Susceptability to Ku-band Radiated Fields, ISEE/AIAA Conference on Payload Susceptability to Space Shuttle Ku-band Radiated Fields, May 30, 1984.

6. Aertec Application Notes, D18Z Zero Bias Schottky Detector, Aertech Corporation, 1981.

7. King, A. P., The Radiation Characteristics of conical horn antennas, Proc IRE, Vol 35, pp. 1462-1471, Dec. 1947.

8. King, A. P., The Radiation Characteristics of conical horn antennas, Proc IRE, Vol 35, pp. 1462-1471, Dec. 1947.

9. Ramo, Winnery, Van Duzen, Fields and Waves in Communications Electronics, p. 430, Wiley, 1965.

10. Ramo, Winnery, Van Duzen, Fields and Waves in Communications Electronics, p. 431, Wiley, 1965.

11. Ramo, Winnery, Van Duzen, Fields and Waves in Communications Electronics, p. 433, Wiley, 1965.

12. Teggart, H. E., Radiated EMI instrumentation errors, EMC Technology, pp. 26-35, Oct. 1982.

13. Walton, K. L., V. C. Sundberg, Broadband ridged horn design, Microwave J., Vol 7, pp. 96-101, March, 1964.

14. Kerr, J. L., Short axial length broadband horns, IEEE Trans. Antennas Propagation, Vol. AP-21, pp. 710-715, Sept., 1973.

15. Hollis, J. S., T. J. Lyon, L. Clayton, Microwave Antenna Measurements, Chapter 6, Scientific Atlanta, 1970.

16. Hockensmith, R. P., R. W. Moss, Information and Concerns Relating to Payload Susceptability to Ku-band Radiated Fields, IEEE/AIAA Conference on Payload Susceptability ot Space Shuttle Ku-band Radiated Fields, May 30, 1984.

17. Diaz, R. E., Erickson, S. A., Determination of electromagnetic fields in the Fresnel zone of the Ku-band system, Contract NAS9-14000, Rockwell International, Report #STS 82-0473, August 22, 1982.

18. Lu, Ba P., L. A. Johnson, J. R. Carl, P. M. Hopkins, Shuttle orbiter OV-099 S-band quad switch beam antenna pattern data. Lockheed Engineering and Management Services Co., Inc. Report #LEMSCO-20904, NASA JSC #EE3-84-14202.

PLASMA PARAMETERS IN THE VICINITY OF THE SHUTTLE ORBITER

by

Alan C. Tribble

A thesis submitted in partial fulfillment
of the requirements for the Master
of Science degree in Physics
in the Graduate College of
The University of Iowa

May 1986

Thesis supervisor: Professor Nicola D'Angelo

Graduate College
The University of Iowa
Iowa City, Iowa

CERTIFICATE OF APPROVAL

MASTER'S THESIS

This is to certify that the Master's thesis of

Alan C. Tribble

has been approved by the Examining Committee for the thesis requirement for the Master of Science degree in Physics at the May 1986 graduation.

Thesis committee: _____
Thesis supervisor

_____
Member

_____
Member

ACKNOWLEDGMENTS

I wish to thank my advisor Professor Nicola D'Angelo, for his numerous helpful comments concerning the preparation of this manuscript. His suggestions regarding the presentation of the data often aided me in gaining a better understanding of the physics involved. The other members of my committee, Professors Goertz and Merlino, also deserve special mention. In addition, I appreciate the time spent by Gerald Murphy and Jolene Pickett helping to familiarize me with the data reduction process. Thanks are also due Alice Shank for typing this thesis.

ABSTRACT

Plasma parameters in the vicinity of the Space Shuttle are studied using a Langmuir probe on the University of Iowa's Plasma Diagnostics Package. First, we examine electron density, temperature, and plasma potential as well as their dependence on the attitude of the orbiter. We then examine density fluctuations in the ambient ionosphere, in the wake of the orbiter, and during an OMS burn.

TABLE OF CONTENTS

LIST OF TABLES

LIST OF FIGURES

I. INTRODUCTION

The Plasma Diagnostics Package

The region of the Earth's atmosphere higher than 60 km above the surface is chiefly composed of negatively charged electrons and positively charged ions commonly called a plasma. A spacecraft moving through this region of the atmosphere, traditionally referred to as the ionosphere, disturbs the plasma in much the same way water is disturbed by a boat sailing on its surface. Spacecraft have been flying through this region of the Earth's atmosphere for over 25 years, but there have been few opportunities to study the wake generated in the plasma. Many scientific and engineering investigations are underway which will use the Space Shuttle as a platform for experiments in the Earth's ionosphere. Therefore, it is essential that we understand the environment near the orbiter since the orbiter's wake or any electromagnetic emissions from the orbiter may have an effect on in situ observations.

For this reason the Plasma Diagnostics Package (PDP) was built by the University of Iowa Department of Physics and Astronomy under the direction of Professor Stanley D. Shawhan. The PDP contains fourteen instruments which can make measurements of magnetic and electric fields, particle distributions, radio waves, as well as plasma

composition, density, and temperature. In addition to making measurements of the ambient medium, the PDP can be teamed with other experiments to perform " active" experiments. For example, the PDP can be used to measure changes deliberately provoked by the operation of the Fast-Pulse Electron Gun, which is part of the Vehicle Charging and Potential experiment (VCAP).

The PDP has flown on two shuttle missions. First, in March of 1982 the PDP took part in the third shuttle flight as one of the experiments on the Office of Space Science payload, the OSS-1 mission. After returning to Earth, the PDP was modified and took part in the Spacelab-2 flight in July of 1985. For the remainder of this thesis note that all data taken during March, i.e., on day 083, 084, etc., is from the OSS-1 mission. All data taken during July or August, i.e., on day 211, 212, etc., is from the Spacelab-2 mission. The altitude for the OSS-1 mission averaged 240 km while the altitude for the Spacelab-2 mission averaged 380 km. The angle of inclination for the OSS-1 mission was 38°, for the Spacelab-2 mission the angle was 49.5°.

During landing and re-entry the PDP is stowed on a pallet in the orbiter's cargo bay. Over the course of each mission, several hours of data were obtained from this location which yielded a good deal of information about conditions in the bay. In addition, on both missions the crew maneuvered the Remote Manipulation System (RMS), the arm of the shuttle, to grapple the PDP, unlatch it, and moved it

around in predetermined sweeps to map the orbiter's environment near the cargo bay and out to 15 m distance. On Spacelab-2 the PDP was released as a spin-stabilized sub-satellite while the orbiter executed a complex series of maneuvers around it at distances up to 200 m. As the two slowly separated, the PDP was able to make more distant measurements of the orbiter's fields.

At this time plans are currently underway to construct the Recoverable Plasma Diagnostics Package (RPDP). The RPDP will be designed to be released from the orbiter for days at a time so that a great deal of in situ observations can be made of the ambient ionosphere. The RPDP is expected to make its first flight sometime around 1990.

Operation of the Langmuir Probe

The Langmuir probe on the PDP is a relatively simple instrument which has two operational modes. In the first mode the probe can determine the electron density, temperature, and plasma potential. In the second mode the probe can observe density fluctuations over a wide frequency range. The probe that was part of the OSS-1 mission was a 6 cm diameter gold-plated spherical sensor mounted on a fixed boom approximately 30 cm from the body of the PDP (see Figure 1). The probe on the Spacelab-2 mission was a 3 cm diameter gold-plated sphere mounted on a moveable boom. When deployed the probe is 78.53 in from the center of the PDP, this is shown in Figure 2. The probe can measure density fluctuations in the frequency range 0 to 178 kHz,

plasma densities from 10^3 to 10^7 electrons/cm^3, and plasma temperatures from about 1000 K to 5000 K.

The electronics that control the probe's operation alternate between two different modes, one complete cycle requires 12.8 seconds. The first is an 11.8 second lock mode. During this time the Langmuir probe is biased at +10 volts relative to the PDP chassis. The lock mode is followed by a 1 second sweep mode where the voltage is swept from +10 volts to -5 volts in increments of 0.125 volts. The performance characteristics of the probe are listed in Table 1.

During the lock mode the probe measures density fluctuations in the following manner. The probe is sampled 120 times a second to see how much charge has accumulated. In this way we are able to obtain the charge collected as a discrete function of time. By taking the Fast Fourier Transform (FFT) of these data, we obtain current fluctuations as a function of frequency. The output is then sampled through three filters: 1 Hz low pass; 1 - 6 Hz bandpass; and 6 - 40 Hz bandpass. The sample rates of the filters are 5 Hz, 20 Hz, and 120 Hz, respectively. A fourth filter (30 Hz high pass) routes the output to a wideband receiver and spectrum analyzer which can look at details of the current fluctuations up to a frequency of 178 kHz. However, data from the fourth filter will not be presented here.

During the sweep mode the data collected by the probe is sent through a 0 - 50 Hz bandpass filter and can be used to determine the electron density, temperature, and the plasma potential. From

elementary plasma physics we know the effect of introducing a potential, such as a point charge or a probe, into a plasma. If we make the assumption that the mobility of the ions can be neglected in comparison to the mobility of the electrons, then, as done by Nicholson [1983], the potential around a test charge q is given by

$$V(r) = \frac{q}{r} \exp\left(\frac{-r}{\lambda_e}\right) \quad ,$$

where

$$\lambda_e = \left(\frac{T_e}{4\pi n_0 e^2}\right) \quad .$$

T_e is the electron temperature and λ_e is the Debye length for electrons. Because the potential falls off so rapidly as r increases, electrons or ions further than one Debye length away from the probe will be virtually unaffected by the probe's presence. If we apply a large positive bias to the probe, we can expect to attract all of the electrons and repel all of the ions within one Debye length of the probe. We can compute the current collected by the probe in the following manner.

If the radius of the probe is much larger than the Debye length, we may assume that all of the particles passing within one Debye length of the probe, through thermal motions, for example, will

hit the probe. If the probe is perfectly absorbing, then the current collected by the probe will be

$$I = J_r A_S \quad .$$

J_r is the random current flux and A_S is the surface area of the sheath one Debye length away from the probe. Since the radius of the probe is much larger than the Debye length, we can approximate the area of the sheath by the surface area of the probe. We now have

$$A_S = 4\pi r^2 \quad .$$

By definition,

$$J_r = Q_S \times (\text{number of particles hitting probe each second}) \quad .$$

Q_S refers to the charge of each species present in the plasma, a sum over each species in the plasma is implied. To determine the quantity in parenthesis, we can look at a differential volume element located at the edge of the sheath farthest from the probe. The particles here are far enough away from the probe that we only need consider their thermal motions. Therefore, half of the particles in this volume element would be entering the Debye sheath, half would be leaving it. We conclude that the number of particles entering the sheath each

second, i.e., the number that will eventually impact the probe, is $(N_S/2)A_S v_S$. N_S is the density of each species in the plasma and v_S is their velocity. This tells us that

$$J_r = Q_S \frac{N_S}{2} A_S v_S \quad .$$

If we assume a Maxwellian distribution, then

$$P(v) = 4\left(\frac{M_S}{2\pi kT_S}\right)^{3/2} v^2 \exp\left(-\frac{M_S v}{2kT_S}\right)$$

is the probability that a given particle will have its velocity between v and v + dv. The average velocity is given by

$$\langle v_S \rangle = \int_{-\infty}^{+\infty} v_S P(v_S) dv_S = 2\left(\frac{2kT_S}{\pi M_S}\right)^{1/2} \quad .$$

The direction of the velocity vector, for the particles entering the sheath, will be randomly distributed over 180°. Therefore, we can define the vector so that the component of velocity directed at the probe is given by $v_S \cos\theta$. When we integrate over the factor $\cos\theta$ to find the average component of velocity in the direction of the probe, we pick up a factor of 1/2 which cancels a factor of 2 in the previous expression for v_S. Therefore, when we combine this

definition of v_s with the definition of J_r, we find that the current collected by the probe is

$$I = Q_s(4\pi r^2)\,\frac{N_s}{2}\left(\frac{2kT_s}{\pi M_s}\right)^{1/2} \quad .$$

Again there is an implied sum over all the species present in the plasma.

If we apply a large positive bias voltage to the probe, we may assume that only electrons will contribute to the current collected, since the number of ions impacting the probe will be negligible. Therefore, the value of the electron current, before the probe saturates, is

$$I = -e(4\pi r^2)\,\frac{N_e}{2}\left(\frac{2kT_e}{\pi M_e}\right)^{1/2} \quad .$$

This equation is dependent on both density and temperature. However, we can make use of the Boltzmann relation from statistical mechanics. In the presence of a potential, in this case the probe, the density is given by

$$N_e = N_0 \exp\left(\frac{-eV}{kT_e}\right) \quad .$$

Plugging this into the previous equation gives

$$I = -e(4\pi r^2)\,\frac{N_0}{2}\left(\frac{2kT_e}{\pi M_e}\right)^{1/2}\exp\left(\frac{-eV}{kT_e}\right) \quad .$$

Now we have an equation involving the electron temperature and the probe bias voltage V. Taking the natural log of both sides of the equation gives

$$\ln I = \text{constant} + (\text{constant}\ \ln T_e) + \left(\frac{-e}{kT_e}\right)V \quad .$$

The ln of T_e will vary much slower than T_e itself, therefore, we may approximate ln T_e as a constant. The equation becomes

$$\ln I = \text{constant} + \left(\frac{-e}{kT_e}\right)V \quad .$$

If we graph ln I vs V, before the probe saturates, the slope will be given by $(-e/kT_e)$. Using this we have an expression for T_e,

$$T_e = \frac{-e}{k\ \text{slope}} \quad .$$

Once we have T_e we can plug this into the expression for I and deduce an expression for N_0, which is

$$N_0 = \text{constant } I\ T_e^{1/2} \quad .$$

The constant is determined if we know the radius of the probe, the mass of the electron, Boltzmann's constant, etc.

In this manner the Langmuir probe can give us the electron density and temperature. If we define the plasma potential as the bias voltage at which the probe saturates, a graph of ln I vs V will also give us the plasma potential. A typical sweep is shown in Figure 3. Note that the value of I that we use in the determination of N_0 is chosen so that V is as positive as possible without saturating the probe. For a further discussion of the theory behind Langmuir probes see, for example, Huddlestone and Leonard [1965].

II. TYPICAL DENSITIES AND TEMPERATURES

In the Ambient Ionosphere

On day 213, 1985 the PDP was released from the orbiter as a free-flying sub-satellite for about 6 hours. During this time the Langmuir probe took measurements of the plasma parameters as the orbiter backed away from the PDP and executed a series of maneuvers around it. The booms were deployed throughout free flight so that the Langmuir probe, VLF spheres, and search coil would be further from the body of the PDP. In addition to this, the PDP used a momentum wheel to cause it to spin with a period of 13.06 seconds. As is shown in Figure 4, the PDP was spinning counterclockwise if viewed from the top. The spin plane, i.e., the plane of the paper in Figure 4, was the plane in which the orbiter executed the majority of its maneuvers after releasing the PDP. The predicted position of the shuttle, relative to the PDP, is shown in Figure 5 for the time that it took the orbiter to execute one complete fly-around. The chronological sequence of events is given in Table 2.

The data taken during this first fly-around are shown in Figures 6-7. (We should first point out that the apparent "density depletion regions" that occur approximately every 9 1/2 minutes are attributed to instrumental effects and are not rapid fluctuations in

the ionospheric electron density. This effect is discussed in Appendix A.) The data reveal the daily fluctuations in electron density and temperature that we could expect to see from the orbiter. Two points are worth noting. First, the plasma potential shows little variation during the day but appears to increase after sunset. Second, the electron density appears lowest at sunrise and sunset but also appears to increase after sunset. One possible explanation for this is that the altitude at which the Spacelab-2 mission took place, 380 km, is in the F region of the Earth's ionosphere. The peak in electron density in the F region usually occurs between 250 - 300 km during the day, and about 50 km higher at night. Therefore, what we may be seeing after sunset is the peak in the electron density shifting to a higher altitude. However, while radar observations confirm that the peak of the electron density shifts to a higher altitude at night, they also show that in most cases the value of the peak density is less at night than it was during the day. Consequently, there may be other factors contributing to the increase in the electron density.

The ambient ionosphere has been studied for many years and a great deal of data has accumulated. For comparison see, for example, Hess and Mead [1968] or Kasha [1969].

Near the Orbiter's Cargo Bay

During most of the OSS-1 and Spacelab-2 missions the PDP was kept on a pallet in the orbiter's cargo bay. The location for the

OSS-1 mission is shown in Figure 8, and the location for the Spacelab-2 mission is shown in Figure 9. During the OSS-1 mission the crew of the orbiter placed the shuttle in several different attitudes designed to subject the orbiter to the most extreme temperature differences that could be expected on later flights. The four attitudes used are shown in Figure 10 and are referred to as "nose to sun," "tail to sun," "bay to sun," and "passive thermal control" or PTC. During the "nose-to-sun" and "tail-to-sun" attitudes, the bay is in the shade and is bitterly cold. The "bay-to-sun" attitude places the pallet in direct sunlight which causes the temperature to soar. PTC, also known as the barbecue mode, is designed to equalize temperatures on all surfaces.

Data obtained during the "nose-to-sun" attitude is shown in Figures 11-12. Note that in Figures 12, 14, 16 the pitch and azimuth angles are measured with respect to the plasma flow vector and not the velocity vector of the shuttle. As we can see from Figure 11 when the bay is in the ram of the plasma flow, electron densities are typically $10^6/cm^3$ and the corresponding electron temperature is less than 1000 K. However, as is discussed in Appendix B, we suspect that we are underestimating the electron temperature when the probe is in ram. Consequently, the corresponding drop in electron density by three orders of magnitude when the bay is facing the wake may be overestimated. Data obtained during PTC is shown in Figures 13-14. Here we see more vividly the effects of rolling the orbiter. Note that the

electron temperature increases in the wake of the shuttle. Similar results have been reported by Oran et al. [1975] and Samir and Wrenn [1972].

For completeness Figures 15-16 show a segment of data obtained during the "nose-to-sun" attitude when the PDP was on the RMS about 7 m above the cargo bay. Even in this position the PDP notices a decrease in the electron density as the orbiter turns so that the PDP is in the wake of the shuttle.

During the Spacelab-2 mission the orbiter executed a series of maneuvers designed to yield information about the extent of the orbiter's near wake. This series of maneuvers is referred to as XPOP (X-axis Perpendicular to Orbital Plane) roll and is described in Figure 17. The location of the PDP during this time is shown in Figure 18. During XPOP roll the orbiter rolls at a rate of 1°/second. Consequently, one complete roll requires 6 minutes. At the same time that the orbiter is rolling, the RMS can be unwound at the same rate so that the orientation of the PDP, relative to the plasma flow, remains unchanged.

Unfortunately, the software that computes the electron density and temperature was unable to make use of most of the raw data collected during XPOP roll. However, we are able to use the second point of the Langmuir probe sweep as an approximation to density. By second point of the sweep, we mean the current collected when the probe is biased at +9.875 volts. Past experience has shown that the value of

the second point of the sweep is proportional to the value of the density. Using the Orbiter Body Axis System (OBAS), a noninertial coordinate system that moves with the orbiter, we can compute the roll angle of the orbiter. The OBAS coordinate system is defined in Figure 19 and the roll angle is defined as the angle between the orbiter's velocity vector and the z-axis of the orbiter. Figure 20 shows the relationship between the interpolated electron density and the roll angle.

These data clearly indicate the presence of a density depletion region in the wake of the shuttle. The velocity of the shuttle is approximately 8 km/s. If we make the assumptions that $n_i = n_e = 10^6$ cm^{-3} and $T_i = T_e = 2500$ K then the thermal velocity of atomic oxygen is 1.1 km/s and the thermal velocity of an electron is 180 km/s. Because the electrons are moving much faster than the shuttle, they will be able to move into the region directly in the wake of the orbiter whereas the majority of the ions will be unable to do so. As a result the majority of the particles in the wake of the orbiter will be mostly electrons and this will be a region of negative potential. This negative potential will prevent other electrons from reaching the wake, consequently, the electron density in the near wake of the shuttle will be lower than the electron density in ram. The density depletion region is also associated with enhanced electron temperatures. As postulated by Samir and Wrenn [1972], this temperature enhancement may be due to wave-particle interactions that apply

an energy-filtering mechanism to the electrons that enter the region. One other possible explanation would be heating through adiabatic compression.

We have now given an overview of the characteristic plasma parameters that the Langmuir probe can measure in the vicinity of the shuttle. The next chapter will deal with an examination of how rapidly these parameters fluctuate.

III. DENSITY FLUCTUATIONS

In the Ambient Ionosphere

As was mentioned in Chapter I, when the Langmuir probe is in the lock mode, we are able to use it to determine the current collected by the probe as a function of frequency. Data obtained during the first 15 minutes of free flight, which occurred during the Spacelab-2 mission, is shown in Figure 21. As shown in Table 2, the PDP was released from the orbiter at 0010 on day 213. The 0 - 1 Hz channel remains relatively constant at about 1 volt until this time. After release the voltage rises rapidly for about 10 minutes before finally leveling off at about 0020. This indicates that there is an increase in the DC current collected by the probe as the shuttle backs away from it. This is to be expected because when the PDP was attached to the RMS, it was directly in the wake of the orbiter. However, as the orbiter moves away the density of the plasma near the PDP increases slightly. The voltage from the 1 - 6 Hz filter remains constant after the release of the PDP. However, there is a marked increase in the turbulence in this channel when the PDP is no longer grounded to the orbiter. After its release the PDP used a momentum transfer wheel to spin up so that it would rotate with a period of 13.06 seconds. The turbulence in the 1 - 6 Hz channel exhibits a

periodicity that leads us to suspect that it is related to the spin of the PDP. That is, the turbulence is either a maximum or minimum depending on the orientation of the PDP relative to the plasma flow. The 6 - 40 Hz channel was not shown because it shows similar turbulence during this time. It is believed that this turbulence is actually interference from another instrument on the PDP. This is the same interference alluded to in Chapter II, and an explanation for it is offered in Appendix A. We believe that we can attribute most if not all of the turbulence in the 1 - 6 Hz and 6 - 40 Hz channels to this interference. Therefore, we conclude that the PDP sees very little turbulence in the ambient ionosphere during free flight. The most notable difference is an increase in the DC current collected by the probe. This is due to the fact that the PDP is no longer in the electron density depletion region found in the orbiter's wake.

We should note that Rubin and Besse [1986] have reported that a free-flying satellite, such as the PDP, could charge to a potential of -1400 volts in the wake of the orbiter. If this potential were distributed nonuniformly over the surface of the PDP, it could produce a surface discharge. However, this does not appear to have caused any problems during free flight.

During XPOP Roll

In Chapter II we explained the attitude known as XPOP roll. A set of data for ten wake crossings was obtained on day 212 when the orbiter was in this attitude and shows us the turbulence associated

with the wake of the orbiter. The raw data are shown for two wake crossings in Figure 22. In both cases we see that there is very little turbulence when the PDP is exactly in the wake of the shuttle. However, we see a good deal more turbulence when the PDP passes from the wake of the orbiter into the ram of the plasma flow and vice versa. This may be due to the presence of the negative potential well in the wake of the shuttle. When the probe is exactly in the wake of the the orbiter, at 180°, there will be very few ions present to affect current collection by the probe. However, as we pass into the ram of the plasma flow, the probe will be bombarded by the ions that are flowing past the bay doors on the shuttle. The presence of this ion-density gradient on either side of the geometrical wake of the shuttle is responsible for turbulence which causes the data to look noisier.

We can also point out that the data for both of the wake crossings look noisier when the probe moves from the wake of the orbiter to the ram of the plasma flow than the other way around. This may be due to the $\vec{v} \times \vec{B}$ force on the ions. Using the OBAS coordinate system, we can compute the magnitude of $\vec{v} \times \vec{B}$ as shown in Figure 23. Note that the charge on the ions/electrons has not been included nor has the factor 1/c. In this figure $\vec{v}$ was taken to be the velocity of the shuttle. However, if we want the force on the ions, we can make use of the fact that the velocity of the ions is comparable to the velocity of the shuttle. Therefore, the majority of the ions

contributing to the turbulence near the wake of the shuttle will be ions moving with their velocity vectors antiparallel to the velocity of the shuttle. Therefore, the $\vec{v} \times \vec{B}$ force on these ions will be in the direction of the positive y-axis during the time that the Langmuir probe is in the wake of the shuttle. Consequently, the turbulence in the negative y-direction has been minimized because the force on the ions that pass the shuttle on this side elongates the ion-density gradient. That is, the force due to $\vec{v} \times \vec{B}$ is in the same direction as the force due to the negative potential well. The turbulence in the positive y-direction is magnified because the $\vec{v} \times \vec{B}$ force opposes the force due to the negative potential well and effectively compresses the density gradient. Other factors, such as the $\vec{E} \times \vec{B}$ drift, will also affect the shape of the orbiter's wake.

After an OMS Burn

During the Spacelab-2 mission a ground-based experiment was conducted to investigate the effects of an OMS (Orbiter Maneuvering System) burn on the plasma cloud surrounding the orbiter. On day 216, 1985 the orbiter conducted a 6 second OMS burn over the radar observatory at Millstone Hill, Massachusetts, starting at 19:14:44. The PDP was located in the bay of the shuttle during this time and made in situ observations of the effects of the burn. The raw data are shown in Figure 24. The data from the 0 - 1 Hz filter shows us that there was a rapid drop in the voltage sent to this filter as the burn started. However, the burn significantly affects this channel only

for about 15 seconds, although there appears to be residual affects which last up to 90 seconds after completion of the burn. The 1 - 6 Hz filter shows an increase in turbulence during and immediately after the burn, although the majority of the turbulence subsides after about 15 seconds here as well. The 6 - 40 Hz filter is essentially saturated during the first 15 seconds after the burn, and it takes another 90 seconds after the burn has stopped for the turbulence to return to the level that it was at before the burn. Therefore, it seems reasonable to conclude that the turbulence associated with an OMS burn affects all three channels for at least 90 seconds after the OMS engines were shut off. The 6 - 40 Hz channel suggests that the decay in the turbulence is roughly exponential. If so, the time required for turbulence to decrease by a factor of 1/e is approximately 30 seconds. It is quite possible that the wideband data, which shows us oscillations up to a frequency of 178 kHz, would indicate that the OMS burn induces most of its turbulence at even higher frequencies. However, the wideband data have yet to be examined.

IV. SUMMARY

In conclusion, we have seen that the Langmuir probe on the PDP has made in situ observations of the ambient ionosphere. These observations are in general agreement with previous studies. However, the electron density enhancement that is seen immediately after sunset still lacks a complete explanation. Data taken from the bay of the shuttle indicate a density depletion region in the wake of the shuttle. This density depletion region forms because the electrons are able to "fill in" the near wake of the shuttle more rapidly than the ions. This produced a region of negative potential and, consequently, a region of electron density depletion and enhanced electron temperatures. Explanations for the elevated electron temperatures have been offered by several authors and three realistic possibilities are:

(i) Hot electrons result from a selection effect by the negative potential found in the wake.

(ii) Electrons may be energized by wave-particle interactions in the turbulent region.

(iii) Adiabatic compression of electrons as they enter the region of negative potential results in thermal excitation.

The density fluctuation data reveal that the orbiter's wake is not totally symmetric. Several factors may contribute to this, for example, $\vec{v} \times \vec{B}$ forces and $\vec{E} \times \vec{B}$ drifts. These data also indicate that there is a great deal of turbulence in the bay of the shuttle following an OMS burn. This turbulence is greatest in the 6 - 40 Hz channel and appears to decay exponentially.

Table 1

Performance Characteristics of the Langmuir Probe

Current Sensor	0.1 μa - 1 ma
T_e	(800 - 5000) °K
n_e	$(10^3 - 10^7)$ cm^{-3}
ΔN/N	
< 1 Hz	1.8% - 460%
1 - 6 Hz	0.12% - 30%
6 - 40 Hz	0.012% - 3%
> 30 Hz (spectrum analyzer)	-30 dB ΔN/N to -80 dB ΔN/N

Table 2

Free-Flight Sequence of Events

Point	GMT	Event Description
1	213/00:10	Deploy and Separation
2	213/00:34	Establish Stationkeeping at 300 feet
3	213/00:52	Begin Electromagnetic Interference Tests
4	213/01:37	Burn to out-of-plane point 1
5	213/01:47	Out-of-plane point 1 midcourse burn
6	213/01:57	Burn to Flux Tube connection
7	213/02:02	Flux Tube connection
8	213/02:04	Burn to Phantom point 1
9	213/02:16	Burn to Flux Tube connection
10	213/02:35	Midcourse burn, lower Flux Tube 1
11	213/02:40	Flux Tube connection
12	213/02:42	Burn to wake transit 1
13	213/02:49	Midcourse burn, wake transit 1
14	213/02:58	Begin wake transit 1
15	213/03:04	Midpoint of wake transit 1

A-G85-598

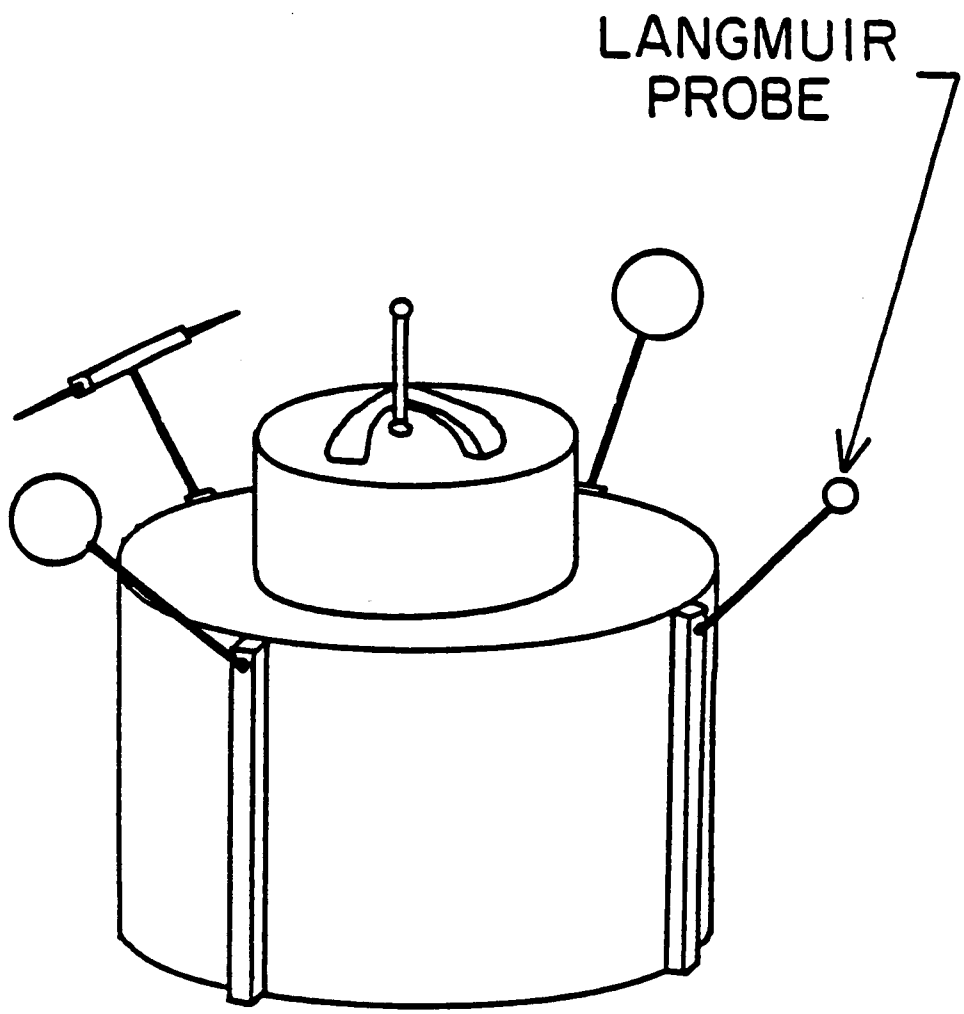

Figure 1. The PDP for the OSS-1 mission.

PDP BOOMS DEPLOYED CONFIGURATION

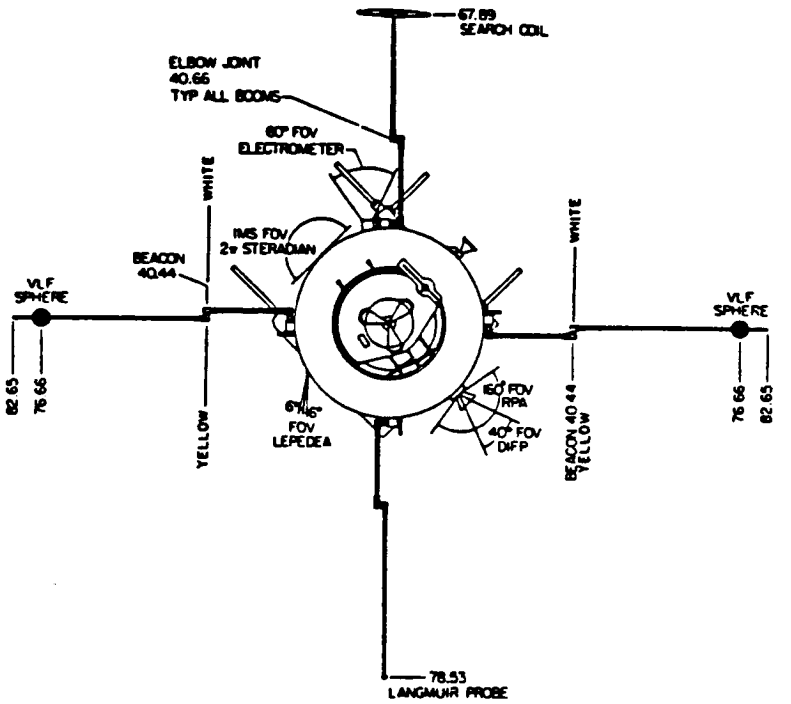

TOP VIEW

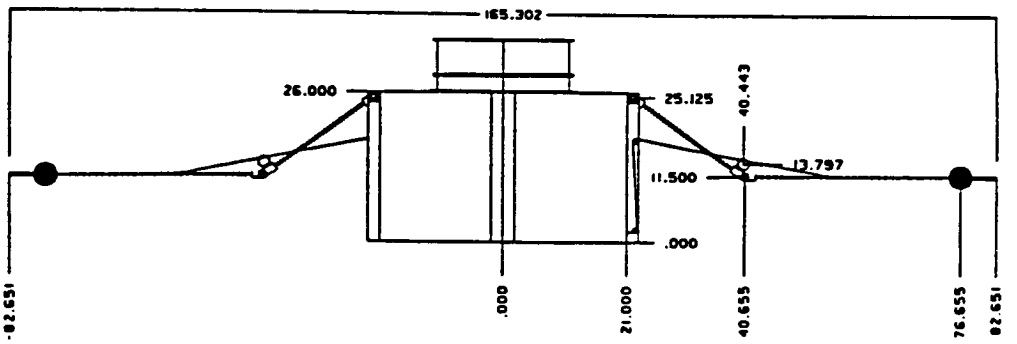

SIDE VIEW

Figure 2. The PDP for the Spacelab-2 mission. The scale is marked in inches.

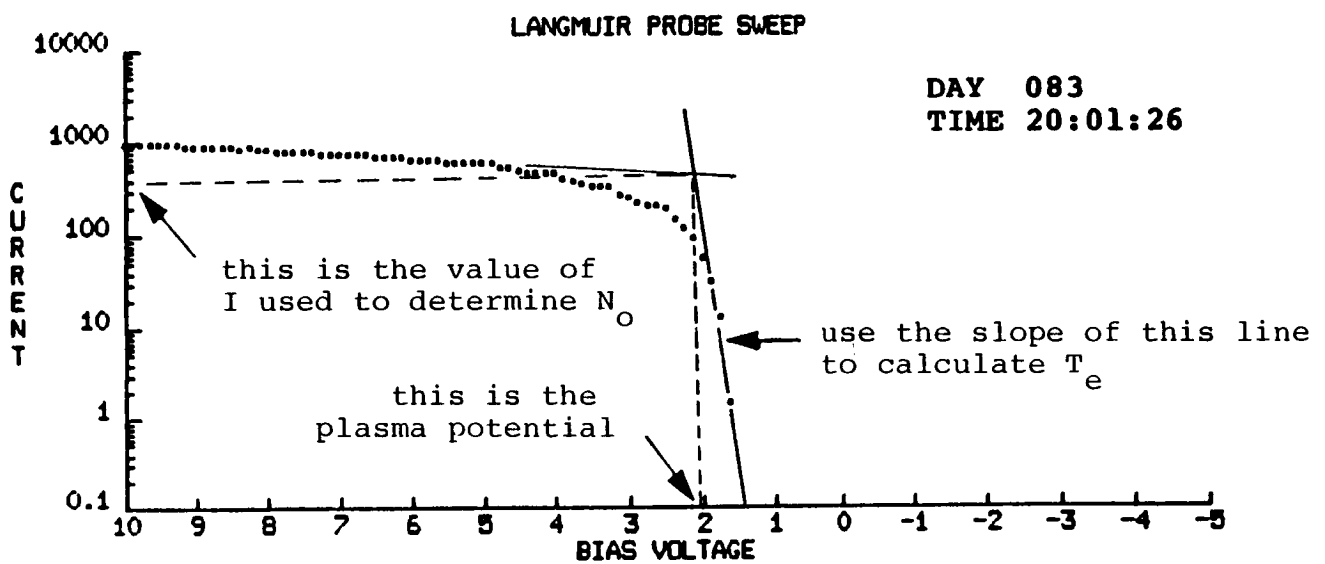

Figure 3. A typical Langmuir probe sweep. The current is in microamperes.

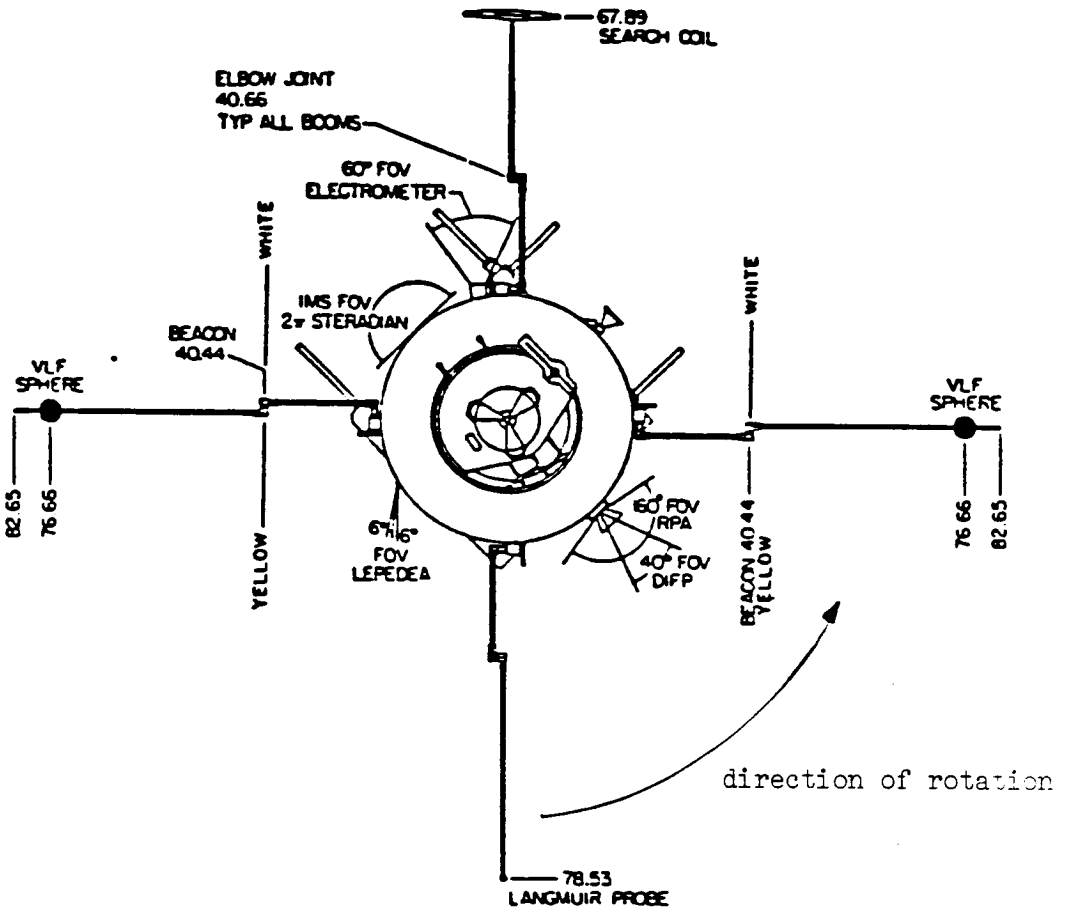

TOP VIEW

Figure 4. The rotation of the PDP during free flight.

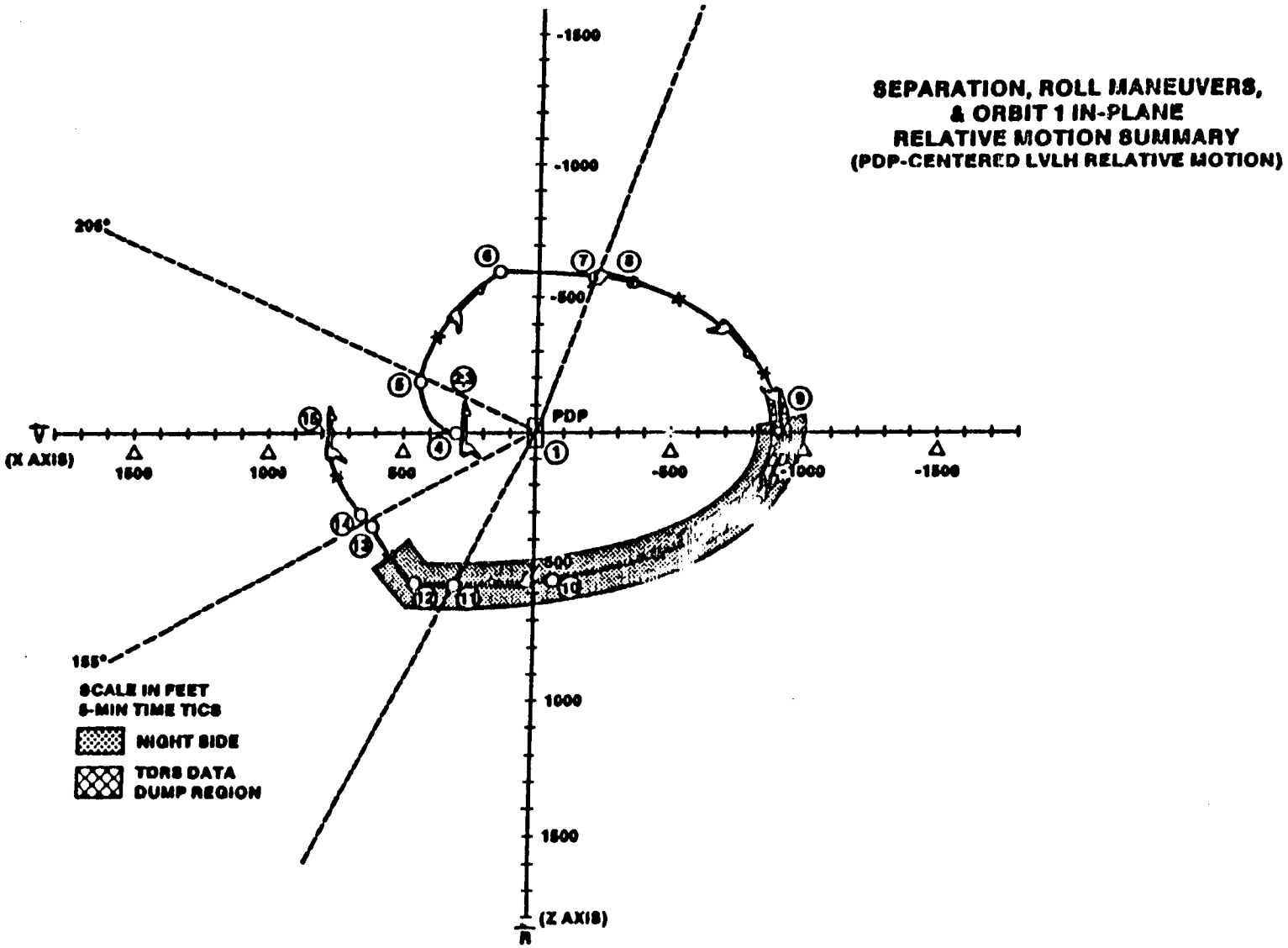

Figure 5. Position of the Shuttle, relative to the PDP.

SPACELAB-2 DATA

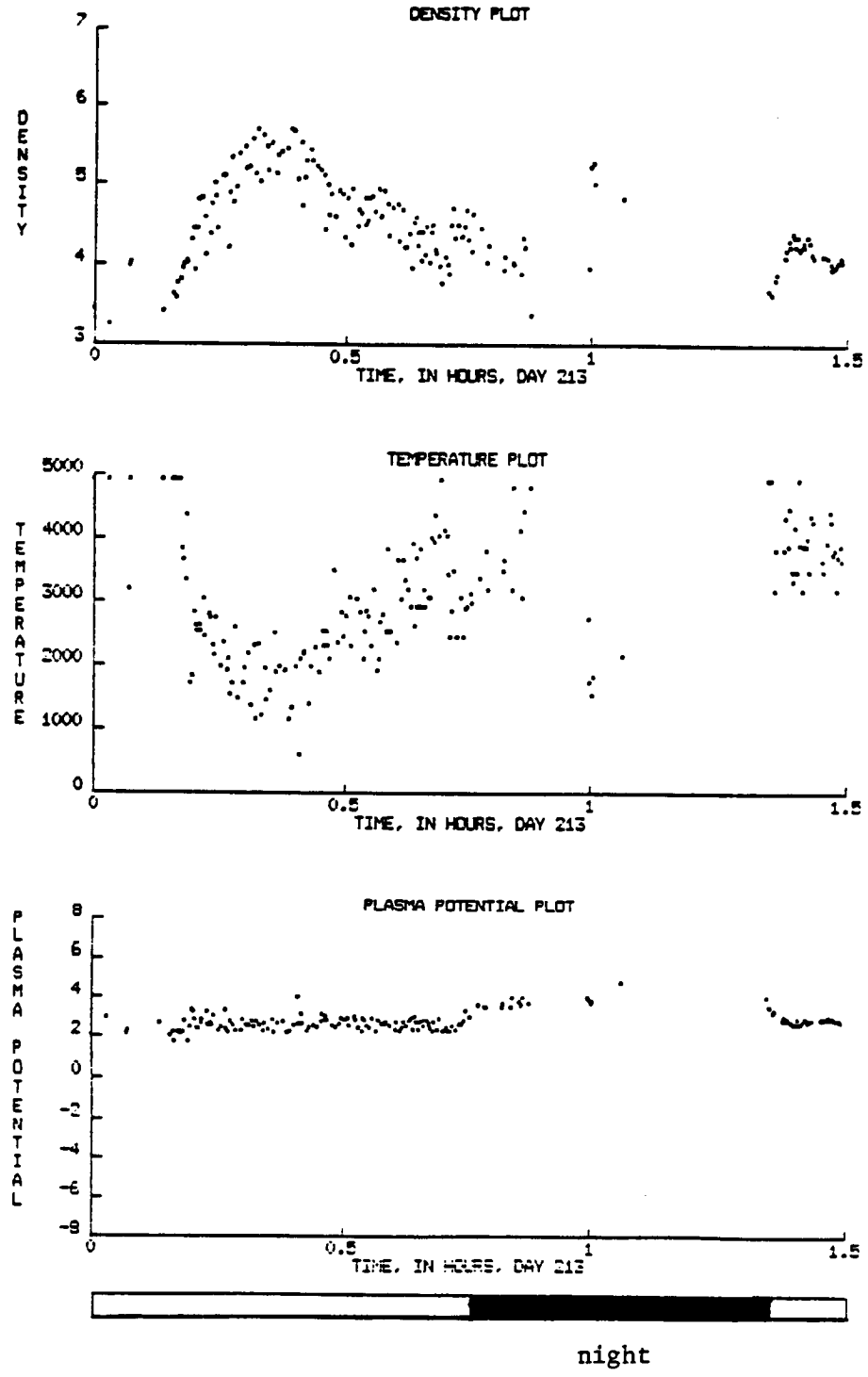

Figure 6. Free-flight densities and temperatures.

SPACELAB-2 DATA

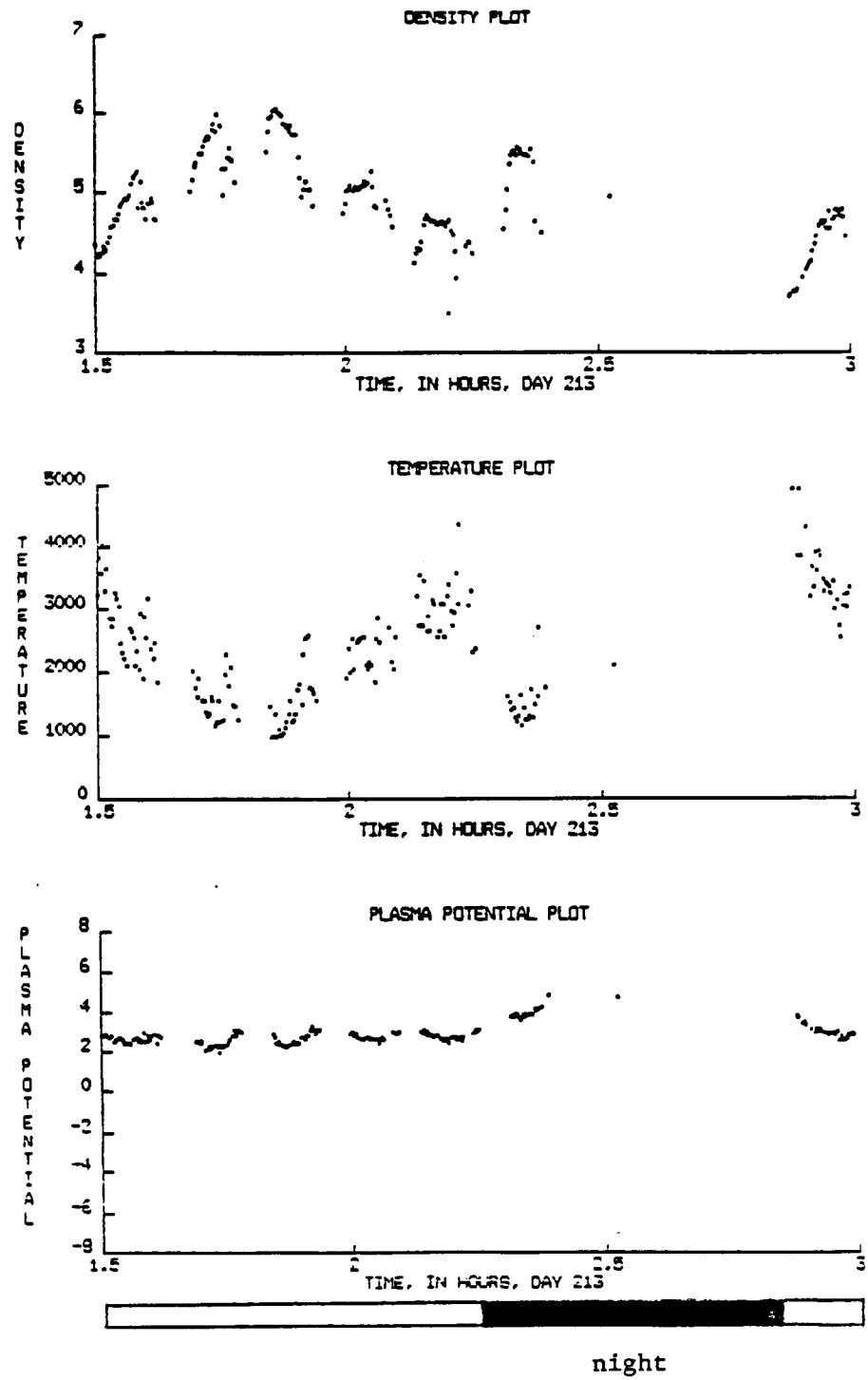

Figure 7. Free-flight densities and temperatures.

A-G83-851-1

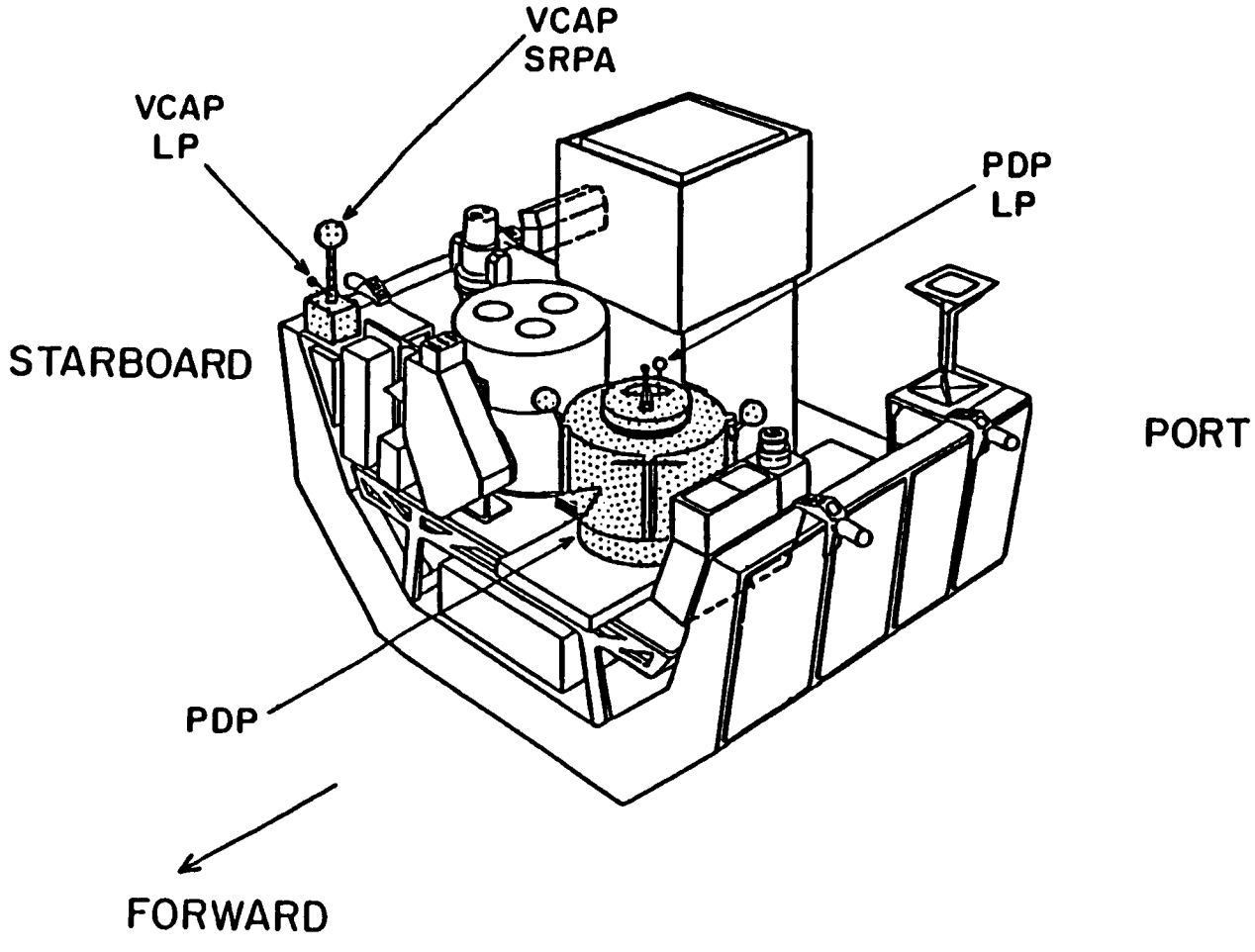

Figure 8. The pallet for the OSS-1 mission.

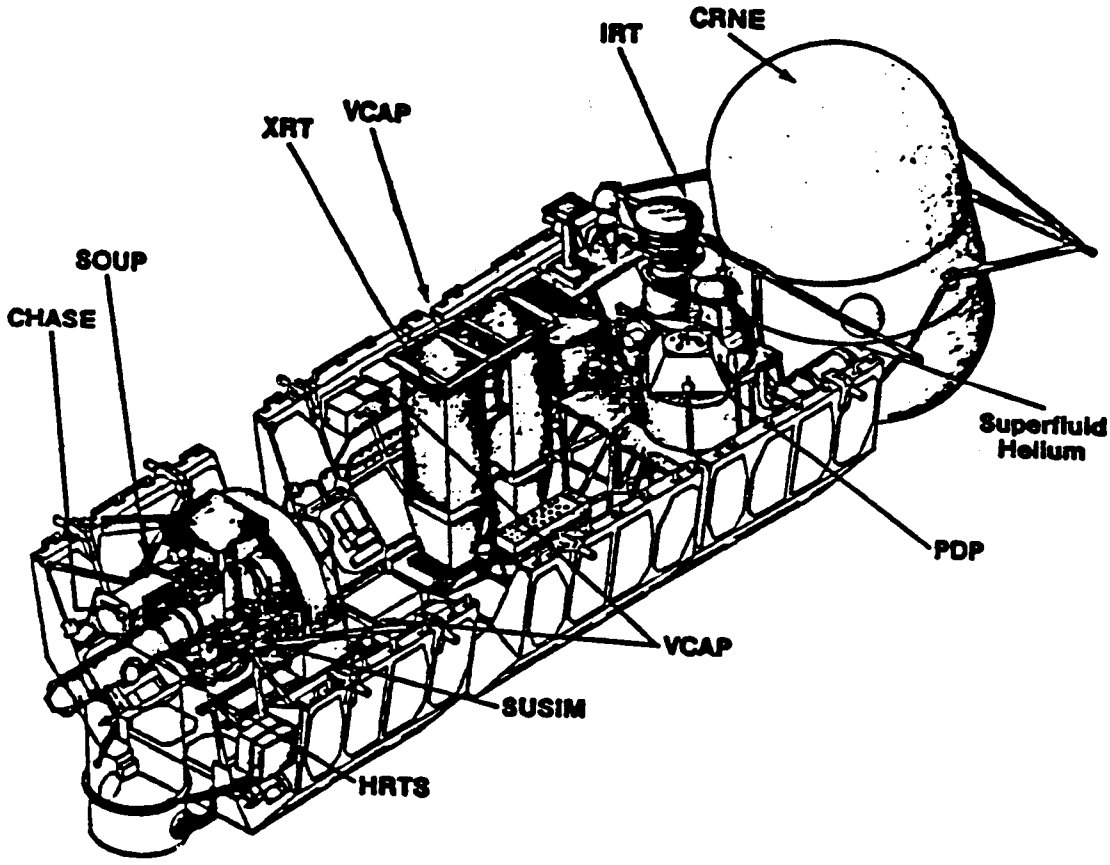

Figure 9. The pallet for the Spacelab-2 mission.

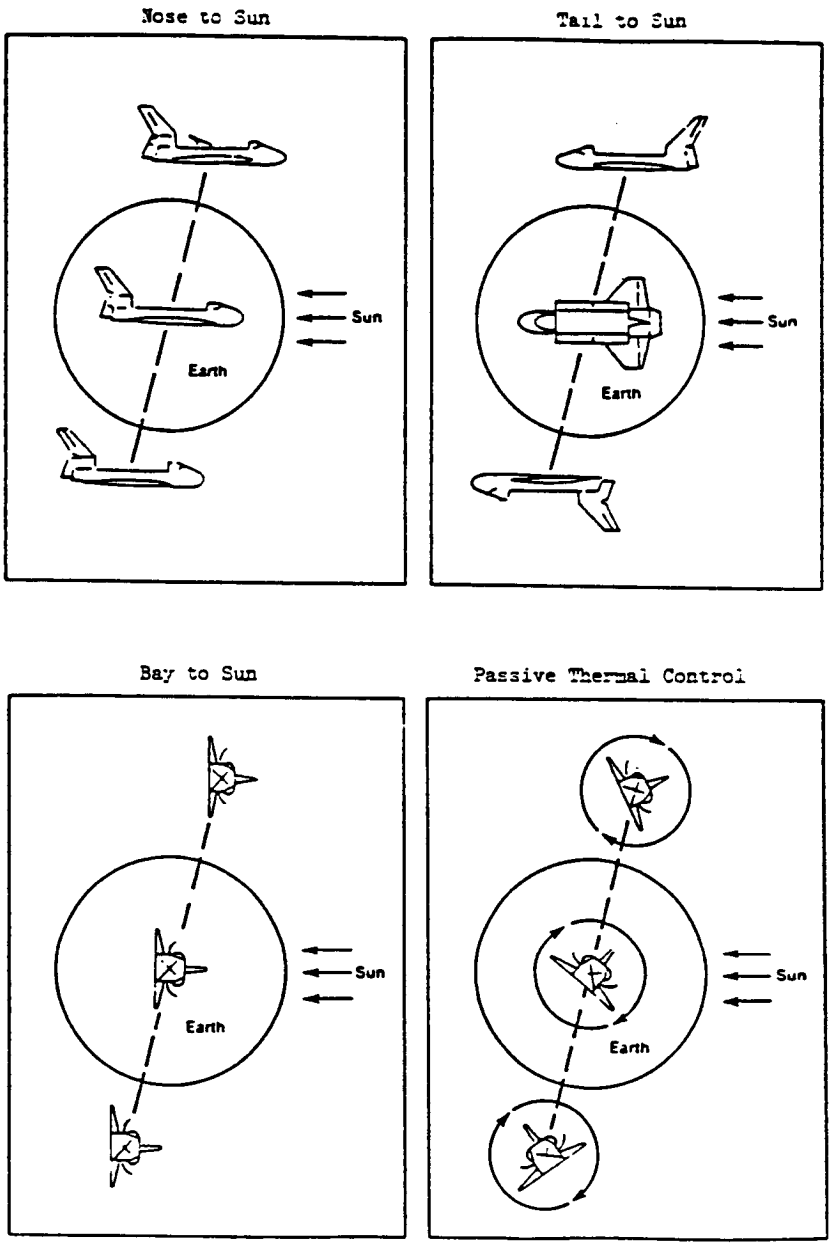

Figure 10. Shuttle attitudes.

OSS-1 DATA

PDP LOCATION: ORBITER BAY

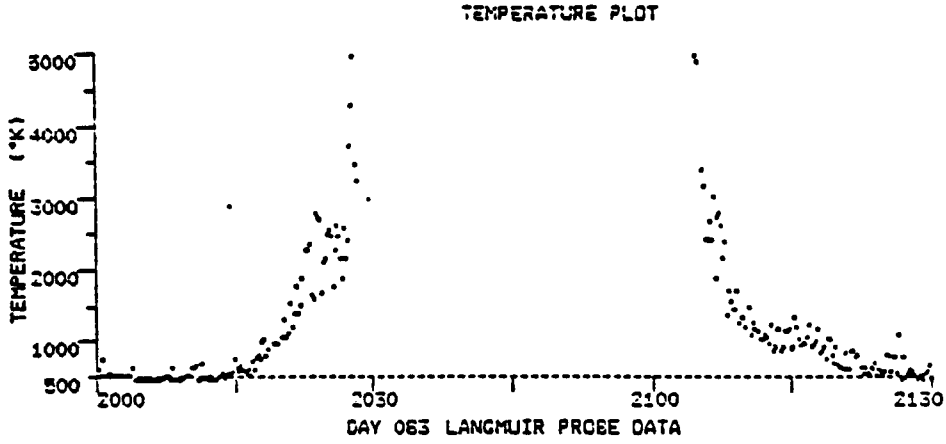

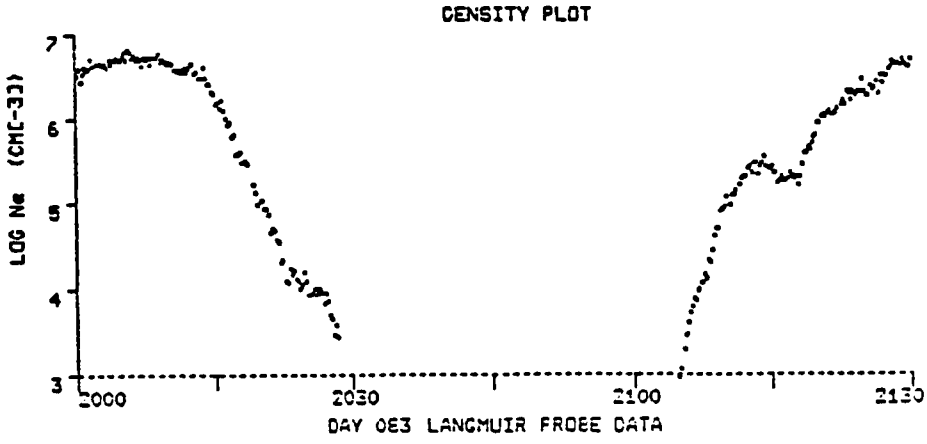

OTHER EVENTS OF INTEREST: Electron Gun Firings, 2013-2029
2059-2101
2126-2128

Figure 11. "Nose-to-Sun" data, PDP in cargo bay.

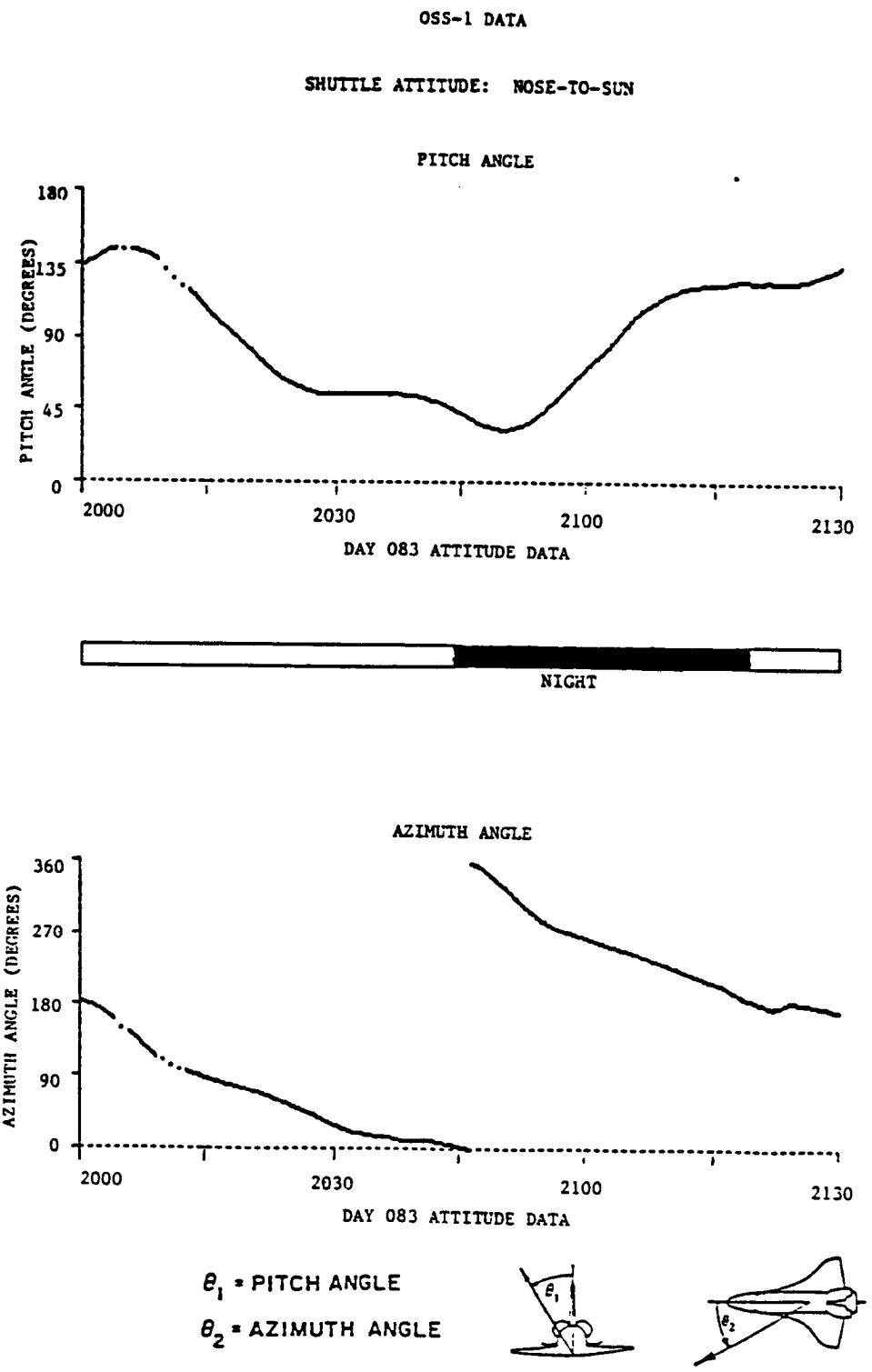

Figure 12. "Nose-to-Sun" data, attitude timeline, PDP in cargo bay.

OSS-1 DATA

PDP LOCATION: ORBITER BAY

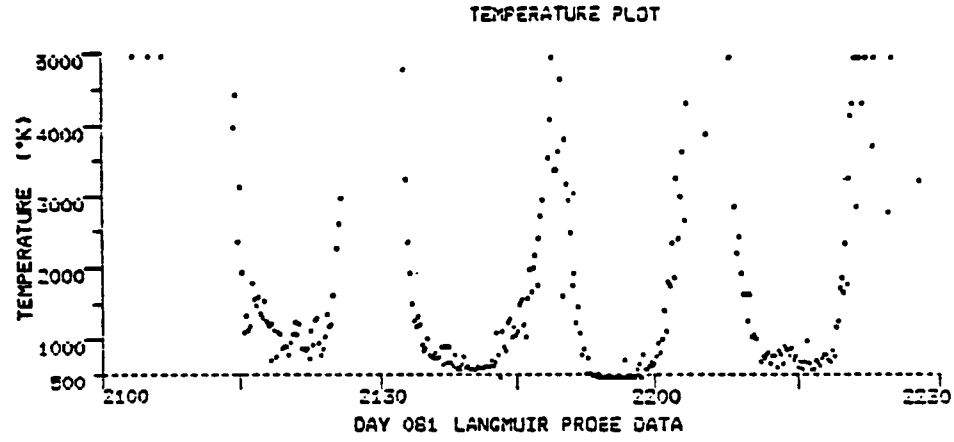

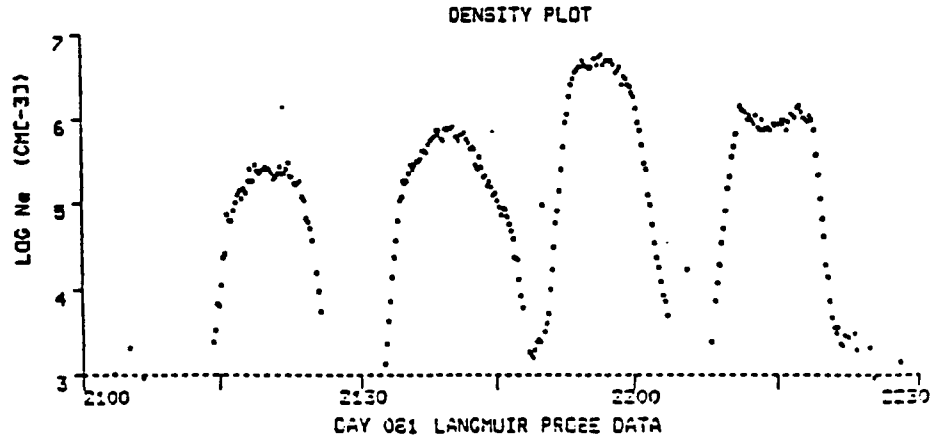

Figure 13. "PTC" data, PDP in cargo bay.

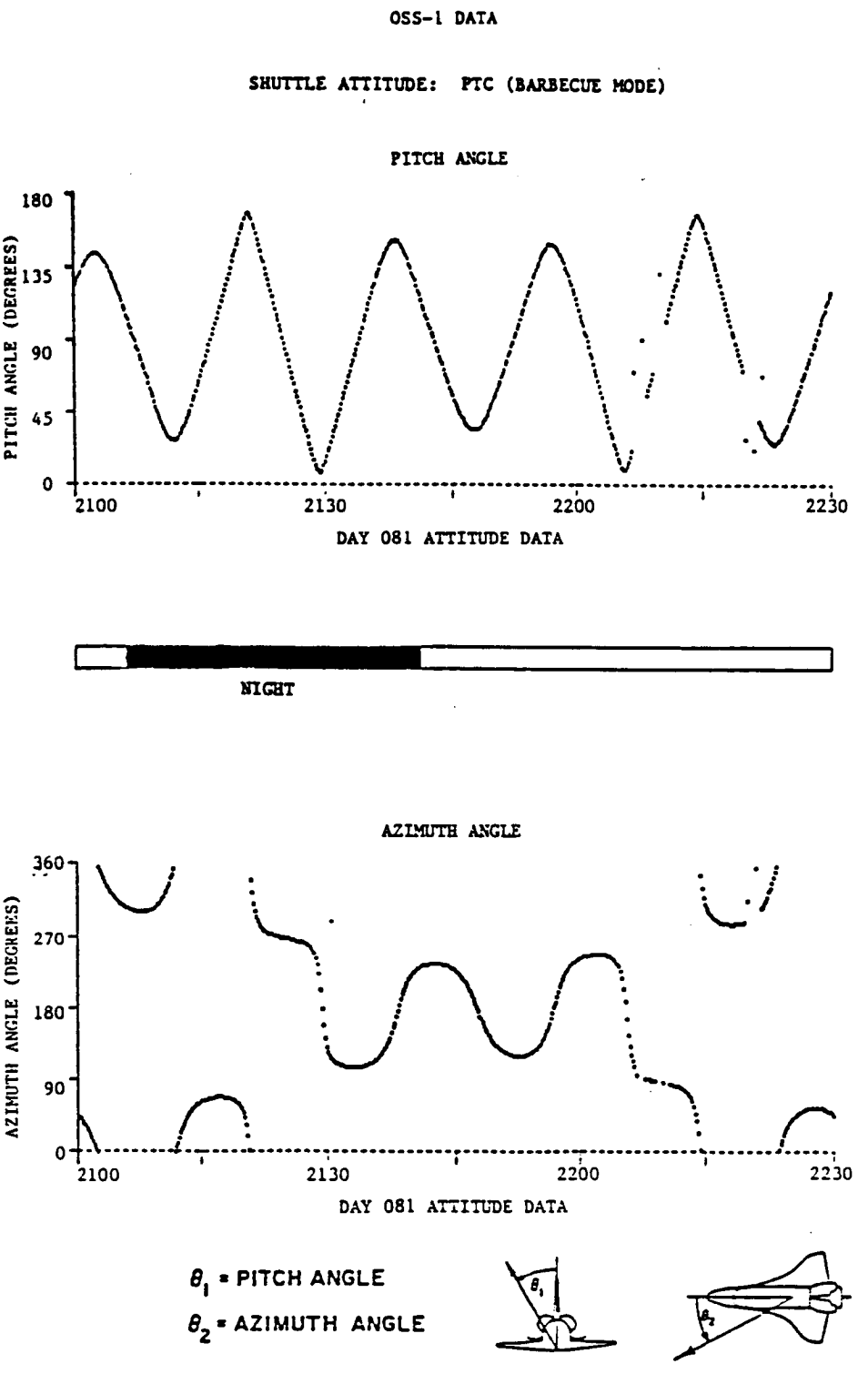

Figure 14. "PTC" attitude timeline, PDP in cargo bay.

OSS-1 DATA

PDP LOCATION: REMOTE MANIPULATOR SYSTEM ARM

TEMPERATURE PLOT

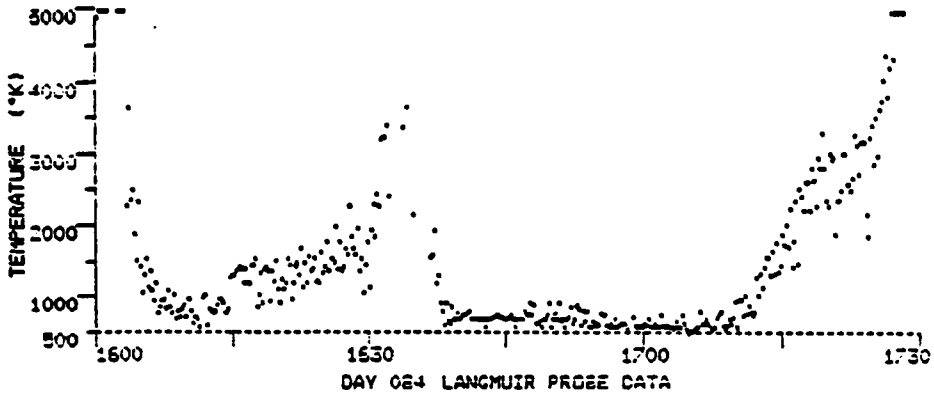

DENSITY PLOT

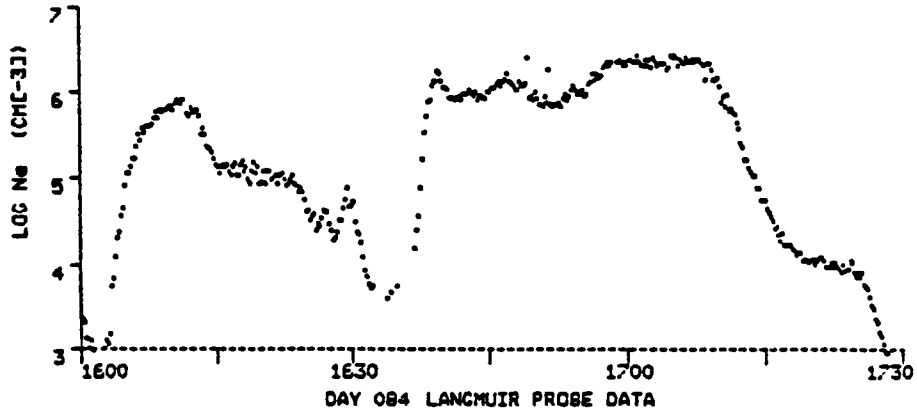

OTHER EVENTS OF INTEREST: Electron Gun Firings, 1653-1710

Figure 15. "Nose-to-Sun" data, PDP on RMS.

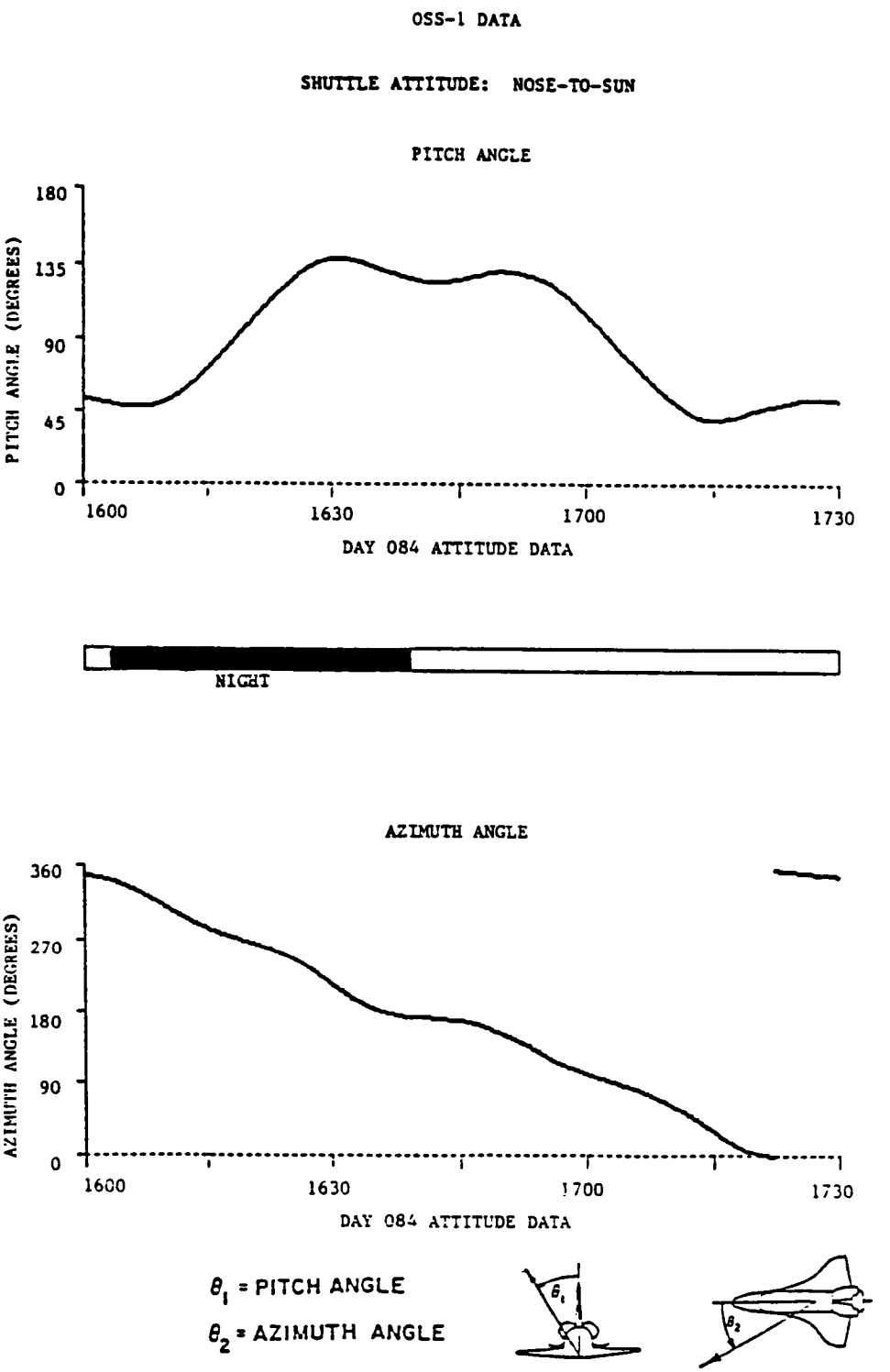

Figure 16. "Nose-to-Sun" attitude timeline, PDP on RMS.

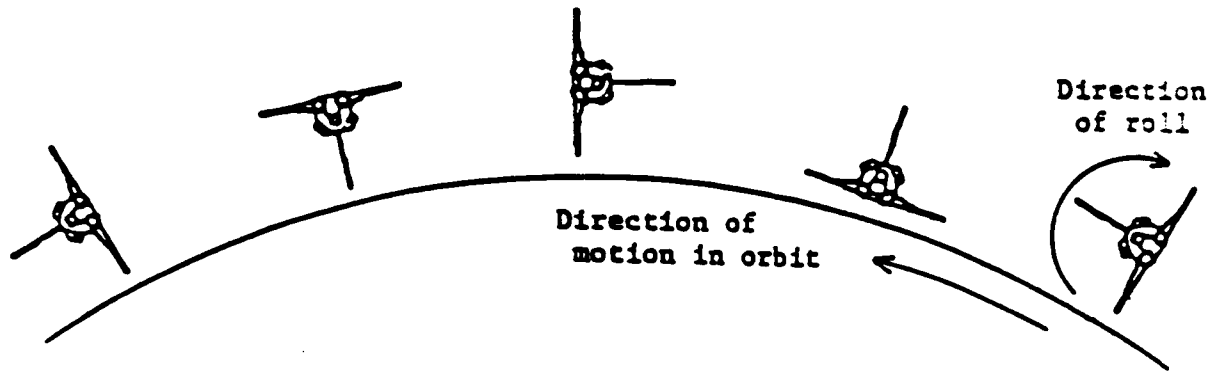

Figure 17. XPOP Roll. Attitude: XPOP Roll (note: tail out of page). Specifics: 0.933°/second retrograde roll around x-axis. x-axis remains perpendicular to the orbit plane. It takes 6 minutes to complete one roll. A total of 10 rolls is made over 1 hour of time. Characteristics: Used to study azimuthal dependence of wake structure.

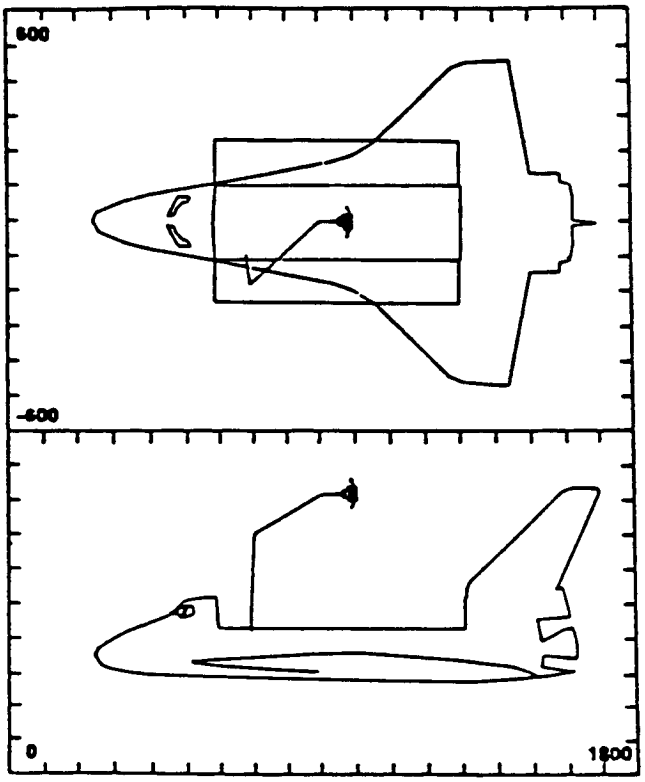

Figure 18. The location of the PDP during XPOP Roll. The scale is marked in inches.

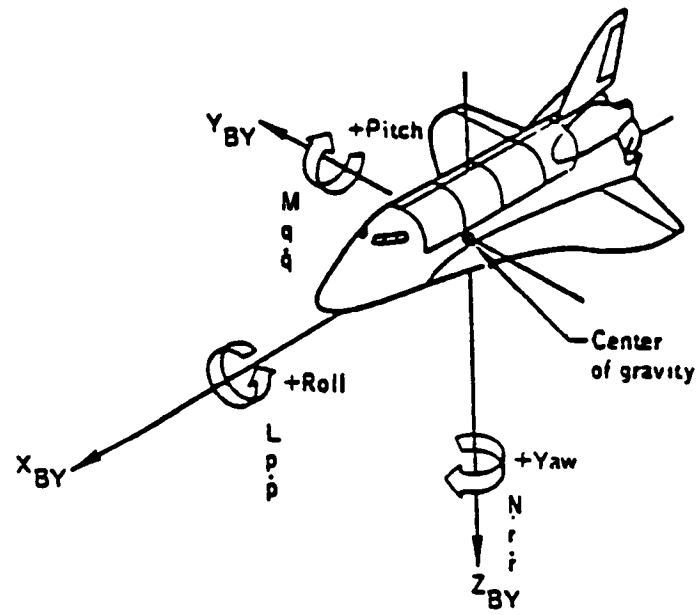

Figure 19. The Orbiter Body Axis System (OBAS). Origin: Center of mass (X = -1100", Y = 0", Z = -370"). Orientation: X_{BY} axis is parallel to the orbiter structural body X_O axis; positive toward the nose. Z_{BY} axis is parallel to the orbiter plane of symmetry and is perpendicular to X_{BY}, positive down with respect to the orbiter fuselage. Y_{BY} axis completes the right-handed orthogonal system. Characteristics: Rotating, right-handed, Cartesian system. L, M, N: Moments about X_{BY}, Y_{BY}, and Z_{BY} axes, respectively. p, q, r: Body rates about X_{BY}, Y_{BY}, and Z_{BY} axes, respectively. $\dot{p}$, $\dot{q}$, $\dot{r}$: Angular body acceleration about X_{BY}, Y_{BY}, and Z_{BY} axes, respectively. The Euler sequence that is commonly associated with this system is a yaw, pitch, roll sequence, where ψ = yaw, θ = pitch, and ϕ = roll or bank. This attitude sequence is yaw, pitch, and roll around the Z_{BY}, Y_{BY}, and X_{BY} axes, respectively.

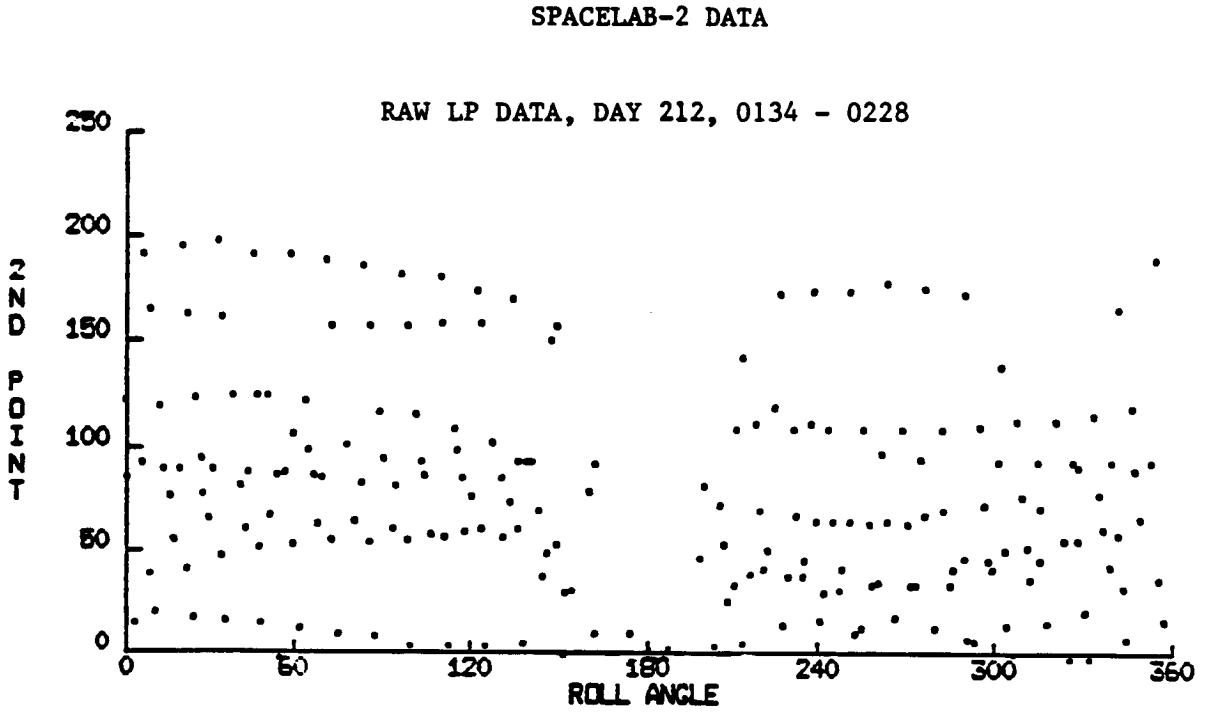

Figure 20. Electron density vs roll angle.

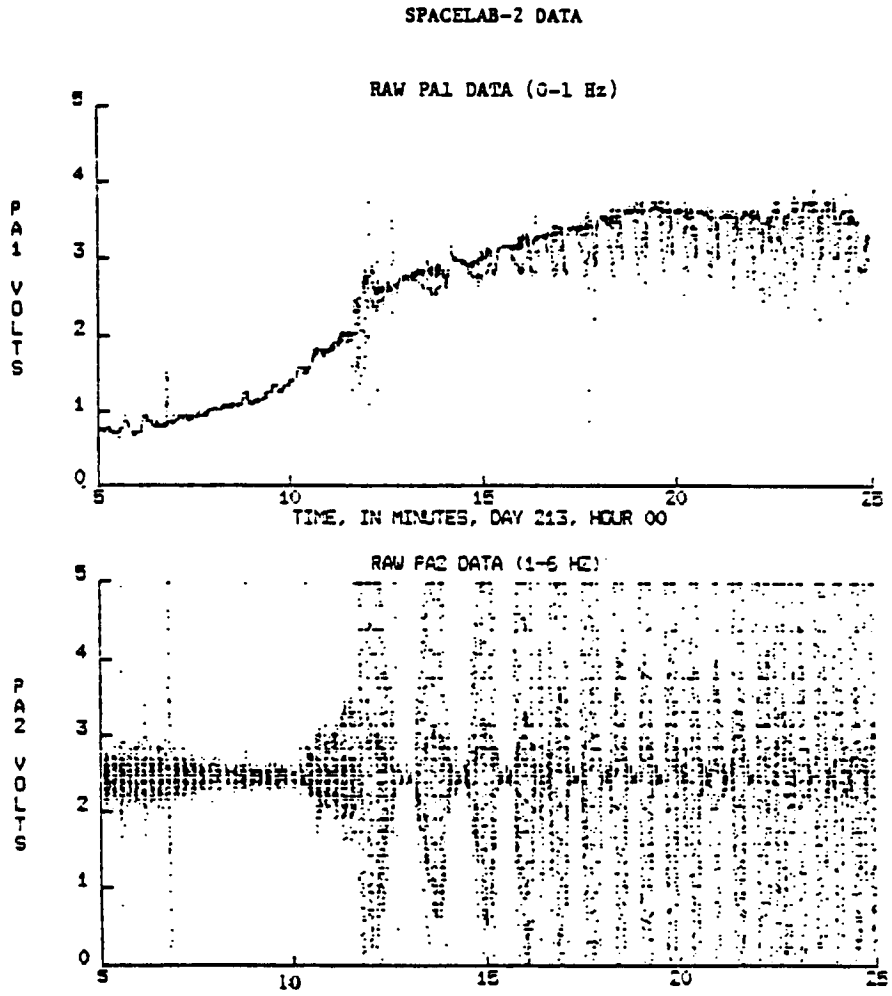

Figure 21. Free-flight density fluctuations.

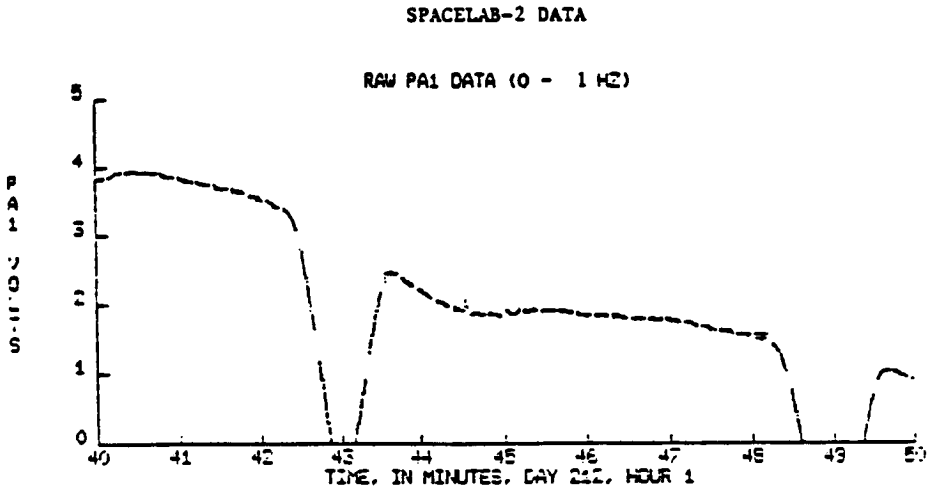

The PDP is in the wake of the orbiter at 43 and 49 minutes.

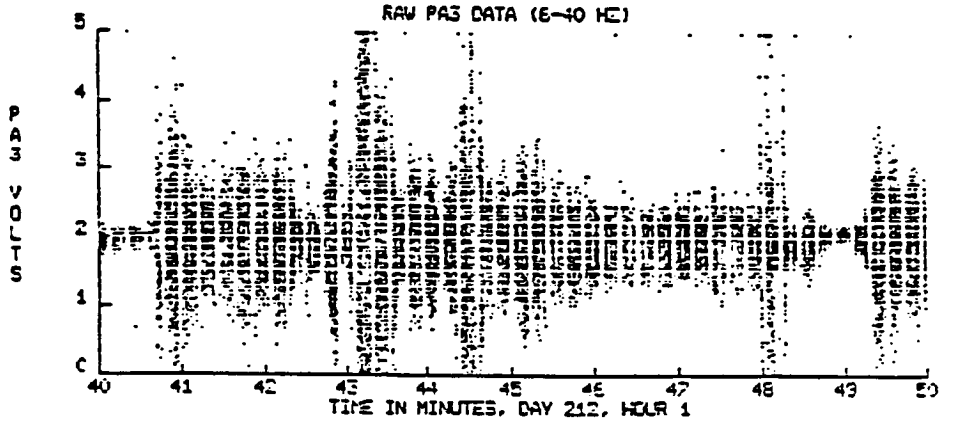

Figure 22. The wake of the orbiter.

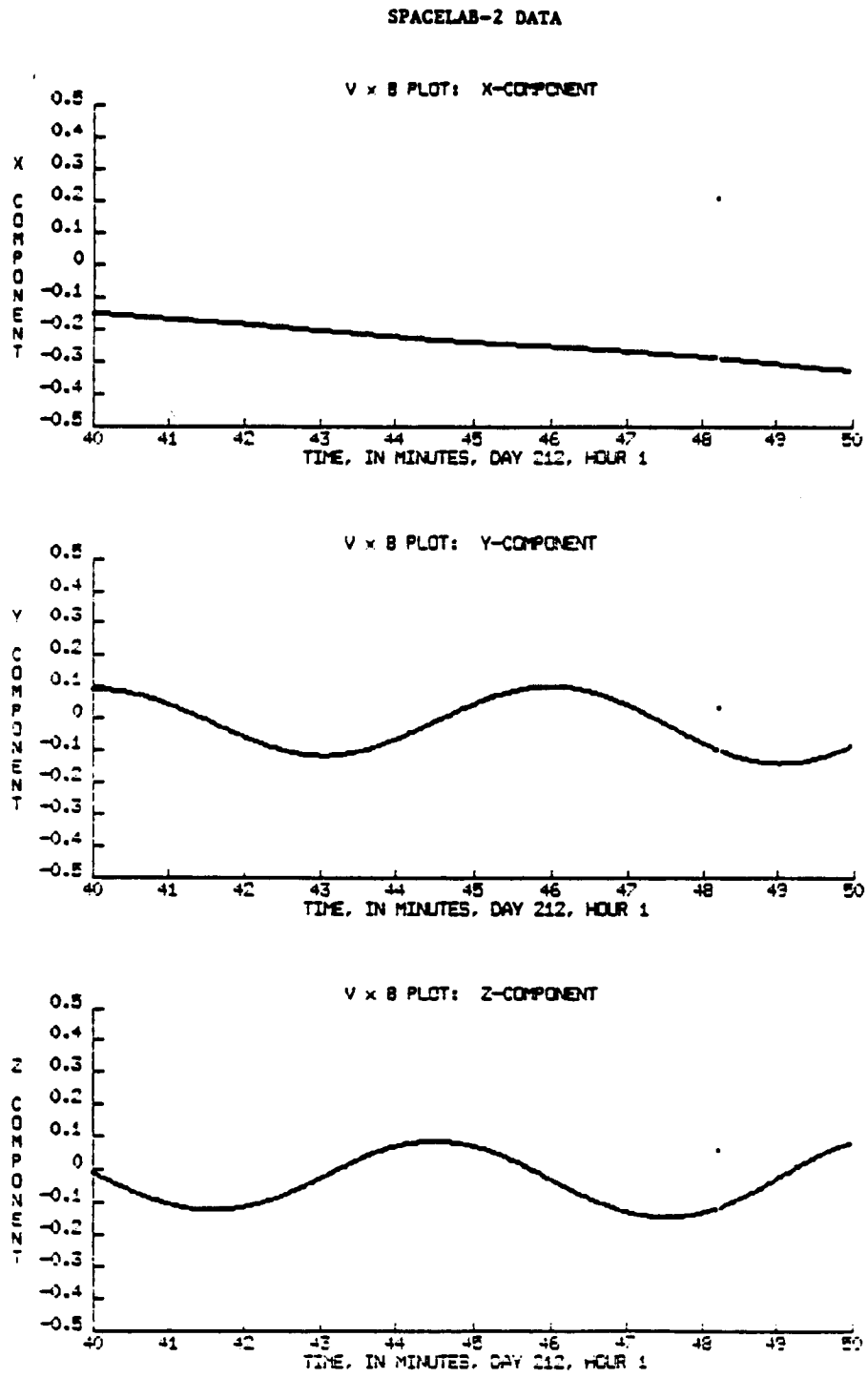

Figure 23. $\vec{v} \times \vec{B}$.

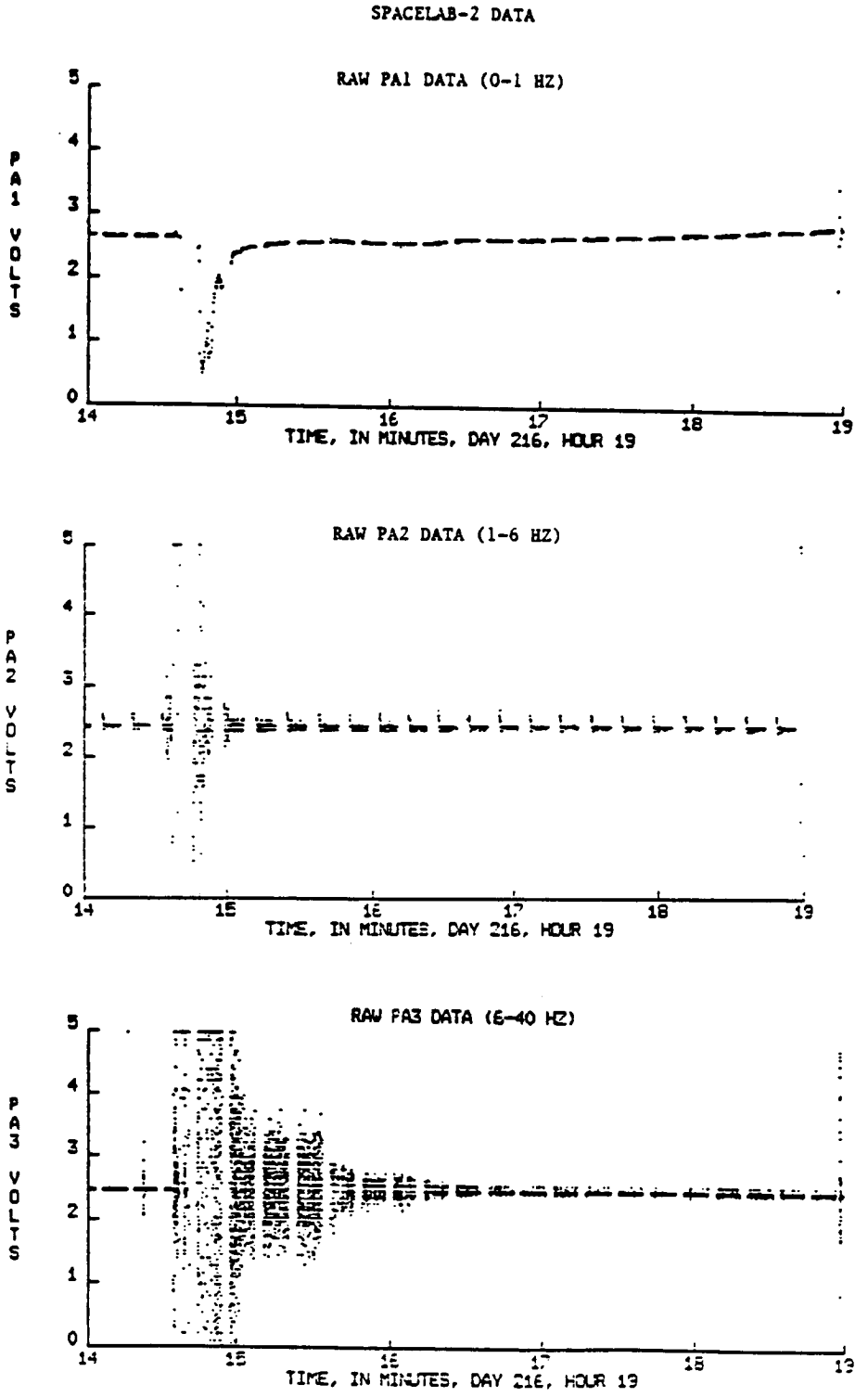

Figure 24. Density fluctuations during an OMS burn.

APPENDIX A

ELECTROSTATIC NOISE

After the completion of the Spacelab-2 mission, we realized that data reduction for the free-flight times would be complicated because the sweep period of the Langmuir probe was approximately equal to the rotation period of the PDP. The probe has a sweep period of 12.80 seconds. That is, every 12.80 seconds the probe starts a new sweep. During free flight the PDP is rotating with a period of 13.06 seconds. To help visualize some of the consequences of this problem, we define the phase angle as shown in Figure A-1. The phase angle is the angle between the velocity vector of the PDP and the vector that points from the center of the PDP to the Langmuir probe. Thus, if the probe starts a sweep when the phase angle is -180°, the next sweep will begin when the phase angle is approximately -172.9°. The difference in phase angles occurs because the PDP will rotate through 352.9° in 12.80 seocnds. Consequently, even though the PDP is rotating in a counterclockwise direction, the probe appears to precess in the clockwise direction.

If the probe travels 7.1° in 12.80 seconds, it will take 10 minutes 42 seconds before the probe will start a new sweep at a

phase angle of -180°. Therefore, the apparent precession period of the probe is just 10 minutes 42 seconds. The velocity vector of the PDP precesses with a period of 90 minutes because this is the time it takes to complete one orbit. Consequently, the probe will start a new sweep in the same position, relative to the velocity vector, after a time T defined by

$$\frac{1}{T} = \frac{1}{10m\ 42s} + \frac{1}{90m} \quad .$$

Solving this gives T = 9 minutes 45 seconds.

This is the time between the recurrences of the so-called "density depletion" regions seen during free flight. Part of the data are shown in Figure A-2. Originially, it was thought that these regions were actually times when the probe was in the wake of the PDP. If this was the case then a graph of phase angle vs time would show the phase angle to be approximately 180° during the times associated with the density depletions. However, as we see in Figure A-3, the phase angle is centered at about -60° not 180°. Therefore, the wake of the PDP is not the explanation for the density depletions.

The computer program that calculates densities and temperatures from a given sweep is sometimes unable to do this if the sweep is too noisy. When we examine the sweeps taken during the "density depletions" region, we notice an anomaly in these sweeps. Figure A-4 shows

an example of a Langmuir probe sweep taken during the middle of the first "density depletion" region, which starts at 1 hour 36 minutes on day 213. As we can see from this sweep, there appears to be something affecting the probe's ability to collect current whenever the probe is biased at approximately +7 volts relative to the PDP chassis. However, this problem only manifests itself when the phase angle is between +30° and -150°.

When we look at the data obtained when the PDP is in the lock mode, we notice some anomaly as well. As shown in Figure A-5, the instrument appears to detect some type of noise every 1.6 seconds. Note that in this figure the individual data points have been connected by lines. In order to understand why this is significant, we must first explain how the data are taken from the PDP.

All of the instruments on the PDP have their output formatted so that one complete sampling, what is referred to as one major frame of data, takes 1.6 seconds. Some instruments are sampled every major frame, others may only be sampled periodically. For example, the sweep mode of the Langmuir probe is sampled every eighth major frame. We conclude that the Langmuir probe sees some type of noise at the beginning of every major frame. For this reason we start to suspect that the source of this noise is either the probe itself, or another instrument on the PDP.

When the probe is in the lock mode, it collects 192 data points every major frame. If we look only at the last 100 points, as shown

in Figure A-6, the data clean up immensely, but we are still able to see the effects of this noise. Figure A-7 is a sample of the data obtained during the "density depletion" region starting at 1 hour 36 minutes on day 213. Note that the first 92 points of every major frame have been removed so that we may see the time evolution of the noise more clearly. This is the source of the small gaps in the data. The large gaps in the data are the time intervals when the probe was in the sweep mode. These data are also not plotted. As shown in this figure, we see that there is a shape to the "noise" which we see at the beginning of every major frame. If we follow the maximum of this noise in time, we notice that in some cases the maximum falls in the middle of the lock mode and in some cases the maximum is not present because it falls in the middle of a sweep. The times this noise falls during a sweep mode are also the times that the probe is unable to calculate densities and temperatures. Therefore, we can conclude that the problem we occasionally see during the sweep mode is always present. However, we only notice it during the sweep mode if the noise maximizes there.

As previously mentioned, the fact that we see this "noise" at the beginning of every major frame makes us suspect that there is either a problem with the probe itself or another instrument on the PDP. We are hesitant to place the blame with the probe itself because the instrument appears to have performed as expected at all other times during the Spacelab-2 mission. Also, other instruments on the

PDP record a similar effect. This leads us to believe that the probe is actually measuring some type of physical disturbance, rather than malfunctioning. Most instruments on the PDP, such as the Retarding Potential Analyzer, the Ion Mass Spectrometer, etc., operate at low voltages which would make them unlikely candidates as a source for this disturbance. The most likely source of this noise is the Low Energy Proton Electron Differential Energy Analyzer (LEPEDEA). At the beginning of every major frame LEPEDEA jumps to +2.2 kilovolts, relative to the chassis of the PDP, then decays exponentially, with a time constant of 4 msec, before the start of the next major frame. This is shown in Figure A-8. Also, as shown in Figure A-9, if we examine the orientation of LEPEDEA relative to the velocity vector, we seem to have a plausible explanation for the strange dependence on phase angle that the noise seems to have. The noise begins when the phase angle is +30°, at this point LEPEDEA is just beginning to look into the ram of the plasma flow. The noise ends when the phase angle is -150°, the point at which LEPEDEA looks into the wake. On the basis of this circumstantial evidence, we seem to have good reason for labeling LEPEDEA as the source of the noise.

The velocity of the shuttle is comparable to the thermal velocity of the ions. Therefore, ions will be colliding with the PDP in great numbers only on the side of the PDP facing the ram of the plasma flow. The thermal velocity of the electrons is much greater than the velocity of the shuttle, and they can be expected to impact

the PDP in equal numbers on all surfaces. When LEPEDEA jumps to +2.2 kilovolts, this creates a large positive potential hill near its opening. Because the ions are also positively charged, they will be deflected by this well as they approach the LEPEDEA. This will cause a number of them to alter their course so that they do not strike the PDP. When LEPEDEA is facing the wake, only those ions whose thermal velocities are greater than that of the PDP will be affected. However, when LEPEDEA is facing the ram, a substantially greater number of ions will be affected because this is the side of the PDP where most of the collisions with ions take place. As a result when LEPEDEA is in ram, there will be less positive current flow to the body of the PDP. This makes the potential of the chassis more negative. Consequently, whenever LEPEDEA is in ram the current-collecting ability of the probe is affected because its reference potential changes momentarily as LEPEDEA fires.

If the LEPEDEA is responsible for changing the reference potential of the PDP, we would expect to see the effect of this within a few milliseconds after LEPEDEA fires. However, as was previously mentioned, the anomaly appears to "maximize" whenever the bias voltage is +7 volts. This is 0.2 seconds after the LEPEDEA has fired. We believe that this delay is caused by the electronics that controls the operation of the Langmuir probe. Recall that when in the sweep mode the output is sent through a 0 - 50 Hz bandpass filter. Whenever an electrical pulse is sent through such a filter, there will be a delay

between the time that the pulse arrives at the filter and the time that the low-frequency components of the pulse are seen as output. It is believed that this delay could be as long as 0.2 seconds. However, this has yet to be experimentally verified.

At this point we begin to wonder why we did not see this effect at other times during either the Spacelab-2 mission or the OSS-1 mission. However, with the exception of the 6 hours of free-flight data, the remainder of the time we were always grounded to the orbiter. Its larger surface area essentially cancelled the effects of the potential well. Also, LEPEDEA has never before been flown in a region where the ion density is this high. Therefore, we had no reason to expect to see this phenomenon before the free-flight data were collected. As it turns out, when we go back and look at the data for other times, we are able to see the effects of this potential difference. However, the magnitude of the effect appears to have been greatly minimized when the PDP is grounded to the orbiter.

In conclusion, we believe that the regions of "density depletion" are actually regions where LEPEDEA has changed the reference potential of the PDP. This potential difference affects the current-gathering ability of the probe and produces sweeps that we are unable to use when we calculate densities and temperatures.

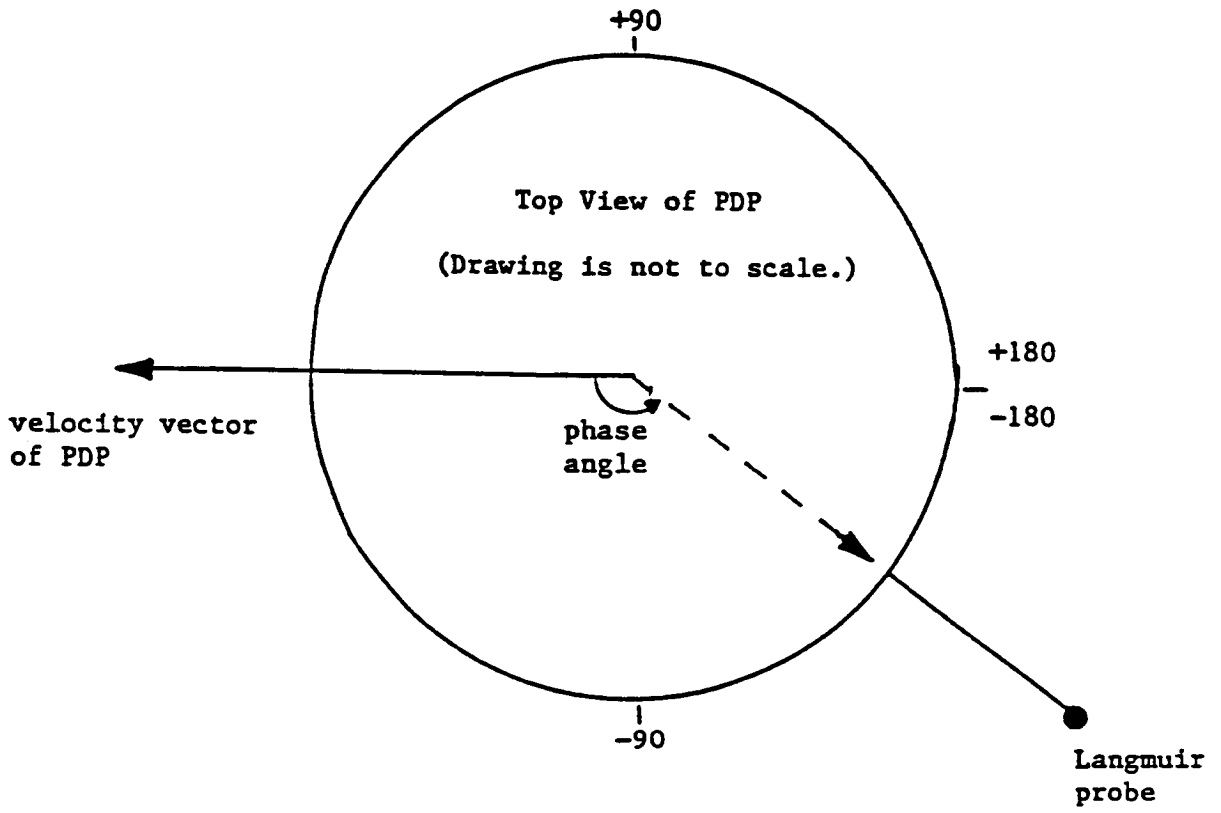

Figure A-1. The phase angle. A phase angle of -90 indicates that the Langmuir probe vector points toward the Earth.

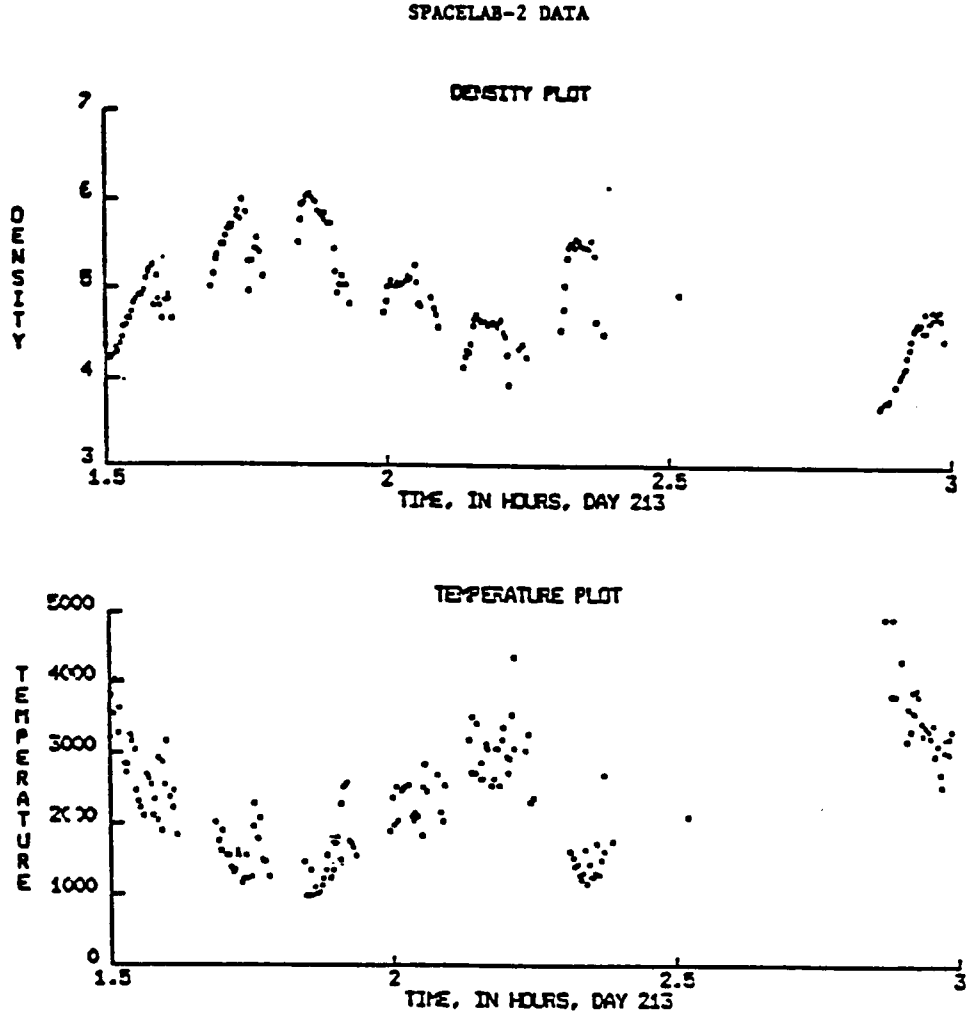

Figure A-2. The density depletion regions.

SPACELAB-2 DATA

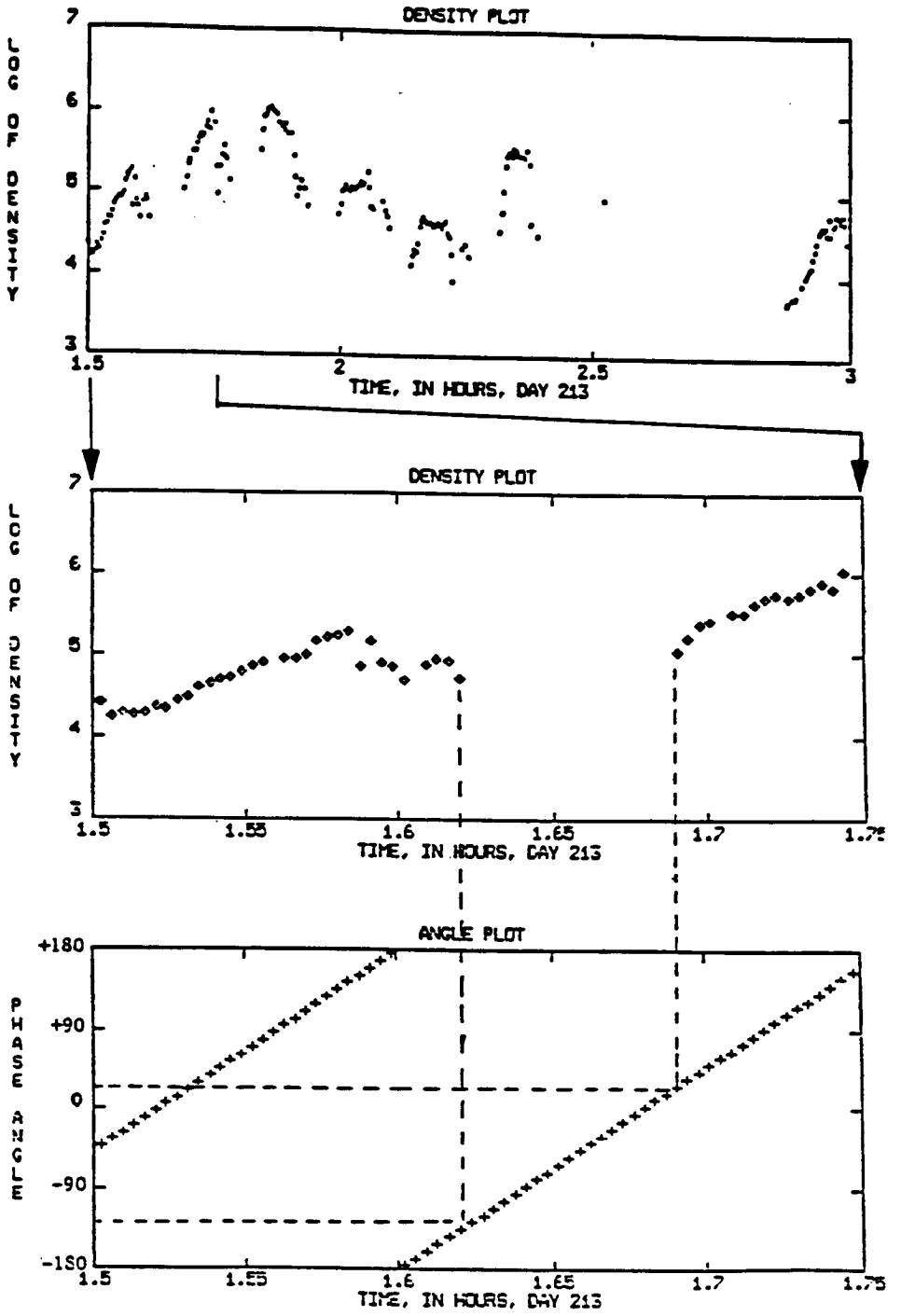

Figure A-3. Density depletions as a function of phase angle.

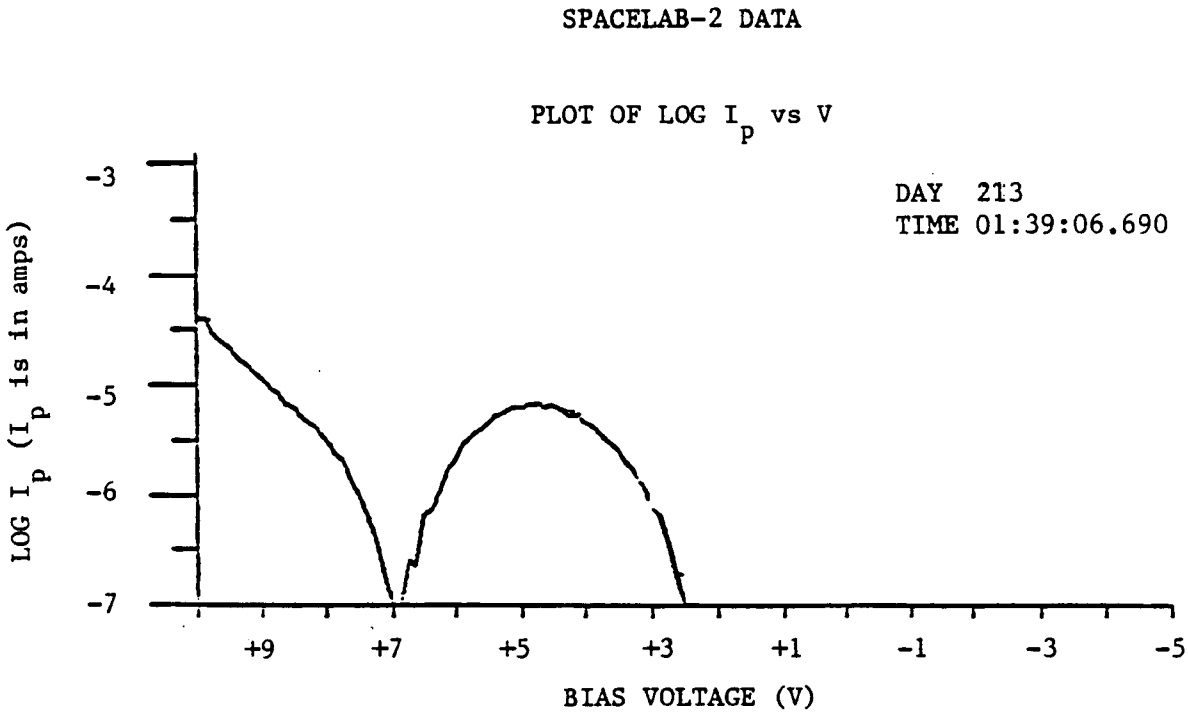

Figure A-4. An anomaly in the Langmuir probe sweep.

SPACELAB-2 DATA

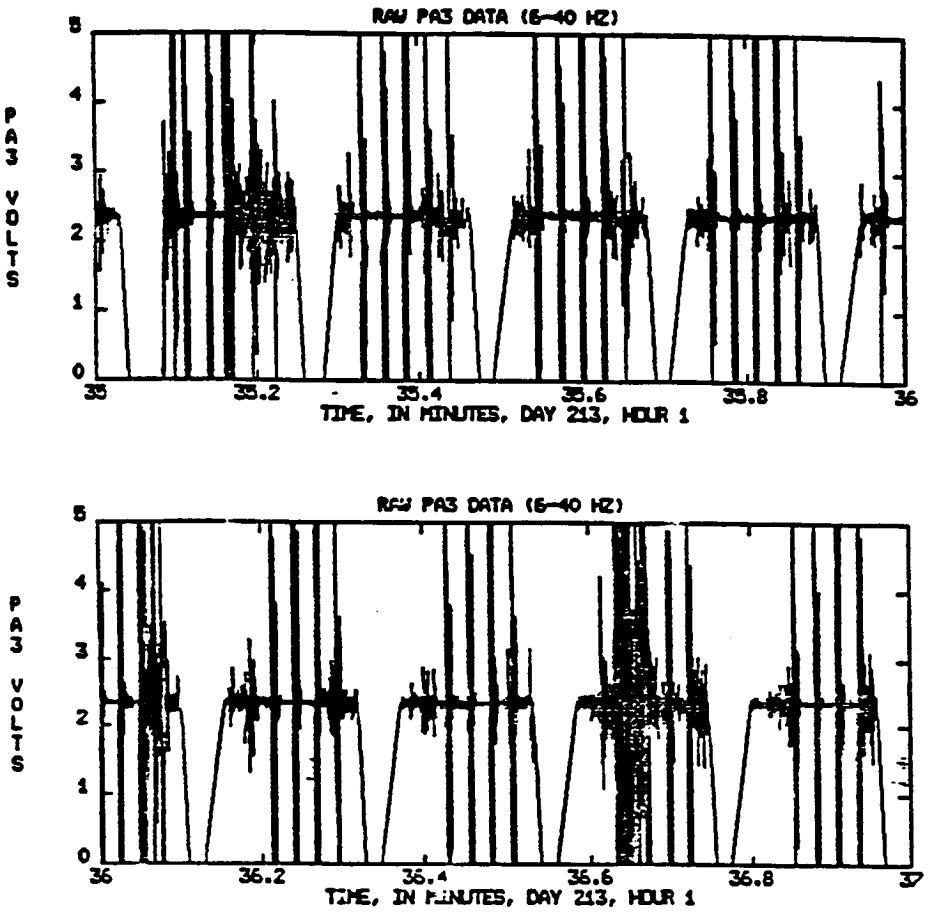

Figure A-5. An anomaly in the lock mode data.

SPACELAB-2 DATA

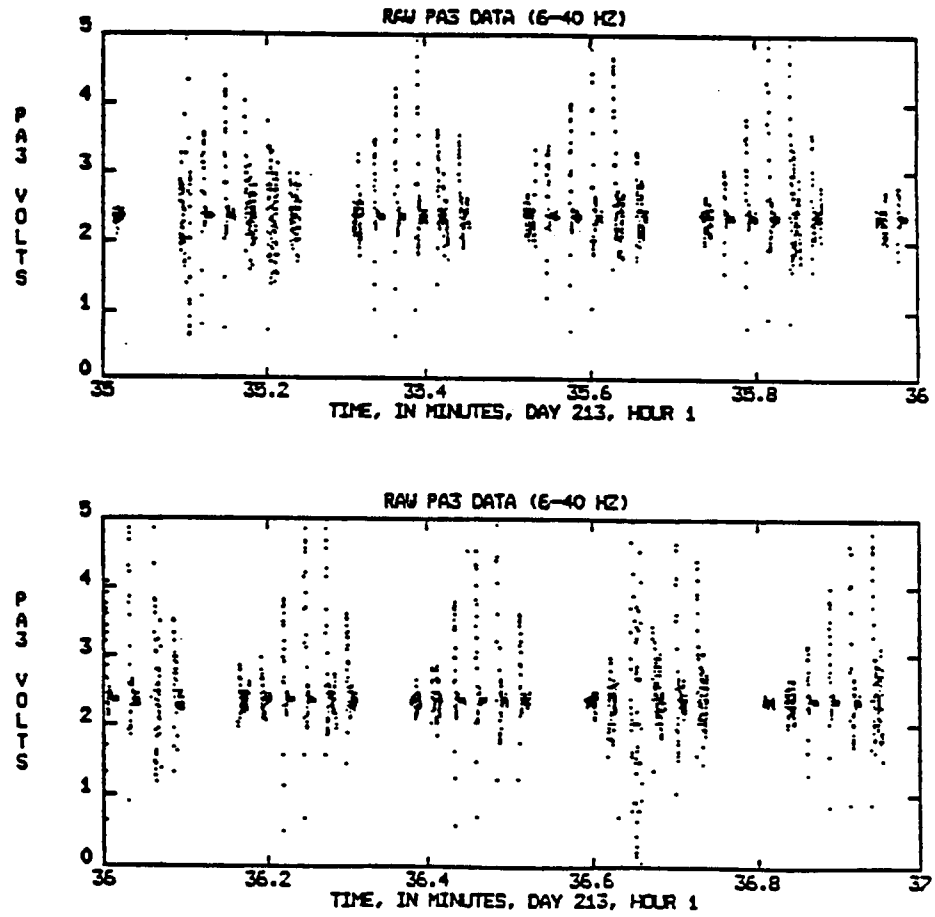

Figure A-6. "Cleaned up" lock mode data.

SPACELAB-2 DATA

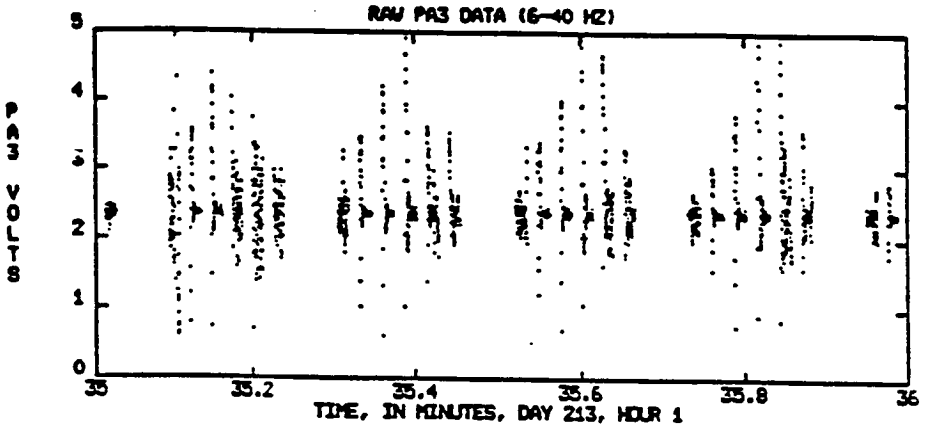

A maximum in the middle of a lock mode at 35.4 hours.

A maximum in the middle of a sweep mode at 39.75 hours.

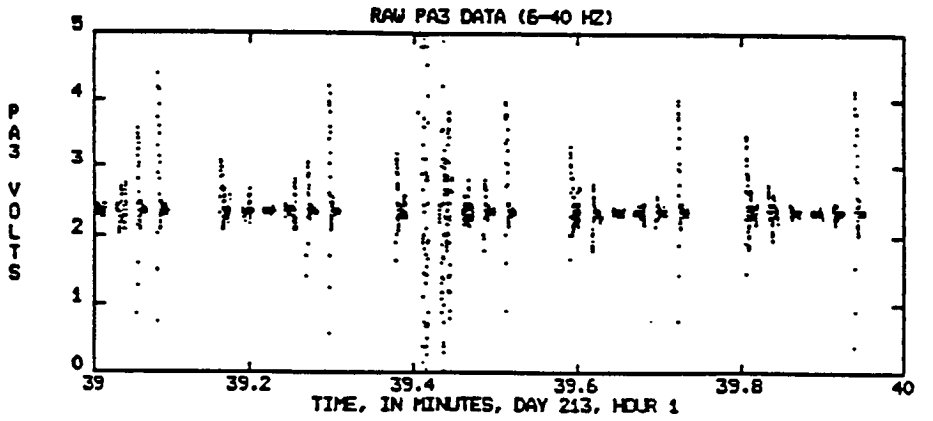

Figure A-7. Lock mode data during density depletion.

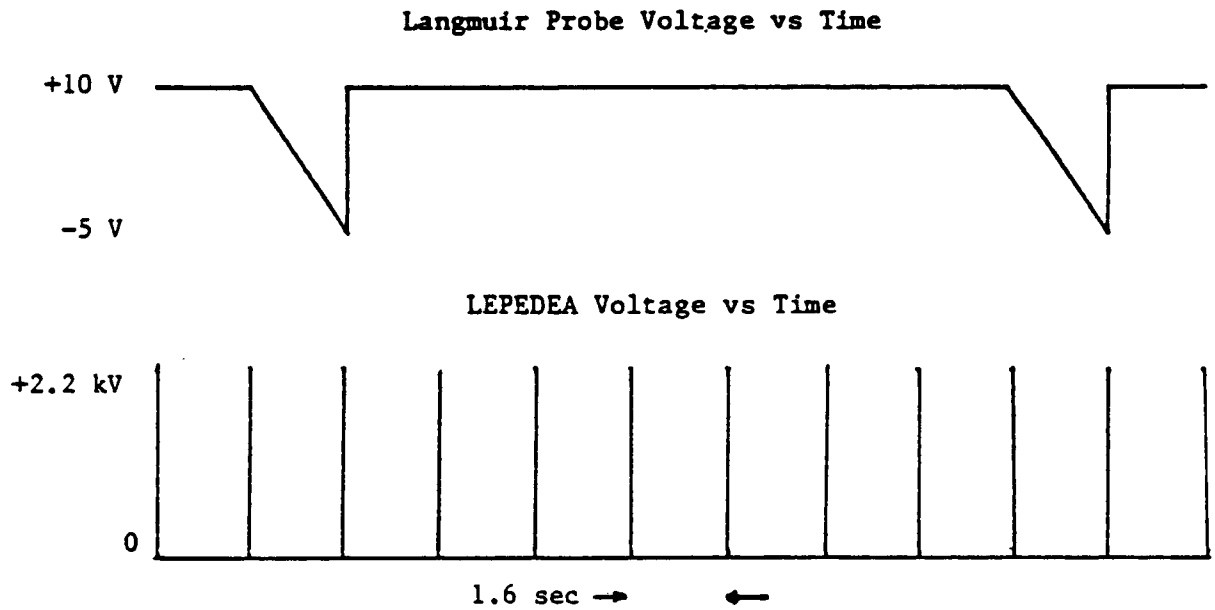

Figure A-8. LEPEDEA firing sequence. LEPEDEA fires at the beginning of the major frame, every 1.6 seconds.

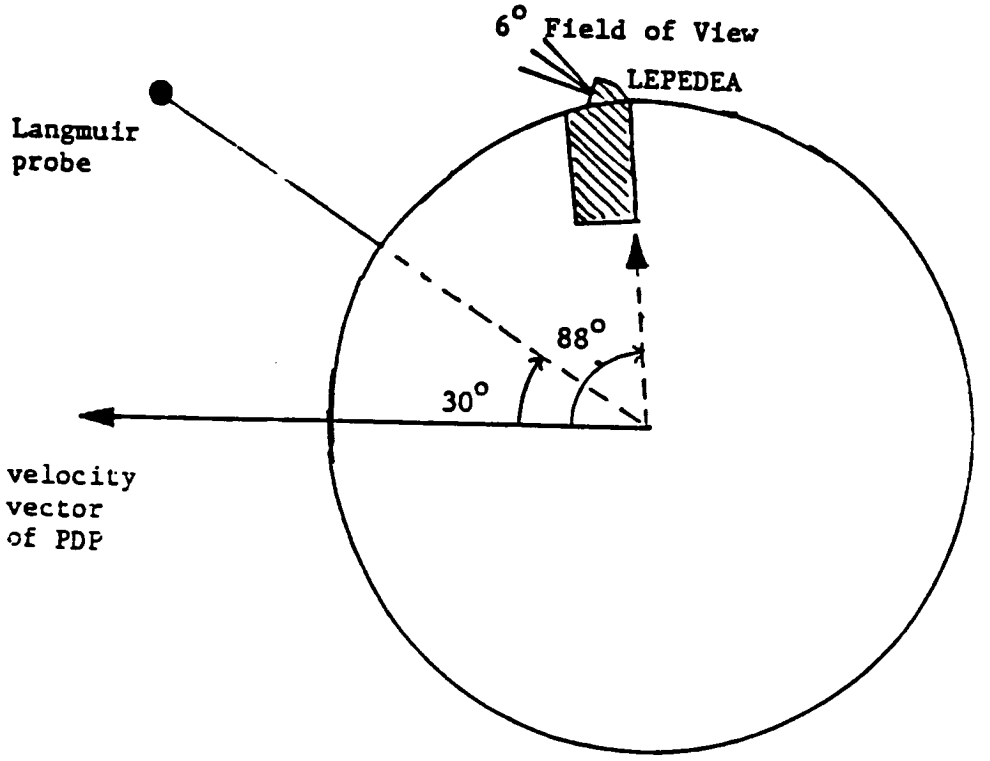

Figure A-9. Location of LEPEDEA at the start of the density depletions.

APPENDIX B

ERROR ANALYSIS

Whenever the Langmuir probe is in the sweep mode, there will be some point in the sweep when the bias voltage of the probe is approximately equal to the plasma potential. Whenever this is the case, the current collected by the probe will be independent of the bias voltage and will depend only on the velocity of the particles in the plasma, relative to the PDP. We can give separate expressions for the magnitude of the current due to the electrons and the current due to the ions. That is,

$$I_{i,e} = q_{i,e} A v_{i,e} n \quad ,$$

where $q_{i,e}$ = charge on the ions/electrons, A = area of probe, $v_{i,e}$ = velocity at which the ions/electrons impact the probe, n = density of the plasma. The current collected by the probe is the sum of both the electron and ion currents. However, when we use the Langmuir probe sweeps to calculate electron density and temperature, we are only interested in the electron current which is given by

$$I_e = I_{total} - I_i \quad .$$

Originally it was thought that the ion current, I_i, would be so small that it could be neglected. However, this is not always the case. The ions are moving with a velocity that is comparable to the speed of the shuttle. Therefore, assuming v_i = 8 km/s, we find that for the OSS-1 mission, when the probe is in ram, the ion current is given by

$$I_i = 3.6 \times 10^{-12}\ n(cm^{-3})\ \text{amperes} \quad .$$

For the Spacelab-2 mission, which used a smaller probe, the value is

$$I_i = 0.9 \times 10^{-12}\ n(cm^{-3})\ \text{amperes} \quad .$$

When the probe is in the wake, I_i is small enough to be neglected.

In Figure 3 we showed a typical Langmuir probe sweep taken during the OSS-1 mission. When taking the slope of the line as shown, we ignored the presence of the ion current, assuming it would be small enough to neglect. However, this particular sweep yielded an electron density of 3.9×10^6 cm^{-3}. Using this as the value for n, we find that the magnitude of the ion current is 14 microamps. Adding 14 microamps to the value of each of the points taken when the bias voltage is approximately equal to the plasma potential, we obtain a corrected Langmuir probe sweep. Table B-1 shows the value of the ion

current for three typical density values. By comparing the two sweeps shown in Figure B-1, we immediately see that the slope of the "corrected" line is different from that of the "uncorrected" line. As a result we find that the uncorrected slope provides an electron temperature of 950 K, whereas the corrected slope provides an electron temperature of 2190 K. The difference that the ion current makes in calculating the electron temperature is shown in Table B-2.

As shown in Table B-2 for OSS-1, when $n = 10^6$ cm^{-3} we underestimate the magnitude of the electron temperature by about 100%. When $n = 10^5$ cm^{-3}, we underestimate the temperature by about 50%, and when $n = 10^4$ cm^{-3} the value of the ion current is so small we do not notice a difference in temperatures.

Because we have failed to take into account the presence of the ion current, we conclude that electron temperatures less than 500 K are not accurate. Data reduction for OSS-1 had been completed and was well underway for the Spacelab-2 mission before this problem was noticed. However, most of the data analysis was concerned with noting differences in the plasma parameters depending on the attitude of the shuttle, orientation of the PDP, etc., and not with determining the exact value of these parameters. Consequently, the values of the electron temperature shown in this thesis have not been changed to reflect the presence of the ion current even though this causes us to underestimate the electron temperature at high densities.

Another problem encountered during data reduction is due to the large step size used by the probe during the sweep mode, 0.125 volts. As is shown in Figure B-1, in some cases this allows us only 3-4 points to use when we take the slope of the line in the log I vs V graph. This limits the accuracy of the probe by introducing an uncertainty in the value of the slope used to calculate the electron temperature and density.

Table B-1

The Magnitude of the Ion Current

	OSS-1	Spacelab-2
n (cm^{-3})	I_i (amps)	I_i (amps)
3.9×10^6	14.04×10^{-6}	3.51×10^{-6}
1.5×10^5	0.54×10^{-6}	0.14×10^{-6}
9.8×10^3	0.03×10^{-6}	0.01×10^{-6}

Table B-2

The Effect of Ion Current on Electron Temperature

$n_e(cm^{-3})$	Uncorrected $T_e(K)$	Corrected $T_e(K)$
3.9×10^6	950	2190
1.5×10^5	1084	1680
9.8×10^3	2221	2221

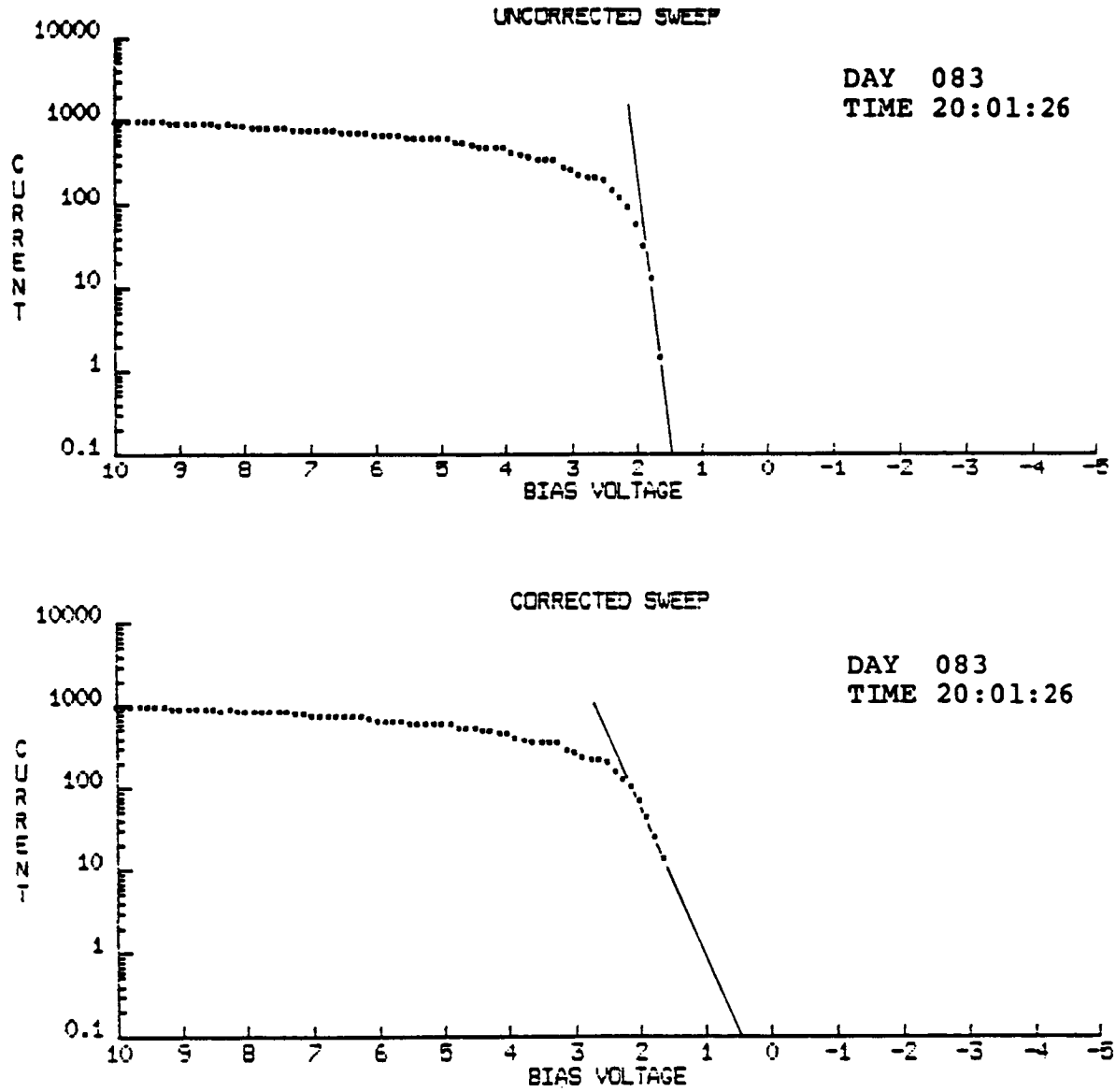

Figure B-1. Corrected and uncorrected Langmuir probe sweeps. The current is in microamperes.

REFERENCES

Hess, W. N., and G. D. Mead (Eds.), Introduction to Space Science, 2d ed., Gordon and Breach, Science Publishers, New York, 1968.

Huddlestone, R. H., and S. L. Leonard (Eds.), Plasma Diagnostic Techniques, Academic Press, New York, 1965.

Kasha, M. A., The Ionosphere and Its Interaction with Satellites, Gordon and Breach, Science Publishers, New York, 1969.

Murphy, G., J. Pickett, N. D'Angelo, and W . S. Kurth, Measurements of plasma parameters in the vicinity of the Space Shuttle, Planet. Space Sci., submitted, 1985.

NASA, Spacelab 2, U.S. Government Printing Office, Washington, DC, n.d.

Nicholson, D. R., Introduction to Plasma Theory, John Wiley & Sons, New York, 1983.

Office of Space Science and Applications, First Goddard Space Flight Center Payload Developed for Flight on Space Shuttle, NASA, Washington, DC, n.d.

Oran, W. A., U. Samir, N. H. Stone, and E. G. Fontheim, Laboratory observations of electron temperature in the wake of a sphere in a streaming plasma, Planet. Space Sci., 23, 1081-1083, 1975.

Rubin, A. G., and A. Besse, Charging of a manned maneuvering unit in the shuttle wake, J. Spacecr. Rockets, 23, No. 1, 1986.

Samir, U., and Wrenn, G. L., Experimental evidence of an electron temperature enhancement in the wake of an ionospheric satellite, Planet. Space Sci., 20, 899-904, 1972.

Solar-Terrestrial Science in Earthspace: A Strategy for Shuttle-Spacelab Missions, H-81-05, Essex Corporation, n.d.

ION PLASMAS IN THE VICINITY OF THE ORBITER:

OBSERVATIONS AND MODELING

by

William R. Paterson

A thesis submitted in partial fulfillment
of the requirements for the Master
of Science degree in Physics
in the Graduate College of
The University of Iowa

July 1987

Thesis supervisor: Professor Louis A. Frank

Graduate College
The University of Iowa
Iowa City, Iowa

CERTIFICATE OF APPROVAL

MASTER'S THESIS

This is to certify that the Master's thesis of

William R. Paterson

has been approved by the Examining Committee for the thesis requirement for the Master of Science degree in Physics at the July 1987 graduation.

Thesis committee: L. A. Frank
Thesis supervisor

David A. Gurnett
Member

John Dorr
Member

ACKNOWLEDGMENTS

I would like to thank Dr. N. D'Angelo for the use of electron density measurements made by the Langmuir probe. Thanks are also due to Dr. L. A. Frank for his advice and support.

ABSTRACT

During the Spacelab-2 mission ions produced from a cloud of neutral gases surrounding the Shuttle-Orbiter were observed by an electrostatic analyzer aboard the PDP spacecraft. These ions, identified primarily as H_2O^+, are distinguishable from ionospheric ions because they form a velocity-space distribution that has the shape of a ring. Distributions of this type were observed at distances up to 400 m from the Orbiter with densities ranging from $100/cm^3$ to $10^4/cm^3$. The production and transport of these ions are modeled in an attempt to reproduce the observed H_2O^+ densities. The water cloud is modeled as radial flow from a spherically symmetric source. Water molecules are removed from the cloud by collisions with atmospheric gases and H_2O^+ ions are produced by charge exchange between neutral H_2O and ionospheric O^+. Once the H_2O^+ ions are produced they are picked up by Earth's magnetic field and removed from the cloud. The density of neutral water is a free parameter in the model which is determined by comparing the modeled H_2O^+ density to the measured ion density. For the Spacelab-2 mission the water density is inferred in this way to be as high as $10^9/cm^3$ at a distance of 50 m from the Orbiter, as much as ten times higher than the density of ambient atmospheric gases.

C-3

TABLE OF CONTENTS

LIST OF TABLES

LIST OF FIGURES

CHAPTER I

INTRODUCTION

Spacelab 2

The Spacelab-2 payload was launched July 29 of 1985 aboard the Shuttle-Orbiter Challenger and landed August 6. This flight was a multidisciplinary science mission which included experiments in physics, astronomy, and biology. Most of the experiments were mounted on a pallet within the Orbiter's payload bay and exposed to space during a major fraction of the eight-day mission. Included among these experiments was the Plasma Diagnostics Package (PDP) designed and built at the University of Iowa. A major role of the PDP during the Spacelab-2 mission was to make measurements of plasmas, plasma waves, and electromagnetic radiation in the vicinity of the Orbiter with the goal of identifying and quantifying the Orbiter environment and the interaction of the Orbiter with the ionosphere.

The PDP

The PDP, shown in Figure 1, is a cylindrical body 1.1 m in height by 1.3 m in diameter with a total mass of 285 kg. Inside are instruments designed to detect and analyze electrically charged particles, electric and magnetic fields, waves, and the neutral gas pressure. Four retractable booms mounted on the PDP allow for the

extension of two electric field probes, a magnetic field probe and a Langmuir probe. The outside of the PDP is covered with a thermal insulation blanket affixed to which is a wire screen so that the surface acts as a conductor. Openings in both the blanket and the screen are provided for instrument apertures.

The PDP is designed so that it can be operated from the pallet within the Orbiter's bay, while attached to the Orbiter's Remote Manipulator System (RMS), or as a free-flying spin-stabilized spacecraft. In March of 1982 the PDP was also flown as part of the STS-3 mission aboard the Orbiter Columbia. During that flight, measurements were made from within the Orbiter's bay and at distances of approximately 15 m from the bay while the PDP was attached to the RMS [1]. During the Spacelab-2 mission measurements were again made from within the bay and from the RMS. In addition, the PDP was operated as a free flyer, and measurements were obtained at distances up to 400 m from the Orbiter. In this thesis these latter free-flight measurements are discussed.

PDP Free Flight

The free flight began on August 1 at 0010 UT, 51 hours into the mission. At this time the PDP was released from the RMS with its spin axis perpendicular to $\vec{R}_e$, the vector pointing from the spacecraft towards the earth, and to $\vec{V}_{sc}$, the velocity vector of the spacecraft, i.e., perpendicular to the orbital plane (see Figure 4). The rotation of the PDP was accomplished by means of a mechanical momentum wheel

inside the spacecraft. This wheel was spun-up prior to release while the PDP was attached to the RMS. After release, angular momentum was transferred from the wheel to the rest of the spacecraft causing the spacecraft to rotate. A constant period of rotation equal to 13.1 sec was maintained throughout most of the free flight. During this time, the Orbiter was maneuvered around the PDP. Two circuits of the PDP were completed, essentially one per orbit. The projection of the Orbiter's trajectory into the orbital plane of the PDP during this time is shown in Figures 2 and 3 in a coordinate system centered on the PDP. The distance of the Orbiter out of the orbital plane during the free flight was as much as 300 m. The PDP was recovered by maneuvering the Orbiter to within approximately 15 m of the satellite and grappling it with the RMS. The recovery was successfully completed at 0620 UT.

The Lepedea

During the free flight, the differential directional intensities of charged particles with energy-per-charge in the range of 2 V to 36 kV were observed with an electrostatic analyzer aboard the PDP. This instrument, known as the Low Energy Proton and Electron Differential Energy Analyzer (Lepedea) is of a type described in detail by Frank et al. [2]. The Lepedea simultaneously measures the fluxes of electrons and positively charged ions in seven separate fields-of-view. Each field-of-view includes one detector for electrons and one detector for ions so that there are fourteen separate detectors in

all. Particles of different mass are not distinguished. The fields-of-view of the Lepedea and their orientations with respect to the PDP spin axis are shown in Figure 4. As can be seen in the figure, these fields-of-view form a fan which rotates with the spacecraft, thus providing excellent sampling of the possible particle trajectories.

A single instrument cycle for the Lepedea is 1.6 sec in duration and includes 0.2 sec of dead-time followed by a 1.4 sec energy sweep. Each sweep consists of forty-two 33-msec samples at a sequence of energies-per-charge which approximate a decreasing exponential. Because of the rotation of the PDP the fan of the Lepedea sweeps through 360 degrees in azimuth once every 13.1 sec. During each 1.6 sec instrument cycle the detectors sweep through 44 degrees of azimuth so that approximately 8 energy sweeps occur during each rotation. Figure 5 is a polar plot showing the azimuth angles of samples during a single spacecraft rotation. Radial distance in this plot is proportional to the logarithm of the center energy of the samples. Azimuthal resolution is improved by collecting data for more than one rotation. The samples are then sorted according to azimuth. In Figure 6 the azimuth angles of samples collected during 41 energy sweeps are shown, corresponding to 5 spacecraft rotations or a time period of 65.6 sec. For this situation, samples at a given center energy are separated by approximately 8 degrees in azimuth. Sampling of polar angles is fixed by the geometry of the detectors as shown in Figure 4.

Data Analysis

A useful quantity in the analysis of plasmas is the density of particles per unit volume, $\Delta x \Delta y \Delta z$, and per unit volume of velocity space, $\Delta v_x \Delta v_y \Delta v_z$. This density is known as the particle velocity distribution and is denoted functionally as $f(\vec{x},\vec{v},t)$. While the velocity distribution is, in general, a function of position, $\vec{x}$, and time, t, as well as velocity, $\vec{v}$, it is often written as simply $f(\vec{v})$.

When the velocity distribution of a group of particles is known, certain bulk properties of the particles can be determined such as the density per unit volume,

$$n = \int f(\vec{v}) dv_x dv_y dv_z \quad ,$$

the mean velocity,

$$\langle \vec{v} \rangle = \frac{1}{n} \int \vec{v} f(\vec{v}) dv_x dv_y dv_z \quad ,$$

or the mean kinetic energy,

$$\langle E \rangle = \frac{1}{n} \int \frac{1}{2} m v^2 f(\vec{v}) dv_x dv_y dv_z \quad ,$$

where the integrals are over all possible values of v_x, v_y, and v_z, and m is the mass of a single particle. The functional form of the velocity distribution is also important for the analysis of plasma

instabilities and waves [3]. In particular, multiply peaked distributions can drive plasma waves which in turn alter the particle velocity distributions.

The velocity distribution, $f(\vec{v})$, is related to the differential particle intensity or differential flux denoted by $j'(E)$. Consider the flux through a surface of unit area of particles with speeds within dv of v and coming from within the differential solid angle $d\Omega$ which is centered about the vector $\vec{v}$. This flux is given by

$$dj = vf(\vec{v})v^2 dv d\Omega \quad .$$

Since $E = 1/2\ mv^2$, we may also write

$$\frac{d^2j}{dEd\Omega} = \frac{2}{m^2} Ef(\vec{v}) \quad , \quad \text{or}$$

$$j'(E) = \frac{2}{m^2} Ef(\vec{v}) \quad , \qquad (1)$$

where $j'(E) = d^2j/dEd\Omega$.

If an ion plasma consists of more than one species of particle, as is generally the case, then there exist separate velocity distributions, $f_k(\vec{v}_k)$, for each species in the plasma, where the subscript k denotes the particle species. In this case,

$$j'(E) = \sum_k j'_k(E) \quad ,$$

where the summation includes a term for each species, and $E = 1/2\ m_k v_k^2$.

Count rates observed by the Lepedea are proportional to the differential flux into the detectors. In the case of electrons, where only a single species is observed, the conversion to $f(\vec{v})$ is straightforward. In the case of positive ions, however, several species may be observed simultaneously. Because the Lepedea does not distinguish between ions of different mass, it is not possible to unambiguously deconvolve the f_k's from the total flux $j'(E)$.

At times during the mission the ion flux into the Lepedea was of sufficient intensity to saturate the ion detectors. For these times it is not possible to determine the ion fluxes directly from the ion count rates. Ions impacting surfaces within the instrument, however, give rise to a flux of a secondary electrons, and some of these electrons are observed by the electron detectors. Since the flux of secondaries is proportional to the ion flux, the observed electron count rate due to these electrons is proportional to the ion count rate. The constant of proportionality relating the rates is found by comparing the electron rates to the ion rates at times when the ion detectors are not saturated. The flux of secondary electrons is much less than the ion flux, so that when the ion detectors are saturuated, the true ion rate can be deduced from the electrons. This analysis assumes that the electron counting rate remains proportional to the ion flux even when the ion detectors are saturated.

CHAPTER II

IONOSPHERIC IONS AND ION PICK-UP

During the PDP free flight, two different kinds of ion distributions are observed by the Lepedea. One of these distributions is due to ambient ionospheric ions which flow past the spacecraft with a velocity equal to $-\vec{V}_{sc}$. The other distribution is interpreted as ions created by the ionization of contaminant gases which co-orbit with the Orbiter. Before presenting these observations it is useful to discuss some of the processes which maintain the ionosphere. The goal of this discussion is to develop an understanding of the kinds of ion distributions which are to be expected at the 320 km altitude of the Orbiter.

Atmospheric Gases and Ionospheric Ions

Ionospheric ions are produced by the ionization of neutral atmospheric gases. At the altitude of the Orbiter the atmosphere is composed primarily of atomic oxygen, OI, molecular nitrogen, N_2, and molecular oxygen, O_2. The density of neutral gases in the ionosphere depends on the atmospheric temperature. Since the upper atmosphere is heated primarily by solar radiation, the temperature depends in turn upon the solar flux incident at Earth. The Spacelab-2 mission was accomplished during conditions approaching solar minimum when the

solar flux and hence the atmospheric temperature and densities were relatively low. Figure 7 shows the atmospheric temperature and the neutral-gas concentrations at the position of the spacecraft during the free flight, as predicted by the MSIS-83 atmospheric model [4]. Variations in temperature and density at the 90-minute period of the orbit are evident, due primarily to diurnal variations in the atmosphere. The dominant species is clearly OI, with a density ranging from 1×10^8 to $3 \times 10^8/cm^3$. The concentrations of N_2 and O_2 are lower than those for OI, but the amplitude of the diurnal variations is greater. The densities for these molecules range from 4×10^6 to $4 \times 10^7/cm^3$ for N_2 and from 2×10^5 to $2 \times 10^6/cm^3$ for O_2.

Ion production and losses at 320 km are dominated by the reactions

$$O + h\nu \rightarrow O^+ + e^- \quad , \tag{2}$$

where $h\nu$ and e^- denote photons and electrons respectively,

$$e^- + O \rightarrow O^+ + 2e^- \quad , \tag{3}$$

$$N_2 + O^+ \rightarrow NO^+ + N \quad , \tag{4}$$

$$O_2 + O^+ \rightarrow O_2^+ + O \quad , \tag{5}$$

$$NO^+ + e^- \rightarrow N + O \quad , \quad \text{and} \tag{6}$$

$$O_2^+ + e^- \rightarrow O + O \quad . \tag{7}$$

Reactions (2) through (7) and their associated rates are discussed in detail in reference [5] and are summarized in Table 1. The primary source of ions is photoionization of OI as described by reaction (2). The photoionization rate, I_ν, depends upon the flux of solar ultraviolet radiation. For solar-minimum conditions $I_\nu \approx 1.7 \times 10^{-7}$/sec [5]. Reaction (3) refers to ionization of OI by energetic photoelectrons created in reaction (2). A sample photoelectron spectrum observed with the Lepedea during the free flight at 0208 UT is shown in Figure 8. The rate, I_e, for reaction (3) is determined by the cross section for electron impact ionization of OI [6] and by the spectrum of the photoelectrons. For the free flight this rate is calculated to be $I_e < 2 \times 10^{-8}$/sec, approximately 10 percent of the rate for photoionization. The neutral molecules N_2 and O_2 are also subject to photoionization and ionization by electron impact. These molecules, however, form ions more rapidly through reactions (4) and (5). These reactions are also the dominant mechanisms for removal of O^+ since direct recombination of O^+ with electrons is a slow process with a rate $\approx 10^{-12}$ cm^3/sec [7]. The molecular ions NO^+, and O_2^+, on the other hand, recombine rapidly via the dissociative recombination processes (6), and (7) with the result that their net concentrations remain low compared to the concentration of O^+.

The velocity distributions of ionospheric ions are Maxwellian with temperatures approximately equal to the temperature of the

neutral gas, i.e., $T_i \approx 1000$ °K. The thermal speeds of these ions are given by $C_i = [2kT_i/m_i]^{1/2}$, where m_i is the mass of the ions and k is Boltzmann's constant. This results in speeds of 1000 m/sec for O^+ ions and 700 m/sec for NO^+ and O_2^+. The Orbiter and the PDP fly through the ionosphere with a speed approximately equal to V_{sc}, where V_{sc} is the orbital speed of these spacecraft, equal to 7800 m/sec. Because V_{sc} is much greater than C_i, in the reference frame of the spacecraft the ions form a narrow beam centered at a velocity equal to $-\vec{V}_{sc}$. The kinetic energies of these ions in the rest frame of the PDP are given approximately by $E = 1/2\ m_i V_{sc}^2$, which predicts energies of 5 eV for O^+ ions and 10 eV for NO^+ and O_2^+.

Reactions (2) through (7) lead to a set of first-order differential equations for the ion concentrations. Denoting the density of species X by [X], these equations are written,

$$\frac{\partial}{\partial t}[O^+] = I[O] - \gamma_1[O^+][N_2] - \gamma_2[O^+][O_2] \tag{8}$$

$$\frac{\partial}{\partial t}[NO^+] = \gamma_1[O^+][N_2] - \alpha_1[NO^+][e^-] \tag{9}$$

$$\frac{\partial}{\partial t}[O_2^+] = \gamma_2[O^+] - \alpha_2[O_2^+][e^-] \tag{10}$$

$$[e^-] = [O^+] + [NO^+] + [O_2^+] \quad , \tag{11}$$

where the coefficient, I, in equation (8) is the combined rate for ionization of OI by solar radiation and energetic electrons. Equations (8) through (11) describe the major features of the ionospheric chemistry of interest for the present problem. By assuming steady-state conditions, these equations can be solved to give an estimate of the ambient ion densities to be expected at the 320 km altitude of the Orbiter.

If we assume a combined ionization rate $I = 1.9 \times 10^{-7}$/sec, and typical daytime atmospheric densities predicted by the MSIS-83 model of $[O] = 2.3 \times 10^8/cm^3$, $[N_2] = 2.1 \times 10^7/cm^3$, and $[O_2] = 7.3 \times 10^5/cm^3$, equations (8) through (11) yield ion densities of $[O^+] = 2.8 \times 10^6/cm^3$, $[NO^+] = 120/cm^3$, and $[O_2^+] = 240/cm^3$. The electron density is approximately equal to the density of O^+, and this value is consistent with peak daytime electron densities $\sim 10^6/cm^3$ measured by the Langmuir probe aboard the PDP.

The velocity distributions of the ambient ions can be modeled by assuming Maxwellian velocity distributions of the form

$$f_i(\vec{v}) = n_i\left(\frac{m_i}{2\pi kT_i}\right)^{3/2} \exp\left[-\frac{m_i(\vec{v} - \vec{V}_{sc})^2}{2kT_i}\right] \quad . \tag{12}$$

The results of such modeling are shown in Figure 9. In that figure, the V axis is chosen so that it is parallel to $\vec{V}_{sc}$, and the ion densities are from the steady-state solution of equations (8) through (11). An ion temperature of 1000 °K is assumed. The distributions

peak at $V = -V_{sc}$. By applying equation (1), the differential flux due to these ions can be computed. The total flux, $j'(E)$, is shown in Figure 10 for the direction opposite to the vector $\vec{V}_{sc}$. This flux peaks at 5 eV corresponding to the orbital ram energy of the dominant species, O^+. Fluxes at energies greater than 10 eV are due primarily to NO^+ and O_2^+ which have ram energies of approximately 10 eV.

Orbiter Gas Cloud and Ion Pick-Up

The Orbiter releases gases in several different ways as it flies through the ionosphere. Water, which is produced as a byproduct of the generation of electricity, is periodically dumped, and thrusters are fired frequently to change or correct the Orbiter attitude. The thrusters rely on a reaction between N_2O_4 and MMH (monomethyl hydrazine). This reaction is predicted to result in a complex set of products which include H_2O, N_2, CO_2, H_2, H, and $MMH-NO_3$ [8]. In addition to these sources, outgassing from Orbiter surfaces and leakage from pressurized systems probably occur as well.

With the exception of the thrusters, these gases are released at a temperature approximately equal to the temperature of the Orbiter surface, about 300 °K, so that the thermal speed of the gas, C, is small compared to V_{sc}. The result is a cloud of gas which, in the reference frame of the Orbiter, expands slowly with a speed approximately equal to C. Thruster gases, on the other hand, are emitted with a high velocity relative to the Orbiter. Thruster firings have been observed on several shuttle flights by neutral mass spectrometers

and by plasma instruments, and the effects of the thrusters are seen to dissipate on a time scale on the order of seconds or less [8,9]. At times when the thrusters are inactive, neutral gases and ions which are not usually found in the upper atmosphere are still observed. The commonly observed species include H_2O, He, H_2O^+, and H_3O^+ [10,11,12].

Gases co-orbiting with the Orbiter are subject to collisions with atmospheric gases, reactions with ionospheric ions, and ionization by solar ultraviolet radiation or by the impact of energetic photoelectrons. Collisions with the atmospheric constituents scatter and thermalize the molecules released from the Orbiter so that a trail of contaminants is left behind the spacecraft. Molecules which are ionized produce a distinctive velocity-space distribution, and can be detected by the Lepedea.

Consider the situation shown in Figure 11. A neutral molecule of mass m_i moves in the X-Z plane with a velocity equal to $\vec{V}$. There is a magnetic field $\vec{B}$ directed parallel to Z, and the components of $\vec{V}$ perpendicular to $\vec{B}$ and parallel to $\vec{B}$ are $V_\perp = V \sin(\alpha)$ and $V_\parallel = V \cos(\alpha)$. The molecule is unaffected by the magnetic field, and has a trajectory which is a straight line as shown in Figures 11(a) and 11(b). At a time $t = t_o$ when the molecule is at a point A, the molecule is ionized by charge exchange or by absorbing an energetic photon, processes which have little effect on the momentum of the molecule. The newly formed ion experiences a Lorentz force $\vec{F} = q\,\vec{V} \times \vec{B}$, where q is the charge of the ion. The subsequent ion velocity, as a function of time, is given by

$$\vec{V}_i = V_\perp \cos[\omega(t - t_o)]\hat{x} + V_\perp \sin[\omega(t - t_o)]\hat{y} + V_\parallel \hat{z} \quad , \qquad (13)$$

where $\hat{x}$, $\hat{y}$, and $\hat{z}$ are unit vectors in the X, Y, and Z directions. The ion motion is a combination of translation parallel to $\vec{B}$ and gyration perpendicular to $\vec{B}$, resulting in a helical trajectory as shown in Figures 11(c) and 11(d). The radius of the helix is given by $R_g = m_i V_\perp / qB$ and the frequency of the gyration by $\omega_g = qB/m_i$.

Now consider a cloud of molecules co-orbiting with the Orbiter, as shown in Figure 12. If these molecules have thermal velocities which are small compared to V_{sc}, then in the rest frame of the ionosphere each molecule has a velocity given approximately by $\vec{V} = \vec{V}_{sc}$. The components parallel to and perpendicular to the Earth's magnetic field are $V_\parallel = V_{sc} \cos(\alpha)$ and $V_\perp = V_{sc} \sin(\alpha)$. A molecule which is ionized at $t = t_o$ will have a velocity given by

$$\vec{V}_i = V_{sc} \sin(\alpha)\cos[\omega(t - t_o)]\hat{x} + V_{sc} \sin(\alpha) \times \sin[\omega(t - t_o)]\hat{y} + V_{sc} \cos(\alpha)\hat{z} \quad . \qquad (14)$$

In the rest frame of the spacecraft the velocity is equal to

$$\vec{V}'_i = \vec{V}_i - \vec{V}_{sc} \quad ,$$

so that

$$\vec{V}_i' = V_{sc} \sin(\alpha)\{\cos[\omega(t - t_o)] - 1\}\hat{x}$$

$$+ V_{sc} \sin(\alpha)\sin[\omega(t - t_o)]\hat{y} \quad . \qquad (15)$$

In velocity space, equation (15) describes a circle of radius $V_\perp = V_{sc} \sin(\alpha)$. This circle lies in a plane perpendicular to $\vec{B}$ and is centered at $V_x = -V_\perp$ as shown in Figure 13. The ion velocity ranges from zero to $-2\ V_{sc} \sin(\alpha)\hat{x}$ resulting in a kinetic energy, $1/2\ m_i V_i'^2$, which ranges between zero and $2\ m_i V_{sc}^2 \sin^2(\alpha)$. The time average of this velocity is

$$\langle \vec{V}_i' \rangle_t = -V_{sc} \sin(\alpha)\hat{x} \quad ,$$

which is equal to the component of $-\vec{V}_{sc}$ projected into the plane perpendicular to $\vec{B}$. To an observer on the spacecraft, the ion appears to gyrate about a center which moves away from the spacecraft with a velocity equal to $\langle \vec{V}_i' \rangle_t$. If $\vec{V}_{sc}$ and $\vec{B}$ are perpendicular so that $\alpha = 90$ degrees, then $\langle \vec{V}_i' \rangle_t = -\vec{V}_{sc}$, and the center of gyration moves past the spacecraft with the same velocity as the ambient ionospheric ions. If $\alpha \neq 90$ degrees, then the velocities of flow of the ambient ions and the ions created from the co-orbiting gas cloud are not the same. For the case where $\alpha = 0$ degrees, the Lorentz force on the newly created ions is zero, so that these ions continue to co-orbit with the spacecraft until colliding with atmospheric gases.

If many molecules are ionized then, in the absence of other forces or collective effects, the resulting ion velocity distribution is ring shaped with a diameter equal to 2 V_{sc} sin(α). The ring lies in the plane perperpendicular to $\vec{B}$ and is centered at V_x = $-V_{sc}$ sin(α). In this discussion, the finite temperature of the contaminant gas has been neglected. A finite thermal spread in velocities would tend to give the ring a finite width. Also ignored are collective plasma effects resulting in waves which would alter the ion velocity distributions.

The ionization of a neutral gas moving transverse to a magnetic field is a process known as "ion pick-up" [13]. Velocity distributions resulting from this process have been observed in the solar wind as it interacts with cometary atmospheres [14,15] and helium of interstellar origin [16]. In these cases, however, the ions appear to have been scattered both in energy and in direction so that the ion velocity-space distributions form either a sphere or a spherical shell rather than a ring.

CHAPTER III

OBSERVATIONS

Figure 14 is a plot of the differential ion flux from the direction of orbital motion, i.e., along $-\vec{V}_{sc}$, on August 1 of 1985 at 0208 UT. At this time the PDP is at a distance of 280 m from the Orbiter, and the angle between $\vec{B}$ and $\vec{V}_{sc}$ is 86 degrees. The spectrum shown in Figure 14 peaks at an energy-per-charge < 5 V. This peak saturates the ion detector in which it is observed and the fluxes for this peak are derived from the electron count rates as discussed in Chapter I. A secondary peak is observed at an energy-per-charge ≈ 18 V, while between 20 V and 60 V the spectrum gradually decreases, and at 60 V drops sharply by almost two orders of magnitude.

The low energy peak is due to ambient ionospheric ions that flow past the spacecraft with a velocity equal to $-\vec{V}_{sc}$, as discussed in Chapter II. These ions are expected to have energies approximately equal to $1/2\ m_i V_{sc}^2$. For atomic oxygen ions this corresponds to an energy of 5 eV which is consistent with the observed energy of the peak. Because this ion distribution is so sharply peaked, it cannot be properly resolved by the Lepedea so it is not possible to make estimates of either the density or the temperature of these thermal ions from the observations.

For singly charged ions, the higher energy peak is at an energy ≈ 18 eV. This energy is somewhat lower than the maximum energy of water-group ions (i.e., OH^+, H_2O^+, H_3O^+) picked up from a cloud of gases moving with the Orbiter. The maximum energy of H_2O^+ picked up from such a cloud is 23 eV, 22 percent higher than the energy of the observed peak. Water and water ions, however, are observed to be the predominant contaminants in the near vicinity of the Orbiter [10,11], and H_2O^+ was observed throughout the free flight by the ion mass spectrometer aboard the PDP [12]. In addition, the velocity-space contours of the ion velocity distribution, shown in Figures 15 and 16 and discussed below, indicate that these ions are pick-up ions. The contours show that the peak at 18 V is actually a cross section through an extended ring-like distribution rather a single localized peak. This kind of distribution is consistent with pick-up ions, but not with ambient ionospheric ions which have a distribution that forms a single well-defined peak. For these reasons, the secondary maximum observed at 18 V is interpreted as water ions gyrating about Earth's magnetic field with a speed approximately equal to the orbital speed of the spacecraft. The discrepancy between the observed energy of these ions and the expected energy may be due to the mechanism by which neutral water is ionized, or may be caused by collective plasma processes after the ions are formed.

Neutral water molecules in the vicinity of the Orbiter are subject to charge exchange with ionospheric O^+ resulting in H_2O^+ ions and neutral OI. As will be shown in Chapter IV, this process is the

dominant mechanism for ionization of H_2O at the altitude of the Orbiter. Charge exchange reactions generally proceed with little exchange of momentum between the interacting particles, however, some momentum transfer can occur [17]. The fact that the ions observed by the Lepedea have an energy somewhat lower than expected may be an indication that some momentum transfer does occur or that some of the kinetic energy of the H_2O molecule is converted to internal energy during the charge exchange process. An alternative explanation is that the H_2O^+ ions lose energy through wave-particle interactions. The spectrum of Figure 14 clearly shows a multiply peaked distribution, and such distributions are known to be unstable to the generation of plasma waves. An instability arising from this distribution could alter the velocity distribution of the plasma and might be the reason why the H_2O^+ ions are observed at an energy which is lower than the energy predicted by the simple arguments presented in Chapter II.

Ions with energy greater than 20 eV are also shown in Figure 14. The broad plateau-like region between 20 V and 60 V is also a cross section through an extended distribution, and is probably due to the pick-up of ions with masses greater than 18 AMU. It is interesting to note that CO_2, which is predicted to be one of the contaminants produced by thrusters, would have a maximum pick-up energy of 55 eV, which corresponds closely to the cut-off energy of the spectrum of Figure 14.

Figure 15 displays contours of constant $f(\vec{v})$ at 0208 UT in the velocity-space plane containing V_x and V_y. This plane is

perpendicular to the magnetic field which lies along the V_z axis. The projection of $\vec{V}_{sc}$ into this plane lies along the V_x axis, and for this case $\vec{V}_{sc}$ is out of the plane by only 4 degrees. To calculate $\vec{v}$ and $f(\vec{v})$, a mass of 16 AMU corresponding to the mass of O^+ ions is assumed. For water ions, which have a mass of 18 AMU, the contours are approximately accurate. For more massive ions, however, the contours and velocities should be recomputed. The outermost contour in Figure 15, which crosses the V_x axis at -2.9×10^6 cm/sec, corresponds to $f = 10^{-19}$ sec^3/cm^6. Successive interior contours increase in value by factors of 10. The maximum in f near $V_x = -0.8 \times 10^6$ cm/sec is the signature of the ambient ionospheric ions. The maximum seen in the energy spectrum of Figure 14 at 18 V is represented in Figure 15 by the contour which crosses V_x at -1.5×10^6 cm/sec. This contour and adjacent contours are nearly circular and similar in placement and shape to the velocity-space trajectory of a single ion picked up by a magnetic field (Figure 13). The low-energy threshold of the Lepedea is 2 V corresponding to a speed of 0.5×10^6 cm/sec, so the region near the origin where these circular contours would be expected to close is not accessible to observation. To demonstrate that the distribution is ring-like rather than spherical, it is necessary to look at the distribution in a plane perpendicular to the plane of Figure 15.

Figure 16 is a second contour plot, also at 0208 UT, but for the plane containing V_x and V_z. The magnetic field is parallel to the V_z axis, and this plane is perpendicular to the plane of Figure 15.

From this figure and Figure 15, it is clear that the extent of the distribution parallel to $\vec{B}$ is much less than in the direction perpendicular to $\vec{B}$. With the exception of the three innermost contours near $V_x = -0.8 \times 10^6$ cm/sec that are due to the ionospheric ions, the velocity-space contours show a broad distribution that occupies a ring-like or disk-like region of velocity space, with the plane of the disk lying perpendicular to the magnetic field. As discussed in Chapter II, this is consistent with the type of distribution expected for pick-up ions. For the distribution shown in Figures 15 and 16, however, the ring-like nature of the pick-up ion distribution is partially obscured by the ambient ions which fill the center of the ring.

When $\vec{B}$ and $\vec{V}_{sc}$ are not perpendicular, the plane of the ring remains perpendicular to $\vec{B}$, however the diameter of the ring, which is proportional to $\sin(\alpha)$, decreases. The ambient ionospheric ions, on the other hand, always lie in a direction opposite to $\vec{V}_{sc}$, so that in general they do not lie in the plane of the ring. A distribution that demonstrates this behavior is observed at 0237 UT when $\vec{B}$ and $\vec{V}_{sc}$ are at an angle of 125 degrees.

Figure 17 shows the differential ion flux along the $-V_x$ axis at 0237 UT. At this time the angle between the V_x axis and $\vec{V}_{sc}$ is equal to 35 degrees. In this figure the low-energy peak, seen in Figure 14 at an energy-per-charge < 5 V, is absent. This is as expected since that peak is due to ambient ionospheric ions which have velocities approximately equal to $-\vec{V}_{sc}$, and the vector $\vec{V}_{sc}$ no longer lies along the V_x axis. The higher energy peak is still present, but has

decreased in energy to an energy-per-charge of 12 V. This peak is a cross section through the ring, and this decrease in energy is consistent with the expectation that the diameter of the ring should shrink as sin(α) decreases.

Contours of constant $f(\vec{v})$ are shown in Figure 18 for the plane perpendicular to $\vec{B}$. As in Figure 15, the contours are ring-like, however in this case, the distribution has a smaller diameter. Also, the distribution decreases near $V_x = -0.8 \times 10^6$ cm/sec due to the fact that the distribution of ambient ionospheric ions is no longer centered in this plane. The two innermost contours in Figure 18 correspond to the same value, $f = 10^{-16}$ sec^3/cm^6, and the region of velocity space interior to the innermost contour is a slight depression in $f(\vec{v})$ rather than a peak. This is shown more clearly in Figure 19 which is a cross section through both the ring and the distribution of ionospheric ions.

Figure 19 displays the contours in the V_x, V_z plane. The dashed line in this figure is parallel to $\vec{V}_{sc}$. It is clear from this figure that the ambient ions have been "lifted" from the plane of the ring. The ionospheric ions lie along the direction opposite to $\vec{V}_{sc}$ while the rest of the distribution, which is due to pick-up, remains in the plane perpendicular to $\vec{B}$. Again, this is as expected and helps confirm the identification of the separate pick-up ion and ambient ion distributions.

Distributions similar to those discussed above were observed throughout the free flight, indicating that the contaminant ions reach

at least as far as the maximum distance of the PDP from the Orbiter, 400 m. The essentially ring-like nature of the pick-up ion distributions indicates that these ions follow trajectories which are generally consistent with the single-particle motion of ions created from a cloud of gas moving with the Orbiter. The energy at which the contaminant distribution peaks is somewhat lower than the energy expected of water ions formed from such a cloud. This may be due to the charge-exchange process through which the ions are formed, or to an instability associated with the ion velocity distribution. The identification of these ions as water ions is consistent with measurements made by the ion mass spectrometer on the PDP and with observations of neutral H_2O and H_2O^+ ions on other Shuttle flights. Heavier ions appear to be present as well, but in lower concentrations than H_2O^+. The density of heavy ions is estimated to be less than ten percent of the density of H_2O^+. The distributions have a finite spread both in energy and in pitch angle, α. These features may be due to the finite temperature of the source cloud, or they may indicate that the ions are scattered by either plasma waves or collisions. However, it is clear that scattering has not progressed to such an extent that the ion distributions have become isotropic, forming a spherical shell or filled sphere in velocity space.

The observed pick-up ion distributions can be integrated numerically to obtain a quantitative estimate of the density of these ions. To determine the density of the pick-up ions, it is necessary to remove the contribution from the ionospheric ions. Also, part of

the pick-up distribution lies below the low-energy threshold of the detectors, and it is also necessary to account for this unobserved portion of the distribution. The ionospheric ions are eliminated by removing from the integration a spherical region of velocity space centered at the velocity of the ambient-ion peak. The diameter of this sphere is chosen to be large enough to remove the bulk of the ambient ions, but not so large as to include a significant part of the pick-up distribution. The unobserved part of the pick-up distribution is accounted for in the following way. Rather than attempt to integrate the entire distribution, only that part which is at $V_x < -V_{sc} \sin(\alpha)$ is included in the integration. This accounts for half of the ring, and the resulting density is multiplied by a factor of two to account for the rest. This procedure could lead to a significant error if a large fraction of the pick-up ions are bunched at a given phase rather than spread out gyrotropically about the ring. Bunches of this sort, however, are not clearly observed in the data, and therefore do not appear to be significant for the distributions observed during the free flight. The pick-up densities calculated in this way at 0208 UT and 0237 UT are $490/cm^3$ and $210/cm^3$.

CHAPTER IV

MODELING

A number of simplifying assumptions are made about the processes affecting the contaminant molecules and ions surrounding the Orbiter. These assumptions are incorporated into a model which predicts spatial and temporal variations in the density of the contaminant ions at the position of the PDP. The rate at which the Orbiter releases neutral gas is a free parameter in this model, and an estimate of this rate is obtained by normalizing the modeled pick-up densities to the densities measured by the Lepedea.

The Orbiter's Gas Cloud

In order to model the pick-up of ions it is first necessary to develop a model of the cloud of gases which is their source. To simplify the chemistry, only H_2O molecules are included in this model. As discussed in Chapter III, water and water ions have been observed to be the dominant contaminant species near the Orbiter, and the energy spectrum of ions observed by the Lepedea is consistent with these observations. Therefore, it is expected that the major features of the gas and ion clouds can be reproduced by considering H_2O to be the only molecule released. The water is assumed to leave the Orbiter with a temperature of 300 °K, the approximate temperature of the

Orbiter surfaces. The density of the resulting water cloud is assumed to be low enough that collisions between the water molecules are unimportant. The shape of the Orbiter is fairly complicated, and the actual source of the water is unknown. To simplify, the contaminant cloud is modeled as radial flow from a spherically symmetric source with a radius R_o = 10 m, the approximate linear dimension of the Orbiter. The gas expands radially with a speed relative to the Orbiter of C = 525 m/sec corresponding to the thermal speed of H_2O at 300 °K.

The cloud is shaped by collisions with the ambient atmospheric gases, predominantly OI. The mean free path for such collisions is $\lambda = 1/(n_a\sigma)$, where n_a is the atmospheric density, and σ is the cross section for the collisions. The cross section for collisions between OI and H_2O is not known but can be estimated assuming diameters of 4.6×10^{-8} cm for H_2O and 2.6×10^{-8} cm for OI [17], where the diameter of OI is assumed to be equal to the diameter of Ne. Using these diameters, and assuming hard-sphere collisions leads to an estimate of $\sigma = 4 \times 10^{-15}$ cm^2. Since $C \ll V_{sc}$, the water molecules have a velocity relative to the atmosphere approximately equal to $\vec{V}_{sc}$, and the mean collision time is given approximately by $\tau = \lambda/V_{sc}$. Relative to the Orbiter, then, these gas molecules travel a distance $d = C\tau = C\lambda/V_{sc}$ before colliding with the atmosphere. The parameter d is an "effective" mean free path which is also a measure of the scale of the cloud. The effect of collisions is to transfer momentum from the atmospheric gases to the water. Assuming hard-sphere elastic

collisions, approximately 90 percent of all such collisions result in H_2O molecules with speeds > 5 C relative to the Orbiter. Therefore, these molecules are rapidly scattered away from the spacecraft. The density of contaminant molecules that have not suffered collisions can be derived in an approximate way from the equation of continuity by assuming that losses are proportional to the flux of atomic oxygen molecules through the cloud and that the flux of atomic oxygen is unperturbed by the collisions. This approximation is valid so long as the mean free path for collisions in the cloud remains greater than the dimension of the cloud. The equation of continuity may be written

$$\frac{\partial n}{\partial t} + \vec{\nabla} \cdot (n\vec{C}) = L \quad , \tag{16}$$

where L represents the losses due to collisions, n is the density of H_2O, and $\vec{C}$ is the radial velocity of expansion of the cloud in a frame of reference centered on and moving with the Orbiter. The loss term L may be written

$$L = - nV_{sc}n_a\sigma = - \frac{nV_{sc}}{\lambda} \quad .$$

In spherical coordinates, and assuming steady-state conditions so that $\partial n/\partial t = 0$, equation (16) may be written as

$$\frac{1}{r^2}\frac{\partial}{\partial r}(r^2 nC) = -\frac{nV_{sc}}{\lambda} \quad .$$

The derivatives on the left-hand side of this equation are evaluated and the equation rearranged algebraically to yield

$$\frac{1}{n}\frac{\partial n}{\partial r} = -\frac{2}{r} - \frac{V_{sc}}{\lambda C} \quad .$$

The solution may be written

$$n(r) = n(R_o)\frac{R_o^2}{r^2}\exp\left[-\frac{(r - R_o)}{d}\right] \quad , \tag{17}$$

where $d = C\lambda/V_{sc}$ is the "effective" mean free path which has already been predicted through qualitative arguments. This equation is valid for $r > R_o$, $C \ll V_{sc}$, and for a cloud of water that does not significantly affect the flow of OI through the cloud. It can be seen from equation (17) that if there are no collisions with the atmosphere, then d becomes infinite and the density of water within the cloud varies as $1/r^2$, a result which can be obtained directly by setting the loss term, L, in equation (16) to zero. The constant $n(R_o)$ may be rewritten in terms of the rate at which gas escapes the spherical surface at R_o. This rate, $\dot{N}$, is given by

$$\dot{N} = 4\pi R_o^2 n(R_o) C \quad .$$

Equation (17) is used to model the H_2O cloud from which H_2O^+ ions are created. The goal of the model is to account for the H_2O^+ ion densities observed by the PDP. Water molecules that have collided with the atmosphere are scattered away from the spacecraft. Since these molecules have speeds relative to the spacecraft which are much greater than C, they disperse rapidly. Therefore, the principal contribution to the distribution of pick-up ions observed by the PDP is expected to be water molecules that have not yet suffered collisions. The validity of equation (17) is probably somewhat better ahead of the Orbiter than behind, since collisions generally scatter the H_2O into the region behind the Orbiter. The actual density of water within the cloud, however, is probably no greater than it would be in a collisionless cloud, and during the PDP free flight the density predicted by equation (17) varied from the density within a collisionless cloud by no more than a factor of two.

Ionization and Losses

Possible sources for ionization of H_2O at Orbiter altitudes include photoionization by solar ultraviolet radiation, ionization caused by the impact of energetic photoelectrons, and charge exchange with O^+ ions through the reaction

$$O^+ + H_2O \rightarrow O + H_2O^+ \quad . \qquad (18)$$

Momentum transfer during the charge exchange process is small [15], so that an H_2O^+ ion created in this way initially has a velocity about the same as the neutral H_2O molecule. Of these three processes, reaction (18) dominates and the other two processes can be neglected by comparison. To see that this is so, it is possible to estimate the ionization rates for photoionization and electron impact ionization. The ionization potential of H_2O is 12.6 eV which corresponds to a photon wavelength of 986 Å. The solar flux between 2 Å and 1000 Å for low-average solar conditions can be computed from the tables in reference [5] to be $< 5 \times 10^{10}/cm^2$ sec. The photoionization cross section between 400 Å and 1000 Å has been measured by Wainfan et al. [18] to be $< 2.5 \times 10^{-17}$ cm^2. If it is assumed that this represents an upper limit to the cross section for the entire range of wavelengths then the photoionization rate is $< 10^{-6}$/sec. The rate for ionization of H_2O by electron impact is calculated using the observed spectrum of energetic photoelectrons and the measured cross section for this process [19]. For the free flight this rate is calculated to be less than 1.5×10^{-8}/sec, about the same as the rate for electron impact ionization of OI. The cross section for charge exchange between H_2O and O^+ for the 5 eV energy of O^+ ions relative to the cloud appears uncertain. Measured cross sections for this reaction range from 0.6×10^{-15} cm^2 to 2.6×10^{-15} cm^2 [20,21]. We adopt the cross section measured by Turner and Rutherford [21] which is equal to 2.6×10^{-15} cm^2. This value is a factor of two lower than the cross section for charge exchange for H_2^+ incident on H_2O at an energy of

30 eV [22]. For a relative velocity of 7.8×10^5 cm/sec, this cross section leads to a reaction rate $\gamma_3 = 2 \times 10^{-9}$ cm^3/sec. If it is assumed that this value is a reasonable estimate of the reaction rate for reaction (18), then for typical ionospheric O^+ densities ranging from 10^4 to $10^6/cm^3$, the rate for ionization of H_2O by charge transfer with O^+ can be estimated to be between 2×10^{-5} and 2×10^{-3}/sec, much faster than the estimated rates for either photoionization or electron impact ionization.

Water ions can be lost through dissociative recombination with electrons

$$H_2O^+ + e^- \rightarrow OH + H \qquad (19)$$

or through an ion-molecule reaction with neutral H_2O

$$H_2O^+ + H_2O \rightarrow H_3O^+ + OH \quad . \qquad (20)$$

The H_3O^+ ions resulting from reaction (20) may recombine with electrons

$$H_3O^+ + e^- \rightarrow \text{products} \quad . \qquad (21)$$

The reaction rates for reactions (19) and (21) are $\alpha_3 \approx 1.7 \times 10^{-7}$ cm^3/sec and $\alpha_4 \approx 1.9 \times 10^{-7}$ cm^3/sec, respectively [23]. For

reaction (20), the kinetic energy of the H_2O^+ relative to the H_2O cloud ranges from zero to approximately 23 eV, due to the fact that these ions are gyrating about the magnetic field. The rate used in the model is the rate at 300 °K which is $\gamma_4 = 1.7 \times 10^{-9}$ cm^3/sec [24]. The reactions involving H_2O, H_2O^+, and H_3O^+ that are included in the model are summarized in Table 2.

Reactions (19) through (21) lead to a pair of differential equations for the concentrations of H_2O^+ and H_3O^+. These equations are

$$\frac{\partial}{\partial t}[H_2O^+] = \gamma_3[H_2O][O^+] - \gamma_4[H_2O^+][H_2O] - \alpha_3[H_2O^+][e^-] \qquad (22)$$

$$\frac{\partial}{\partial t}[H_3O^+] = \gamma_4[H_2O^+][H_2O] - \alpha_4[H_3O^+][e^-] \quad . \qquad (23)$$

Equations (22) and (23) are solved numerically with a fifth-order Runge-Kutta routine. As discussed in Chapter II, the pick-up ions leave the water cloud with a time-averaged velocity equal to $-\vec{V}_\perp$. To account for this motion the equations are solved in a reference frame that is at rest with respect to the instantaneous center of gyration of the pick-up ions.

Consider the geometry shown in Figure 20. The coordinate system used in the model is one in which the V axis points along $\vec{V}_{sc}$ and the vector $\vec{R}$ from the Orbiter to the PDP lies in the plane defined

by V and W. Integration of equations (22) and (23) is performed at the point P which, sliding along the field line $\vec{B}$ with velocity $\vec{V}_{\parallel} = \vec{V}_{sc} \cdot \vec{B}/B$, intercepts the PDP at time $t = t_o$. The density of H_2O at P is found from equation (17) with $r(t) = |\vec{R} + \vec{V}_{\perp}(t_o - t)|$. In practice, the integration is started at a time $t = 0$ when P is sufficiently far from the center of the water cloud that the density of H_2O at P is approximately zero. The fact that the ions have a finite radius of gyration of about 30 m is neglected.

CHAPTER V

MODEL RESULTS

Pick-up ion densities measured during the free flight and densities calculated from the model are shown in Figure 21. Also shown in this figure are the angle, θ, between $\vec{R}$ and $\vec{V}_{sc}$ and the distance, R, between the two spacecraft. The angle θ is an indication of whether the PDP is ahead of or behind the Orbiter. The Orbiter's thrusters are not fired during any of the density measurements shown in Figure 21. Most of the calculations are performed assuming that the density of O^+ is equal to the density of electrons measured with the Langmuir probe, however, between 0232 and 0250 UT and between 0405 and 0422 UT reliable Langmuir probe sweeps are not available and the O^+ density is assumed to be $10^4/cm^3$. Poor agreement between the model and the data for the first of these intervals may be due to O^+ densities which are higher than have been assumed. The density of H_2O at 10 m from the Orbiter is a free parameter in the model and has been chosen by normalizing the model results to the data for the peak near 0350 UT. This normalization yields a density of H_2O at R_o equal to $3.8 \times 10^{10}/cm^3$ and a corresponding water release rate of $\dot{N} = 2.5 \times 10^{22}/cm^3$ sec. If this rate is constant for the entire eight-day mission, a total of 500 kg of water is released. The integrated column density for the cloud is $\simeq 4 \times 10^{13}/cm^2$. This can be compared

to maximum column densities inferred from neutral mass spectrometer measurements from within the Orbiter's bay during the STS-2, STS-3, and STS-4 missions [25]. These column densities range from 1.5×10^{11} to $3.2 \times 10^{13}/cm^2$. For these flights, the measured water densities are largest at the beginning of the flight, and decrease with a time constant of approximately 10 hours.

It should be noted that the density of the neutral water cloud inferred from the model is inversely proportional to the cross section for charge exchange between O^+ and H_2O. If the actual cross section is a factor of five lower than the value estimated in Chapter IV, then the density of H_2O inferred from the model would be a factor of five higher than the estimate discussed above.

Because the water density near the Orbiter is so high, approximately two orders of magnitude greater than n_a at R_o, the assumption that the fluxes of OI and O^+ through the cloud are unperturbed is probably not correct for distances from the Orbiter $\leq$ 50 m, or in the region directly behind the Orbiter. Directly behind the Orbiter these assumptions are not satisfied in any case because the Orbiter itself obstructs the flow and is known to produce a plasma wake [26]. Between 0420 UT and 0500 UT the PDP traversed the region directly behind the Orbiter, and the divergence of modeled and measured densities during this time may be due to the wake of the Orbiter or to a depletion of O^+ near the dense center of the cloud. Between 0115 and 0130 UT, however, the PDP was also in this near-downstream region and the agreement during this time period appears to be quite good. The

fit to the model is also poor between 0310 and 0330 UT. This may be due to a variation in the water release rate or to difficulties integrating the observed distributions to obtain the density. During this time period the angle α between $\vec{B}$ and $\vec{V}_{sc}$ becomes relatively small, ranging from 30 to 60 degrees. When this occurs it is difficult to remove the ambient ions from the integration without removing a significant part of the pick-up ion distribution as well.

Despite the discrepancies at the times mentioned above, the modeled and observed densities are in good qualitative agreement, and for some portions of the free flight the model provides a good quantitative fit to the data as well. We note that the agreement is also good near the first and second sunrise of the free flight even though a variation in the rate of release of water might be expected at these times, when Orbiter surfaces are suddenly exposed to sunlight.

As can be seen in Figure 21, the variation in density of the pick-up ions ranges over more than two orders of magnitude. Much of this is due to variations in the ionospheric plasma density, since the rate of pick-up is proportional to $[O^+]$. The position of the PDP relative to the spacecraft, however, is also important. In Figure 22 the calculated densities of the H_2O cloud and of H_2O^+ and H_3O^+ pick-up ions are shown along an axis parallel to the V axis of Figure 20 but displaced 50 m from the center of the cloud. For this calculation, $\vec{B}$ and $\vec{V}_{sc}$ are taken to be perpendicular and typical daytime densities of $[OI] = 2.3 \times 10^8/cm^3$ and $[O^+] = 4.3 \times 10^5/cm^3$ are assumed. The scale

length, d, of the H_2O cloud is equal to 714 m. In the region ahead of the Orbiter the H_2O^+ density generally follows the density of H_2O, but is five orders of magnitude lower. The formation of H_3O^+ is proportional to the densities of H_2O^+ and H_2O, so that $[H_3O^+]$ becomes significant only near the center of the cloud where $[H_2O]$ and $[H_2O^+]$ are relatively large. Behind the Orbiter $[H_2O^+]$ and $[H_3O^+]$ remain approximately constant. This happens because the ions are transported downstream with a velocity equal to $-\vec{v}_{sc}$, and are many kilometers behind the spacecraft before recombination occurs.

The density of the H_2O cloud falls off as

$$\frac{1}{r^2} \exp\left[-\frac{(r - R_o)}{d}\right] \quad ,$$

where d is proportional to $1/(n_a\sigma)$. Therefore, changes in n_a, the atmospheric density, affect the density of the neutral water cloud and hence the density of the pick-up ions as well. Figure 23 is similar to Figure 22, but is calculated for an atmospheric density five times higher than the density used for the calculation of Figure 22. This density would be observed at an altitude of 270 km, 50 km lower than the altitude of the free flight, during moderate solar conditions. In this case, the scale length of the water cloud is only 143 m, and the density of water ions falls below $1/cm^3$ at a distance approximately 700 m upstream from the Orbiter.

The dependence of the pick-up densities on the angle between $\vec{B}$ and $\vec{V}_{sc}$ is illustrated in Figure 24. This figure shows a calculation of $[H_2O^+]$ and $[H_3O^+]$ along the same axis as in Figures 22 and 23, but for the case where the angle α between $\vec{B}$ and $\vec{V}_{sc}$ is equal to 60 degrees. The densities of OI and O^+ are the same as in Figure 22. Upstream, the pick-up densities are approximately the same as for the case of Figure 22. However, behind the Orbiter the ion density drops rapidly as a consequence of the transport of the pick-up ions along the magnetic field. This transport speed is equal to $V_{sc}\cos(\alpha)$, so the further α is from 90 degrees, the higher the speed of transport. Limiting cases of $\alpha = 0°$ and $\alpha = 180°$ would result in pick-up ions which flow along the field with speed V_{sc}. In these cases, the ions would co-orbit with the spacecraft and would be removed only by recombination with electrons or collisions with the atmosphere. For the Spacelab-2 mission, $30° < \alpha < 150°$, so these cases are not observed.

Table 1. Ionospheric Reactions

Reaction	Rate
$O + h\nu \rightarrow O^+ + e^-$	$I_\nu = 1.7 \times 10^{-7}$/sec
$O + e^- \rightarrow O^+ + 2e^-$	$I_e = 2 \times 10^{-8}$/sec
$N_2 + O^+ \rightarrow NO^+ + N$	$\gamma_1 = 1.2 \times 10^{-12}(300/T)$ cm^3/sec
$O_2 + O^+ \rightarrow O_2^+ + O$	$\gamma_2 = 2 \times 10^{-11}(300/T)^{1/2}$ cm^3/sec
$NO^+ + e^- \rightarrow N + O$	$\alpha_3 = 4.2 \times 10^{-7}(300/T_e)$ cm^3/sec
$O_2^+ + e^- \rightarrow O + O$	$\alpha_2 = 2.2 \times 10^{-7}(300/T_e)^{(0.7 \text{ to } 1.0)}$ cm^3/sec

Note: The symbols T and T_e in the expressions for the rates refer to the temperatures of the gas and the electrons, respectively.

Table 2. Model Reactions

Reaction	Rate
$H_2O + O^+ \rightarrow H_2O^+ + O$	$\gamma_3 = 5 \times 10^{-9}$ cm^3/sec
$H_2O^+ + e^- \rightarrow OH + H$	$\alpha_3 = 1.7 \times 10^{-7}$ cm^3/sec
$H_2O^+ + H_2O \rightarrow H_3O^+ + OH$	$\gamma_4 = 1.7 \times 10^{-9}$ cm^3/sec
$H_3O^+ + e^- \rightarrow$ products	$\alpha_4 = 1.9 \times 10^{-7}$ cm^3/sec

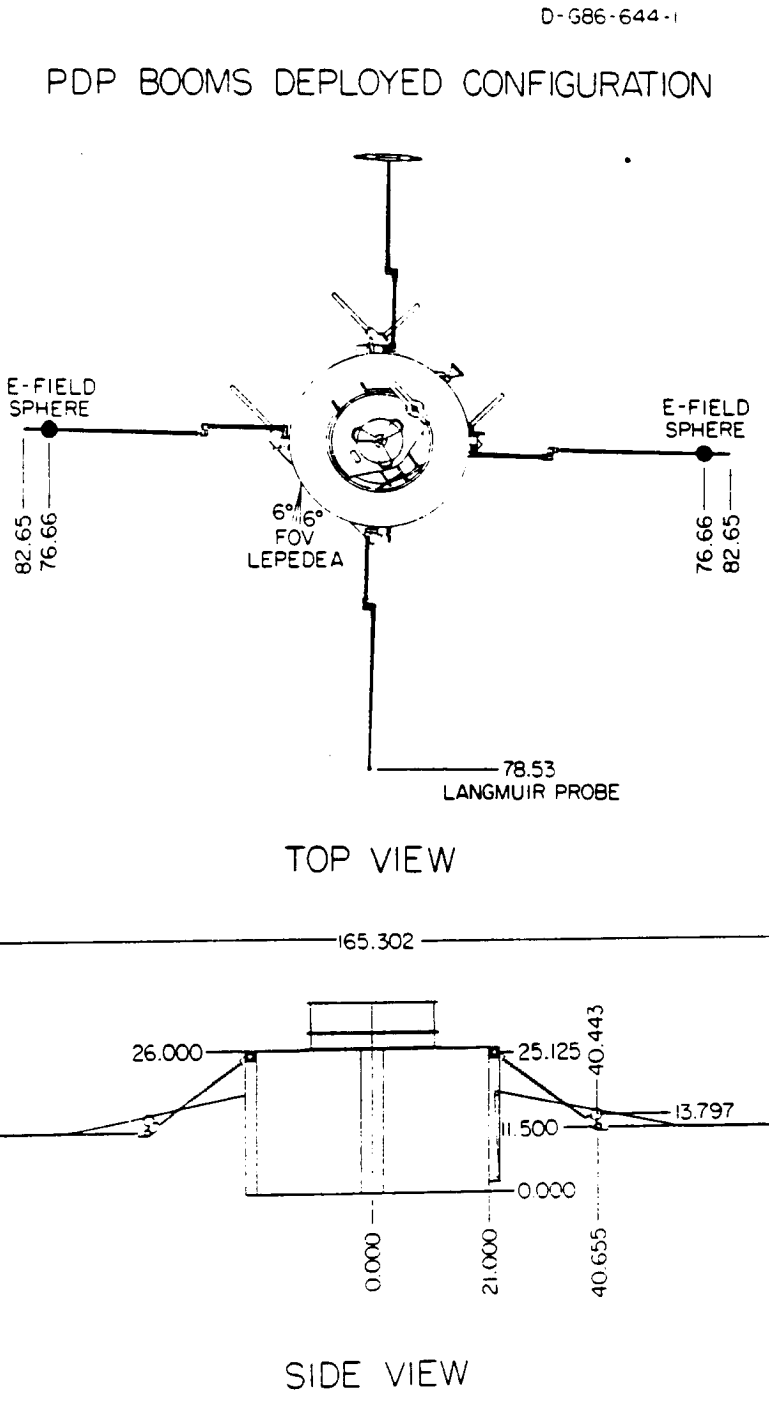

Figure 1. Top and side views of the PDP with the booms deployed as in free flight. Distances are in inches.

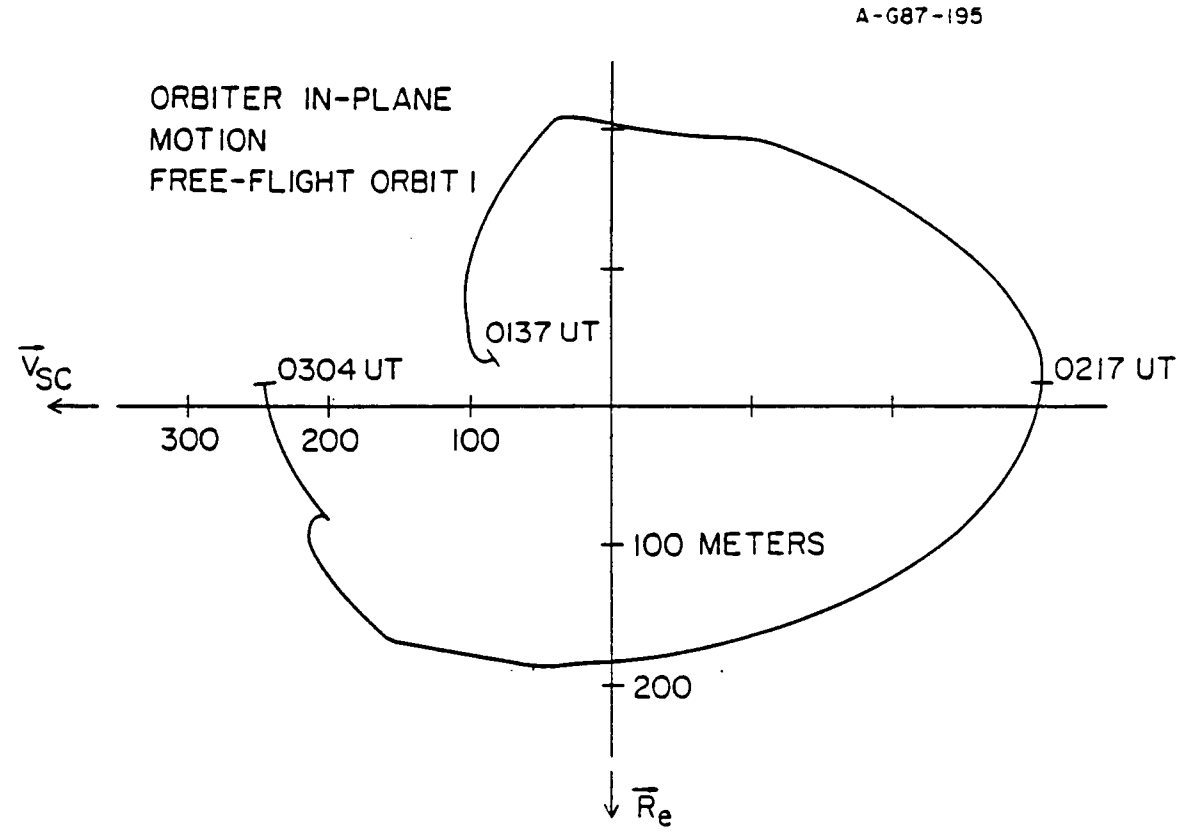

Figure 2. Orbital-plane motion of the Orbiter relative to the PDP between 0137 and 0304 UT.

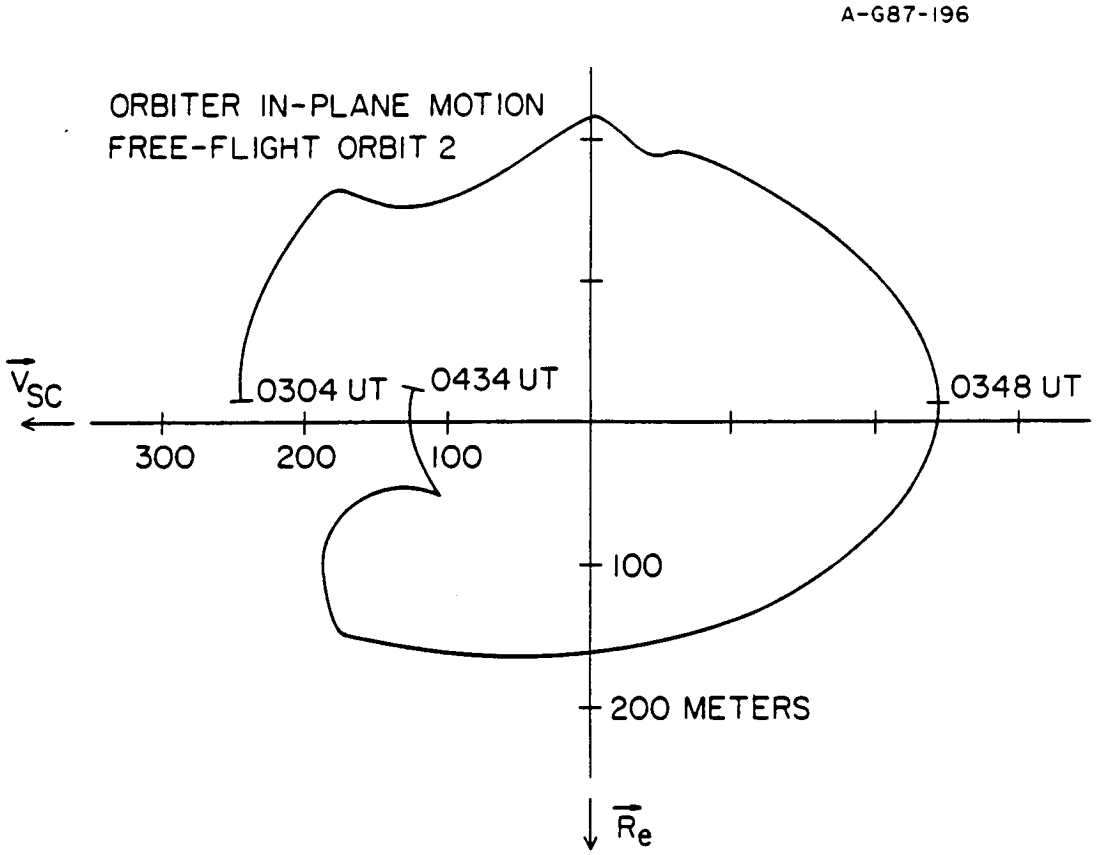

Figure 3. Orbital-plane motion of the Orbiter relative to the PDP between 0304 and 0434 UT.

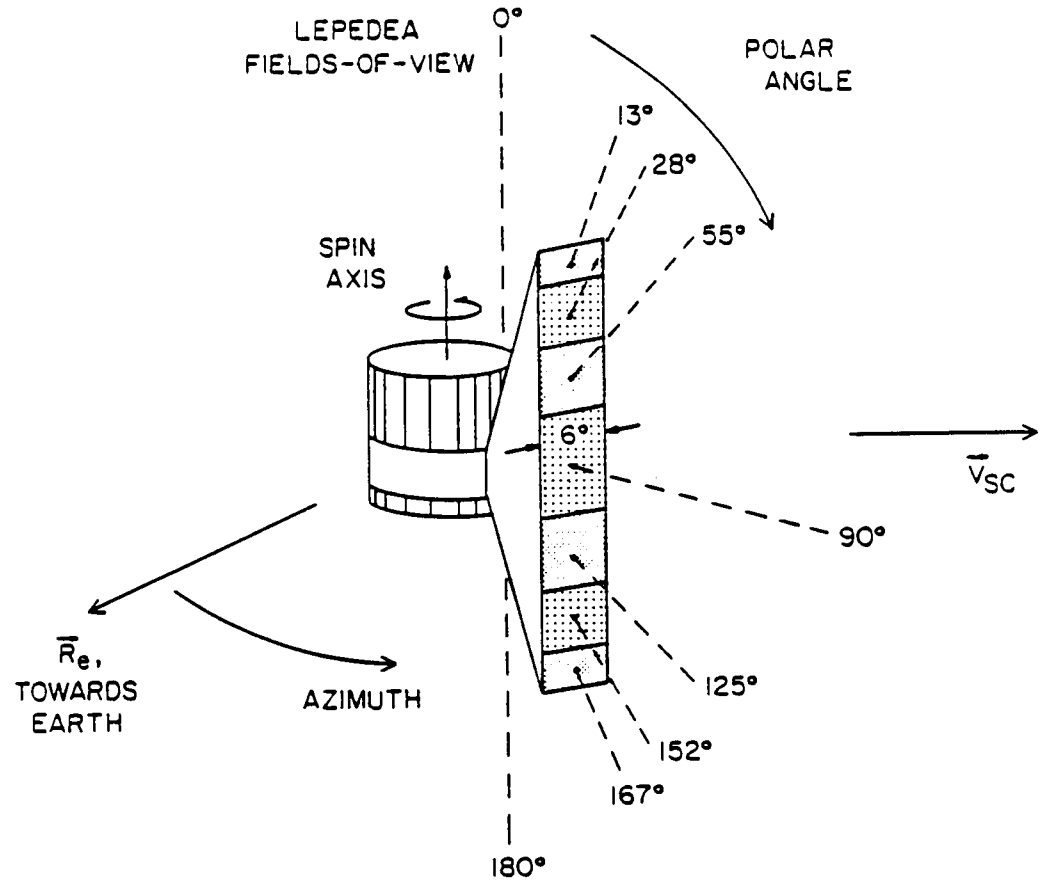

Figure 4. Relative orientations of $\vec{R}e$, $\vec{V}_{SC}$, the PDP spin axis, and the fields-of-view of the Lepedea (adapted from Frank [2]).

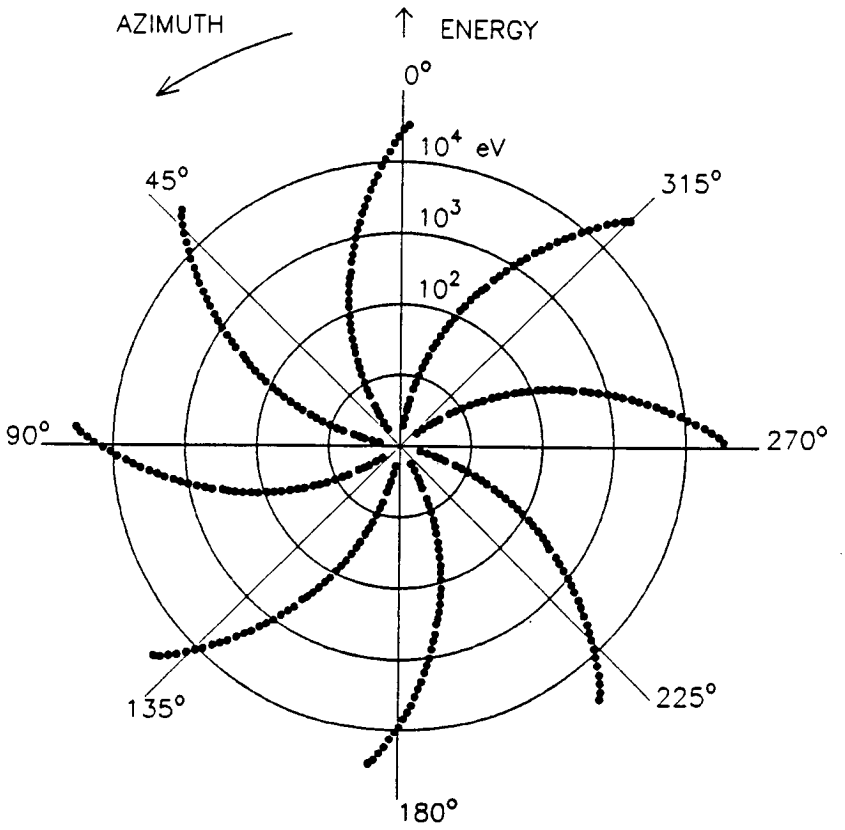

Figure 5. Polar plot showing the azimuth angles of samples from the Lepedea during eight consecutive energy sweeps for a spin period of 13.1 sec. Radial distance is proportional to the logarithm of the energy of the sample.

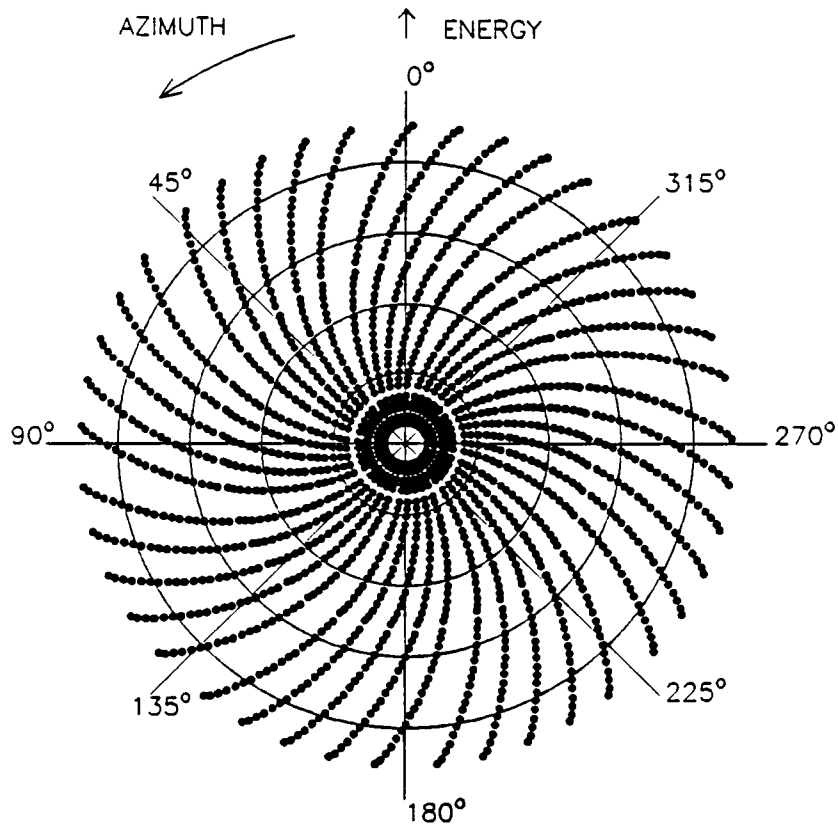

Figure 6. Same as Figure 5 except that 41 consecutive energy sweeps are shown.

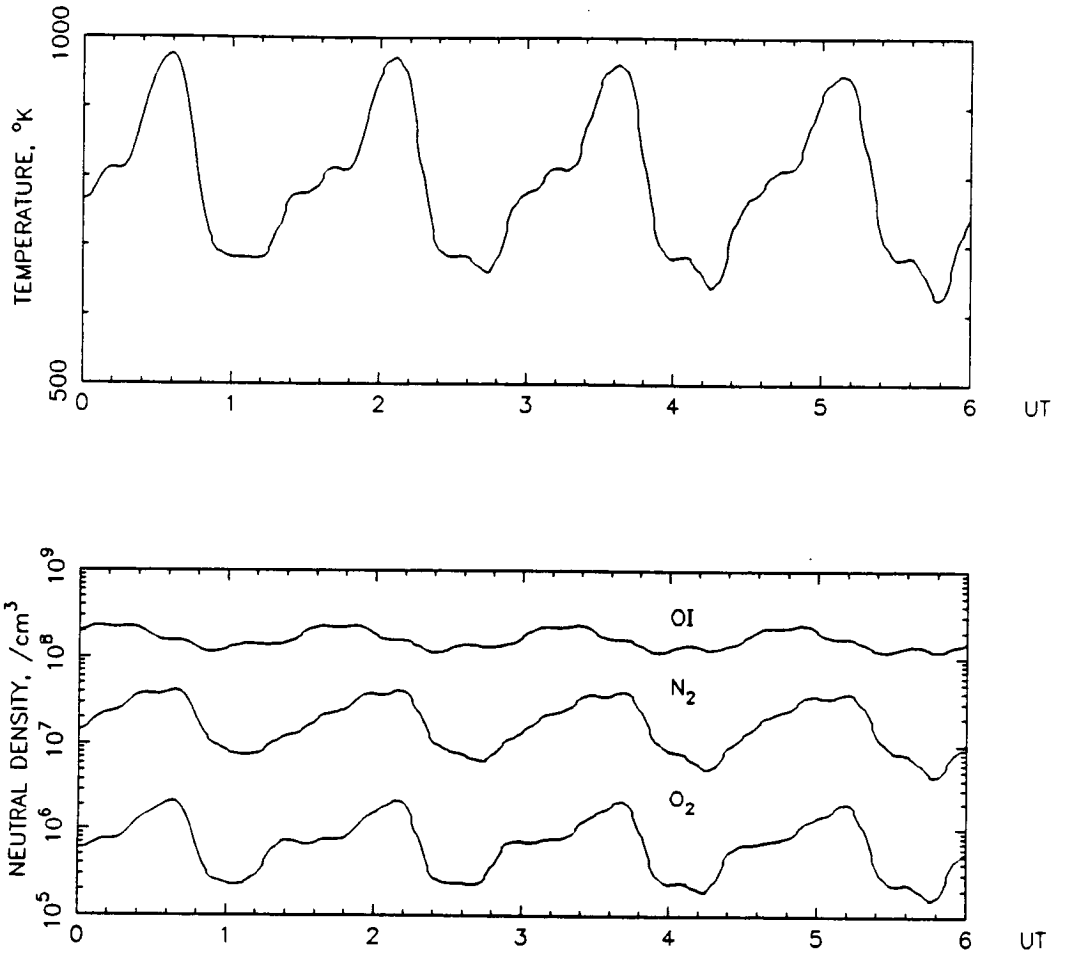

Figure 7. Atmospheric temperature and densities at the position of the spacecraft during the free flight. Calculated from the MSIS-83 atmospheric model (Hedin [4]).

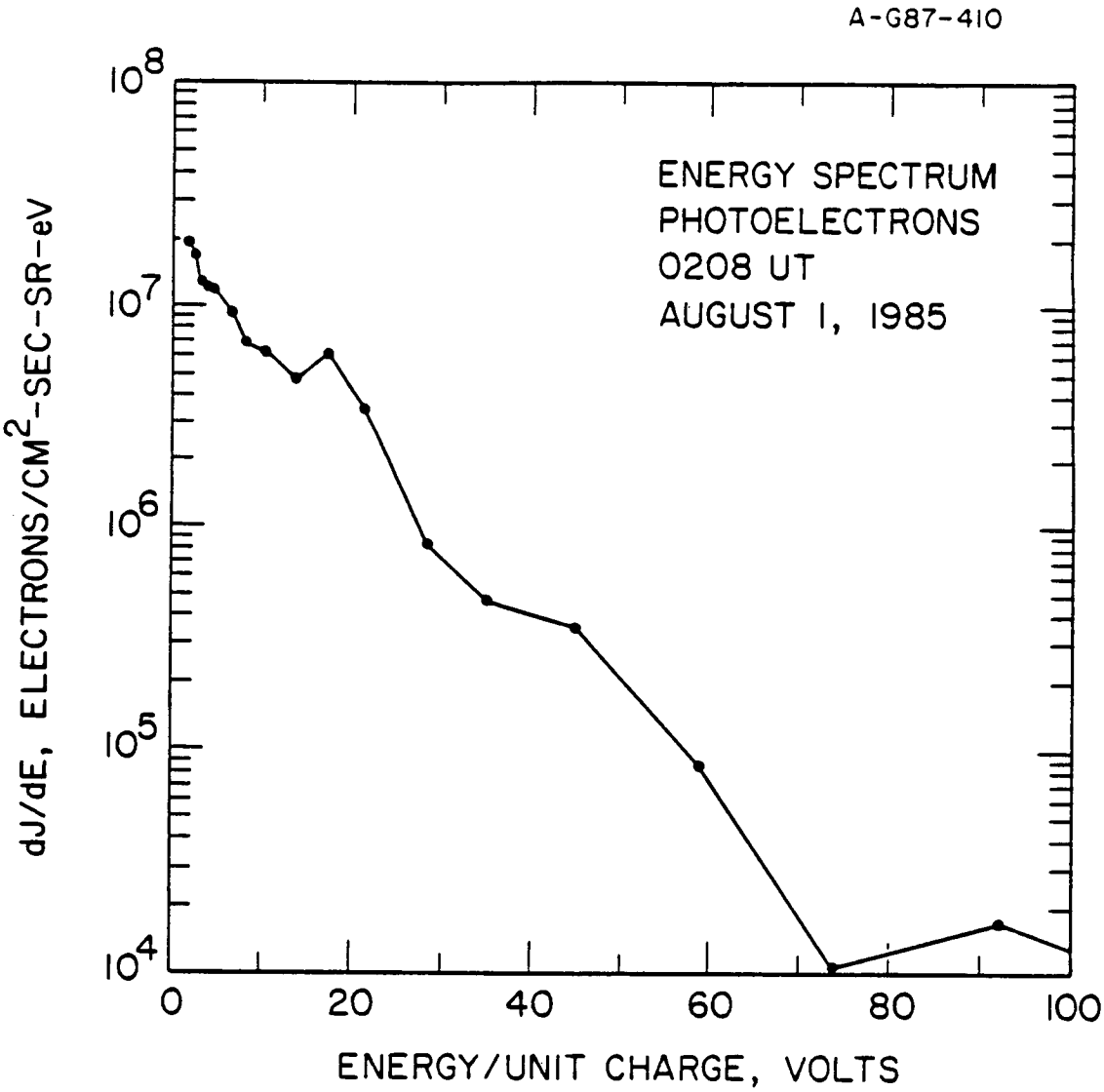

Figure 8. The energy spectrum of photoelectrons observed at 0208 UT.

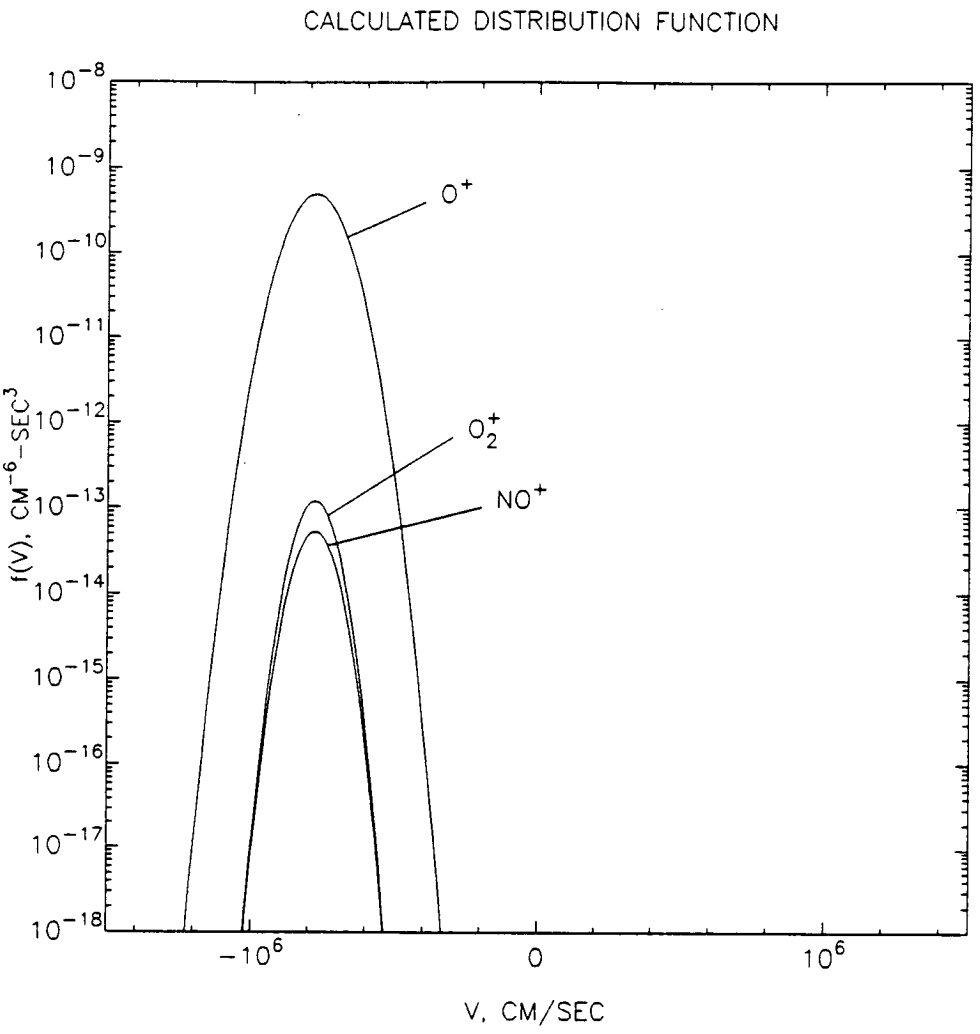

Figure 9. Calculated ion distributions in a reference frame moving with velocity V = 7.8 × 10^3 m/sec with respect to the rest frame of the ions.

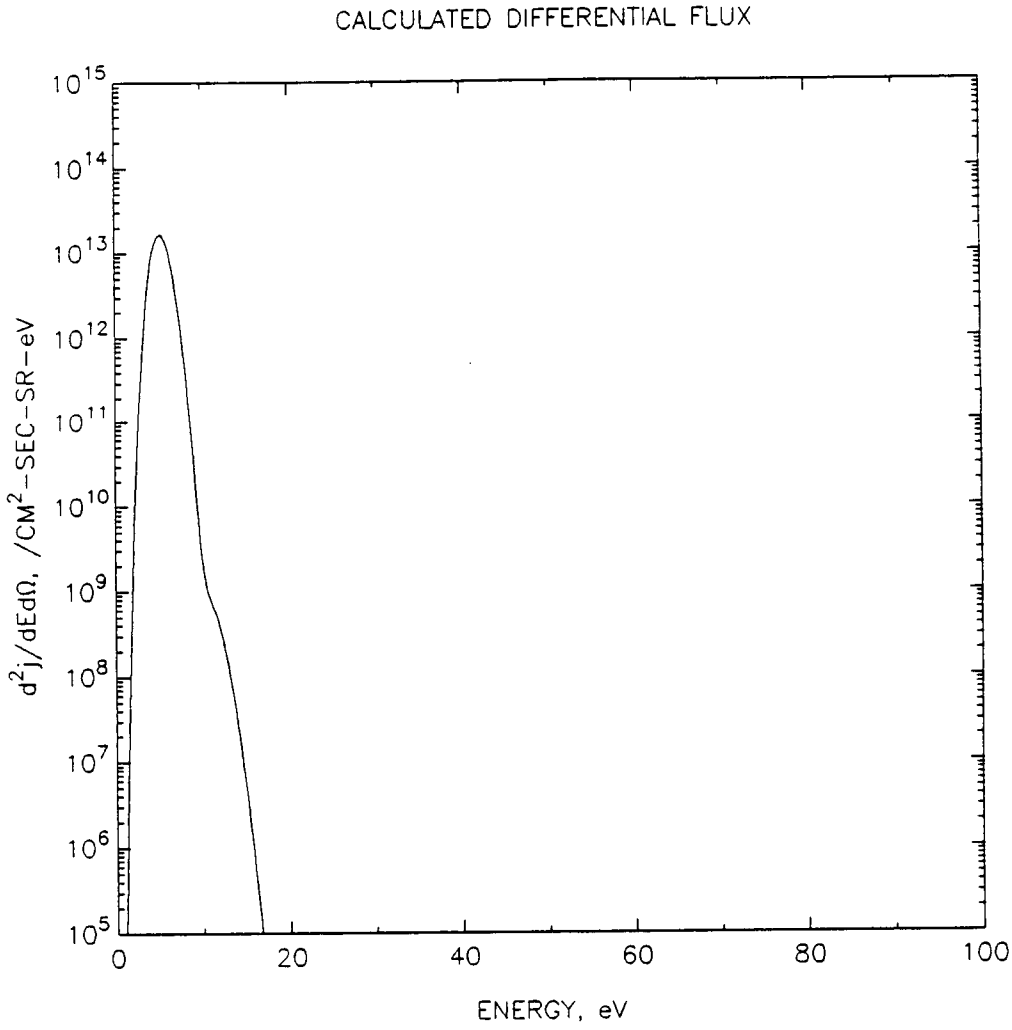

Figure 10. Energy spectrum calculated for the distributions of Figure 9.

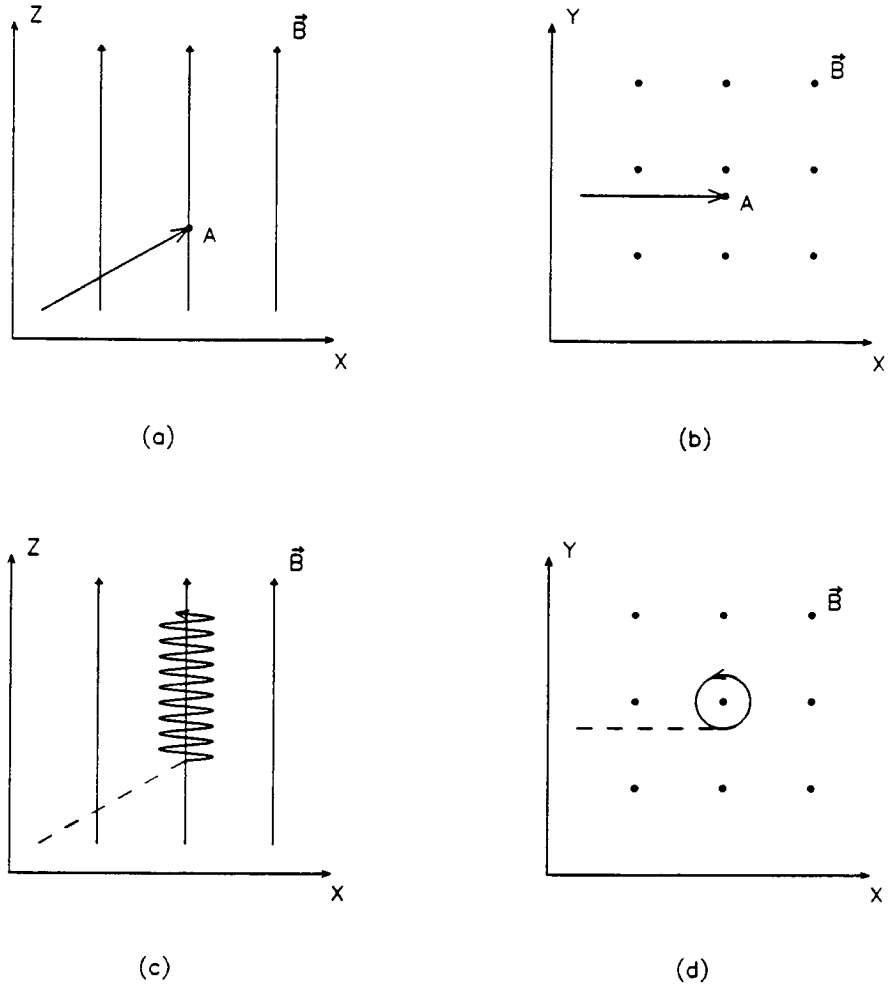

Figure 11. Motion of a particle in a magnetic field before and after ionization. The particle is ionized at point A. (a) Trajectory of the particle in the X, Z plane before ionization. (b) Trajectory of the particle in the X, Y plane before ionization. (c) Trajectory of the particle in the X, Z plane after ionization. (d) Trajectory of the particle in the X, Y plane after ionization.

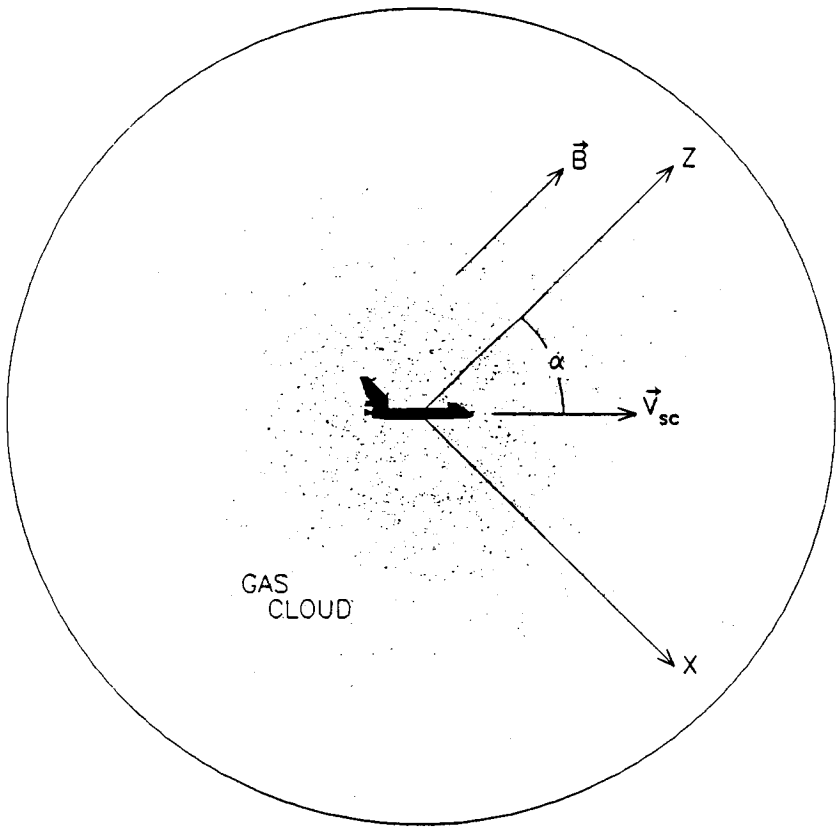

Figure 12. Coordinates used to describe pick-up of ions from a cloud of gases co-orbiting with the Orbiter.

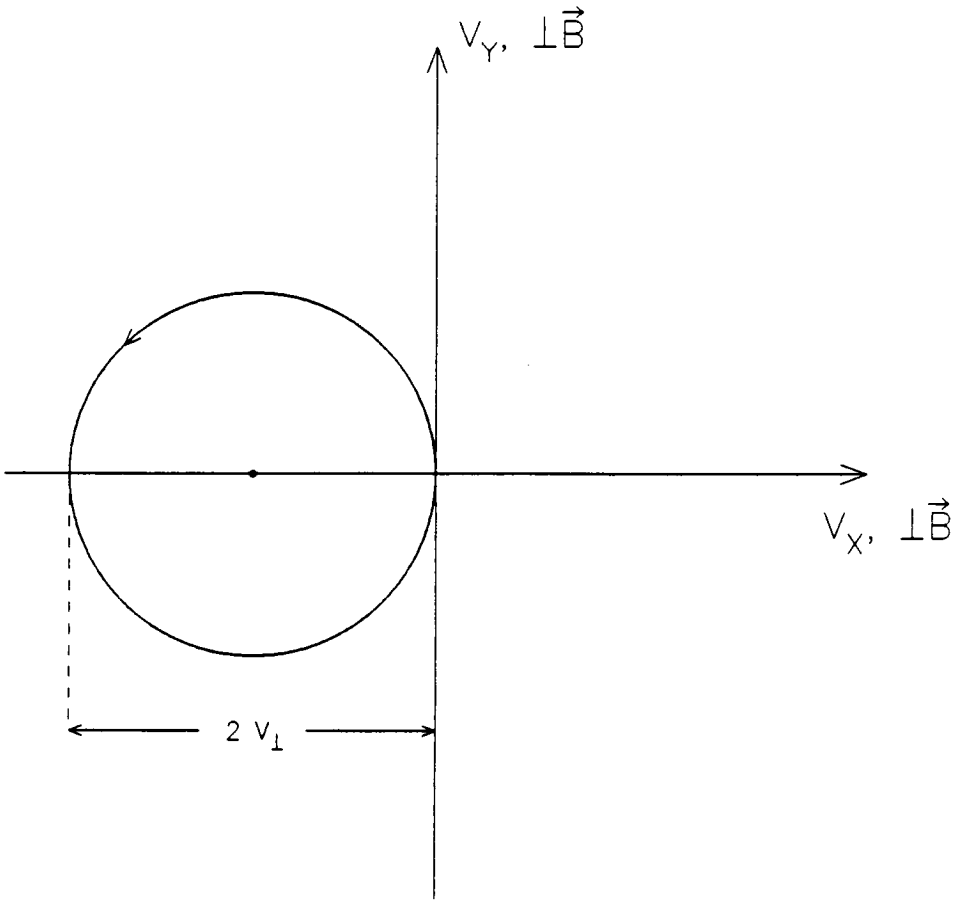

Figure 13. The velocity-space trajectory of a single pick-up ion. The magnetic field is out of the plane of the figure. The ion speed ranges from zero to 2 $V_\perp$.

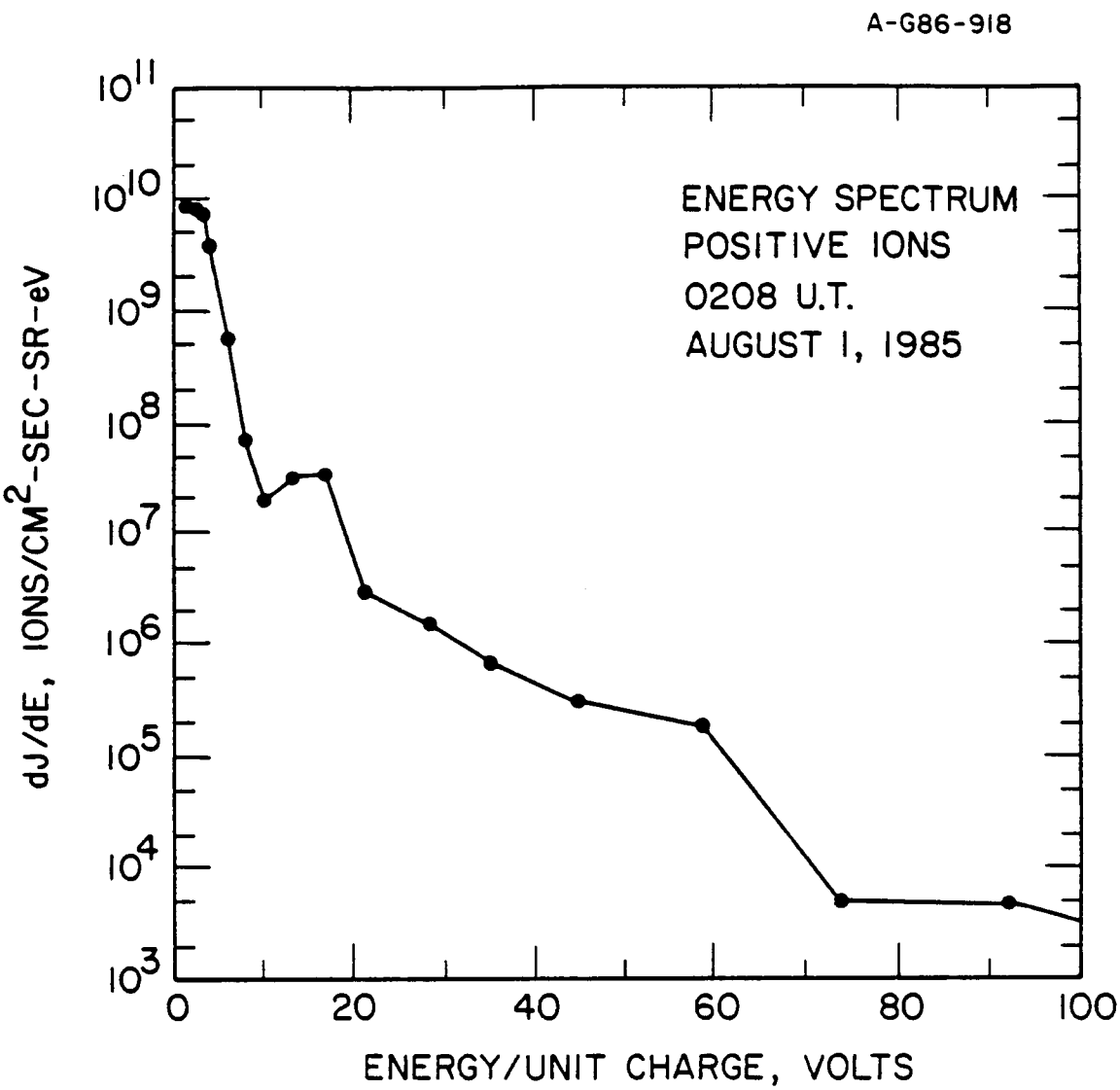

Figure 14. The energy spectrum of positive ions observed by the Lepedea at 0208 UT in the direction of orbital motion.

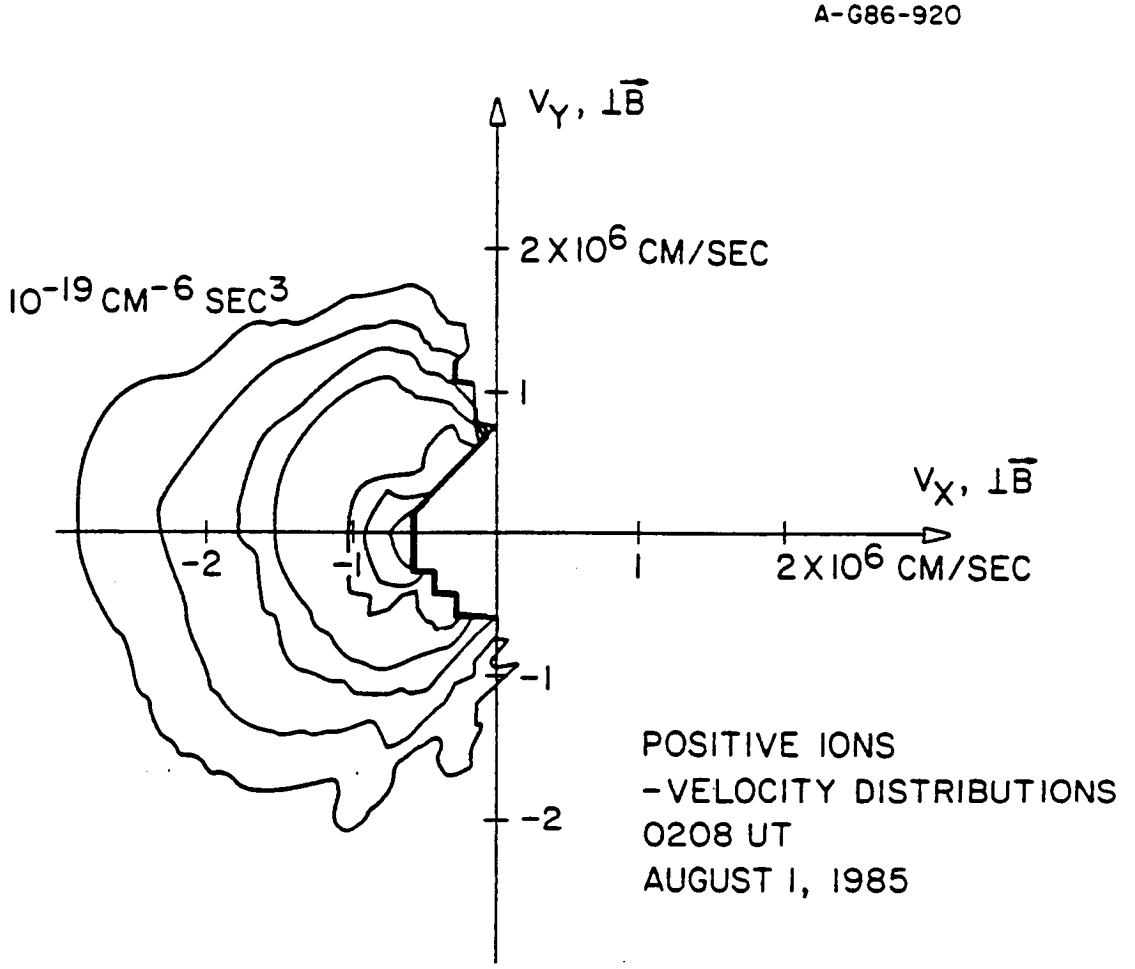

Figure 15. Contours of constant $f(\vec{V})$ at 0208 UT in the V_x, V_y plane. Both V_x and V_y are perpendicular to $\vec{B}$. The projection of $\vec{V}_{sc}$ into the plane is along V_x. At this time, $\vec{V}_{sc}$ and $\vec{B}$ are at an angle of 86°. The outermost contour is for $f = 10^{-19}$ sec^3/cm^6. Contours interior to this increase by factors of ten.

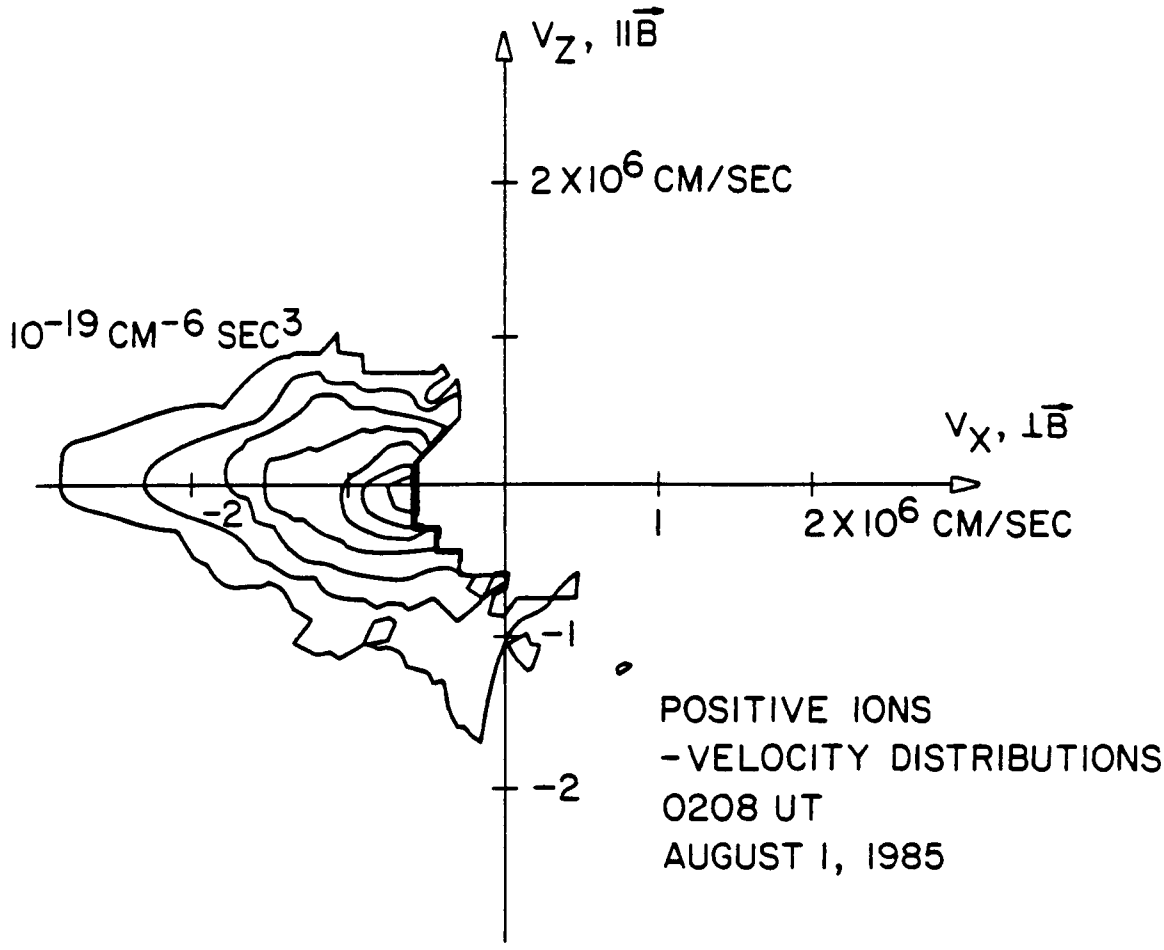

Figure 16. Contours of constant $f(\vec{v})$ at 0208 UT in a plane perpendicular to the plane of Figure 15. The magnetic field is parallel to the V_z axis.

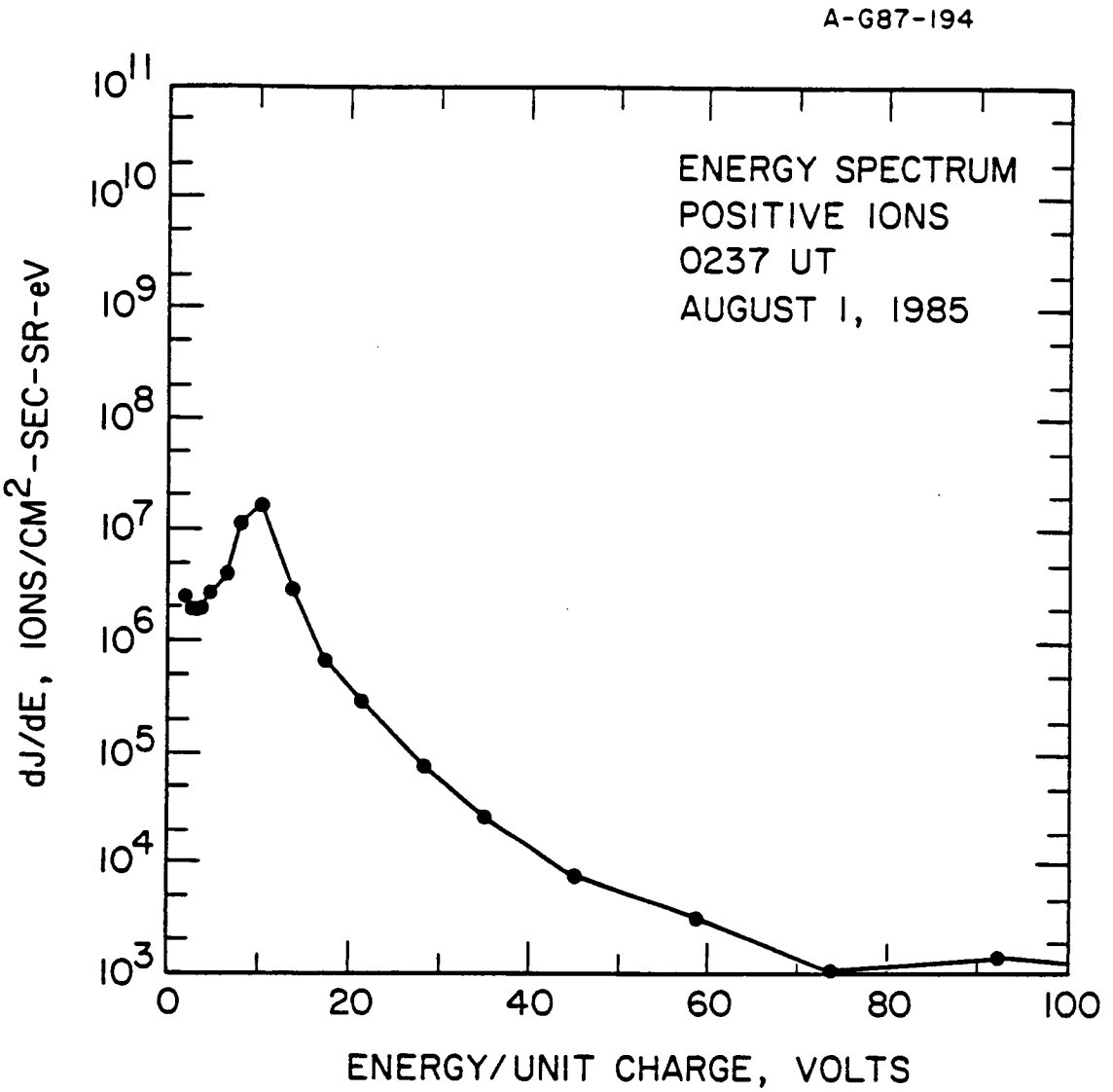

Figure 17. Energy spectrum of positive ions at 0237 UT in the direction of V_x.

A-G87-197

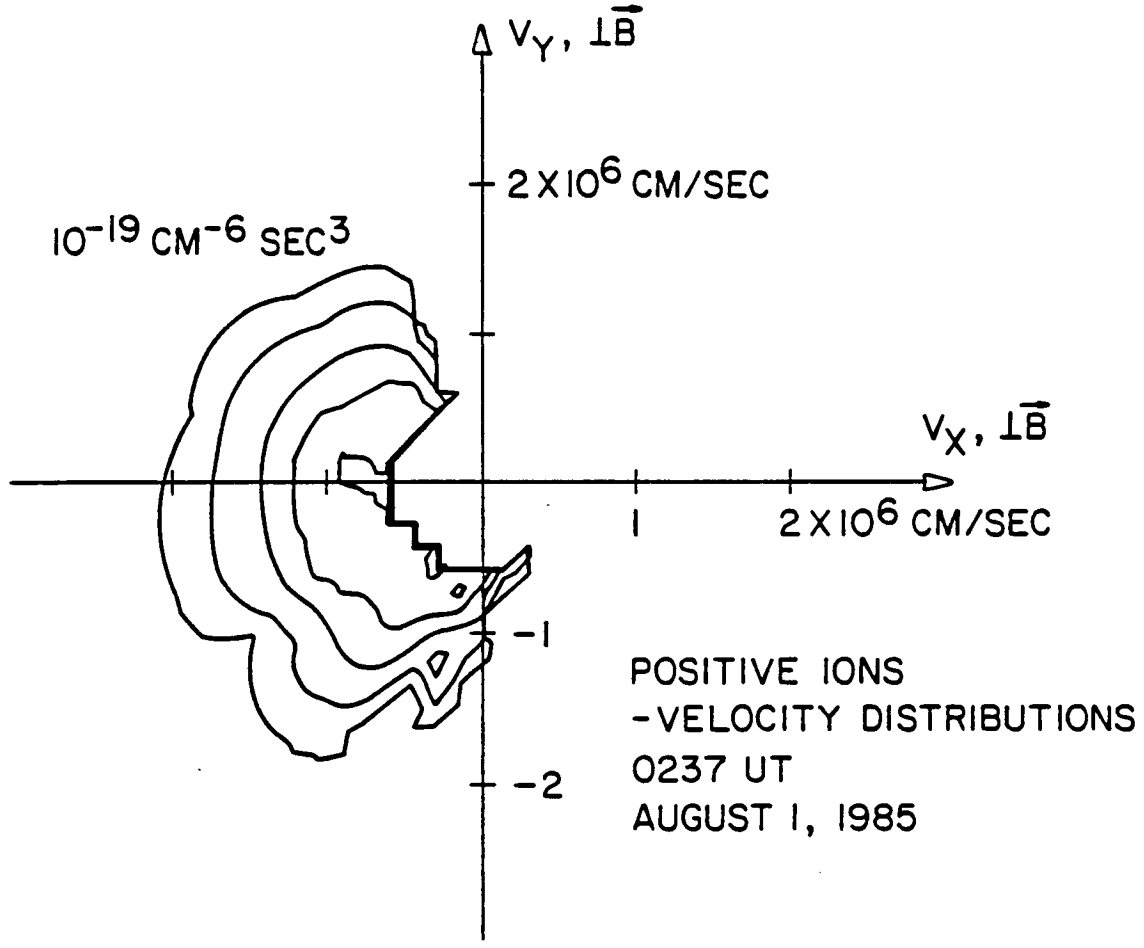

Figure 18. Contours of constant $f(\vec{V})$ in the V_x, V_y plane at 0237 UT.

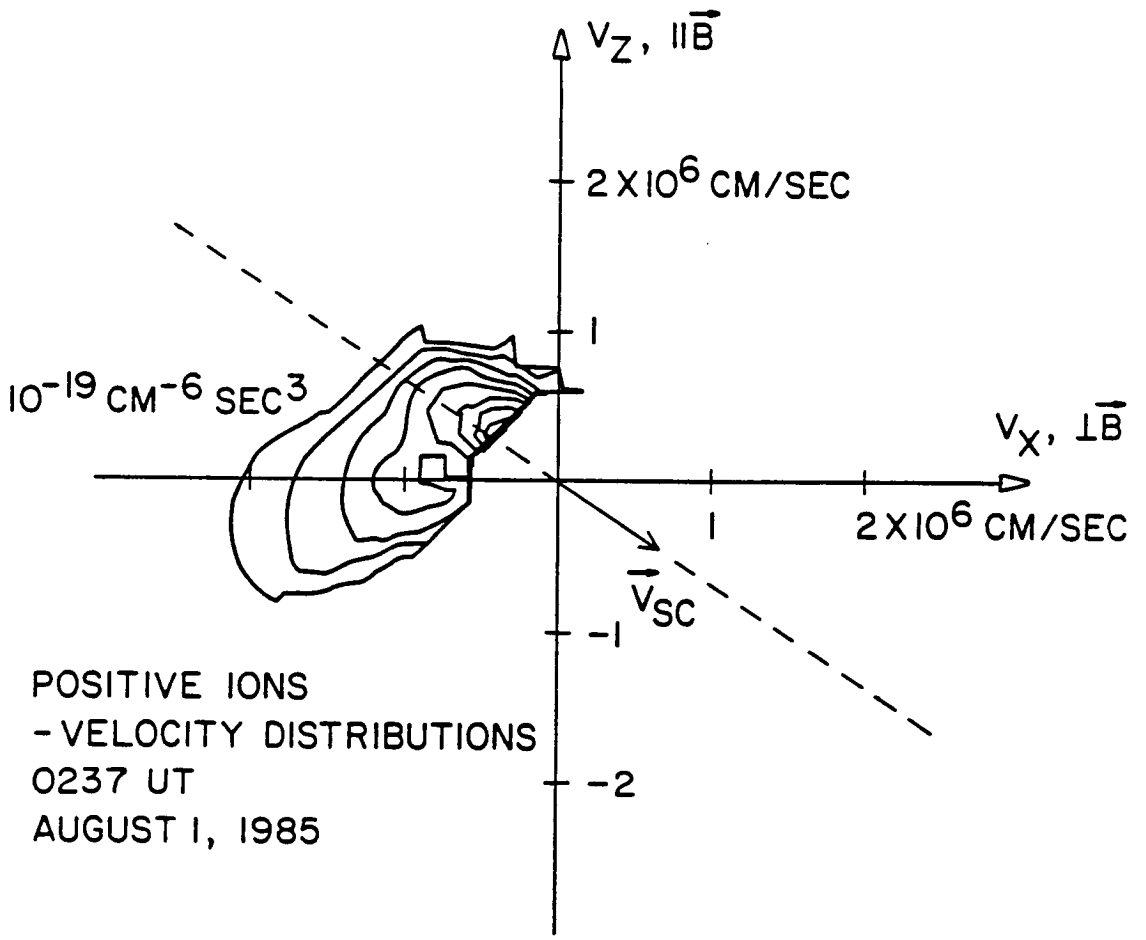

Figure 19. Contours of constant $f(\vec{V})$ in the V_x, V_z plane at 0237 UT. The direction of orbital motion is indicated by the dashed line and the arrow marked $\vec{V}_{sc}$.

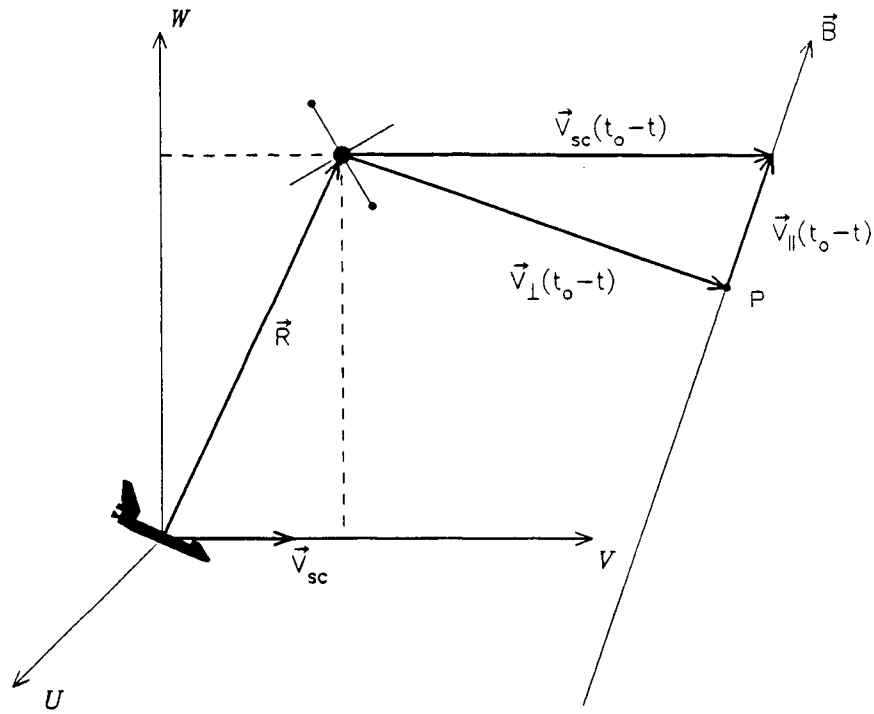

Figure 20. The coordinate system used to integrate equations (22) and (23). The integration is performed at the point P on the field line $\vec{B}$. The point P moves along $\vec{B}$ with a velocity equal to $\vec{V}_{\parallel}$. Magnetic field lines sweep past the Orbiter with velocity $-\vec{V}_{sc}$. The PDP lies in the U, V plane at a distance R from the Orbiter.

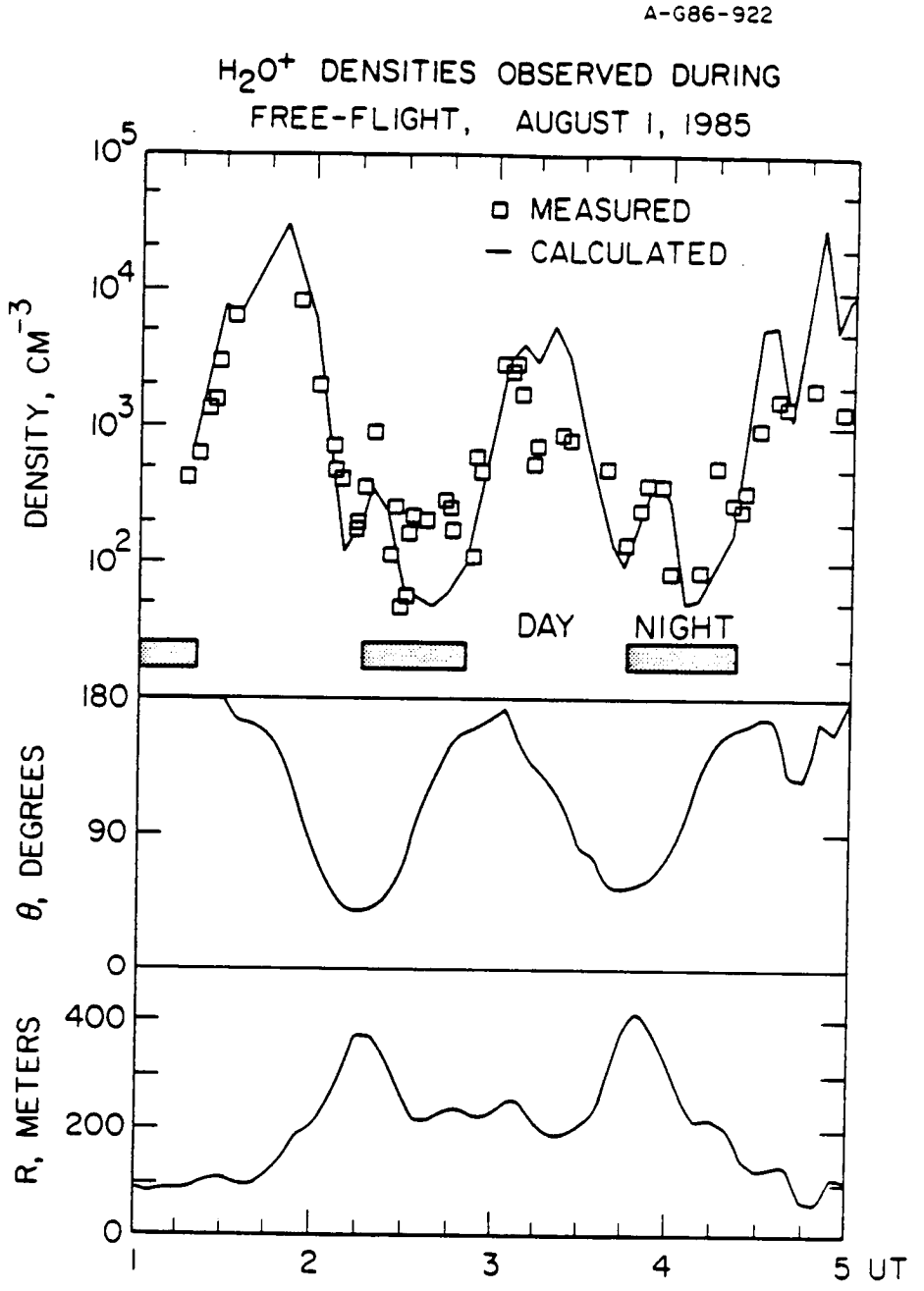

Figure 21. Comparison of observed and calculated pick-up ion densities during the free flight. The lower panels show the angle θ between $\vec{R}$ and $\vec{V}_{sc}$, and the distance R between the PDP and the Orbiter.

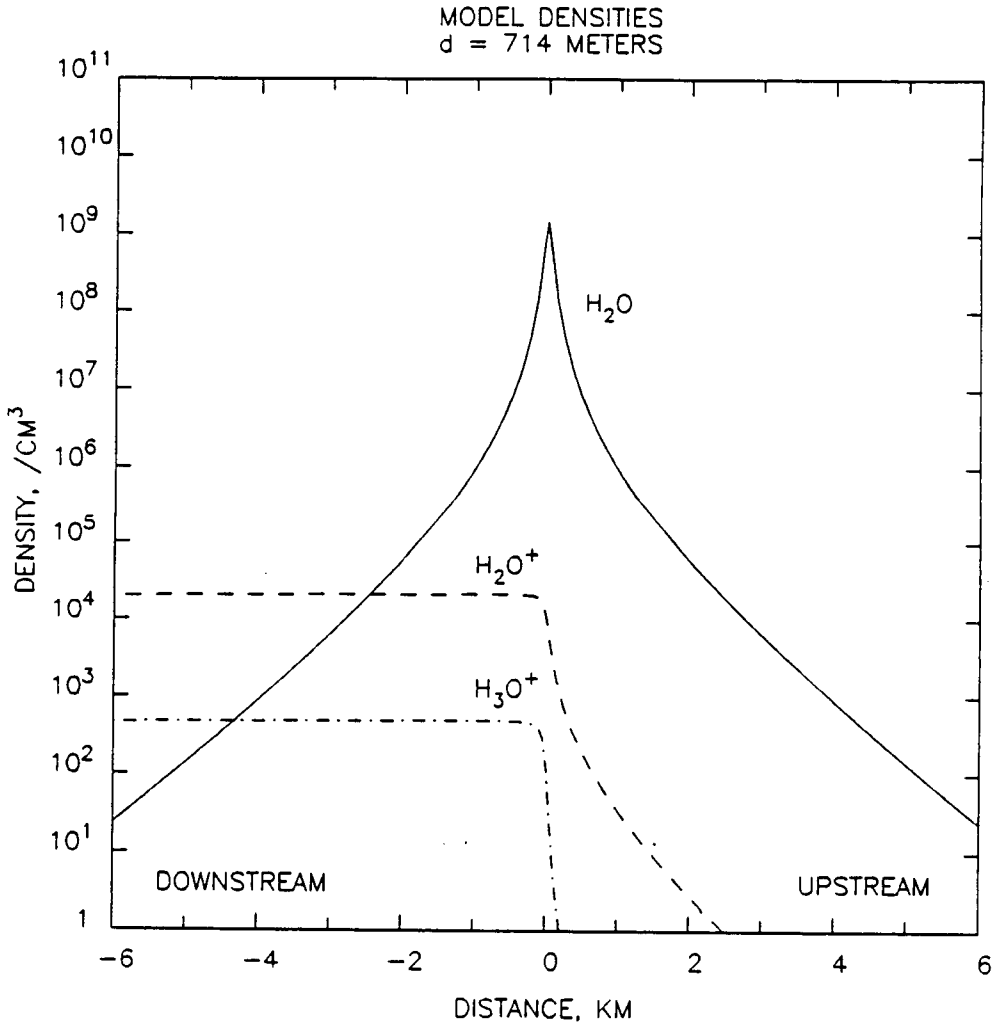

Figure 22. Calculated H_2O, H_2O^+, and H_3O^+ densities along a line which is parallel to the V axis of Figure 20 and which passes within 50 m of the center of the water cloud. Parameters used in the calculation are discussed in the text. The angle between $\vec{B}$ and $\vec{V}_{sc}$ is 90°.

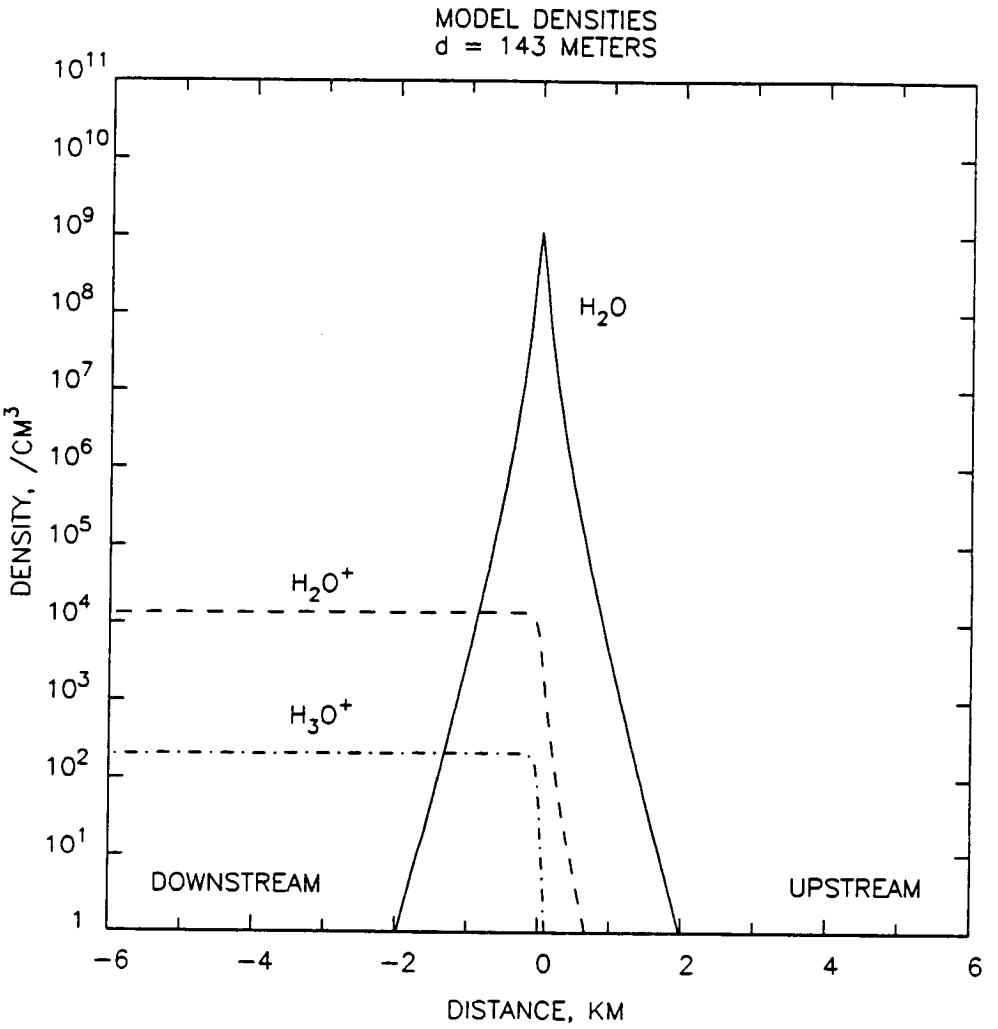

Figure 23. Same as Figure 22 but calculated for an atmospheric densitiy five times higher than the density of Figure 22.

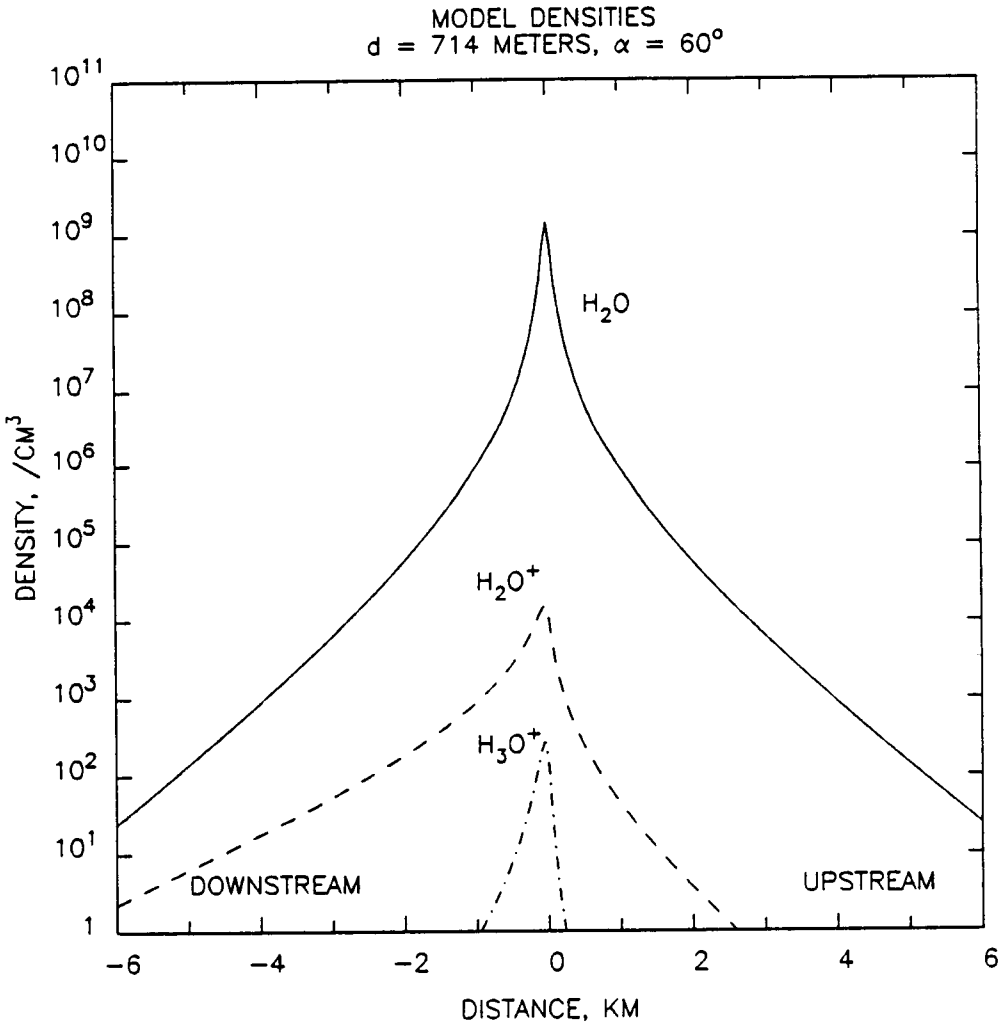

Figure 24. Same as Figure 22 but for an angle between $\vec{B}$ and $\vec{V}_{sc}$ of 60°.

REFERENCES

[1] S. D. Shawhan, G. B. Murphy, and J. S. Pickett, "Plasma Diagnostics Package Initial Assessment of the Shuttle Orbiter Plasma Environment," J. Spacecr. Rockets, 21, 387, 1984.

[2] L. A. Frank, D. M. Yeager, H. D. Owens, K. L. Ackerson, and M. R. English, "Quadrispherical LEPEDEAS for ISEE's-1 and -2 Plasma Measurements," IEEE Trans. Geosci. Electron., 3, 221, 1978.

[3] F. F. Chen, Introduction of Plasma Physics and Controlled Nuclear Fusion, 2nd ed., Vol. 1 (Plenum Press, New York, 1984).

[4] A. E. Hedin, "A Revised Thermospheric Model Based on Mass Spectrometer and Incoherent Scatter Data," J. Geophys. Res., 88, 10,170, 1983.

[5] P. M. Banks and G. Kockarts, Aeronomy, Part A (Academic Press, New York, 1973).

[6] E. Brook, M. F. A. Harrison, and A. C. H. Smith, "Measurements of the Electron Impact Ionisation Cross Sections of H_e, C, O, and N Atoms", J. Phys. B, 11, 3115, 1978.

[7] A. Dalgarno, "Charged Particles in the Upper Atmosphere," Ann. Geophys., 17, 16, 1961.

[8] J. S. Pickett, G. B. Murphy, W. S. Kurth, C. K. Goertz, and S. D. Shawhan, "Effects of Chemical Releases by the STS 3 Orbiter on the Ionosphere," J. Geophys. Res., 90, 3487, 1985.

[9] E. Wulf and U. von Zahn, "The Shuttle Environment: Effects of Thruster Firings on Gas Density and Composition in the Payload Bay," J. Geophys. Res., 91, 3270, 1986.

[10] R. Narcisi, E. Trzcinski, G. Frederico, L. Wlodyka, and D. Delorey, "The Gaseous and Plasma Environment around the Space Shuttle, " AIAA Paper 83-2659, 1983.

[11] D. E. Hunton and J. M. Calo, "Low Energy Ions in the Shuttle Environment: Evidence for Strong Ambient-Contaminant Interactions," Planet. Space Sci., 33, 945, 1985.

[12] J. M. Grebowsky, H. A. Taylor, M. W. Pharo, and N. Reese, "Thermal Ion Perturbations Observed in the Vicinity of the Space Shuttle," Planet. Space Sci., **35**, 501, 1987.

[13] C. K. Goertz, "Io's Interaction with the Plasma Torus," J. Geophys. Res., **85**, 2949, 1980.

[14] F. M. Ipavich, A. B. Galvin, G. Gloecker, D. Hovestadt, B. Klecker, and M. Scholer, "Comet Giacobini-Zinner: In Situ Observation of Energetic Heavy Ions," Science, **232**, 366, 1986.

[15] T. Mukai, W. Miyake, T. Terasawa, M. Kitayama, and K. Hirao, "Plasma Observation by Suisei of Solar-Wind Interaction with Comet Halley," Nature, **321**, 299, 1986.

[16] E. Möbius, D. Hovestadt, B. Klecker, M. Scholer, G. Gloecker, and F. M. Ipavich, "Direct Observation of He^+ Pick-Up Ions of Interstellar Origin in the Solar Wind," Nature, **318**, 1985.

[17] E. W. McDaniel, Collision Phenomenon in Ionized Gases (John Wiley and Sons, New York, 1964).

[18] N. Wainfan, W. C. Walker, and G. L. Weissler, "Photoionization Efficiencies and Cross Sections in O_2, N_2, A, H_2O, H_2, and CH_4," Phys. Rev., **99**, 542, 1955.

[19] T. D. Mark and F. Egger, "Cross-Section for Single Ionization of H_2O and D_2O by Electron Impact from Threshold up to 170 eV," Int. J. Mass Spectrom. Ion Phys., **20**, 89, 1976.

[20] E. Murad and S. T. F. Lai, "Some Charge Exchange Reactions Involving H_2O," Chem. Phys. Lett., **5**, 427, 1986.

[21] B. R. Turner and J. A. Rutherford, "Charge Transfer and Ion-Atom Interchange of Water Vapor Ions," J. Geophys. Res., **73**, 6751, 1968.

[22] M. A. Coplan and K. W. Ogilvie, "Charge Exchange for H^+ and H_2^+ in H_2O, CO_2, and NH_3^*," J. Chem. Phys., **52**, 4154, 1970.

[23] G. W. Sjolander and E. P. Szuszczewicz, "Chemically Depleted F_2 Ion Composition: Measurements and Theory," J. Geophys. Res., **84**, 4393, 1979.

[24] D. L. Albritton, "Ion-Neutral Reaction-Rate Constants Measured in Flow Reactors through 1977," At. Data Nucl. Data Tables, **22**, 1, 1978.

[25] G. R. Carignan and E. R. Miller, "STS-2, -3, -4 Induced Environment Contamination Monitor (IECM) Summary Report, NASA Technical Memorandum TM-82524, 1983.

[26] G. B. Murphy, J. S. Pickett, N. D'Angelo, and W. S. Kurth, "Measurements of Plasma Parameters in the Vicinity of the Space Shuttle," Planet. Space Sci., **34**, 993, 1986.

AN ANALYSIS OF WHISTLER-MODE RADIATION FROM THE SPACELAB-2 ELECTRON BEAM

by

William Michael Farrell

An Abstract

Of a thesis submitted in partial fulfillment
of the requirements for the Doctor of
Philosophy degree in Physics
in the Graduate College of
The University of Iowa

July 1987

Thesis supervisor: Professor Donald A. Gurnett

ABSTRACT

During the Spacelab-2 mission, the University of Iowa's Plasma Diagnostics Package (PDP) was released from the space shuttle to investigate plasma effects in the near-shuttle environment. At times during this freeflight when the PDP was magnetically connected to the shuttle, an electron gun in the shuttle cargo bay ejected a nearly field-aligned 1 keV - 50 mA electron beam. During these beam ejections, the plasma wave instrument onboard the Plasma Diagnostics Package detected intense whistler-mode radiation from the beam. This thesis presents a detailed study of a whistler mode emission detected during one period when the beam was ejected continuously for about 7 minutes. The electric field polarization of the detected whistler mode signal is consistent with propagation near the resonance cone. Calculations indicate that the beam radiated approximately 1.6 mW in the whistler mode as the beam traversed the 200 meters from the shuttle to the PDP. The emissivity also decreased by about a factor of 10 over this same distance. The measured wave powers are 10^7 greater than wave powers expected from incoherent Cerenkov radiation, verifying that the radiation is generated by a coherent process.

One coherent wave generation mechanisms considered in this study is the whistler-mode instability in the beam; however, it has been concluded that this instability cannot sufficiently amplify the

radiation to the measured power levels since the path length for wave growth in the beam is much smaller than the estimated whistler-mode wavelength.

Another wave generation process considered is coherent Cerenkov radiation from electron bunches formed in the beam by an electrostatic beam-plasma instability. A one-dimensional simulation of the SL-2 electron beam verifies the existence of these electron bunches, and the calculated coherent power radiated from this modeled beam is near the power levels measured from the SL-2 electron beam in the whistler mode. Including coherent Cerenkov radiation effects in the calculation of the power increases their values by nearly 90 dB's above incoherent power levels. Consequently, this mechanism can account for the whistler-mode radiation detected by the PDP during its encounter with the 1 keV - 50 mA electron beam.

Abstract approved: _____
Thesis supervisor

_____
Title and department

_____
Date

AN ANALYSIS OF WHISTLER-MODE RADIATION FROM THE SPACELAB-2 ELECTRON BEAM

by

William Michael Farrell

A thesis submitted in partial fulfillment
of the requirements for the Doctor of
Philosophy degree in Physics
in the Graduate College of
The University of Iowa

July 1987

Thesis supervisor: Professor Donald A. Gurnett

ACKNOWLEDGEMENTS

I would like to thank Dr. Donald A. Gurnett for his ideas, patience and support throughout all phases of this project. I would also like to thank Dr. Christoph K. Goertz, Terry Whelan and Shinobu Machida for their timely ideas concerning the simulation and radiated power calculations. I would also like to thank John Steinberg for the useful discussions. Terry Averkamp deserves thanks for his valuable input on PDP data analysis and John Birkbeck deserves thanks for a fine drafting job. I would also like to thank Kathy Kurth for the time and effort spent typing this thesis.

Part of this research was funded by NASA Graduate Student Researchers Training Grant NGT-50034. The research at the University of Iowa was also supported by NASA through contract 32807, grants NGL 16-001-002 and NGL 16-001-043, and by the Office of Naval Research through contract N00014-85-K-0404. The research at Stanford University was supported by NASA through grant NAGW-235.

ABSTRACT

During the Spacelab-2 mission, the University of Iowa's Plasma Diagnostics Package (PDP) was released from the space shuttle to investigate plasma effects in the near-shuttle environment. At times during this freeflight when the PDP was magnetically connected to the shuttle, an electron gun in the shuttle cargo bay ejected a nearly field-aligned 1 keV - 50 mA electron beam. During these beam ejections, the plasma wave instrument onboard the Plasma Diagnostics Package detected intense whistler-mode radiation from the beam. This thesis presents a detailed study of a whistler mode emission detected during one period when the beam was ejected continuously for about 7 minutes. The electric field polarization of the detected whistler mode signal is consistent with propagation near the resonance cone. Calculations indicate that the beam radiated approximately 1.6 mW in the whistler mode as the beam traversed the 200 meters from the shuttle to the PDP. The emissivity also decreased by about a factor of 10 over this same distance. The measured wave powers are 10^7 greater than wave powers expected from incoherent Cerenkov radiation, verifying that the radiation is generated by a coherent process.

One coherent wave generation mechanisms considered in this study is the whistler-mode instability in the beam; however, it has been concluded that this instability cannot sufficiently amplify the

radiation to the measured power levels since the path length for wave growth in the beam is much smaller than the estimated whistler-mode wavelength.

Another wave generation process considered is coherent Cerenkov radiation from electron bunches formed in the beam by an electrostatic beam-plasma instability. A one-dimensional simulation of the SL-2 electron beam verifies the existence of these electron bunches, and the calculated coherent power radiated from this modeled beam is near the power levels measured from the SL-2 electron beam in the whistler mode. Including coherent Cerenkov radiation effects in the calculation of the power increases their values by nearly 90 dB's above incoherent power levels. Consequently, this mechanism can account for the whistler-mode radiation detected by the PDP during its encounter with the 1 keV - 50 mA electron beam.

TABLE OF CONTENTS

LIST OF TABLES

LIST OF FIGURES

CHAPTER I

GENERAL INTRODUCTION

The results of a study of a whistler-mode emission detected from an artificial electron beam during the space shuttle's Spacelab-2 (SL-2) mission are presented in this thesis. The study includes a measurement of the total radiated power from the beam in the whistler-mode and a comparison of this power to the power predicted by various whistler-mode radiation mechanisms.

The Spacelab-2 flight, which was launched on July 29, 1985, included an electron gun called the Fast Pulsed Electron Generator (FPEG) from Stanford University, and a spacecraft called the Plasma Diagnostics Package (PDP) from the University of Iowa. During a 6-hour period on August 1, 1985, the PDP was released from the shuttle to investigate plasma effects in the vicinity of the shuttle. During the PDP free flight, the shuttle was maneuvered so that the PDP passed near magnetic field lines connected to the shuttle. Four such magnetic conjunctions were achieved. During one of these magnetic conjunctions a 1 keV - 50 mA electron beam was continuously ejected from the shuttle so that radiation effects could be monitored as the PDP passed near the magnetic field line carrying the beam. Figure 1 shows a frequency vs. time spectrogram from the PDP plasma wave instrument during this electron beam event. The funnel-shaped signal extending from the electron cyclotron frequency, f_c, down to approximately 30

kHz is whistler-mode radiation from the electron beam. This whistler-mode radiation was first described by Gurnett et al. [1986] and is the subject of this thesis.

The observation of this beam-generated whistler-mode signal is not unusual; in fact, whistler-mode radiation is frequently detected from both artificial and natural electron beams in the ionosphere. The following briefly describes some of these electron beams and the corresponding radiation detected.

The first artificial electron beam experiment was performed in the ionosphere in 1969. An electron accelerator was flown on an Aerobee 350 rocket and injected a 9.5 keV/490 mA pulsed electron beam into the ionospheric medium [Hess et al., 1971]. Although ground-based radio receivers did not detect any beam-generating emissions, the beam did propagate ~ 200 km into the lower ionosphere where it was observed optically. This experiment demonstrated that artificial electron beams could propagate great distances without being destroyed by beam-generated instabilities.

During the seventies and eighties, an investigative group at the University of Minnesota performed a number of electron beam experiments in the ionosphere with two stated purposes: first, to study the electron beam, including its emitted radiation and its effect on the beam-ejecting spacecraft; and second, to use the beam as a diagnostic tool to further understand processes occurring in the magnetosphere and ionosphere [Winckler, 1980]. Specifically, their electron Echo experiments were designed to inject an electron beam on closed field lines

into the conjugate hemisphere and analyze the returning electrons (electron "echoes") to identify any physical processes involved. To study the plasma and radio waves emitted from these beams, a radio receiver, typically located in the rocket nose cone, was separated from the main payload. During beam injections these receivers detected waves in the whistler mode, at the upper hybrid/plasma frequencies and at electron cyclotron harmonics (ECH) [Cartwright and Kellogg, 1974; Kellogg et al., 1976; Monson et al., 1976; Winckler, 1980]. Recently, the scientific objectives of the latest Echo experiment, Echo 7, were presented and again include an extensive electron beam investigation [Winckler et al., 1986].

Observations of beam-generated emissions were also made during the joint Franco-Soviet Artificial Radiation and Aurora between Kerguelen and the Soviet Union (ARAKS) experiments in 1975 (Lavergnat et al., 1980). Like the Echo experiments, a diagnostics package was carried in the nose cone of the rocket and separated from the main payload. During electron beam injections, radio receivers flown on this package detected waves in the whistler mode, near the local plasma frequency, and near the fourth harmonic of the electron cyclotron frequency (an ECH emission) [Lavergnat et al., 1980; Dechambre et al., 1980a, Dechambre et al., 1980b].

Electron beams have also been used to probe structures occurring in the auroral region. Such an example is the "E∥B" experiment that was launched into an auroral arc. During the flight, an electron beam was injected along geomagnetic field lines to locate the regions of

parallel electric field that generated the arc. It was believed that part of the injected electron beam would reflect from these regions; however, few reliable signatures of the returning electrons were detected during the experiment [Wilhelm et al., 1980]. A second flight under the same investigation, the NVB-06 flight, was launched in December of 1979. During pulsed electron beam injections, Kellogg et al. [1986] again reported observing waves in the whistler mode, at the upper hybrid frequency, and at the fundamental and first harmonic of the electron cyclotron frequency. The relative intensity and frequency spectra of the waves were also observed to vary with the beam energy and current, and may have been associated with beam plasma discharge (BPD) effects (see Bernstein et al. [1979]).

A unique facility used for beam-plasma research is the Johnson Space Center (JSC) plasma chamber. This cylindrical chamber has a height of 27.4 m and a diameter of 16.8 m, and is large enough to allow space-like experiments to be performed in a laboratory environment. Such experiments performed on injected electron beams include measurements of the emitted radiation and a study of BPD effects [Shawhan, 1982]. For a review of the results from these experiments, see Grandel [1982].

Electron beam injection experiments in the ionosphere have also been performed on the space shuttle. Since the electron beams and corresponding diagnostics packages (particularly the PDP) could be maneuvered into favorable positions, wave and particle measurements unobtainable from rocket experiments were made in and around the beam

environment. The first electron beam experiment performed on the shuttle was in March of 1982 as part of the STS-3 mission. On this flight, the PDP was maneuvered using the shuttle's Remote Manipulator Arm (RMS) while the FPEG, located in the shuttle cargo bay, produced an electron beam. During beam injections, strong emissions near the local plasma frequency and possibly in the whistler mode were detected by the PDP radio receivers [Shawhan et al., 1984]. In December of 1983, the shuttle carried the PICPAB (Phenomenon Induced by Charged Particle Beams) and SEPAC (Space Experiments with Particle Accelerators) investigations into the ionosphere as part of the Spacelab-1 mission. During electron beam injections, the PICPAB radio receivers detected emissions in the whistler mode, at the plasma frequency and at the fourth harmonic of the cyclotron frequency [Beghin et al., 1984] while the SEPAC radio receivers detected an intense VLF signal between 0.7 and 10 kHz that varied in intensity depending on the beam pitch angle [Neubert et al., 1986]. As mentioned previously, in July/August of 1985, the shuttle again carried the PDP and FPEG into the ionosphere as part of the Spacelab-2 mission. The PDP was released to fly around the shuttle and during magnetic conjunction with the shuttle the FPEG was fired. Besides detecting the whistler-mode radiation, emissions near the local plasma frequency and intense electrostatic emissions below 30 kHz were detected by the PDP during beam injections [Gurnett et al., 1986]. During pulsed electron beam events electromagnetic waves at the fundamental and harmonics of the pulsing frequency were also observed [Reeves et al., 1986; Bush et al., 1986].

From the discussion above, it seems evident that whistler-mode radiation is commonly detected from artificial electron beams. This radiation is also produced naturally in the auroral zone in association with the field-aligned electron beams that are responsible for the aurora [Gurnett, 1966] and is usually called auroral hiss. Both upward and downward propagating auroral hiss has been observed [Mosier and Gurnett, 1969]. The downward propagating auroral hiss is associated with downward moving electron beams with characteristic energies of a few hundred eV [Gurnett, 1966; Hartz, 1969; Gurnett and Frank, 1972; Laaspere and Hoffman, 1976]. The upward propagating auroral hiss often has a V-shaped spectrum called a "saucer" [Smith, 1969; Mosier and Gurnett, 1969; James, 1976] or a "funnel" [Gurnett et al., 1983]. Upward propagating auroral hiss has been observed in association with upward moving field-aligned electron beams [Lin et al., 1984]. The characteristic frequency-time shape of the "saucer" or "funnel" is a propagation effect that occurs for whistler-mode waves propagating near the resonance cone.

Although whistler-mode waves and electron beams are closely related, the exact wave-particle interaction generating the waves is unknown. It is hoped that the study of the whistler-mode radiation from the SL-2 electron beam will aid in the understanding of the processes that create these other artificial and natural beam-generated whistler-mode emissions.

The specific outline of this thesis is as follows. In Chapter II measurements of the polarization and power of the whistler-mode

radiation from the SL-2 electron beam are presented. In Chapter III, the measured power is compared and contrasted to the calculated power predicted from possible incoherent and coherent wave generation mechanisms. By the end of Chapter III, it will be evident that coherent Cerenkov radiation from electron bunches in the beam is the only mechanism able to account for the measured power in the whistler mode. Chapters IV and V involve the detailed modeling of the electron bunches responsible for the coherent Cerenkov radiation. Specifically, an expression for the radiated power from an electron beam is derived in Chapter IV and the Appendix. In Chapter V, the results of a computer simulation of the SL-2 electron beam are presented, which includes the modeling of the electron beam distribution. Electron bunches in the simulated beam resulting from a beam-plasma instability are clearly evident. The radiated power from this simulated beam will then be calculated using the derived power expressions and will be compared to the measured power from the SL-2 electron beam in the whistler-mode.

CHAPTER II

POLARIZATION AND POWER OF THE WHISTLER-MODE RADIATION FROM THE SL-2 ELECTRON BEAM

In this section, measurements of the electric field polarization and radiated power of the whistler-mode emission from the 1 keV - 50 mA SL-2 electron beam are presented. As will be shown, both measured quantities are important in determining the wave generation mechanism of the whistler-mode emission.

A. Electric Field Polarization

The whistler mode has a polarization that depends on the wave frequency, f, the wave normal angle, θ, the cyclotron frequency, f_c, and the plasma frequency, f_p. Using cold plasma theory [Stix, 1962], the electric-field and index of refraction vectors can be calculated as a function of these parameters. The variation of the index of refraction as a function of θ is often presented as an index of refraction surface $\bar{n}(\theta)$, which defines the locus of points the index of refraction vectors make as a function of the wave normal angle for constant f, f_p and f_c. Figure 2 shows a typical index of refraction surface for the whistler mode. At a limiting wave normal angle, known as the resonance cone angle, θ_{Res}, the index of refraction goes to infinity. This angle is defined by $\tan^2\theta_{Res} = -P/S$, where $P = 1 - f_p^2/f^2$ and $S = 1 - f_p^2/(f^2 - f_c^2)$. As the wave normal approaches the resonance cone,

the electric field $\overline{E}$ becomes linearly polarized with $\overline{E}$ parallel to $\overline{n}$. In this limit the electric field is quasi-electrostatic and the group velocity, $\overline{v}_g$, is perpendicular to $\overline{E}$ and $\overline{n}$ (see Figure 2).

In a previous paper [Gurnett et al., 1986], the funnel-shaped frequency versus time pattern of the radiation from the SL-2 electron beam was explained as a frequency dependent propagation effect for whistler-mode emissions propagating near the resonance cone. As the wave frequency increases, the resonance cone angle, θ_{Res}, decreases and the ray path direction, $\overline{v}_g$, becomes increasingly oblique to the magnetic field, approaching 90° as the frequency approaches the electron cyclotron frequency. As the PDP approaches the beam, emissions near the gyrofrequency are detected first, since their ray paths are almost perpendicular to the beam. Lower and lower frequencies are then detected as the distance between the PDP and beam decreases. This frequency dependent wave propagation effect causes the funnel-shaped emission pattern observed in Figure 1 and provides strong evidence that the radiation is propagating near the resonance cone.

In order to provide further confirmation that the radiation from the SL-2 electron beam is propagating near the resonance cone, an additional test was performed. This test compares model electric-field directions in the PDP spin plane to their actual directions as measured by the PDP plasma wave instrument. To perform this test a computer program was developed that calculates the angle, ϕ, between the projection of a model electric field onto the spin plane and a fixed reference direction. The fixed reference direction selected was

the spin plane projection of the spacecraft-sun vector. To compute ϕ, the group velocity was assumed to be directed from a point on the beam toward the PDP with the electric field vector, $\overline{E}$, at an angle θ_{Res} relative to the beam. This field geometry is the expected configuration for an upward propagating whistler-mode wave near the resonance cone. Figure 3 shows the corresponding geometry of $\overline{E}$, $\overline{v}_g$ and $\overline{k}$.

The electric-field directions in the spin plane calculated using the model described above are compared to the measured electric-field directions found from spin modulation maximums in the receiver data. The spin modulation maximums occur when the PDP electric antennas are aligned with the measured electric field in the spin plane, thus allowing a direct determination of this measured electric field direction. Figure 4 shows the results of this comparison at four frequencies: 562, 311, 178, and 100 kHz. This figure shows the phase angle, ϕ, between the projected electric field and the sun vector as a function of time. The dots represent the modeled electric-field directions computed assuming a resonance cone propagation scheme while the X's represent the measured electric-field directions. The close agreement between the computed and measured electric field directions provides strong confirmation that the waves are propagating near the resonance cone and in the beam direction (i.e., $\overline{k}\cdot\overline{v}_b > 0$), as indicated in Figure 3.

B. Emitted Power

In this section the total power radiated from the beam in the whistler mode is estimated. By comparing the radiated power to the

total power in the beam, the efficiency of the wave-beam interaction can be determined and compared with various generation mechanisms.

The power emitted from the beam in the whistler mode is obtained by integrating the Poynting flux over a surface surrounding the beam. An inherent difficulty with this calculation is the determination of the phase and magnitude of the electric and magnetic fields in the Poynting flux expression, $\overline{S} = \overline{E} \times \overline{H}$. Since three axis measurements are not available and since phase measurements were not made, the Poynting vector cannot be determined directly. The situation is further complicated by the fact that the emission is propagating near the resonance cone and is quasi-electrostatic. Consequently, the ratio of the electromagnetic to electrostatic components of the wave electric field is a sensitive function of the wave normal angle. Therefore, to compute the wave normal angle it is assumed that the radiation is produced by the Landau resonance, i.e., $\frac{\omega}{k_\parallel} = \frac{c}{n_\parallel} = v_b$. Since the beam velocity is known, this assumption gives a well-defined value for the wave normal direction. The fact that the radiation is propagating in the same direction as the beam ($\overline{k} \cdot \overline{v}_b > 0$) provides a strong indication that the Landau resonance is involved. For example, the $s = -1$ cyclotron resonance produces radiation propagating in the opposite direction of the beam and is therefore completely ruled out, since the radiation is observed to be propagating in the direction of the beam. Also, as will be discussed later, the Landau resonance gives the best agreement with the measured electric to magnetic field ratios.

To compute the Poynting vector, $\overline{S}$, the electrostatic and electromagnetic component of the whistler-mode electric field must be determined. Since the PDP did not measure the relative phase between $\overline{E}$ and $\overline{H}$, these important components of $\overline{E}$ cannot be directly calculated. However, by using the assumption that the waves are generated via a Landau resonance, $\overline{n}$ and $\overline{E}$ can be calculated exactly using cold plasma theory. Consider, first, the whistler-mode wave electric field. Since the emission is propagating near the resonance cone, $\overline{E}$ lies almost entirely in the plane defined by $\overline{n}$ and the geomagnetic field (see Figure 3). The electrostatic and electromagnetic components of $\overline{E}$ are then given by $E_o \cos \Delta\theta$ and $E_o \sin \Delta\theta$, respectively, where $\Delta\theta$ is the angle between $\overline{E}$ and $\overline{n}$, and E_o is amplitude of the total electric field. The angle $\Delta\theta$ is determined by the Landau resonance condition and cold plasma theory. The Landau resonance condition specifies the component of n parallel to the geomagnetic field, i.e.,

$$n_{\parallel} = n \cos \theta = c/v_b \quad . \qquad (2\text{-}1)$$

where c is the speed of light. For a 1 keV electron beam moving parallel to the magnetic field $n_{\parallel}$ is approximately 15.9. A program was written that solves Equation (1-20) of Stix [1962] for the magnitude and directions of $\overline{n}$ and $\overline{E}$. Using this program, $\overline{n}$ and $\Delta\theta$ at a particular wave frequency can be calculated by constraining values of $\overline{n}(\theta)$ using (2-1). Since $\Delta\theta$ is now determined, the electrostatic and electromagnetic components of $\overline{E}$ can be calculated. The calculated $\Delta\theta$ values are very small, typically ranging from .06° to 1.1° from 31.1

kHz to 562 kHz, indicating that the wave is nearly electrostatic. It is easy to show that the magnitude of the Poynting vector is given by

$$|\overline{S}| = \frac{n E_o^2}{2} \left(\frac{\varepsilon_o}{\mu_o}\right)^{1/2} (A^2 + B^2)^{1/2} \quad , \qquad (2\text{-}2)$$

where $A = 1 - \cos^2\Delta\theta$ and $B = \sin \Delta\theta \cos \Delta\theta$. In the derivation of Equation 2 Faraday's Law was used to eliminate the magnetic field in the $\overline{E} \times \overline{H}$ term. Note, also, that as θ approaches the resonance cone angle, $\overline{n}$ and $\overline{E}$ become parallel and $|\overline{S}|$ goes to zero. This behavior near θ_{Res} is similar to an expression derived by Mosier and Gurnett [1971] in their paper addressing Poynting flux measurements of VLF hiss emissions.

Figure 5 shows, pictorially, the PDP trajectory during the 1 keV - 50 mA electron beam event. As can be seen, near the magnetic conjunction, the PDP trajectory was nearly perpendicular to the beam, and, at closest approach, passed within about 3 meters of the beam at a distance of about 200 meters along the field line from the shuttle. To compute the total radiated power, the Poynting flux is integrated over an imaginary surface perpendicular to the beam that includes the PDP trajectory. Assuming that the sampled intensities along this trajectory are constant around an annular ring of the area, $dA = 2\pi RdR$, centered on the beam, the radiated power from the beam segment can be obtained by evaluating the integral $P = \int S_{\parallel} 2\pi RdR$, where $S_{\parallel}$ is the field-aligned component of the Poynting vector and R is the

perpendicular distance from the beam to the PDP. Note that the evaluation of this integral will yield two values for the radiated power: one value from the inbound pass where the limits of integration extend from $R = \infty$ to $R \cong 0$ and one value from the outbound pass where the limits of integration now extend from $R \cong 0$ to $R = -\infty$. Figure 6 shows the average power spectral density from these two passes as a function of wave frequency. The error bars in the figure represent the standard deviations of the power values. Note that the power spectral density, dP/df, is on the order of 10^{-9} W/Hz in the frequency range extending from 30 kHz to 1 MHz. Adding $\frac{dP}{df}$ over the 30 kHz to 1 MHz frequency range, the total emitted power in the 200-meter beam segment from the shuttle to the PDP is found to be P = 1.6 mW. If the power were emitted uniformly along the beam, the radiated power per unit length, $dP/d\ell$, would be approximately 1.6 mW/200 m = 8×10^{-6} W/m. Since the total power of the beam was 50 W, the beam converted approximately 1.6 mW/50 W = 3.2×10^{-5} of its power to whistler-mode radiation in the first 200 meters. As a rough indication of the radiation efficiency, if the beam continued to radiate at this level and this radiation was the only beam energy dissipation mechanism, the beam would only propagate about 6000 km before converting all of the beam energy to radiation.

The linear emissivity of the whistler-mode radiation, $dP/df d\ell$, from different locations along the beam can also be calculated. To calculate the linear emissivity, a knowledge of a signal's exact source location from the beam is required; however, by using the ray

path, the source of the signal at a particular point along the PDP trajectory can be located. The power radiated from an infinitesimal beam radiation source, $d\ell$, is $P = \int S_\perp 2\pi R d\ell$, where $S_\perp$ is the perpendicular component of the Poynting vector measured at the perpendicular distance R from the beam and corresponds to the Poynting flux emitted from a cylinder of radius, R, and length, $d\ell$, surrounding the beam. The linear emissivity from this source, $dP/df d\ell$, is then obtained by using the differential form of the power integral. The calculated linear emissivity of the whistler-mode waves is shown in Figure 7. Note that the emissivity drops by a factor of ten from 100 to 200 meters along the beam. This decrease in emissivity indicates that the efficiency of whistler-mode generation decreases with increasing distance along the beam and that the generation mechanism is capable of dynamic changes in tens of meters. If the emissivity continues to drop at the rate observed between 100 to 200 meters, the radiation would be undetectable by the PDP at source distances more than about 1 km from the shuttle. This result may explain why DE-1, which was magnetically connected to the shuttle during a gun firing on the STS-3 mission, did not see beam-generated whistler-mode radiation in the vicinity of the streaming electrons [Inan et al., 1984]. From the SL-2 measurements, it appears that strong whistler-mode emissions are probably generated only in close proximity to the source of the beam.

As mentioned earlier, the electric and magnetic field measurements also provide direct evidence that the whistler-mode waves were generated via a Landau resonance process. This evidence comes from a

comparison of computed and measured cB/E ratios. Assuming a specific resonance condition and using the solution of Equation (1-20) of Stix [1962], a unique value for $\bar{n}$ and $\Delta\theta$ can be computed. Faraday's law can then be used to obtain the relationship

$$\bar{n} \times \bar{E} = c\bar{B} \qquad (2\text{-}3)$$

where $\bar{E}$ is the electric component and $\bar{B}$ is the magnetic component of the whistler-mode waves. For the assumed field geometry, Equation 3 can be rewritten as

$$n E_o \sin \Delta\theta = cB_o \quad ,$$

or

$$\frac{cB_o}{E_o} = n \sin \Delta\theta \quad . \qquad (2\text{-}4)$$

Using Equation (2-4), n sin $\Delta\theta$ is computed for various resonance conditions and compared with the measured cB/E ratio. The spectrum analyzer used with the PDP search coil can only provide measurements up to 178 kHz; therefore, the magnetic to electric field ratio can only be obtained in the 56 kHz, 100 kHz, and 178 kHz frequency channels. Also, the measured values of B at high frequencies using the search coil are highly uncertain, due to inaccuracies in the calibration of the instrument. The preflight calibration was performed by placing a calibration

coil in the search coil and surrounding the system in a μ-metal can. A problem arises at high frequencies (>10 kHz), where frequency dependent capacitances and inductances affect the current and the expected value of $\overline{B}$ from the calibration coils. Unfortunately, post-flight calibrations under more ideal condition (specifically, without the μ-metal can) have failed to reproduce the preflight calibrations. This suggests that the high frequency gain of the search coil may have shifted during the flight. Our current best estimates are that B (and cB/E) are accurate only to within a factor of 2 - 4 at high frequencies. The range of measured cB/E values lies between 1.3 and 15.3. Assuming a Landau resonance, n sin $\Delta\theta$ is computed to be .54, .52, and .54 for 56 kHz, 100 kHz, and 178 kHz, respectively. Note that these values lie just outside the range of measured cB/E values, and fall in the range when considering the factor of 2 - 4 uncertainty in the calibrations. For an s = +1 cyclotron resonance, however, n sin $\Delta\theta$ is computed to be between .05 to .08 for 56 kHz, 100 kHz, and 178 kHz. These values are about a factor of 20 smaller than the lowest measured cB/E value. Similar computed values are obtained for the s = -1 cyclotron resonance. These comparisons show that the measured cB/E ratio is closest to those expected for a Landau resonance.

CHAPTER III

POSSIBLE WHISTLER-MODE WAVE GENERATION MECHANISMS

From the power measurements alone it is not clear whether the beam-generated whistler-mode radiation detected by the PDP during the SL-2 mission results from a coherent or incoherent generation process. A coherent mechanism involves large numbers of particles acting together to generate the emitted waves. The total power from a coherent source goes as N^2, where N is the number of particles in coherence. Common coherent sources are plasma instabilities, lasers and radio antennas. Incoherent mechanisms involve particles that are radiating independently. The power from the individual radiators must be added to get the total power emitted; thus the total power is proportional to N, the number of radiators. A common incoherent source is an incandescent light bulb. In this chapter possible incoherent and coherent mechanisms for generating whistler-mode radiation are described.

A. Incoherent Generation Mechanisms

One possible incoherent mechanism involves incoherent Cerenkov radiation from beam electrons. Cerenkov radiation is generated by charged particles moving with speeds greater than the phase speed of the wave in the medium. The whistler-mode waves from the SL-2 electron beam are propagating near the resonance cone with large indices of refraction, typically $n \sim 30$ to 500. The phase speed of the wave is therefore much

less than the speed of a 1 keV electron. Since the beam electrons are moving faster than the phase speed of the whistler mode, Cerenkov radiation should be produced.

The measured whistler-mode power from the beam is next compared to the calculated power from Cerenkov radiation, assuming that the beam electrons are incoherent radiators. This calculation is similar to those performed by Jorgenson [1968] and Taylor and Shawhan [1973], who both calculated the power from this process and compared it to the radiated powers from VLF hiss. Mansfield [1967] derived an equation that gives the power spectral density radiated from a single electron moving through an ambient ionized gas with a speed greater than the wave phase speed. For an incoherent mechanism, the total power radiated from the beam is the power radiated from each electron $(\frac{dP}{df})_e$, added up over all the electrons in a given beam volume, N_V: $(\frac{dP}{df})_{total} = N_V(\frac{dP}{df})_e$. Using Mansfield's formula, the radiated power from each beam electron can be calculated and is shown in Figure 8. In obtaining this result, it is assumed that the radiation is produced via a Landau resonance. It is also assumed, for this calculation, that the pitch angle of the electrons is 10°. The actual pitch angles varied from 0° to 20°; however, the results are relatively insensitive to pitch angles in this range. From Figure 8 it can be seen that the most intense radiation occurs between the electron cyclotron frequency and the lower hybrid frequency, f_{LHR}. Outside this range the power drops by a factor of 10^4. Note that this frequency range corresponds rather well to the frequency range of the radiation observed by the

PDP. Multiplying the power from each electron by the number of electrons in the first 200 meter segment of the beam (3×10^{12} particles) yields $(\frac{dP}{df})_{total} \sim 10^{-16}$ W/Hz in the frequency range from f_c to f_{LHR}. These power spectral densities are much lower than the measured power spectral densities, by about a factor of 10^7 (compare with Figure 6, where $dP/df \sim 10^{-9}$ W/Hz). Therefore, an incoherent process cannot account for the measured wave powers. Some coherent wave process must be involved. In Taylor and Shawhan's [1973] analyses of the generation of VLF hiss emissions by auroral electron beams, the calculated powers for the incoherent Cerenkov process were found to be a factor of 10^2 - 10^3 lower than those measured, again indicating a coherent process.

B. Coherent Generation Mechanisms

As concluded in the previous section, some coherent process must be involved in the whistler-mode wave generation from the SL-2 electron beam. Coherent processes can be divided into two classes: direct and indirect. Direct mechanisms involve the direct conversion of energy from an unstable particle distribution to electromagnetic radiation; whereas indirect mechanisms involve the intermediate generation of one or more electrostatic modes which are coupled to the escaping electromagnetic radiation. This section will discuss possible direct and indirect mechanisms that may explain the whistler-mode radiation.

Since an unstable electron distribution is present in the beam the escaping electromagnetic radiation may result from direct conversion of the beam energy to electromagnetic radiation. Such a mechanism

has been proposed by Maggs [1976] for the generation of auroral hiss. In his model, incoherent Cerenkov radiation produced by an auroral electron beam is directly amplified via a whistler-mode plasma instability within the beam. It seems reasonable that this wave generation mechanism could be applied to the whistler-mode waves emitted from the SL-2 electron beam; however, a problem arises in doing so. Unlike auroral beams, the path length for wave growth in the SL-2 beam is very short, only two to three electron cyclotron radii (6 to 9 meters). Using the Landau resonance condition and the fact that the emission is propagating near the resonance cone, the wavelength of the whistler-mode radiation is given by

$$\lambda \cong \frac{V_b}{f} \cos \theta_{Res} \quad , \tag{3-1}$$

which, for the nominal parameters has a value of about 20 meters. This wavelength is greater than the path length, which completely invalidates any mechanism involving exponential growth. Even if that were not the case, for typical whistler-mode group velocities of 10^7 m/sec, the amount of time the wave spends in the beam is so short, only about 10^{-6} sec, that unreasonably high growth rates ($\gamma > \omega_c \cong 10^6$ sec^{-1}) would be required to generate the radiation. No whistler-mode instability is known that can produce such large growth rates from realistic electron distribution functions. These same conclusions were also reached by Jones and Kellogg [1973] in their paper

addressing the growth rates of whistler-mode radiation from artificially-created electron beams.

Mechanisms involving the intermediate generation of electrostatic waves in the beam are now considered. Any density perturbation or bunch created by an electrostatic wave in the beam is capable of emitting coherent Cerenkov radiation. The radiated power from a bunch will have a frequency spectrum similar to that of a single radiating electron; however, the wave power will be much greater since the emitted power goes as N^2, where N is the number of electrons in a bunch. Coherent Cerenkov radiation from a bunched beam has been considered previously by Bell [1968].

Beam-plasma instabilities are known to be capable of creating intense electrostatic waves and density perturbations in the beam. An estimate of the number of coherently bunched electrons required to account for the observed whistler-mode radiation is presented. A first-order expression for the total power emitted from the electron bunches in the beam is $(\frac{dP}{df})_{TOT} = (\frac{dP}{df})_e (\Delta N)^2 \alpha$, where $(\frac{dP}{df})_e$ is the power radiated by each electron, ΔN is the typical number of electrons in a bunch, and α is the number of bunches in the 200-meter segment of the beam. Consequently,

$$\Delta N = \left(\frac{(\frac{dP}{df})_{TOT}}{(\frac{dP}{df})_e \alpha}\right)^{1/2} . \qquad (3\text{-}2)$$

Beam-plasma instabilities are known to create an electrostatic wave near the local electron plasma frequency (3 MHz). Such an emission is, in fact, observed near 3 MHz [see Gurnett et al., 1986]. The corresponding wavelength of this emission is $V_b/f_p \approx 7$ meters, which is assumed to be the approximate length of each bunch. This wavelength can then be used to calculate α, the number of bunches in the first 200 meters of the beam. This number is $\alpha \approx 29$. The radiated power from the 200-meter beam segment, $(\frac{dP}{df})_{total}$, is about 10^{-9} W/Hz. From Mansfield, $(\frac{dP}{df})_e$ is about 10^{-29} W/Hz. Using (3-2), it is calculated that each bunch must contain about $\Delta N = 2 \times 10^9$ electrons in order to account for the observed radiated power.

An estimate can now be made of the required electric field strength of the electrostatic wave in the beam that forms the bunches. Assuming that the beam diameter is about 2 cyclotron radii, the electron number density in the bunch can be estimated using the formula:

$$\Delta n = \frac{\Delta N}{\pi r_c^2 \Delta L} \qquad (3\text{-}3)$$

where ΔL is the bunch length and r_c is the cyclotron radius (2 to 3 meters). The required number density is found to be about $\Delta n = 1 \times 10^7$ electrons/m^3. Again assuming a beam diameter of 2 r_c, the average beam density is $n_o = 1 \times 10^9$ electron/m^3. Note that the fractional density perturbation in the beam $\Delta n/n_o$ is only about 0.01. Consequently, a relatively small density perturbation can account for the

measured whistler-mode power. Poisson's equation can be used to determine the magnitude of the self-consistent electric field needed to generate this density perturbation

$$\frac{\Delta E}{\Delta L} = \frac{e\Delta n}{\varepsilon_o} \quad . \tag{3-4}$$

From Equation (3-4), an electric field on the order of 1-2 V/m is needed to create the required coherence in the beam electrons.

Although the PDP did not fly directly through the beam during free flight, when the PDP was on the Remote Manipulator Arm, it did provide electric field measurements in the beam. During these times, an intense field-aligned electric-field signal near f_{pe} was measured with amplitudes greater than 0.3 V/m, sufficiently large to saturate the receiver. This value is within a factor of 10 of the required amplitudes needed for radiative coherence of the beam electrons. The good agreement between the calculated and measured electrostatic field strengths strongly suggests that electron bunches generated by a beam-plasma instability can account for the observed whistler-mode power.

In the analysis above, it is assumed that the electron beam has fully expanded to a diameter of 2 r_c after being injected. This assumption, however, may not actually be valid near the generator since the beam is still expanding after being ejected from the small generator oriface. As will be shown in Chapter V, this expansion can effect beam structure and should be considered in a detailed power calculation.

In the rest of this thesis, a detailed model of the coherent Cerenkov radiation mechanism described above is presented. A computer simulation of the beam is performed, and the radiated power from this beam is calculated and compared to the measured power from the SL-2 beam in the whistler mode.

CHAPTER IV

EMITTED POWER VIA CERENKOV RADIATION PROCESSES

In this chapter an expression will be derived for the power emitted from an electron beam in a plasma by the Cerenkov radiation process. This expression can be used with known electron beam distributions to compute the radiated power from a beam, and can be applied to the SL-2 electron beam to determine its radiated power.

The derivation is similar to that of Mansfield's [1967], who derived an expression for the radiated power from a single test particle in a plasma medium. His approach was to use the Fourier transforms of the source current and electric field to obtain the radiated power; a method that differed from Liemohn [1965], who derived a similar power expression using the solution of the Hamiltonian of the test particle's radiation field. Mansfield [1967] claimed that there was 'excellent quantitative and qualitative agreement' between his expression and Liemohn's.

Either of these expressions for single particle radiation can be used to calculate the incoherently-radiated power from an electron beam. In performing this calculation it is assumed that each electron in the beam radiates independently from all others. The radiated power from each individual electron in a given volume of the beam is then added to obtain the total radiated power.

In the previous section, a calculation of the incoherently-radiated power from the SL-2 electron beam was performed. It was found that this radiation mechanism could not account for the measured whistler-mode wave power, and concluded that coherent effects among the beam electrons must be included in the calculation.

Harker and Banks [1983] derived an expression for the power radiated from a pulsed electron beam in a plasma which included the coherent effects between the radiating electrons in the beam. They, like Mansfield, used the Fourier transforms of the pulsed current source and electric field to obtain the radiated power. In their derivation, it was assumed that all beam electrons travelled with the same velocity, $\overline{v}$, in pulses of length, ℓ, with a distance, d, separating each pulse. Compared to the incoherently-radiated power from a beam, the inclusion of coherent effects between radiating beam-electrons in a pulse leads to much higher radiated powers; however, the derived expression for radiated power did not include effects from bunches that occur due to instabilities in the beam.

In this section, a general expression will be derived for the radiated power from an electron beam that includes the coherent radiation from particle bunches. The derived expression allows one to calculate the radiated power from N field-aligned particles with arbitrary velocity and position. If a distribution of beam particles is known, the velocity and position of these particles can be used to compute the radiated power.

A. Derivations

There will be two expressions derived in this section: first, the power radiated from a single test particle in a plasma medium will be obtained. Except for a simplification, this derivation will follow the identical steps as Mansfield [1967]. Second, this derivation will be generalized to include the radiated power from N particles of arbitrary velocity and position.

In deriving these expressions, it is assumed that all particles are moving parallel to a static magnetic field in a plasma. This choice of particle trajectory will simplify the integrations involved in the derivations. It will be shown that these field-aligned particle trajectories only allow the $s = 0$ Landau resonance interaction between beam particles and waves. This is not a problem, however, since it is believed that the detected whistler-mode signal from the SL-2 electron beam was generated by the Landau interaction. It should be noted that the SL-2 electron beam was not actually field aligned, but varied in pitch angle from 0° to 20°; however, this variation causes only a 6% change in the beam electron's parallel velocity and, as mentioned previously, is not enough variation to significantly alter the radiated power from a 1 keV beam electron. Cyclotron motion of the electrons can, however, alter the radiative coherence of the beam. As will be shown, coherent effects between beam electrons is a function of their relative position. If a beam has a relatively large pitch angle, the beam electrons will deviate from their field-aligned trajectories which alter their relative position and

coherence; however, the SL-2 beam had, at most, a pitch angle of 20° and during most of the encounter was nearly field aligned. Consequently, the calculated power assuming a field-aligned beam trajectory should not be significantly different from that of the real SL-2 beam with small variations in pitch angle.

Some further assumptions will be made in deriving the two power expressions in this section. These assumptions are identical to those made by Mansfield [1967] and they are:

(1) That the plasma medium is represented by a homogeneous, cold, collisionless plasma in a static magnetic field, $\overline{B}_o$.

(2) That the presence of the test particle(s) may be neglected in the description of the medium.

(3) That the radiated waves from the test particle(s) do not significantly alter the medium and have magnetic fields much weaker than $\overline{B}_o$.

(4) That the magnetic permability is equal to the free space value.

1. Radiated Power From a Single Test Charge In A Plasma Medium

An expression is now be derived for the radiated power from a single test charge in a plasma medium. The steps taken in this derivation are identical to Mansfield's [1967], except for the simplification of making the particle trajectories field aligned.

The first step is to write Ampere's and Faraday's Laws for the Fourier transforms of $\overline{E}(\overline{r},t)$ and $\overline{H}(\overline{r},t)$:

$$\bar{k} \times \bar{H}(\bar{k},\omega) = -\omega\ \varepsilon_o \overleftrightarrow{K} \cdot \bar{E}(\bar{k},\omega) + i\ \bar{J}_q(\bar{k},\omega) \tag{4-1}$$

$$\bar{k} \times \bar{E}(\bar{k},\omega) = \omega\ \mu\ \bar{H}(\bar{k},\omega) \tag{4-2}$$

where $\bar{J}_q(\bar{k},\omega)$ is the Fourier transform of the external source current and $\overleftrightarrow{K}$ is the dielectric tensor for the plasma medium. Substituting $\bar{H}(\bar{k},\omega)$ from (4-2) into (4-1) yields the homogeneous equation:

$$\bar{n} \times \bar{n} \times \bar{E}(\bar{k},\omega) + \overleftrightarrow{K} \cdot \bar{E}(\bar{k},\omega) = \frac{i\ \bar{J}_q(\bar{k},\omega)}{\omega\ \varepsilon_o} \tag{4-3}$$

where $\bar{n} = \frac{\bar{k}c}{\omega}$ is the index of refraction. This equation can be reexpressed as

$$\overleftrightarrow{T} \cdot \bar{E}(\bar{k},\omega) = \frac{i\ \bar{J}_q(\bar{k},\omega)}{\omega\ \varepsilon_o} \quad . \tag{4-4}$$

A static magnetic field, $\bar{B}_o$, is present in the plasma medium and is assumed to lie along the $\hat{z}$-axis. Radiation from a field-aligned test particle will be azimuthally symmetric; however, for simplicity, it is assumed that $\hat{k}$ is entirely in the y-z plane at an angle θ relative to the $\hat{z}$-axis. This coordinate system can be rotated to analyze radiation from any specific aximuth angle, thus these assumptions can be made without any loss of generality. With these assumptions, $\overleftrightarrow{T}$ can be expressed as:

$$\bar{\bar{T}} = \begin{bmatrix} \varepsilon_1 - n^2 & i\,\varepsilon_2 & 0 \\ -i\,\varepsilon_2 & \varepsilon_1 - n^2\cos^2\theta & n^2\sin\theta\cos\theta \\ 0 & n^2\sin\theta\cos\theta & \varepsilon_3 - n^2\sin^2\theta \end{bmatrix} \qquad (4\text{-}5)$$

where

$$\varepsilon_1 = 1 + \frac{f_{pe}^2}{f_{ce}^2 - f^2} + \frac{.1836\, f_{pe}^2}{f_{ce}^2 - (1836f)^2} \quad ,$$

$$\varepsilon_2 = \frac{f_{pe}^2\, f_{ce}}{f(f^2 - f_{ce}^2)} + \frac{f_{pe}^2\, f_{ce}}{f[f_{ce}^2 - (1836f)^2]} \quad ,$$

$$\varepsilon_3 = 1 - \frac{f_{pe}^2}{f^2} - \frac{f_{pe}^2}{1836f^2} \quad ;$$

and f, f_{ce} and f_{pe} are the wave frequency, local cyclotron frequency and local plasma frequency, respectively.

The electric field, $\bar{E}(\bar{r},t)$, is obtained by taking the inverse Fourier transform of $\bar{E}(\bar{k},\omega)$:

$$\bar{E}(\bar{r},t) = \frac{1}{\varepsilon_o} \iint \bar{\bar{T}}^{-1} \cdot \bar{J}_q(\bar{k},\omega) e^{i(\omega t - \bar{k}\cdot\bar{r})} d\bar{k}\, \frac{d\omega}{\omega} \quad . \qquad (4\text{-}6)$$

For a single test particle in the medium, the source current is expressed as:

$$\bar{J}_q(\bar{r},t) = q\,\bar{V}_q\,\delta(\bar{r} - \bar{r}_q(t)) \tag{4-7}$$

where for field-aligned trajectories, $\bar{V}_q$ is

$$\bar{V}_q = V_o\hat{z} \tag{4-8}$$

and

$$\bar{r}_q = (r_o + V_o t)\hat{z} \quad . \tag{4-9}$$

The variable r_o is defined as the particle's initial position. The Fourier transform of the source current is:

$$\bar{J}_q(\bar{k},\omega) = \frac{1}{(2\pi)^4}\iint \bar{J}_q(\bar{r},t)e^{i(\bar{k}\cdot\bar{r}-\omega t)}d\bar{r}dt = \frac{\hat{z}qV_o}{(2\pi)^4}\int e^{i(\bar{k}\cdot\bar{r}_q-\omega t)}dt \quad . \tag{4-10}$$

As mentioned previously, $\hat{k}$ is assumed to lie in the y-z plane, at an angle θ relative to the $\hat{z}$-axis, which allows $\bar{k}$ to be expressed as:

$$\bar{k} = \hat{y}\,k\sin\theta + \hat{z}\,k\cos\theta \tag{4-11}$$

and

$$\bar{k}\cdot\bar{r}_q = \frac{n\omega\cos\theta_o}{c}\,r_o + n\omega\cos\theta\,\beta t \tag{4-12}$$

where $\beta = \frac{V_o}{c}$ and $\frac{n\omega}{c}$ has been substituted for k. The transform of the source current is then:

$$\bar{J}_q(\bar{k},\omega) = \frac{\hat{z}\, q\, V_o}{(2\pi)^4} e^{\frac{in\omega}{c} \cos\theta\, r_o} \int_{-\infty}^{\infty} e^{i(n\omega \cos\theta\, \beta - \omega)t} dt$$

$$= \frac{\hat{z}\, q\, V_o}{(2\pi)^3} e^{\frac{in\omega}{c} \cos\theta\, r_o}\, \delta(n\omega \cos\theta\, \beta - \omega) \quad . \tag{4-13}$$

where $\int_{-\infty}^{\infty} e^{i(n\omega \cos\theta\, \beta - \omega)t} dt = 2\pi\delta(n\omega \cos\theta\, \beta - \omega)$ is used to obtain (4-13). Substituting (4-13) into Equation (4-6) yields:

$$\bar{E}(\bar{r},t) = \frac{qiV_o}{(2\pi)^3 \varepsilon_o} \iint (\bar{\bar{T}}^{-1} \cdot \hat{z})\, e^{\frac{in\omega \cos\theta}{c} r_o}\, \delta(n\omega \cos\theta\, \beta - \omega)$$

$$e^{i(\omega t - \bar{k}\cdot\bar{r})} d\bar{k}\, \frac{d\omega}{\omega} \tag{4-14}$$

for the electric field.

The radiated power from this test particle is

$$P(t) = q\, \bar{E}(\bar{r}_q,t) \cdot \bar{V}_q(t)$$

$$= \frac{q^2 iV_o^2}{(2\pi)^3 \varepsilon_o} \iint (\hat{z} \cdot \bar{\bar{T}}^{-1} \cdot \hat{z}) e^{\frac{in\omega}{c} \cos\theta\, r_o}\, e^{i(\omega t - \bar{k}\cdot\bar{r}_q)} \delta(n\omega \cos\theta\, \beta - \omega) \partial\bar{k}\, \frac{d\omega}{\omega}. \tag{4-15}$$

Substituting (4-12) for $\bar{k}\cdot\bar{r}_q$ in the exponential term of (4-15) yields:

$$P(t) = \frac{q^2 i V_o^2}{(2\pi)^3 \varepsilon_o} \iint (\hat{z}\cdot\bar{\bar{T}}^{-1}\cdot\hat{z})\delta(n\omega \cos\theta\ \beta-\omega)e^{i(\omega-n\omega\cos\theta\ \beta)t} d\bar{k}\ \frac{d\omega}{\omega} \quad . \tag{4-16}$$

Note that the dependence of the power on r_o, the initial position of the particle, cancels out of the expression. The element $d\bar{k}$ can be reexpressed as

$$d\bar{k} = n^2 \frac{\omega^3}{c^3}\, dn \sin\theta\, d\theta\, d\phi \quad .$$

Since there is no ϕ dependence in (4-16), the integration over ϕ yields a 2π. The integration over θ is more complicated since cos θ is in both the delta function and exponential. An integral of the form

$$I = \int f(x)\ \delta(Ax+B)dx = \frac{f(x_o)}{|A|}$$

now has to be evaluated. For (2-16), $A = |n\omega\beta|$, $B = \omega$, and $x_o = \frac{1}{n\beta}$. Note, in the integration, that a nonzero value is obtained only if

$$\cos\theta_o = \frac{1}{n\beta} \tag{4-17}$$

is satisfied. This is the Landau resonance condition. The expression for radiated power now becomes:

$$P(t) = \frac{-q^2 i V_o^2}{(2\pi)^2 \varepsilon_o c^3 \beta} \iint (\hat{z}\cdot\bar{\bar{T}}^{-1}\cdot\hat{z})|n||\omega| dn d\omega \quad . \tag{4-18}$$

From Mansfield [1967], it is found that

$$(\hat{z}\cdot\bar{\bar{T}}^{-1}\cdot\hat{z}) = \frac{\varepsilon_1^2 - \varepsilon_2^2 - \varepsilon_1 n^2 + (n^4 - \varepsilon_1 n^2)\cos^2\theta_o}{\varepsilon_1 (n^2 - n_1^2)(n^2 - n_2^2)} \tag{4-19}$$

where θ_o is the angle that satisfies the Landau resonance condition and $n_{1,2}^2 = [-B \pm (B^2 - 4C\varepsilon_1)^{1/2}]/2\varepsilon_1$. The quantity $B = (\frac{c}{V_o})^2(\varepsilon_3 - \varepsilon_1) + \varepsilon_2^2 - \varepsilon_1^2 - \varepsilon_1\varepsilon_3$ and $C = (\frac{c}{V_o})^2(\varepsilon_1^2 - \varepsilon_2^2 - \varepsilon_1\varepsilon_3) + \varepsilon_3(\varepsilon_1^2 - \varepsilon_2^2)$ where ε_1, ε_2 and ε_3 are those previously defined. If the numerator of (4-19) is defined as $T_{33}(n)$, the power expression can now be written as:

$$P(t) = \frac{-q^2 i V_o^2}{(2\pi)^2 \beta \varepsilon_o c^3 \varepsilon_1} \int \left[\int_o^\infty \frac{T_{33}(n)\ |n| dn}{(n^2 - n_1^2)(n^2 - n_2^2)} \right] |\omega| d\omega \quad . \tag{4-20}$$

Since the real part of the power is needed, the imaginary part of the quantity in brackets in (4-20) has to be calculated. To obtain this imaginary part, the Plemelj formula was used with the result that

$$\int_0^\infty \frac{T_{33}(n)\,|n|\,dn}{(n^2-n_1^2)(n^2-n_2^2)} = \frac{\pi i}{2(n_2^2-n_1^2)}\,[T_{33}(n_2) - T_{33}(n_1)]$$

$$= \frac{\pi i}{2(n_2^2-n_1^2)} \sum_{k=1}^{2} (-1)^k T_{33}(n_k) \qquad (4\text{-}21)$$

Equation (4-20) now becomes

$$P(t) = \int_{-\infty}^{\infty} \frac{q^2\,|\omega|\,d\omega}{8\pi\varepsilon_o\varepsilon_1(n_2^2-n_1^2)} \left(\frac{V_o}{c^2}\right) \sum_{k=1}^{2} (-1)^k T_{33}(n_k) \quad . \qquad (4\text{-}22)$$

This expression for the radiated power can be compared to Equation 32 of Mansfield [1967]. Assuming that the particle's perpendicular velocity is zero and that wave generation is via the s = 0 Landau resonance, then out of the six terms in brackets in Mansfield's Equation 32, only one remains. In the limit that the particle's perpendicular velocity goes to zero, the Bessel function, $J_o(L)$, in Mansfield's Equation 32 goes to one. Consequently, Equation (4-22) is identical to Mansfield's Equation 32 when considering the radiated power from a field-aligned test particle.

2. Radiated Power From N Particles in a Plasma Medium

An expression for the radiated power from N field-aligned test particles is now derived. This derivation is similar to the single particle case derived previously; however, coherence effects between these N radiators will be included.

The source current for the N test particles can be written as:

$$\bar{J}_q(\bar{r},t) = \sum_{i=1}^{N} q\, \bar{V}_i(t)\delta(\bar{r} - \bar{r}_i(t)) \tag{4-23}$$

with

$$\bar{V}_i(t) = V_{io}\hat{z} \tag{4-24}$$

and

$$\bar{r}_i(t) = (r_{io} + V_{io}t)\hat{z} \tag{4-25}$$

being the velocity and position of the ith particle. Like the single particle case, each of the N particles are field-aligned and are initially located at point r_{io} along the $\hat{z}$-axis. Using (4-12), $\bar{k}\cdot\bar{r}_i$ can be expressed as

$$\bar{k}\cdot\bar{r}_i = \frac{n\omega}{c}\cos\theta\ r_{io} + n\omega\cos\theta\ \beta_i t \tag{4-26}$$

where $\frac{n\omega}{c}$ has been substituted for k and $\beta_i = \frac{V_{io}}{c}$. The Fourier transform of the source current is

$$\bar{J}_q(\bar{k},\omega) = \frac{1}{(2\pi)^4} \iint \bar{J}_q(\bar{r},t) e^{i(\bar{k}\cdot\bar{r}-\omega t)} d\bar{r}dt$$

$$= \sum_{i=1}^{N} \frac{q\, V_{io}\hat{z}}{(2\pi)^4} \int e^{i(\bar{k}\cdot\bar{r}_i-\omega t)} dt \quad . \qquad (4\text{-}27)$$

Substituting (4-26) into (4-27) and using the identity $\int_{-\infty}^{\infty} e^{i(n\omega \cos\theta\, \beta_i-\omega)t} dt = 2\pi\delta(n\omega \cos\theta\, \beta_i-\omega)$ yields:

$$\bar{J}_q(\bar{k},\omega) = \sum_{i=1}^{N} \frac{q\, V_{io}\hat{z}}{(2\pi)^3} e^{\frac{in\omega}{c}\cos\theta\, r_{io}} \delta(n\omega \cos\theta\, \beta_i-\omega) \quad . \qquad (4\text{-}28)$$

The electric field can now be solved by substituting (4-28) into (4-6):

$$\bar{E}(\bar{r},t) = \sum_{i=1}^{N} \frac{q\, i\, V_{io}}{(2\pi)^3\varepsilon_o} \iint (\bar{\bar{T}}^{-1}\cdot\hat{z})\, e^{\frac{in\omega}{c}\cos\theta\, r_{io}}\, \delta(n\omega \cos\theta\, \beta_i-\omega)$$

$$e^{i(\omega t-\bar{k}\cdot\bar{r})} d\bar{k}\, \frac{d\omega}{\omega} \quad . \qquad (4\text{-}29)$$

The radiated power from these particles is

$$P(t) = q \sum_{j=1}^{N} \bar{E}(\bar{r}_j,t)\cdot\bar{V}_j(t)$$

$$= \sum_{j=1}^{N}\sum_{i=1}^{N} \frac{q^2 i\, V_{io} V_{jo}}{(2\pi)^3 \varepsilon_o} \iint (\hat{z}\cdot\bar{\bar{T}}^{-1}\cdot\hat{z})\, e^{\frac{in\omega}{c}\cos\theta\, r_{io}}\, \delta(n\omega\cos\theta\,\beta_i-\omega) \tag{4-30}$$

$$e^{i(\omega t-\bar{k}\cdot\bar{r}_j)} d\bar{k}\,\frac{d\omega}{\omega} \quad .$$

The element $d\bar{k}$ can be written as:

$$d\bar{k} = n^2\,\frac{\omega^3}{c^3}\, dn \sin\theta\, d\theta\, d\phi$$

and

$$\bar{k}\cdot\bar{r}_j = \frac{n\omega}{c}\cos\theta\, r_{jo} + n\omega\cos\theta\,\beta_j t$$

where $\beta_j = \frac{V_{jo}}{c}$. The radiated power, after performing the integration over ϕ, then becomes:

$$P(t) = \sum_{j=1}^{N}\sum_{i=1}^{N} \frac{q^2 i V_{io} V_{jo}}{(2\pi)^2 \varepsilon_o c^3} \iint (\hat{z}\cdot\bar{\bar{T}}^{-1}\cdot\hat{z}) e^{\frac{in\omega}{c}\cos\theta(r_{io}-r_{jo})} \tag{4-31}$$

$$e^{i(\omega-n\omega\cos\theta\, B_j)t}\, \delta(n\omega\cos\theta\,\beta_i-\omega) n^2\omega^2 dn \sin\theta d\theta d\omega \quad .$$

Like the single particle case, the evaluation of the integral

$$I = \int f(x)\ \delta(Ax+B) = \frac{f(xo)}{|A|}$$

is needed to complete the integration over θ. For (4-31), $A = |n\omega\ \beta_i|$, $B = \omega$ and $x_o = \frac{1}{n\ \beta_i}$. This integration is nonzero only for

$$\cos\ \theta_{oi} = \frac{1}{n\ \beta_i} \tag{4-32}$$

which is the Landau resonance condition for the ith particle. Equation (4-31) can now be expressed as:

$$P(t) = -\sum_{j=1}^{N}\sum_{i=1}^{N} \frac{q^2 i V_{io} V_{jo}}{(2\pi)^2 \varepsilon_o c^3 \beta_i} \iint (\hat{z}\cdot\bar{\bar{T}}^{-1}\cdot\hat{z}) e^{\frac{in\omega}{c}\cos\ \theta_{io}(r_{io}-r_{jo})} e^{i\omega(1-\frac{\beta_j}{\beta_i})t}\ |n|\ |\omega|\ dn\ d\omega \quad . \tag{4-33}$$

The quantity $(\hat{z}\cdot\bar{\bar{T}}^{-1}\cdot\hat{z})$ is, again,

$$(\hat{z}\cdot\bar{\bar{T}}^{-1}\cdot\hat{z}) = \frac{T_{33}(n)}{\varepsilon_1(n_1^2-n^2)(n_2^2-n^2)} \tag{4-34}$$

where $T_{33}(n)$ is the numerator of (4-19) and $n_{1,2} = n_{1,2}(\beta_i)$. Equation (4-33) is reexpressed as

$$P(t) = -\sum_{j=1}^{N}\sum_{i=1}^{N} \frac{q^2 i\, V_{io} V_{jo}}{(2\pi)^2 \varepsilon_o c^3 \beta_i \varepsilon_1} \int \left[\int_o^\infty \frac{T_{33}(n)|n| e^{inA} dn}{(n^2-n_1^2)(n^2-n_2^2)}\right] e^{i\omega(1-\frac{\beta_j}{\beta_i})t} |\omega| d\omega \tag{4-35}$$

where $A = \frac{\omega}{c} \cos\theta_{io}(r_{io}-r_{jo})$. Since the real part of the power is desired, the imaginary part of the quantity in brackets must be calculated. In this evaluation, only the real part of the exponential, e^{inA}, is considered since only the relative phase of the electron radiators is needed. Using the Plemelj formula, the imaginary part of the integral is

$$\int_o^\infty \frac{T_{33}(n)|n| e^{inA} dn}{(n^2-n_1^2)(n^2-n_2^2)} = \frac{\pi i}{2(n_2^2-n_1^2)} \sum_{k=1}^{2} (-1)^k T_{33}(n_k) e^{in_k A} \quad . \tag{4-36}$$

Substituting (4-36) for the bracketed expression in (4-35) yields the expression for the radiated power from N particles:

$$P(t) = \int_{-\infty}^{\infty} \sum_{j=1}^{N}\sum_{i=1}^{N} \frac{q^2|\omega| d\omega}{8\pi\varepsilon_o\varepsilon_1} \frac{1}{(n_2^2(\beta_i)-n_1^2(\beta_i))} \left(\frac{V_{jo}}{c^2}\right) e^{i\omega(1-\frac{\beta_j}{\beta_i})t}$$

$$\times \sum_{k=1}^{2} (-1)^k T_{33}(n_k(\beta_i)) e^{i\frac{n_k(\beta_i)\omega}{c} \cos\theta_{io}(r_{io}-r_{jo})} \quad . \tag{4-37}$$

The radiated power is reexpressed as

$$P(t) = \int_{-\infty}^{\infty} \sum_{i=1}^{N} \frac{q^2|\omega|d\omega}{8\pi\ \varepsilon_o\varepsilon_1} \left(\frac{1}{n_2^2(\beta_i) - n_1^2(\beta_i)}\right) \left(\frac{V_{io}}{c^2}\right) \sum_{k=1}^{2} (-1)^k T_{33}(n_k(\beta_i))$$

$$+ \int_{-\infty}^{\infty} \sum_{i=1}^{N} \sum_{j\neq i}^{N} \frac{q^2|\omega|d\omega}{8\pi\ \varepsilon_o\varepsilon_1} \left(\frac{1}{n_2^2(\beta_i) - n_1^2(\beta_i)}\right) \left(\frac{V_{jo}}{c^2}\right) \tag{4-38}$$

$$e^{i\omega(1 - \frac{\beta_j}{\beta_i})t} \sum_{k=1}^{2} (-1)^k T_{33}(n_k(\beta_i))$$

$$e^{i\frac{n_k(\beta_i)}{c}\omega \cos\theta_{io}(r_{io} - r_{jo})} \quad .$$

In this expression, the first-term represents the incoherently radiated power from the N test particles while the second-term represents the additional power from coherent effects between the N particles. Note these coherent effects depend on a particle's velocity and position relative to all other particles.

The time-averaged power is defined as

$$\overline{P} = \frac{1}{2T} \int_{-T}^{T} P(t)dt \quad .$$

Averaging (4-37) over time yields the expression:

$$\overline{P} = \int_{-\infty}^{\infty} \sum_{j=1}^{N} \sum_{i=1}^{N} \frac{q^2|\omega|d\omega}{8\pi\ \varepsilon_o\varepsilon_1} \frac{1}{n_2^2(\beta_i) - n_1^2(\beta_i)} \left(\frac{V_{jo}}{c^2}\right) \tag{4-39}$$

$$\frac{\sin x}{x} \sum_{k=1}^{2} (-1)^k T_{33}(n_k(\beta_i))\ e^{i\frac{n_k(\beta_i)}{c}\omega \cos\theta_{io}(r_{io} - r_{jo})}$$

where $x = \omega T (1 - \beta_j/\beta_i)$. Note that if $\beta_i = \beta_j$ ($V_{io} = V_{jo}$), then $\sin x/x \to 1$ and the radiation coming from particles i and j can be coherent, depending only on the particle's relative position. If a distribution of particles exist with $\beta_i \neq \beta_j$ then the power averaged over very long periods will be nearly equal to the incoherently radiated power from the particles. This result is obtained because $\underset{T\to\infty}{\text{LIM}} \frac{\sin x}{x} = 0$ for $\beta_i \neq \beta_j$, allowing only the terms that describe the incoherently radiated power to remain in (4-39). Note, from (4-39), that if all particles were moving at the same velocity and each had the same initial position, the exponential terms would be unity and the radiated power would be $P = N^2 P_1$, where P_1 is te radiated power from a single test charge.

As an example, the radiated power from two test particles will be written from (4-39):

$$\overline{dP} = \frac{q^2 |\omega| d\omega}{8\pi\varepsilon_o\varepsilon_1} \left| \frac{1}{(n_2^2(\beta_1) - n_1^2(\beta_1))} \frac{V_{1o}}{c^2} \sum_{k=1}^{2} (-1)^k T_{33}(n_k(\beta_1)) \right.$$

$$+ \frac{1}{(n_2^2(\beta_2) - n_1^2(\beta_2))} \frac{V_{2o}}{c} \sum_{k=1}^{2} (-1)^k T_{33}(n_k(\beta_2))$$

$$\left. + \frac{1}{(n_2^2(\beta_2) - n_1^2(\beta_2))} \frac{V_{1o}}{c} \frac{\sin x_1}{x_1} \sum_{k=1}^{2} (-1)^k T_{33}(n_k(\beta_2)) \right|$$

$$\times e^{\frac{in_k(\beta_2)\omega}{c}\cos\theta_{2o}(r_{2o}-r_{1o})} \tag{4-40}$$

$$+ \frac{1}{(n_2^2(\beta_1)-n_1^2(\beta_1))} \frac{V_{2o}}{c^2} \frac{\sin x_2}{x_2} \sum_{k=1}^{2} (-1)^k T_{33}(n_k(\beta_1))$$

$$\times e^{\frac{in_k(\beta_2)\omega}{c}\cos\theta_{1o}(r_{1o}-r_{2o})} \Bigg]$$

where $x_1 = \omega\ T\ (1 - \beta_1/\beta_2)$ and $x_2 = \omega\ T\ (1 - \beta_2/\beta_1)$. The first two terms in the brackets represent the radiated power from single test charge #1 and single test charge #2. These two terms, together, represent the incoherent radiation from the two particles. The last two terms in the brackets represent the effects of coherence on the radiated power from these two test particles. Again, if the particles are moving at the same velocity and have the same initial position, the radiated power is

$$P = 4P_1$$

where P_1 is the radiated power from a single test particle.

Although it is not completely obvious in the analysis, expression (4-37) does indeed describe a Cerenkov radiation process. This fact is easily demonstrated using the Cerenkov (Landau) resonance condition:

$$n_{\parallel} = n \cos \theta = \frac{c}{V_b} \quad . \tag{4-41}$$

Recall that if this condition is not met, the radiated power from the beam is zero (see Equation 4-32). Since the phase velocity of the emitted radiation is $V_{PH} = c/n$, the expression

$$V_b = \frac{V_{PH}}{\cos \theta} > V_{PH} \tag{4-42}$$

can be written using (4-41). Consequently, a necessary condition to obtain radiation from the beam is that $V_b > V_{PH}$, which describes a Cerenkov process.

B. Practical Applications

Expressions (4-37) and (4-39) calculates the radiated power by determining the coherence effect amongst the individual beam electron radiators. This calculation represents a microscopic approach to determining the radiated power. A general macroscopic approach has also been derived and is presented in the Appendix. In this approach, the radiated power from a beam with current density $J_z(z,t)$ is calculated. The macroscopic approach has a distinct advantage over the microscopic approach since any real calculation of the radiated power can be computed easier when considering the macroscopic variable $J_z(z,t)$. Using the microscopic approach, the position and velocity of all N particles as a function of time must be considered. Keeping track of all these

variables on a computer requires large amounts of CPU time. Using the macroscopic approach, however, only requires a calculation of the macroscopic variable $J_z(z,t)$, which on a computer is far easier to calculate. Consequently, for any practical power calculation, Equation (A-10) will be used.

The microscopic approach derived in this section is still an important original work since it is the theoretical basis on which the macroscopic approach is derived. This approach also considers explicitly the concept of radiative coherence between the beam particles; a concept that is only implicitly dealt with in the macroscopic approach.

Calculating the radiated power using either approach requires a knowledge of the beam phase-space configuration. Considering the SL-2 electron beam, the phase-space configuration must be modeled from a particle simulation, since beam particle distributions were not obtained experimentally. There are two reasons for not measuring these distributions directly: first, when the PDP was in free flight, it did not fly through the beam [W. R. Paterson, personal communication, 1986]. When it was on the RMS, it was maneuvered into the beam; however, the instrument that obtains these distributions, the Low Energy Proton Electron Differential Energy Analyzer (Lepedea) instrument, was turned off, since it was feared that a direct hit of the beam on the instrument would alter its sensitivity [W. R. Paterson, personal communication, 1986]. In either case, direct measurements of the electron beam distributions were not obtainable. Second, even if the Lepedea instrument had been turned on and in a favorable position to

measure the beam distribution, the instrument's temporal resolution (1.6 seconds) is not fine enough to directly measure instability-related electron bunching which occurs on the order of $1/\omega_{pe} \sim 10^{-7}$ seconds.

In the next section, the results of a one-dimensional electrostatic particle simulation of the SL-2 electron beam will be reviewed. The velocities and positions of the beam electrons obtained from modeled phase-space distributions will be used to calculate $J_z(z,t)$, and, using (A-10), the Cerenkov radiated power from the beam will be calculated. This calculated power will then be compared to the measured whistler-mode power obtained during the PDP/beam encounter.

CHAPTER V

A ONE-DIMENSIONAL ELECTROSTATIC SIMULATION OF THE SL-2 ELECTRON BEAM

In order to complete a calculation of the radiated power from the SL-2 electron beam, a knowledge of the electron beam phase-space distribution is required. As mentioned in the previous section, no direct measurement of these distributions were made by the Lepedea instrument on the PDP; thus, the distributions must be modeled. In this section, the results of a particle simulation of the SL-2 electron beam is presented that includes modeled phase-space configurations of the beam that can be used to calculate the radiated power.

To obtain the required beam distribution, a one-dimensional electrostatic model of an electron beam propagating through an ambient plasma is simulated on a computer. Generally, these models use simulation particles that are many times the mass and charge of an electron, and modeling the plasma using these particles is valid only when many of these particles are contained in a Debye cube (Debye length for a one-dimensional system). In this simulation, the ambient plasma consists of electrons represented by simulation particles of negative charge and immobile ions represented by a net positive background charge. The simulation is designed so that initially there is no net charge in the system. The simulation particles representing the

ambient electrons can move freely in this one-dimensional system; however, they are confined to the system by re-injection boundaries. Ambient electrons leaving the system at these boundaries are re-injected with a Gaussian-weighted velocity between zero and the electron thermal speed. The electron beam is represented by simulation particles of negative charge that are injected into the system at the z = 0 boundary with velocities greater than the ambient electron thermal speed. In this one-dimensional simulation, a cold electron beam is always injected into the system. In order to keep the net charge in the system equal to zero, a positive charge equal in magnitude to the amount of negative beam charge in the system is placed at the z = 0 boundary. This boundary charge imitates the spacecraft charging effect observed on the beam-ejecting shuttle [Williamson et al., 1985].

In a one-dimensional simulation, only a particle's velocity and position in one dimension is considered. The total length of the simulation system is divided up into "grids" of a Debye length, λ_D, in size. The charge density in each grid, ρ_n, is calculated and the numerical solution to Poisson's equation, $E_{n+1} = E_n + 1/2(\rho_{n+1} + \rho_n)$, is used to calculate the electric field in the n+1 grid. The simulation particles are then allowed to move in the system under the influence of this electric field for a period of time $\Delta t \leq \lambda_D/V_B$, where V_B is the simulation beam speed. If $\Delta t > \lambda_D/V_B$, the simulated beam particles are moving more than one grid in Δt and will skip grids. Since the ambient particles in the skipped grids will not interact with the beam particle, the modeled system no longer represents reality.

After the simulation particles have evolved, a new charge density and electric field is calculated for each grid and the particles are again allowed to move under the influence of the new electric field. This iterative process continues until the beam-plasma interactions reach a steady-state where then the simulation is terminated.

It is assumed that the particle's position and velocity in the one-dimensional simulated electron beam and plasma is along a static magnetic field line. This alignment allows the simulated particle trajectories to be unaffected by this field. Since the SL-2 electron beam was nearly field aligned during injection, this modeling of the electron beam should yield particle distributions that, for the most part, represent the true physical situation.

Generally, near field-aligned electron beams in test chambers and on shuttle flights tend to expand from twice the radius of the electron generator opening to about two electron cyclotron radii in the radial direction, if the generator opening is less than a gyroradius. This radial or perpendicular expansion decreases the density of the beam as it propagates away from its source. Figure 9 shows pictorially this expansion of the beam. Initially, the beam leaves the electron generator ($z=0$) with a radius r_o and a density n_o. However, an effect is present that causes the beam to expand perpendicular to the magnetic field with a perpendicular expansion speed of $V_{\perp exp}$. This expansion may be related to edge effects of the generator opening or to Coulomb repulsion of beam electrons. As the beam propagates along the $\hat{z}$-axis at a speed of V_B, the beam radius is expanding according to

the first-order expression $r = r_o + \frac{V_{\perp exp}}{V_B} z$ with the local density of the beam, n(z), changing proportionally. The beam expansion continues until $r \cong r_c$, where r_c is the cyclotron radius. By equating the current at the generator to that at other points along z ($J_o A_o = J(z)A(z)$), a first-order expression for n(z) is obtained:

$$n(z) = \frac{n_o r_o^2}{(r_o + \frac{V_{\perp exp}}{V_B} z)^2} = \frac{n_o}{(1 + \frac{z}{L})^2} \qquad (5\text{-}1)$$

where

$$L = (\frac{V_B}{V_{\perp exp}}) r_o \quad . \qquad (5\text{-}2)$$

The scale length, L, represents the beam length where the beam density decreases to $n_o/4$, and is expressed in units of gun radii.

This perpendicular expansion is modeled in the simulation of the SL-2 electron beam. To include this effect, the density of the beam electrons in the simulation are weighted by the factor $\frac{1}{(1+z/L)^2}$, where L is treated as a free parameter. Consequently, the simulation is able to model the density decreases associated with beam expansion which affect the modeled electric fields and beam distributions.

The parameter, L, also indirectly affects the amount of positive charge at the z=0 boundary during simulated beam injections. As

mentioned previously, the amount of positive charge at the z=0 boundary is equal to the amount of negative beam charge in the system. This charge is placed there in order to conserve the total charge in the system, and effectively simulates spacecraft charging known to occur on beam-ejecting spacecraft. As L decreases, the beam density and total beam charge in the system decreases which also causes the amount of positive charge placed at the z=0 boundary to decrease. Consequently, by varying L, both the modeled beam expansion and boundary charging are altered.

Including these effects in the modeling of the SL-2 electron beam makes this one-dimensional simulation rather unique. Usually, to observe the beam character under varying beam expansion and boundary charge, a two-dimensional or three-dimensional simulation is needed; however, by weighting the beam particles properly, this simple one-dimensional simulation copies processes occurring in these more advanced simulations. As an example, results from a two-dimensional simulation performed by Pritchett and Winglee [1986] are compared to the results from this one-dimensional simulation under similar simulated plasma conditions. Pritchett and Winglee's simulation is very advanced. In their two-dimensional simulation system, a simulated spacecraft immersed in a simulated plasma is able to eject a simulated electron beam. Diagnostic software is included that analyzes the electric fields and return currents that develop around the beam and spacecraft. Unlike the one-dimensional simulation, both electron and ion motion parallel and perpendicular to the static magnetic field are

modeled. Electric fields and currents are also allowed to develop both inside and outside the region where the beam propagates. It would seem that such an advanced simulation would have very different results for the electron beam distributions as compared to this study's one-dimensional simulation; however, this is not the case. Figure 10(a) and (b) shows the V_z versus z phase-space configuration of the beam electrons from Pritchett and Winglee's two-dimensional simulation. For this particular simulation, the ratio of the beam to ambient electron densities, n_b/n_A, is 1/16 and the ratio of the beam to ambient thermal velocities, V_b/V_{TE}, is 10. These figures show the phase-space distribution of the beam after the simulation has run for 32 and 64 plasma periods. Note, in both cases, that particle trapping is evident by the looping structures in phase space. In Figure 10(b), particle heating is occurring between 0-.5 V_B and the front edge of the beam has a filament structure associated with it. Figure 11(a,b) shows the V_z versus z phase-space configuration of the beam electrons from this study's one-dimensional simulation run with similar beam-plasma parameters as Pritchett and Winglee's. For this run, the expansion scale length parameter, L, is 100. Note that the phase-space configuration of the beam has trapping, heating and filament structures very similar to those of Pritchett and Winglee's, and indicates that similar physical processes are being modeled in both simulations.

The beam phase-space configurations from the one-dimensional simulation are dependent on the expansion scale length parameter, L.

Figure 12(a) and (b) show the beam phase-space configuration from the one-dimensional simulation run with similar beam-plasma parameters as Figures 10 and 11, only now $L = \infty$ (no expansion). The phase-space configurations shown in this figure appear noticeably different, particularly at the leading edge of the beam, compared to those shown in Figures 10 and 11 and indicates that particle trapping dominates at this leading edge. Consequently, beam expansion alters the beam phase-space distributions by reducing wave trapping effects.

The modeling of an electron beam using the one-dimensional code works equally well when simulating an overdense beam ($n_b > n_A$) in an ambient plasma. Figure 13 shows a V_z versus z phase-space configuration from the one-dimensional simulation for an overdense beam with $n_b/n_A = 8$, $V_b/V_{TH} = 15$ and $L = 10$. This configuration can be compared with those obtained by Winglee and Pritchett [1986], who also performed a one-dimensional simulation of an overdense beam ($n_b/n_A = 2$). The beam phase-space distribution obtained from their simulation is shown in Figure 14. Note, in both cases, that a large charge build up of the beam particles is present at the injection boundary, with electron bunches forming near the boundary.

The results of these one-dimensional simulations can be compared to the results obtained from Pritchett and Winglee's two-dimensional simulation of an overdense beam. The V_z versus z beam phase-space configuration from their simulation with $n_b/n_A = 8$ and $V_b/V_{TH} \sim 15$ is shown in Figure 15. Note that a charge build up near the injection boundary is again present, along with bunches of slow moving electrons.

For the modeling of both the underdense and overdense beam injections, this study's one-dimensional simulation is capable of replicating the results obtained from the one-dimensional and two-dimensional simulations performed by Pritchett and Winglee. There is one distinct advantage to the one-dimensional simulation and that is, unlike Pritchett and Winglee's two-dimensional simulation, it can run for very long times; thus, allowing the study of the steady-state nature of the beam. Pritchett and Winglee's simulation has to be terminated as soon as about 1% of the beam particles leave the system in order to maintain charge neutrality based on the simulation boundary conditions; and this usually occurs after 60-100 plasma periods when the beam and plasma are still in a transient state. To determine the steady-state beam character, the simulation should be run for longer times.

A. Results of the Simulation of the SL-2 Electron Beam

The one-dimensional electron beam simulation was performed under similar conditions that prevailed during the SL-2 1 keV-50 mA electron beam injection. The simulated plasma parameters during these runs are displayed in Table 1. The 1 keV-50 mA electron beam was initially injected with a density much greater than the ambient electron density. In order to model this overdense beam in the simulation, an electron beam consisting of simulated electron particles was injected into the simulated plasma with a density fives times greater than the ambient electron density. This beam was injected with a velocity $V_B > V_{th}$, where V_{th} is the ambient electron thermal velocity. In the

region of the ionosphere where the SL-2 electron beam experiment was performed, $V_b \cong 100\ V_{th}$. Simulations were performed with this

Table 1. Simulation Parameters

n_b/n_A at $z = 0$	5
V_b/V_{th}	20
z	1200 λ_D (~ 60 meters)
L	2, 3, 5, 10 Gun Radii
t	270 ω_{pe}^{-1} (~ 1.3×10^{-5} sec)
Total number of ambient particles	24000

velocity ratio; however, it was found that V_b/V_{th} could be as low as 20 without significantly altering the beam velocity distributions. Lowering this ratio, however, allows the beam-plasma interactions to occur over shorter length scales, which increases the effective length of the simulation system. Consequently, the simulations were run with $V_b/V_{th} = 20$, which then increased the effective beam length being simulated by a factor of five without altering the interactions being modeled.

The length of the simulation system was selected to be 1200 simulation units long, which corresponds to a length of approximately 60 meters. This length was selected since it is much larger than the size of the expected beam density perturbations, and allows the simulation to be run in a couple CPU hours.

The results of four simulations run with different L values (2, 3, 5, 10) will be presented. Based on practical arguments of beam expansion, spacecraft charging and wave activity, the model that is most consistent with the SL-2 electron beam will be selected.

A simulation was performed with the plasma parameters shown in Table 1, with L, the beam expansion parameter, equal to 10. Figure 16 shows the V_z versus z phase-space distribution for the first 60 meters (1200 simulation units) of the beam at $t = 270\ \omega_p^{-1}$. Note that the beam is strongly decelerated near the z=0 boundary. Figure 17 shows the electric field versus z for this time. The electric field is measured in dimensionless simulation units, where one of these units corresponds approximately to 6 V/m. Note that a very large positive field is present near the z=0 boundary. This electric field is similar to those obtained by Pritchett and Winglee for an overdense beam and results from the strong charging at the boundary. Figure 18 shows the total number of electrons in the beam versus z, and indicates that randomly-spaced density fluctuations are present in the beam; however, as Figure 16 indicates, their velocities are significantly smaller than the initially injected 1 keV-beam velocity. Note from Figure 16 that there is an accumulation of electrons almost lying directly on the z=0 boundary. Many of these electrons have significant negative velocities ($V \sim -V_b/2$). This return electron current has been described in great detail by Katz et al. [1986] and is a result of the large potential that develops near z=0 due to charging.

Beam expansion is increased and spacecraft charging is decreased for the simulation run with L = 5. Figure 19 shows the V_z versus z phase-space distribution of the injected beam for the first 60 meters at t = 270 ω_p^{-1}. The distribution does not appear significantly different from that obtained from the run with L = 10 (Figure 16); however, more electrons are able to escape the region near the charged boundary. Figure 20 shows the electric field versus z at t = 270 ω_{pe}^{-1}. Note that a strong electric field is again generated near the z=0 boundary; a result from charging effects at the boundary. Figure 21 shows the total electron number versus z, again indicating that randomly-spaced density perturbations are escaping from the region near the charged boundary.

Note for both the L = 5 and 10 simulation runs that after 270 ω_{pe}^{-1}, the bulk of the beam electrons have not propagated 30 meters past the injection boundary. In contrast, if the beam had propagated unperturbed, it would have extended out to 135 meters; thus, spacecraft charging is drastically altering the character of the beam in these runs. In reality, it may be that large return currents are flowing back to the shuttle along paths unrelated to the beam; such as along magnetic field lines connected to a conducting surface on the shuttle. Such currents may neutralize the spacecraft charge substantially. If this charge is significantly reduced, the beam phase-space distribution will appear as that shown in Figure 22. This result was obtained from a simulation run with L = 3. Note that the beam can propagate freely from the injection boundary. The initially

cold beam becomes thermalized and bunches of electrons propagate from the z=0 boundary. Note that the beam has a significant number of particles with speeds greater than the initial beam velocity. This is an effect of particle acceleration from an electrostatic wave in the beam. This wave is clearly evident in Figure 23, which displays the electric field versus z. Also note from this figure that the strong charging-related electric field near the z=0 boundary is reduced. Figure 24 shows the total number of beam electrons versus z, and indicates that nearly periodic, highly-localized bunches of electrons are present and, from Figure 22, it is concluded that the collective bunch velocity is near or above the initial beam velocity.

Figure 25 shows the V_z versus z beam phase-space distribution from the simulation run with L = 2 at t = 270 ω_p^{-1}. Note that the beam can again propagate freely from the z=0 boundary. Also, note from this figure, that electron bunches are clearly evident at the top of the elongated looping phase-space structures. Figure 26 displays the electric field versus z at this time. Note that strong electrostatic wave turbulence is present in the beam; however, the relative amplitude of this wave decreases as a function of z. This wave amplitude decrease is an effect of the extreme width-wise beam expansion being simulated. This expansion causes the beam density to strongly decrease as a function of $1/z^2$, which strongly decreases the turbulent electric field according to Poisson's equation. The magnitude of the wave then decreases as the density of the perturbing electrons

decreases. Figure 27 shows the total number of beam electrons versus z. Note that highly localized bunches are evident in the beam.

In Chapter III, calculations were made assuming the bunches had a length, ΔL, of about 7 meters. This bunch length is clearly quite different from those obtained from the simulation. For the runs at L = 2 and 3, the bunches are highly localized ($\Delta L \sim .1-.5$ m), nearly periodic, fast-moving groups of charges, while for L = 5 and 10, only small randomly-spaced density fluctuations exist in the beam. The density character of the beam in both cases differ from that described in Chapter III, since the simulation is modeling nonlinear wave and spacecraft charging effects occurring in the beam. These effects can drastically alter the beam character and were not included in the simple calculations performed in Chapter III.

As mentioned previously, a choice between the four different beam models must be made to determine which correctly models the SL-2 electron beam. The models presented can be classified according to spacecraft charging's influence on beam propagation. For the runs with L = 5 and 10, spacecraft charging is able to drastically alter the injected beam, while for runs with L = 2 and 3, the beam is only slightly influenced by charging effects. In reality, the importance of charging depends on the ability of the shuttle to effectively conduct return currents that neutralize the positive charge created during electron beam ejections.

Williamson et al. [1985] have shown that during SL-2 electron beam injections, the shuttle only charged up to between 0 and 40

volts. Consequently, enough return current was drawn from the ionospheric plasma to sufficiently neutralize the positive spacecraft charge, and this charge neutralization allowed the beam to propagate freely from the shuttle [Banks et al., 1985]. A beam freely escaping the near-shuttle region is consistent with the simulations run with L = 2 and 3, and rules out the L = 5 and 10 simulation runs as possible models of the SL-2 beam.

Figure 26 displays E_z versus z for the simulation run with L = 2. As mentioned previously, a self-consistent electrostatic wave is present in the beam with an amplitude that decreases with increasing z, and has a frequency near ω_{pe}. From the figure it appears that the wave has an amplitude barely above simulation noise level in regions of the beam where z > 7 meters (150 simulation units). This modeled wave activity is inconsistent with observations made by the PDP on the RMS, where strong electrostatic wave turbulence near ω_{pe} was detected by the PDP radio receivers in regions of the beam where z > 7 meters. This model of the beam is then ruled out as a realistic model of the SL-2 electron beam.

From the above arguments, it seems that the simulation run with L = 3 is the best model of the SL-2 electron beam. There are two more points to support this conclusion. The first point involves the energy spectrum of the backscattered beam electrons detected near magnetic conjunction by the Lepedea instrument. Apparently, these electrons were not monoenergetic, but were observed at all energies from 2 eV, the lowest Lepedea channel, to about 1 keV [W. R. Paterson,

personal communication]. If nearly-elastic collisional processes dominated the backscattering, the beam distribution would also have a similar energy spectra, which is consistent with the L = 3 simulation run (see Figure 22). Also, from Figure 23, strong wave activity is present in the beam for this run. These waves have a frequency near ω_{pe} and are similar to those observed by the PDP in the beam. Consequently, the beam model with L = 3 is consistent with the observed beam spectra, wave activity, and spacecraft charging during the 1 keV -50 mA electron beam injection, and is clearly the best beam model.

B. The Radiated Power From a Model of the SL-2 Electron Beam

The radiated power from the modeled SL-2 electron beam will now be calculated. This power will be compared to the measured whistler-mode power to determine if coherent Cerenkov radiation from a bunched beam is a viable wave generation mechanism.

It has been assumed throughout this analysis, that the magnitude of the electric field of the generated Cerenkov radiation is much smaller than that of the electrostatic wave generated within the beam, $E_{ES} >> E_{RAD}$. This assumption implies that the radiation electric field did not significantly alter the SL-2 beam electron trajectories, and is consistent with the modeling of the beam where radiation field effects are neglected. This assumption is also consistent with observations made during the SL-2 experiment, where $E_{ES} > .3$ V/m in the beam while $E_{RAD} \sim 10^{-3}$ V/m for the whistler-mode waves.

The radiated power from N particles in a specific length segment of the beam can be calculated using equations (4-37) and (4-39). To

actually compute the power using these expressions, however, requires large amounts of costly computer time. An easier way to calculate the power is to use the expression (A-10):

$$P(t) = \overline{P} = \int_{-\infty}^{\infty} \left(\frac{|\omega| d\omega}{8\pi\, \varepsilon_o \varepsilon_1 c^2 V_s}\right) \frac{1}{(n_2^2 - n_1^2)} \sum_{k=1}^{2} (-1)^k\, T_{33}(n_k) \times \left[2\pi\, J_z(k_z(n_k, \theta_o)) J_z^*(k_z(n_k, \theta_o))\right] \quad . \tag{A-10}$$

In this expression, V_s is the velocity of the frame moving with the beam such that the current density, $J_z(z,t)$, is considered time independent. In deriving (A-10), a transformation to this frame was made in order to calculate the radiated power from a specific beam segment. Consequently, $J_z(z,t)$ becomes $J_z(z')$ in this new frame, where $z' = z - V_s t$. In (A-10), $J_z(k_z)$ represents the spatial Fourier transform of $J_z(z')$. Once $J_z(k_z)$ of a specific beam segment is known, the power radiated from that segment is easily calculated. As mentioned in Chapter IV, calculating the power using macroscopic variable $J_z(z,t)$ requires less computer time than calculating the radiated power from each particle. In deriving expression (A-10), it has been assumed that a frame of reference exists where the current density is completely independent of time. In this frame, all beam density perturbations have to propagate at identically the same speed, V_s. The transform of the current density is then properly expressed as (A-4), with the delta function specifying the speed of the density

perturbations. This subtle condition placed on the propagation speed of the perturbations reduces the generality of equation (A-10) compared to equation (4-37) which expressed the radiated power from N electrons with arbitrary speeds. Despite this reduction in generality, it will be shown that (A-10) is quite capable of yielding a reasonable estimate of the radiated power from the modeled SL-2 electron beam with bunches moving at or near V_s. It should be noted that in the frequency range of consideration, $n_1 >> n_2$, $n_1 \cong n$ where n is the whistler-mode index of refraction obtained from cold plasma theory and $T_{33}(n_1) \cong 10^3\ T_{33}(n_2)$. Also, based on arguments of the typical density structure size in the beam, $J_z(k_z(n_1,\theta_0) > J_z(k_z(n_2,\theta_0))$. Consequently, the k=2 term in the summation of Equation (A-10) is very small and can be neglected. The radiated power can then be expressed as

$$P(t) = \overline{P} \cong \int_{-\infty}^{\infty} \left[\frac{-|\omega| d\omega}{8\pi\ \varepsilon_o \varepsilon_1 c^2 V_s} \frac{1}{(n_2^2 - n_1^2)} \right] [2\pi J_z(k_z') J_z^*(k_z')] T_{33}(n_1) \qquad (5\text{-}3)$$

where $k_z' = \dfrac{n \cos \theta_o \omega}{c}$. Note that $n_1 > n_2$ which makes the term in brackets positive in the frequency range considered.

A simulation of the SL-2 electron beam was run with a simulation length three times longer than those run previously. This simulation length now extends 3600 grid lengths and represents a model of the first 180 meters of the SL-2 electron beam. This increased length was

added to improve the resolution of $J_z(k_z)$ in the whistler-mode range of k_z'. The V_z versus z phase-space configuration for this modeled beam at $t = 840\ \omega_{pe}^{-1}$ is displayed in Figure 28. Note that this phase-space configuration is very similar to the phase-space configuration of the 60-meter beam segment displayed in Figure 22. Both configurations have two electron components: a strongly heated component found in phase-space regions where $V < V_b$ and electron bunches found in phase-space regions where $V > V_b$. These bunches are particularly pronounced in the first 75 meters of the beam (from z = 0 to 1500). Using Equation (5-3), the radiated power will be calculated from a beam-segment extending 175 meters in length from z = 100 to 3500. The first five meters of the beam is not included in the calculation since the beam phase-space configuration near the generator (z = 0 boundary) is atypical of the rest of the beam. The power radiated from this 175-meter segment is equal to the Poynting flux through a cylindrical surface of radius R and length L = 175 meters surrounding the beam:

$$P_{175m} = S_{\perp}\ 2\pi R\ L\ (175m) \quad . \tag{5-4}$$

Since the radiated power varies directly with L, the power from a 200-meter beam segment can be approximated by

$$P_{200m} = (200/175)\ P_{175m} \quad . \tag{5-5}$$

A quantity that has to be determined in (A-10) is V_s, the velocity where the current density, $J_z(z,t)$, is considered independent of time. This current density consists of two parts, $J_z(z,t) = J_o(z,t) + J_1(z,t)$. The quantity $J_o(z,t)$ represents the current density from the randomized electrons found in regions of phase space where $V_z < V_b$. The current from these electrons is flowing continuously at a nearly constant value thus $J_o(z,t) = J_o(z)$. The quantity $J_1(z,t)$ represents the current density from the density perturbations or bunches in the beam found in regions of phase space where $V_z > V_b$. The current from these perturbations is time dependent, with bunches passing a point $z = z_o$ at a periodicity of approximately $1/\omega_{pe}$. Consequently, the current density can be rewritten as $J_z(z,t) = J_o(z) + J_1(z,t)$. The frame of reference where $J_z(z,t)$ appears stationary is then a frame that is moving with the bunches since $J_1(z,t)$ is the only time-dependent term in the current density. From Figure 28 it is evident that the bunches are propagating at $V \cong 1.5\ V_b = 2.8 \times 10^7$ m/s; thus, $V_s = 2.8 \times 10^7$ m/s.

Bunches created by an electrostatic wave in the beam propagate near the phase speed of the wave, $V_{ph} = \omega/k_z$. The frame where $J_z(z,t)$ is considered time independent is then a frame moving with this wave, $V_s = V_{ph}$. To determine the wave phase speed, the Fourier transform of $J_z(z,t)$, in both time and space for the 175-meter beam segment is calculated and plotted as a function of ω and k_z. This plot is displayed in Figure 29. If the perturbations in current density result from beam interaction with an electrostatic wave, then J_z

(k_z,ω) will be most intense near V_{ph}. Note from the figure that J_z (k_z,ω) does indeed peak near $\omega/k = V_{ph} = 2.8 \times 10^7$ m/sec, which is represented by the solid line in the figure. Consequently, if a transformation is made to a frame moving at $V_s = V_{ph} = 2.8 \times 10^7$ ms/s, the current density appears nearly stationary. Note also from the figure that all the bunches are not moving exactly at V_{ph}, but have a spread in velocity in a range $\pm\Delta V$ about V_{ph}. Consequently, in the moving frame, some second-order temporal perturbations in the current density will be present and must be considered in the calculation of the radiated power. As will be shown later, these second-order perturbations will not significantly alter the calculation of the radiated power.

The current density calculated from the 175-meter segment is considered the density in the frame moving at V_s, $J_z(z')$, where $z' = z - V_s t$; and the Fourier transform of this current density, $J_z(k_z)$, will be used in (5-3) to determine the radiated power from this segment. The transform of a 175-meter beam segment will yield discrete values of $J_z(k_z)$ at each $k_z = 2\pi m/175$ meters where m is an integer from 0 to 1750. A plot of $J_z(k_z)$ versus k_z is displayed in Figure 30. The resulting transform appears as a white-noise type k-spectra for $k_z > 22$; however, for $k_z < 22$, $J_z(k_z)$ appears to increase as k_z decreases. The white-noise type k-spectra found in $k_z > 22$ results from the randomized position and velocity of the simulation electrons used in the computer model. This noise is inherent in the modeled system since simulation electrons many times the mass and charge of real electrons

were used in the model. Although not feasible, if real electrons had been modeled, this noise would be reduced to nearly zero. The average noise level was calculated by summing the $J_z(k_z)$ values between k_z = 28.7 and 62.8 and dividing by the number summed. This level is represented by the dotted line in the figure. The increase in $J_z(k_z)$ found in $k_z < 22$ results from wave-particle interactions within the beam that create localized charged regions or bunches. If bunching had not occurred, the simulated beam electrons would be randomly spaced in both velocity and position and the resulting $J_z(k_z)$ would appear as a white noise type k-spectra at all k_z values.

To solve (5-3), $J_z(k_z)$ evaluated at $k_z' = n \cos \theta_o \omega/c$ is required. This $k_z'(\omega)$ represents the wave numbers that satisfy the Landau resonance condition and varies from .01 at 31.1 kHz to .25 at 1 MHz. The $J_z(k_z)$ values that correspond to k_z' are presented, graphically, in Figure 30. Note from this figure that six values of $J_z(k_z)$ fall in the range of k_z' for the whistler-mode. Table 2 lists these $J_z(k_z)$ values with the simulation noise level subtracted at their corresponding k_z' and $f(= V_s k_z'/2\pi)$. Using Equation (5-3) and (5-5), the radiated power spectral density, dP/df, from a 200-meter beam segment is evaluated at each of the six frequencies. These values are plotted as a function of wave frequency in Figure 31 (represented by x's) along with the calculated incoherent Cerenkov power spectra (represented by o's) and measured whistler-mode power spectra (represented by .'s) from the 200-meter SL-2 electron beam segment.

Table 2. Values of $J_z(k_z)$

k_z (1/m)	f (kHz)	$J_z(k_z)$ (Noise Level Subtracted)
.0395	176	.092
.0790	352	.035
.1185	529	.192
.1580	705	.067
.1975	881	.123
.2370	1057	.112

Note that the inclusion of coherent effects amongst the beam electrons increases the wave powers by almost 10^9 (90 dB's) above incoherent power levels. Also note that the coherent power level is near the measured whistler-mode powers. It is clear from the figure that coherent Cerenkov radiation from the beam can indeed account for the measured whistler-mode wave power. In fact, the calculated power from the modeled beam overestimates the measured power by about a factor of 10. This disagreement may result from the fact that both the computer simulation of the beam and the power calculations were performed in only one dimension. In this case, motion of the beam electrons perpendicular to the static magnetic field have been neglected. Such motion, as the electron's gyromotion, can change the radiative coherence of the beam electrons by giving them a significant displacement perpendicular to the geomagnetic field. Also, the one-dimensional

simulation of the beam has completely neglected any finite radius effects that occurred in the SL-2 electron beam. These effects can reduce the amplitude of the electrostatic wave in the beam, which correspondingly reduces Δn, the beam density perturbations. The radiated power from the SL-2 electron beam with its finite radius should then be less than the predicted radiated power from the model. Landau damping of the whistler-mode waves in the SL-2 electron beam may also reduce wave powers. This damping occurs because the Cerenkov radiation emitted by the bunches with a phase speed, $V_{ph} < V_s$, is able to interact with the heated component of the beam. This damping is not considered significant, however, since the path length for damping (as well as wave growth) in the SL-2 electron beam is very short. Consequently, the radiation will not interact with the thermalized beam component long enough to be altered significantly.

Note in Figure 31 that the frequency range of the modeled coherently radiated power does not extend below 176 kHz. This low frequency limit results from the discreteness of the $J_z(k_z)$ values used in the calculations. For a 175-meter beam segment, values of $J_z(k_z)$ can only be obtained at specific k_z and f values; namely, at $k_z = 2\pi m/175$ meters and $f = mV_s/175$ meters, where m is an integer extending from 0 to 1750. Consequently, the first nonzero frequency where a $J_z(k_z)$ value exists and the power can be determined is at 176 kHz. Values of power spectral density cannot be obtained below this frequency for a beam of this length. Increasing the beam length will allow the radiated power to be determined at lower frequencies;

however, the computer run time will also be increased, possibly beyond practical considerations. As an example, a calculation of the radiated power at 50 kHz would require nine times the CPU time currently used (from 24 to 216 VAX CPU hours) and a similar calculation at 31 kHz would require a twenty-five times increase in CPU time (from 24 to 600 VAX CPU hours). Clearly, power calculations at these lower frequencies are not feasible.

Based on the results of the simulation, the measured whistler-mode powers calculated in Chapter II and displayed in Figures 6 and 31 should be corrected to account for the radiation emitted by bunch electrons moving at speeds 1.5 times greater than the initial injection speed. The original calculation of this power assumed that all the beam electrons were moving at their initial injection velocity of 1.89×10^7 m/sec which, from the Landau resonance condition, corresponds to a value of $n_\parallel = 15.9$. This value of $n_\parallel$ was used to constrain the values of $\bar{n}(\theta)$ obtained from cold plasma theory and specified the values of n and $\Delta\theta$ used in the magnitude of the Poynting vector, expression (2-2). From the simulation, however, it is evident that the radiation is emitted from electron bunches moving at $V_s = 2.8 \times 10^7$ m/sec, which corresponds to a value of $n_\parallel = 10.7$. As a consequence, the measured power is about 50% greater when considering radiation from the faster moving bunches. Although this increase is insignificant compared to the factor of 10 difference between measured and coherent Cerenkov power values, it still should be mentioned. Recall that the Landau resonance had to be incorporated into the

measured power calculations since complete information on $\overline{E}$ and $\overline{B}$ of the measured whistler-mode waves was unavailable. The measured power is then considered a model dependent quantity based on values of $n_{\parallel}$.

As mentioned previously, all the bunches in the beam are not propagating at exactly V_s, but instead propagate in a range of velocities, $V_s \pm \Delta V$, where ΔV is the typical velocity spread. Consequently, in the moving frame, the current density is not completely independently of time as assumed in the derivation of (5-3), but has second-order temporal variations that can alter the radiative coherence of the beam. The effect of these temporal variations on the radiated power will now be considered.

Consider a current density that varies as $J_z(z')\ e^{-t^2/t_o^2}$, where t_o represents the typical time of the temporal variations in the current density. The corresponding transform of this current density in space and time is written as

$$\overline{J}_q(\overline{k},\omega) = \frac{\hat{z}}{(2\pi)^3}\sqrt{2\pi}\ J_z(k_z)\left[\frac{t_o}{2\sqrt{\pi}}\ e^{-a^2t_o^2/4}\right] \qquad (5\text{-}6)$$

where $J_z(k_z)$ is the spatial transform of the current density and $a = k_zV_s - \omega$.

If the electrostatic wave in the beam is monochromatic, the corresponding density perturbations propagate at the phase speed of

this wave. The transform of the current density is then peaked at ω/k_z values where $\omega/k_z = V_{ph} = V_s$, with no spread in ω or k_z. In this case, the current density is properly represented by (A-4). However, as Figure 29 indicates, the transform of the current density has a significant spread about $\omega/k_z = V_{ph} = V_s$. Consequently, this transform is best represented by (5-6), where the delta function in (A-4) is replaced by Gaussian function centered at $\omega/k_z = V_s$. Note as $t_o \to \infty$, the two expressions become identical.

Following a similar analysis as that of the Appendix, the radiated power is found to be

$$P(t) = \frac{i}{(2\pi)^3 \varepsilon_o} \iint (\hat{z}\cdot\bar{\bar{T}}^{-1}\cdot\hat{z})\,[2\pi\, J_z(k_z)J_z(k_z)^*] \; \frac{t_o}{2\sqrt{\pi}}\, e^{\frac{-a^2 t_o^2}{4}} \; e^{-\left(\frac{t^2}{t_o^2} + iat\right)} dk\, \frac{d\omega}{\omega} \qquad (5\text{-}7)$$

The time-averaged radiated power is now calculated. This power is defined to be

$$\bar{P} = \frac{1}{2T} \int_{-T}^{T} P(t)\, dt \qquad (5\text{-}8)$$

where T is the time interval over which the power is averaged. An integral of the form

$$I = \frac{1}{2T} \int_{-T}^{T} e^{-\left(\frac{t^2}{t_o^2} + iat\right)} dt \qquad (5\text{-}9)$$

must now be solved. Expression (5-9) can be reexpressed as

$$I = \frac{e^{\frac{-a^2 t_o^2}{4}}}{2T} \int_{-T}^{T} e^{-(\frac{t}{t_o} + \frac{iat_o}{2})^2} dt \quad . \tag{5-10}$$

The whistler-mode radiation detected by the PDP radio receivers at any instant in time is generated from a beam length segment, ℓ. The typical time an electron spends in ℓ is $\varepsilon = \ell/V_b$. Consequently, (5-10) can be rewritten as

$$I = \frac{e^{\frac{-a^2 t_o^2}{4}}}{\varepsilon} \int_{o}^{\varepsilon} e^{-(\frac{t}{t_o} + \frac{iat_o}{2})^2} dt \quad . \tag{5-11}$$

Since ℓ is small, $\varepsilon << t_o$ and (5-11) is near unity.

The average radiated power is then

$$\overline{P} = \frac{1}{(2\pi)^2 \varepsilon_o c^2} \int (\hat{z} \cdot \tilde{\bar{T}}^{-1} \cdot \hat{z}) [2\pi \, J_z(k_z) J_z^*(k_z)] \frac{t_o}{2\sqrt{\pi}} e^{\frac{-a^2 t_o^2}{4}} n\omega \, dn \, d\omega \, dk_z \tag{5-12}$$

where $d\overline{k} = \frac{n^2\omega^3}{c^3} dn \sin\theta \, d\theta \, d\phi = \frac{n\omega^2}{c^2} dn \, dk_z \, d\phi$. Equation (5-12) can be expressed as

$$\left.\frac{\overline{dP}}{d\omega}\right|_{\omega=\omega_o} = \int F(k_z, \omega_o) \frac{t_o}{2\sqrt{\pi}} e^{\frac{-a^2 t_o^2}{4}} dk_z \quad . \tag{5-13}$$

Thus, to obtain the radiated power, a Gaussian weighted integration of $F(k_z,\omega_o)$ over dk_z must be performed. Using (A-10), a similar expression can be written when $J_z(k_z\omega)$ has no spread about $\omega/k_\parallel = V_s$:

$$\left.\frac{dP}{d\omega}\right|_{\omega=\omega_o} = \int F(k_z,\omega_o)\ \delta(k_zV_s - \omega_o)e^{i(k_zV_s-\omega_o)t}dk_z$$

$$= \left.\frac{F(k_{zo},\omega_o)}{V_s}\right|_{k_{zo}=\frac{\omega_o}{V_s}} . \qquad (5\text{-}14)$$

Expression (5-13) and (5-14) should yield similar results as long as $F(k_z,\omega_o)$ approximates $F(k_{zo},\omega_o)$ in dk_z. A numerical integration of (5-13) was performed and this result was indeed found to be true. The radiated power varied only slightly when considering a spread in $J_z(k_z,\omega)$ equal to k_{zo}. The deviations of the radiated power due to such a spread are shown in Table 3. In this table, the power from a Gaussian-like $J_z(k_z,\omega)$ distribution with a spread, Δk_z, equal to k_{zo} is calculated using (5-13) and compared to the power expected using (5-14). From these results it is evident that the radiated power does not vary significantly when considering a spread in $J_z(k_z,\omega)$ about $\omega/k_z = V_s$. Consequently, the radiated power calculated using (5-3) is an accurate representation of the radiated power from the modeled beam.

Table 3. The Change in Radiated Power From Considering a Current Density With a Spread, Δk.

Frequency	$\frac{dP}{d\omega}(\Delta k_z = k_{zo})/\frac{dP}{d\omega}(\Delta k_z \to 0)$
562 kHz	.930
311 kHz	.887
178 kHz	.924
100 kHz	.942
56.7 kHz	.979
31.1 kHz	1.031

CHAPTER VI

THE ELECTRON BEAM AS AN EFFICIENT ANTENNA

In this study, it has been concluded that the whistler-mode emission detection from the SL-2 electron beam is created by coherent Cerenkov radiation from electron bunches in the beam. Consequently, the electron beam is considered an antenna radiating the whistler-mode radiation. As will be shown, by positioning the radiating bunches properly in the beam, the radiation efficiency of this "antenna" can be improved. Consider, first, the bunches formed in the continuous SL-2 electron beam. From Figure 22 it is evident that these bunches have a length, ℓ = .1-.5 meters and have a spacing, d $\cong$ 6 meters, apart from each other. This bunching of the modeled beam is clearly evident in Figure 30 which displays $J_z(k_z)$ versus k_z. In this figure the maximum $J_z(k_z)$ value is near $k_z \cong 2\pi/d \cong 1$ corresponding to the typical bunch spacing. Note that this maximum value lies outside the range of k_z' of the whistler-mode radiation. More power in the whistler-mode would have been obtained from the beam if this maximum $J_z(k_z)$ value had been in the k_z' range. In this case, the spacing between the bunches would then be equal to the parallel component of a whistler-mode wavelength, $d = \lambda_{\parallel}$; and the coherent radiation from the bunches in the beam at $f = V_s/\lambda_{\parallel}$ would constructively interfere. This

process would significantly increase the wave powers above those measured from the SL-2 electron beam to near 10^{-6} W/Hz at $f = V_s/\lambda_{\parallel}$.

This effect can be artificially induced by pulsing the electron beam near the whistler-mode range of frequencies. Unlike the continuous beam, a beam-plasma instability is now undesirable, since it tends to destroy the highly coherent pulses ejected from the gun. Consequently, to reduce the effects of the instability, the length of the pulses, ℓ, should be $\ell << V_b/f_{pe}$, where V_b/f_{pe} represents the characteristic length over which the instability acts and is the wavelength of the instability-related electrostatic wave. Also, the spacing between the pulses, d, should be equal to a parallel component a whistler-mode wavelength, $\lambda_{\parallel}$. If these two conditions are met, the radiated power at $f = V_b/d$ will be quite intense. As an example, consider a 1 keV - 50 mA electron beam in the same plasma environment as the continuous SL-2 electron beam, however, pulsed such that

$$J_z(z) = \sum_{n=0}^{p} NqV\ \delta(n\ 31.4\ \text{meters})$$

where p is the number of pulses in a 200-meter segment (equal to 6). In this idealized example, the individual pulses have an infinitesimally small length, ℓ, and are spaced 31.4 meters apart from each other. For a 1 keV -50 mA electron beam, $V = 1.89 \times 10^7$ m/sec and $N = 4.9 \times 10^{11}$ electrons. The value of k_z corresponding to the pulse spacing, d, is $k_z = .2$. The Fourier transform of $J_z(z)$ is

$$J_z(k_z) = \sum_{n=0}^{p} \frac{NqV}{\sqrt{2\pi}} \int_{-\infty}^{\infty} \delta\,(n\ 31.4)\ e^{ik_z z}\,dz = \sum_{n=0}^{p} \frac{NqV}{\sqrt{2\pi}}\ e^{in\ 31.4\ k_z}\ .$$

Note that at $k_z = .2$, $J_z(k_z)$ is a maximum since the exponential term, representing the relative phase difference between the pulses, goes to unity. Consequently,

$$J_z(k_z = .2) = \frac{6NqV}{\sqrt{2\pi}} = 3.56\ .$$

From the Landau resonance condition, this value of k_z corresponds to a frequency of 600 kHz. The radiated power is then a maximum at this frequency and is calculated to be $\sim 3 \times 10^{-4}$ W/Hz from a 200-meter pulsed beam segment. Note that this power is over 10^5 greater than those measured by the PDP. Consequently, the constructive interference amongst the pulses increases the radiated powers drastically.

CHAPTER VII

CONCLUSIONS

The whistler-mode radiation detected by the PDP during its flyby of a 1 keV - 50 mA electron beam has these characteristics:

A) The radiation is propagating near the resonance as determined by the electric field polarization.

B) About 1.6 mW of the radiation is emitted from the first 200 meters of the beam, corresponding to about 8×10^{-6} W/m of emitted radiation from the beam.

C) The calculated wave powers from the beam are well above those expected from incoherent Cerenkov radiation processes in the beam.

Many mechanisms have been discussed to account for the detected signal; however, the best mechanism is coherent Cerenkov radiation from density perturbations or bunches in the beam. These bunches are created by an electrostatic beam-plasma instability occurring within the beam.

The existence of these bunches is verified in two ways: first, when the PDP was in the beam, radio receivers detected very intense waves near ω_{pe}. These waves are believed to be associated with the instability creating the bunches. Second, a one-dimensional computer simulation of the beam clearly shows the presence of electron bunches in the beam.

The calculated power from the simulated beam indicates that the radiation from electrons in bunches is coherent enough to account for the measured whistler-mode power. Consequently, from this study it is concluded that the whistler-mode radiation from the SL-2 electron beam is generated by coherent Cerenkov radiation from a bunched electron beam.

Figure 1 A frequency vs. time spectogram from the PDP plasma wave instrument showing intense emissions during a D.C. electron gun firing. The funnel-shaped structure that extends from the electron cyclotron frequency, f_c, to about 30 kHz is whistler-mode radiation from the beam.

ORIGINAL PAGE
BLACK AND WHITE PHOTOGRAPH

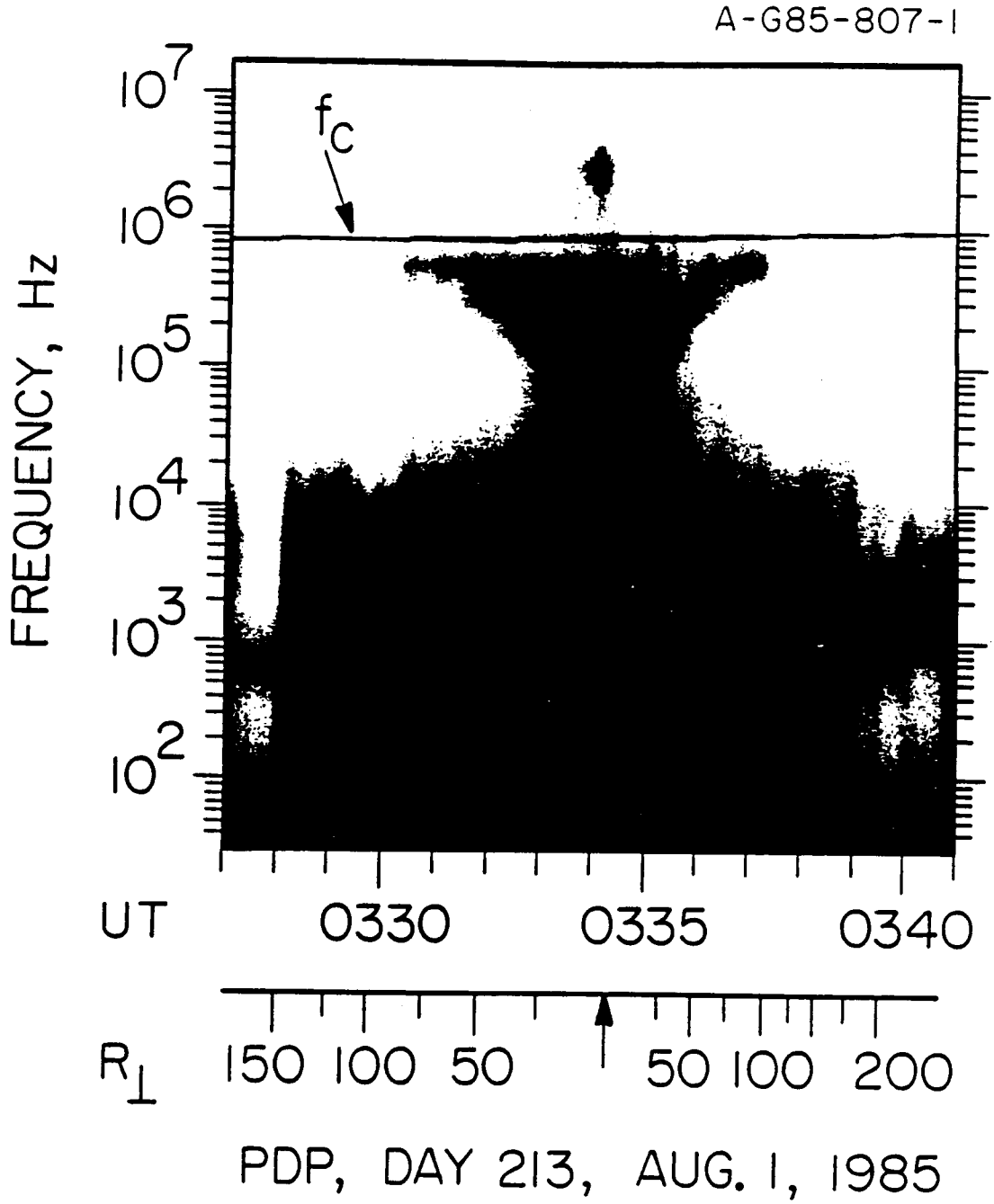

Figure 2 This diagram shows the index of refraction surface for the whistler mode and the associated $\overline{E}$, $\overline{k}$, and $\overline{v}_g$ vectors for propagation near the resonance cone ($\theta \approx \theta_{Res}$). For propagation near the resonance cone, $\overline{k}$ and $\overline{E}$ are parallel and nearly perpendicular to $\overline{v}_g$. In this limit $\overline{E}$ is linearly polarized and quasi-electrostatic.

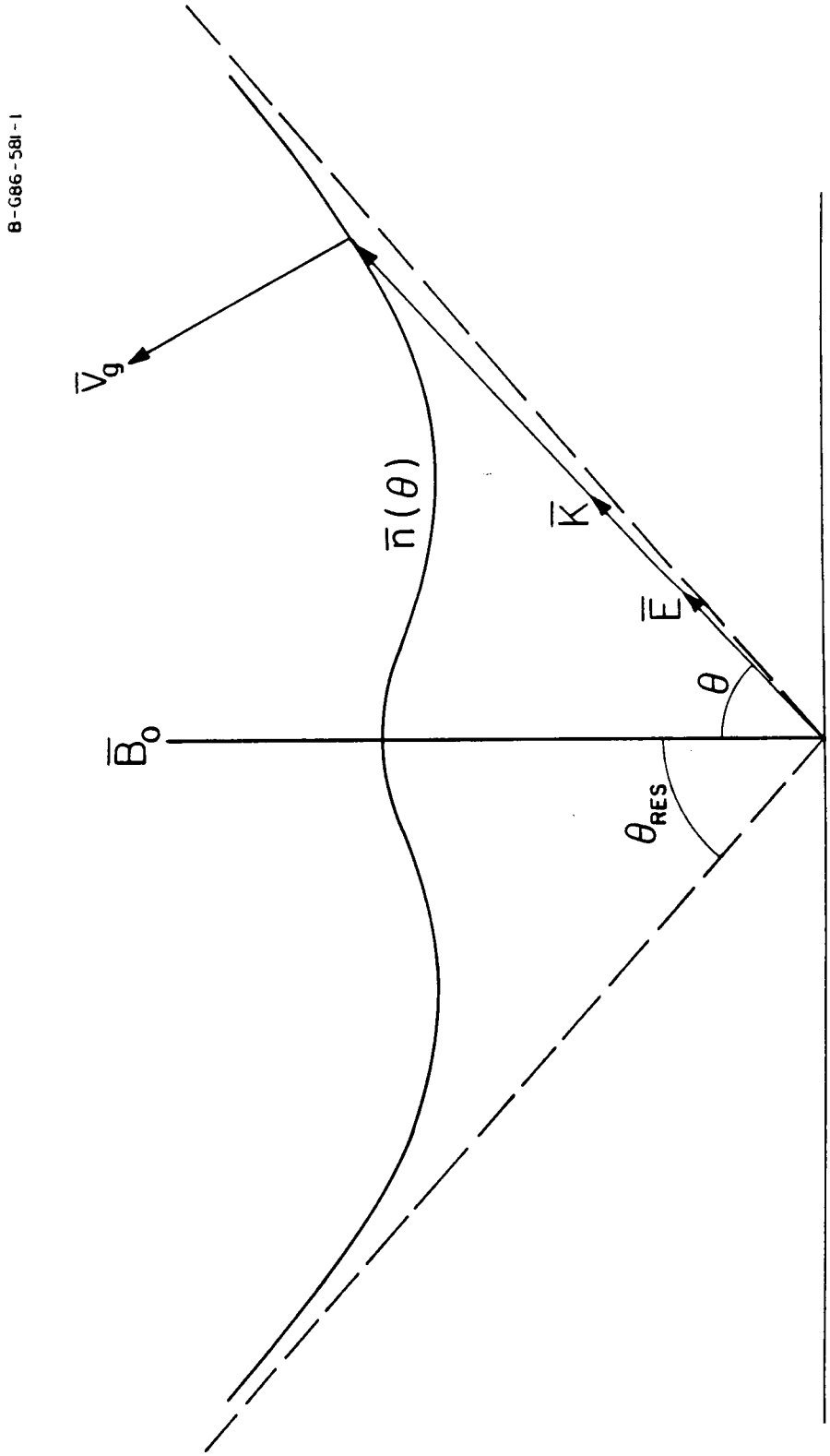
B-G86-581-1
$\overline{V}_g$
$\overline{n}(\theta)$
$\overline{K}$
$\overline{E}$
θ
$\overline{B}_o$
θ_{RES}

Figure 3 This diagram shows the ray path and $\overline{E}$, $\overline{k}$, and $\overline{v}_g$ vectors used to confirm the electric field polarization. The assumed electric field is projected into the PDP spin plane and the angle relative to the projection of the sun vector is calculated. The projected electric field direction can then be compared to the measured directions calculated from spin modulation maximums in the electric field intensity (see Figure 4).

B-G86-582-1

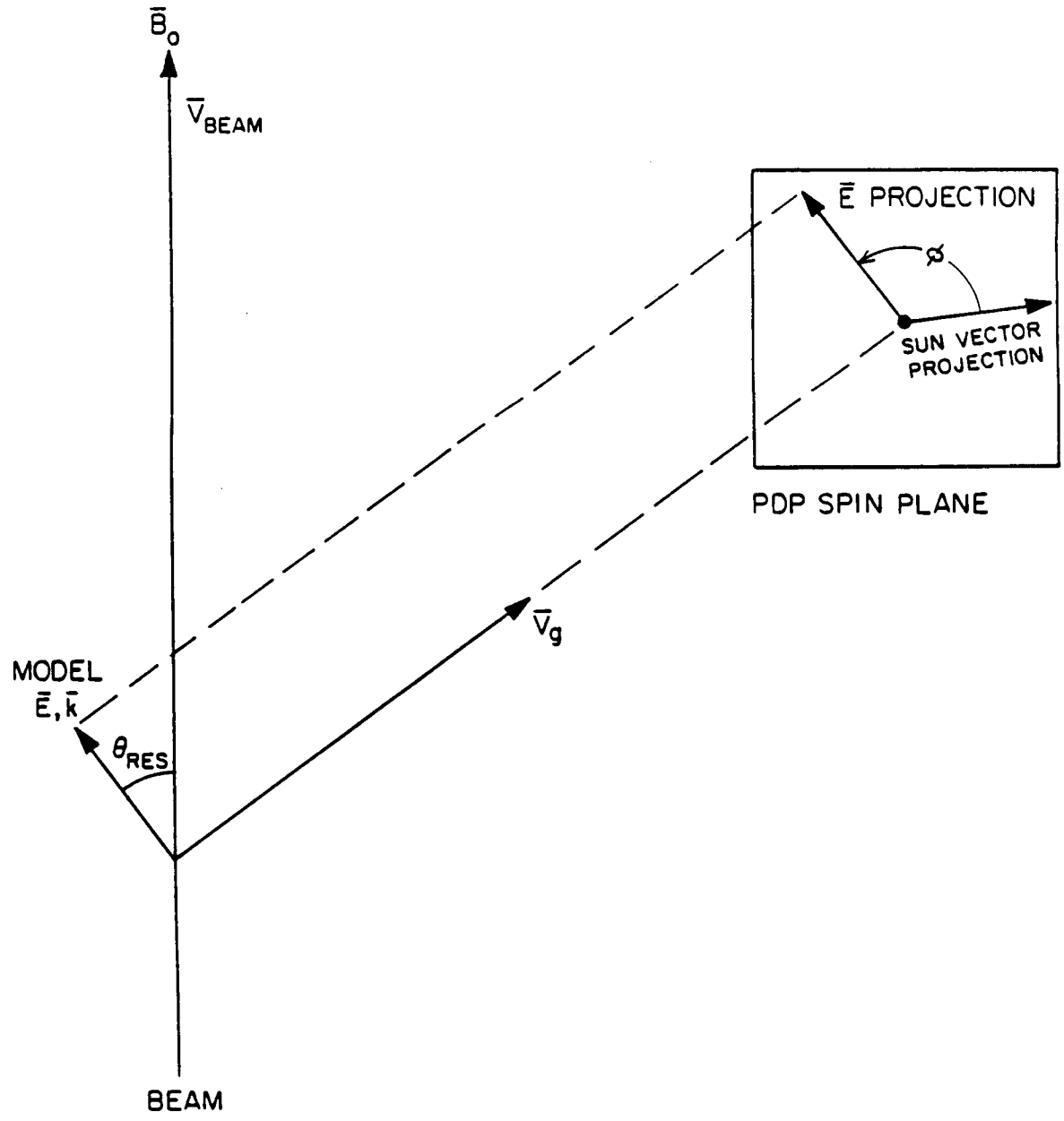
$\bar{B}_o$
$\bar{V}_{BEAM}$
$\bar{E}$ PROJECTION
ø
SUN VECTOR PROJECTION
PDP SPIN PLANE
$\bar{V}_g$
MODEL
$\bar{E}, \bar{k}$
θ_{RES}
BEAM

Figure 4(a), (b), (c), and (d) These plots show the relative directions of the computed and measured electric-field vectors in the PDP spin plane for the 562 kHz, 311 kHz, 178 kHz, and 100 kHz frequency channels. The dots represent the computed electric field directions assuming that the wave vector is near the resonance cone with $\bar{k} \cdot \bar{v}_b > 0$, and the x's represent measured electric-field directions. The close agreement between the measured and modeled directions indicates that the whistler-mode radiation is propagating near the resonance cone in the same direction as the beam.

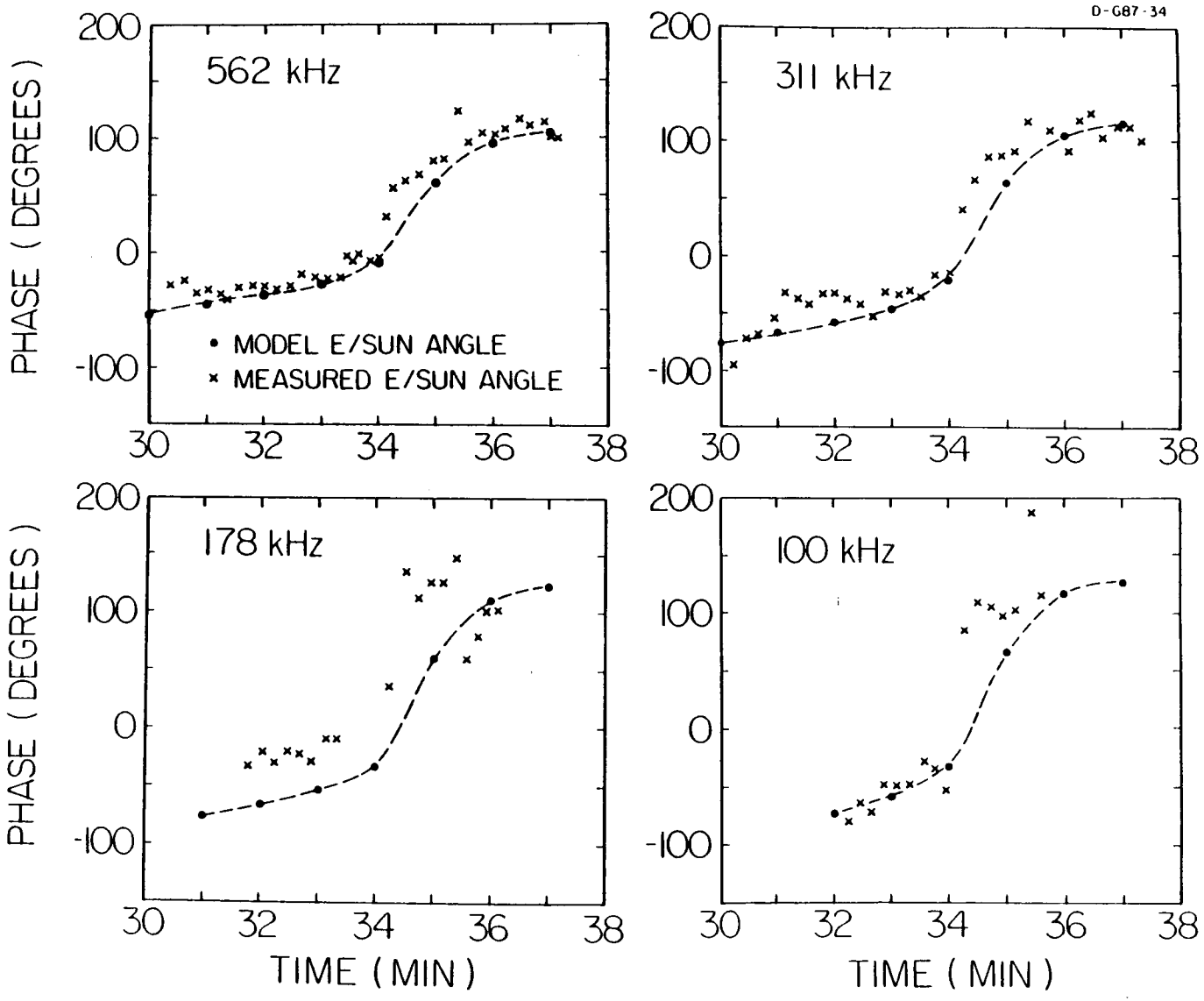
D-G87-34
562 kHz
311 kHz
178 kHz
100 kHz
• MODEL E/SUN ANGLE
× MEASURED E/SUN ANGLE
PHASE (DEGREES)
PHASE (DEGREES)
TIME (MIN)
TIME (MIN)
200
100
0
-100
30
32
34
36
38

Figure 5 This diagram shows the integration surface used to calculate the power emitted from the beam in the whistler mode. At closest approach, the PDP passed within 3 meters of the beam at a distance of about 200 meters from the shuttle.

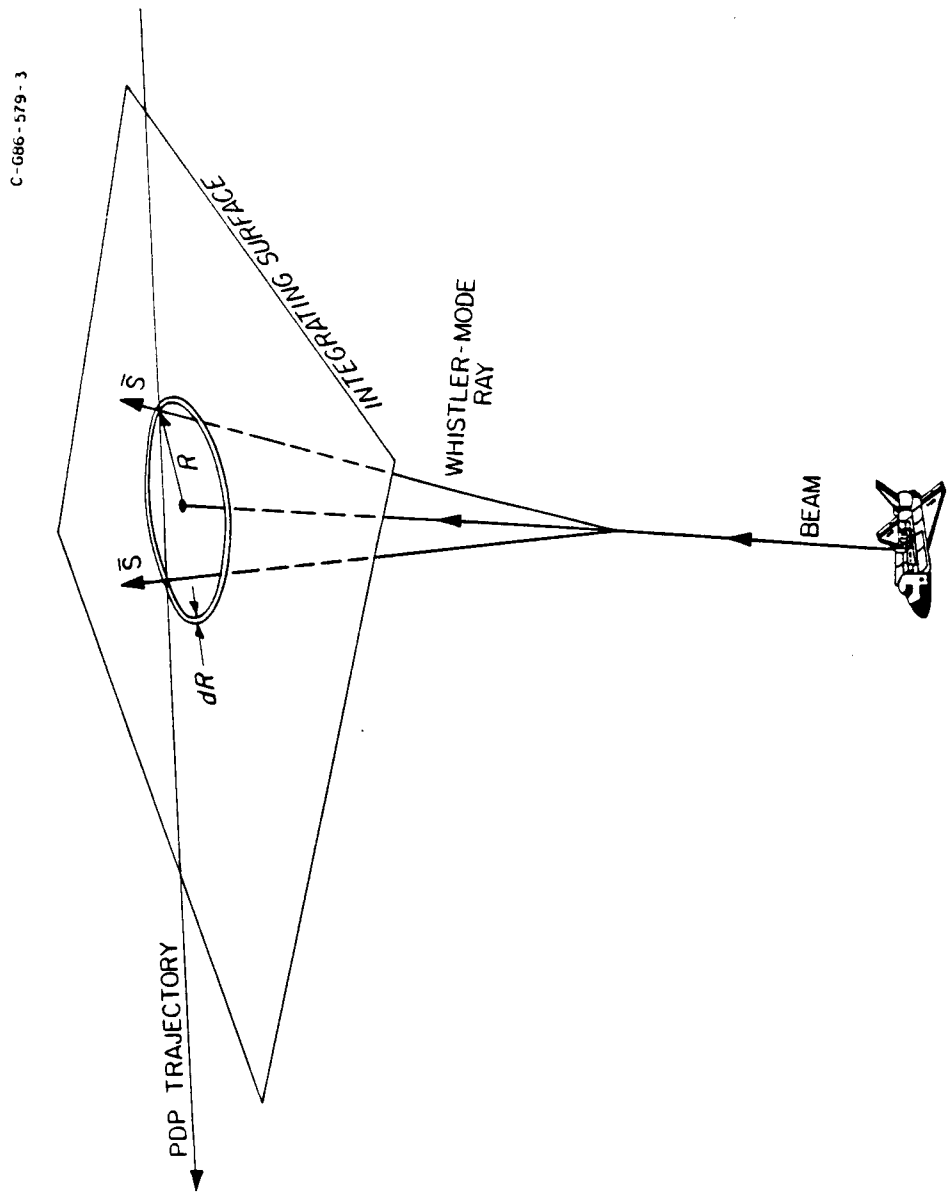
C-686-579-3
INTEGRATING SURFACE
WHISTLER-MODE RAY
BEAM
PDP TRAJECTORY
R
dR
S̄
S̄

Figure 6 The calculated power spectral density from the beam in the whistler mode is shown as a function of frequency.

A-G86-219

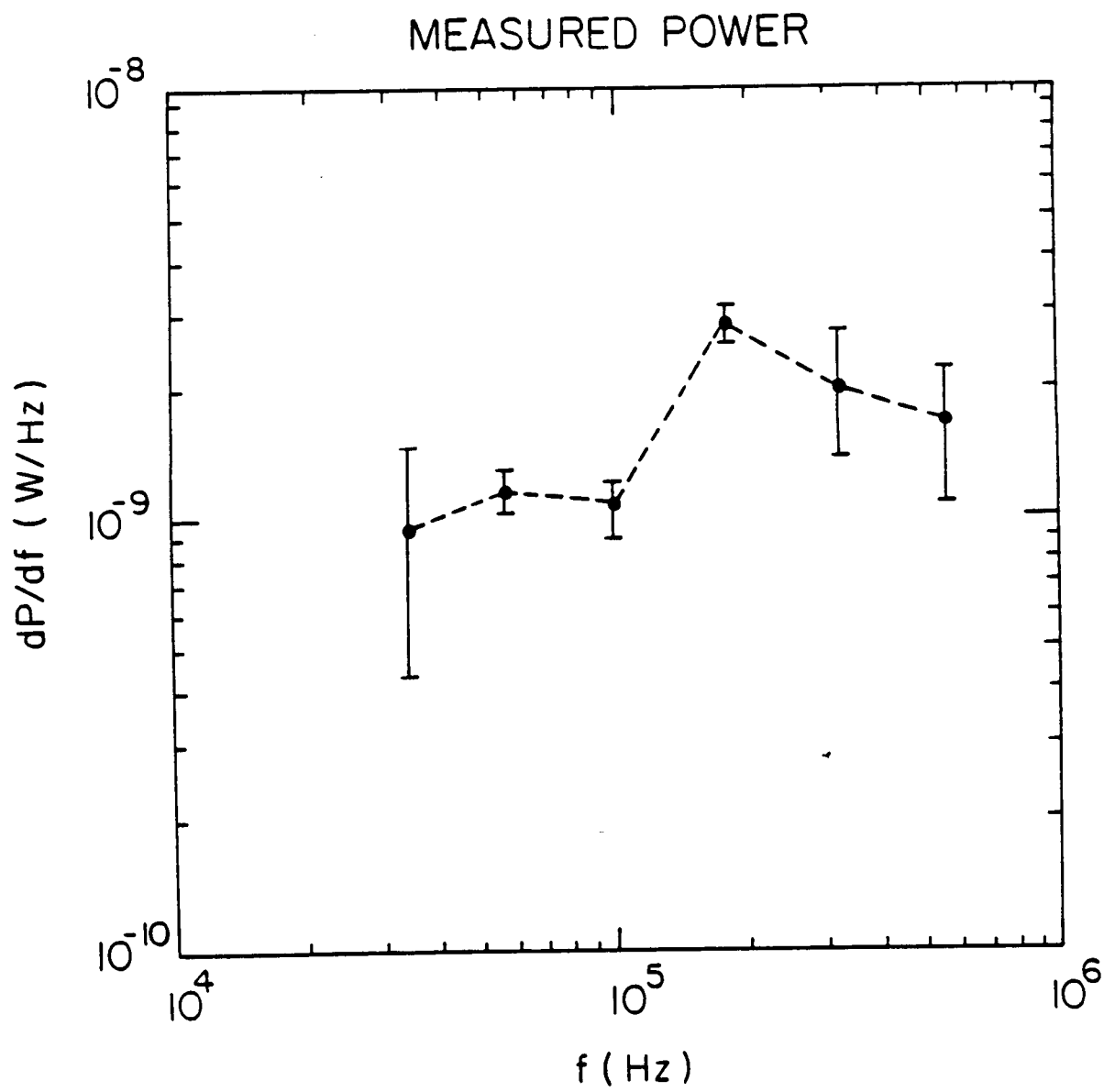

Figure 7(a) and (b) The linear emissivity, $dP/df d\ell$, is shown as a function of the distance, L, along the beam for the 562 kHz and 311 kHz frequency channels. Note that the emissivity starts to decrease rapidly beyond about 100 meters.

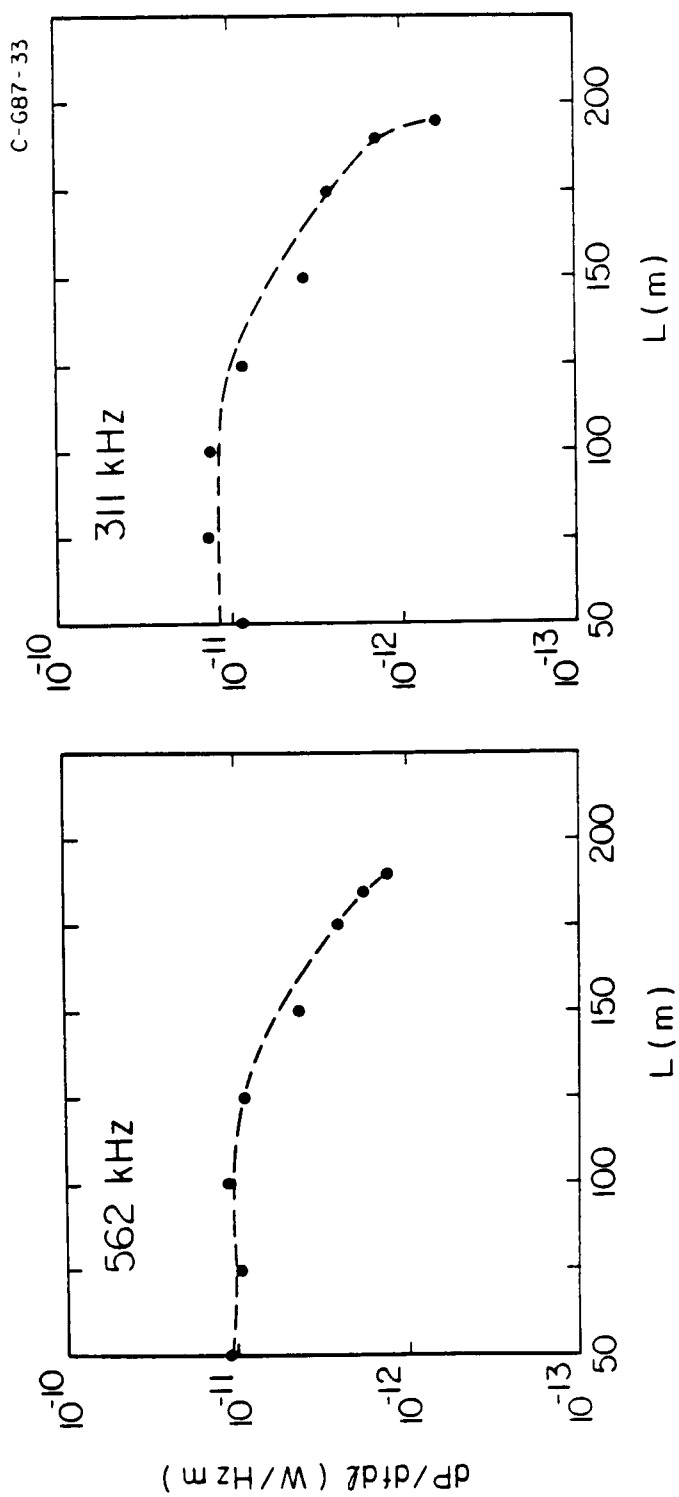
C-687-33
311 kHz
562 kHz
dP/df dℓ (W/Hz m)
L (m)
L (m)
10^-10
10^-11
10^-12
10^-13
50
100
150
200

Figure 8 The power spectra from a single electron radiating via the Cerenkov processes is shown in a plasma environment similar to that surrounding the SL-2 beam. These calculations assume the wave/beam interaction is by a Landau resonance process and that the particle pitch angle is 10°. This power calculation is based on formulas derived by Mansfield [1967].

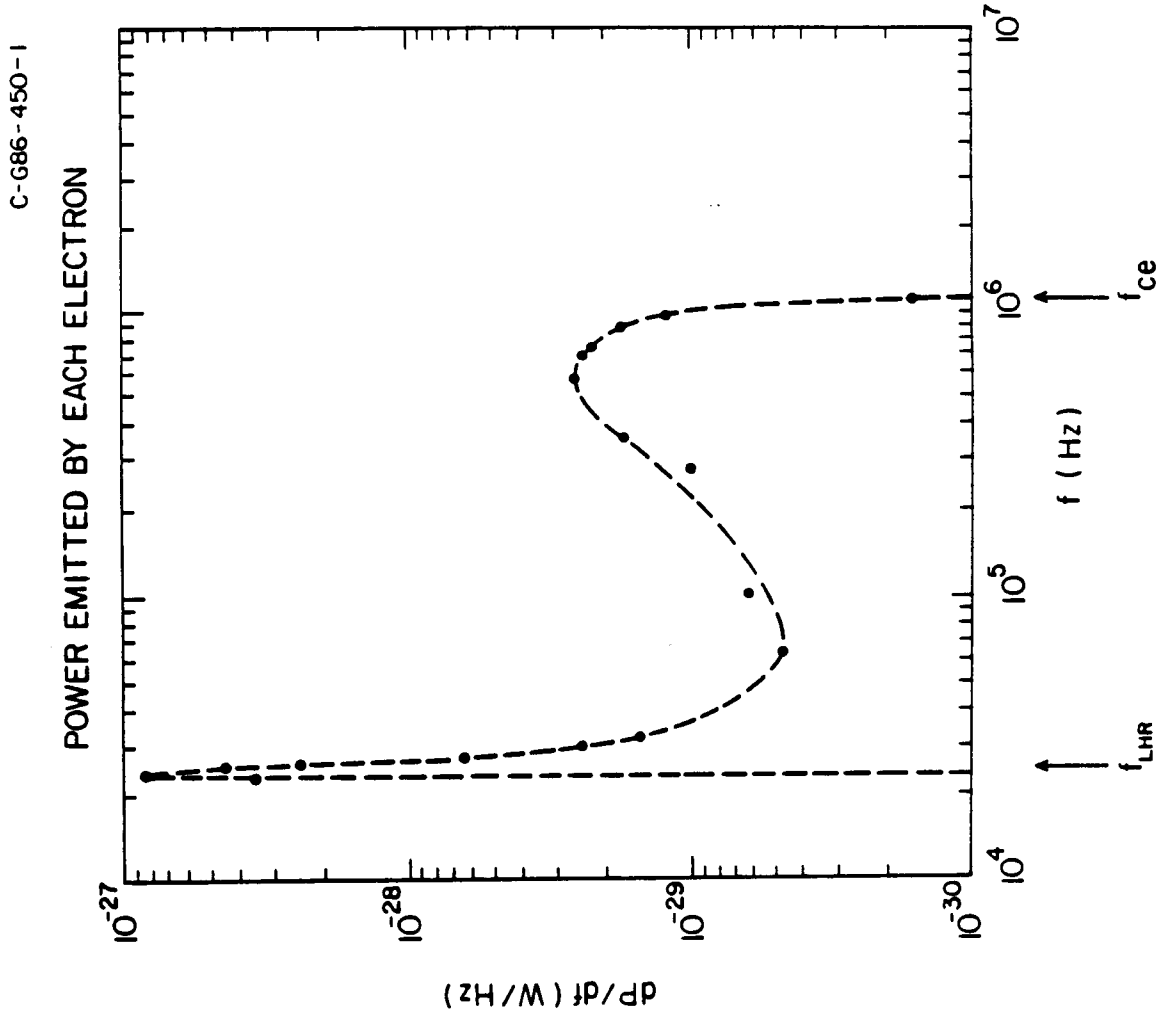
C-G86-450-1
POWER EMITTED BY EACH ELECTRON
dP/df (W/Hz)
10^-27
10^-28
10^-29
10^-30
10^4
10^5
10^6
10^7
f (Hz)
f_LHR
f_ce

Figure 9 This figure displays the radial expansion of a field-aligned electron beam after it is initially ejected from a gun of radius r_o. As the beam propagates, the radius expands according to $r = r_o + \frac{V_{\perp exp}}{V_b} z$.

B-G87-143

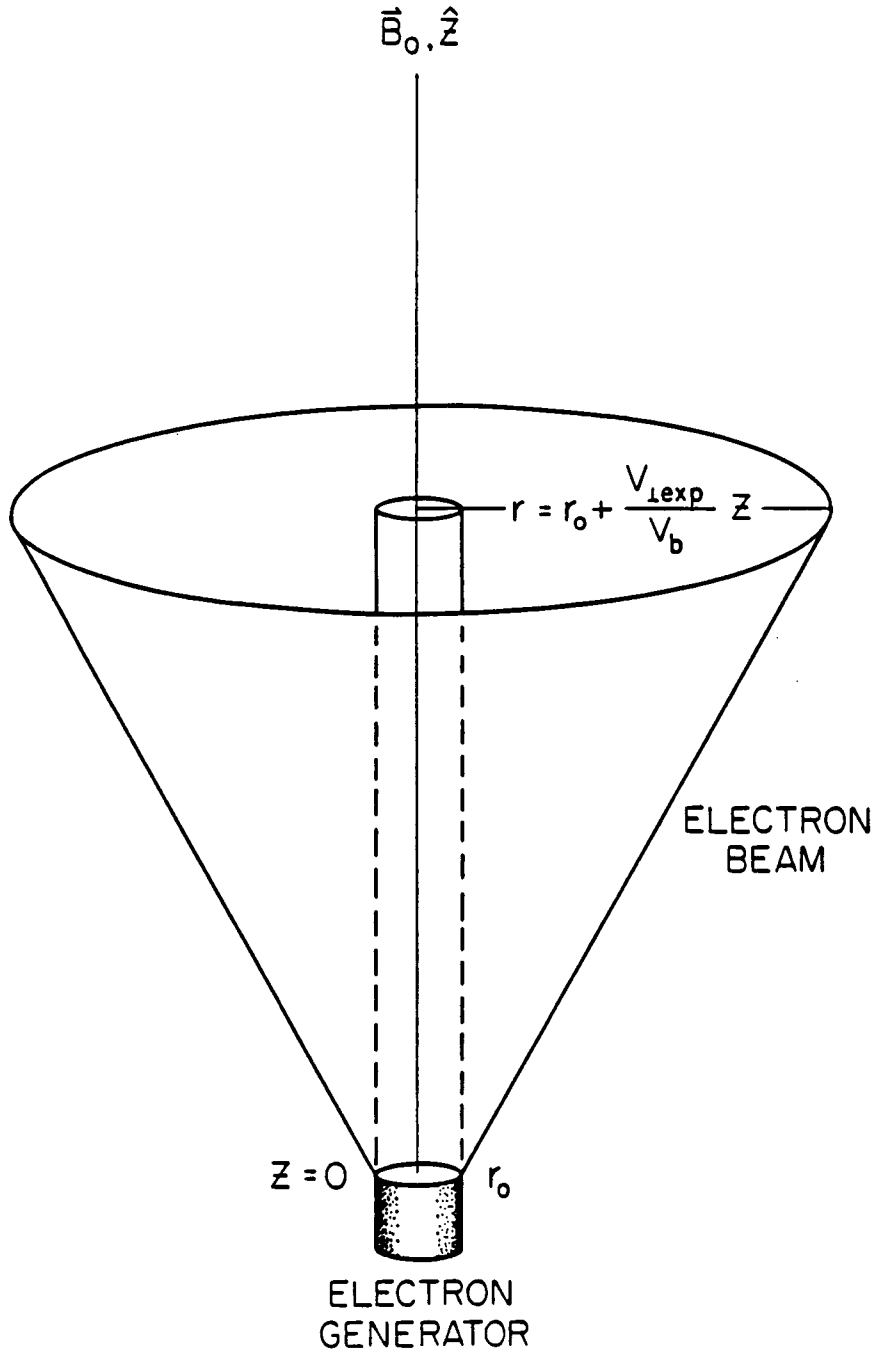
$\vec{B}_0, \hat{z}$
$r = r_o + \frac{V_{\perp exp}}{V_b} z$
ELECTRON BEAM
$z = 0$
r_o
ELECTRON GENERATOR

Figure 10 This figure is a V_z versus z phase-space configuration of electrons from a beam of density $n_b = 1/16\ n_A$ and $V_b = 10\ V_{th}$ after (a) 32 ω_{pe}^{-1} and (b) 64 ω_{pe}^{-1}. This configuration is obtained from Pritchett and Winglee's two-dimensional simulation [1986]. The beam is injected from a spacecraft located at z = 125.

A-G87-149-1

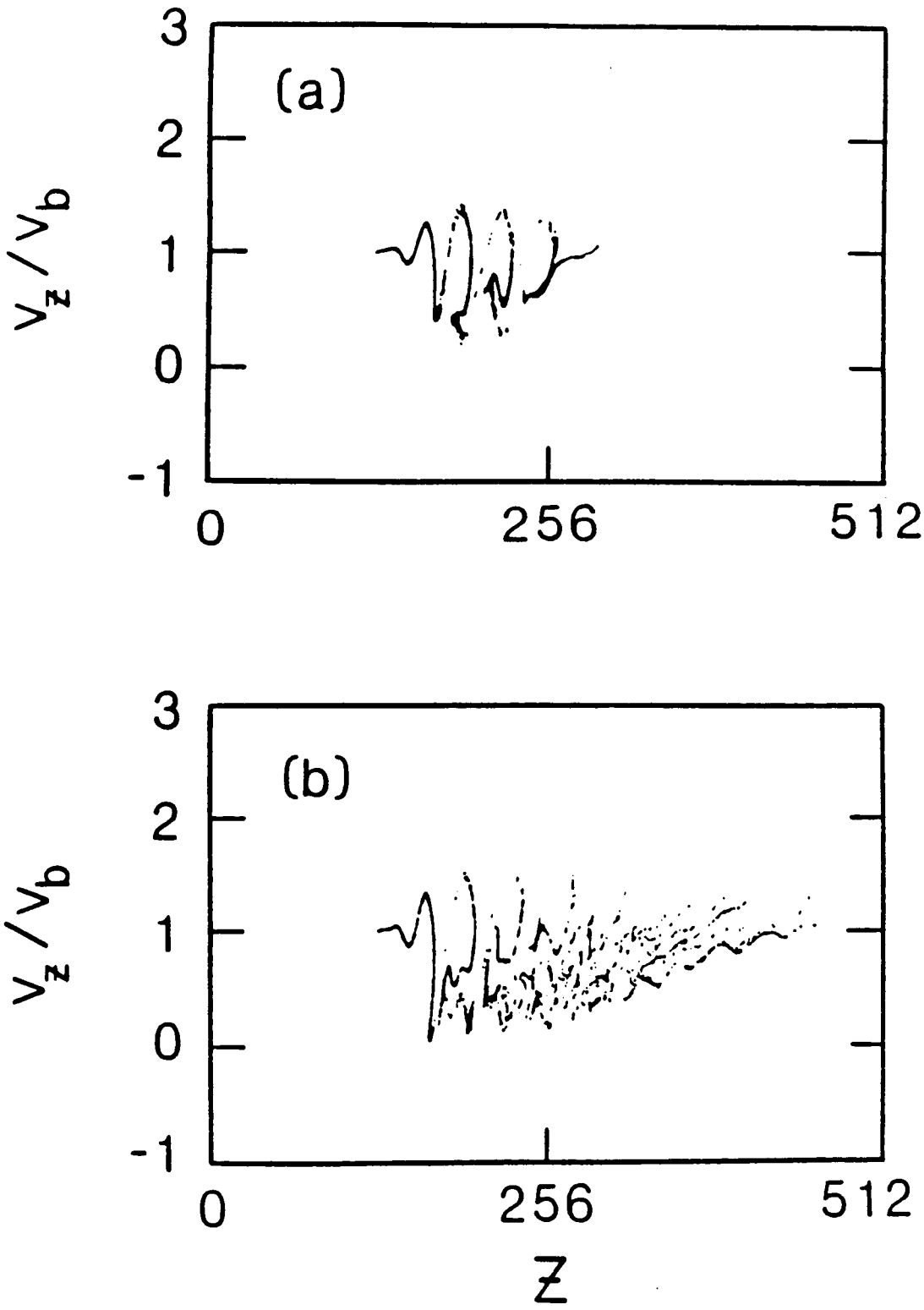

Figure 11 This figure is a V_z versus z phase-space configuration of an electron beam with similar density and velocity as that of Figure 10 taken from the one-dimensional simulation developed in this study. Note that L = 100.

A-G87-124

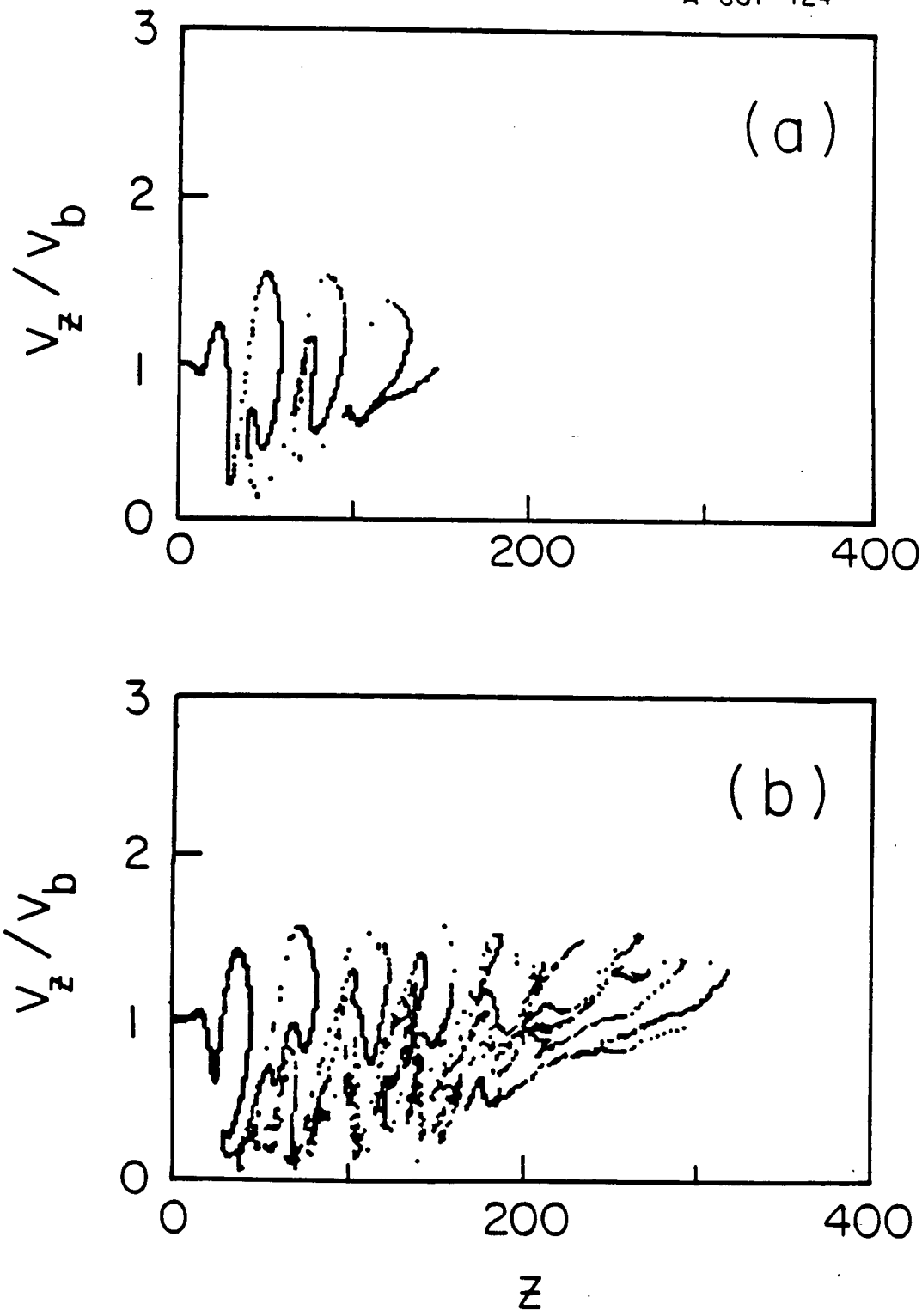

Figure 12 Again, a beam phase-space configuration is shown from the one-dimensional simulation developed in this study run with similar parameter as those of Figures 10 and 11, only now $L = \infty$ (no radial beam expansion).

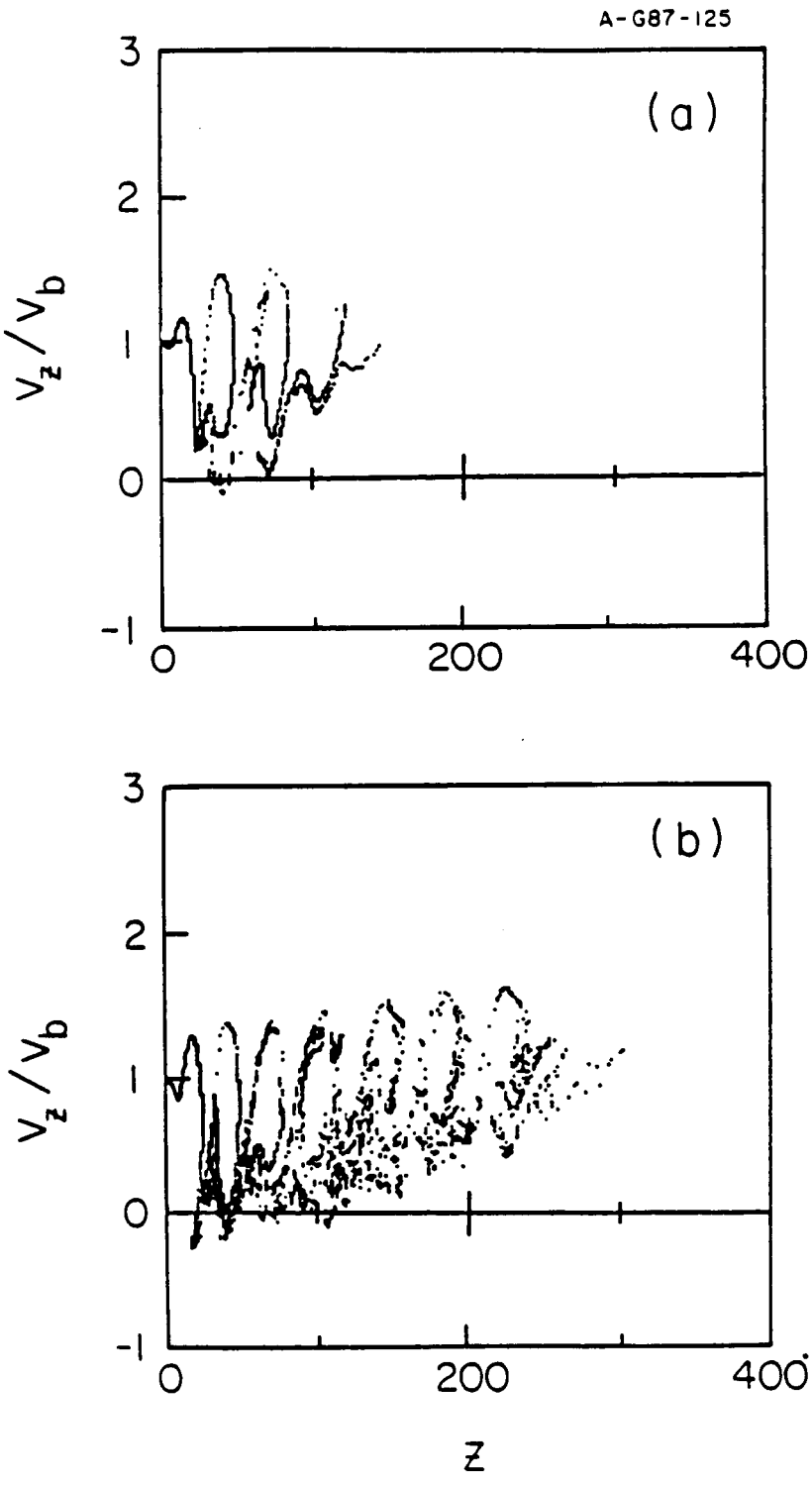
A-G87-125
(a)
(b)
V_z / V_b
3
2
1
0
-1
0
200
400
z

Figure 13 This V_z versus z beam phase-space configuration is from the one-dimensional simulation run with $n_b = 8\ n_A$, $V_b = 15\ V_{TH}$ and L = 10 for two different times: (a) 20 ω_{pe}^{-1} and (b) 30 ω_{pe}^{-1}.

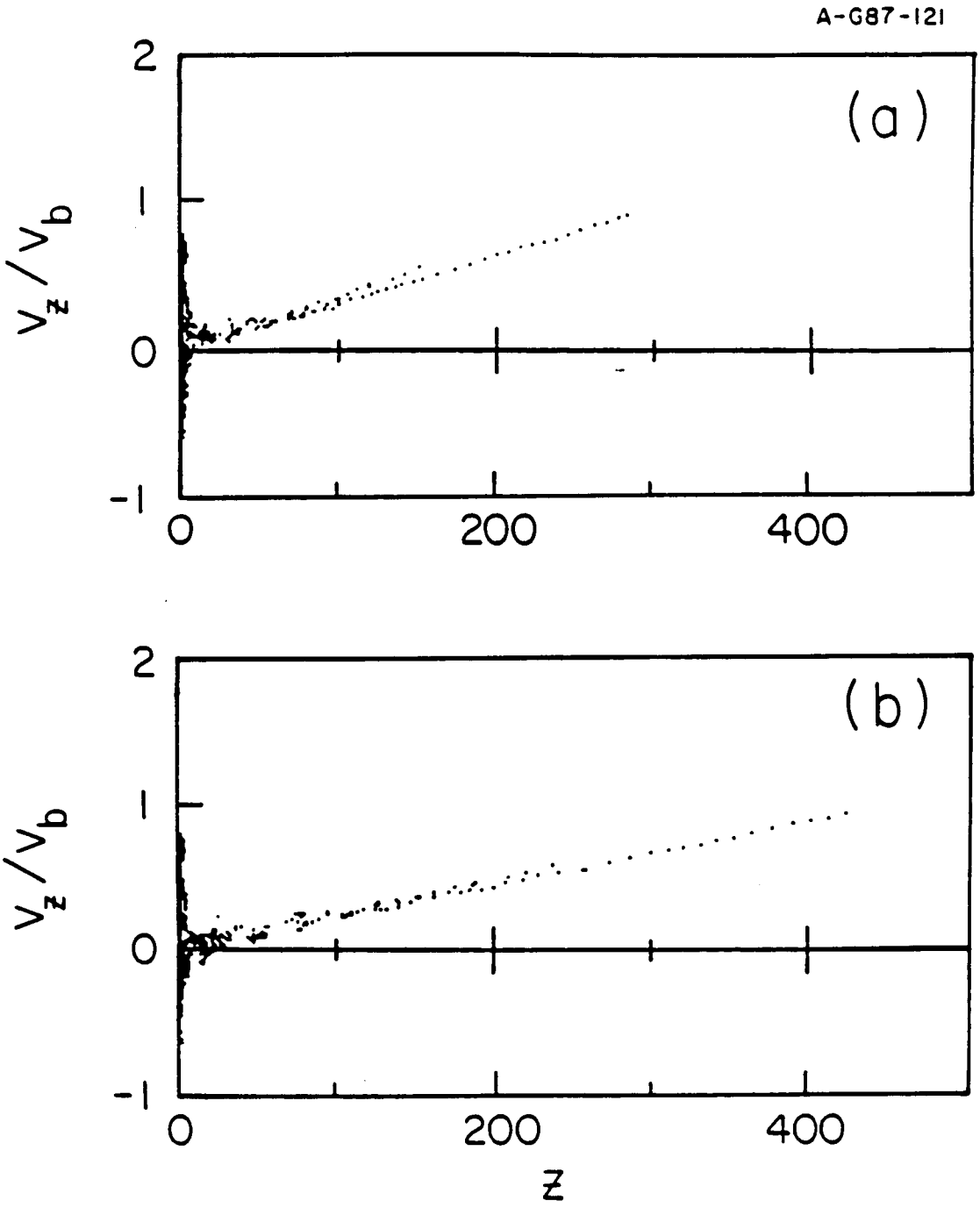
A-G87-121
(a)
(b)
v_z/v_b
2
1
0
-1
0
200
400
z

Figure 14 This figure is a beam phase-space configuration taken from Winglee and Pritchett [1986] for an overdense beam ($n_b/n_A = 2$). Note that the beam structure looks similar to that of Figure 13.

A-G87-150

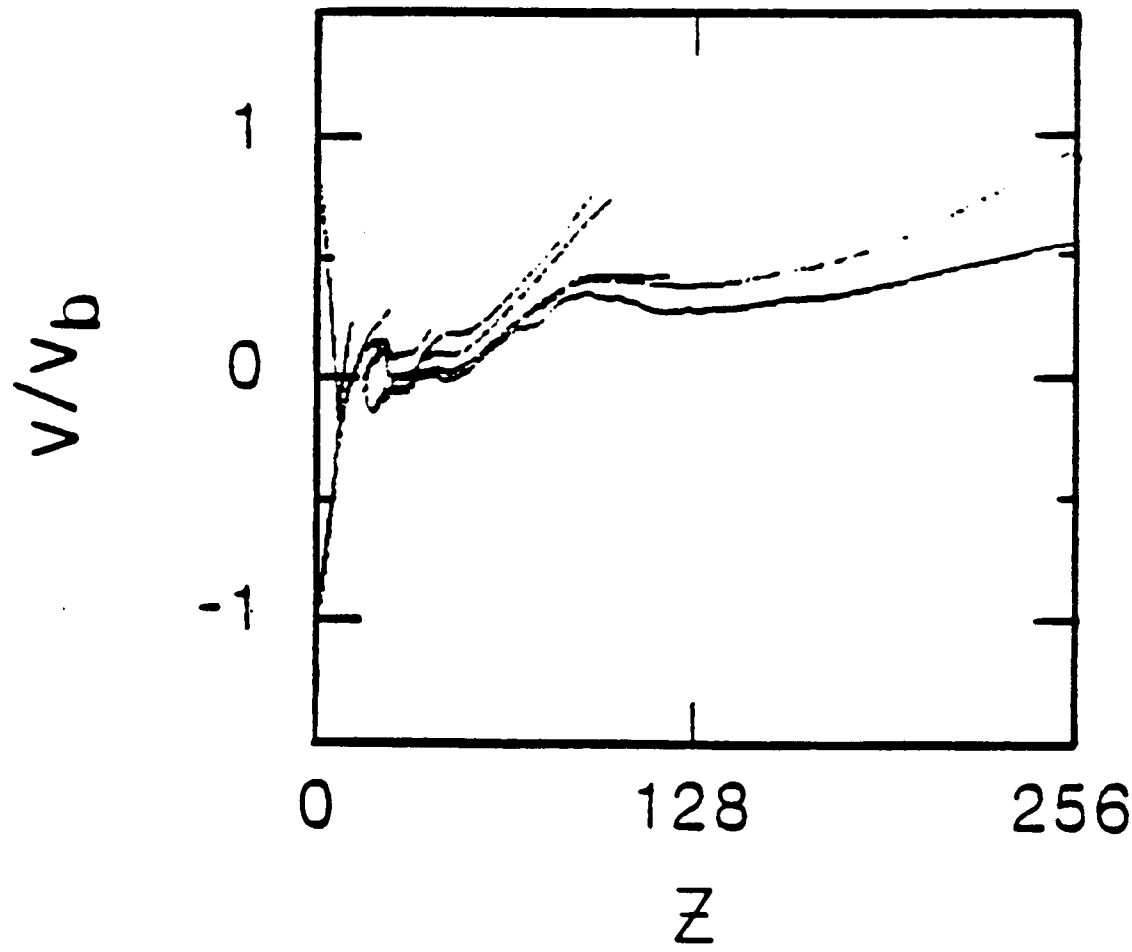

Figure 15 This figure is a beam phase-space configuration taken from Pritchett and Winglee [1986] for an overdense beam ($n_b = 8\ n_A$) at two different times: (a) 16 ω_{pb}^{-1} and (b) 32 ω_{pb}^{-1}.

A-G87-151-1

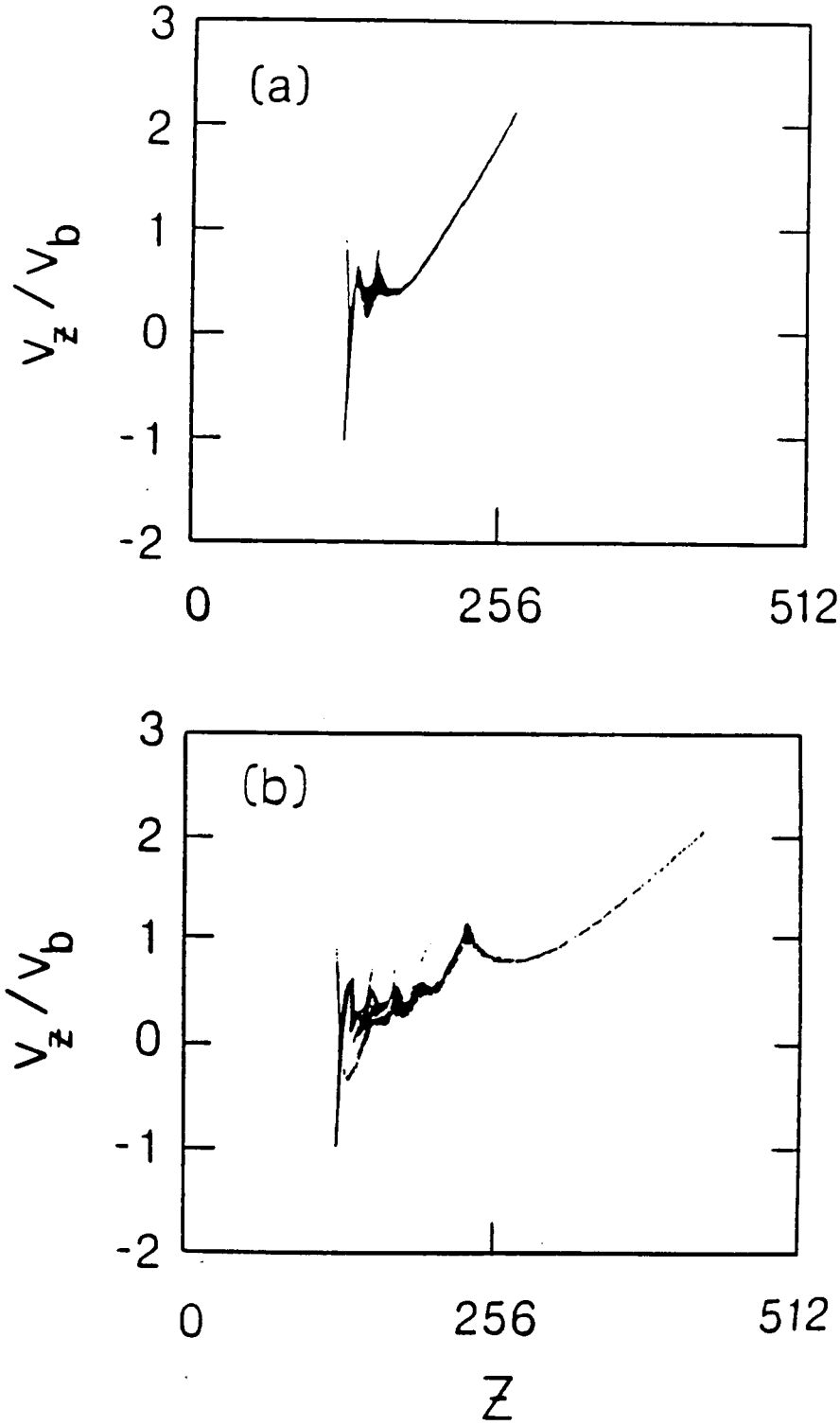

Figure 16 This figure is a V_z versus z phase-space configuration of the modeled SL-2 electron beam obtained from the one-dimensional simulation run with the parameters shown in Table 1, with L = 10.

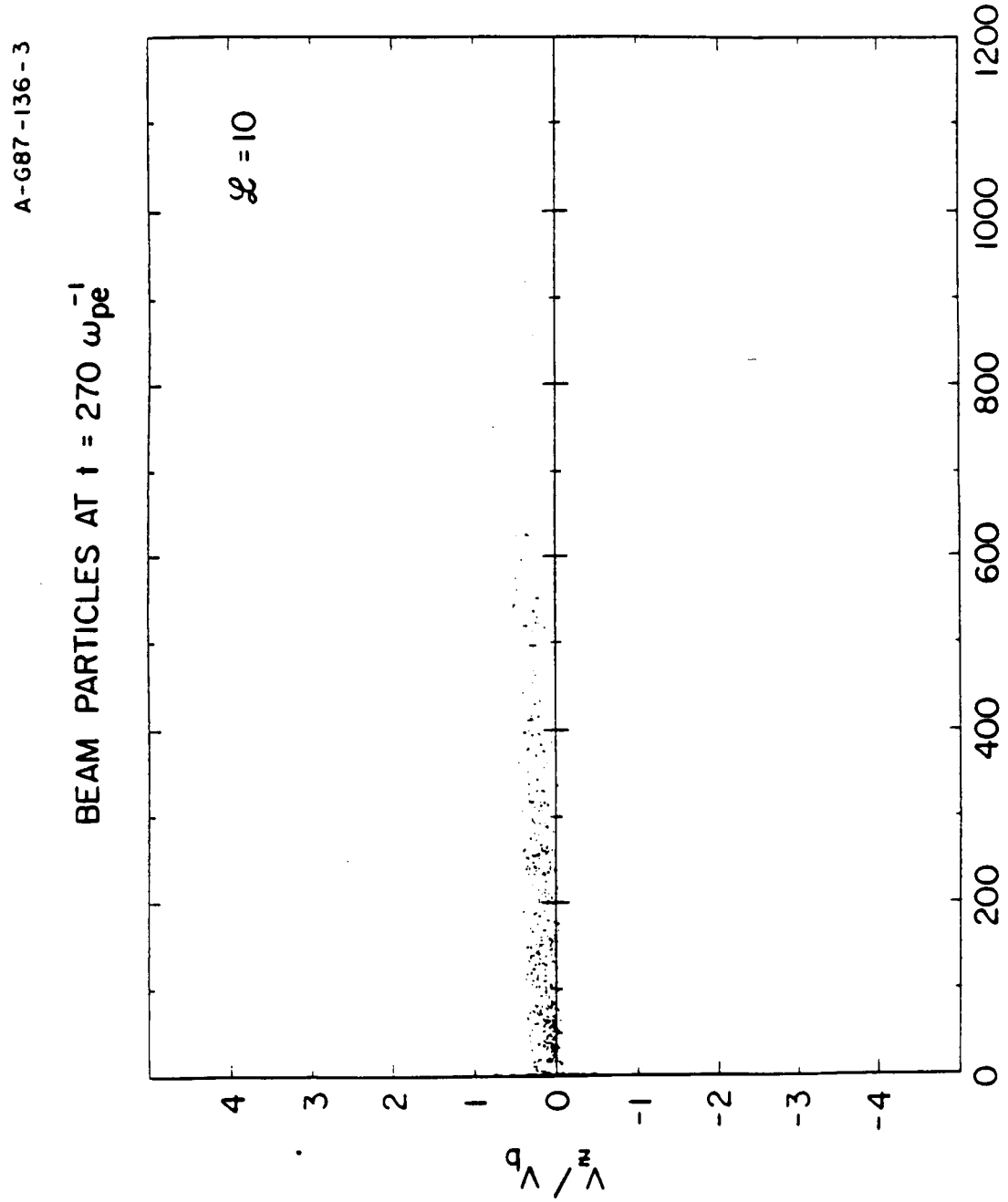
A-G87-136-3
BEAM PARTICLES AT t = 270 ω_{pe}^{-1}
$\mathcal{L}$ = 10
v_z / v_b
z
4
3
2
1
0
-1
-2
-3
-4
0
200
400
600
800
1000
1200

Figure 17 This figure displays E_z versus z from the one-dimensional simulation run with L = 10. Note that a strong electric field is located near z = 0.

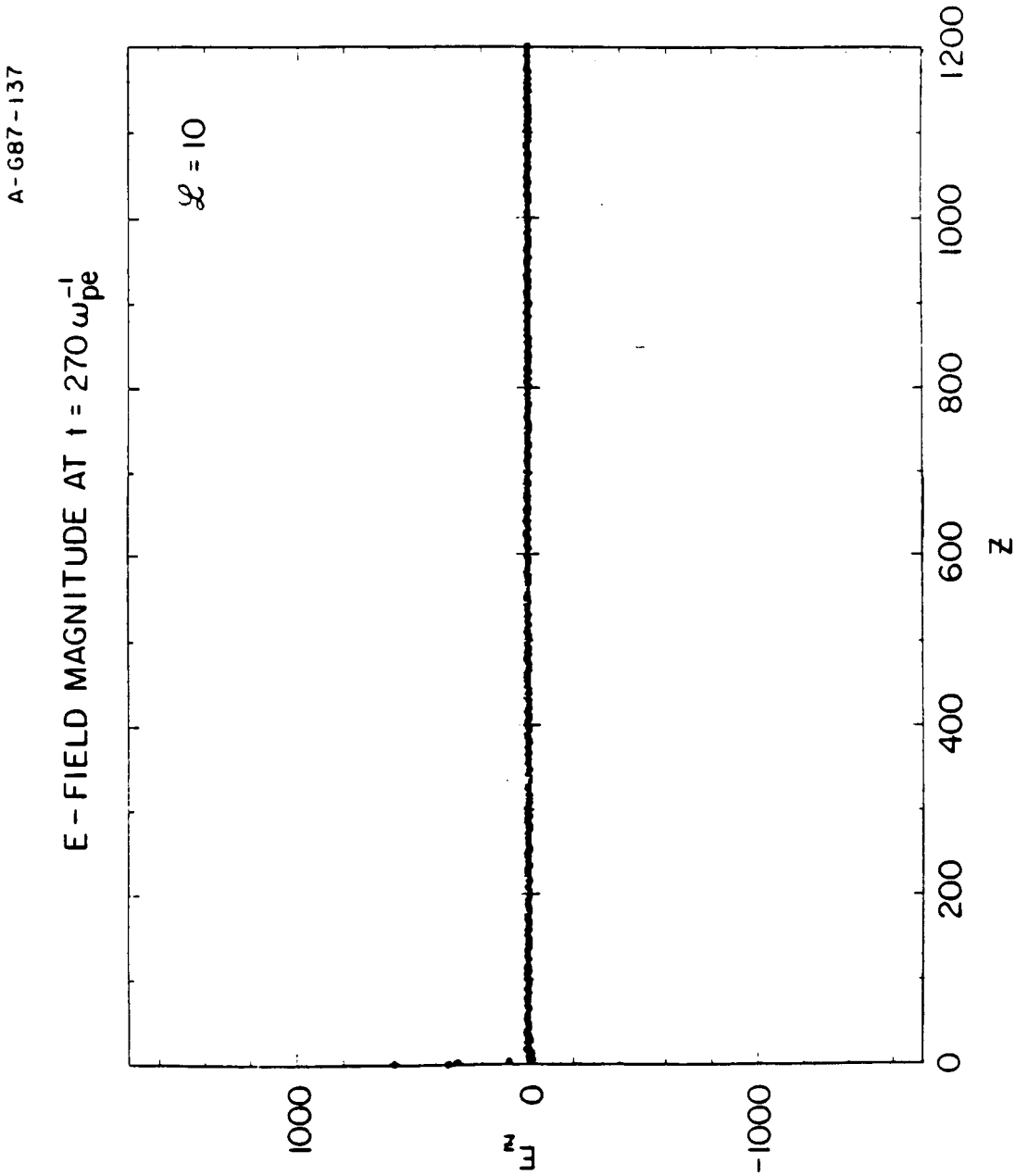
A-687-137
E-FIELD MAGNITUDE AT t = 270 ω_{pe}^{-1}
$\mathcal{L}$ = 10
1000
0
-1000
E_z
0
200
400
600
800
1000
1200
Z

Figure 18 This figure displays the number of electrons, N, versus z from the modeled beam run with L = 10.

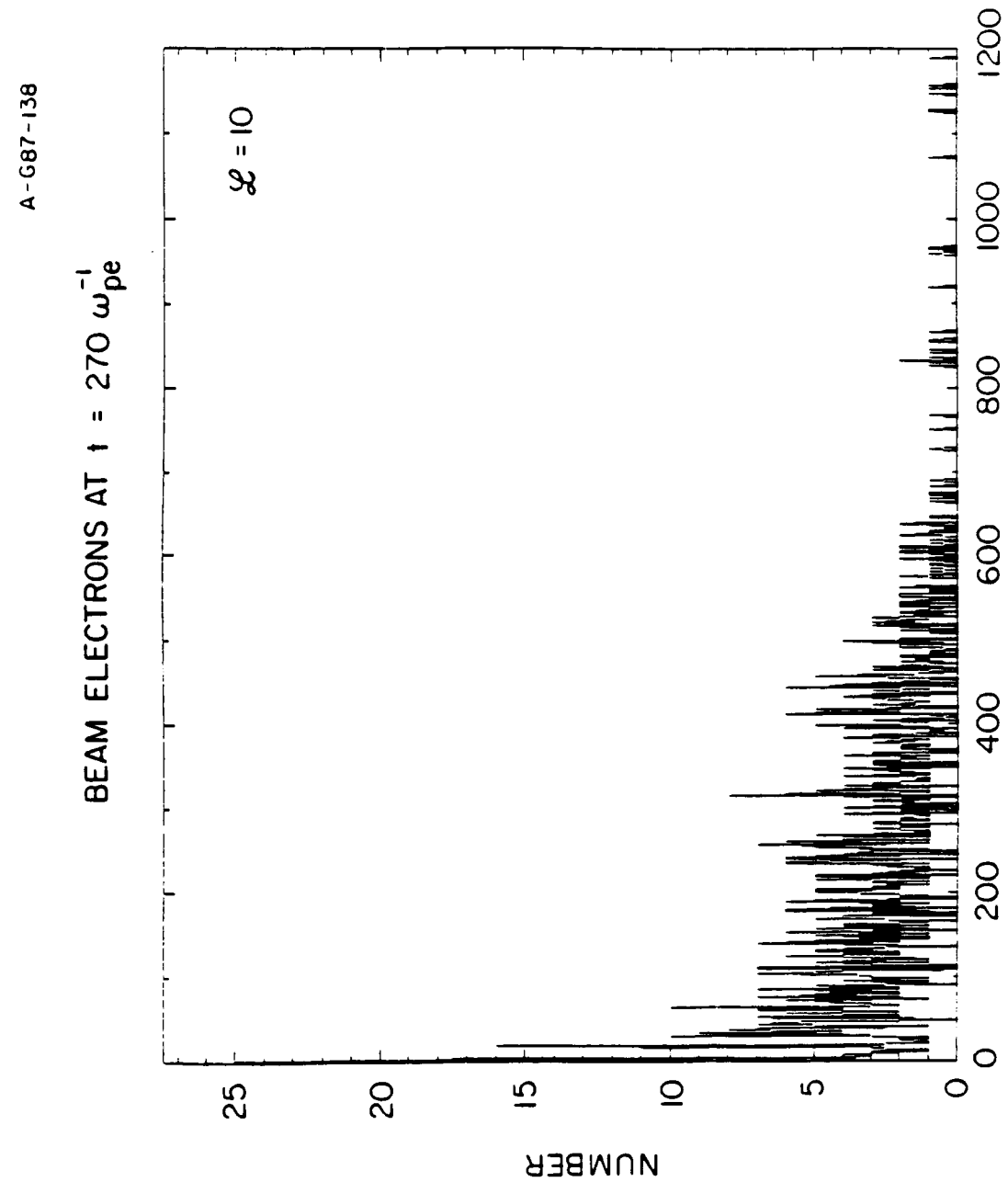
A-G87-138
BEAM ELECTRONS AT t = 270 ω_{pe}^{-1}
$\mathscr{L}$ = 10
NUMBER
Z
0
5
10
15
20
25
0
200
400
600
800
1000
1200

Figure 19 This figure is a V_z versus z phase-space configuration of the modeled SL-2 electron beam obtained from the one-dimensional simulation run with the parameters shown in Table 1, with L = 5.

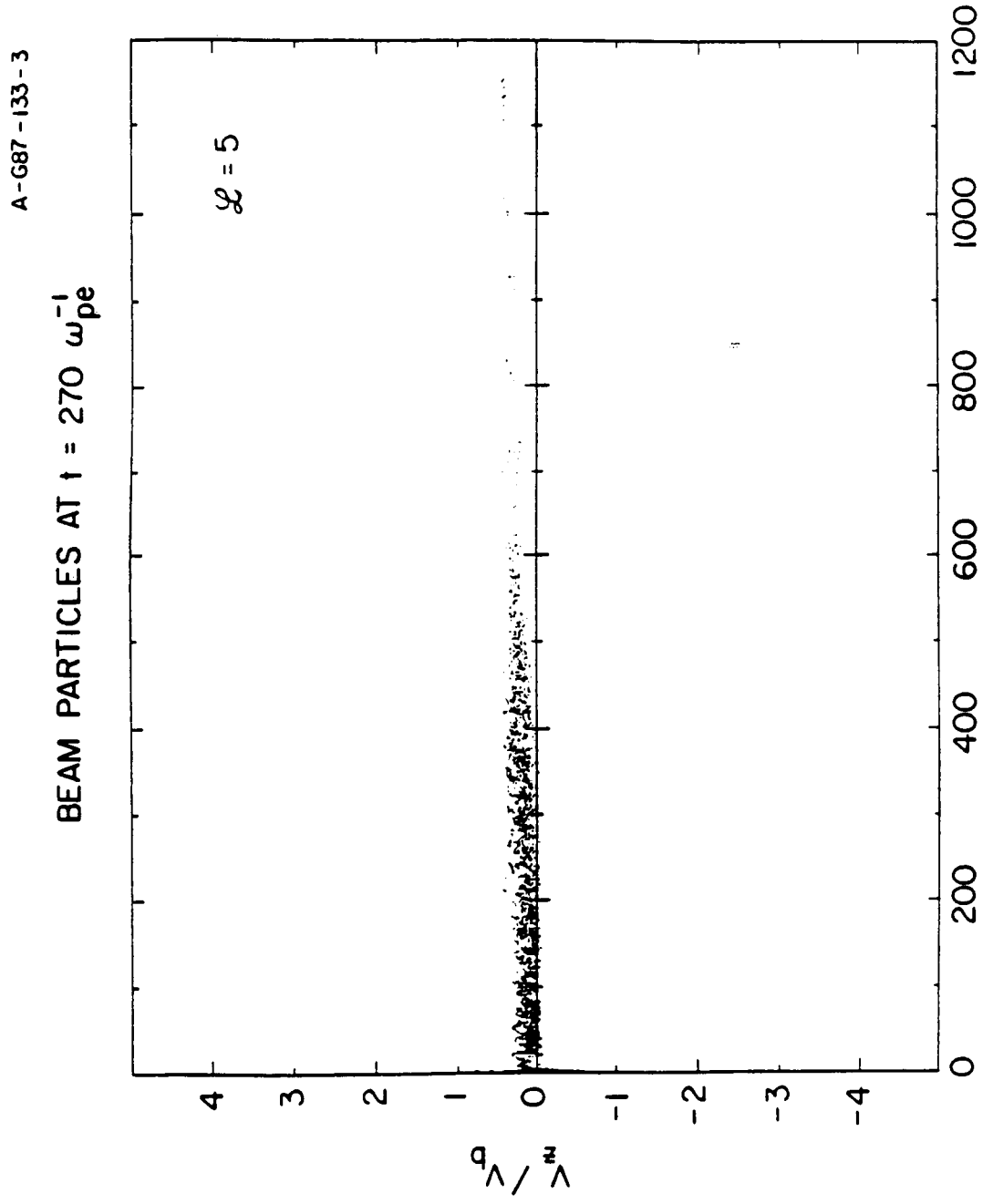
A-G87-133-3
BEAM PARTICLES AT t = 270 ω_{pe}^{-1}
$\mathscr{L} = 5$
v_z / v_b
z
4
3
2
1
0
-1
-2
-3
-4
0
200
400
600
800
1000
1200

Figure 20 This figure displays E_z versus z from the one-dimensional simulation run with L = 5. Note that a strong electric field is located near z = 0.

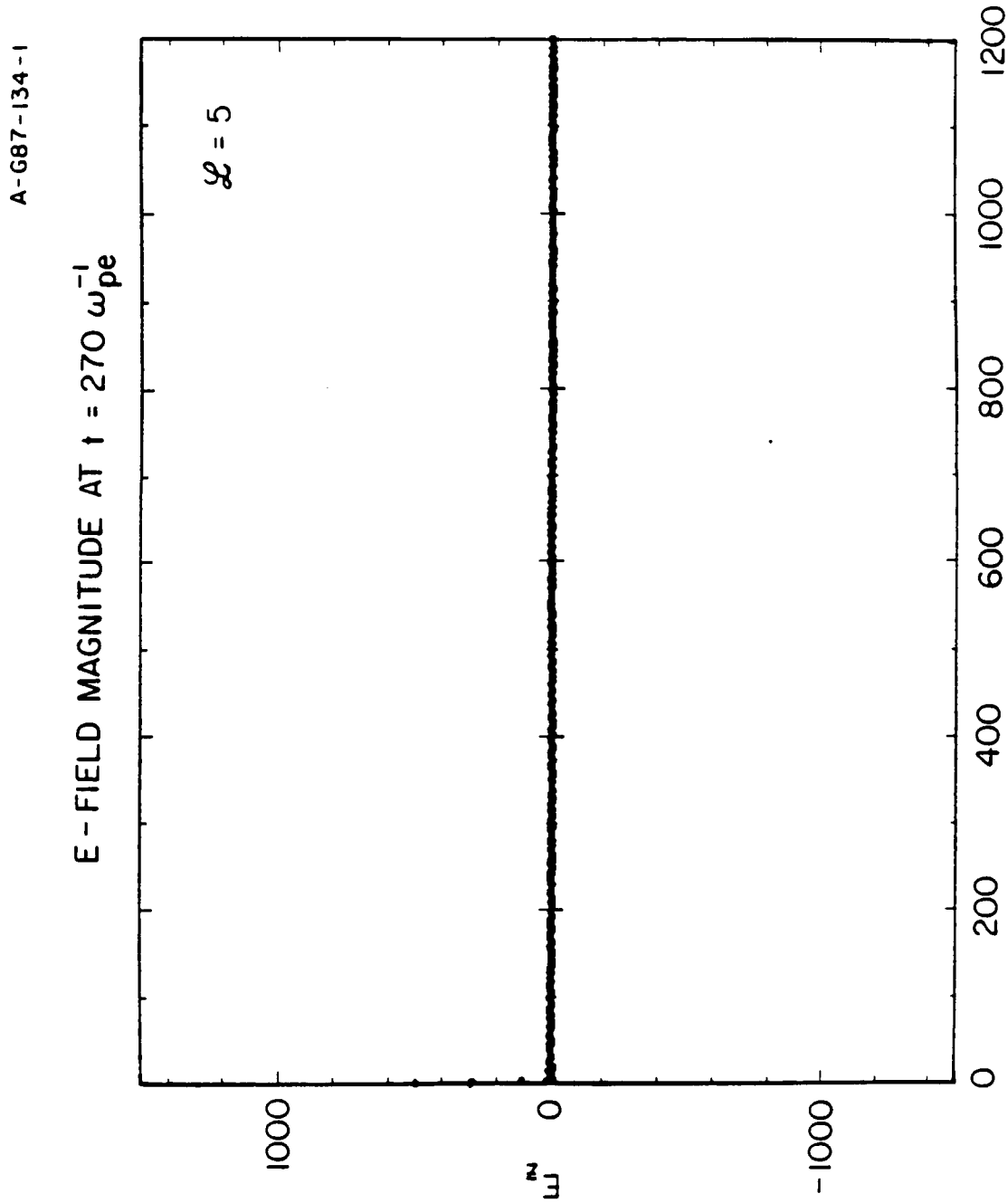
A-G87-134-1
E-FIELD MAGNITUDE AT t = 270 ω_{pe}^{-1}
$\mathcal{L}$ = 5
1000
0
-1000
E_z
0
200
400
600
800
1000
1200
z

Figure 21 This figure displays the number of electrons, N, versus z from the modeled beam run with L = 5.

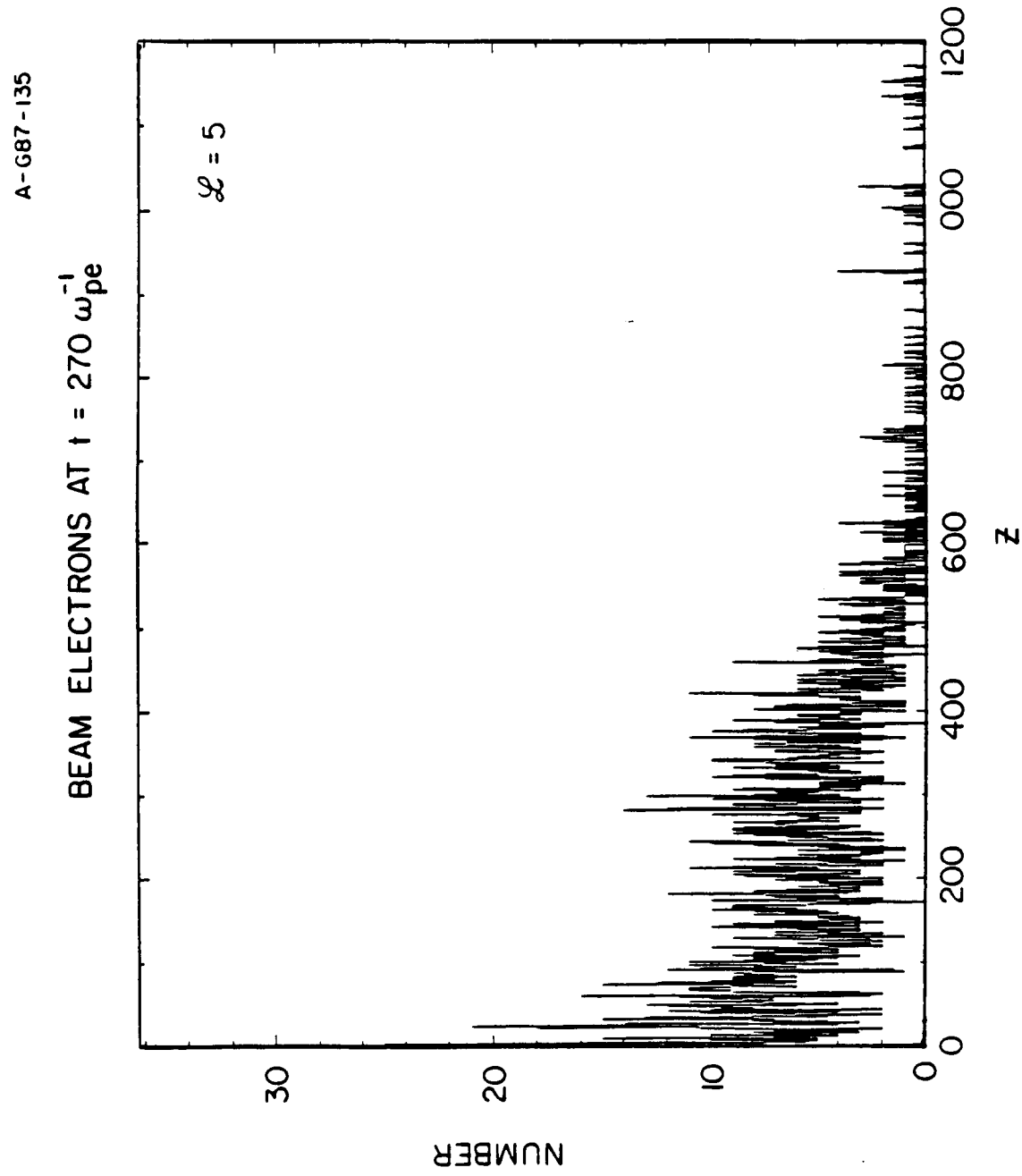
A-687-135
BEAM ELECTRONS AT t = 270 ω_{pe}^{-1}
$\mathscr{L}$ = 5
NUMBER
0
10
20
30
0
200
400
600
800
000
1200
Z

Figure 22 This figure is a V_z versus z phase-space configuration of the modeled SL-2 electron beam obtained from the one-dimensional simulation run with the parameters shown in Table 1, with L = 3.

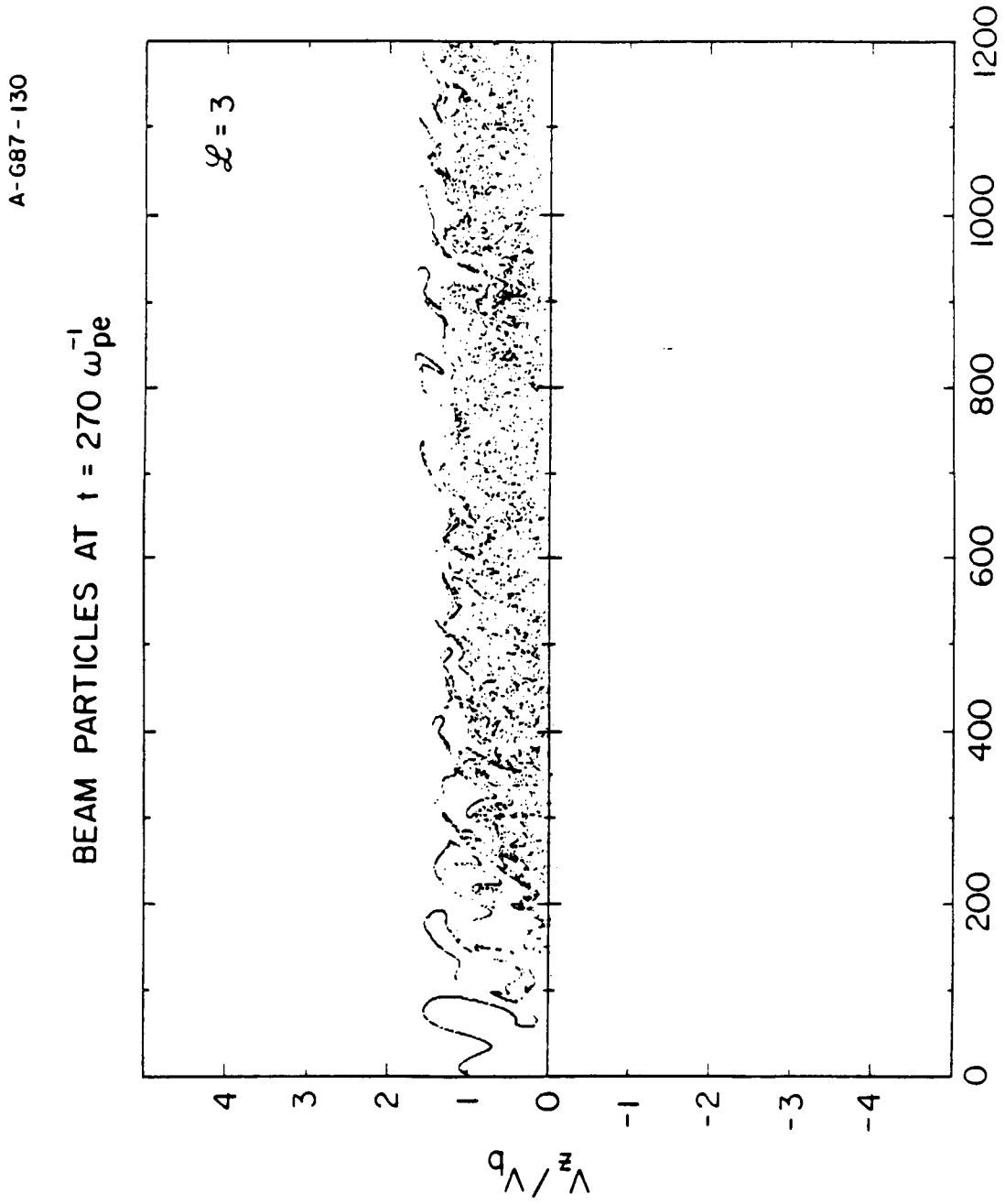
A-G87-130
BEAM PARTICLES AT t = 270 ω_{pe}^{-1}
$\mathcal{L} = 3$
v_z / v_b
z
4
3
2
1
0
-1
-2
-3
-4
0
200
400
600
800
1000
1200

Figure 23 This figure displays E_z versus z from the one-dimensional simulation run with L = 3. Note that wave activity is present in the beam.

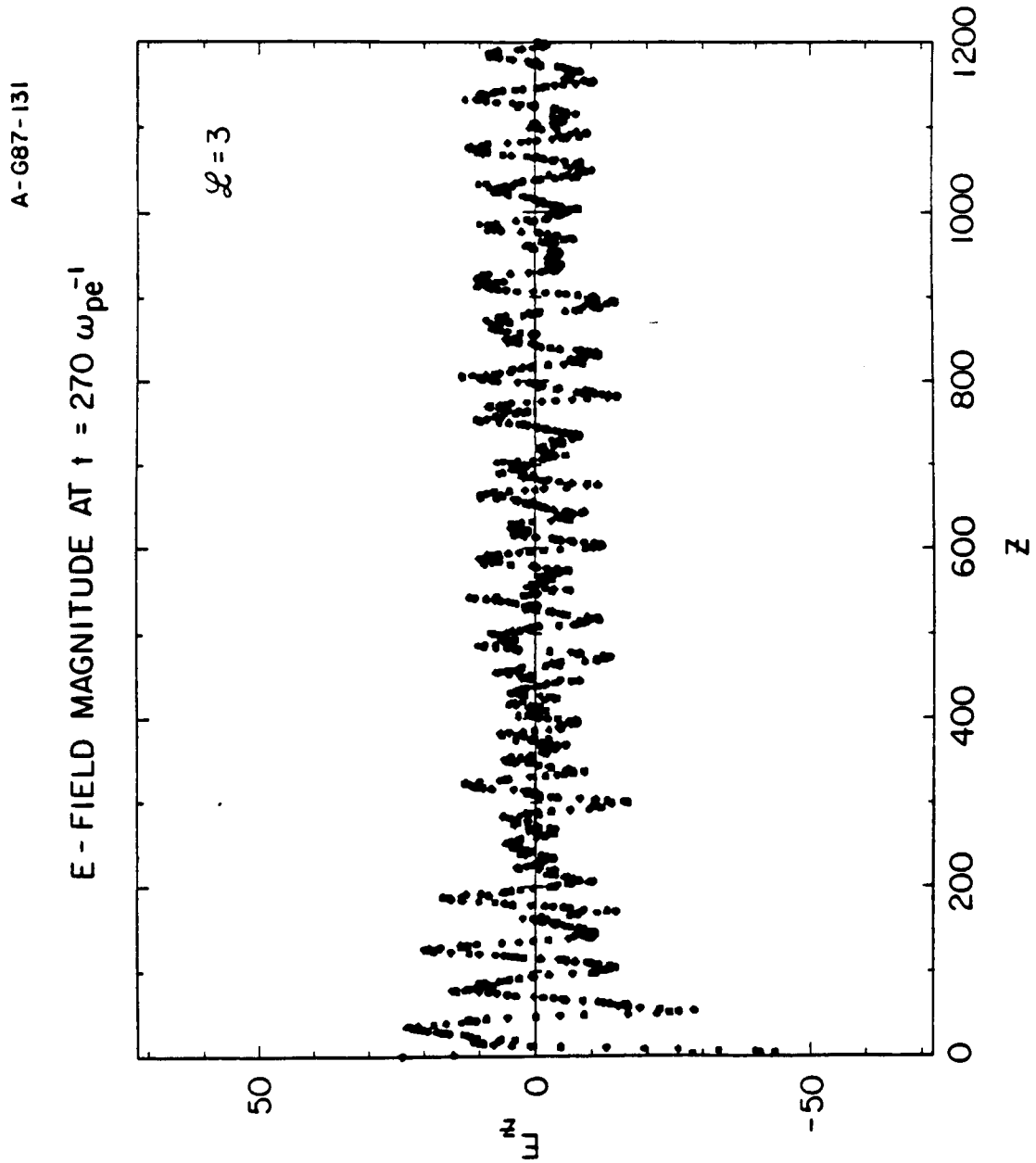
A-G87-131
E - FIELD MAGNITUDE AT t = 270 ω_{pe}^{-1}
$\mathscr{L}$ = 3
E_z
50
0
-50
0
200
400
600
800
1000
1200
z

Figure 24 This figure displays the number of electrons, N, versus z from the modeled beam run with L = 3.

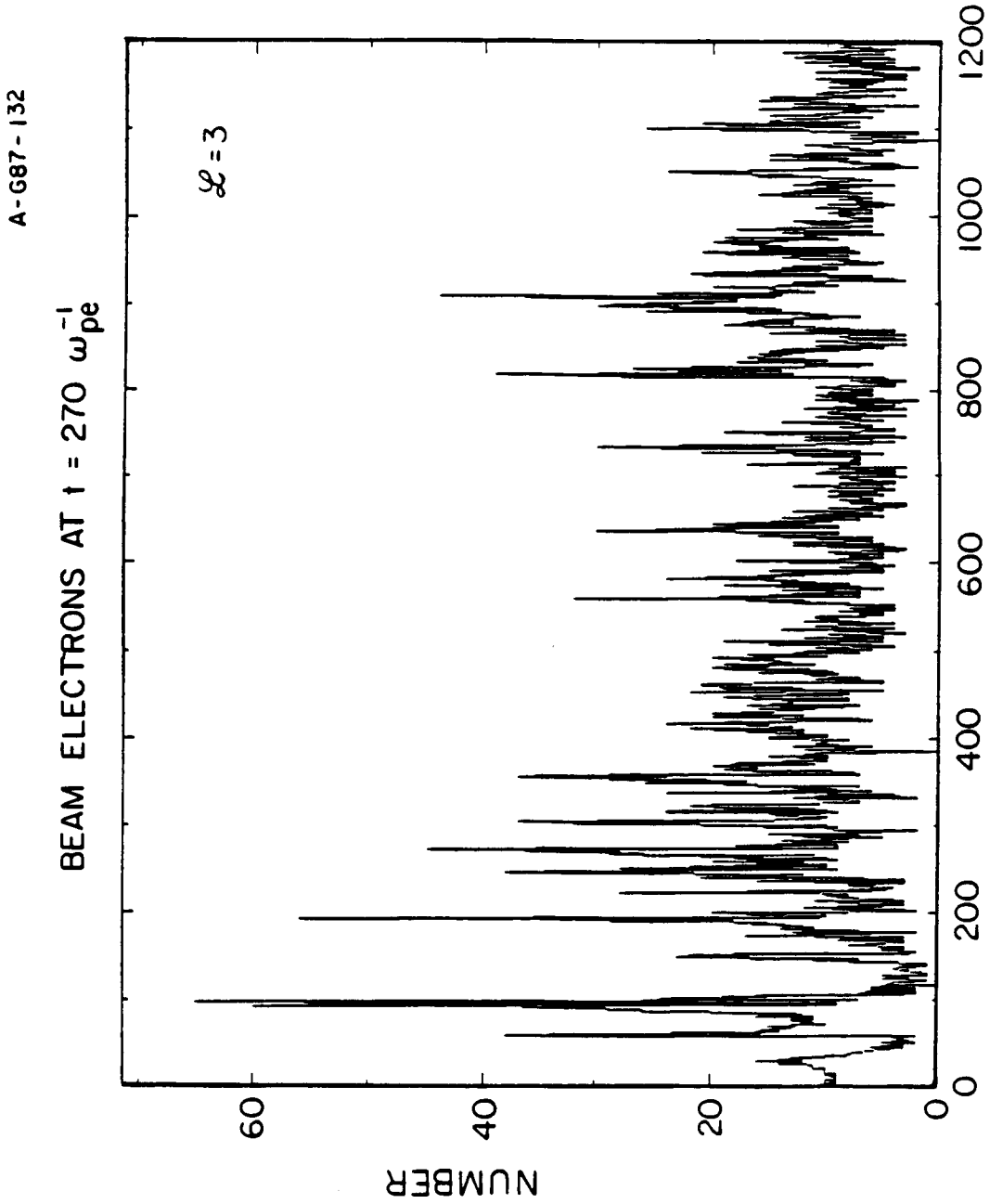
A-687-132
BEAM ELECTRONS AT t = 270 ω_{pe}^{-1}
$\mathcal{L}$=3
NUMBER
0
20
40
60
0
200
400
600
800
1000
1200
z

Figure 25 This figure is a V_z versus z phase-space configuration of the modeled SL-2 electron beam obtained from the one-dimensional simulation run with the parameters shown in Table 1, with L = 2.

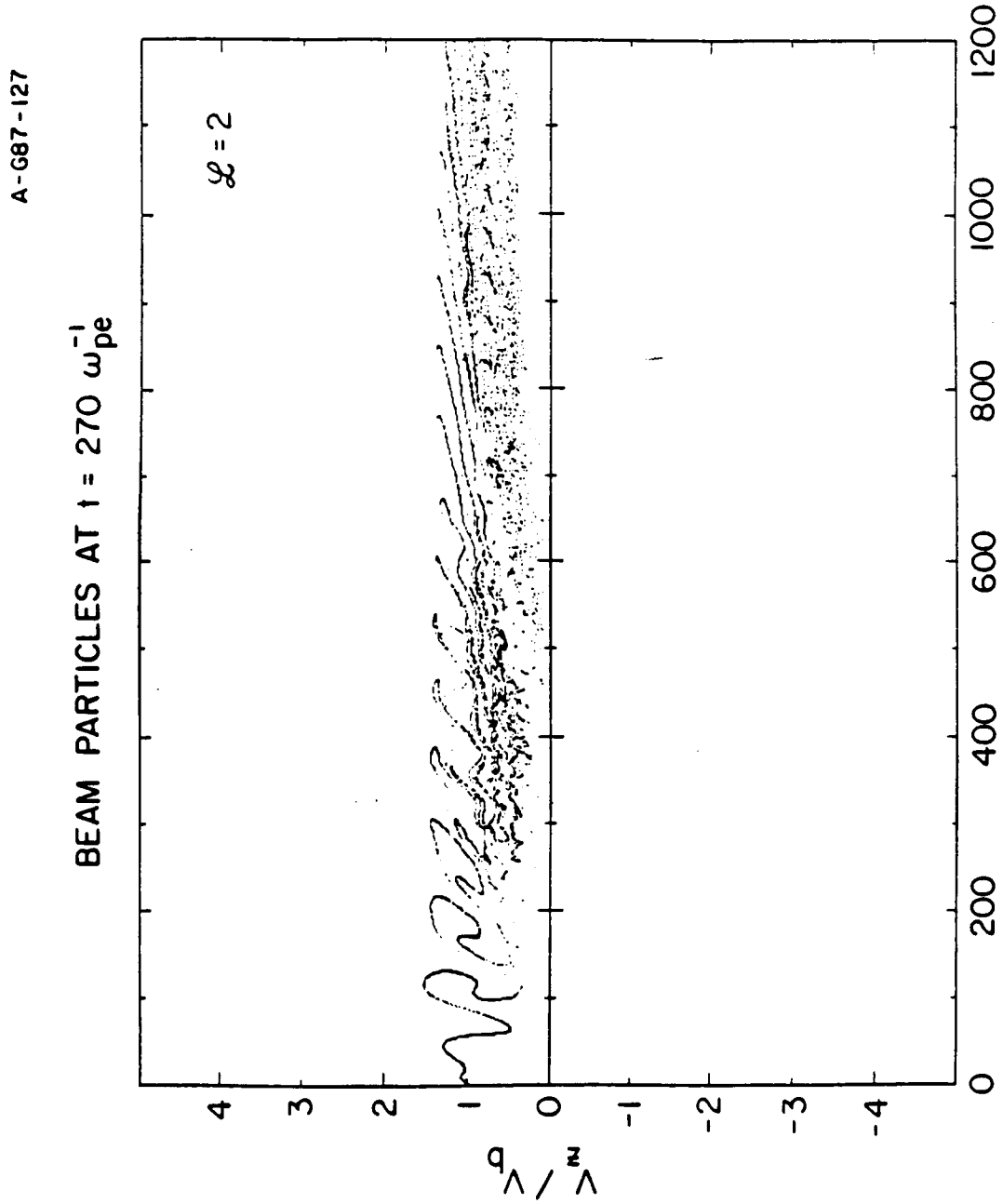
A-G87-127
BEAM PARTICLES AT t = 270 ω_{pe}^{-1}
$\mathscr{L} = 2$
v_z / v_b
z
4
3
2
1
0
-1
-2
-3
-4
0
200
400
600
800
1000
1200

Figure 26 This figure displays E_z versus z from the one-dimensional simulation run with L = 2. Note that wave activity is present in the beam.

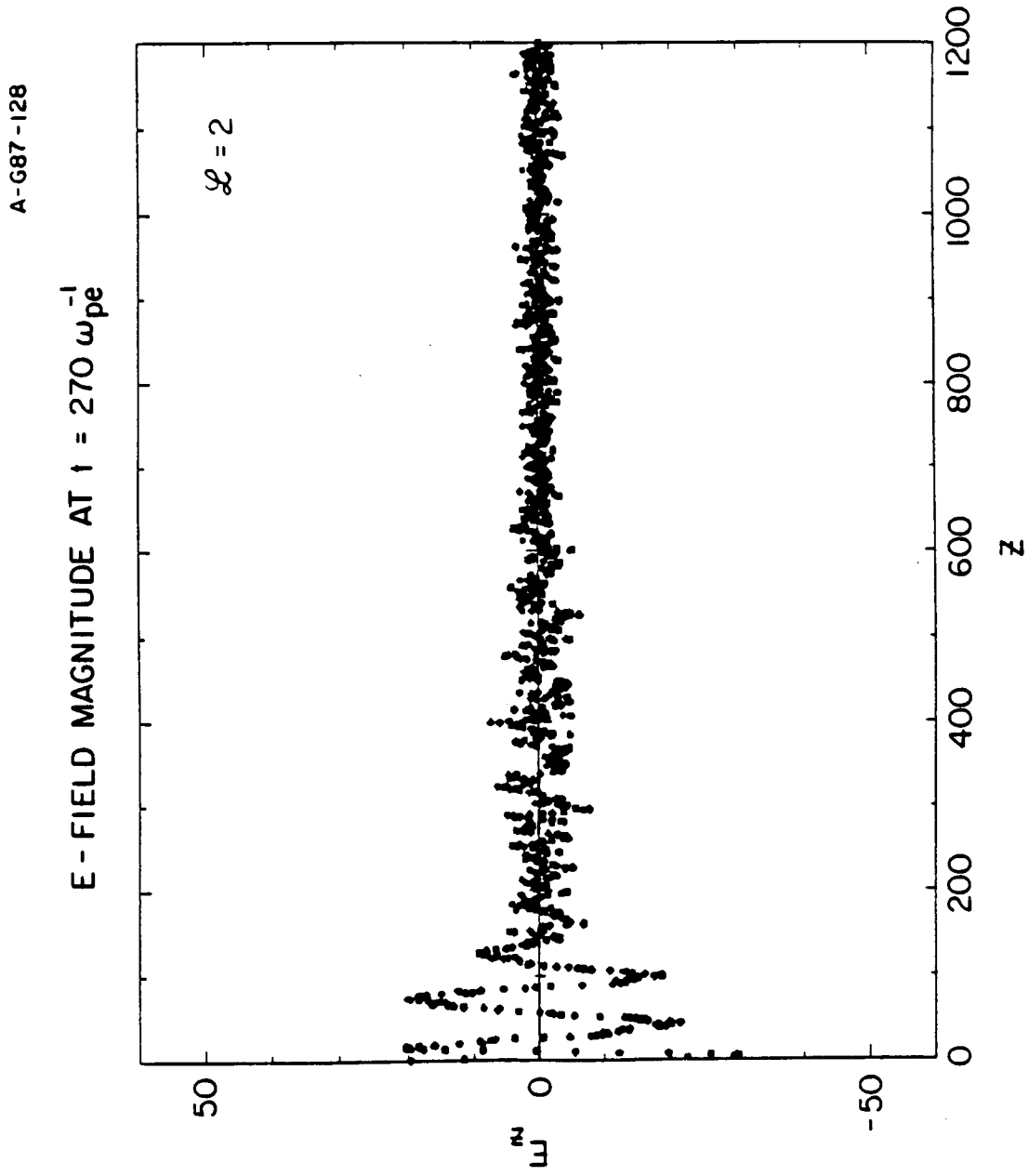
A-G87-128
E - FIELD MAGNITUDE AT t = 270 ω_{pe}^{-1}
$\mathscr{L} = 2$
E_z
50
0
-50
0
200
400
600
800
1000
1200
z

Figure 27 This figure displays the number of electrons, N, versus z from the modeled beam run with L = 2.

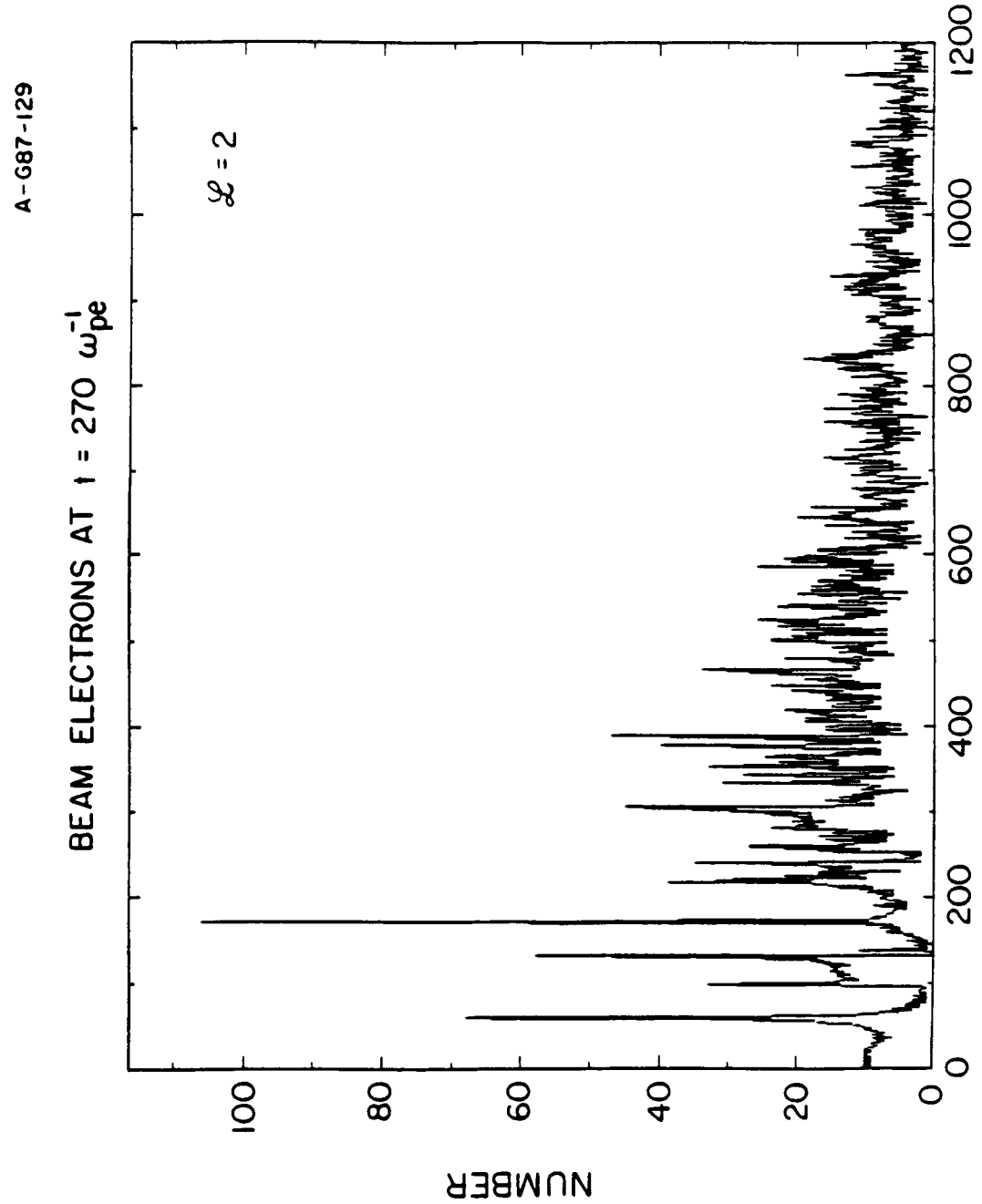
A-G87-129
BEAM ELECTRONS AT t = 270 ω_{pe}^{-1}
$\mathscr{L} = 2$
NUMBER
Z
0
20
40
60
80
100
0
200
400
600
800
1000
1200

Figure 28 This figure is a V_z versus z phase-space configuration of the modeled SL-2 electron beam obtained from the one-dimensional simulation run with L = 3 and a length of 3600 grids corresponding to 180 meters. Note that the beam phase-space configuration is similar to that shown in Figure 22 for a 60-meter beam segment.

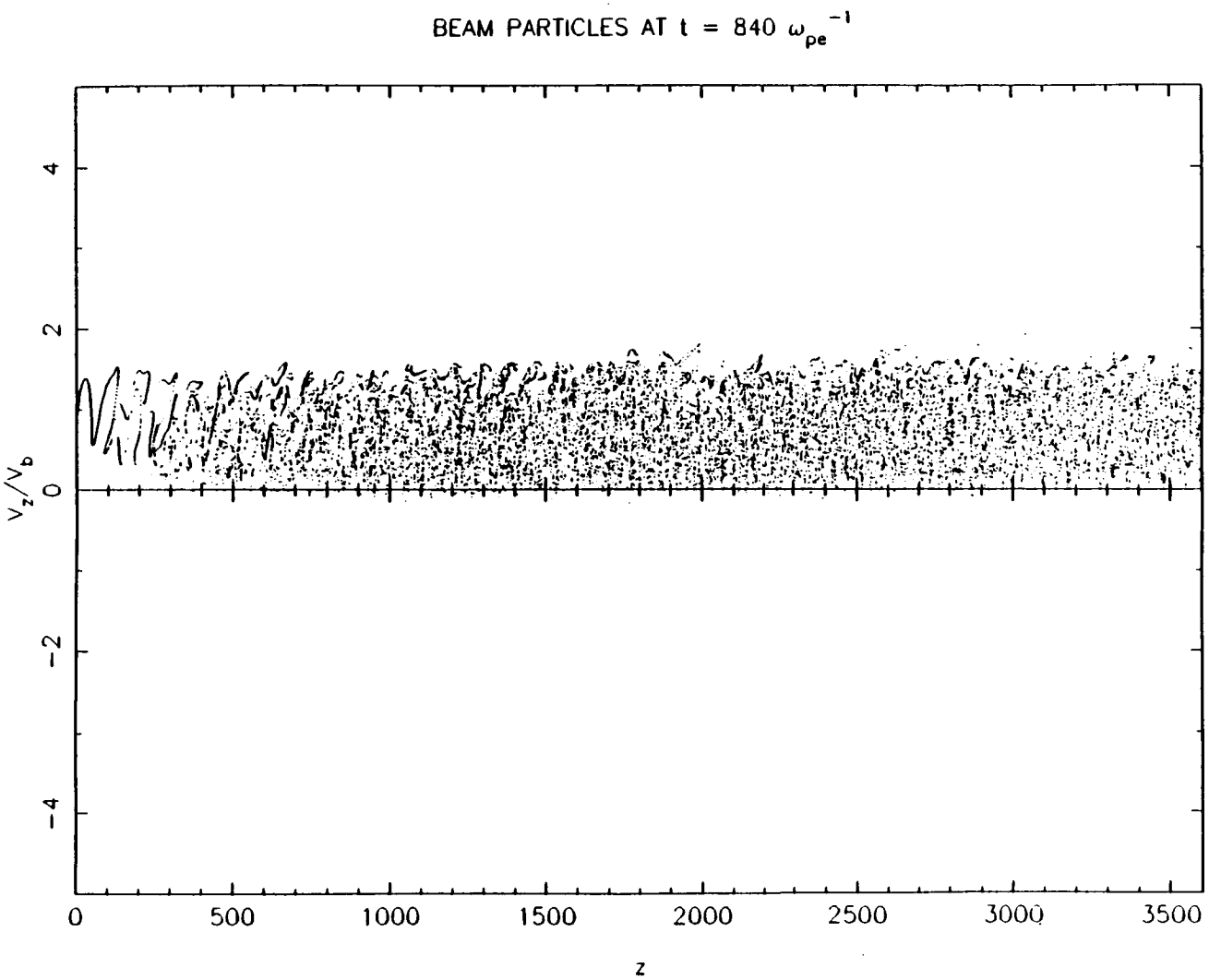
BEAM PARTICLES AT t = 840 ω_{pe}^{-1}
v_z/v_b
4
2
0
−2
−4
0
500
1000
1500
2000
2500
3000
3500
z

Figure 29 This diagram is a plot of $J_z(k_z,\omega)$ as a function of ω and k_z for the 175-meter beam segment. The largest values of $J_z(k_z,\omega)$ are completely dark, while o's and .'s represent continually lower intensities. Note that the values of $J_z(k_z,\omega)$ peaks at about $\omega/k_z = 2.8 \times 10^7$ m/s.

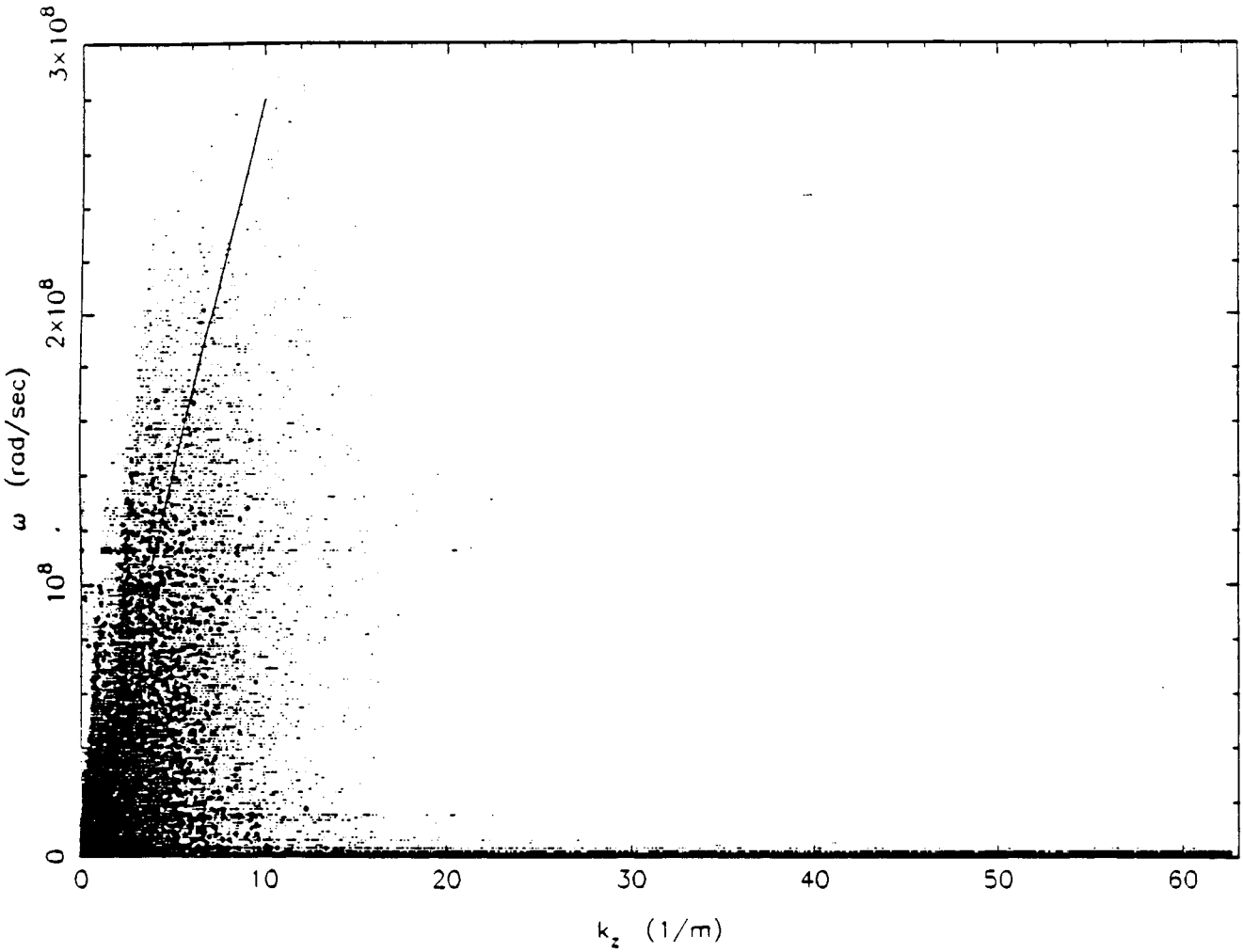
3×10^8
2×10^8
10^8
0
ω (rad/sec)
0
10
20
30
40
50
60
k_z (1/m)

Figure 30 This figure shows the variation of $J_z(k_z)$ for the 175 meter beam segment as a function of k_z. Note for k_z < 22 that $J_z(k_z)$ increases as k_z decreases. This variation in $J_z(k_z)$ results from the density perturbations in the beam created by a beam-plasma instability. Also shown in the figure is the simulation noise level. This noise is obtained since simulation electrons many times the mass and charge of real electrons were used in the computer model. The range of k_z' of the whistler-mode waves is also shown in the figure.

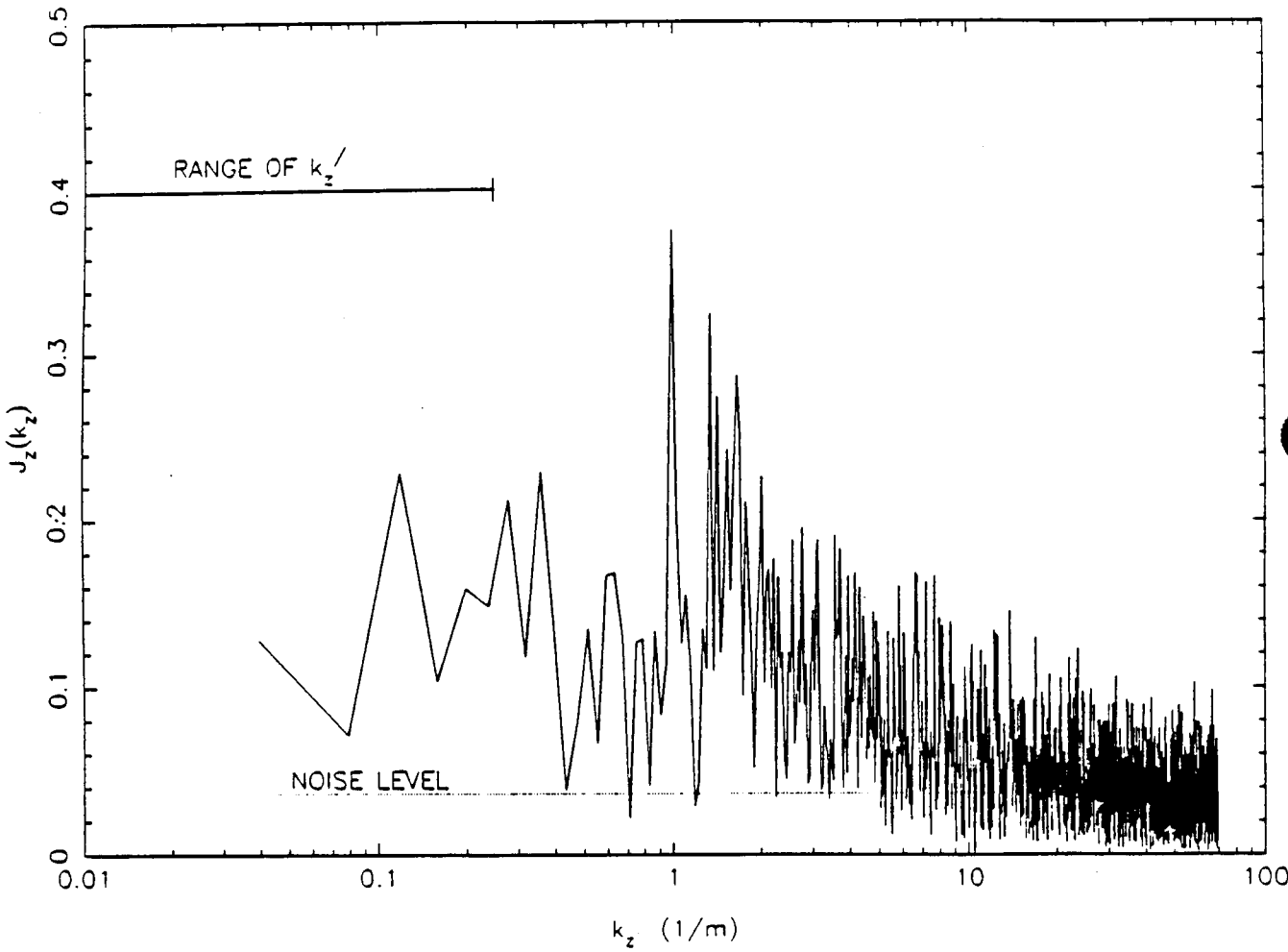
RANGE OF k_z'
NOISE LEVEL
$J_z(k_z)$
0
0.1
0.2
0.3
0.4
0.5
0.01
0.1
1
10
100
k_z (1/m)

Figure 31 This figure shows the power spectra of the measured whistler-mode radiation from the first 200 meters of the SL-2 electron beam along with the calculated power spectra of the incoherent and coherent Cerenkov radiation from a 200-meter beam segment. Note that the inclusion of coherent radiation effects increases the calculated powers to those measured from the SL-2 electron beam. Based on these results, it is concluded that coherent Cerenkov radiation from a bunched electron beam generates the detected whistler-mode radiation.

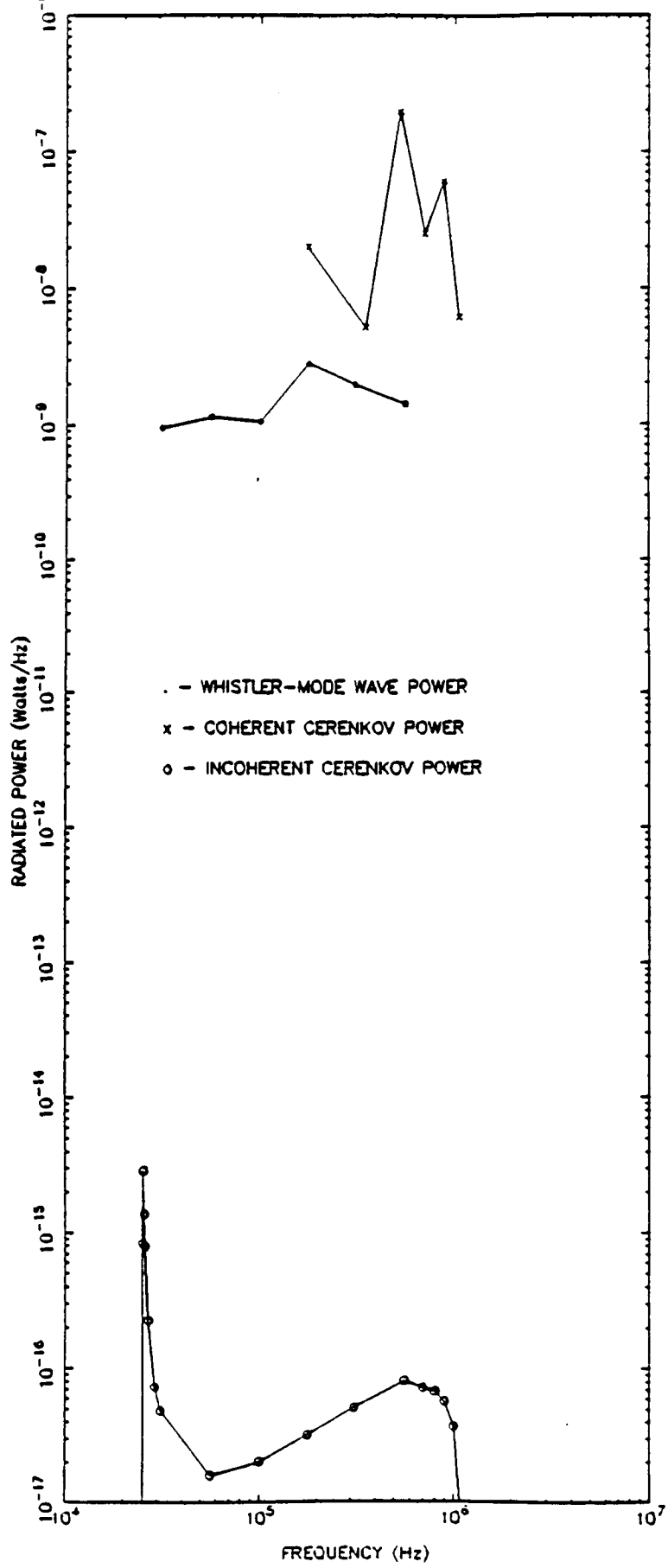
RADIATED POWER (Watts/Hz)
FREQUENCY (Hz)
. – WHISTLER-MODE WAVE POWER
x – COHERENT CERENKOV POWER
o – INCOHERENT CERENKOV POWER

APPENDIX

A general formula for the radiated power from a field-aligned beam of current density $J_z(z)$ has been derived by C. K. Goertz. From this very general formalism, the radiated power from a single particle, N particles and a pulsed beam can be easily obtained.

First, the current density is written as

$$\overline{J}_q(\overline{r},t) = \hat{z} \langle nev \rangle_z \delta(x)\delta(y) = \hat{z}\, J_z(z,t)\, \delta(x)\delta(y) \qquad (A-1)$$

where $J_z(z)$ is the field-aligned component of the current density. The Fourier transform of the current can be written as

$$\overline{J}_q(\overline{k},\omega) = \frac{\hat{z}}{(2\pi)^4} \iint J_z(z,t)\, e^{i(k_z z-\omega t)} dzdt \quad . \qquad (A-2)$$

In order to calculate the radiated power from a group of charges, a transformation must be made to a frame of reference moving with the charges. In this frame, the current density becomes independent of time:

$$J_z(z,t) = J_z(z') \quad .$$

And, consequently, the current density appears stationary. The new coordinate z' is defined as $z' = z - V_s t$, where V_s represents the velocity of this moving frame. Expression (A-2) is then

$$\bar{J}_q(\bar{k},\omega) = \frac{\hat{z}}{(2\pi)^4} \int_{-\infty}^{\infty} J_z(z')\, e^{ik_z z'}\, dz' \int_{-\infty}^{\infty} e^{i(k_z V_s - \omega)t} dt \,. \qquad \text{(A-3)}$$

The quantity $\int_{-\infty}^{\infty} J_z(z')\, e^{ik_z z'} dz' = \sqrt{2\pi}\, J_z(k_z)$ where $J_z(k_z)$ is the Fourier transform of J(z'). Using the definition of the delta function, $\int_{-\infty}^{\infty} e^{i(k_z V_s - \omega)t} dt = 2\pi\, \delta(k_z V_s - \omega)$, and using the fact that $k_z = \frac{n\omega}{c}\cos\theta$, (A-3) now becomes

$$\bar{J}_q(\bar{k},\omega) = \frac{\hat{z}}{(2\pi)^3} (\sqrt{2\pi}\, J_z(k_z))\, \delta(n\omega \cos\theta\beta - \omega) \qquad \text{(A-4)}$$

where $\beta = V_s/c$.

Using Equation (4-6), the electric field is written as

$$\bar{E}(\bar{r},t) = \frac{i}{(2\pi)^3 \varepsilon_o} \iint (\bar{\bar{T}}^{-1} \cdot \hat{z})\, (\sqrt{2\pi}\, J_z(k_z))$$

$$\delta(n\omega\cos\theta\beta - \omega) e^{i(\omega t - \bar{k}\cdot\bar{r})} d\bar{k}\, \frac{d\omega}{\omega} \qquad \text{(A-5)}$$

Knowing the electric field and source current, an expression for the radiated power can be obtained:

$$P(t) = \int E(r,t)\cdot J(r,t)\, dr$$

$$= \frac{i}{(2\pi)^3 \varepsilon_o} \iiint (\hat{z}\cdot\bar{\bar{\Gamma}}^{-1}\cdot\hat{z})\ (\sqrt{2\pi}\ J_z(k_z)) \qquad \text{(A-6)}$$

$$\delta(n\omega\cos\ \theta\ \beta - \omega)\ e^{i(\omega t - k_z z)} J_z(z,t) dz\ d\bar{k}\ \frac{d\omega}{\omega}$$

where the current is again described by (A-1). Moving to the frame $z'' = z - V_s t$, (A-6) can be rewritten as

$$P(t) = \frac{i}{(2\pi)^3 \varepsilon_o} \iiint (\hat{z}\cdot\bar{\bar{\Gamma}}^{-1}\cdot\hat{z})\ (\sqrt{2\pi}\ J_z(k_z))$$

$$\delta(n\omega\ \cos\ \theta\ \beta - \omega)\ e^{i(\omega - n\omega\ \cos\ \theta\ \beta)t} \qquad \text{(A-7)}$$

$$[J_z(z'')\ e^{-ik_z z''} dz'']\ d\bar{k}\ \frac{d\omega}{\omega} \quad .$$

The quantity in brackets is equal to $\sqrt{2\pi}\ J_z^*(k_z)$ where $J_z^*(k_z)$ is the conjugate Fourier transform of $J(z'')$. The element $d\bar{k}$ is

$$d\bar{k} = n^2 \frac{\omega^3}{c^3}\, dn\ \sin\ \theta\ d\theta\ d\phi \qquad \text{and}$$

$$k_z = \frac{n\ \cos\ \theta\ \omega}{c} = k_z(n,\theta) \quad .$$

Substituting these into (A-7) and integrating over ϕ yields:

$$P(t) = \frac{i}{(2\pi)^2\varepsilon_o} \iint (\hat{z}\cdot\bar{\bar{T}}^{-1}\cdot\hat{z})\ (2\pi)J_z(k_z(n,\theta))$$

$$J_z^*(k_z(n,\theta))\ \delta(n\omega\cos\theta\,\beta - \omega) \qquad \text{(A-8)}$$

$$e^{i(\omega - n\,\omega\cos\theta\,\beta)t}\, n^2\omega^2 dn\sin\theta\, d\theta\, d\omega \quad .$$

Integrating over θ, an integral of the form

$$I = \int f(x)\ \delta(Ax - B)dx = \frac{f(x_o)}{A}$$

must be solved where $A = |n\ \omega\ \beta|$, $B = \omega$ and $x_o = \cos\theta_o = \frac{1}{n\beta}$. The radiated power then becomes

$$P(t) = \frac{-i}{(2\pi)^2\varepsilon_o c^3\beta} \iint (\hat{z}\cdot\bar{\bar{T}}^{-1}\cdot\hat{z})\ (2\pi)J_z(k_z(n,\theta_o)) \qquad \text{(A-9)}$$

$$J_z^*(k_z(n,\theta_o))\ |n|\ |\omega|\ dn\ d\omega \quad .$$

An explicit form for $(\hat{z}\cdot\bar{\bar{T}}^{-1}\cdot\hat{z})$ is obtained using Equation (4-34), and upon obtaining the imaginary part to the integral

$$\int_o^\infty \frac{T_{33}(n)\ |n|\ f(n)\ dn}{(n^2-n_1^2)(n^2-n_2^2)} = \frac{\pi i}{2(n_2^2-n_1^2)} \sum_{k=1}^{2} (-1)^k T_{33}(n_k)\ f(n_k)$$

where f(n) is an arbitrary even with no singularities, the radiated power becomes

$$P(t) = \overline{P} = \int_{-\infty}^{\infty} \left(\frac{\omega\, d\omega}{8\pi\, \varepsilon_o \varepsilon_1 c^2 V_s}\right) \frac{1}{(n_2^2 - n_1^2)} \sum_{k=1}^{2} T_{33}(n_k) \times [2\pi\, J_z(k_z(n_k, \theta_o)) J_z^*(k_z(n_k, \theta_o))] \quad . \tag{A-10}$$

Note that the radiated power is proportional to the square of the Fourier transform of the current density. Once the current density and its transform are known, it can be used in Equation (A-10) to easily calculate the radiated power.

As an example, the radiated power from a single field-aligned point charge moving at velocity, V_o, can be calculated. Moving to a frame where the particle is considered stationary, $V_s = V_o$, the current density becomes

$$J_z(z) = q\, V_o \delta(z - z_o),$$

where z_o represents the position of the particle relative to the center of coordinates for the frame moving at V_s. The current density transform becomes

$$J_z(k_z) = \frac{q\, V_o}{\sqrt{2\pi}} \int_{-\infty}^{\infty} \delta(z - z_o) e^{ik_z z} dz = q\, V_o \frac{e^{i \frac{n\omega}{c} \cos\theta\, z_o}}{\sqrt{2\pi}}$$

where $kz = \frac{n\omega}{c} \cos\theta$. Using Equation (A-4), $\underline{J}_q(\underline{k},\omega)$ is

$$\overline{J}_q(\overline{k},\omega) = \hat{z}\,\frac{q\,V_o}{(2\pi)^3}\,e^{i\,\frac{n\omega}{c}\cos\theta\,z_o}\,\delta(n\omega\cos\theta\,\beta - \omega)$$

and is identical to (4-13). Since $J_z(k_z)\,J_z^*(k_z) = 1/2\pi$, the radiated power is

$$P = \int_{-\infty}^{\infty} \left(\frac{q^2\omega d\omega}{8\pi\epsilon_o\epsilon_1}\right)\left(\frac{V_o}{c^2}\right)\frac{1}{(n_2^2-n_1^2)}\sum_{k=1}^{2} T_{33}(n_k)$$

which is identical to (4-22).

The power radiated from N point charges all moving at velocity V_o, but located at arbitrary positions along a field line can also be calculated. Again, $V_s = V_o$, however, the current density is now

$$J_z(z) = q\,V_o\sum_{i=1}^{N}\delta(z - z_i) \quad ,$$

where z_i is the particle position relative to the center of coordinates of the frame moving with V_s. The transform becomes

$$J_z(k_z) = \sum_{i=1}^{N}\frac{q\,V_o}{\sqrt{2\pi}}\int_{-\infty}^{\infty}\delta(z - z_i)e^{ik_z z}dz$$

$$= \frac{q\ V_o}{\sqrt{2\pi}} \sum_{i=1}^{N} e^{ik_z z_i} = \frac{q\ V_o}{\sqrt{2\pi}} \sum_{i=1}^{N} e^{i \frac{n\ \omega}{c} \cos\ \theta\ z_i}$$

and

$$J_z^*(k_z) = \frac{q\ V_o}{\sqrt{2\pi}} \sum_{j=1}^{N} \frac{e^{-i \frac{n\ \omega}{c} \cos\ \theta\ z_j}}{\sqrt{2\pi}} \quad .$$

The quantity

$$J_z(k_z)\ J_z^*(k_z) = \frac{q\ V_o}{2\pi} \sum_{i=1}^{N} \sum_{j=1}^{N} e^{i \frac{n\ \omega}{c} \cos\ \theta(z_i - z_j)} \quad .$$

Inserting this into Equation (A-10) yields a result identical to that of (4-37) for $\beta_i = \beta_j$ ($V_{io} = V_{jo}$).

A surprising result is obtained for the radiated power if the beam density is completely uniform. In this case, the particles are moving at velocity, V_o; thus, $V_s = V_o$. The current density is

$$J_z(z) = q\ V_o \frac{N}{L} = q\ V_o \lambda_o \quad .$$

The transform is then

$$J_z(k_z) = q\ V_o \lambda_o \int_{-\infty}^{\infty} e^{ik_z z}\ dz = q\ V_o \lambda_o \delta(k_z) = q\ V_o \lambda_o \delta\left(\frac{n\ \omega}{c} \cos\ \theta\right)$$

and $J_z^*(k_z) = q\ V_o \lambda_o \delta(\frac{n\ \omega}{c} \cos\ \theta)$. After substituting these into (A-10), it is found that radiation only at $\omega = 0$ is possible and consequently the radiated power is zero. Therefore, an unperturbed, uniform beam moving at velocity V_o along a magnetic field will not radiate.

Finally, the power from a pulsed electron beam is considered. Using Equations (74), (76), (77) and (78) from Harker and Banks [1983], the Fourier transform of the field-aligned current is

$$\overline{J}(\overline{k},\omega) = \frac{q\ V_o \hat{z}}{(2\pi)^3}\ \delta(k_z V_o - \omega)\ N\ell\ \text{sinc}\ (\frac{k_z \ell}{2\pi}) \sum_{m=-\infty}^{\infty} e^{imk_z d}$$

where ℓ is the pulse length and d is the distance between pulses. Comparing this with Equation (A-4), $J_z(k_z)$ is obtained:

$$J_z(k_z) = q\ V_o \frac{N\ \ell}{\sqrt{2\pi}}\ \text{sinc}(\frac{k_z \ell}{2\pi}) \sum_{m=-\infty}^{\infty} e^{-imk_z d}$$

and $J_z^*(k_z)$ is

$$J_z^*(k_z) = q\ V_o \frac{N\ \ell}{\sqrt{2\pi}}\ \text{sinc}(\frac{k_z \ell}{2\pi}) \sum_{m=-\infty}^{\infty} e^{imk_z d} \quad .$$

The quantity

$$J_z(k_z)\, J_z^*(k_z) = q^2\, V_o^2\, \frac{N^2 \ell^2}{2\pi}\, \mathrm{sinc}^2\left(\frac{k\ell}{2\pi}\right) \left| \sum_{m=1}^{p} e^{-imk_z d} \right|^2$$

where p is the number of pulses. Since

$$\left| \sum_{m=1}^{p} e^{-imk_z d} \right|^2 = \frac{\sin^2(pdk_z/2)}{\sin^2(dk_z/2)} \quad ,$$

$J_z(k_z)\, J_z^*(k_z)$ is

$$J_z(k_z)\, J_z^*(k_z) = \left[q\, V_o\, \frac{N\, \ell}{\sqrt{2\pi}}\, \mathrm{sinc}\, \left(\frac{k_z \ell}{2\pi}\right) \frac{\sin(pdk_z/2)}{\sin(dk_z/2)}\right]^2 \quad .$$

Inserting this into (A-10) yields an expression for the radiated power similar to Equation (91) of Harker and Banks.

REFERENCES

Banks, P. M., R. I. Bush, W. J. Raitt, Observations of electron beam structure on STS-3 and Spacelab 2 (abstract), EOS Trans. AGU, 66, 1053, 1985.

Beghin, C., J. P. Lebreton, B. N. Maehlum, J. Troim, P. Ingsoy, J. L. Michau, Phenomena induced by charged particle beams, Science, 225, 188-191, 1984.

Bell, T. F., Artificial production of VLF hiss, J. Geophys. Res., 73, 4409-4415, 1968.

Bernstein, W., H. Leinbach, P. J. Kellogg, S. J. Monson, and T. Hallinan, Further laboratory measurements of the beam plasma discharge, J. Geophys. Res., 84, 7271-7277, 1979.

Bush, R. I., T. Neubert, P. M. Banks, W. J. Raitt, D. A. Gurnett, Observations of enhanced plasma wave production during pulsed beam emissions (abstract), EOS Trans. AGU, 67, 1176, 1986.

Cartwright, D. G., and P. J. Kellogg, Observations of radiation from an electron beam artificially injected into the ionosphere, J. Geophys. Res., 79, 1439, 1974.

Dechambre, M., G. A. Gusev, Yu. V. Kushnerevsky, J. Lavergnat, R. Pellat, S. A. Pulinets, V. V. Selegei, I. A. Zhulin, High-frequency waves during the ARAKS experiments, Ann. Geophys., 36, 333-340, 1980a.

Dechambre, M., Yu. V. Kushnerevsky, J. Lavergnat, R. Pellat, S. A. Pulinets, and V. V. Seleger, Waves observed by the ARAKS experiment: The whistler mode, Ann. Geophys., 36, 351-359, 1980b.

Grandal, B. (ed.) Artificial Particle Beams in Space Plasma Studies, Plenum, New York, 1982.

Gurnett, D. A., A satellite study of VLF hiss, J. Geophys. Res., 71, 5599, 1966.

Gurnett, D. A., Electromagnetic plasma wave emissions from the auroral field lines, J. Geomag. Geoelectr., 30, 257-272, 1978.

Gurnett, D. A., and L. A. Frank, VLF hiss and related plasma observations in the polar Magnetosphere, J. Geophys. Res., 77, 172, 1972.

Gurnett, D. A., W. S. Kurth, J. T. Steinberg, P. M. Banks, R. I. Bush, and W. J. Raitt, Whistler-mode radiation from the Spacelab-2 electron beam, Geophys. Res. Lett., 13, 225-228, 1986.

Gurnett, D. A., S. D. Shawhan, and R. R. Shaw, Auroral hiss, Z-mode radiation, and auroral kilometric radiation in the polar magnetosphere: DE-1 observations, J. Geophys. Res., 88, 329-340, 1983.

Harker, K. J. and P. M. Banks, Radiation from pulsed electron beams in space plasmas, Radio Sci., 19, 454-470, 1983.

Hartz, T. R., Radio Noise Levels Within and Above the Ionosphere, Proc. ISEE, 57, 1042, 1969.

Hess, W. N., M. G. Trichel, T. N. Davis, W. C. Beggs, G. E. Kraft, E. Stassinopoulos, and E. J. R. Maier, Artificial auroral experiment: Experiment and principal results, J. Geophys. Res., 76, 6067, 1971.

Inan, U. S., M. Pon, P. M. Banks, P. R. Williamson, W. J. Raitt, and S. D. Shawhan, Modulated beam injection from the space shuttle during magnetic conjunction of STS-3 with the DE-1 satellite, Radio Science, 19, 487, 1984.

James, H. G., VLF observations of auroral beams as sources of a class of emissions, Nature, 224, 351, 1969.

Jones, T. W., and P. J. Kellogg, Plasma waves artificially induced in the ionosphere, J. Geophys. Res., 75, 2166, 1973.

Jorgensen, T. S., Interpretation of auroral hiss measured on OGO-2 and at Byrd Station in terms of incoherent Cerenkov radiation, J. Geophys. Res., 73, 1055, 1968.

Katz, I., G. A. Jongeward, D. E. Parks, D. L. Reasoner, and C. K. Purvis, Energy broadening due to space-charge oscillations in high current electron beams, Geophys. Res. Lett., 13, 64-67, 1986.

Kellogg, P. J., D. G. Cartwright, R. A. Hendrickson, S. J. Monson, and J. R. Winckler, The University of Minnesota electron Echo experiment, Space Res., XVI, 589-599, 1976.

Kellogg, P. J., S. J. Monson, W. Bernstein, and B. A. Whalen, Observations of waves generated by electron beams in the ionosphere, J. Geophys. Res., 91, 12065-12078, 1986.

Laaspere, T., and R. A. Hoffman, New results on the correlation between low-energy electrons and auroral hiss, J. Geophys. Res., 81, 524, 1976.

Lavergnat, J., M. Dechambre, R. Pellat, Yu. V. Kushnerevsky, S. A. Pulinets, Waves observed by the ARAKS experiments: Generalities, Ann. Geophys., 36, 323-332, 1980.

Liemohn, H. B., Radiation from electrons in a magnetoplasma, Radio Sci., 690, 741, 1965.

Lin, C. S., J. L. Burch, S. D. Shawhan, and D. A. Gurnett, Correlation of auroral hiss and upward electron beams near the polar cusp, J. Geophys. Res., 89, 925, 1984.

Maggs, J. E., Coherent generation of VLF hiss, J. Geophys. Res., 81, 1707-1724, 1976.

Mansfield, V. N., Radiation from a charged particle spiraling in a cold magnetoplasma, Astrophy. J., 147, 672, 1967.

Monson, S. J., P. J. Kellogg, and D. G. Cartwright, Whistler-mode plasma waves observed on electron Echo II, J. Geophys. Res., 81, 2193, 1987.

Mosier, S. R., and D. A. Gurnett, VLF measurements of the Poynting flux along the geomagnetic field with Injun 5 satellite, J. Geophys. Res., 74, 5675-5687, 1969.

Mosier, S. R., and D. A. Gurnett, Theory of the Injun 5 very-low-frequency Poynting flux measurements, J. Geophys. Res., 76, 972-977, 1971.

Neubert, T., W. W. L. Taylor, L. R. O. Storey, N. Kawashima, W. T. Roberts, D. L. Reasoner, P. M. Banks, D. A. Gurnett, R. L. Williams, and J. L. Burch, Waves generated during electron beam emissions from the space shuttle, J. Geophys. Res., 91, 11321-11330, 1986.

Pritchett, P. L., and R. M. Winglee, The plasma environment during particle beam injection into space plasmas, 1. Electron Beams, J. Geophys. Res., submitted.

Reeves, G. D., P. M. Banks, R. I. Bush, K. J. Harker, An analysis of the harmonic structure of VLF radiation generated by a square wave modulated electron beam in space (abstract), EOS Trans. AGU, 67, 1176, 1986.

Shawhan, S. D., Description of the Plasma Diagnostics Package (PDP) for the OSS-1 shuttle mission and JSC chamber test in conjunction with the Fast Pulsed Electron Gun (FPEG), Artificial Particle Beams in Space Plasma Studies, ed. by B. Grandel, Plenum, NY, pp. 419-430, 1982.

Shawhan, S. D., G. B. Murphy, P. M. Banks, P. R. Williamson, and W. J. Raitt, Wave emissions from D. C. and modulated electron beams on STS-3, Radio Science, 19, No. 2, 471-486, 1984.

Smith, R. L., VLF observations of auroral beams as sources of a class of emissions, Nature, 224, 351, 1969.

Stix, T. H., The Theory of Plasma Waves, McGraw-Hill, New York, 1962.

Taylor, W. W. L., and S. D. Shawhan, A test of incoherent Cerenkov radiation for VLF hiss and other magnetospheric emissions, J. Geophys. Res., 79, 105-117, 1974.

Wilhelm, K., W. Bernstein, B. A. Whalen, Study of electric fields parallel to magnetic lines of force using artificially injected energetic electrons, Geophys. Res. Lett., 7, 117, 1980.

Williamson, P. R., J. G. Hawkins, R. I. Bush, P. M. Banks, W. J. Raitt, Vehicle charging measured during electron beam emission on Spacelab-2 (abstract), EOS Trans. AGU, 66, 1051, 1985.

Winglee, R. M., and P. L. Pritchett, Space-charge effects during the injection of dense electron beams into space plasmas, J. Geophys. Res., submitted.

Winkler, J. R., The application of artificial electron beams to magnetospheric research, Rev. Geophys. Res. and Space Phys., 18, No. 3, 659-682, 1980.

Winkler, J. R., K. N. Erickson, P. R. Malcolm, A new experiment to investigate the conjugate echoes and plasma physics phenomena produced by an electron beam injected in the ionosphere--Echo 7 (abstract), EOS Trans. AGU, 67, 1180, 1986.

THE LARGE SCALE WAKE STRUCTURE OF THE SHUTTLE ORBITER: PLASMA DENSITY, TEMPERATURE, AND TURBULENCE

by

Alan C. Tribble

A thesis submitted in partial fulfillment
of the requirements for the Doctor of
Philosophy degree in Physics
in the Graduate College of
The University of Iowa

May 1988

Thesis supervisor: Professor Nicola D'Angelo

Graduate College
The University of Iowa
Iowa City, Iowa

CERTIFICATE OF APPROVAL

PH.D. THESIS

This is to certify that the Ph.D. thesis of

Alan C. Tribble

has been approved by the Examining Committee for the thesis requirement for the Doctor of Philosophy degree in Physics at the May 1988 graduation.

Thesis committee: Michael D'Angelo
Thesis supervisor

David R. Alan
Member

Kyle Eberg
Member

Dan Schmidt
Member

Robert F. Merlino
Member

ACKNOWLEDGEMENTS

There are a number of people who deserve special recognition and thanks for their help in the preparation of this manuscript. First and foremost I must express my gratitude to my advisor, Nicola D'Angelo, for his insight into many of the problems that were encountered and for his helpful critiques of the resulting presentations. At the same time I cannot underestimate the assistance rendered to me by Gerald Murphy and Jolene Pickett. Being able to rely upon their experience with the Langmuir probe made this job much easier. The other members of my committee, Dr.'s Andersen, Gurnett, Longrenn, and Merlino, all warrant acknowledgement for their comments and advice.

In addition to those just mentioned I also owe my gratitude to Alice Shank, for help with the word processing program, and to John Birkbeck for drafting the numerous figures used in this dissertation. Lastly, I thank my fiancee, Beth Gunion, for her patience and support during the many months it took to finish the research presented here. Maybe I will get to return the favor some day.

This work was supported by grant NAG3-449 from the NASA Lewis Research Center, contract NAS8-32807 from the NASA Marshall Space Flight Center, and grant NGT-50402 from NASA headquarters.

ABSTRACT

The large scale plasma wake structure of the shuttle orbiter is studied using a Langmuir probe on a smaller ionospheric satellite. This satellite, the University of Iowa's Plasma Diagnostics Package (PDP), was flown on shuttle mission STS-51F from 29 July to 6 August 1985. The PDP was carried in the shuttle's payload bay, but during certain times throughout the mission it was placed on the arm of the shuttle, the Remote Manipulator System (RMS), or ejected as a free-flying satellite, so that both the near and far wake of the orbiter could be studied. The resulting data on the electron temperature, electron density, and fluctuations in the electron density in the orbiters wake provide the first in situ observations of the large scale wake of the orbiter. The density profile suggests the possibility of converging ion streams in the orbiters wake and the temperature profile indicates enhanced electron temperatures at distances as great as 250 m downstream from the orbiter. The region of density depletion and temperature enhancement are bounded by the orbiter's Mach cone. The turbulence data indicates an enhancement of about 10 dB on the order of the ion plasma frequency along the Mach cone with no appreciable increase in turbulence detected directly on the wake axis.

TABLE OF CONTENTS

LIST OF TABLES

LIST OF FIGURES

CHAPTER I

INTRODUCTION

The phenomena involved in the expansion of a plasma into a vacuum are of fundamental importance to many areas of plasma physics. This expansion process is qualitatively similar to many naturally occurring processes in the solar system, as well as certain processes in laser fusion. The distribution of charged particles and electric fields in the wake of an object moving supersonically in a plasma is an example of the expansion of a plasma into a void (vacuum) or into a more tenuous plasma. One specific problem of particular interest is the structure of the wake of a satellite as it moves through the Earth's ionosphere. Here the interaction takes place in a flow regime that is both supersonic and sub-Alfvenic. This suggests application to the motion of natural satellites, such as Io and Titan, orbiting their parent planets in the outer solar system. As listed by Martin [1], the interaction of the plasma with the satellite is important in that:

1. The charged particles will contribute to the drag of the body as it moves through the plasma.
2. The disturbance produced by the body must be know if diagnostic and measuring instruments are to be placed on board a vehicle.

3. The redistribution of charged particles and the potentials and screening sheaths will have an effect upon any radio-frequency antennae, aerials, and probes which are mounted on the vehicle.
4. The disturbed wake of the body will be of interest to radar detection and tracking applications.
5. The design of shields for protection against high energy particles, and their radiation, will have to take the disturbed conditions into account.
6. The excitation of plasma waves and other propagating disturbances will be influenced by the changes caused by the vehicle.

Some in situ observational attempts have been made to study these interactions, Samir and Wrenn [2], Samir and Willmore [3], Henderson and Samir [4], however, as reported by Samir [5], and Stone and Samir [6] the available in situ data is meager, fragmentary and applicable only to the very near wake zone.

The object of this dissertation is to obtain a better understanding of the physical processes responsible for the phenomena that are associated with the plasma wake of a large object, in this case the shuttle orbiter. This will be accomplished by examining data collected by a Langmuir probe on The University of Iowa's Plasma Diagnostics Package (PDP). From 30 July to 6 August 1985 the PDP was flown as part of the Spacelab-2 payload on space shuttle flight STS-51F. During this time the shuttle orbiter executed a series of maneuvers designed to allow the PDP to make extensive studies of plasma parameters in both the near and far wake zones. This was the first study of its kind and has produced the only in situ data on the mid and far orbiter wake that is available at this time.

We should note that the Spacelab-2 mission was actually the second shuttle flight for the PDP. The PDP was first flown on the STS-3 mission as part of the first Office of Space Sciences (OSS) payload in March of 1982. That mission yielded some of the first measurements of plasma parameters near the shuttle orbiter, Murphy et al. [7] and Raitt et al. [8]. The OSS-1 mission provided investigators with a general idea of what conditions were like in the vicinity of the orbiter and led to a much more comprehensive study of the orbiters wake during the Spacelab-2 mission.

This dissertation will begin with a review of plasma wakes, Chapter II. The object of this review is two-fold. It will afford us with an idea of the type of phenomena we can expect to see in the wake of an object, such as the shuttle orbiter, and it will also indicate the areas where this study can be expected to make significant contributions. Chapter III will describe the experimental wake studies conducted during Spacelab-2, Chapter's IV and V will present the data, and Chapter VI will summarize our results.

CHAPTER II

REVIEW OF PLASMA WAKES

An Obstacle in a Plasma

When an obstacle is placed in a plasma it will be subjected to a current due to the electrons and ions that are striking it. If there is an imbalance between the electron current and the ion current the obstacle will begin to charge. This charging will continue until the obstacle reaches an electrical potential that will cause the ion flux to balance the electron flux. When this occurs the obstacle is said to be charged to the floating potential, ϕ_{fl}. The equation that describes this is

$$I_{ion} - I_{electron} = 0, \tag{1}$$

where I_{ion} is the sum of the ion currents and $I_{electron}$ is the sum of the electron currents. In the example that follows we will use the word 'ram' to refer to the region within 90^o of the spacecraft velocity vector, while 'wake' will refer to the region within 90^o of the vector antiparallel to the spacecraft velocity vector.

Measurements taken at the altitude of the Spacelab-2 mission, 340 km, indicate a typical electron density given by $n_e = 1 \times 10^{-5}\ cm^{-3}$ and an electron temperature of $T_e = 2500\ K$. This will be examined in more detail in the next chapter. Assuming these to be the nominal values for n_e and T_e and that $n_e \approx n_i$,

$T_e \approx T_i$, as is typical of ionospheric plasmas, we find the ion and electron thermal velocities to be 1.1 km/s and 180 km/s, respectively. Since the velocity of the orbiter, v_o, was 7.7 km/s we are in the regime where $v_{i,th} \ll v_o \ll v_{e,th}$. Under these conditions the ion current to an ionospheric satellite will consist of the ions that are 'rammed' out by the the spacecraft's orbital motion. The equation describing this is

$$I_{i,sc} = A_i e n_i v_o, \tag{2}$$

where A_i is the cross sectional area that is swept out by the spacecraft, n_i is the ambient ion density, and v_o the satellite orbital velocity.

Since the thermal velocity of the electrons is greater than than the orbital velocity of our satellite all surfaces of the satellite will collect electron current, not just the ram side. We assume that the electrons have a Maxwellian velocity distribution given by

$$f_e(v) = n_e \left(\frac{m_e}{2\pi k T_e} \right)^{3/2} exp\left(\frac{-m_e v^2}{2kT_e} \right). \tag{3}$$

The electron current to a satellite at a potential V less than the plasma potential, and measured relative to the plasma potential, consists of those electrons with energies greater than $\mid eV \mid$ that strike the satellite, and is given by

$$I_{e,sc} = A_e e n_e \left(\frac{kT_e}{2\pi m_e} \right)^{1/2} exp\left(\frac{eV}{kT_e} \right), \tag{4}$$

where A_e is the surface area of the satellite, T_e is the electron temperature, k is Boltzmann's constant, n_e is the electron density, and m_e is the electron mass. Combining equations (2), (4), and (1) we find that the floating potential is given by

$$\phi_{fl} = \frac{kT_e}{e} ln \left(\frac{A_i e n_i v_o}{A_e e n_e \left(\frac{kT_e}{2\pi m_e} \right)^{1/2}} \right). \tag{5}$$

The value of the floating potential that we would calculate from this equation for the PDP is -0.86 volts, Tribble et al. [9]. This derivation has ignored the possibility of photoemission of electrons and a number of other factors that may add small corrections to equation (5). These corrections, which are not expected to have an impact on measurements to be presented in this dissertation, are adequately discussed by Kasha [10].

The potential on the body, ϕ_{fl}, is one of two parameters that play an important role in the formation of a plasma wake. The second parameter is known as the space charge field. The space charge field is the electric field that arises because of the differing thermal velocities of the ions and electrons. Since we are in a regime where $v_{i,th} \ll v_o \ll v_{e,th}$ the electrons will be able to fill in the wake of our obstacle quite easily. The ions, having much slower thermal speeds, will not be able to reach the area in the very near wake of the obstacle and a charge separation will result giving rise to the space charge field. The relative abundance of electrons in the near wake of the satellite will be responsible for causing that region to be a region of negative potential. This negative potential

will then act as a barrier to additional electrons and the near wake of the satellite will be characterized by an unequal depletion of both ions and electrons, Samir, Maier, and Troy [11].

It is appropriate to mention that electron temperature enhancements are usually observed in these regions of negative potential. Samir and Wrenn [12], Illiano and Storey [13], and Troy, Maier, and Samir [14] report that these enhancements are typically on the order of 50 -100%, but can sometimes be higher. Samir, Brace, and Brinton [15] report that the magnitude of the enhancement is dependent upon the size of the object and the ambient temperature but not upon the plasma density. Morgan, Chan, and Allen [16] report that the enhancment depends on the ratio of the ion energy to the electrical potential energy of the object. The mechanism for production of this temperature enhancement is not agreed upon in the literature. Two explanations have been offered to account for this effect. One is that a wave-particle interaction may take place in the potential well behind the object. This interaction may apply a filtering mechanism to the electrons that leave the well and result in a population of hotter electrons close to the spacecraft. Alternatively, one may infer the possibility of a heating mechanism related to stream interactions and/or instabilities correlated with plasma oscillations in the near wake, Samir and Wrenn [12].

A simple sketch of the wake, as depicted by Fournier and Pigache [17] and Martin [1], is seen in Figure 1. Because of the electric field due to the body potential, ions passing near the body will be deflected towards the wake axis. These deflected ions may produce an ion density peak in the wake. The

location of the peak, z_{near}, and the deflection angle, θ_D, are both dependent upon the body potential, ϕ_{fl}. Several investigations into the properties and dependencies of these ion density peaks have been carried out. Worthy of special note are the studies by Taylor [18,19], Skvortsov and Nosachev [20,21], Schmitt [22], Bogaschenko et al. [23], Stone, Oran, and Samir [24], and Merlino and D'Angelo [25], in addition to those previously mentioned.

After the ion streams pass the edge of the body they will continue to be accelerated by the space charge field. The transverse velocity acquired by these ions is on the order of the ion acoustic speed. In the far wake of the object we may detect a wave-like disturbance propagating at about the Mach angle $\theta_m = \sin^{-1}(1/M)$. It can easily be seen that this transverse ion acceleration is similar to the process of plasma expansion into a vacuum, which is the subject of the next section.

Plasma Expansion into a Vacuum

Consider a semi-infinite plasma confined to the region $x \leq 0$ at t = 0, Figure 2 a). If the plasma is allowed to expand into the vacuum, the region $x > 0$, how will the density and velocity distribution evolve? As the expansion begins the electrons will enter the vacuum first, because of their higher thermal velocities. This is the charge separation mentioned earlier. The space charge field will accelerate the ions and an 'expansion front' will move into the vacuum. To compensate for this a region of decreased plasma density, a 'rarefaction wave', will move into the ambient plasma. The ion acceleration has been studied by

Gurevich, Pariĭskaya, and Pitaevskiĭ [26], who report that it is the ions nearest the interface that will attain the highest velocities. Since the rarefaction wave is the result of ion motion it can be expected to travel at the ion acoustic velocity.

A numerical simulation by Singh et al. [27] reports that this plasma expansion can account for the electron temperature enhancements mentioned earlier. The picture they present is that as the ambient plasma expands into the vacuum it is the electrons with highest thermal velocities that arrive in the vacuum first. Then, as time elapses progressively slower electrons will stream into the void. The electric potential in the void will grow more negative as the electrons fill in the region. This negative potential slows down the electrons that have yet to arrive. As a result, electrons that are already in the region of negative potential, the electrons in the tail of the original Maxwellian distribution, will account for the majority of electrons seen there. Consequently, we will detect a warm electron population with a thermal spread in the velocity distribution about a factor of 2 larger than the thermal spread in the ambient plasma.

As summarized by Samir, Wright, and Stone [28], the phenomena we may expect to see in the wake of an object in a plasma are as follows:

1. Ions are accelerated to high energies.
2. A rarefaction wave is created which propagates into the ambient plasma.
3. An ion front (shock) moves into the vacuum region.
4. Excitation of instabilities and plasma waves over certain volumes in space take place.

5. Strong (or jump) discontinuities in the plasma occur at the expansion front.

In the next section we will examine how some of the phenomena seen in the wake are dependent upon the plasma and upon the object being studied.

Factors Influencing Wake Phenomena

In order to understand the specific case of a satellite in the ionosphere we need to first understand how the properties associated with a plasma wake are dependent upon both the size and shape of the object and upon the plasma being studied. That is, how do the values of the plasma density and temperature, the satellite floating potential, and the ratio of object size to Debye length affect the wake structure. Let's first examine the effect of body size on wake structure. As reported by Martin [1] the ratio of body size to Debye length plays an important role. In the situation where $R_o < \lambda_D$ the wake will be dominated by the ion deflection effects that are controlled by the potential on the object. If we move to the region where $R_o > \lambda_D$ we find that the body potential loses much of its influence upon the ion trajectories and the wake is controlled mostly by the space charge field. The reason for this is fairly straightforward to understand. Consider a disk 1 cm in diameter in a streaming plasma with a Debye length of 1 cm. Obviously, a sizeable fraction of the ions found in the objects wake must have passed within one Debye length of the object. In contrast, if the disk was 10 m in diameter, then the fraction of ions in its wake that had passed within one Debye length of its edge would be negligible. The shape of the object will

also play an important role in determining wake features. As reported by Oran, Stone, and Samir [29], the cross sectional area is actually more important than the overall size. A highly symmetrical object would be expected to give rise to a highly symmetrical wake with sharp wake features, whereas the converse would be true for an asymmetrical object.

Changing the ratio of T_e/T_i may also have a noticeable effect on some wake features. Könemann [30] reports that in isothermal plasmas no sharp wake features can be expected, because the appropriate waves are heavily damped and other features are smoothed by the thermal motion of the ions. Effects associated with varying the value of the body potential, ϕ_{fl}, have already been discussed.

Summary

We can now summarize some of the results that we would expect to see in the wake of an object like the shuttle orbiter. First, since we are in the realm where $R \gg \lambda_D$ we would not expect to see effects due to deflected streams of ions, as seen in Figure 1. Rather we would expect to see only those effects related to the space charge field, i.e., wake disturbances that propagate outward at the Mach angle. Second, since the ionosphere satisfies the condition $T_i \approx T_e$ we would expect most of the waves in the wake of the orbiter to be heavily damped. Finally, the fact that the orbiter presents a highly asymmetrical cross section to plasma flow indicates that we will not expect any 'sharp' wake features and the regions of density depletion, temperature enhancements, and turbulence would be spatially 'smoothed'.

CHAPTER III

THE EXPERIMENT

Equipment

The data that will be presented in this dissertation was collected by a University of Iowa satellite the Plasma Diagnostics Package (PDP), Figure 3. The PDP was composed of 14 instruments designed to make measurements of magnetic and electric fields, particle distributions, radio waves, plasma composition, as well as plasma density, temperature, and turbulence. In particular, we will be examining data collected by a Langmuir probe on the PDP, which was mounted on one of the PDP's extendable booms. The Langmuir probe consisted of a 3 cm diameter gold-plated sphere and supporting electronics. The probe was used to measure plasma densities from 10^3 to 10^7 electrons/cm^3, plasma temperatures from about 1000 K to 5000 K, and density fluctuations in the frequency range 30 Hz to 178 kHz.

The electronics that control the probe's operation alternate between two different modes, one complete cycle requiring 12.8 seconds. The first is an 11.8 second 'lock' mode. During this time the Langmuir probe is biased at +10 volts, relative to the PDP chassis, and is used to measure electron density fluctuations. The current to the probe is sampled at a rate of 120 Hz. The data is passed through three filters, 1 Hz low pass, 1-6 Hz bandpass, and 6 - 40 Hz bandpass,

with sampling rates of 5 Hz, 20 Hz, and 120 Hz respectively. A fourth filter, 30 Hz high pass, routes the output to a wideband receiver and spectrum analyzer which can look at details of the current fluctuations up to a frequency of 178 kHz.

The 'lock' mode is followed by a 1.0 second 'sweep' mode where the bias voltage on the probe is swept from +10 volts to -5 volts in discrete steps of 0.125 volts and then returned to +10 volts. During the sweep mode the data collected by the Langmuir probe is sent through a 0-50 Hz low pass filter and can be used to determine the electron temperature, electron density, and plasma potential. A derivation of the appropriate equations is given in Appendix A. The data we obtain from the probe therefore consists of one measurement of electron density, temperature, and plasma potential every 12.8 seconds, in addition to the 11.8 seconds of density fluctuation data. Experience has shown that when the Langmuir probe is in the lock mode the output from the 1 Hz low pass filter, which is essentially the DC current to the probe, can be used as a good approximation to the electron density. This will be justified in the section on the ambient ionosphere. The performance characteristics of the probe are listed in Table 1.

It is also possible to perform a spectral analysis on the 0-40 Hz data that we have just described. To do this we first create a data file containing the 11.8 seconds worth of lock mode data. We then apply a cosine weighting function to the first and last 10% of the data, Bingham et al. [31], and set any bad or missing data to zero. By taking the Fast Fourier Transform (FFT) of these data we are

able to look at the spectral density. The output from this FFT is given in units of dB ($\delta N/N$) and is calibrated to have a minimum of 0.01% and a maximum of 2.7%. We will look at the dB average (20 x log(data)) and the peak values over the range -80 to -31.37 dB.

Finally, we will give examples of the spectral density obtained by routing the Langmuir probe data through a spectrum analyzer. The spectrum analyzer consists of 16 channels. The output from each channel is an amplitude spectrum given in units of dB $\left(\frac{\delta N/N}{\sqrt{Hz}}\right)$, found from the relation (20 x log(V_{rms}). Table 2 shows the channels, their bandwidths, their saturation levels and the appropriate multiplying factors (see below). Subsequent to the mission four of the channels were found to contain bad data, these are the channels that are not reported in Table 2. Note that the saturation $\delta N/N$ has been multiplied by the square root of 2 since we wanted peak values rather than RMS values. The multiplying factor is formed by dividing saturation $\delta N/N$ by the square root of the bandwidth.

Procedure

The data used to study the wake of the orbiter was obtained during two separate maneuvers designed to allow the PDP to study both the near and far wake of the orbiter. The first maneuver, designed for near wake studies, involved placing the PDP on the RMS a distance of 10.53 m above the center of the payload bay with the booms partially extended. By keeping the x-axis of the orbiter perpendicular to the orbital plane rolling the orbiter at a rate of 1^o per second would move the PDP alternatively into and out of the orbiter's wake,

Figure 4. This maneuver is referred to as XPOP roll. At this same time, the RMS could be rotated at the same rate so that the orientation of the PDP, relative to plasma flow, remained unchanged. In the plane of rotation the biggest obstacles to plasma flow were the orbiter's payload bay doors, which were 10.35 m wide. Consequently, if we define Z to be the width of our obstacle, 10.35 m, and R to be our downstream distance, 10.53 m, the XPOP roll maneuver occured at a characteristic ratio of $Z/R \approx 1$.

For a period of 6 hours the PDP was released as a free-flying satellite in order to allow the PDP to study the mid and far wake of the orbiter. During this time the booms seen in Figure 3 were extended to their full length. After release from the orbiter the PDP was spin stabilized with an inertial spin period of 13.06 seconds. The plane of PDP rotation was coincident with the orbital plane. During this period of six hours the orbiter executed a series of maneuvers around the PDP designed to allow the PDP to study the wake of the orbiter. Also, on four occasions the PDP and the orbiter were aligned on approximately the same magnetic field line which allowed for a study of flux tube events. The distance from the orbiter to the PDP, in a non-inertial coordinate system using the orbiter as its origin, is shown in Figures 5 - 8. Here the largest obstacle to plasma flow is the body of the orbiter itself, with a length of 35.56 m. The data obtained during this six hours of free flight represents the only in situ observations on the mid and far wake of the shuttle orbiter.

The Ambient Ionosphere

It is appropriate to discuss the characteristics of the ambient ionosphere. The plasma in the Earth's ionosphere arises due to the ionizing effect of the sun's UV radiation striking the neutral gases found there. At the altitude of the Spacelab 2 mission the ionization is 1 - 2% of the neutral gas, with the major constituent being atomic oxygen. Data obtained by the Langmuir probe on the PDP during the period of free flight just described is illustrated in Figures 9 and 10. These data correspond to the times when the distance between the PDP and the orbiter were those given in Figures 6 and 7, respectively. The apparent data drop outs that occur with a periodicity of approximately 9.5 minutes are an indirect result of the operation of another PDP instrument, the LEPEDEA, and are described in more detail by Tribble et al. [9]. For the remainder of this dissertation we will remove any visible perturbations in the data that we can associate with the LEPEDEA so that it will not have an affect on the results we present. At this point we can compare the 0-1 Hz data with the results from the Langmuir probe sweep mode. Earlier we had mentioned that the 0-1 Hz data could be used as our approximation to electron density. This agreement is confirmed in Figure 11. We will use the 0-1 Hz data as our estimate of the electron density in the succeeding chapters since it is sampled at a rate of 5 Hz and not once every 12.8 seconds as is the sweep mode data.

As we can see from Figures 9 and 10, the data we measure agree with the assumptions used in Chapter II. A listing of some of the plasma parameters associated with the ionospheric plasma are given in Table 3.

CHAPTER IV

THE NEAR WAKE

Plasma Density and Temperature

Our discussion of the near wake of the orbiter will center around data taken during XPOP roll. Since the rotation rate of the orbiter was one degree per second we will present the data in terms of an orbiter phase angle, which we define as the angle, in the orbiters' yz plane, between the velocity vector of the orbiter and the vector that points from the center of mass of the orbiter to the center of the PDP.

Measurements of the plasma density and temperature found during the first transit of the orbiters' near wake are shown in Figure 12. Unlike the remaining wake transits, during the first near wake transit the RMS was kept fixed. Two things should be noted about this data. First, the apparent density enhancement at a phase angle of 180° is associated with a thruster firing. Second, the wake of the orbiter appears to be centered around a phase angle of about 185° and not 180° as we might expect. This 5° offset occurs because the physical displacement of the Langmuir probe from the center of the PDP was such that the Langmuir probe did not arrive at the center of the orbiter's wake until the orbiter phase angle was approximately 185°.

If we assume that the ambient plasma conditions can be given by a straight line fit between the data collected at a phase angle of 130° and that collected at 230° we can calculate the density depletions and temperature enhancements in the wake as shown in Figures 12 and 13, respectively. During the maneuver known as XPOP roll we have data on 8 transits of the orbiters wake. The value of the electron density obtained when on wake axis, i.e. when the orbiter phase angle was 180°, was always below the minimum sensitivity of the instrument. But, by interpolating as in Figure 12 we can infer that on the wake axis at a distance of 10 meters behind the orbiter the electron density is approximately 0.1% of its ambient value, while the electron temperature shows an enhancement on the order of 300-500%. The value for the Mach angle calculated for these conditions is approximately 43°. If we allow for the 5° offset due to the physical displacement of the Langmuir probe boom we would expect the Langmuir probe to enter the Mach cone when the orbiter phase angle was 142° and exit it when the phase angle was 228°. This is in excellent agreement with the data. For completeness data on the succeeding two wake transits are shown in Figures 14 through 16. The electron temperature data for the third wake transit is not presented because, as can be seen from Figure 16, there are too few data points available to allow an accurate interpretation of temperature enhancements.

Plasma Turbulence

We can now proceed with an examination of the plasma turbulence in the orbiter's wake. As mentioned in Chapter II, the output from the Langmuir

probe circuitry is broken up into three channels representing the 0-1 Hz, 1-6 Hz, and 6-40 Hz components, respectively. The 1-6 Hz data obtained for near wake transit one is shown in Figure 17, while the 6-40 Hz data is shown in Figure 18. The 1-6 Hz data indicate that there are few, if any, wake effects visible in this frequency range. This data is reproducible throughout XPOP roll. The 6-40 Hz data on the other hand, indicate there there is a great deal of turbulence in this frequency range that is associated with the wake of the orbiter. In addition to the wake structure, Figure 18 indicates the effects of thruster firings at 130° and 230°. Also, the effects of the LEPEDEA are visible when that intrument points into the ram of the plasma flow, phase angles 250° to 270°. The 6-40 Hz data obtained during the two successive wake transits are shown in Figures 19 and 20. Again increases in turbulence which are associated with thruster firings are visible in Figure 20 at a phase angle of approximately 130°. Recall that during near wake transit one there was a thruster firing at an orbiter phase angle of about 180°. We believe that this is the explanation for the fact that turbulence is seen throughout near wake transit one, while transits two and three indicate a decrease in turbulence when directly on the wake axis. These data support the conclusion that we encounter turbulence as we cross the orbiter's Mach cone. This turbulence then decreases to a level below that associated with the ambient ionosphere when directly on wake axis.

A brief aside is in order here to discuss the Langmuir probe circuitry. Recall from Figure 12 that the measurements of electron density when on the wake axis were below the minimum sensitivity of the instrument. We have examined

the possibility that the decrease in turbulence seen when crossing the wake axis was due to instrumental effects. However, the gain of the 6-40 Hz channel is a factor of 154 greater than the gain of the 0-1 Hz channel. We believe that the decrease in curent to the probe, when on the wake axis, would not in itself be sufficient to account for the decrease in turbulence.

We can carry our analysis one step further by performing a Fast Fourier Transform (FFT) on the 0-40 Hz data. Recall that the FFT calculation utilizes 11.8 seconds of data to produce one graph. Since this corresponds to an 11.8° arc through the wake this will limit our spatial resolution. We should also mention that an examination of the FFT data does not indicate any effects that we can associate with the effect of the LEPEDEA.

FFT Data obtained during near wake transit one is presented in Figures 21 through 25. The starting and ending values of the orbiter phase angle that correspond to each graph can be calculated by adding the decimal seconds of the starting and ending time of each graph to 120°. For example, Figure 21, which begins at 04 seconds and ends at 16 seconds, represents data obtained between an orbiter phase angle of 124° and 136°. The conditions indicated by Figure 21, taken just outside of the orbiter's Mach cone, are equivalent to those encountered in the ambient ionosphere. Immediately after crossing the Mach cone, Figure 22, the basic shape of the signature remains the same but the spectral density is shifted downward by about 20 dB. When we reach a phase angle of about 150°, Figure 23, the spectral density of the lowest frequency components, 0 - 1 Hz, are about the same, -50 dB, but the spectral density of the higher frequency

components, 2 - 40 Hz, has increased from -80 dB to -65 dB. This is the increase seen previously in the 6-40 Hz data of Figure 18. This leveling of the spectral density increases as the phase angle progresses to 143°, Figure 24. The data obtained when crossing the wake axis, Figure 25, is essentially the same as that seen in Figure 24 except for an increase in spectral density in the 0-5 Hz range. This particular increase is most likely the result of the thruster firing reported earlier that occured at a phase angle of 180°. The data pertaining to the two subsequent wake axis crossings, Figures 21 and 22, are identical to that seen in Figure 25 except for the increase in the 0-5 Hz range. As the PDP exits the orbiters wake Figures 21 - 25 are essentially repeated in reverse order, confirming the geometrical symmetry that we would expect.

We will now examine the spectral analyzer data which examines details of density fluctuations from 30 Hz to 178 kHz. These data are sampled once every 6.83 minutes for a period of 51.2 seconds at a stretch. The only spectral analyzer data that are available during a near wake transit is that of near wake transit five. The density, temperature, and turbulence data for near wake transit five are quite similar to those presented for near wake transits one through three previously given.

The spectrum analyzer data corresponding to an orbiter phase angle of 159° are given in Figure 26. There appears to be a fairly sharp drop off in spectral density of $\Delta N/N$ past a frequency of 10,000 Hz. This frequency is on the order of the ion plasma frequency, 39,000 Hz. Recall that the Langmuir probe would cross the orbiter's Mach cone at phase angles of 142° and 225°, so

we are well within this range. The data corresponding to a phase angle of 164° is shown in Figure 27. It is fairly similar to that given in Figure 26 in that there is a sharp drop off in the spectral density of $\Delta N/N$ at 10,000 Hz. However, Figure 29 indicates a drop in the spectral density for the frequency range 31 - 200 Hz and an increase for the 200 - 10,000 Hz range. This trend is continued in the next graph, corresponding to a phase angle of 167°, Figure 28. Figure 29, corresponding to a phase angle of 175°, indicates a return to the conditions of Figure 28. This is repeated when the PDP is directly on the orbiter's wake axis, Figure 30.

The same shift, from a spectral density of about -80 dB to -90 dB in the frequency range of 31 - 200 Hz is observed as the PDP continues in its transit of the orbiter's wake. Figures 30 and 31 indicate a spectral density of about -80 dB for this frequency range, while Figure 32, orbiter phase angle 190°, shows the spectral density here depressed by about 10 dB in comparison to the spectral density at 1000 Hz. The conditions return to those originally seen in Figure 26 for phase angles of 198° and 206°, see Figures 33 and 34.

CHAPTER V

THE MID AND FAR WAKE

Plasma Density and Temperature

We have a number of opportunities to view cross sections of data taken downstream from the orbiter during the six hours of free flight. The spatial location of the PDP during the times best suited for wake studies can be culled from Figures 5 - 8, and is given in Figure 35. The first data set that we will examine was taken just after the PDP was released from the orbiter. This maneuver, which we refer to as backaway, is illustrated in Figure 36. The electron density dependence seen during this time is illustrated in Figure 37. The dashed line in Figure 37 a) represents the value associated with the ambient ionosphere. Note that the enhancments seen from 11:45 to 12:00 minutes are associated with a series of thruster firings. The ambient data was obtained at the same local time 1.5 hours later in the mission when the PDP was not in the wake of the orbiter. Similarly, the electron temperature dependence is shown in Figure 38. Note that two symbols are used to indicate the values obtained for the electron temperature. Due to the rotation of the PDP some data points were obtained when the Langmuir probe was in the wake of the PDP and may show effects associated with the PDP's wake. A box is used for these points while an asterisk is used for data points taken when the Langmuir probe was not in the wake of

the PDP. The wake of the PDP is discussed in Appendix B. During backaway the electron density increases exponentially from a low value of approximately 5% of the ambient density as the distance between the PDP and the orbiter increases, while the electron temperature shows an initial enhancement of approximately 100%, which decreases linearly as distance increases.

The first far wake transit is illustrated in Figure 39. The electron density and electron temperature dependencies for this time are given in Figures 40 and 41. Again, the values shown in Figures 40 b) and 41 b) have used a a straight line fit between the unperturbed ambient conditions. Data for wake transit two is given in Figures 42 through 44, wake transit three is shown in Figures 45 through 47, and wake transit four is given in Figures 48 through 50.

It is possible to combine the values obtained from each wake transit into one graph that describes the density depletions measured in the wake of the orbiter, Figure 51. This plot is quite significant in that it represents the first such contour model obtained from in situ data. Also of significance is the fact that the lines associated with the value of N_w/N_a cross approximately 100 m downstream from the orbiter. This may suggest the possibility of crossing streams of ions as measured by Merlino and D'Angelo [25]. The work by Murphy et al., [32], indicates values for the maximum electron density depletion on the wake axis that are slightly different than the values that would be calculated from the data in this dissertation. The difference arises because Murphy assumes an ambient model that allows for slight ionospheric variations over the 4-5 minutes necessary for wake transit. Values for $n_{e,wake}/n_{e,ambient}$ measured by both methods agree

to within the errors of the experiment. In order to compare our results with laboratory observations the data in Figure 51 were used to obtain a graph of density depletions for constant values of Z/R. That is, at fixed distances downstream of the orbiter, measured along the orbiters' z-axis, the value of N_w/N_a that would be encountered at various transverse locations, measured along the orbiters' x-axis, were interpolated from Figure 51. These results are presented in Figure 52.

Our efforts to obtain a similar graph for the electron temperature enhancements were somewhat complicated. As is seen in Figures 44, 47, and 50, some of the temperature data taken inside of the orbiters Mach cone happen to coincide with times when the Langmuir probe was in the wake of the PDP. For this reason we have avoided the use of any data points taken in the wake of the PDP in our attempt to obtain a contour map of the temperature dependence in the wake of the orbiter. The remaining data are not sufficient to obtain an accurate map, but they do indicate a distinct temperature gradient as illustrated in Figure 53.

Plasma Turbulence

Due to the problem with the LEPEDEA, Tribble et al., [9], the 1-6 Hz data is completely unusable during free flight. The 6-40 Hz data is somewhat perturbed, but the majority of these perturbations can be removed from the data. The 6-40 Hz data obtained during backaway is seen in Figure 54. These data indicate that the majority of the turbulence in this frequency range that is seen on axis as we move away from the orbiter is confined to the first 2.5 minutes

of backaway, or a distance of 25 m downstream. The large enhancements seen between 11.75 and 12.0 minutes and the smaller enhancements seen at approximately 14.9 minutes, 16.1 minutes, 16.5 minutes, etc., are all associated with thruster firings. If we move to an examination of the far wake transit one data, Figure 55, we see that there are no large structures that we can associate with the orbiter wake. A very slight enhancement is visible at about 02:58:30, between 03:01 and 03:06, and again between 03:08 and 03:09. The interval 03:01 - 03:06 corresponds to the times when the PDP is inside the orbiter's Mach cone. The times 02:58:30 and 03:08 - 03:09 are times when the LEPEDEA is in ram. Even though we have removed a majority of the data that show the effects of this problem, some perturbations are still visible in the data when the LEPEDEA is in ram. The data corresponding to far wake transit two, Figure 56, indicate a larger enhancement centered at about 04:33:15 and a number of smaller enhancements noticeable throughout this interval. In Figure 56, the PDP was inside of the orbiter's Mach cone from 04:30 to 04:34. Again in far wake transit three, Figure 57, there are a number of sharp, short lived enhancements that we associate with thruster firings. But as in Figure 56 there are no large enhancements to associate with the Mach cone crossings at 04:47 and 04:51. The final far wake transit data are shown in Figure 58, which again shows no large enhancements linked to the Mach cone crossings at 04:58 and 05:03.

The 6-40 Hz data did not indicate any large increases in turbulence that we can associate with the wake of the orbiter. We shall next turn to an examination of the FFT of the 0-40 Hz data. First we will examine data obtained during

backaway 35 m downstream of the orbiter, Figure 59. These data do not differ appreciably from that seen in the ambient ionosphere. Data obtained 120 m downstream, about 20 m past the wake 'crossing point' seen in Figure 51, is presented in Figure 60. These data both indicate a similar drop in spectral density at the higher frequencies. Data taken along the orbiter's Mach cone 200 m downstream are presented in Figure 61. In comparison to the 2 previous figures we see a drop in spectral density on the order of 15 - 20 dB at the higher frequencies. Data taken just outside the orbiter's Mach cone at distances of 20 m and 90 m downstream from the orbiter are shown in Figures 62 and 63, respectively. These bear the general shape of the data obtained on the wake axis, but they also exhibit more rapid variations in spectral density as frequency increases.

The data just presented was choosen so that the LEPEDEA would be facing the wake of the PDP during most of the 11.8 second period covered by the graph. In this manner we have attempted to minimize its effect. However, we previously mentioned that the 1-6 Hz data was completely unusable due to this problem and that the 6-40 Hz data was noticeably perturbed. These perturbations were not removd by the algorithms that computes the FFT of the data. However, by comparing the free flight data with data taken from the RMS or payload bay were are unable to detect any significant differences that we can attribute to either the wake of the PDP or the LEPEDEA.

Due to the different sampling schedule of the spectral analyzer we did not have as many data points available to us as we did for the FFT data. The

locations where we do have spectral analyzer data available to us are shown in Figure 64. The roman numerals will be used to reference the individual data points. For the sake of comparison we will first present data obtained in the ambient ionosphere, Figure 65. Recall the turbulence seen in the very near wake of the orbiter in the 6-40 Hz data. Again, when in the very near wake at location I of Figure 65 we see that the measurements of the turbulence show enhancements, Figure 66. However, the data taken 50 m further downstream, at location II, do not indicate such enhancements, Figure 68. An examination of data obtained on the orbiter's Mach cone at a distance of 250 m, location III, indicates an enhancement of approximately 5 dB at a frequency of 10,000 Hz, Figure 69. This enhancement disappears on wake center, IV, Figure 69, but seems to reappear at the opposite side of the Mach cone, V, Figure 70. Just inside the orbiter's Mach cone at a distance of 150 m downstream, VI, we see an enhancement of approximately 15 dB at a frequency of approximately 20,000 Hz, Figure 71. Again, even at the closer distance, III, the enhancement is not visible on axis, Figure 72. Data obtained at the 5 remaining locations is presented in Figures 73 - 77.

CHAPTER VI

SUMMARY AND CONCLUSIONS

Having completed our analysis of the data we can now present the description of the wake of the orbiter as inferred from the in situ observations. The very near wake of the orbiter, Z/R $\approx$ 1, is a region of electron density depletion and temperature enhancement bounded by the orbiter's Mach cone. The electron density measured on the wake axis is 10^{-3} of the ambient value, while the temperatures measured there are increased by a factor of 3 - 5 over ambient conditions. The turbulence in the 6-40 Hz range exhibits a change from a fraction of a percent to over three percent as the PDP entered the orbiter's Mach cone. This turbulence decreased to a level slightly below that associated with the ambient ionosphere when the PDP was within $2^o - 3^o$ of the orbiter's wake center. The FFT of the low frequency data indicated an overall decrease in the spectral density when crossing the Mach cone and a flattening of the spectral density signature when on the wake axis.

The spectral density of $\Delta N/N$ in the near wake decreased significantly for frequencies higher than $f_{p,i}$ at all times. The turbulence that we associate with crossing the orbiter's Mach cones exhibited an increase in the spectral density for frequencies below about 200 Hz. When in the quieter wake region there was a decrease in the spectral density of these lower frequencies and a slight increase

for frequencies between 200 Hz and 10,000 Hz. When directly on the wake axis, the spectral density at the lowest frequencies was about -80 dB and decayed exponentially as the frequency increased to a spectral density of about -95 dB at a frequency of 10,000 Hz.

In the far wake of the orbiter, the electron density depletion data, Figure 51, indicates a 'crossing point', a region where the electron density on the wake axis was less both upstream of this point and downstream of it. It is important to note that the first far wake transit was at times as much as 15 m out of the orbital plane. Therefore, the density depletions indicated by this farthest wake transit might have indicated densities as low as 0.5 N_a had this transit been completely in plane. In any case, the significance of Figure 51 is that it shows conclusively that the density depletions behind the orbiter extend to a distance of several hundred meters behind the orbiter, perhaps even as far as a kilometer. Similarly, the electron temperature enhancements shown in Figure 53 extend equally far downstream.

The 6-40 Hz data indicate that the region of maximum turbulence is confined to a region on the order of the size of the orbiter itself, 35 m. The fact that there is no minimum on the orbiter's axis seen after release from the orbiter may indicate that the turbulence associated with the Mach cones during XPOP roll converges approximately 15 m downstream of the orbiter. It is difficult to find low frequency turbulence that we associate with the far wake of the orbiter, but the effects of thruster firings are readily visible as far as 250 m downstream. The FFT data support the conclusion that there is a decrease in the overall spectral

density when crossing the orbiter's Mach cone and a slight increase when at the 'crossing point' just mentioned.

The spectral density of $\Delta N/N$ is largest in the near wake, a further confirmation of the fact that the majority of the turbulence is confined to a region on the order of the size of the orbiter. The spectral density is essentially constant along the wake axis both before and after the 'crossing point', however this point exhibits a slight increase in the lower frequency spectral density. The spectrum analyzer data indicate that there are ion plasma waves, excited by the passage of the orbiter, that travel outward at the ion acoustic velocity. Since these ion plasma waves were not observed during XPOP roll this data is consistent with the picture seen in Figure 1. That is, the region of turbulence that expands at the Mach angle originates some distance downstream of the obstacle. Since the signature of these waves can vary by 5 - 10 dB, depending on the location of the sample, it would support the statement that waves in the wake of a large obstacle are heavily damped, [30].

Having completed our analysis we find that our results are in agreement with what was expected in Chapter II. Our results are summarized as follows:

1. The electron density depletions and temperature enhancements associated with the wake of the orbiter extend to distances on the order of 1 km behind the orbiter.
2. There is a great deal of low frequency turbulence confined to the near wake, $\approx$ 35 m, region downstream of the orbiter.

3. The regions of greatest turbulence in the orbiter's wake have essentially a constant spectral density in the 0-40 Hz range.
4. There are ion plasma waves generated in the wake of the orbiter that are traveling at the ion acoustic speed.

APPENDIX A

DERIVATION OF LANGMUIR PROBE EQUATIONS

During the sweep mode the current that is collected by the Langmuir probe is sent through a 0-50 Hz low pass filter and can be used to determine electron density, temperature, and the plasma potential. From elementary plasma physics we know the effect of introducing an object that is charged to a potential, such as a point charge or a probe, into a plasma. If we make the assumption that the mobility of the ions can be neglected in comparison to the mobility of the electrons then the potential around a test charge q is given by

$$V(r) = \frac{q}{r}\exp\left(\frac{-r}{\lambda_e}\right), \tag{A.1}$$

where

$$\lambda_e = \left(\frac{T_e}{4\pi n_o e^2}\right), \tag{A.2}$$

T_e is the electron temperature and λ_e is the Debye length for electrons. Because the potential falls off so rapidly as r increases electrons and ions further than one Debye length away from the probe will be virtually unaffected by the probe's presence. If we apply a large potitive bias to the probe we can expect to attract all of the electrons and repel all of the ions within one Debye length of the probe.

Then, as shown, for example, by Huddlestone and Leonard [33], we can compute the current collected by the probe in the following manner. If the radius of the probe is much larger than the Debye length, we may assume that all of the particles passing within one Debye length of the probe, through thermal motions for example, will hit the probe. If the probe is perfectly absorbing, then the current collected by the probe will be

$$I = J_r A_s, \tag{A.3}$$

where J_r is the random current flux and A_s is the surface area of the sheath one Debye length away from the probe. Since the radius of the probe is assumed to be much larger than the Debye lengnth we can approximate the area of the sheath by the surface area of the probe. We now have

$$A_s = 4\pi r^2. \tag{A.4}$$

By definition,

$$J_r = Q_s \times (\text{number of particles hitting the probe/unit time}). \tag{A.5}$$

Q_s refers to the charge of each species present in the plasma, a sum over each species in the plasma is implied. To determine the quantity in parenthesis we can look at a differential volume element located at the edge of the sheath farthest from the probe. The particles here are far enough away from the probe that

we only need consider their thermal motions. Therefore, half of the particles in this volume element would be entering the Debye sheath, half would be leaving it. We conclude that the number of particles entering the sheath per unit time, i.e. the number of particles that will eventially impact the probe, is $(N_s/2)A_s v_s$, where N_s is the density of each species in the plasma and v_s is their velocity. This tells us that

$$J_r = \frac{Q_s N_s A_s v_s}{2}. \tag{A.6}$$

If we assume each plasma species has a Maxwellian velocity distribution then

$$P(v) = 4\left(\frac{M_s}{2\pi k T_s}\right)^{3/2} v^2 \exp\left(\frac{-M_s v}{2kT_s}\right) \tag{A.7}$$

is the probability that a given particle will have its velocity between v and v + dv. The average magnitude of the velocity is given by

$$< v_s >= \int_{-\infty}^{+\infty} v_s P(v_s) dv_s = 2\left(\frac{2kT_s}{\pi M_s}\right)^{1/2}. \tag{A.8}$$

The direction of the velocity vector, for the particles entering the sheath, will be randomly distributed over 180°. Therefore, we can define the vector so that the component of velocity directed at the probe is given by $v_s \cos\theta$. When we integrate over the factor $\cos\theta$ to find the average component of velocity in the direction of the probe we pick up a factor of 1/2, which cancels a factor of 2 in the previous expression for v_s. Therefore, when we combine this definition of v_s with the definition of J_r, we find that the current collected by the probe is

$$I = Q_s(4\pi r^2)\frac{N_s}{2}\left(\frac{2kT_s}{\pi M_s}\right)^{1/2}. \qquad (A.9)$$

Again, there is an implied sum over all the species present in the plasma. If we apply a large positive bias voltage to the probe we may assume that only electrons will contribute to the current collected, that is, the ion current will be negligible. Therefore, the value of the electron current, before the probe saturates, is given by

$$I = -e(4\pi r^2)\frac{N_e}{2}\left(\frac{2kT_e}{\pi M_e}\right)^{1/2}. \qquad (A.10)$$

This equation is dependent upon both density and temperature. However, we can make use of the Boltzmann relation from statistical mechanics. In the presence of a potential, in this case the probe, the density is given by

$$N_e = N_o \exp\left(\frac{-eV}{kT_e}\right). \qquad (A.11)$$

Plugging this into the previous equation gives

$$I = -e(4\pi r^2)\frac{N_o}{2}\left(\frac{2kT_e}{\pi M_e}\right)^{1/2}\exp\left(\frac{-eV}{kT_e}\right). \qquad (A.12)$$

Now we have an equation involving the electron temperature and the probe bias voltage V. Taking the natural log of both sides of this equation gives

$$lnI = C + (C' lnT_e) + \left(\frac{-e}{kT_e}\right)V. \qquad (A.13)$$

C - 6

where both C and C' are constants depending on the radius of the probe, the mass of the electron, and so on. The term proportional to ln T_e will vary much slower than $1/T_e$, therefore we may approximate the ln T_e term as a constant. The equation becomes

$$lnI = C'' + \left(\frac{-e}{kT_e}\right) V. \tag{A.14}$$

If we graph ln I vs V, before the probe satures, the slope will be given by $(-e/kT_e)$. This gives us an expression for T_e,

$$T_e = \frac{-e}{k \text{ slope}}. \tag{A.15}$$

Once we have T_e we can plug this into the expression for I, equation A.10, and deduce an expression for N_e, which is

$$N_e = \frac{-2I}{e(4\pi r^2)} \left(\frac{\pi M_e}{2kT_e}\right)^{1/2}, \tag{A.16}$$

Consequently, we find that the Langmuir probe can indeed give us temperature. If we define the plasma potential as the bias voltage at which the electron density and the probe saturates, a graph of ln I vs V will also give us the plasma potential. A typical sweep is shown in Figure 78. Note that the value of I that we use in the determination of N_o is chosen so that V is as positive as possible without saturating the probe. This completes our discussion of the equations governing the operation of the Langmuir probe. For a more in depth discussion of probe characteristics under specific plasma conditions see the works by Parrot et al.

[34], Rubinstein and Laframboise [35], Szuszczewicz and Takacs [36], or Makita and Kuriki [37].

APPENDIX B

THE WAKE OF THE PDP

There are times during free flight when the Langmuir probe passes through the wake of the PDP. It is important to understand what effect this may have on the data collected by the probe. Measurements of the electron density depletions in the wake of the PDP are presented in Figure 79 where the PDP phase angle is defined analagously to the orbiter phase angle defined previously. That is, the PDP phase angle is defined as the angle between the PDP's velocity vector and the vector that points from the center of the PDP to the Langmuir probe. Figure 79 seems to indicate that the wake of the PDP is centered around a phase angle of 190° and not the 180° that we might expect. We believe that this ten degree offset arises from uncertainties associated with the calculation of the PDP phase angle and is not indicative of an asymmetric wake.

The data in Figure 79 indicate a density depletion on the order of 30 - 40% of the ambient values when directly in the wake of the PDP. These data also confirm that the density depletions in the wake of the PDP are bounded by the orbiter's Mach cone. Figure 79 represents data collected during four complete rotations by the PDP, so we can conclude that the wake structure is quite stable.

Data pertaining to temperature enhancements in the wake of the PDP are presented in Figure 80. The asterisks are used to indicate data points taken

when the Langmuir probe was outside of the PDP's Mach cone, while the boxes indicate that the probe was inside the Mach cone. We conclude that the wake of the PDP is characterized by a temperature enhancement on the order of 75%, in agreement with previous studies, [12 - 16].

TABLE 1.

Langmuir Probe Performance Characteristics

Current Sensor	$0.1\mu a - 1ma$
T_e	800 - 5000 K
n_e	$10^3 - 10^7\ cm^{-3}$
$\Delta N/N$	
$\leq$ 1 Hz	1.8% - 460%
1 - 6 Hz	0.12% - 30%
6 - 40 Hz	0.012% - 3%
$\geq$ 30 Hz (spectrum	
analyzer)	-30 dB $\Delta N/N$ to -80 dB $\Delta N/N$

TABLE 2.

Spectrum Analyzer Performance Characteristics

Channel	Center Freq. (kHz)	Saturation $\Delta N/N$	Saturation Input (V)	Bandwidth (Hz)	Mult. Factor
0	0.0355	0.113	0.5012	16.1	0.05639822
1	0.0633	0.057	0.2512	21.5	0.04880926
2	0.1200	0.090	0.3981	34.9	0.03830448
3	0.2000	—	—	—	—
4	0.3110	0.226	1.0000	89.1	0.02397155
5	0.5620	—	—	—	—
6	1.0000	0.226	1.0000	353.0	0.01204336
7	1.7800	—	—	—	—
8	3.1100	0.113	0.5012	907.0	0.00751406
9	5.6200	—	—	—	—
10	10.0000	0.113	0.5012	2,050.0	0.00499806
11	16.5000	0.226	1.0000	2,780.0	0.00429158
12	31.1000	0.226	1.0000	3,550.0	0.00379771
13	56.2000	0.226	1.0000	7,110.0	0.00268349
14	100.0000	0.226	1.0000	11,300.0	0.00212861
15	178.0000	0.180	0.7943	12,200.0	0.00204878

TABLE 3.

Ionospheric Plasma Characteristics

Parameter	Symbol and Value
Electron/Ion density	$n_e \approx n_i \approx 1 \times 10^5\ cm^{-3}$
Electron/Ion temperature	$T_e \approx T_i \approx 2500\ K$
Orbital velocity	$v_o = 7.7\ km/s$
Earth's magnetic field strength	$B_E \approx 5 \times 10^{-5}\ T$
Thermal electron velocity	$v_{e,th} = \left(\frac{2kT_e}{m_e}\right)^{1/2} \approx 180\ km/s$
Thermal ion velocity	$v_{i,th} = \left(\frac{2kT_i}{m_i}\right)^{1/2} \approx 1.1\ km/s$
Electron plasma frequency	$f_{p,e} = \frac{1}{2\pi}\left(\frac{4\pi n_o e^2}{m_e}\right)^{1/2} = 440\ kHz$
Ion plasma frequency	$f_{p,i} = \frac{1}{2\pi}\left(\frac{4\pi n_o e^2}{m_i}\right)^{1/2} = 39\ kHz$
Electron gyrofrequency	$\Omega_e = \left(\frac{eB_o}{m_e c}\right) = 3.5 \times 10^{-2}\ s$
Ion gyrofrequency	$\Omega_i = \left(\frac{eB_o}{m_i c}\right) = 1.0 \times 10^{-6}\ s$
Electron Larmor radius	$R_{e,L} = \left(\frac{m_e v_{e,th}}{eB_E}\right) = 2\ m$
Ion Larmor radius	$R_{i,L} = \left(\frac{m_i v_{i,th}}{eB_E}\right) = 46\ m$
Electron Debye length	$\lambda_{e,D} = \left(\frac{T_e}{4\pi n_o e^2}\right) = 1\ cm$
Ion acoustic speed	$C_s = \left(\frac{kT_e + 3kT_i}{m_i}\right)^{1/2} = 1.6\ km/s$
Mach number	$M = \left(\frac{v_o}{C_s}\right) = 3.85$
Mach angle	$\theta_m = tan^{-1} M = 14.5^o$

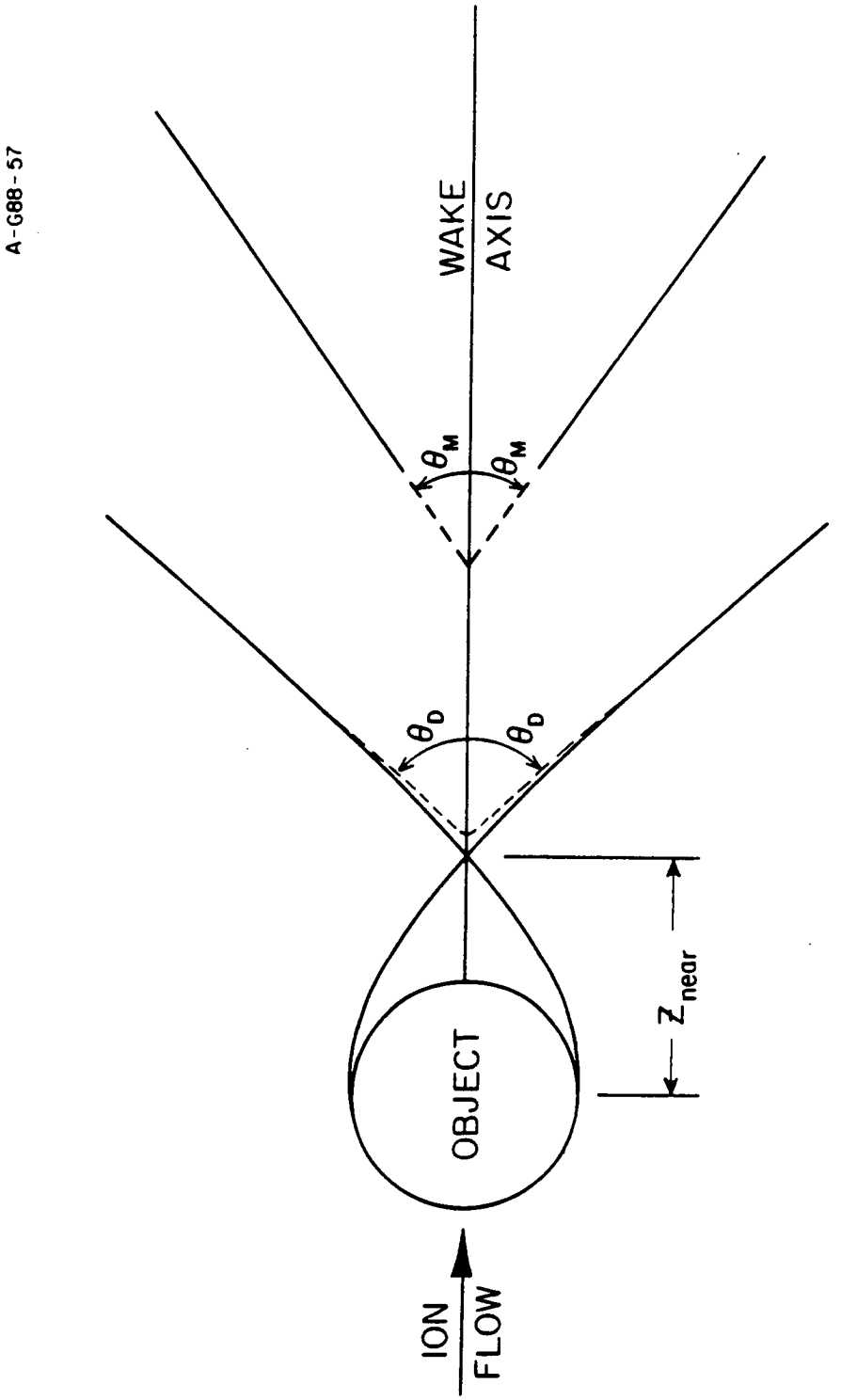

Figure 1. An idealized view of the plasma wake of an object in a flowing plasma.

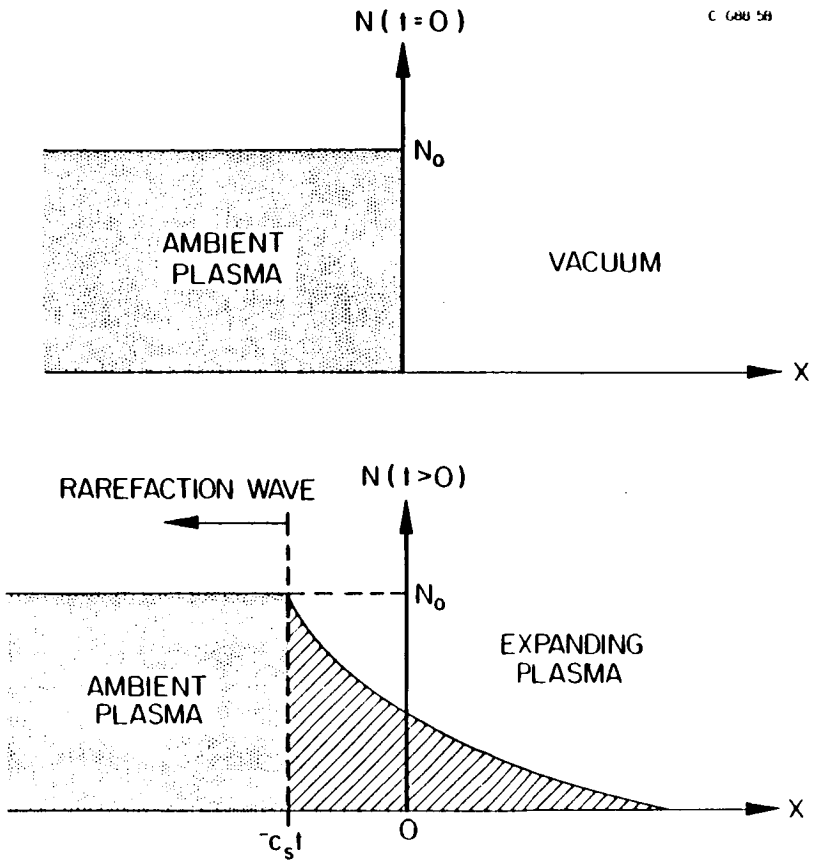

Figure 2. Plasma Expansion into a vacuum.

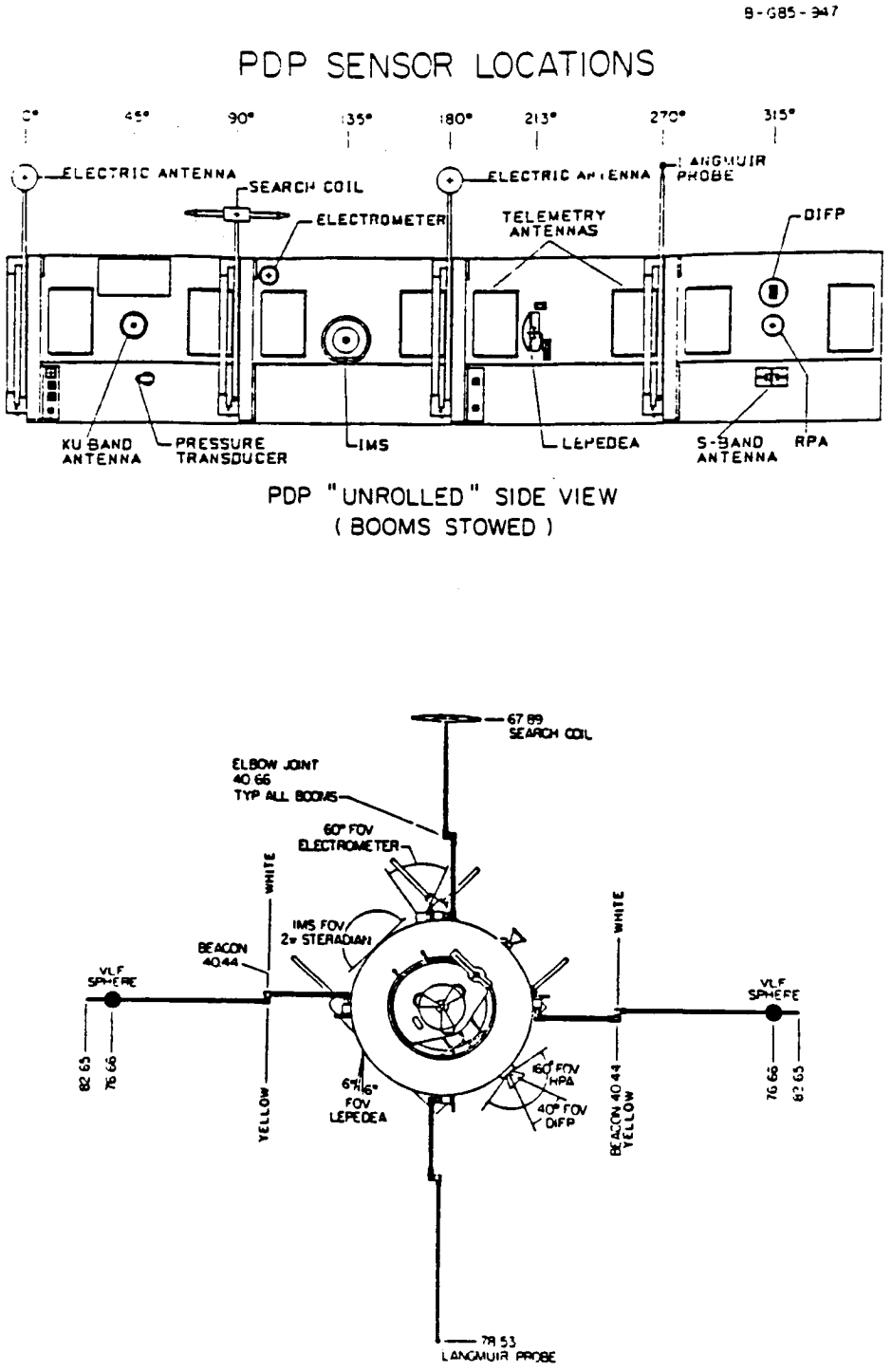

Figure 3. The Plasma Diagnostics Package.

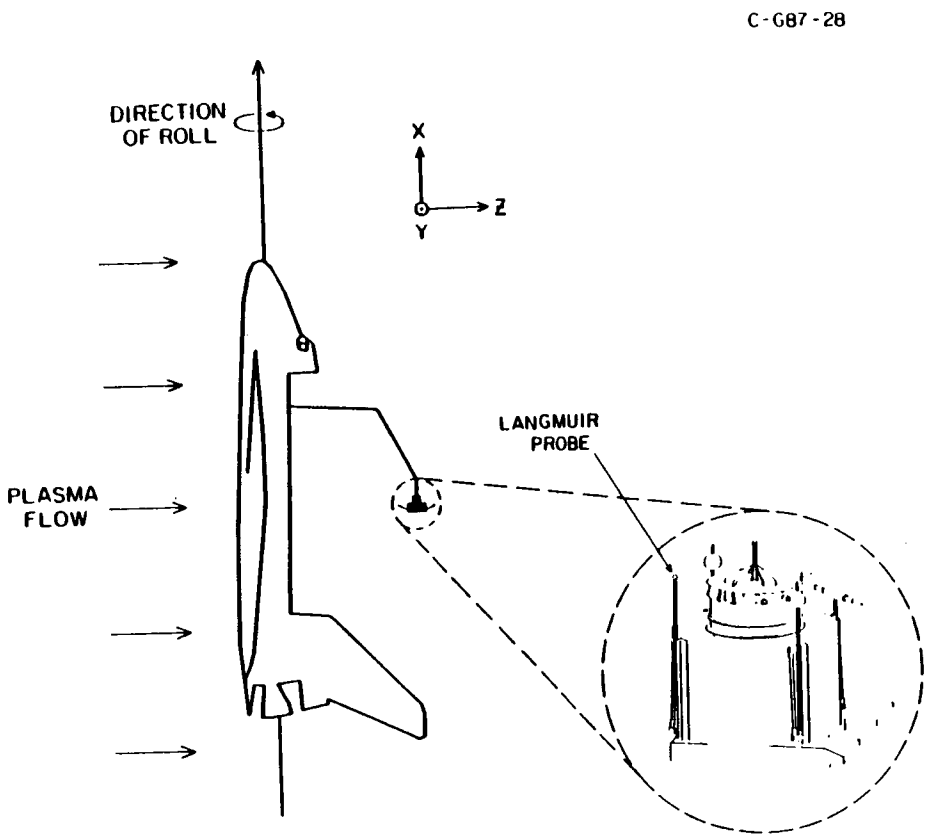

Figure 4. XPOP roll, the procedure used to study the near wake of the orbiter.

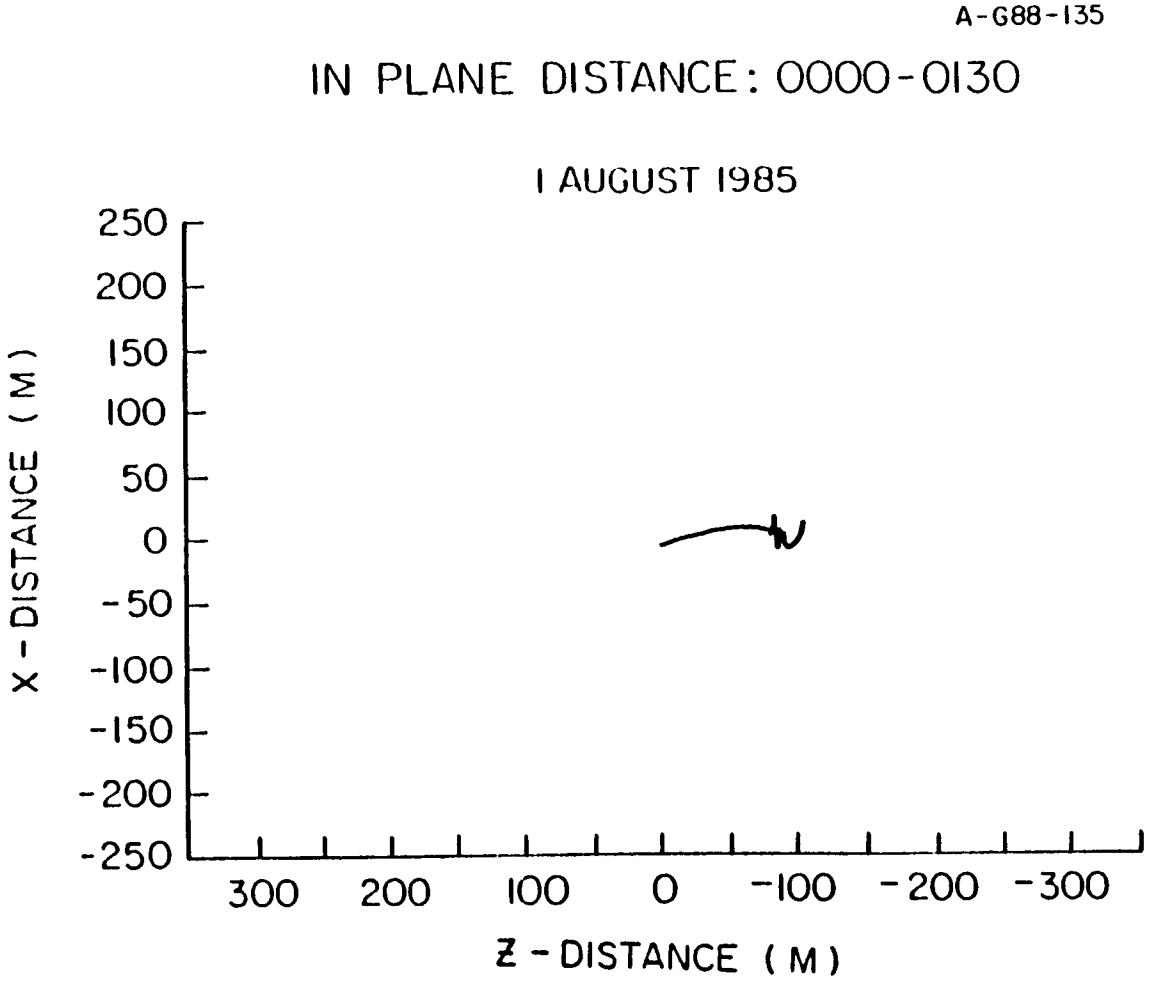

Figure 5. In plane distance between the orbiter and the PDP, 00:00 - 01:30.

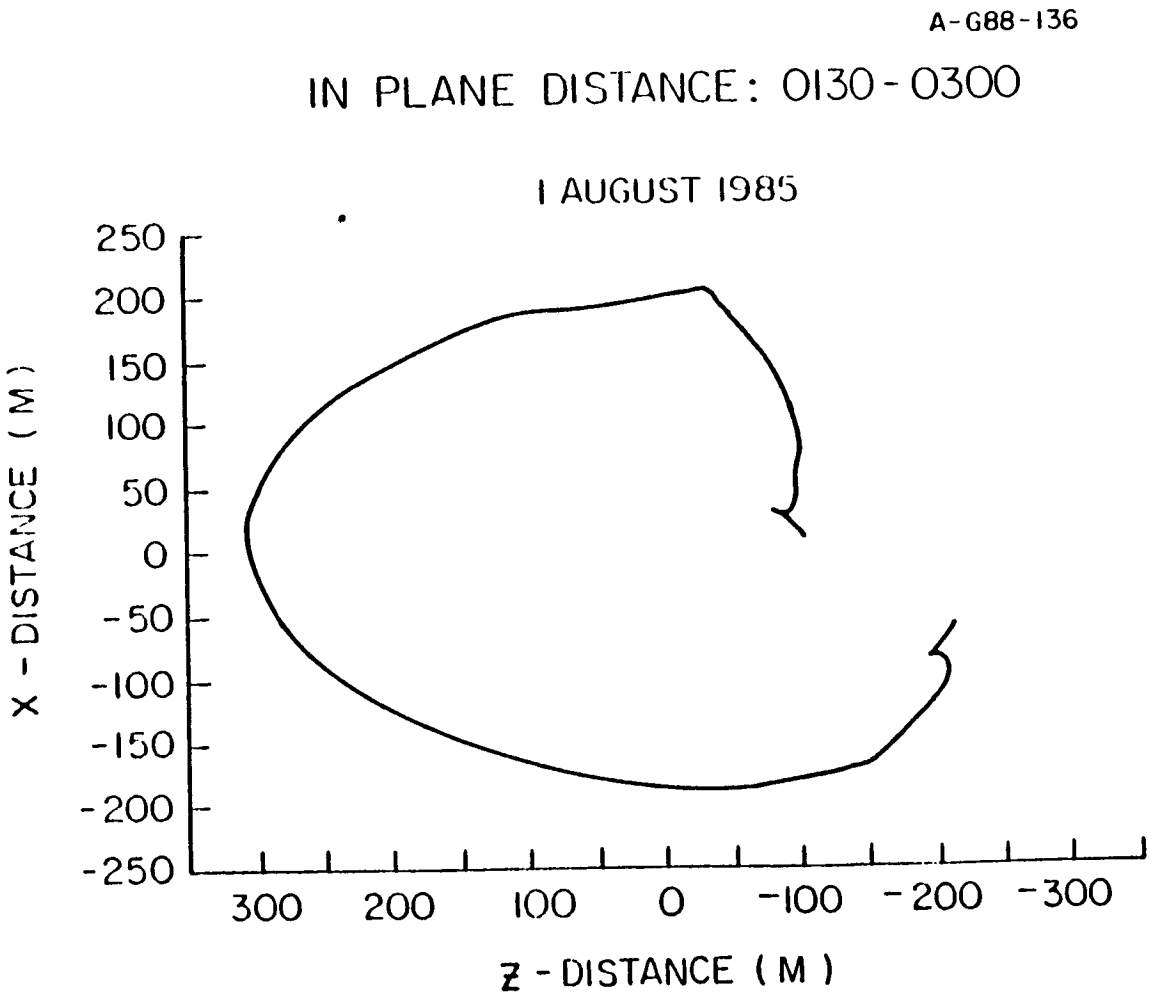

Figure 6. In plane distance between the orbiter and the PDP, 01:30 - 03:00.

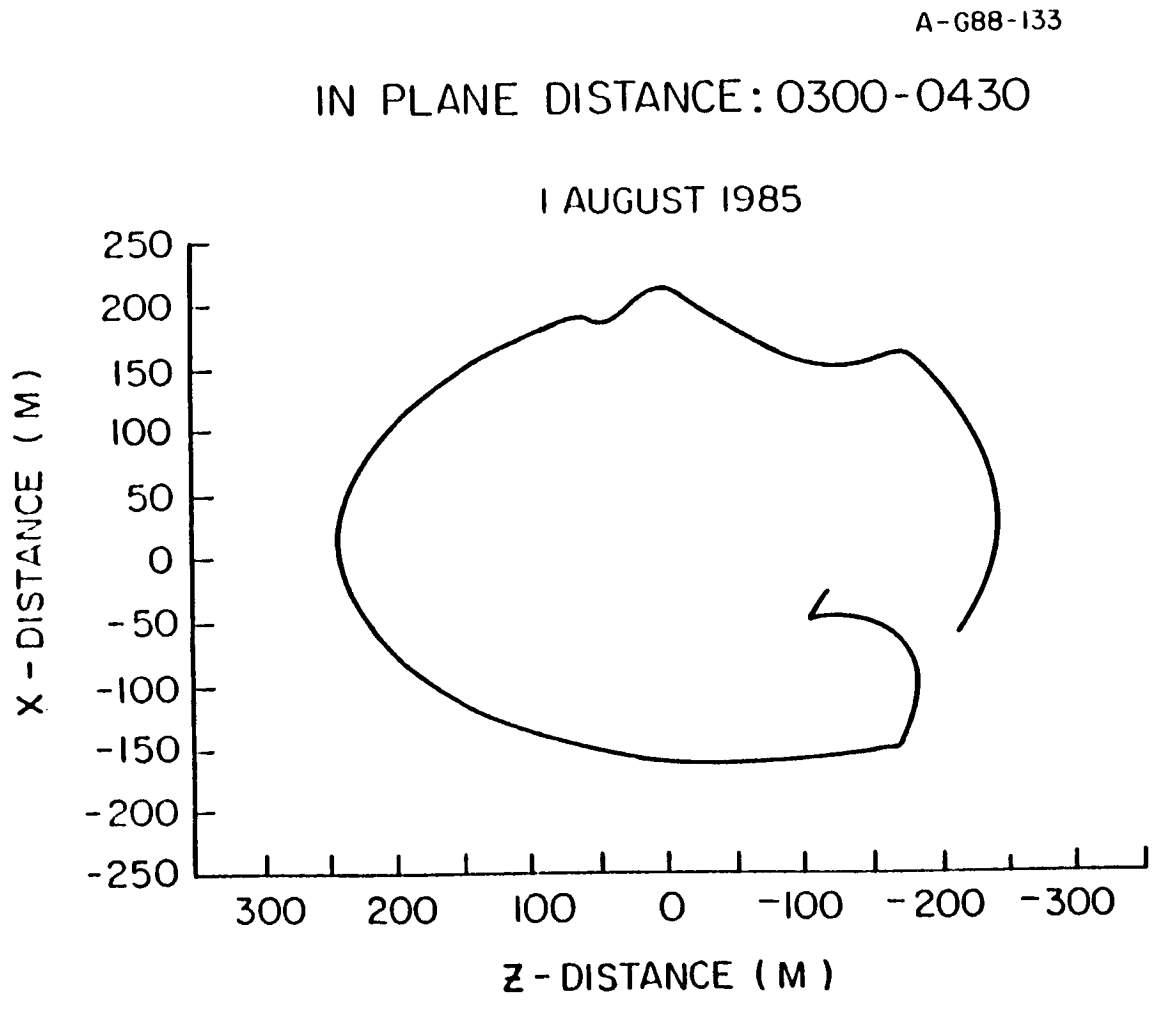

Figure 7. In plane distance between the orbiter and the PDP, 03:00 - 04:30.

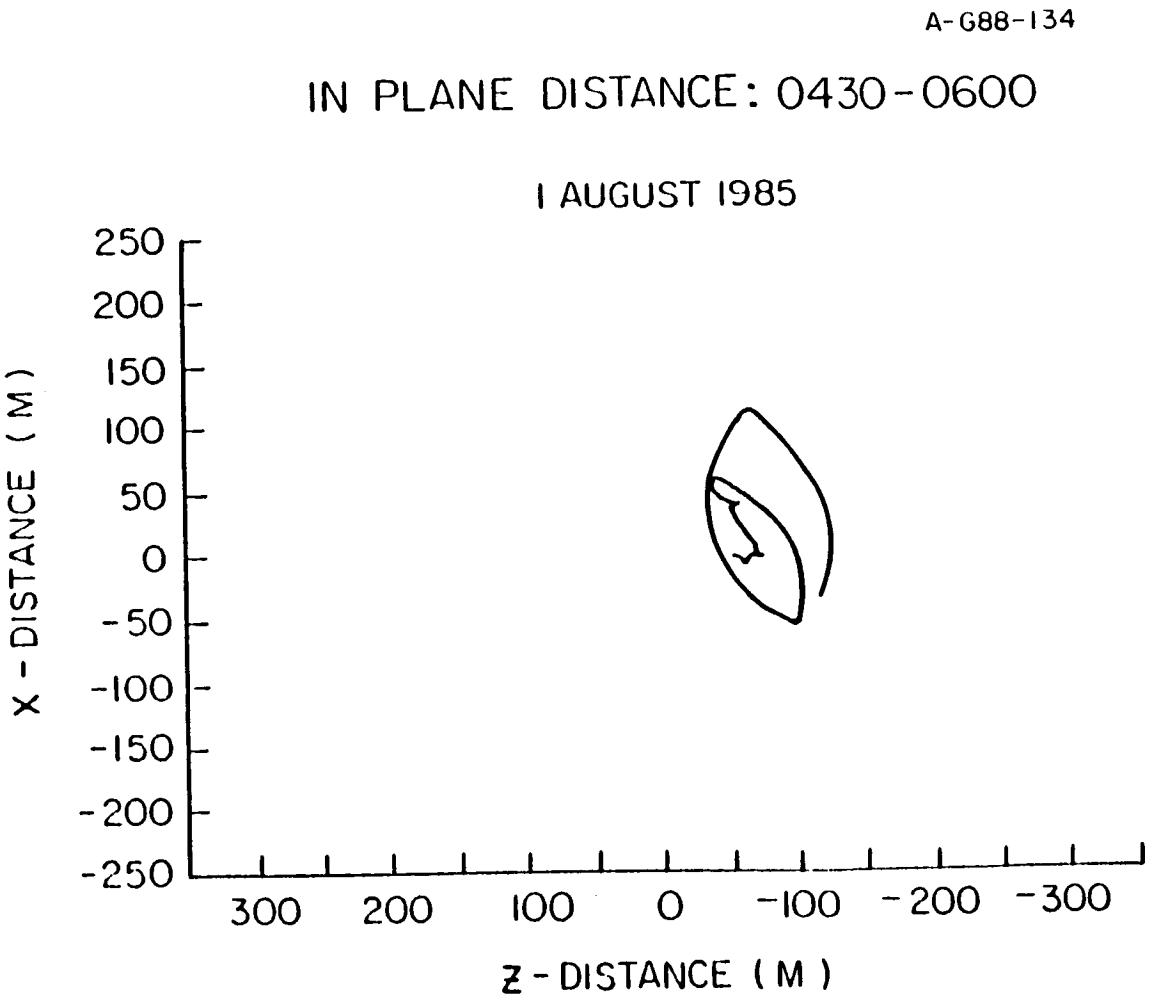

Figure 8. In plane distance between the orbiter and the PDP, 04:30 - 06:00.

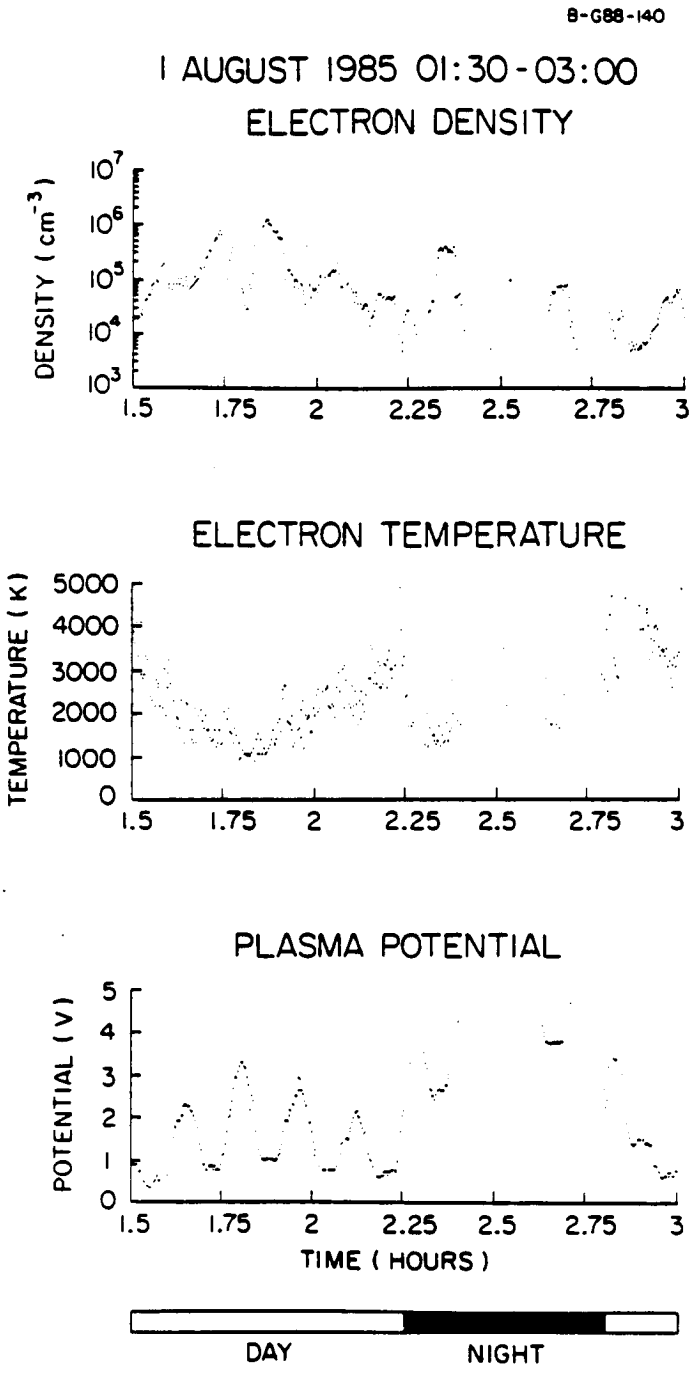

Figure 9. Ambient ionospheric characteristics, 01:30 - 03:00.

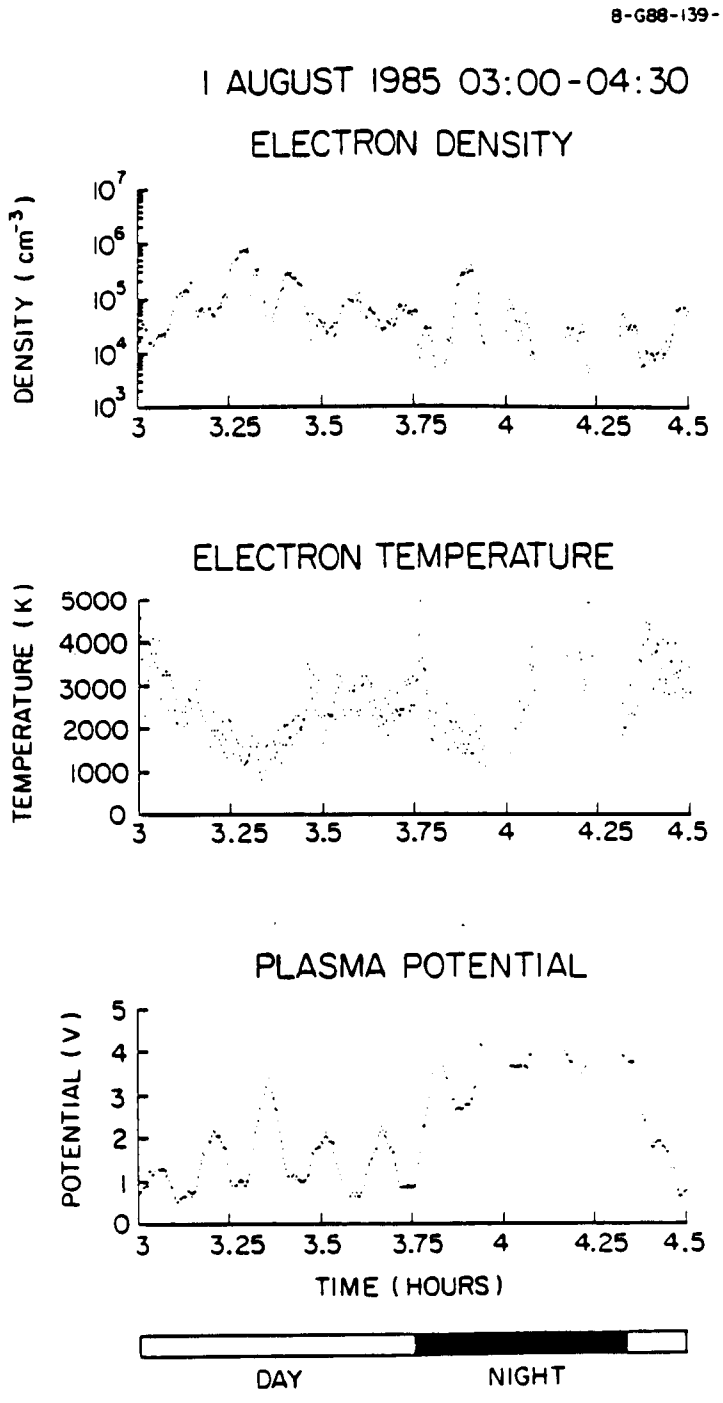

Figure 10. Ambient ionospheric characteristics, 03:00 - 04:30.

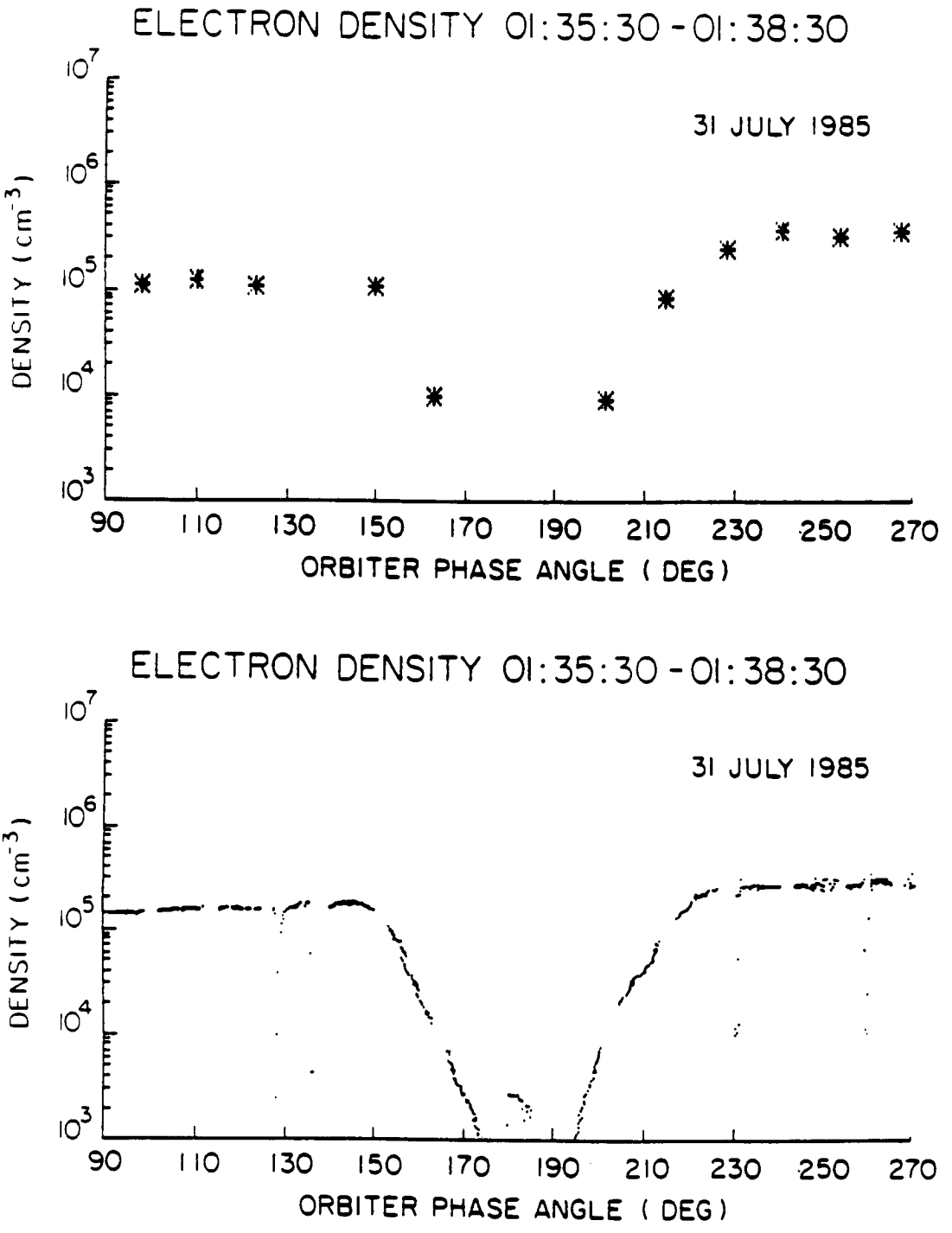

Figure 11. A comparison of the electron density calculated from the Langmuir curves (top) with that calculated from the 0-1 Hz data (bottom).

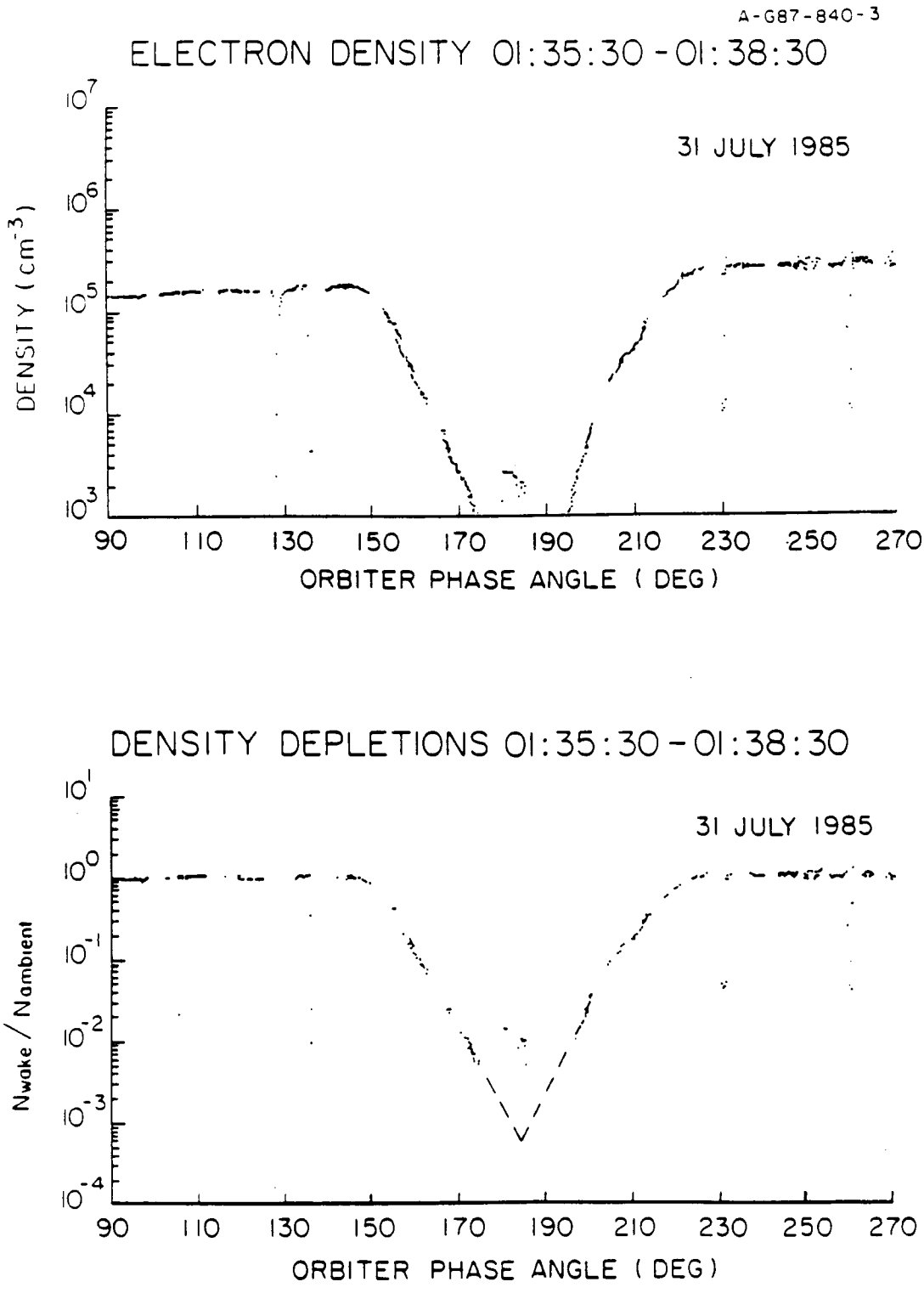

Figure 12. Electron density depletions during near wake transit one.

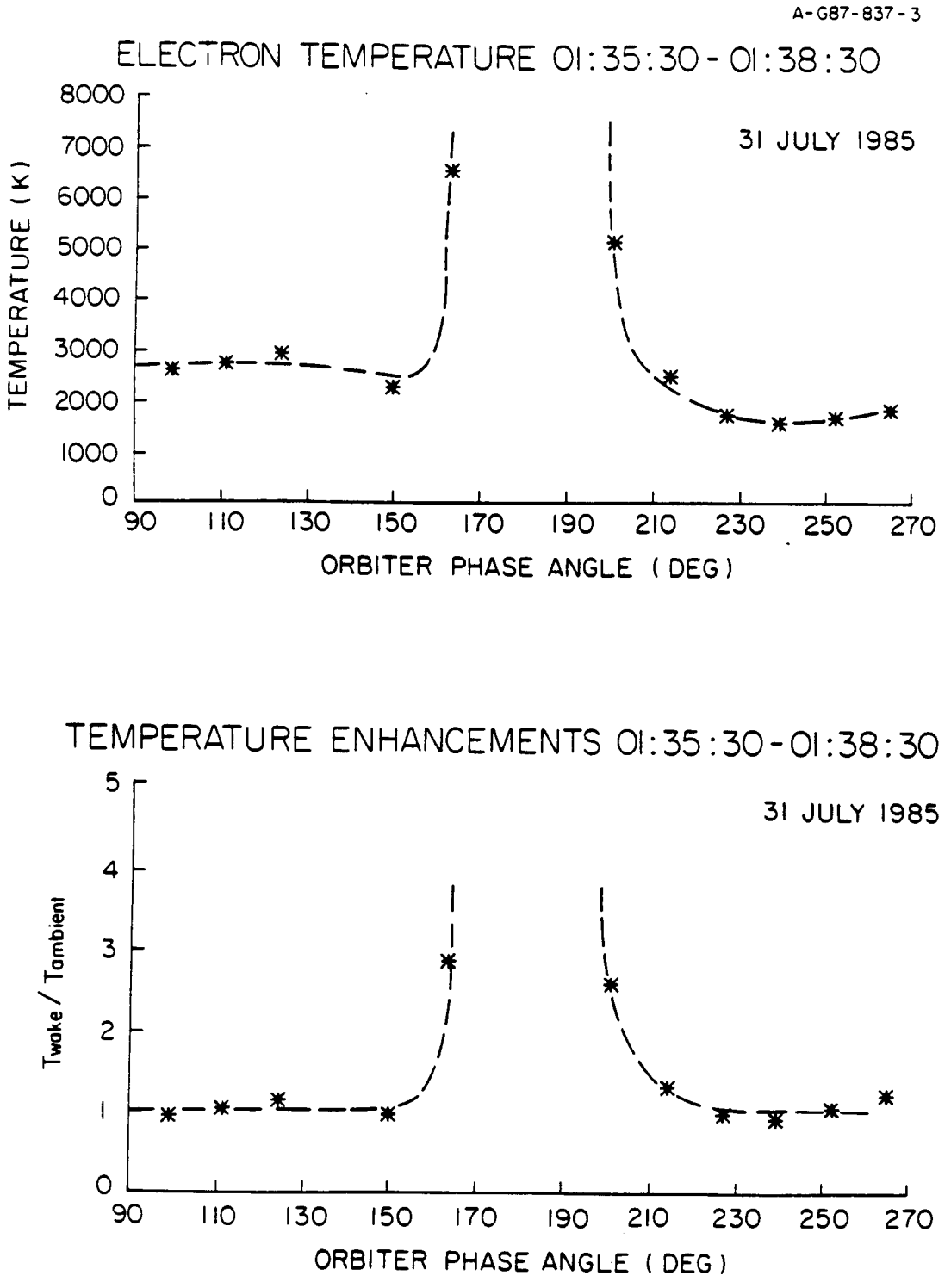

Figure 13. Electron temperature enhancements during near wake transit one.

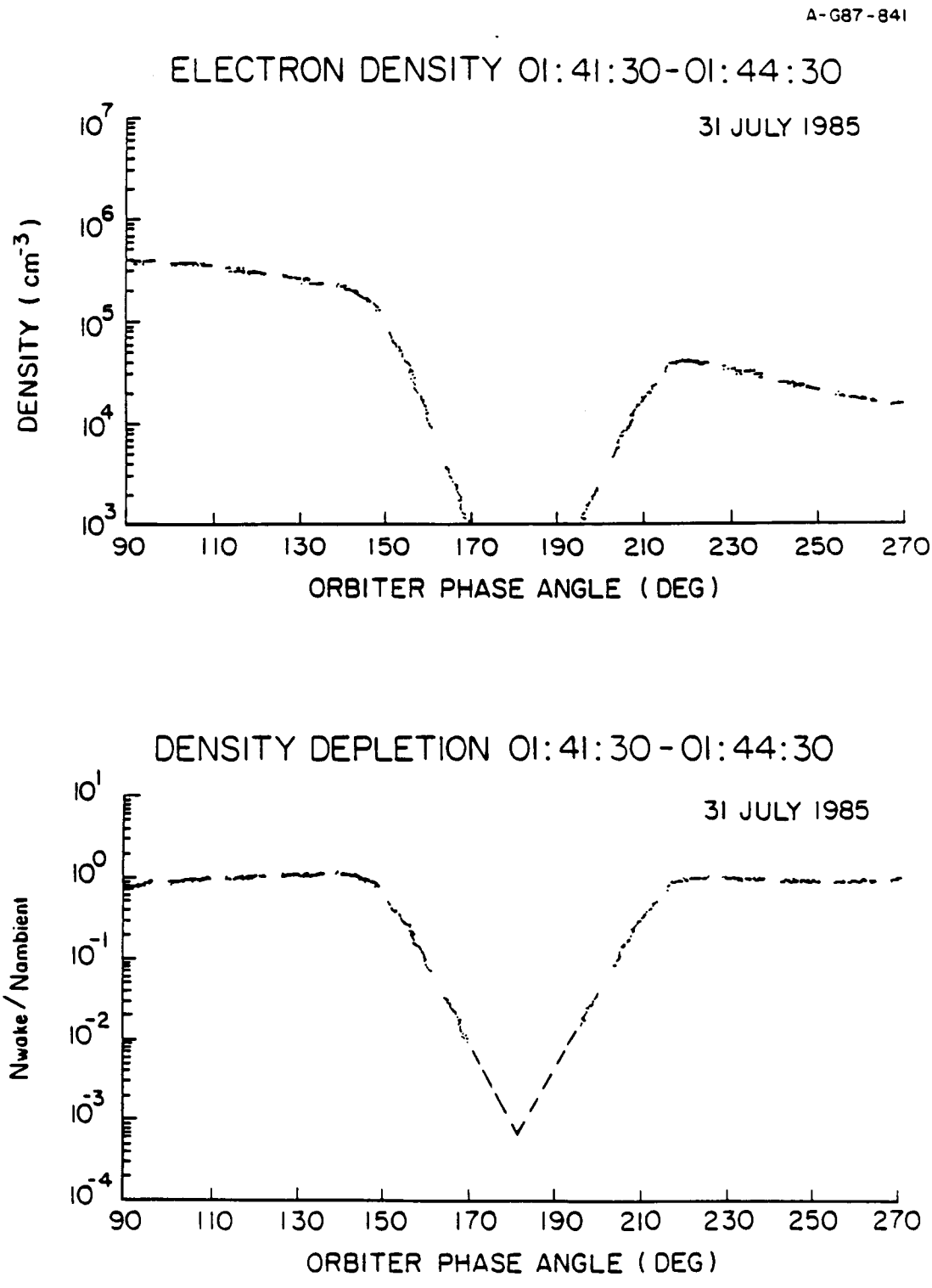

Figure 14. Electron density depletions during near wake transit two.

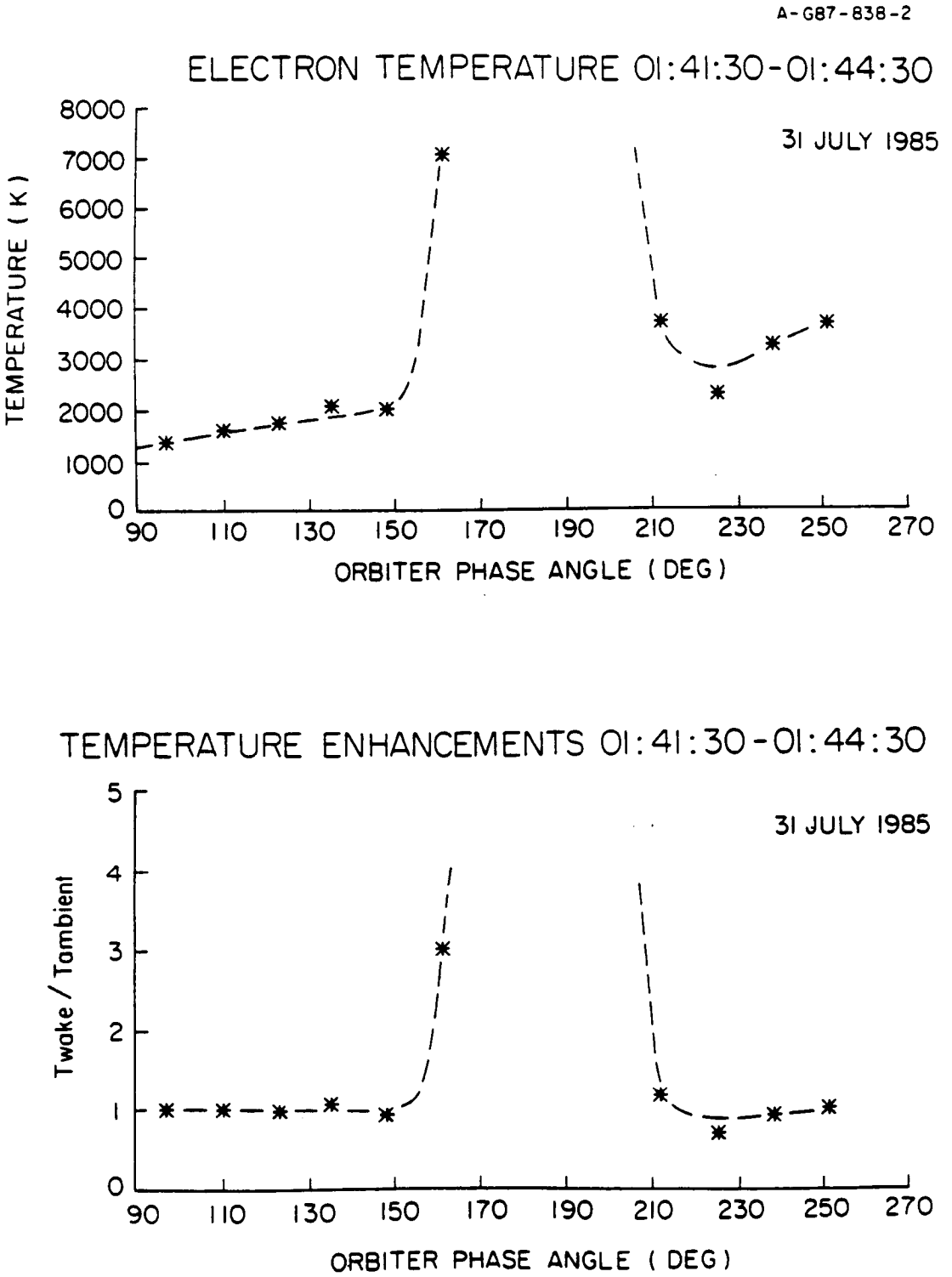

Figure 15. Electron temperature enhancements during near wake transit two.

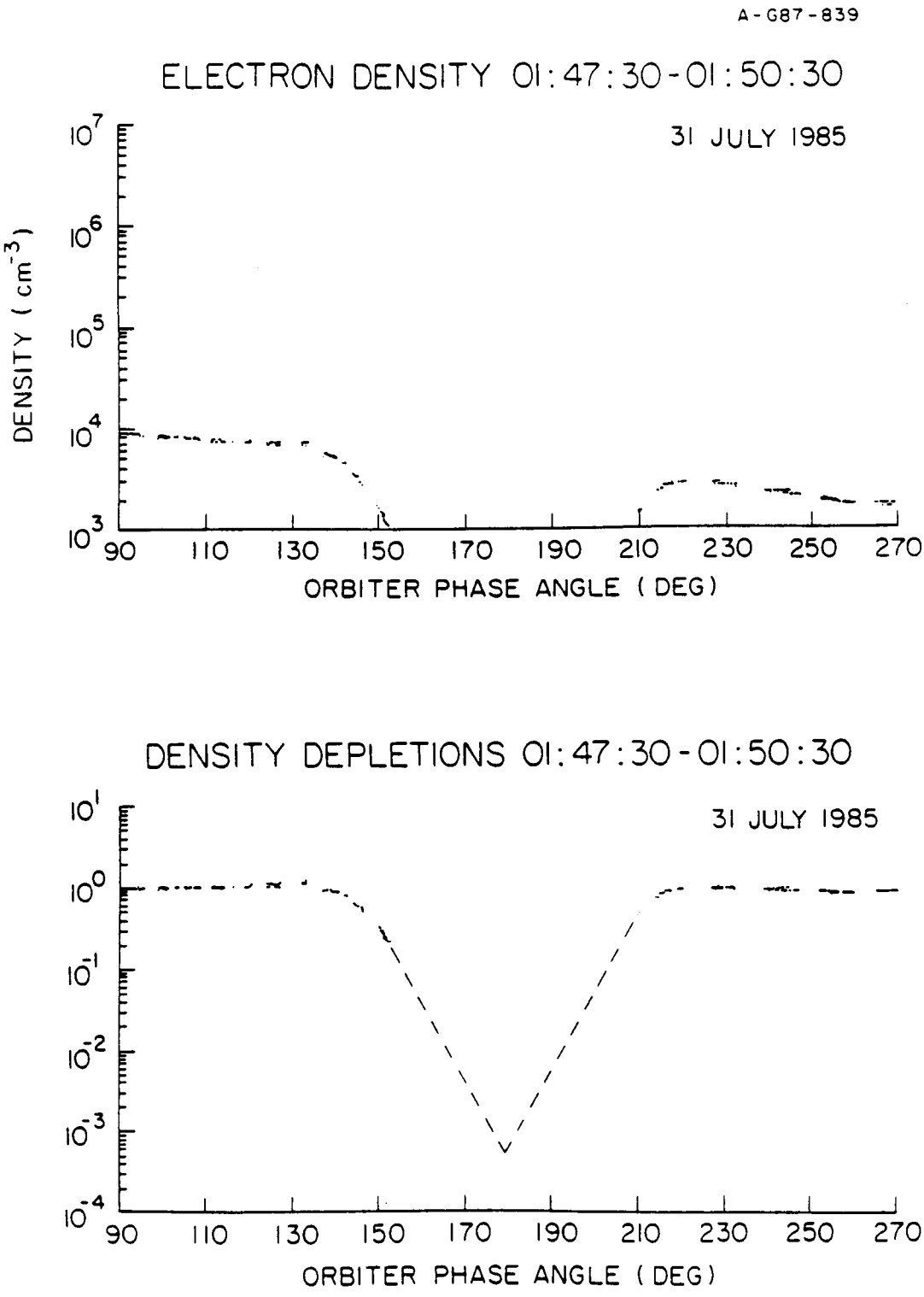

Figure 16. Electron density depletions during near wake transit three.

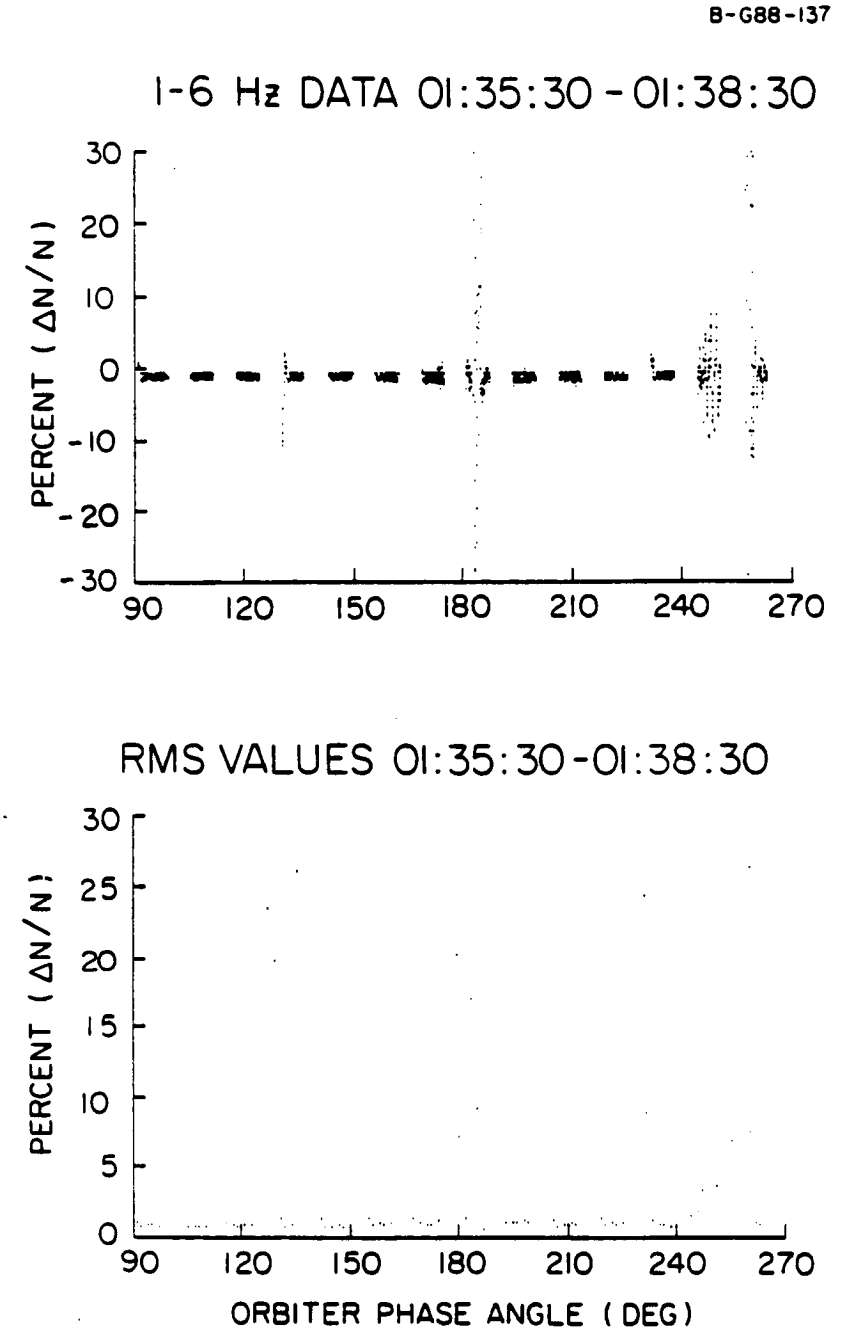

Figure 17. 1-6 Hz data during near wake transit one.

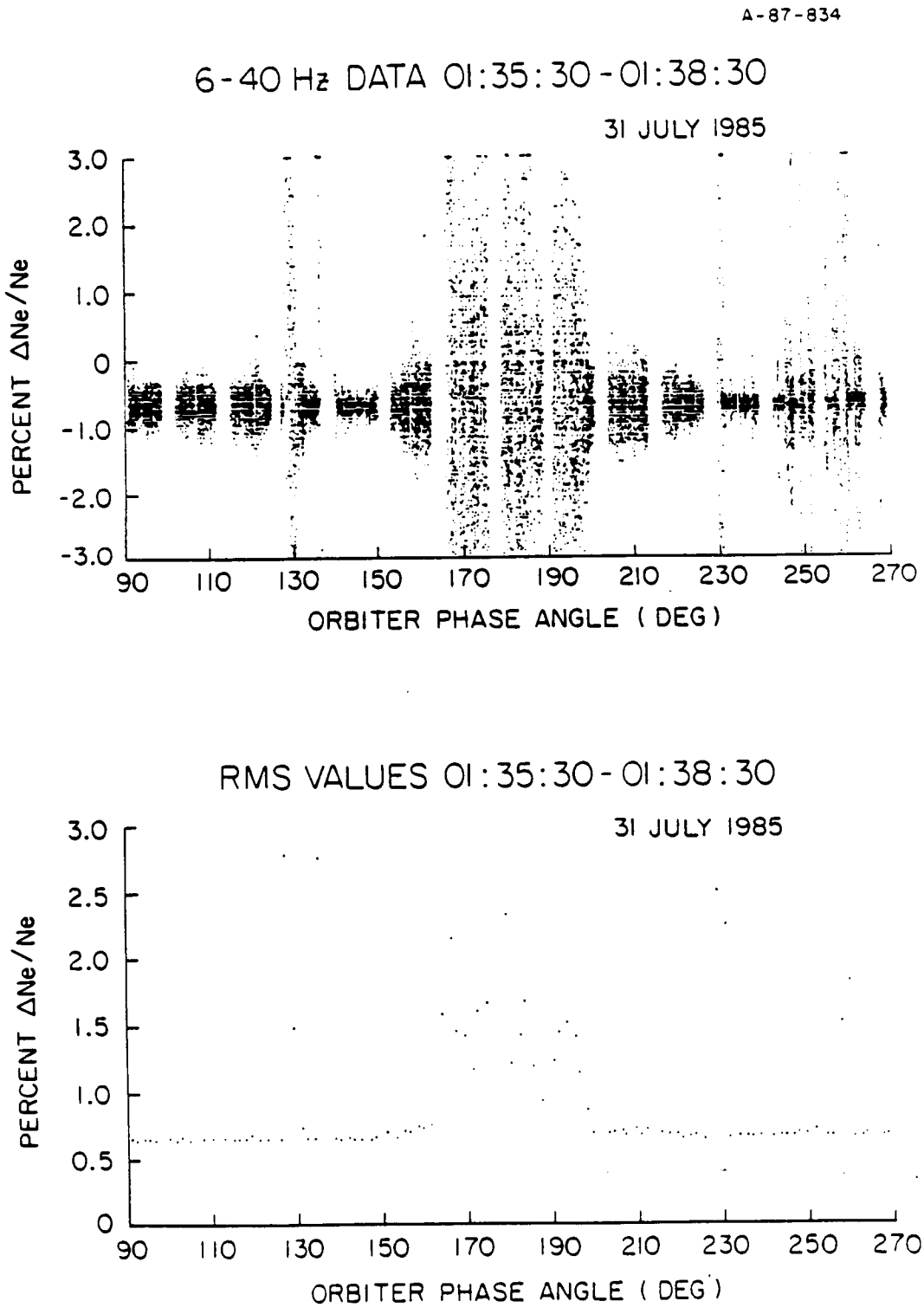

Figure 18. 6-40 Hz data during near wake transit one.

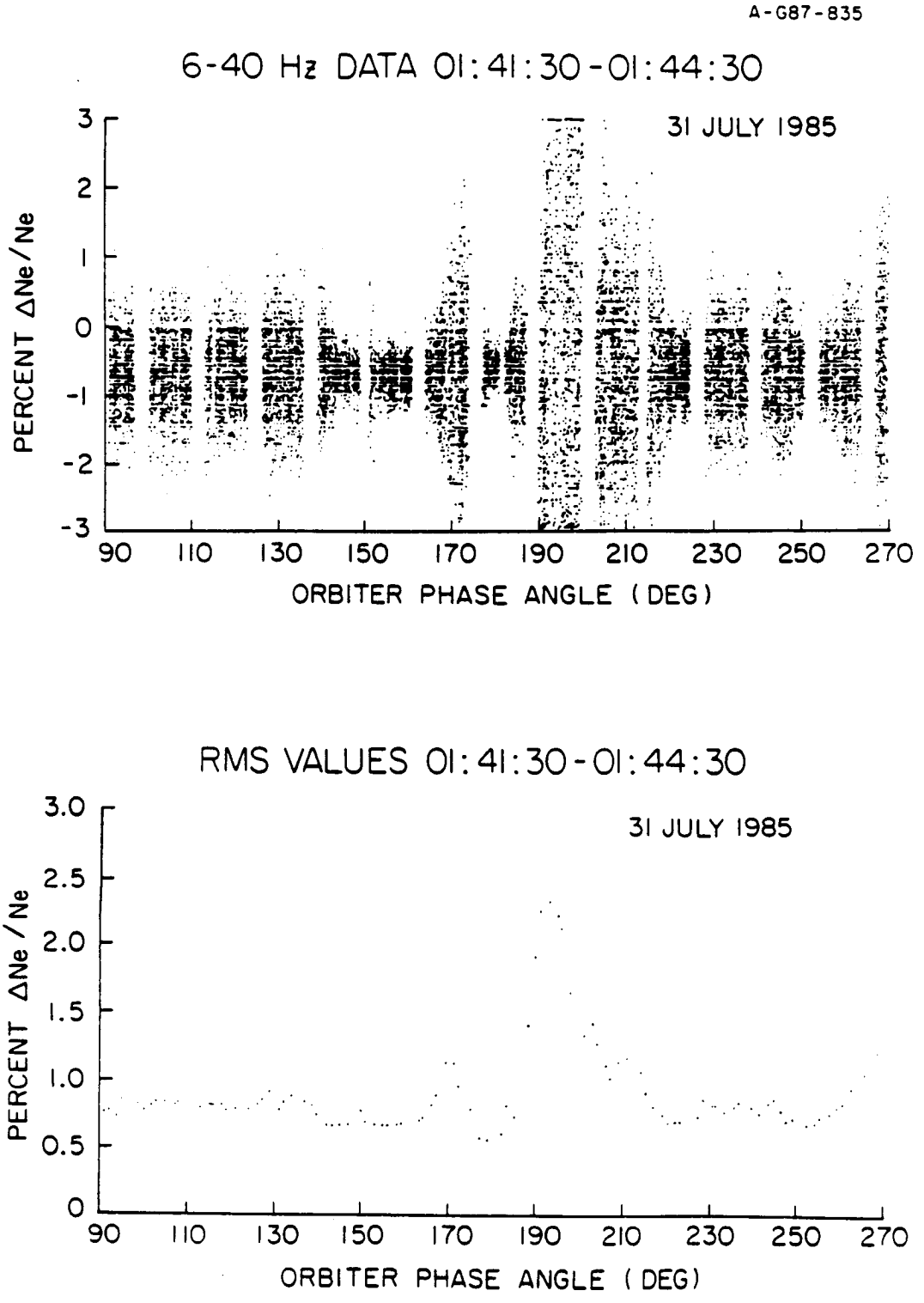

Figure 19. 6-40 Hz data during near wake transit two.

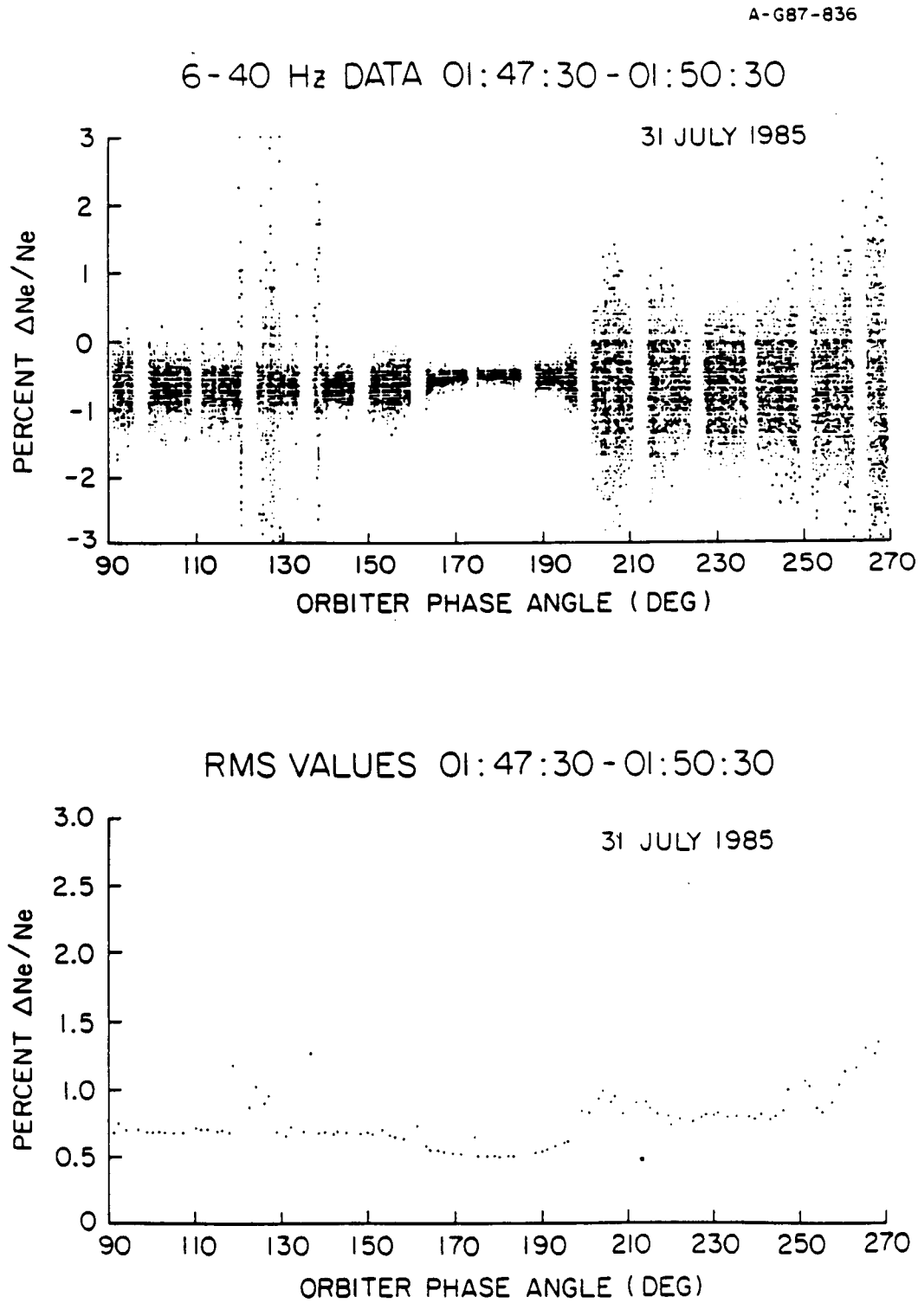

Figure 20. 6-40 Hz data during near wake transit three.

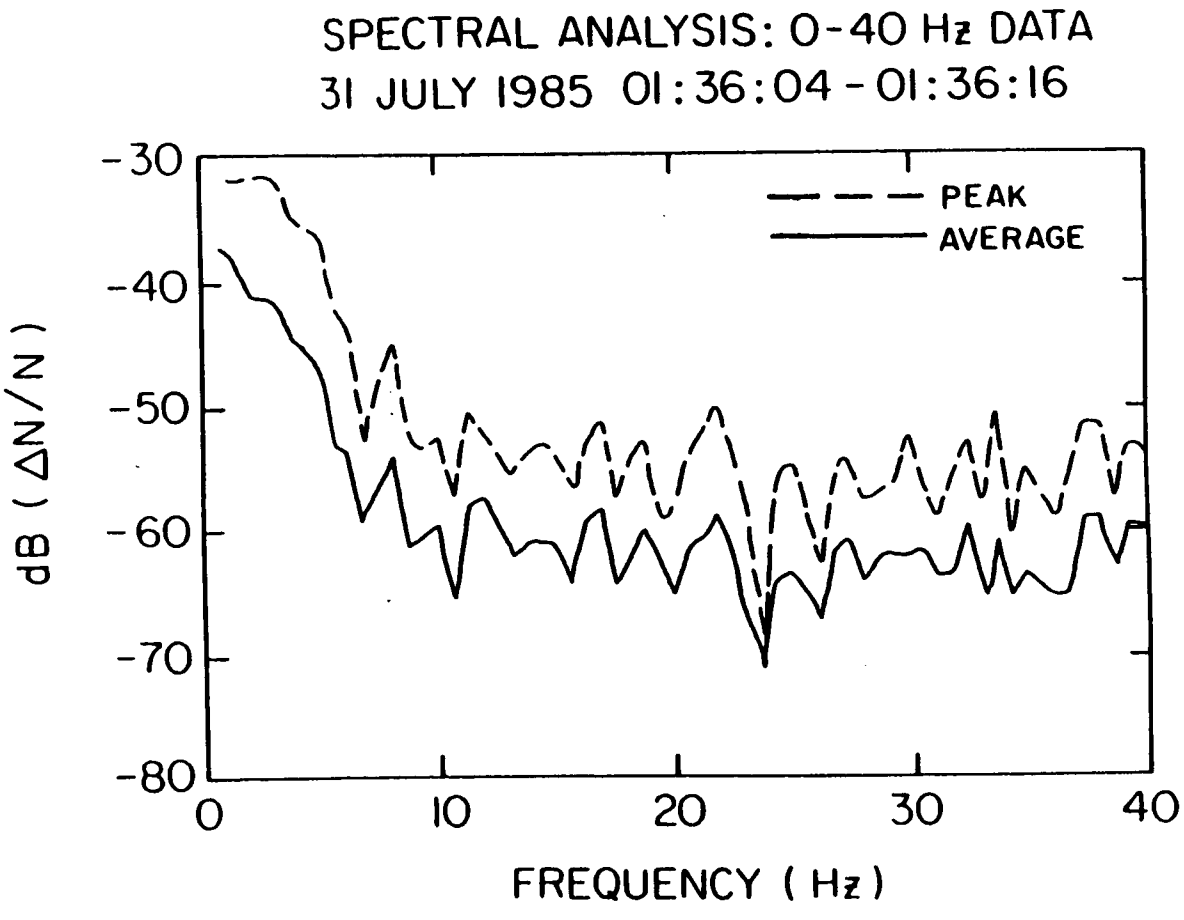

Figure 21. 0-40 Hz FFT data corresponding to orbiter phase angles $124^o - 136^o$.

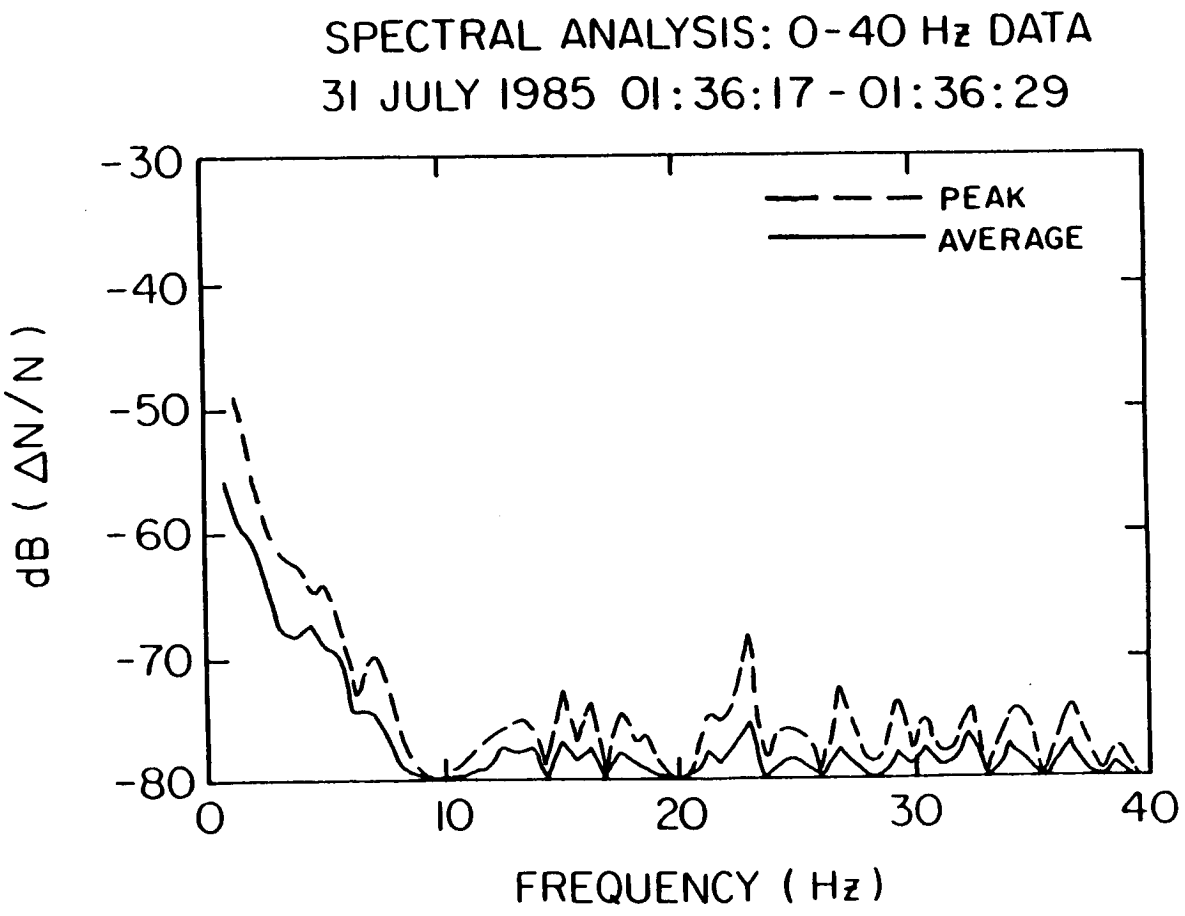

Figure 22. 0-40 Hz FFT data corresponding to orbiter phase angles 137° – 149°.

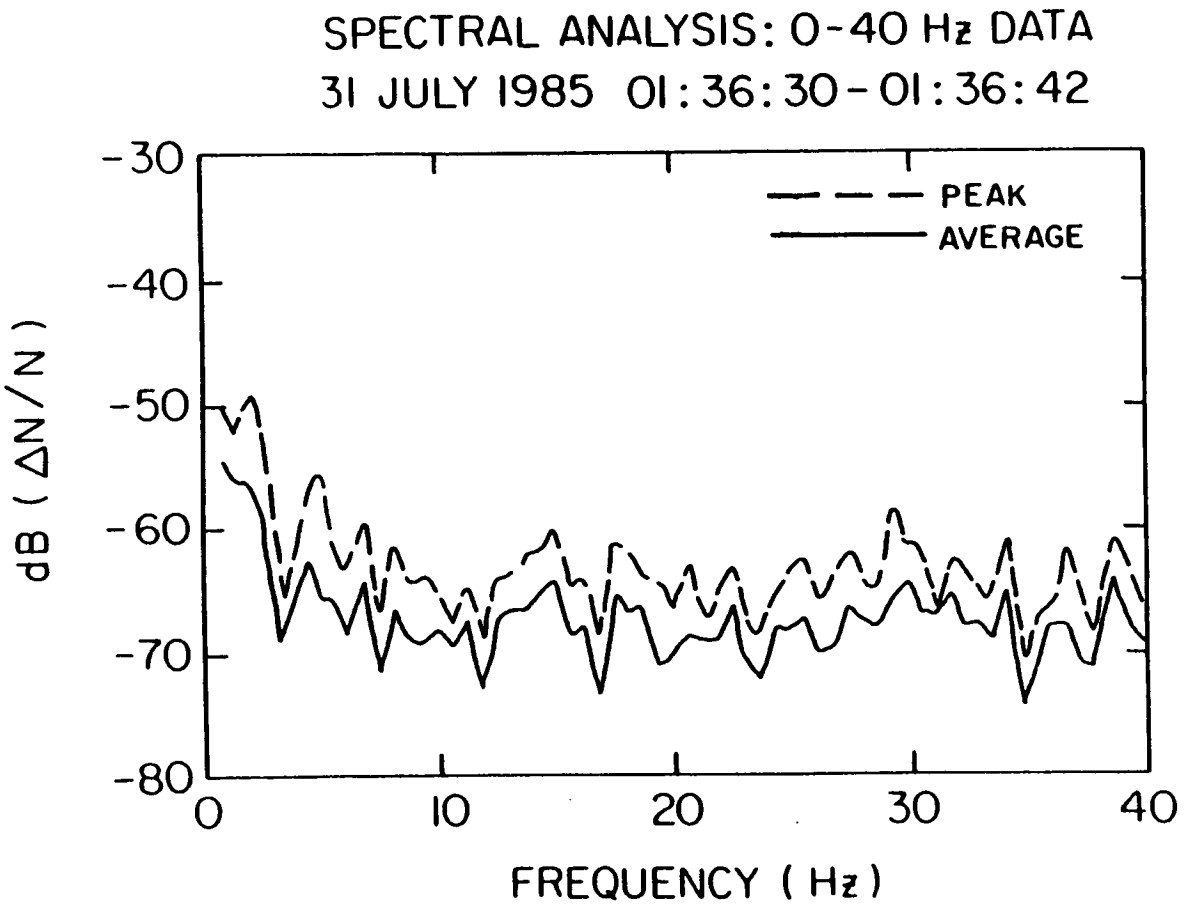

Figure 23. 0-40 Hz FFT data corresponding to orbiter phase angles $150^o - 162^o$.

A-G88-177

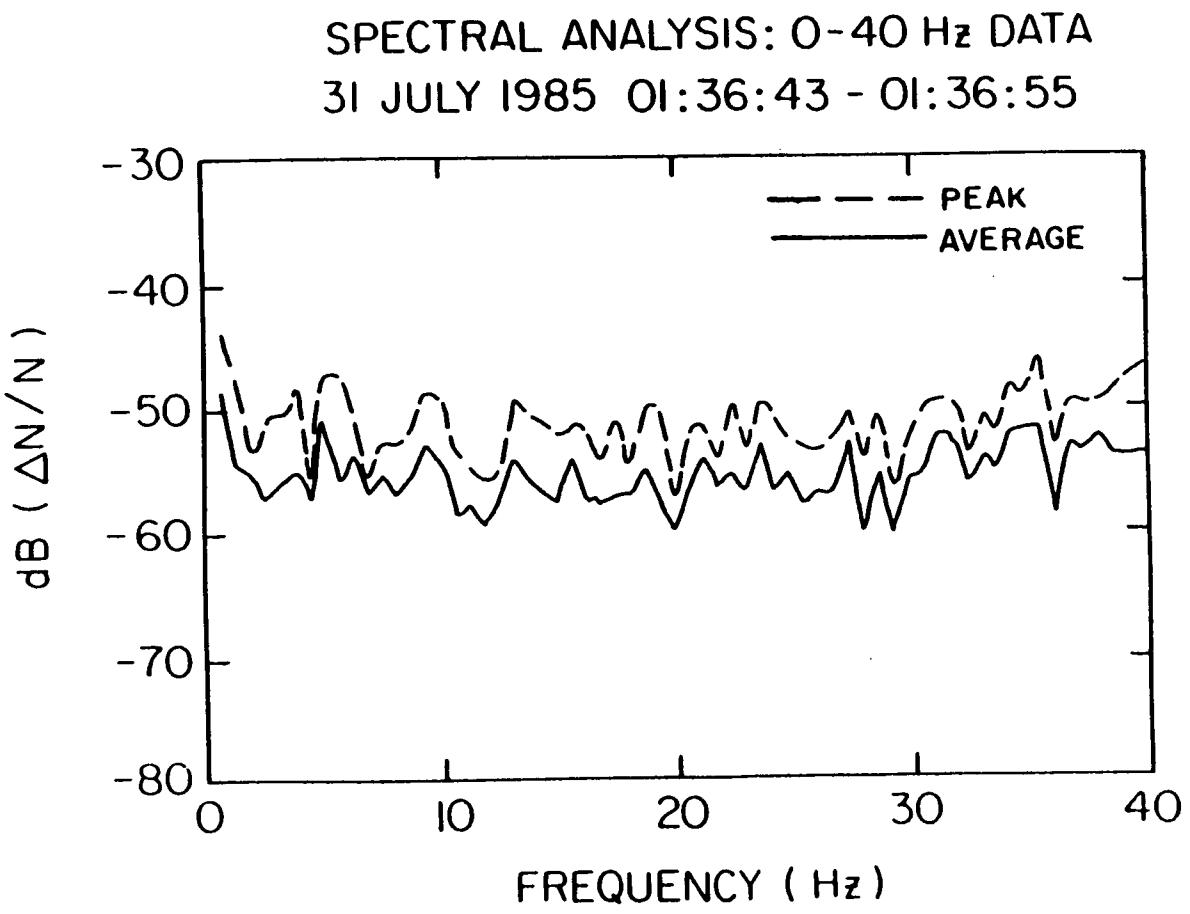

Figure 24. 0-40 Hz FFT data corresponding to orbiter phase angles $163^o - 175^o$.

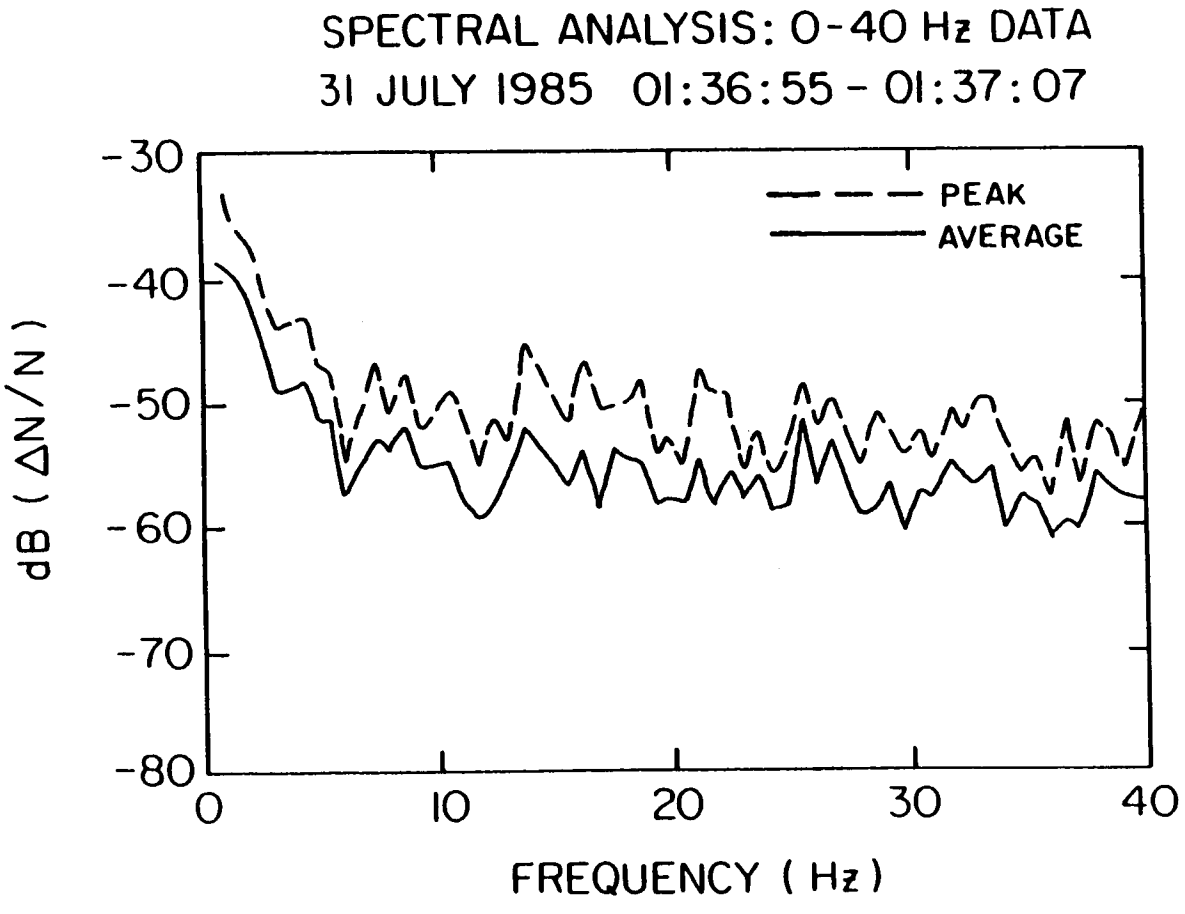

Figure 25. 0-40 Hz FFT data corresponding to orbiter phase angles 175° – 187°.

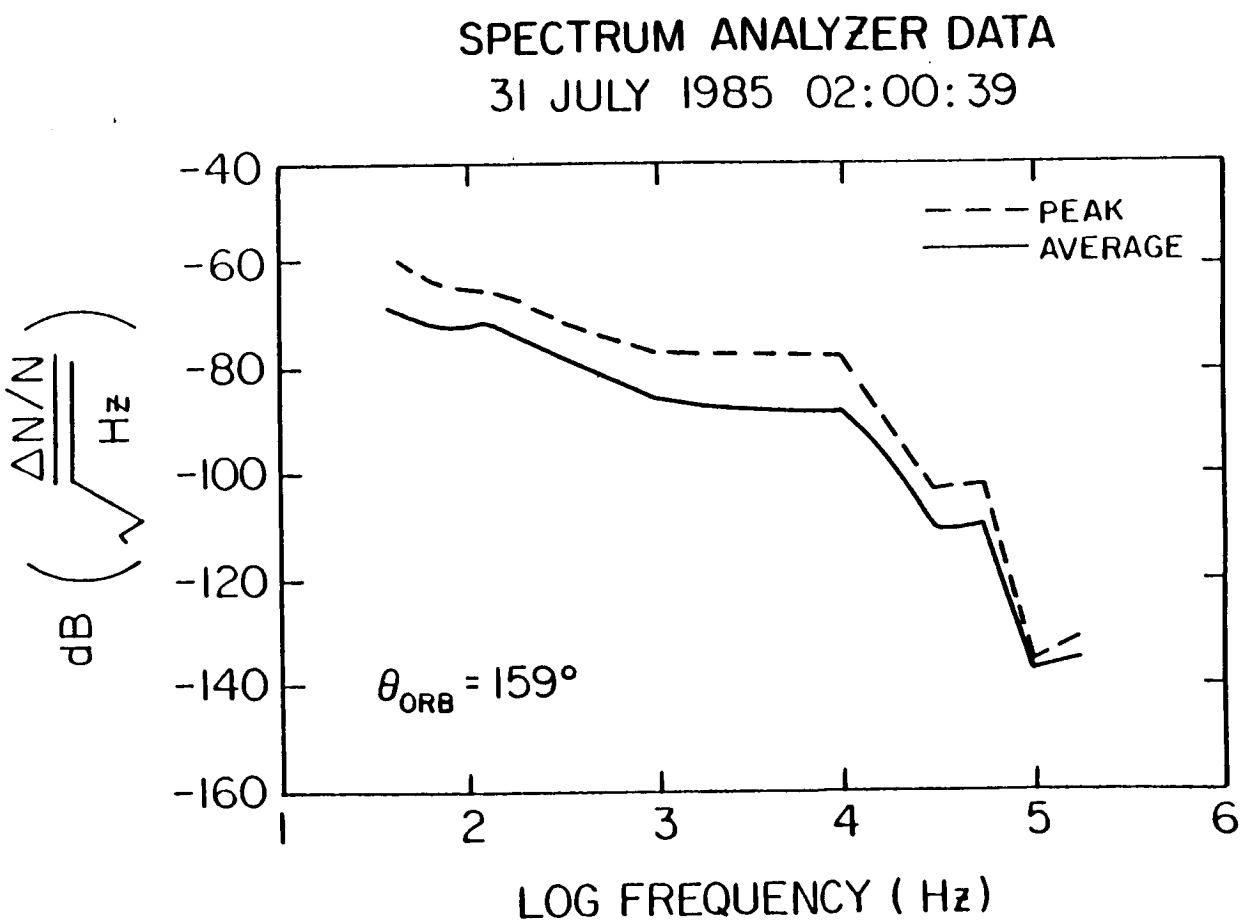

Figure 26. Near wake transit one spectral density data corresponding to orbiter phase angle 159°.

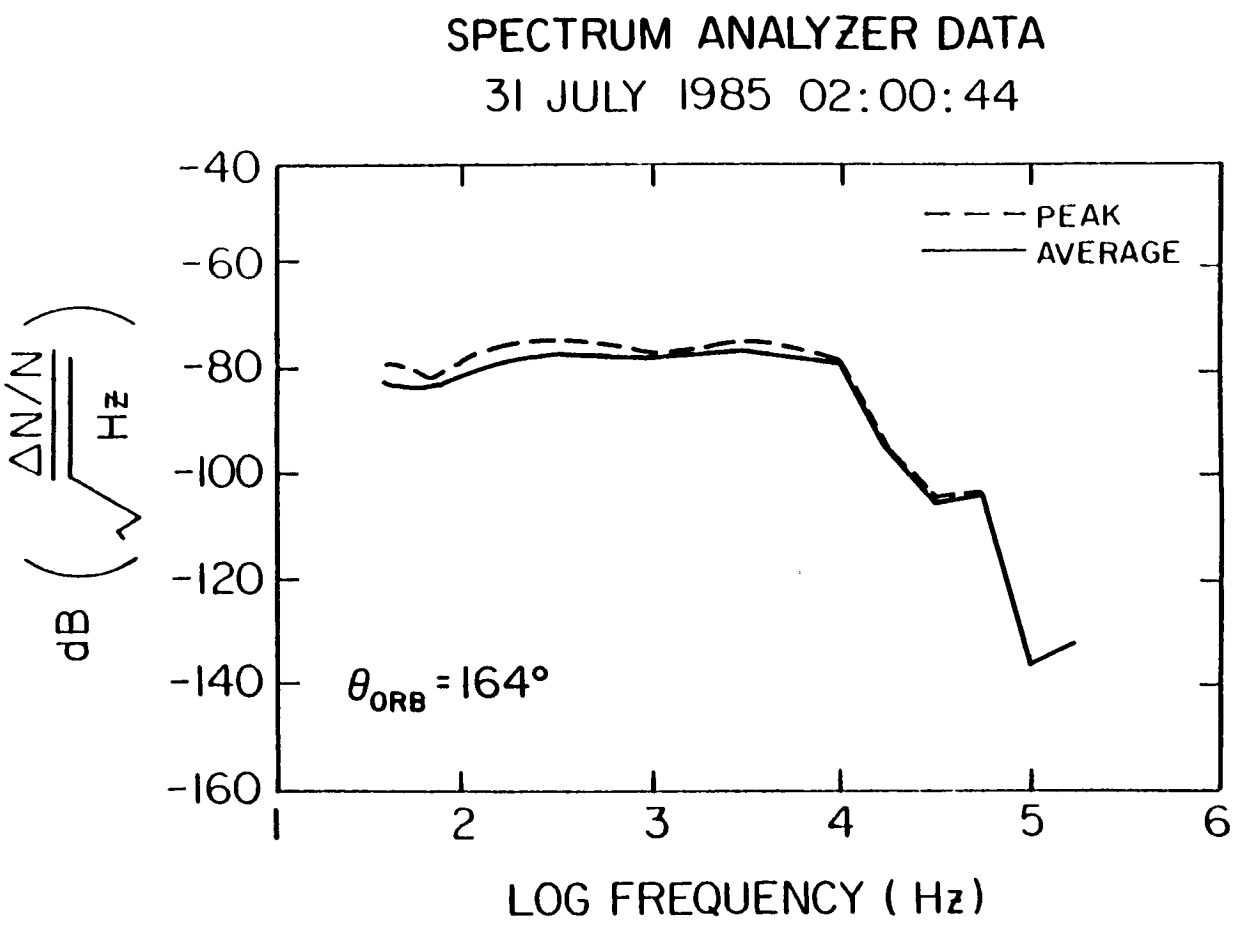

Figure 27. Near wake transit one spectral density data corresponding to orbiter phase angle 164°.

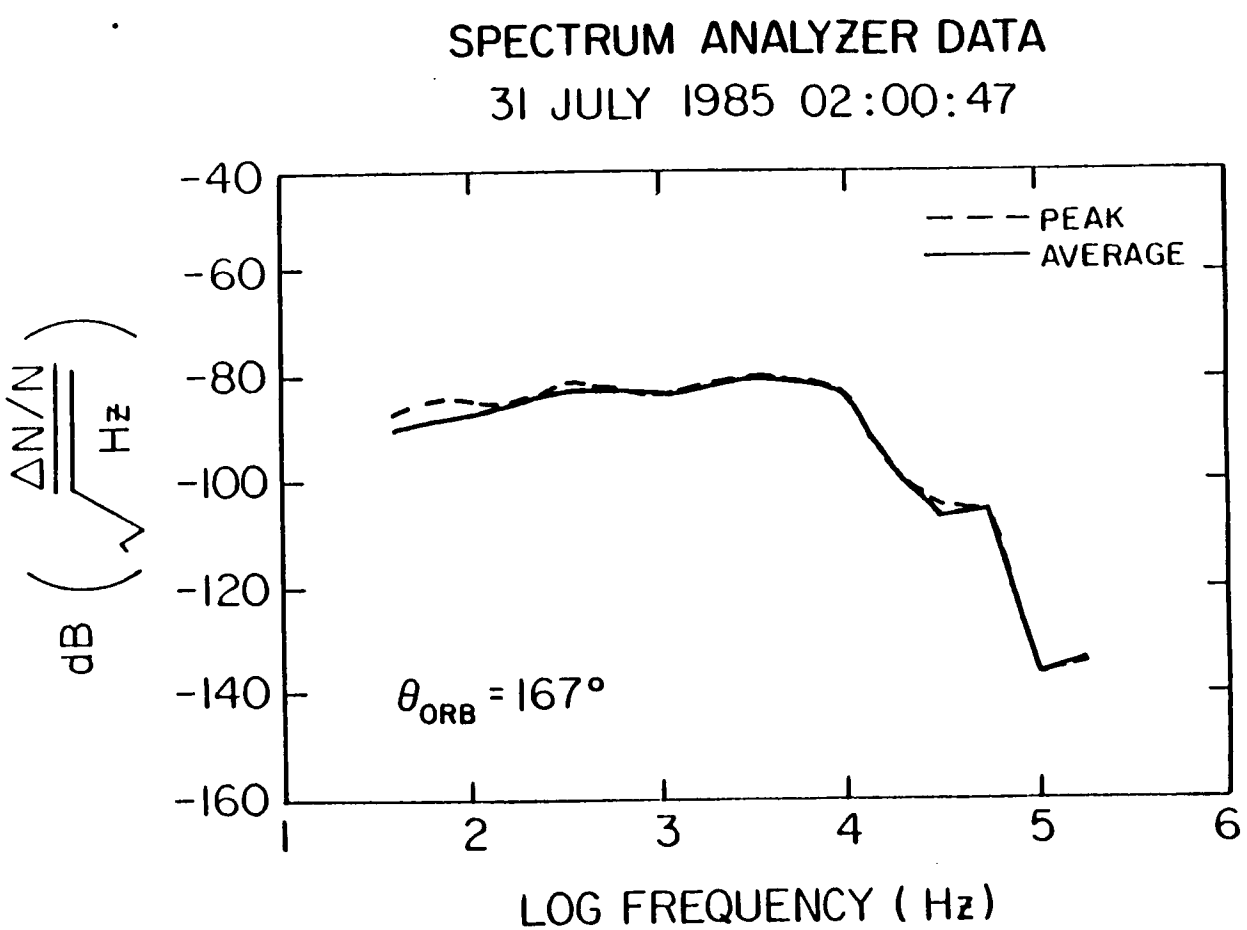

Figure 28. Near wake transit one spectral density data corresponding to orbiter phase angle 167°.

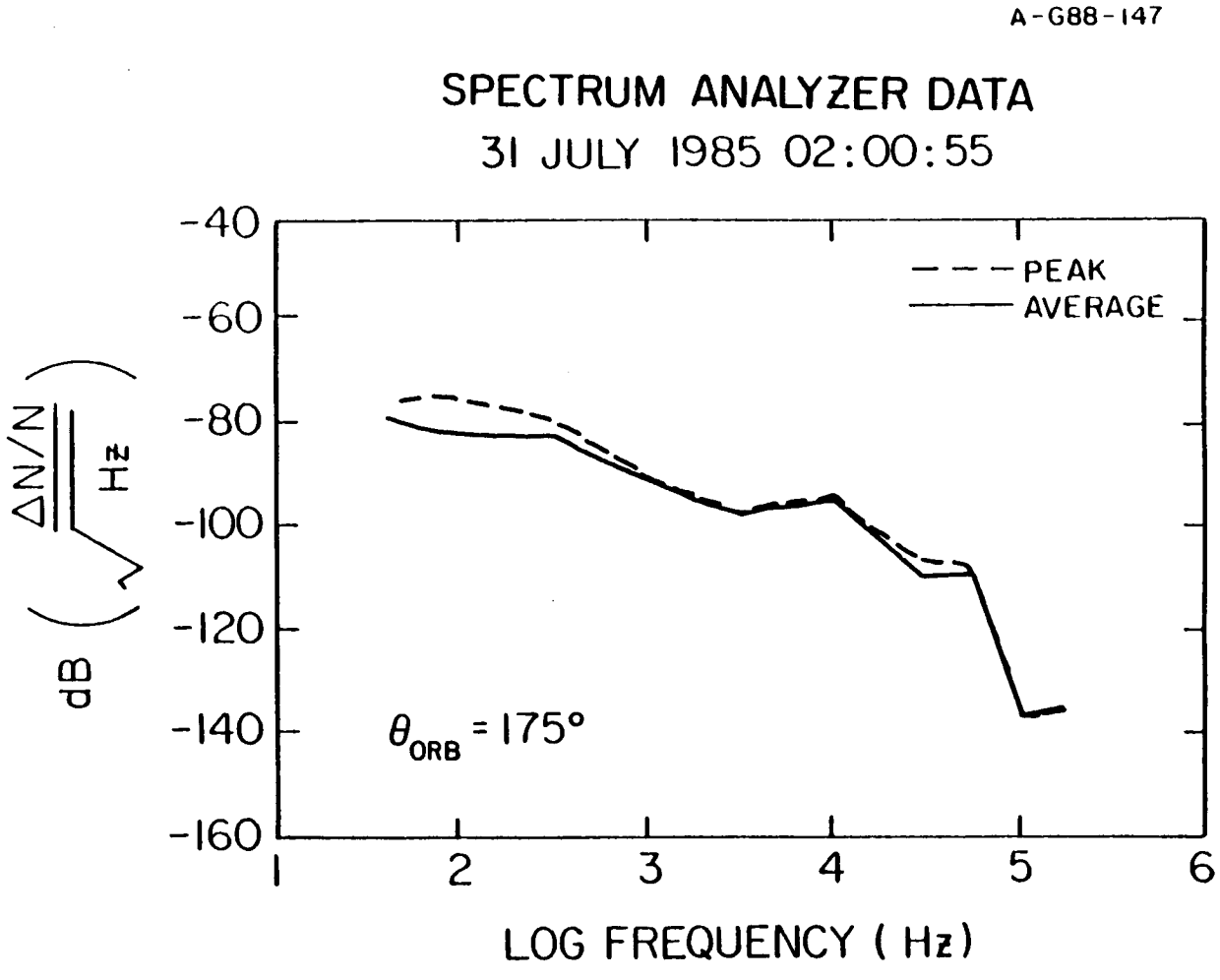

Figure 29. Near wake transit one spectral density data corresponding to orbiter phase angle 175°.

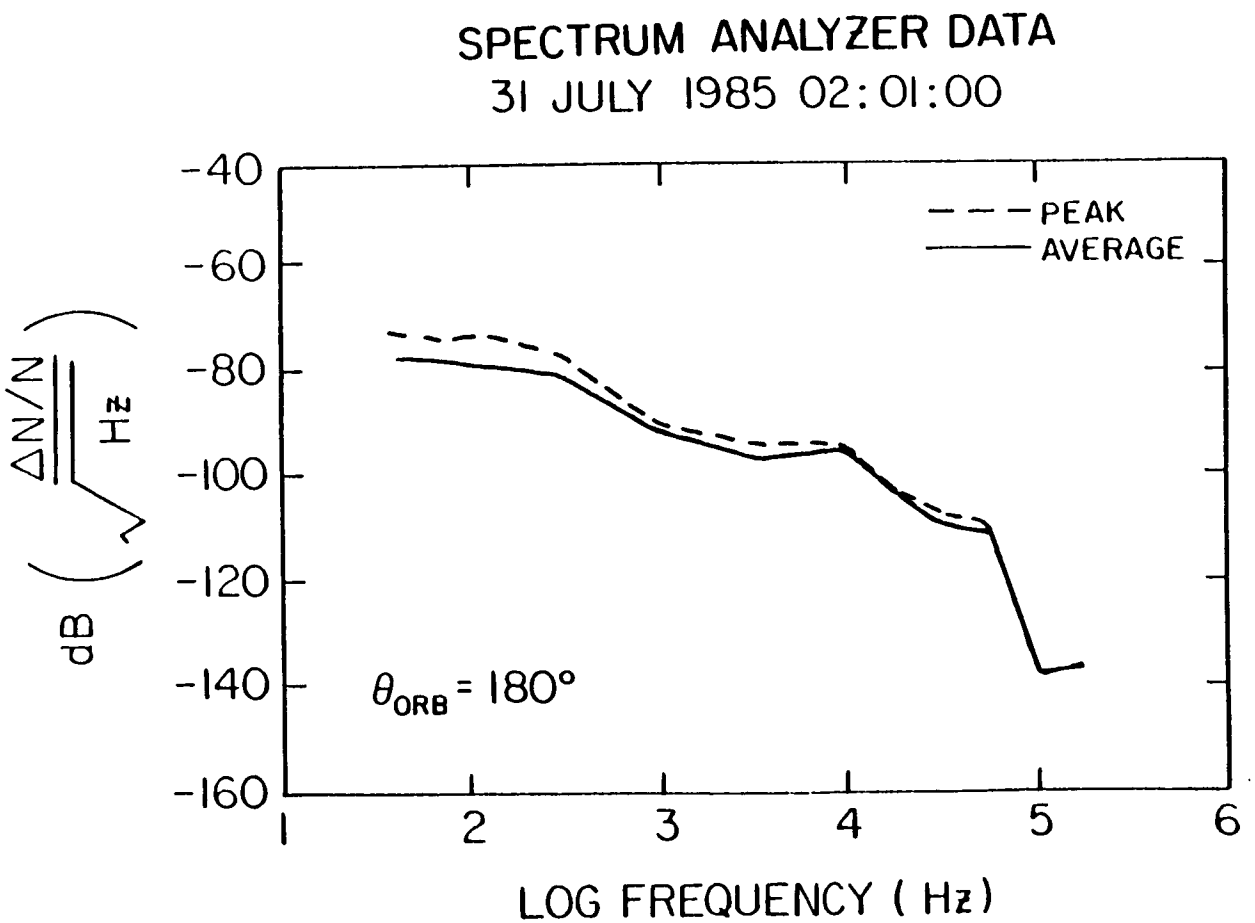

Figure 30. Near wake transit one spectral density data corresponding to orbiter phase angle 180°.

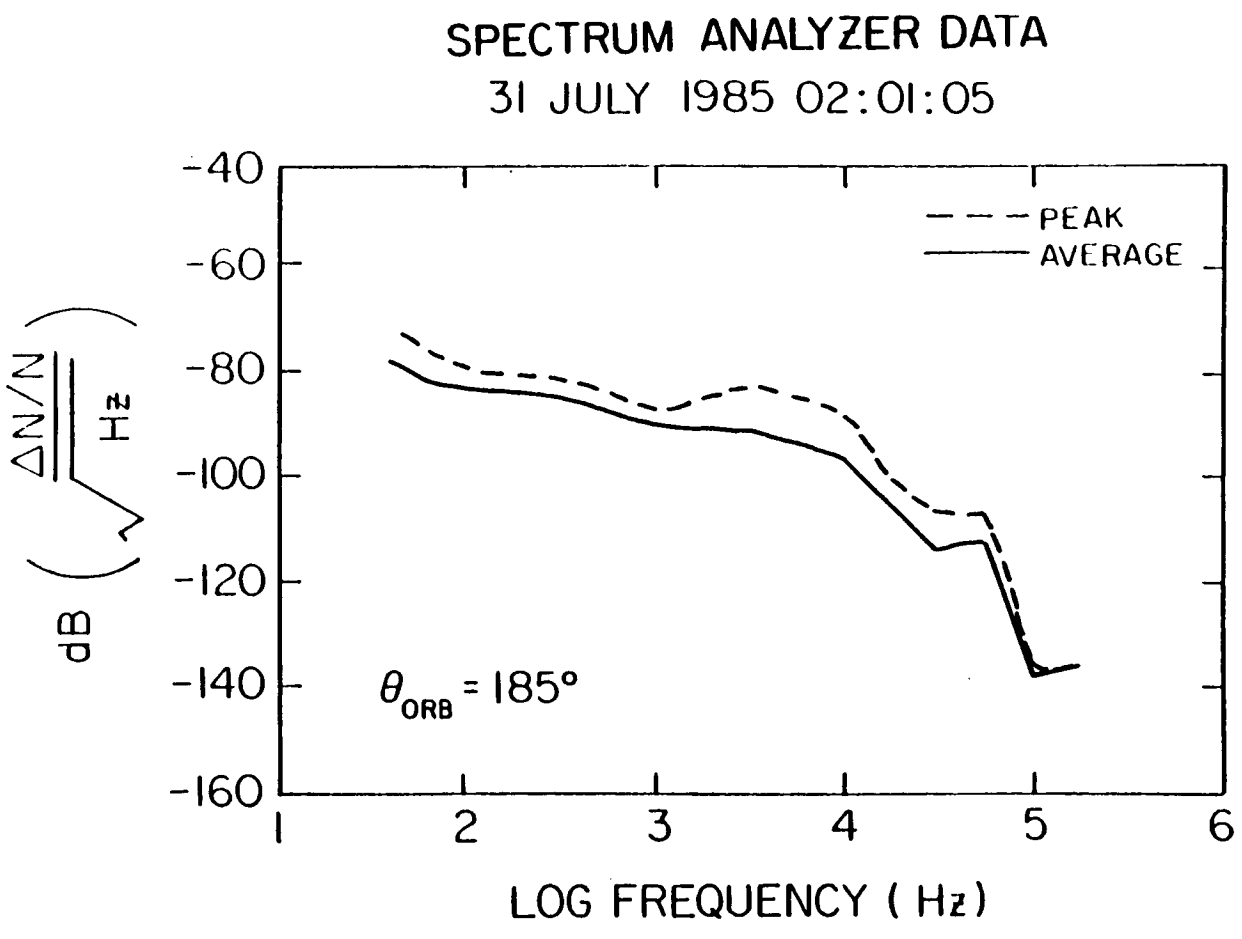

Figure 31. Near wake transit one spectral density data corresponding to orbiter phase angle 185°.

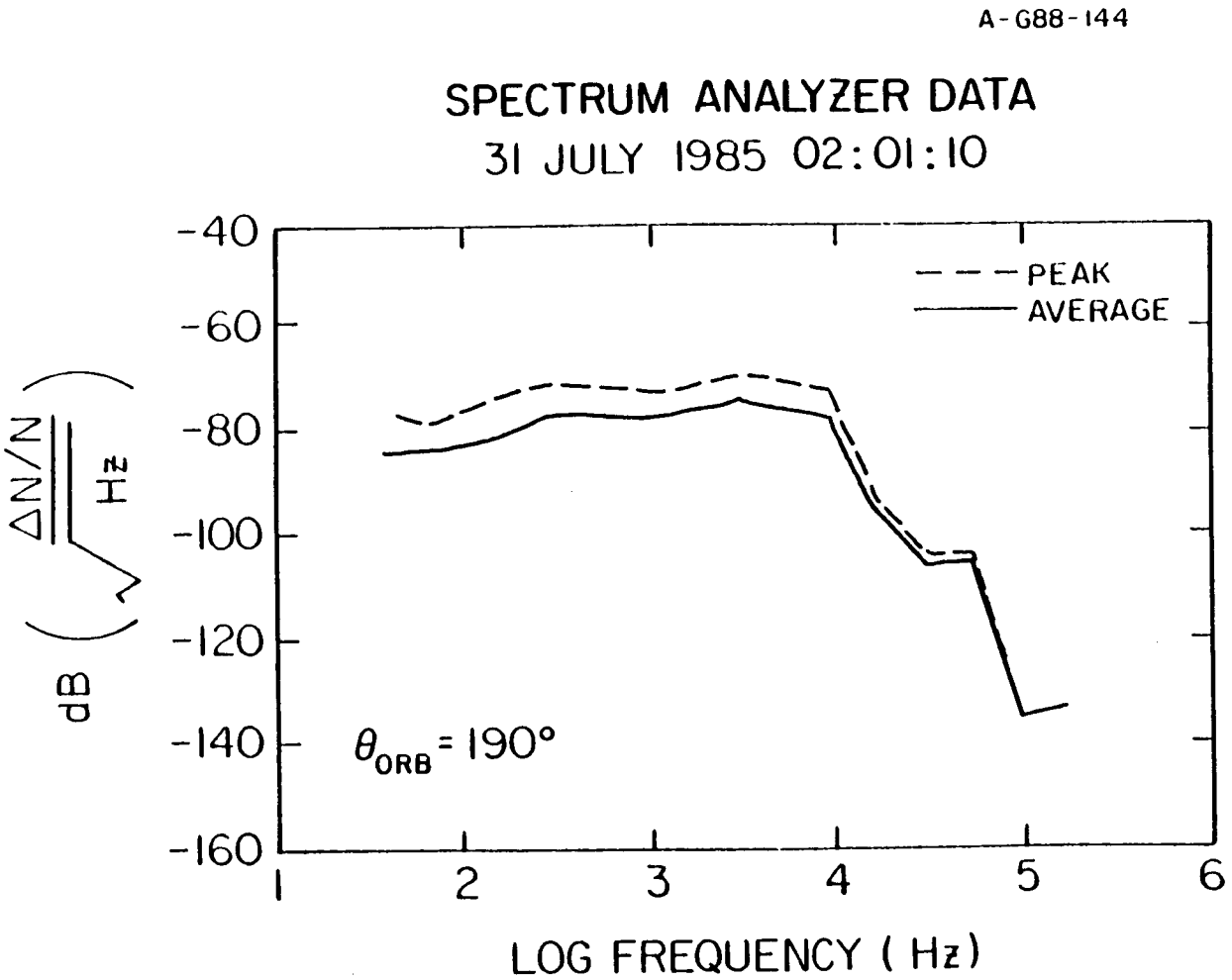

Figure 32. Near wake transit one spectral density data corresponding to orbiter phase angle 190°.

A-G88-143

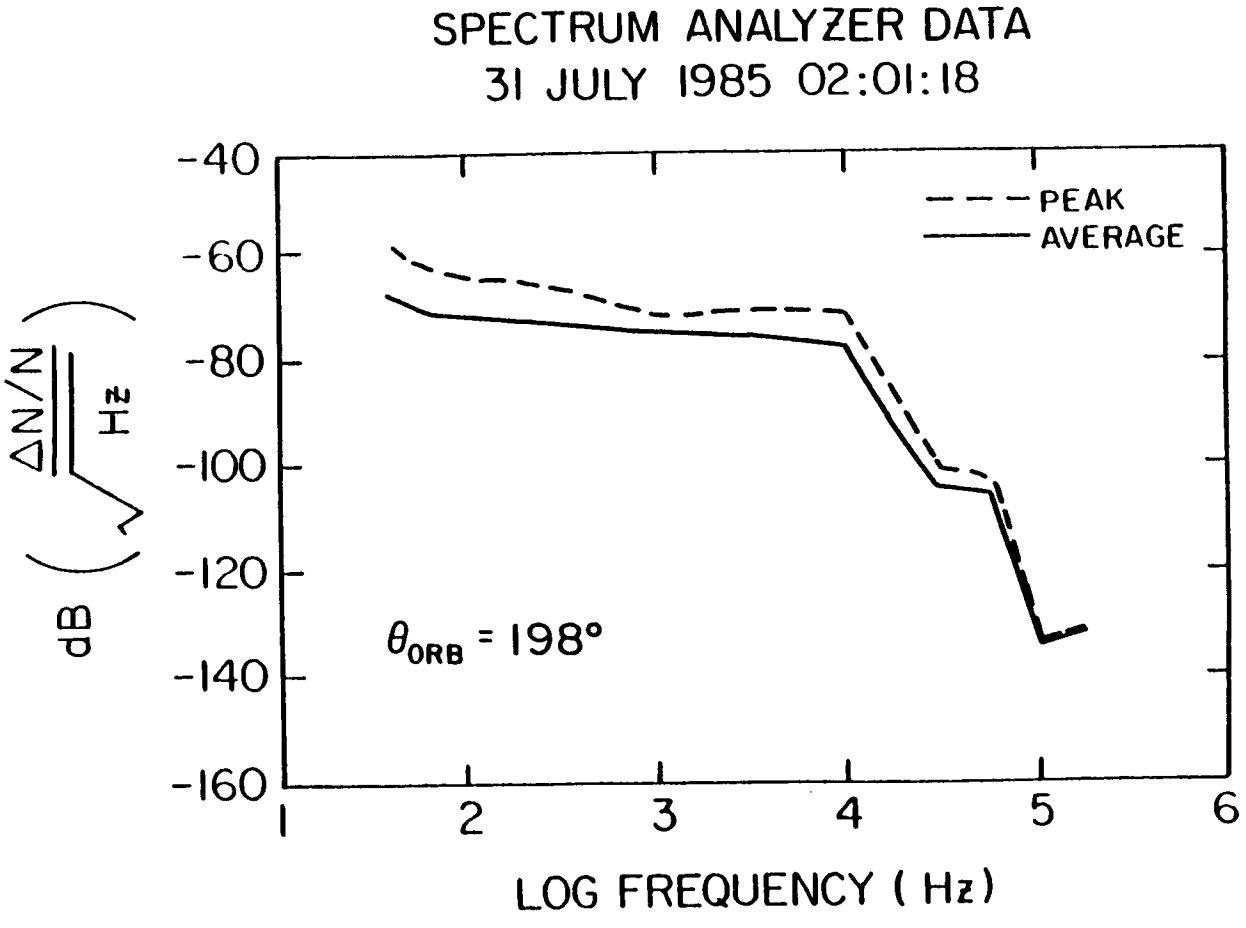

Figure 33. Near wake transit one spectral density data corresponding to orbiter phase angle 198°.

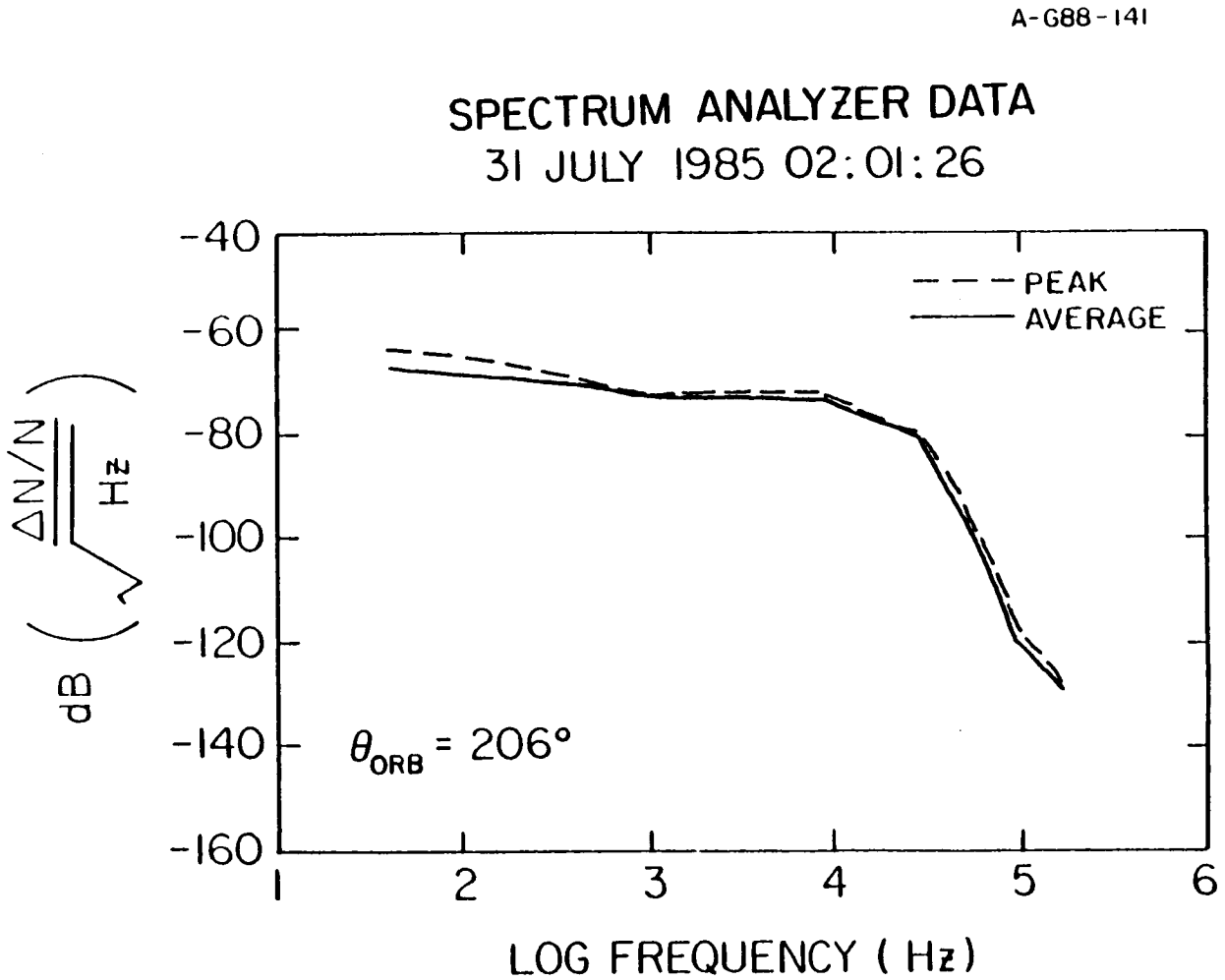

Figure 34. Near wake transit one spectral density data corresponding to orbiter phase angle 206°.

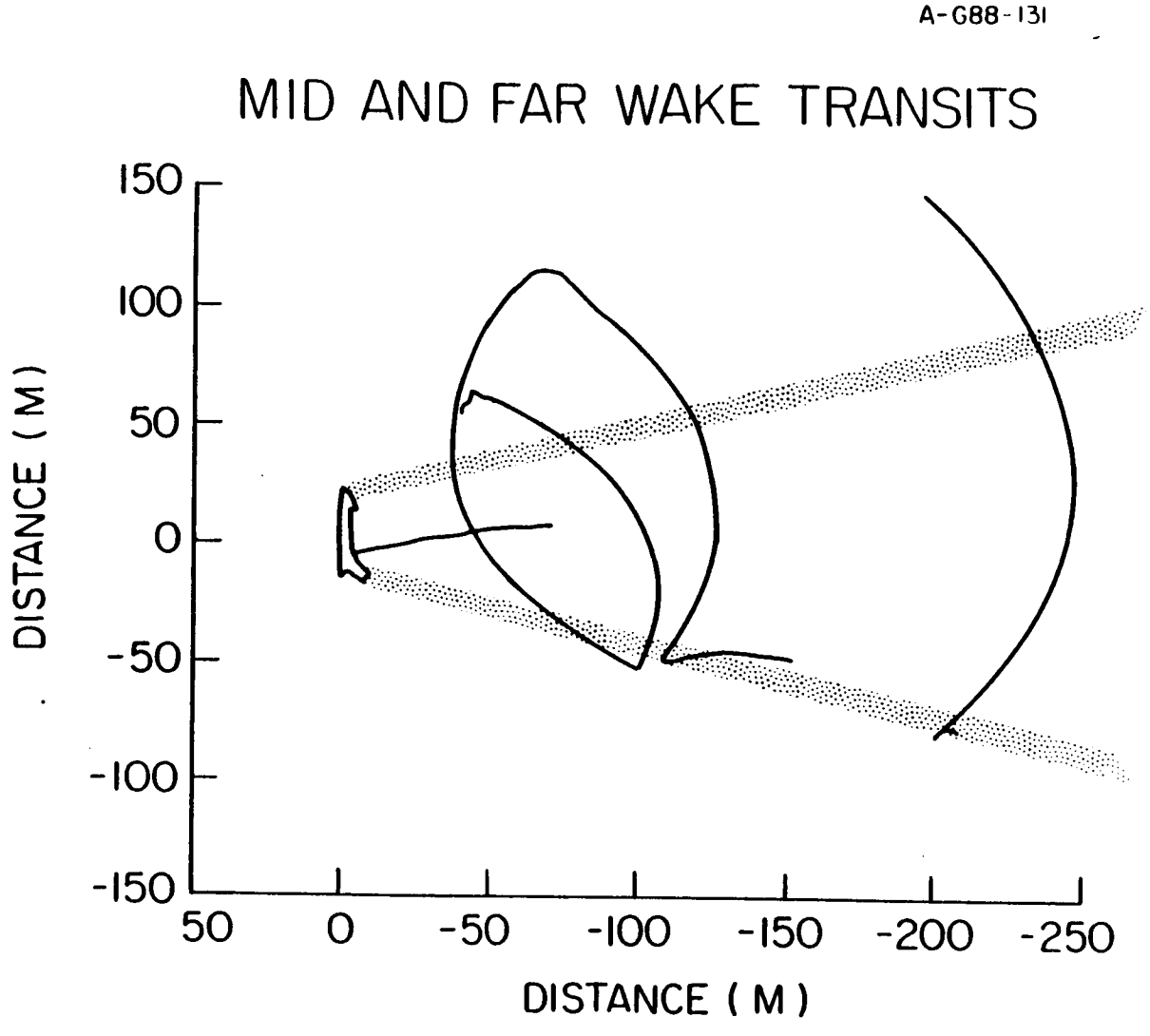

Figure 35. Mid and Far wake transits.

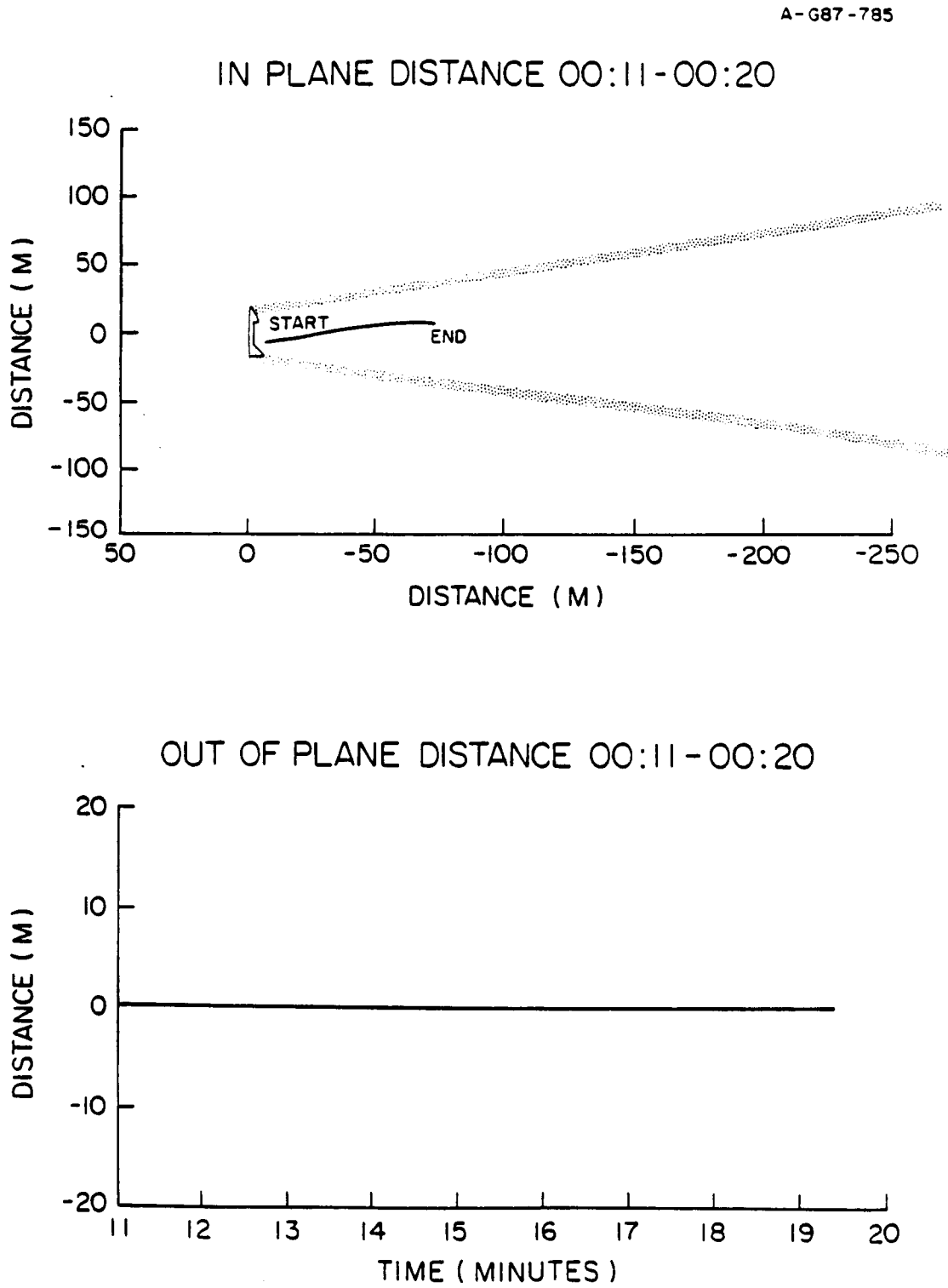

Figure 36. Spatial relationship between the orbiter and the PDP during backaway.

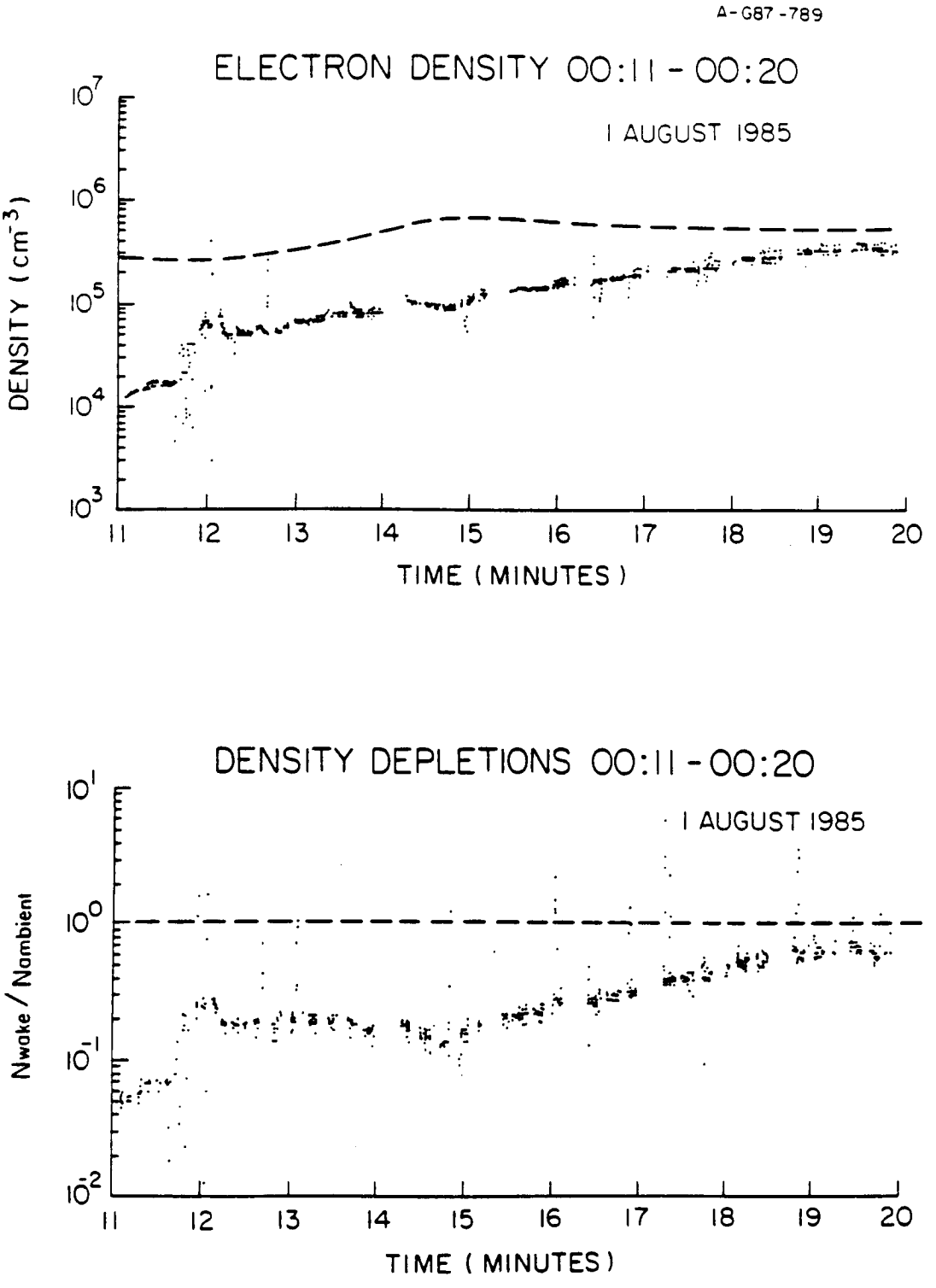

Figure 37. Electron density depletions during backaway.

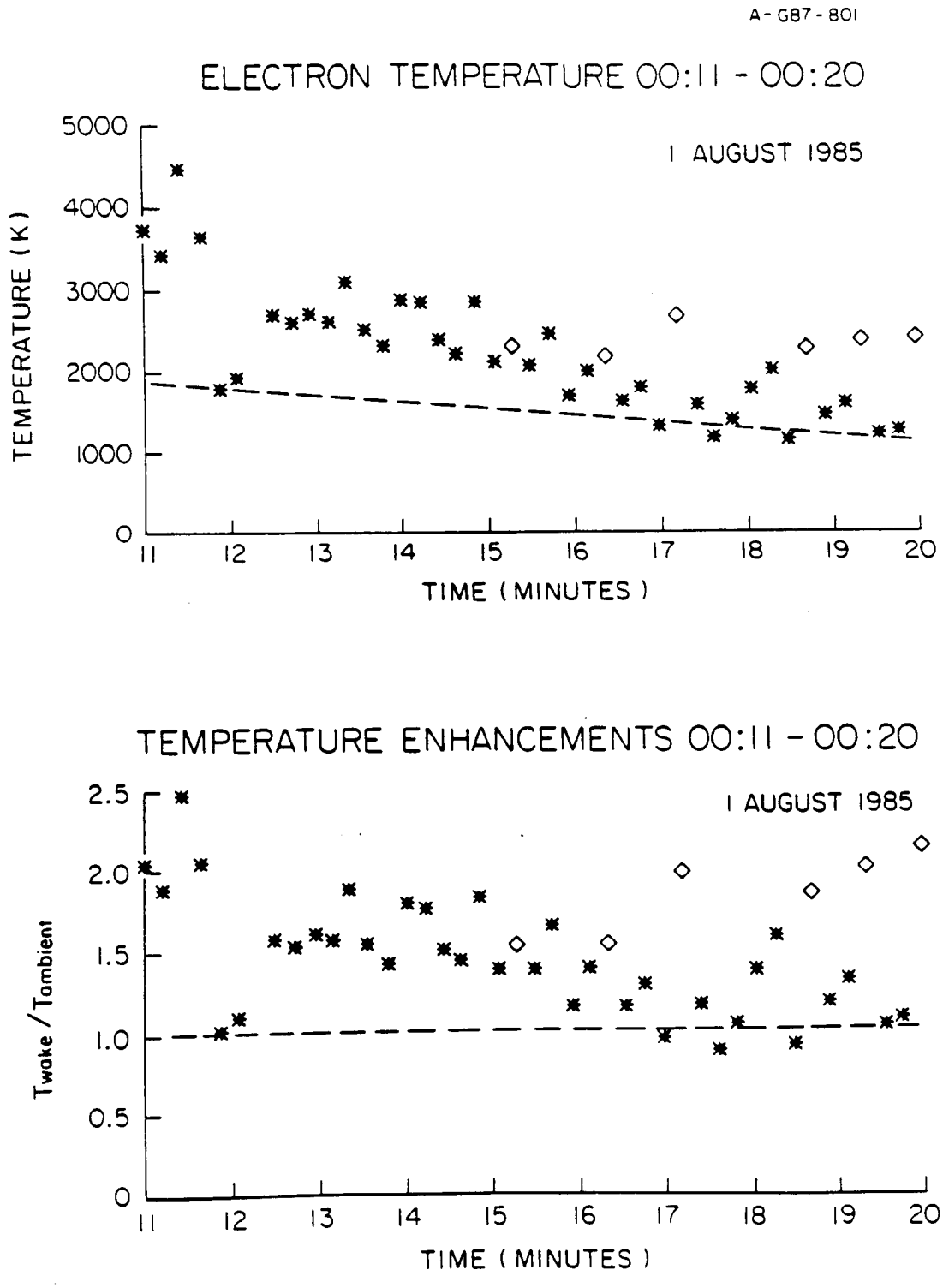

Figure 38. Electron temperature enhancements during backaway.

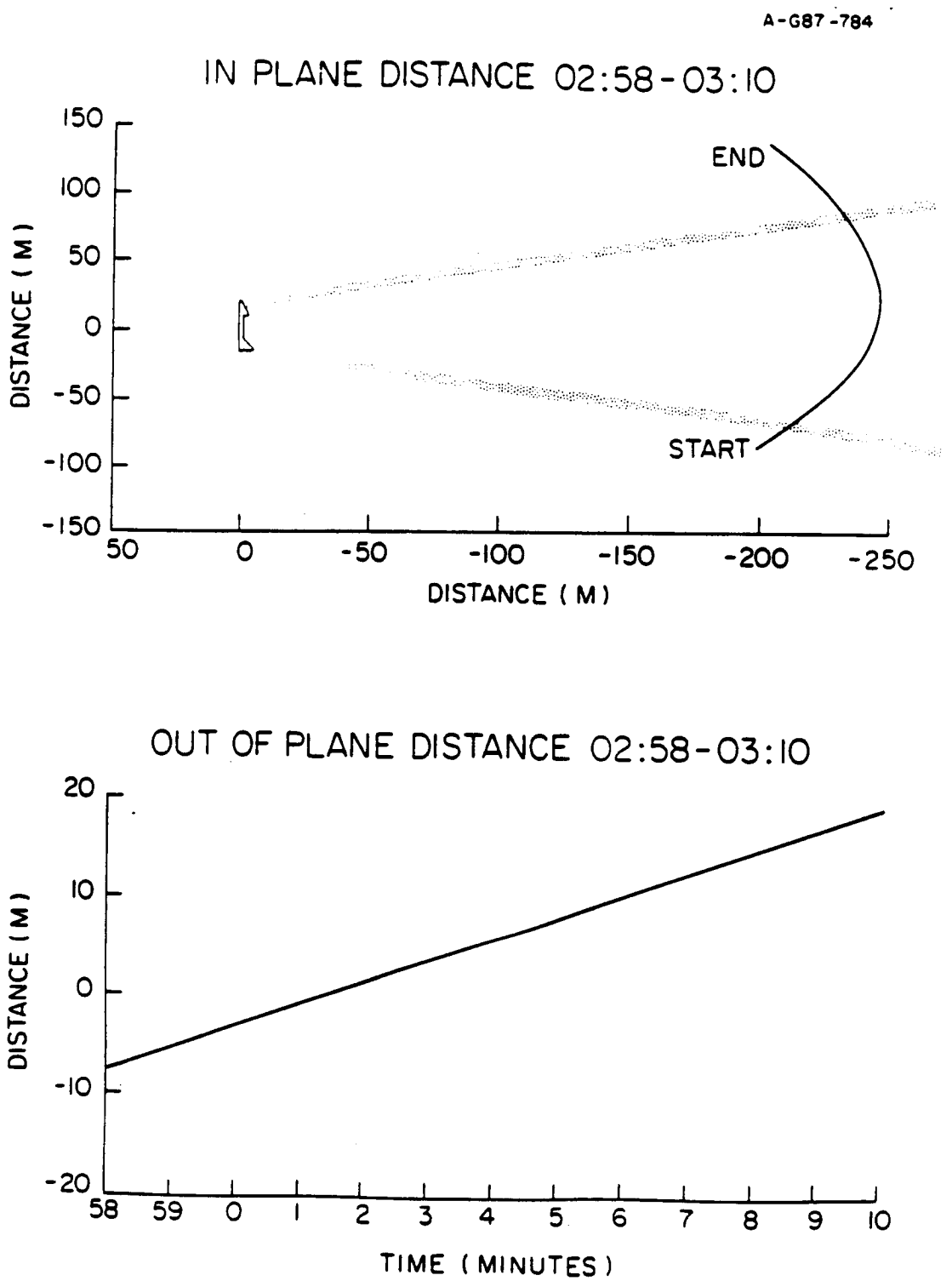

Figure 39. Spatial relationship between the orbiter and the PDP during far wake transit one.

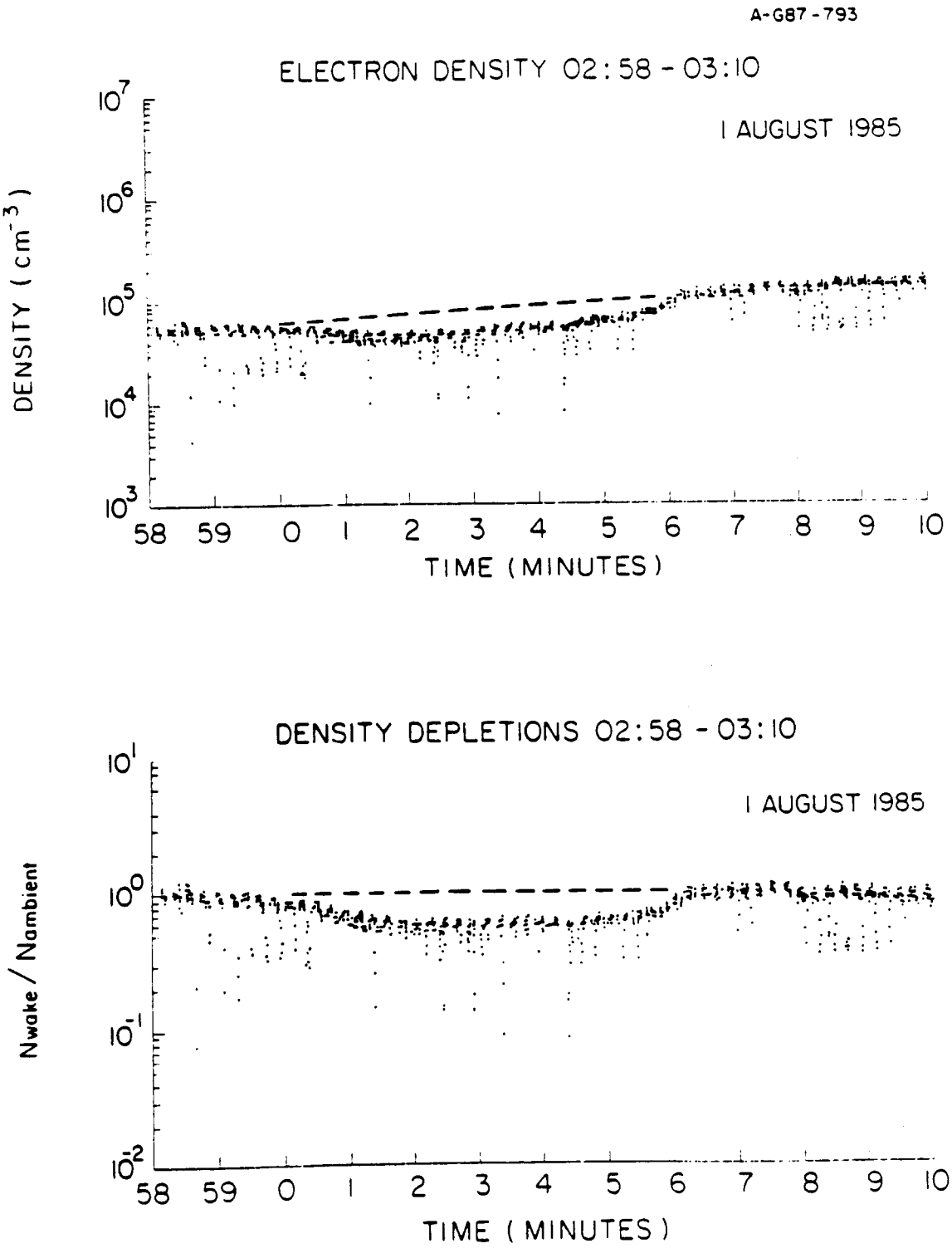

Figure 40. Electron density depletions during far wake transit one.

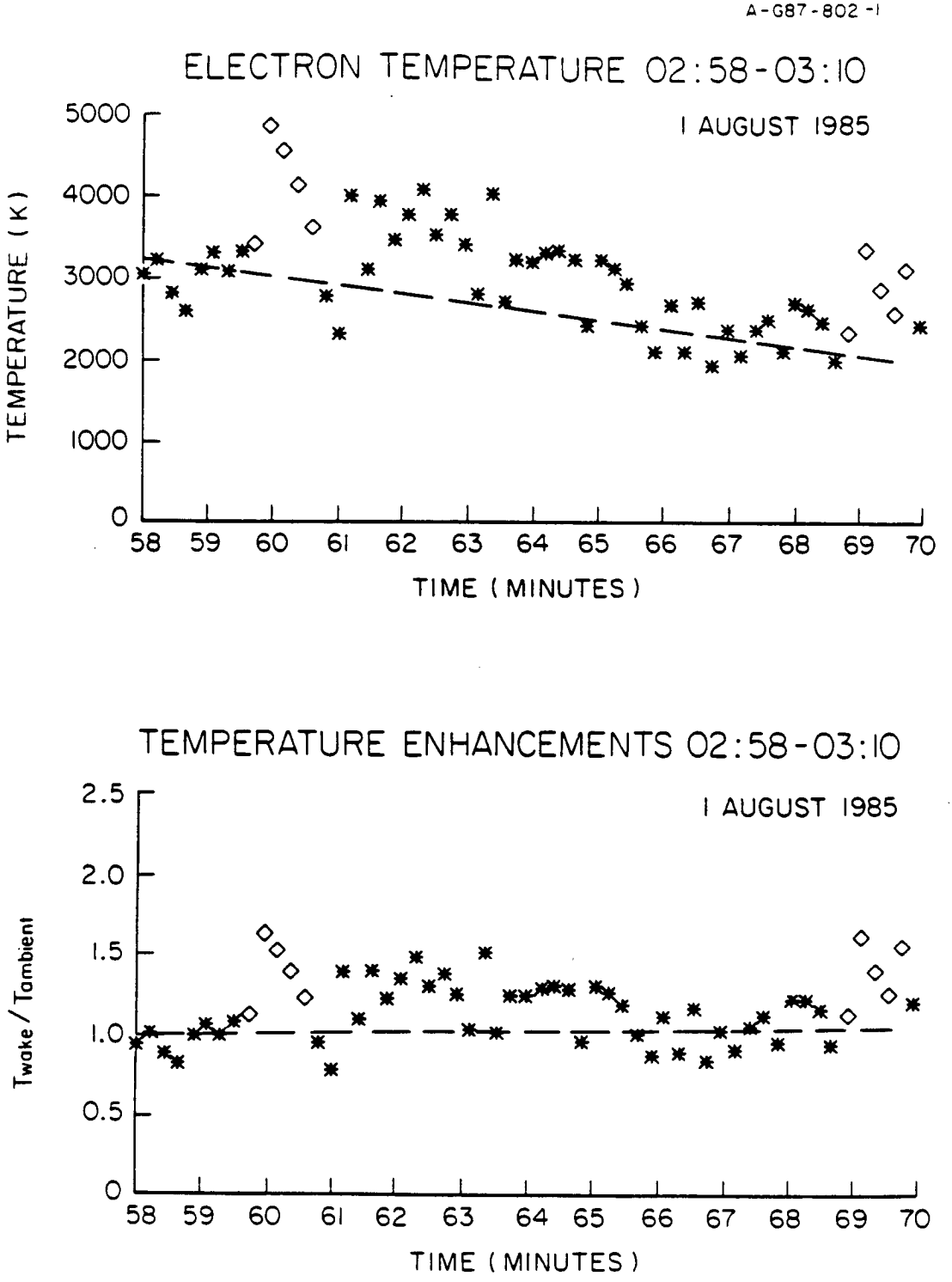

Figure 41. Electron temperature enhancements during far wake transit one.

A-G87-786

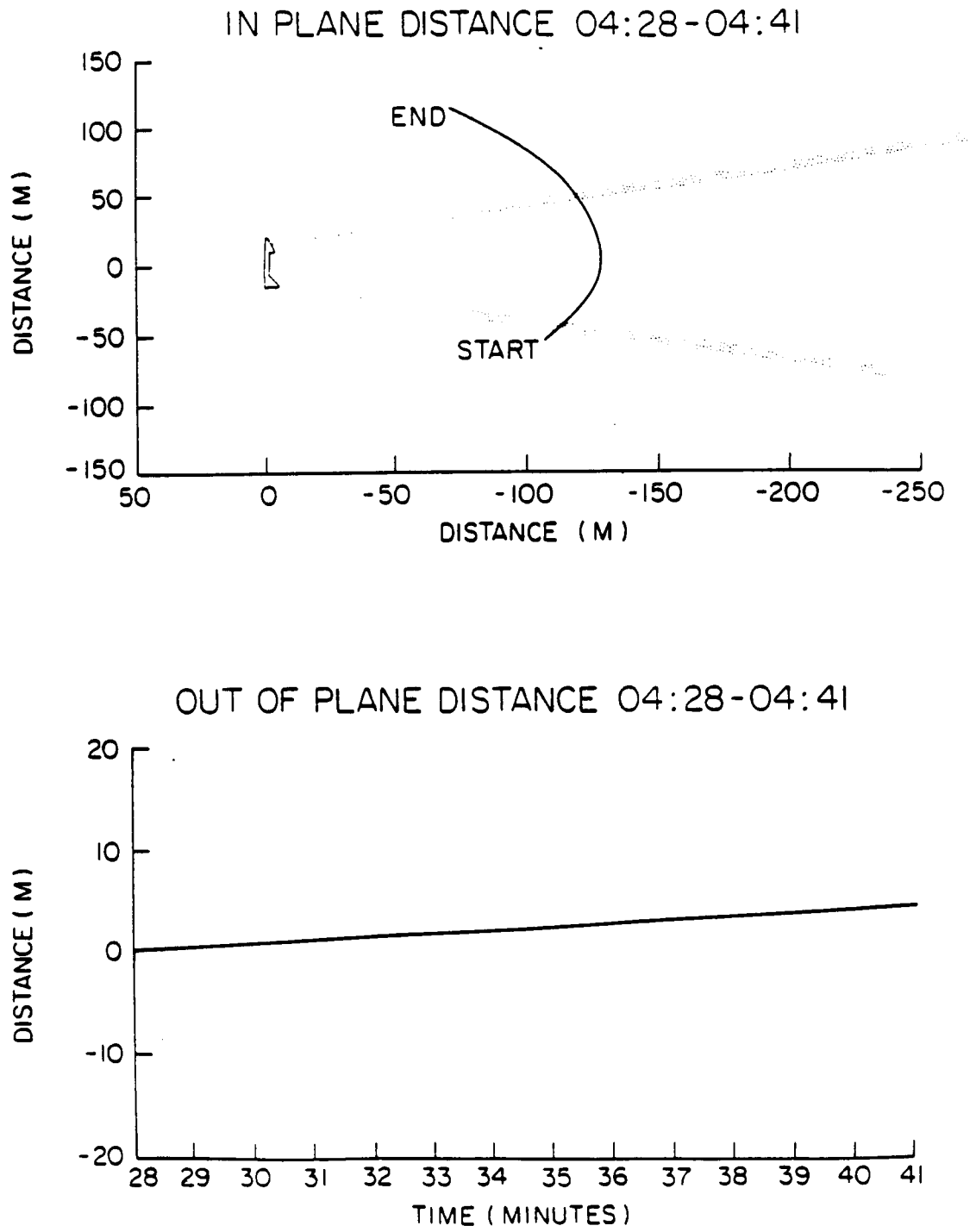

Figure 42. Spatial relationship between the orbiter and the PDP during far wake transit two.

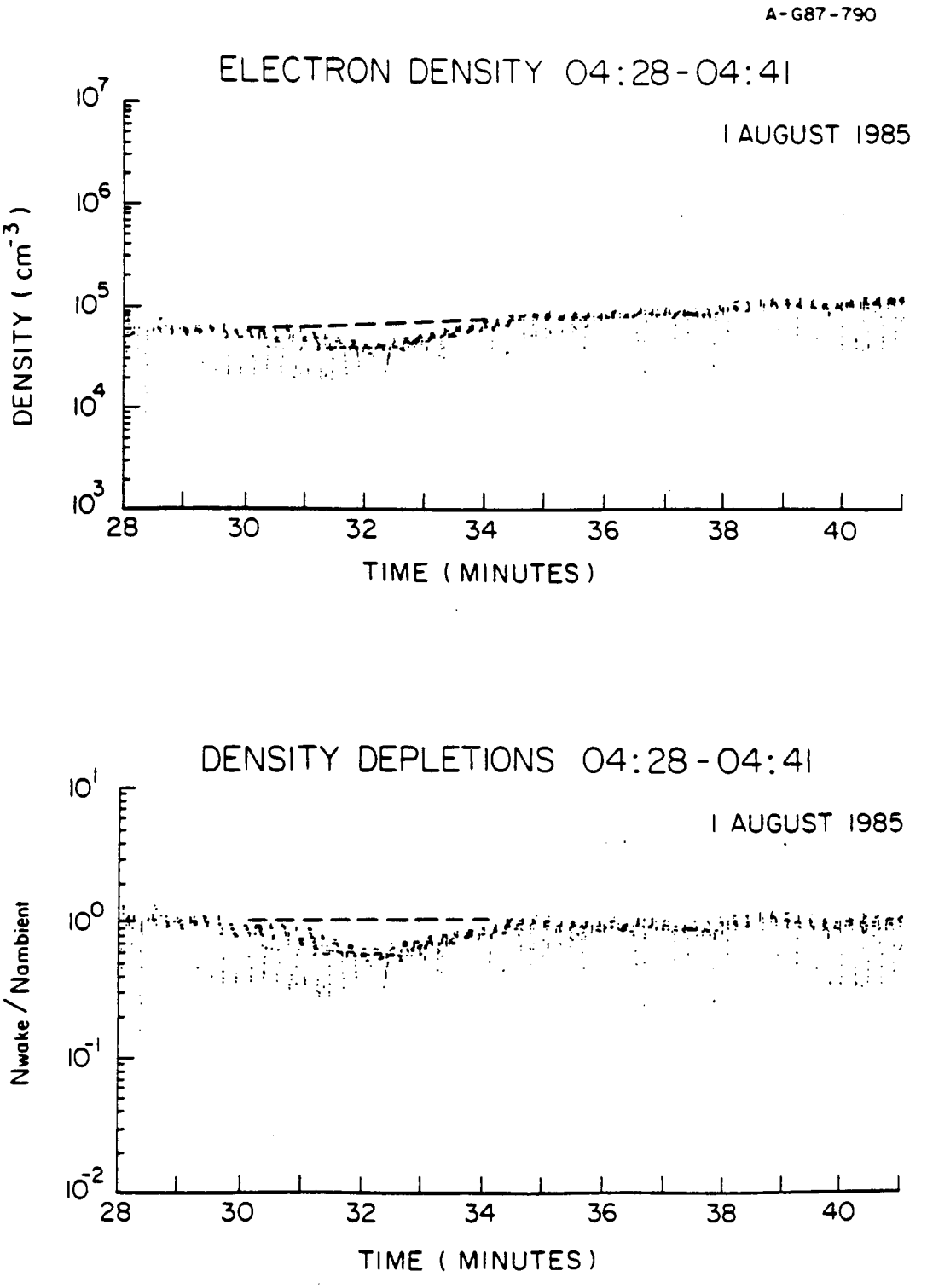

Figure 43. Electron density depletions during far wake transit two.

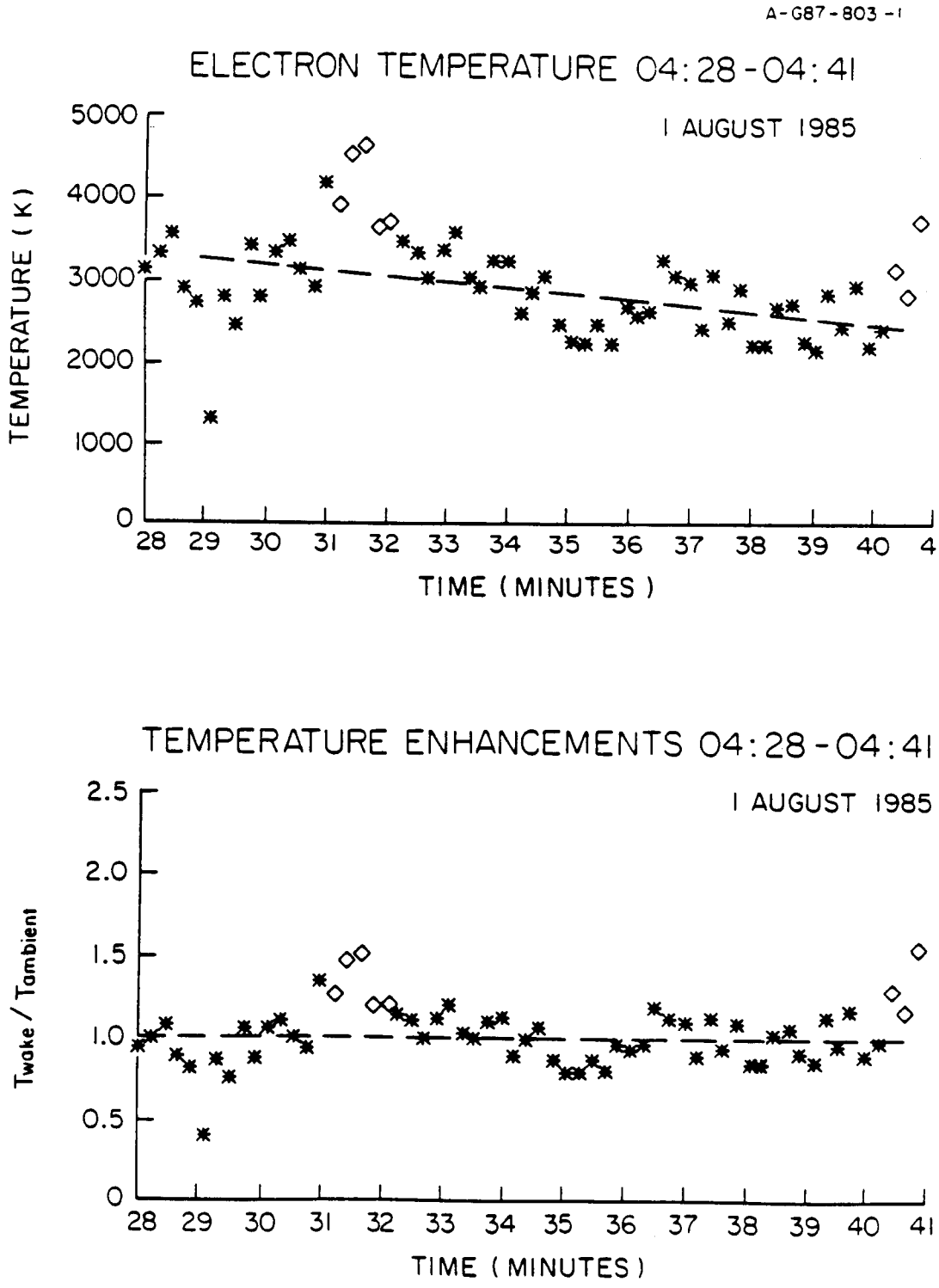

Figure 44. Electron temperature enhancements during far wake transit two.

A-G87-788

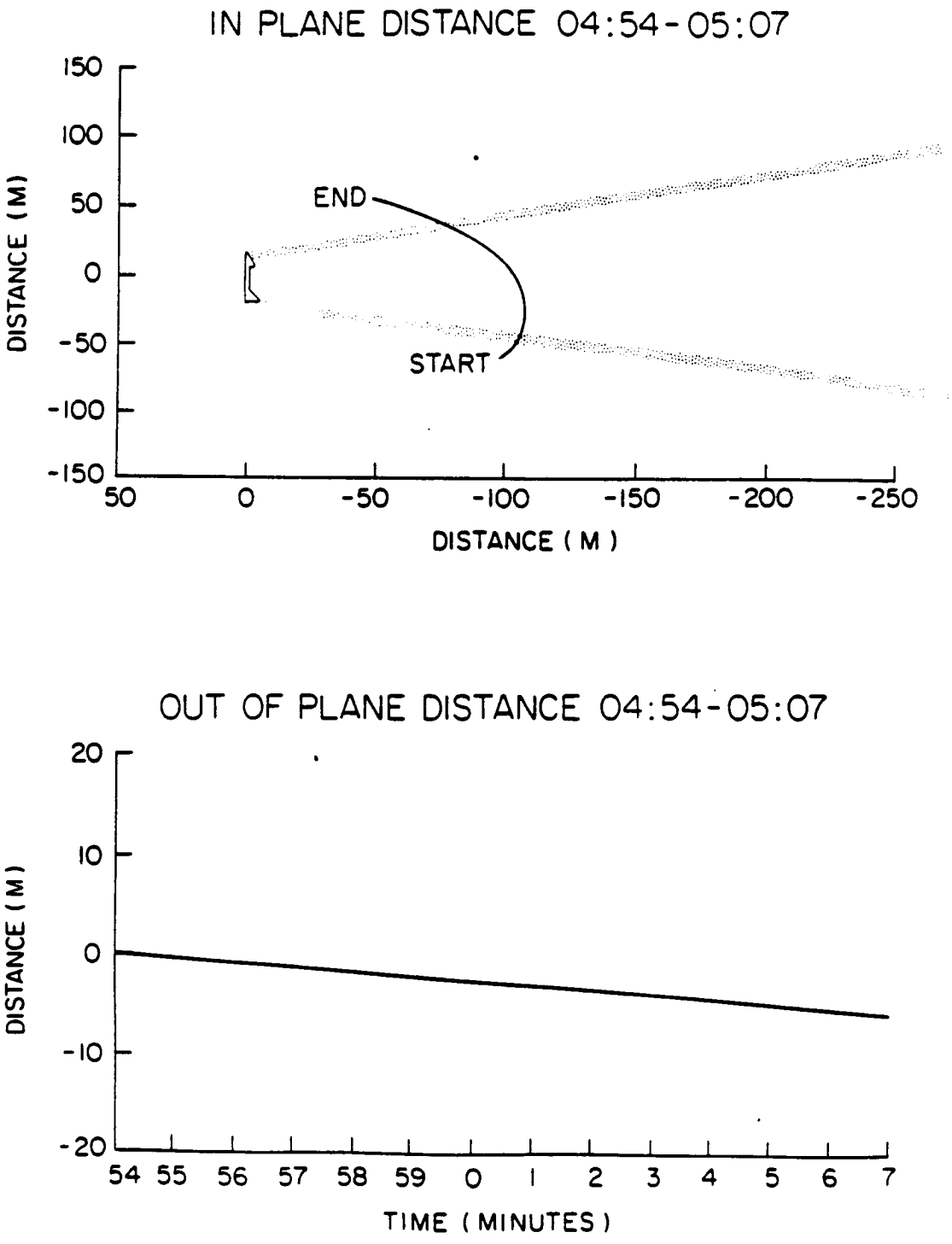

Figure 45. Spatial relationship between the orbiter and the PDP during far wake transit three.

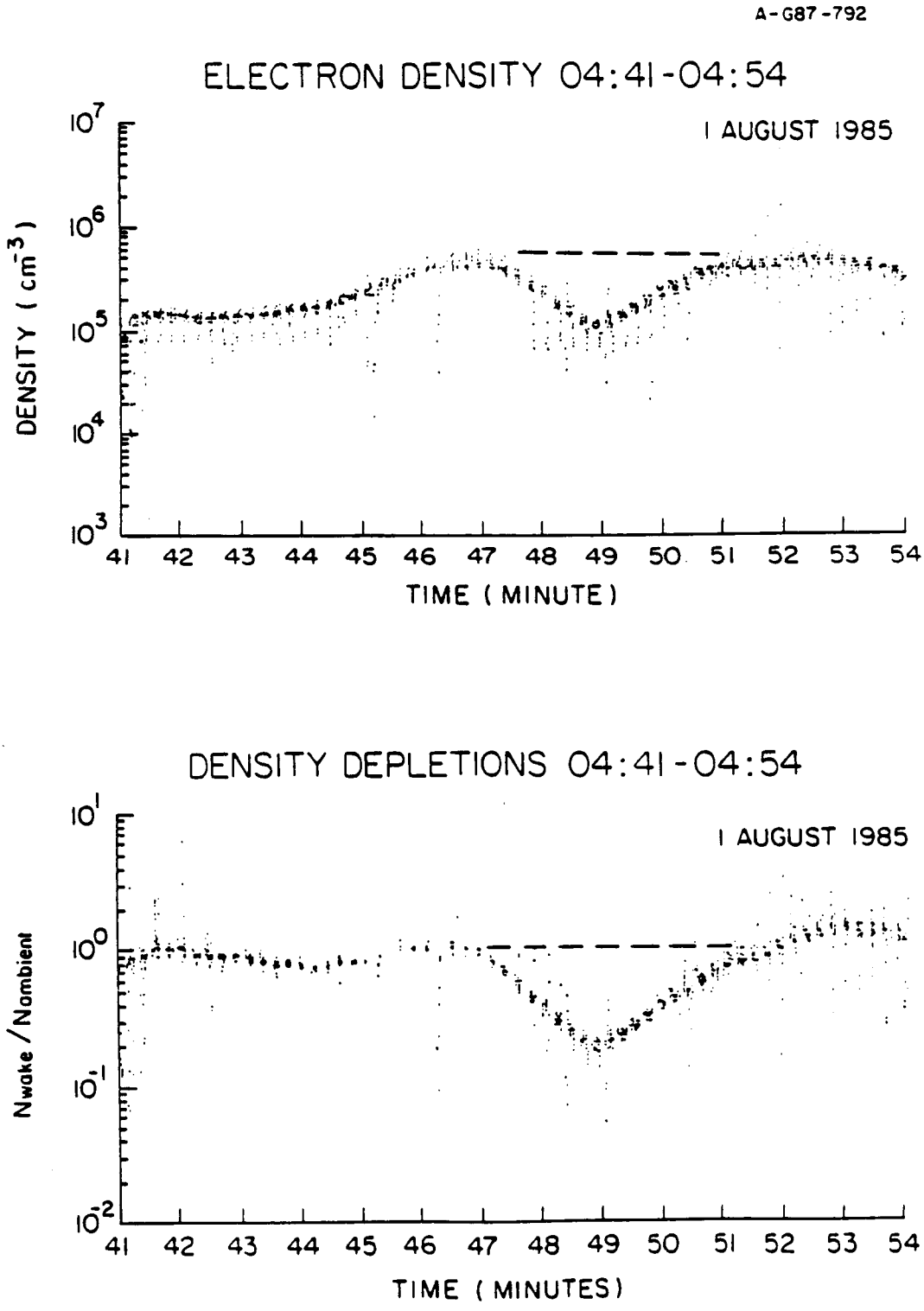

Figure 46. Electron density depletions during far wake transit three.

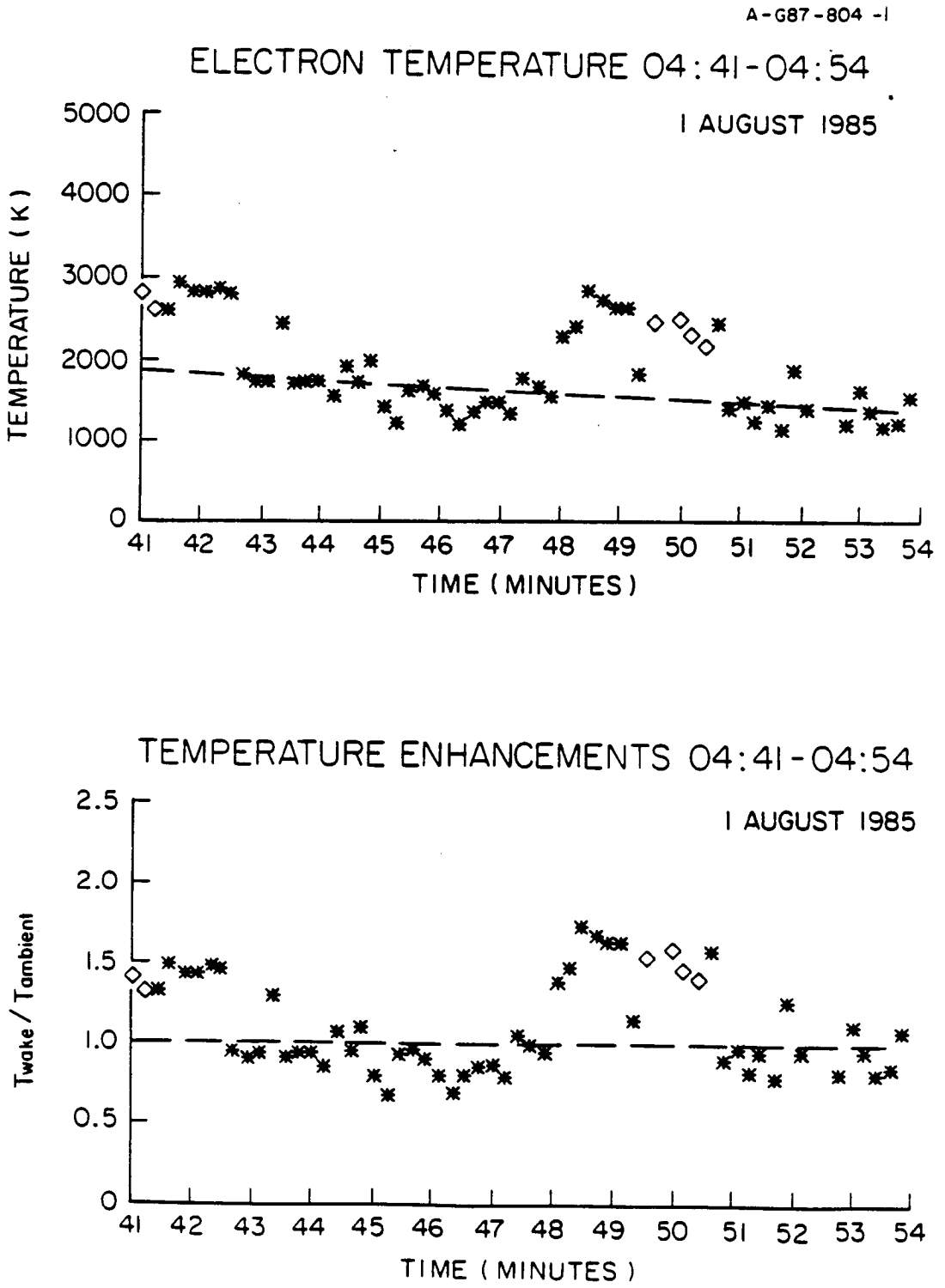

Figure 47. Electron temperature enhancements during far wake transit three.

A-G87-787

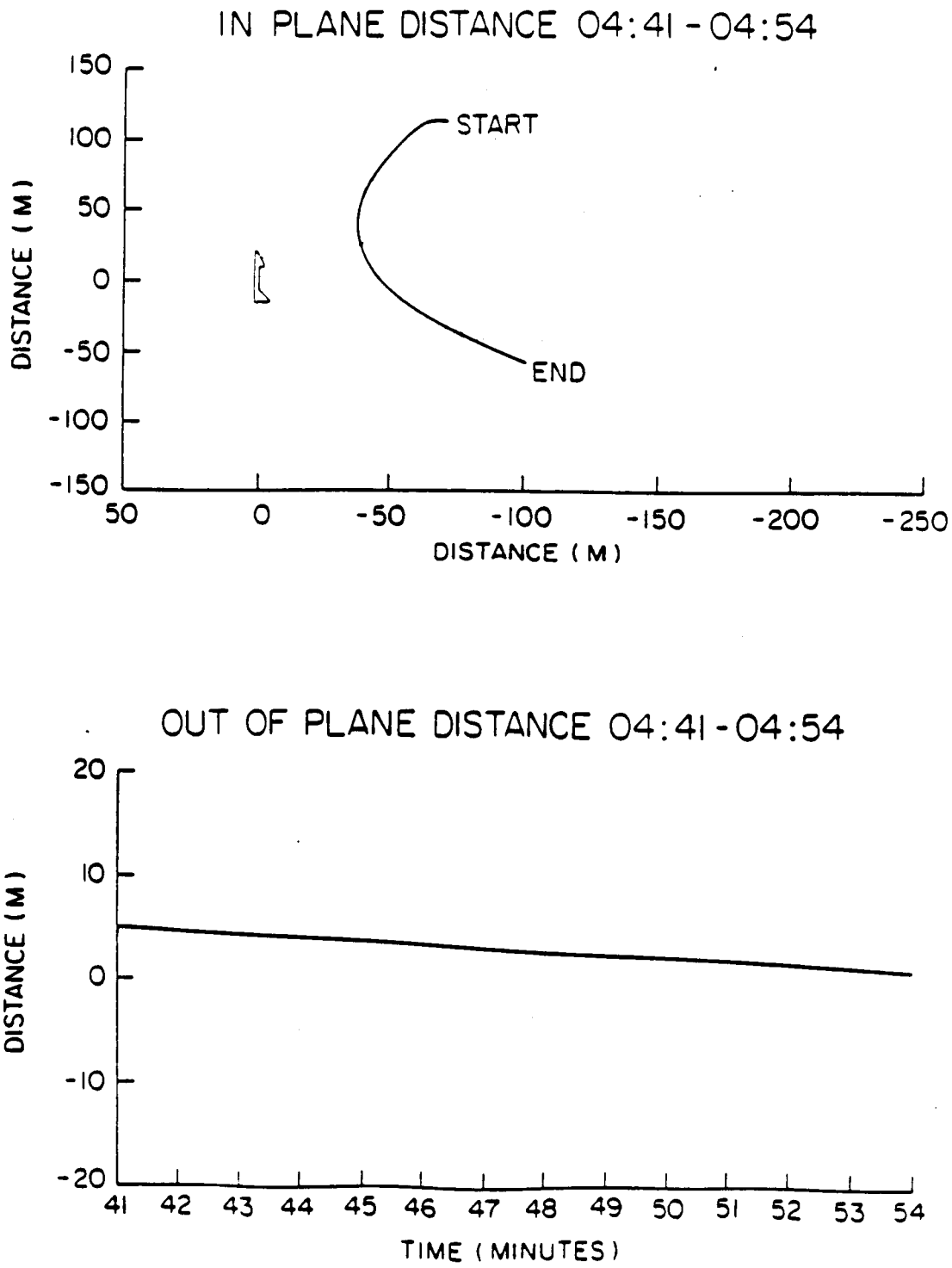

Figure 48. Spatial relationship between the orbiter and the PDP during far wake transit four.

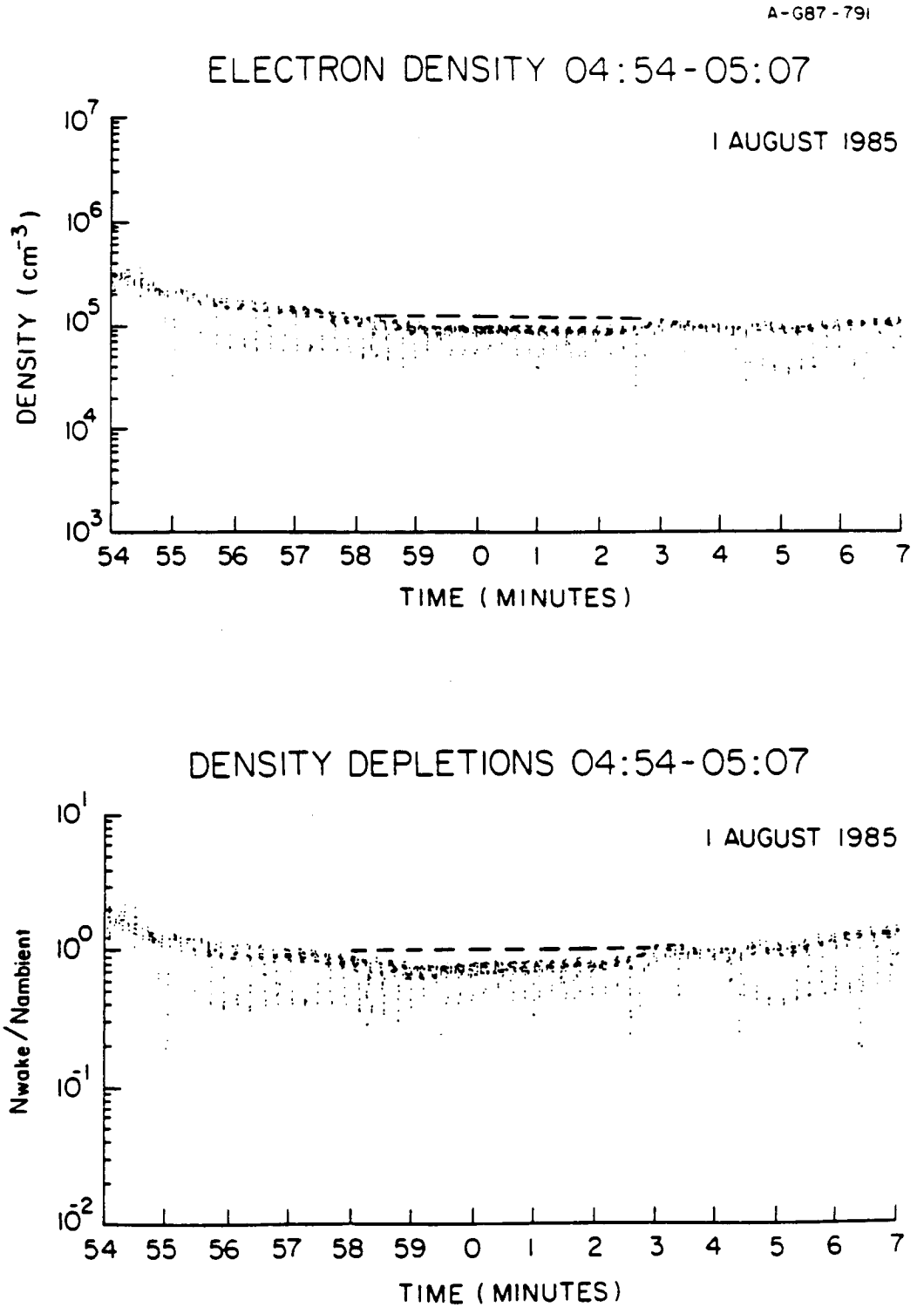

Figure 49. Electron density depletions during far wake transit four.

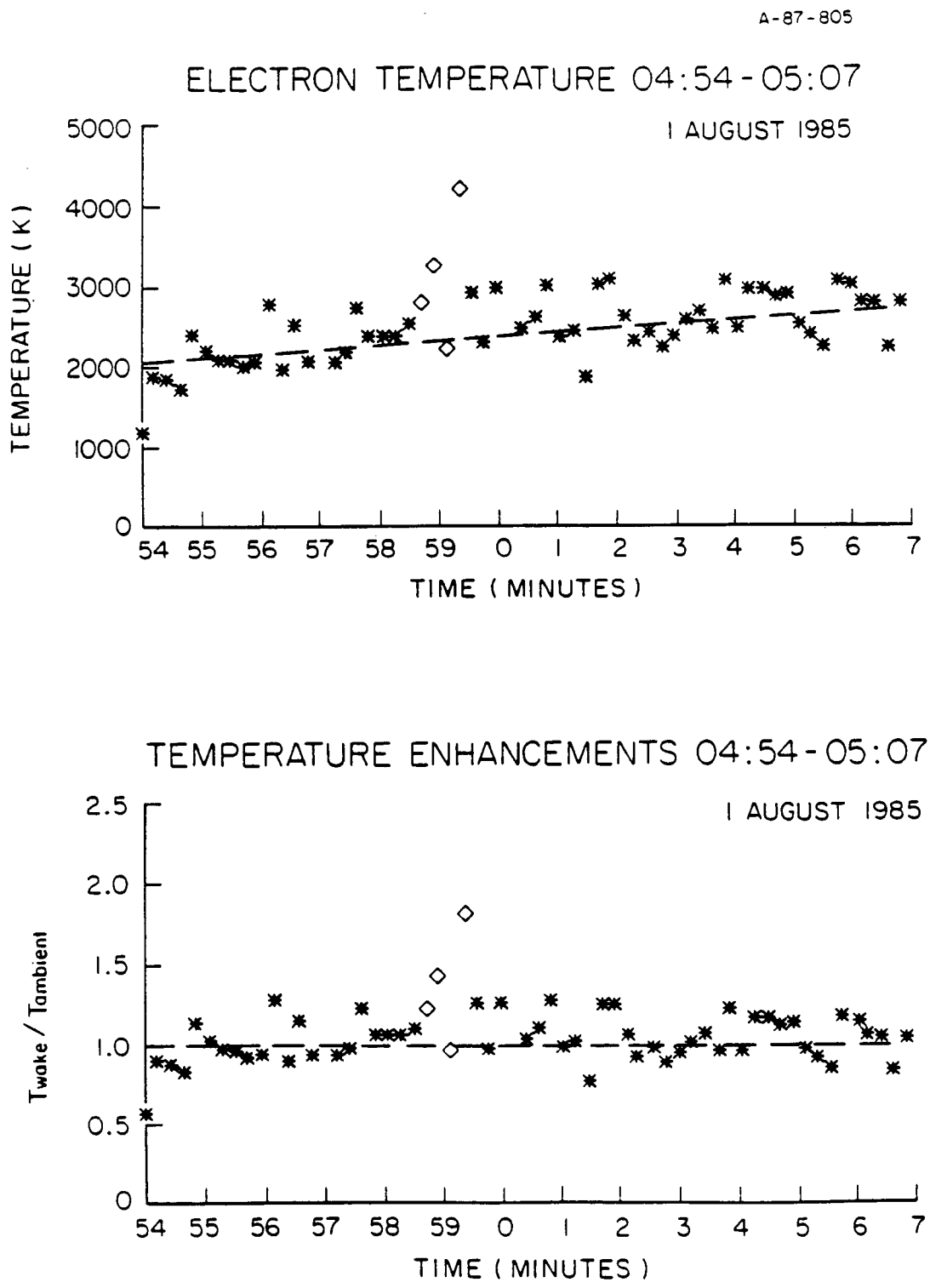

Figure 50. Electron temperature enhancements during far wake transit four.

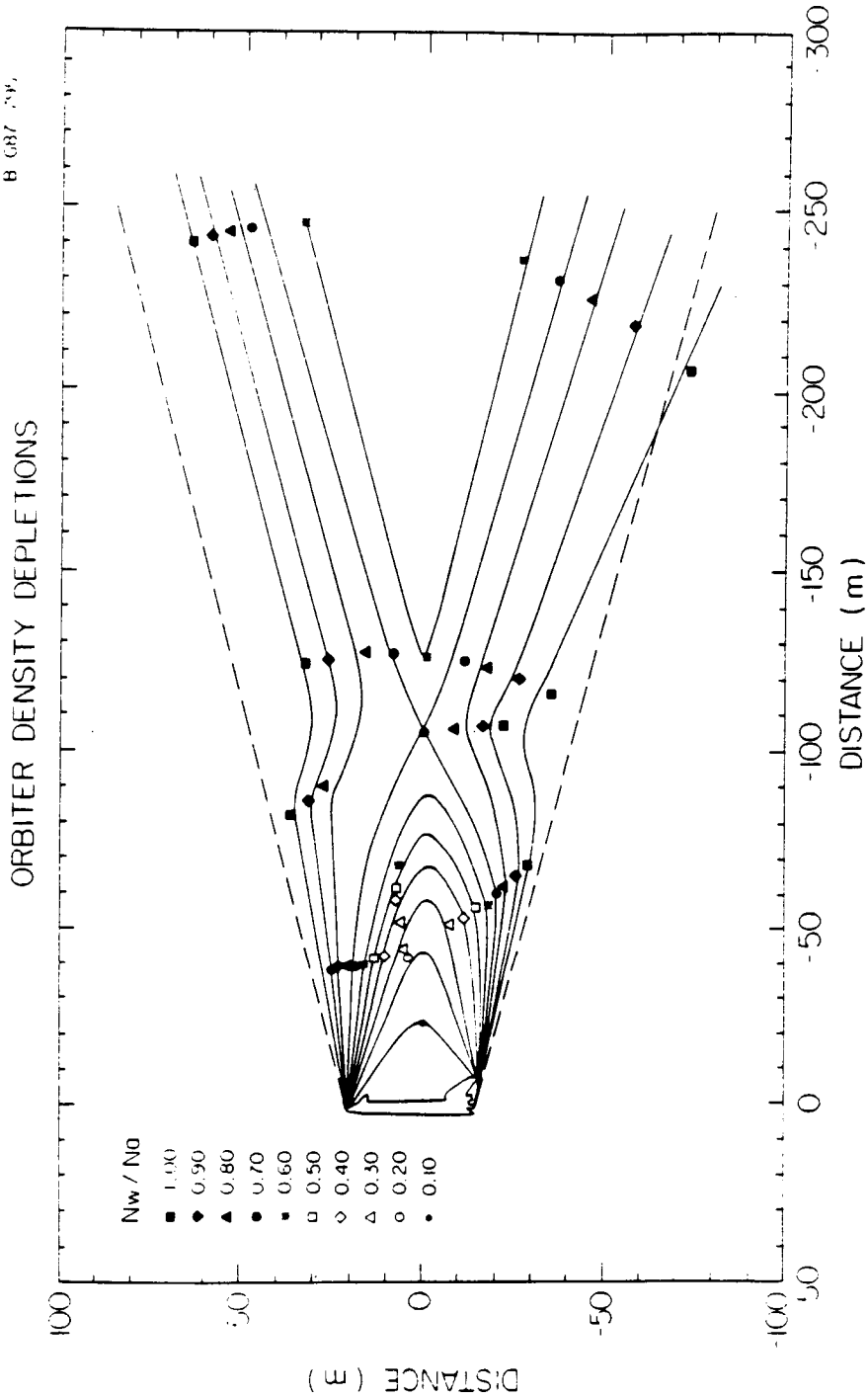

Figure 51. Electron density depletions in the wake of the shuttle orbiter for constant values of N_w/N_a.

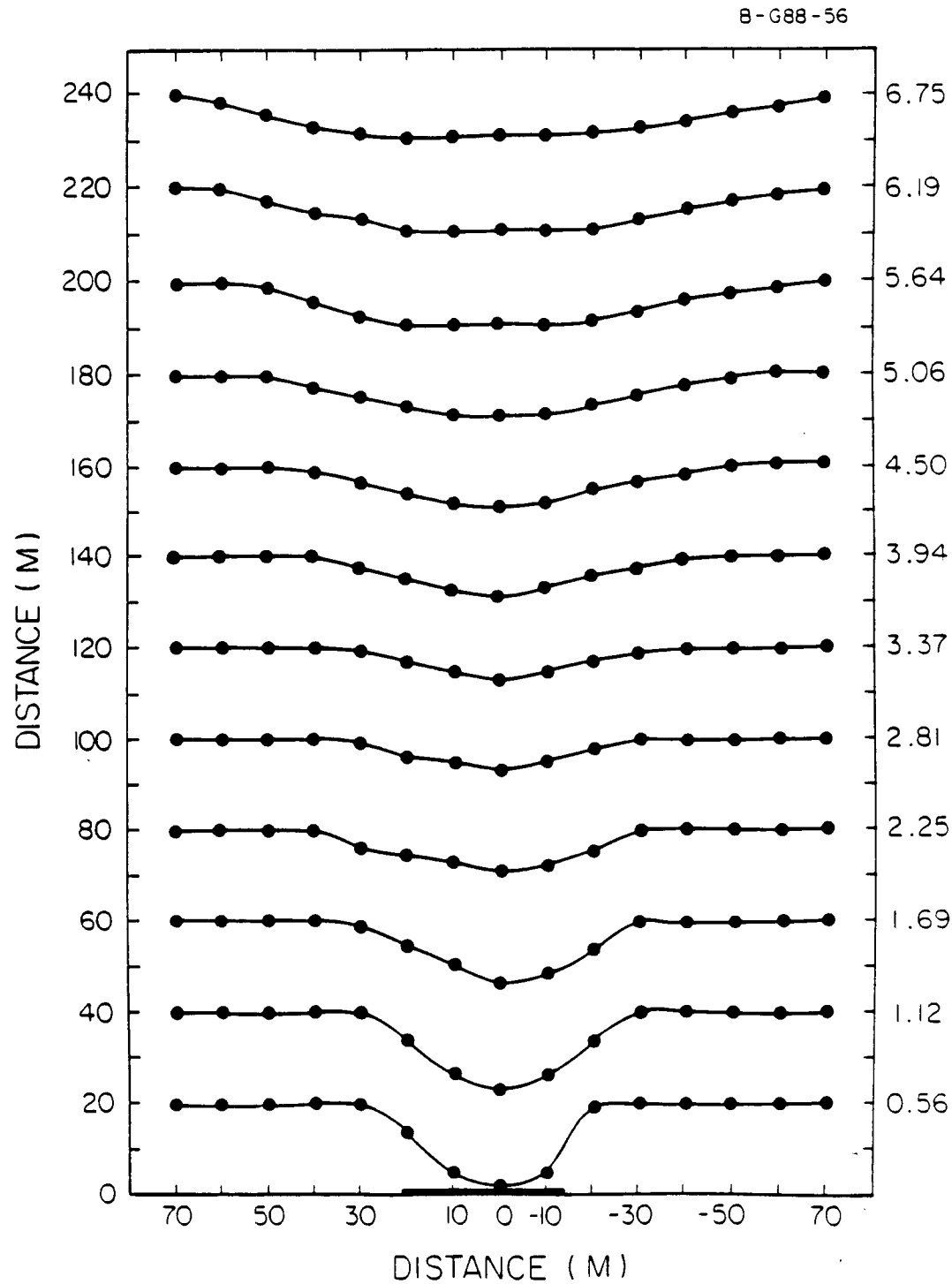

Figure 52. Electron density depletions in the wake of the shuttle orbiter for constant values of Z/R.

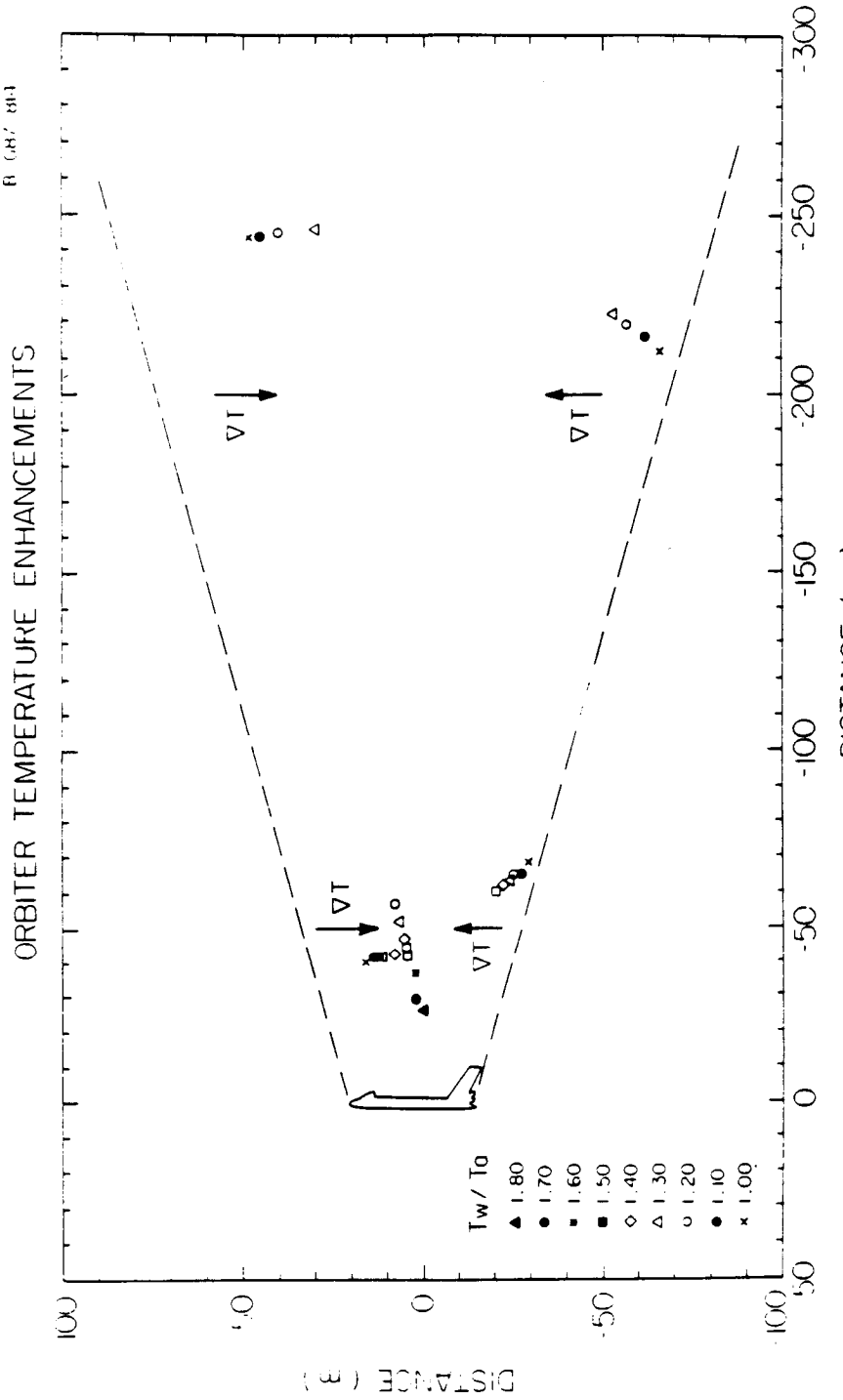

Figure 53. Electron temperature enhancements in the wake of the shuttle orbiter.

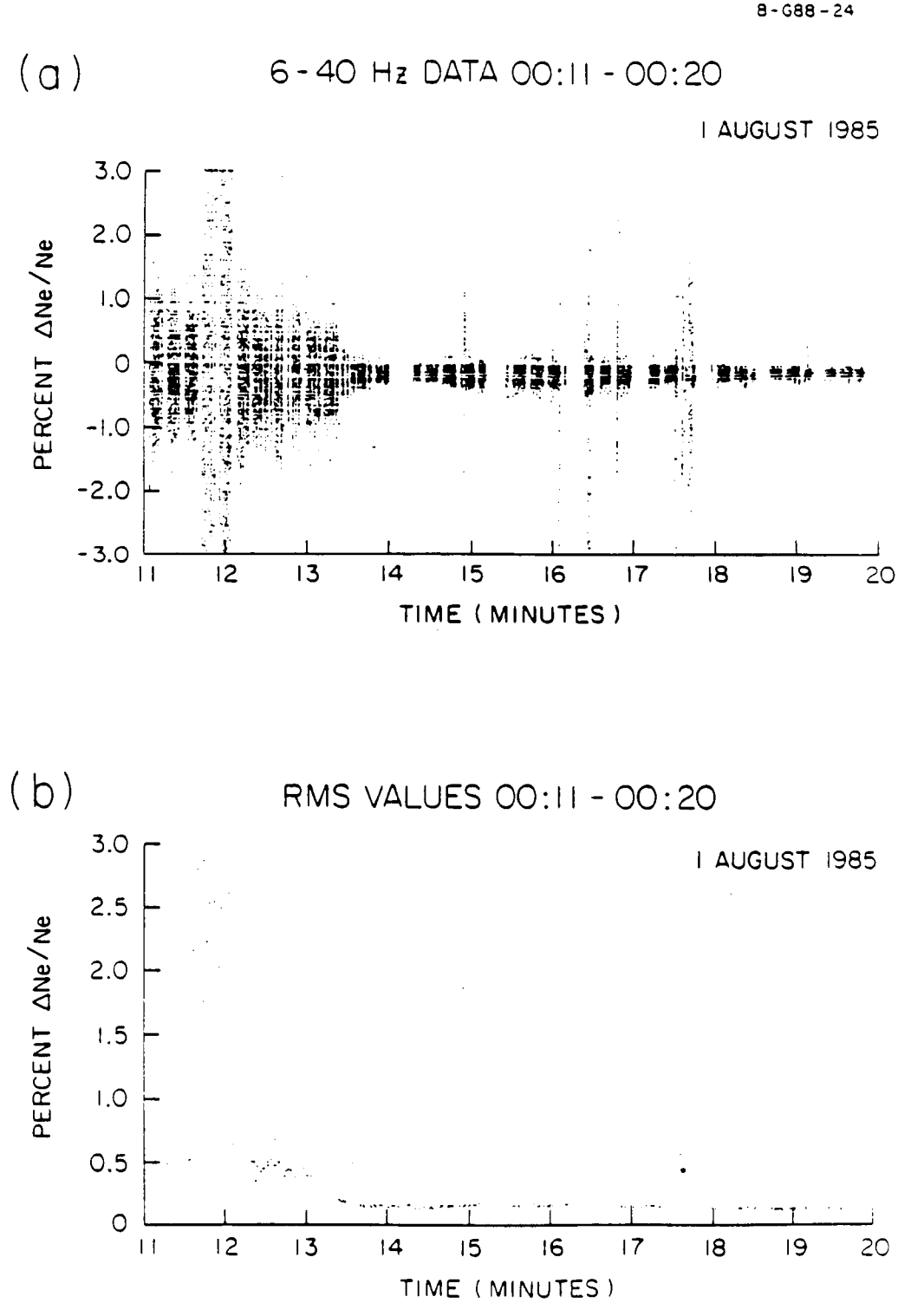

Figure 54. 6-40 Hz data during backaway.

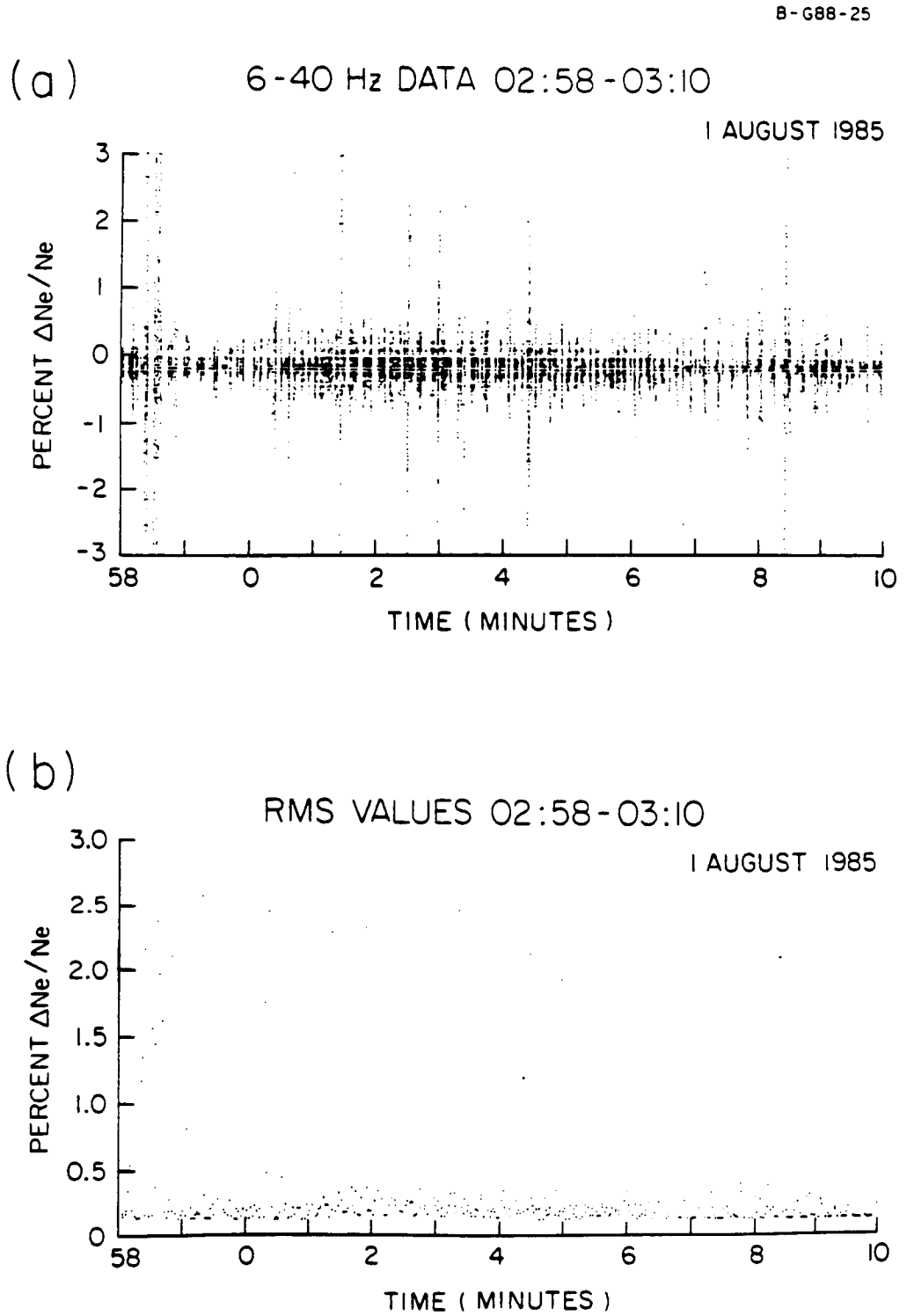

Figure 55. 6-40 Hz data during far wake transit one.

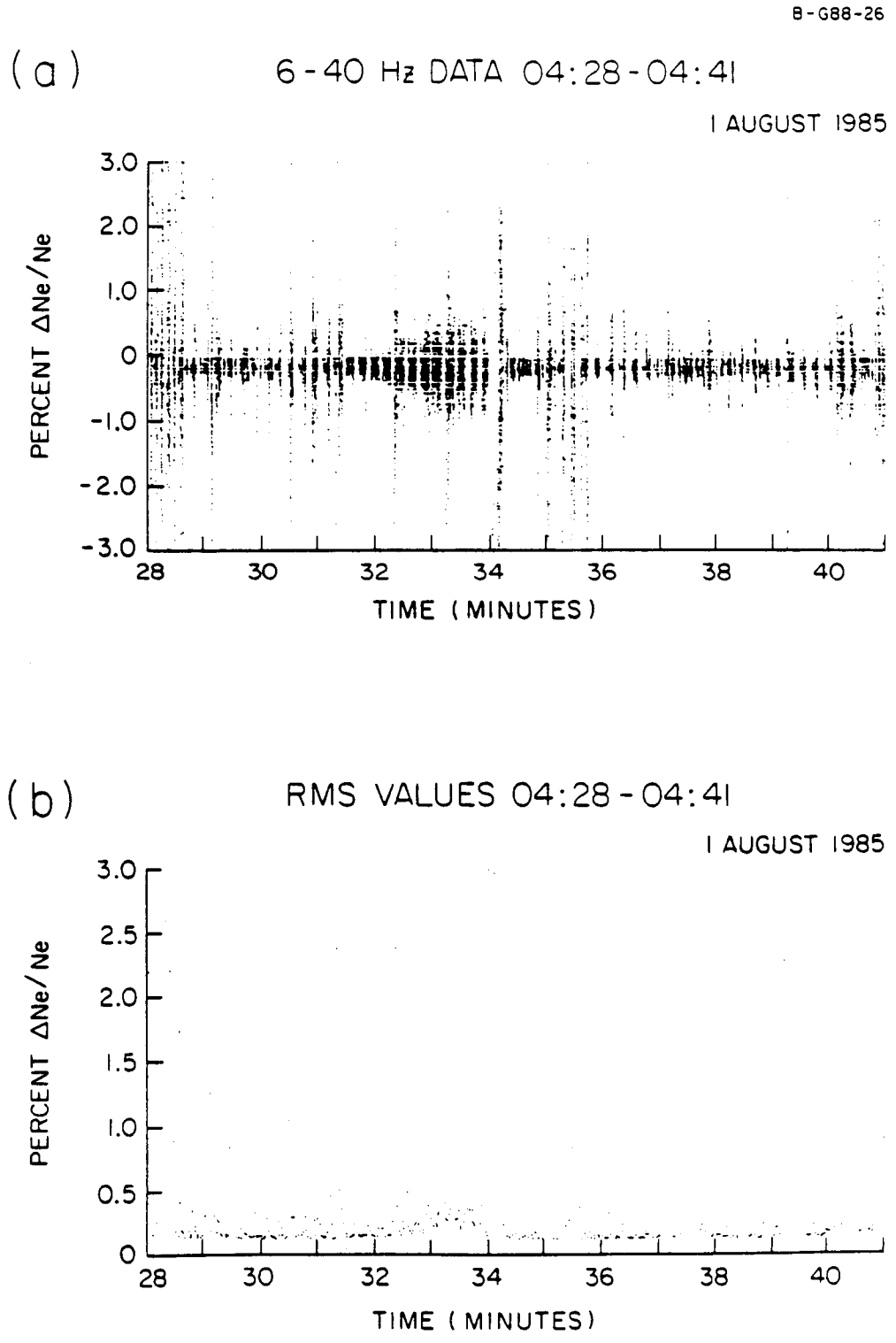

Figure 56. 6-40 Hz data during far wake transit two.

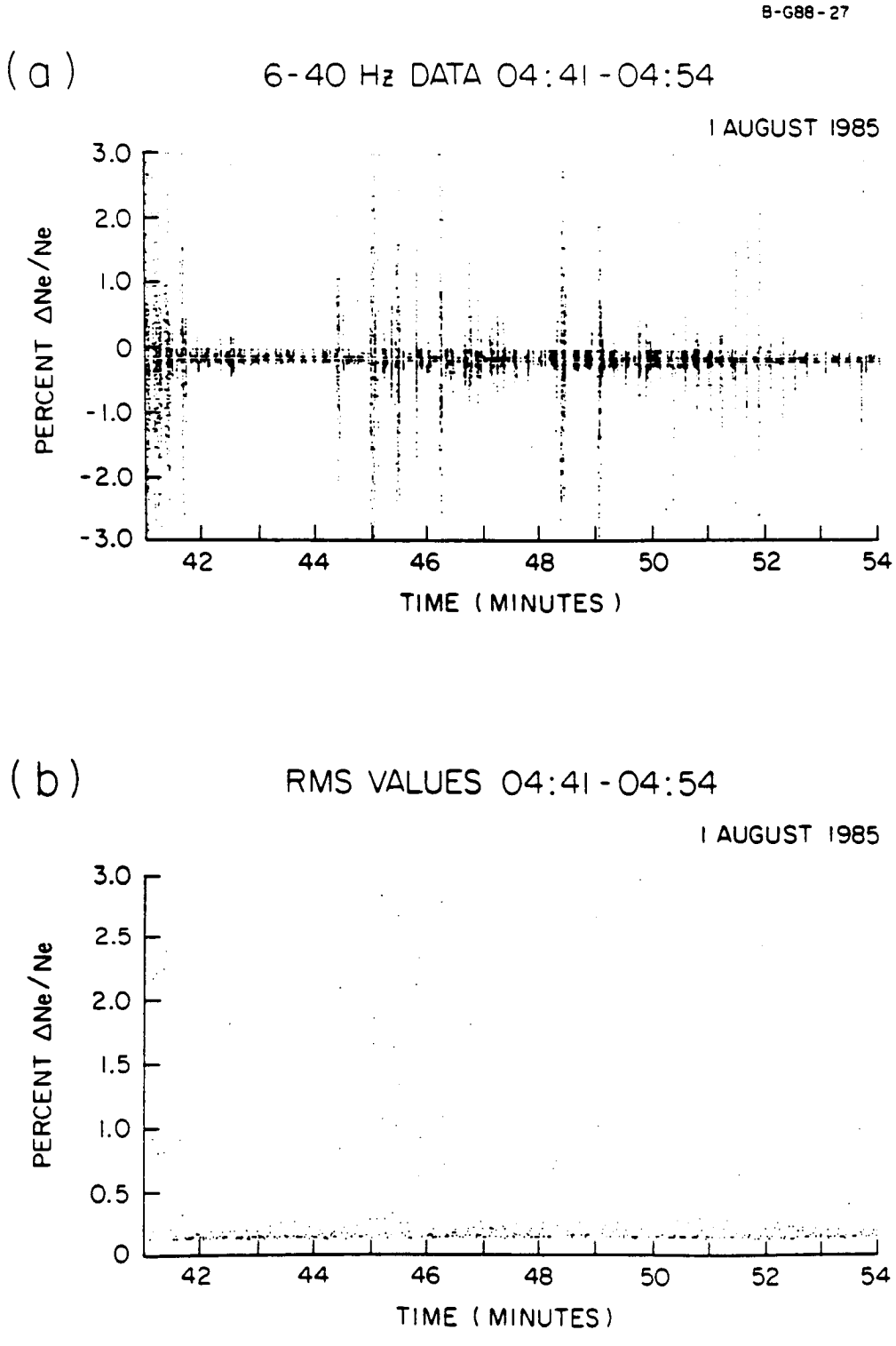

Figure 57. 6-40 Hz data during far wake transit three.

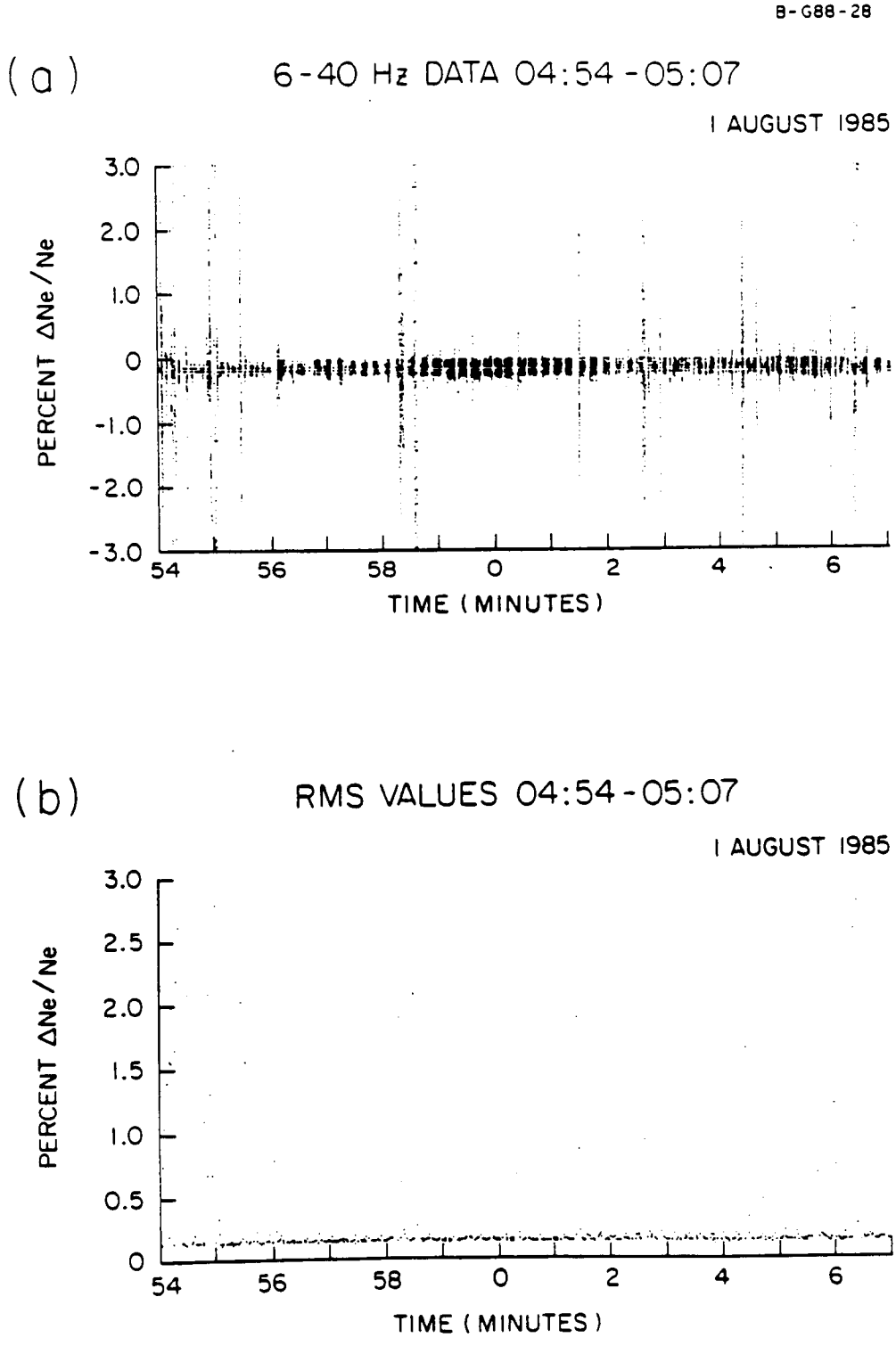

Figure 58. 6-40 Hz data during far wake transit four.

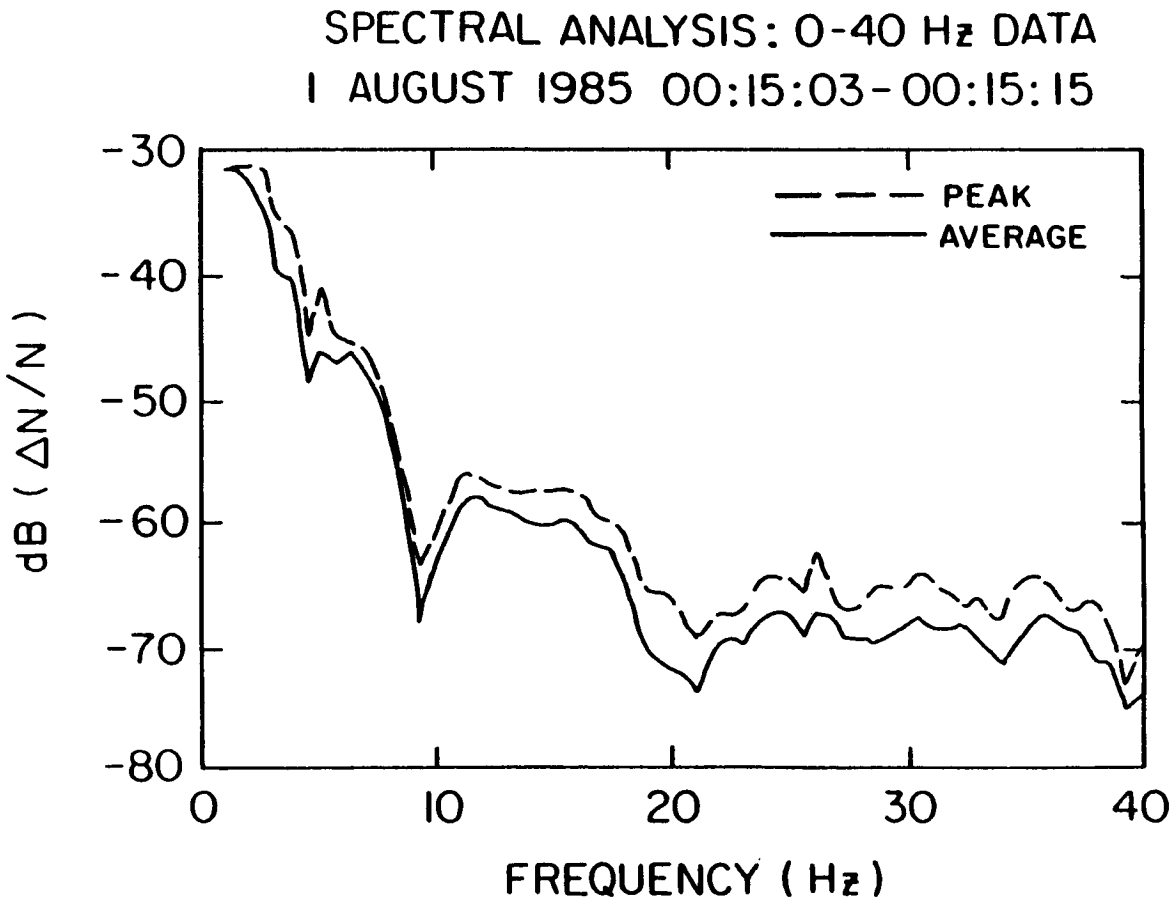

Figure 59. 0-40 Hz FFT data obtained on the wake axis 35 m downstream from the orbiter.

A-G88-181

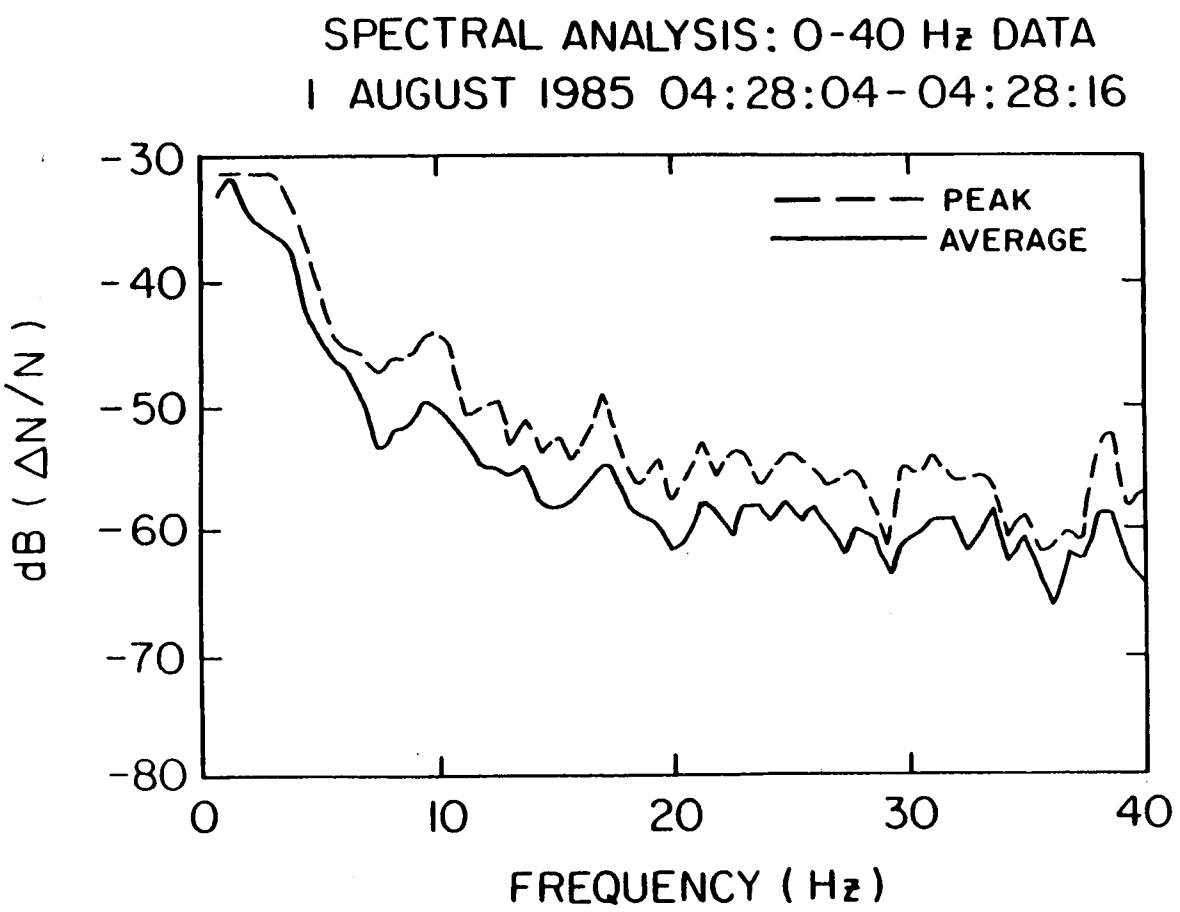

Figure 60. 0-40 Hz FFT data obtained on the wake axis 120 m downstream from the orbiter.

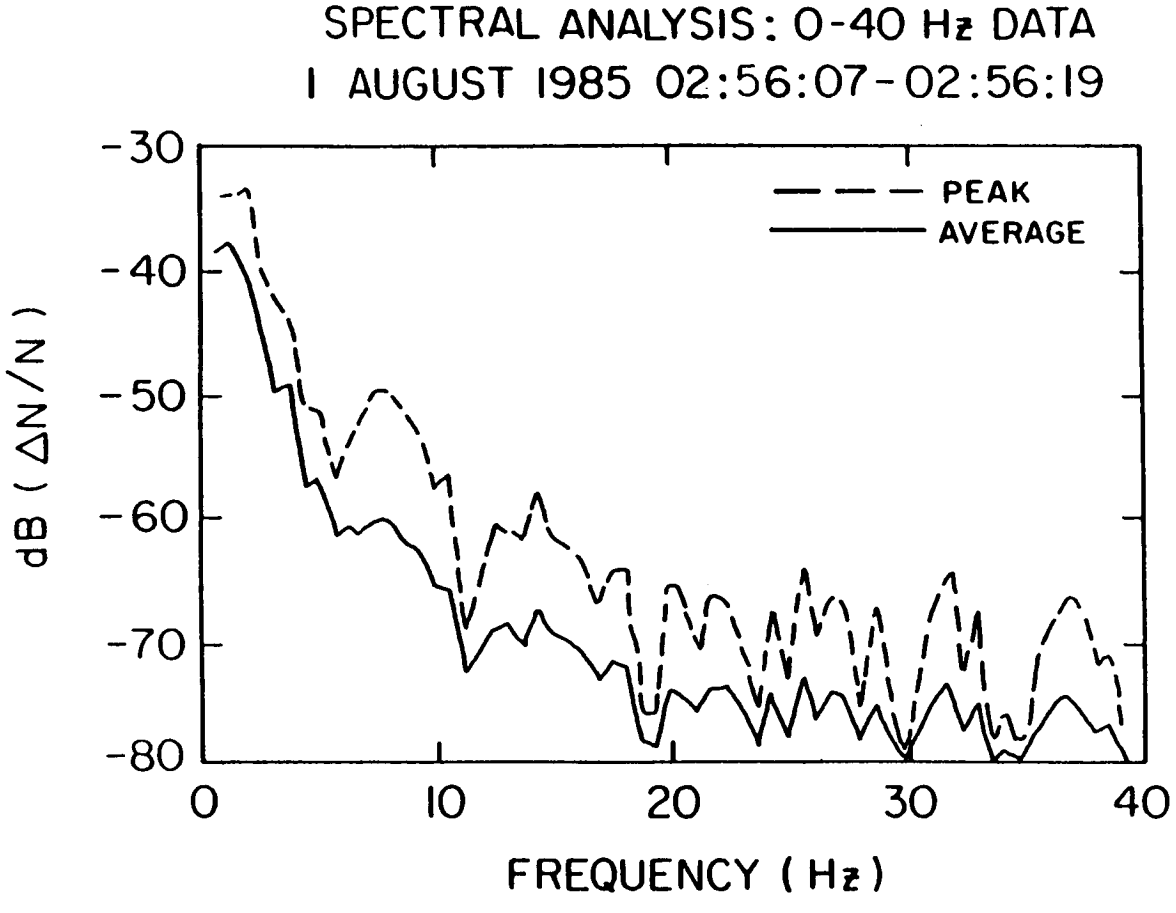

Figure 61. 0-40 Hz FFT data obtained on the Mach cone 200 m downstream from the orbiter.

A-G88-182

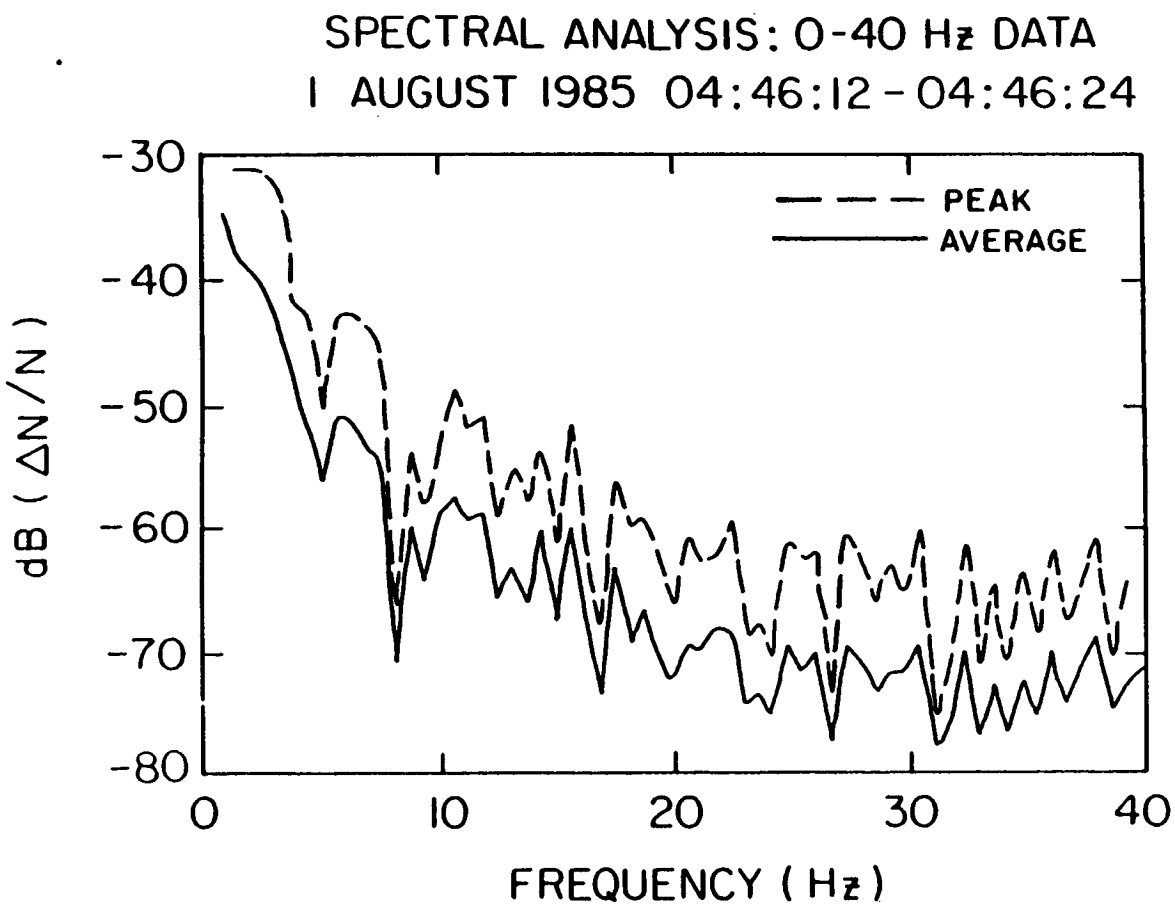

Figure 62. 0-40 Hz FFT data obtained just outside the Mach cone 20 m downstream from the orbiter.

A-G88-183

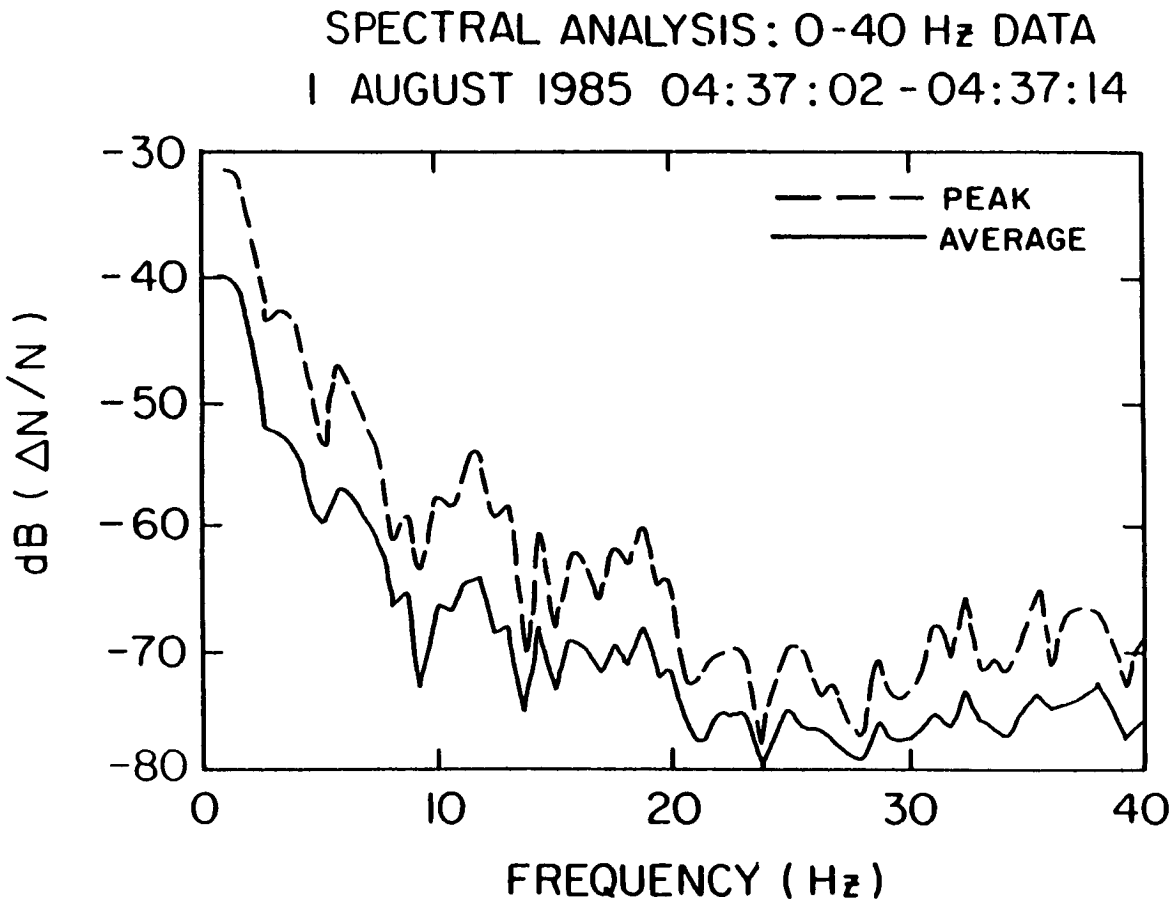

Figure 63. 0-40 Hz FFT data obtained just outside the Mach cone 90 m downstream from the orbiter.

A-688-130

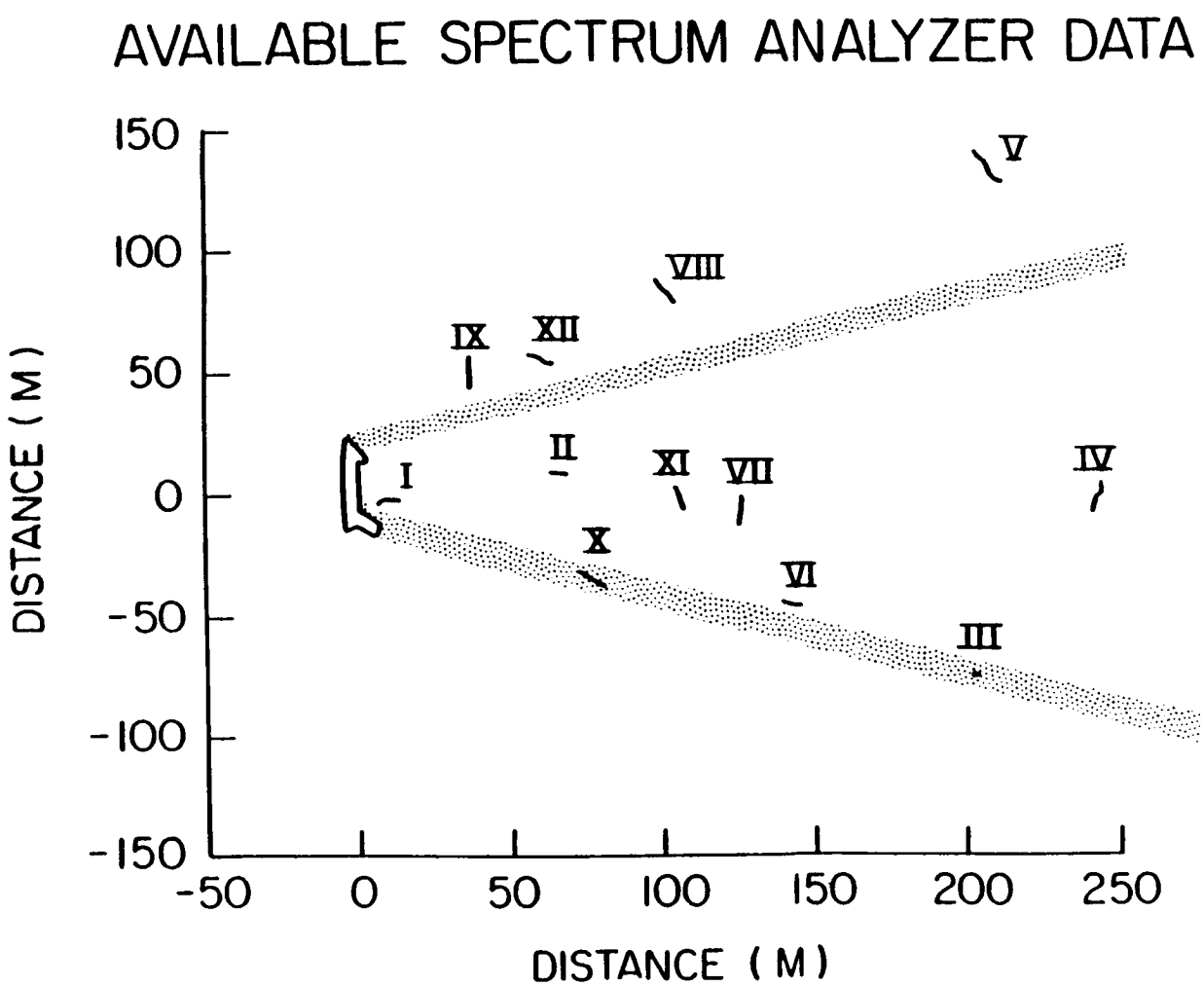

Figure 64. The locations where Langmuir probe spectrum analyzer data is available during wake studies.

A-G88-163

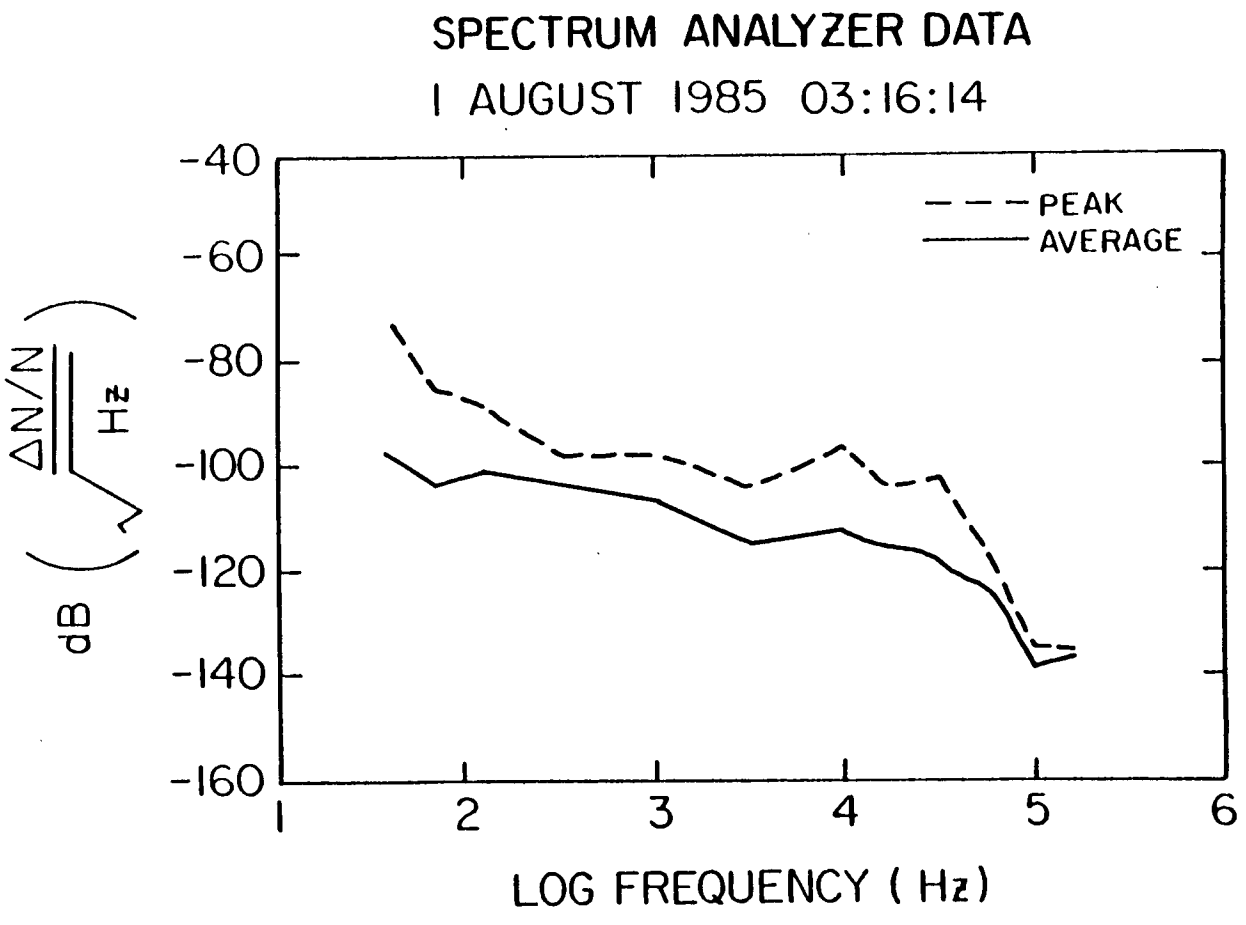

Figure 65. Ambient ionospheric conditions as measured by the spectrum analyzer.

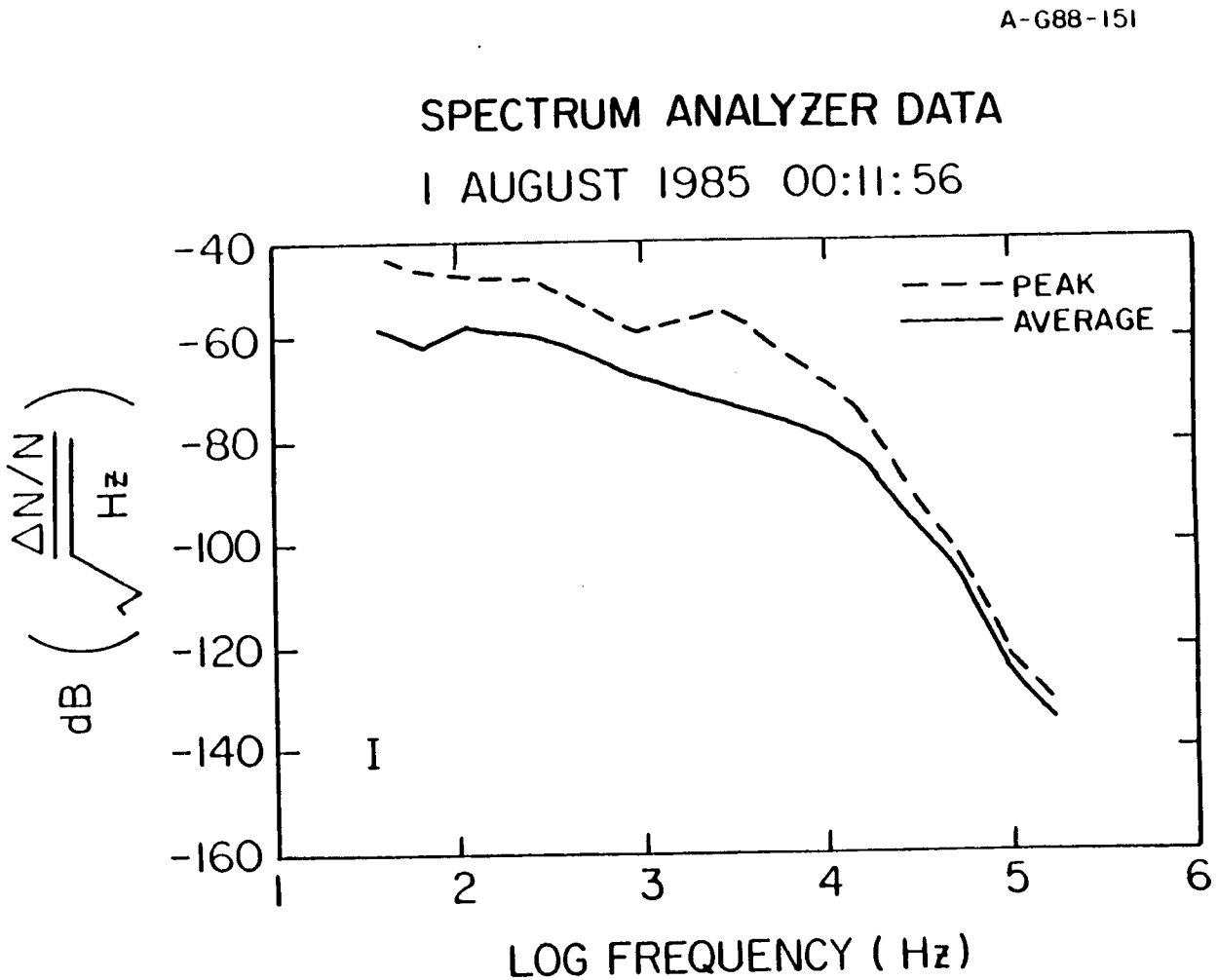

Figure 66. Spectral density of $\Delta N/N$ at location I.

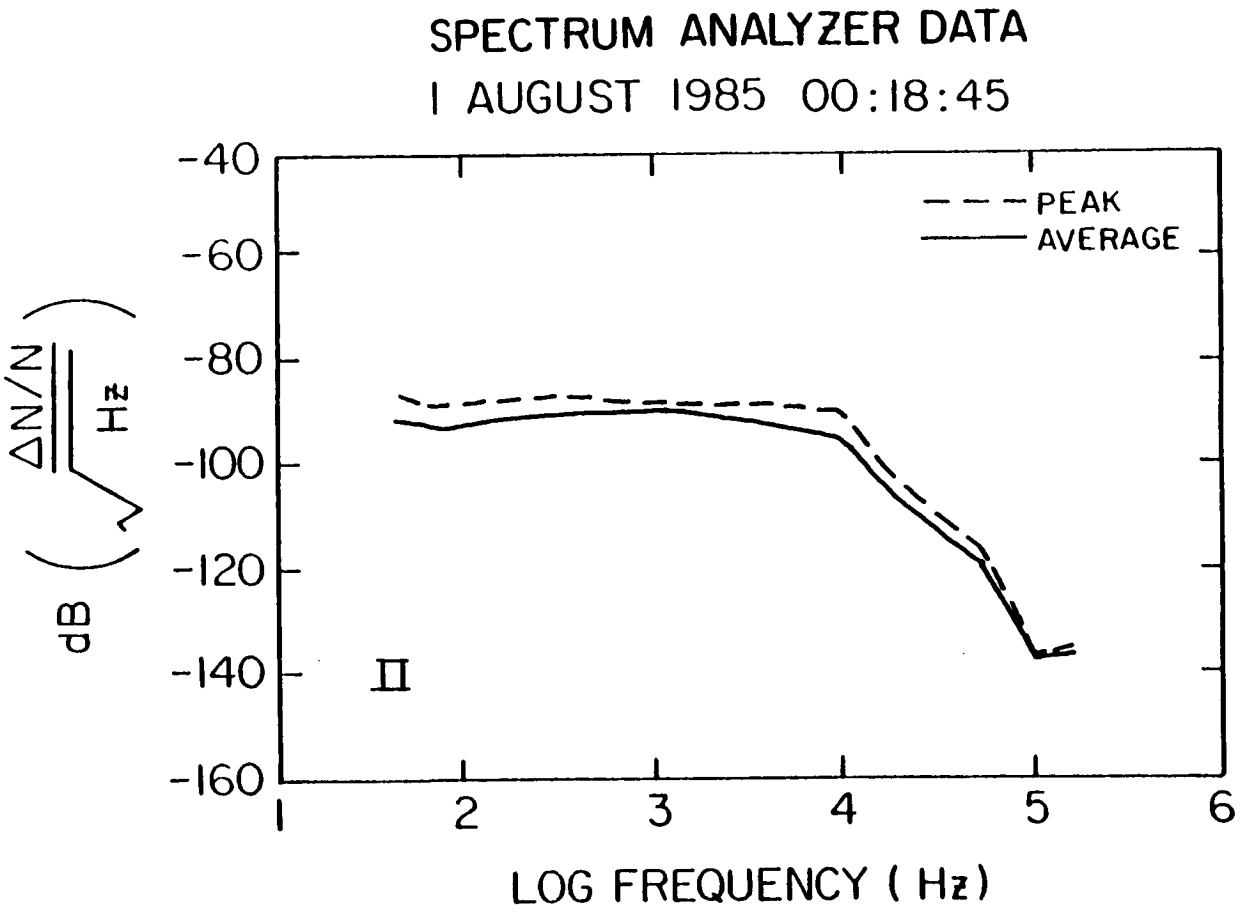

Figure 67. Spectral density of $\Delta N/N$ at location 11.

A-G88-153

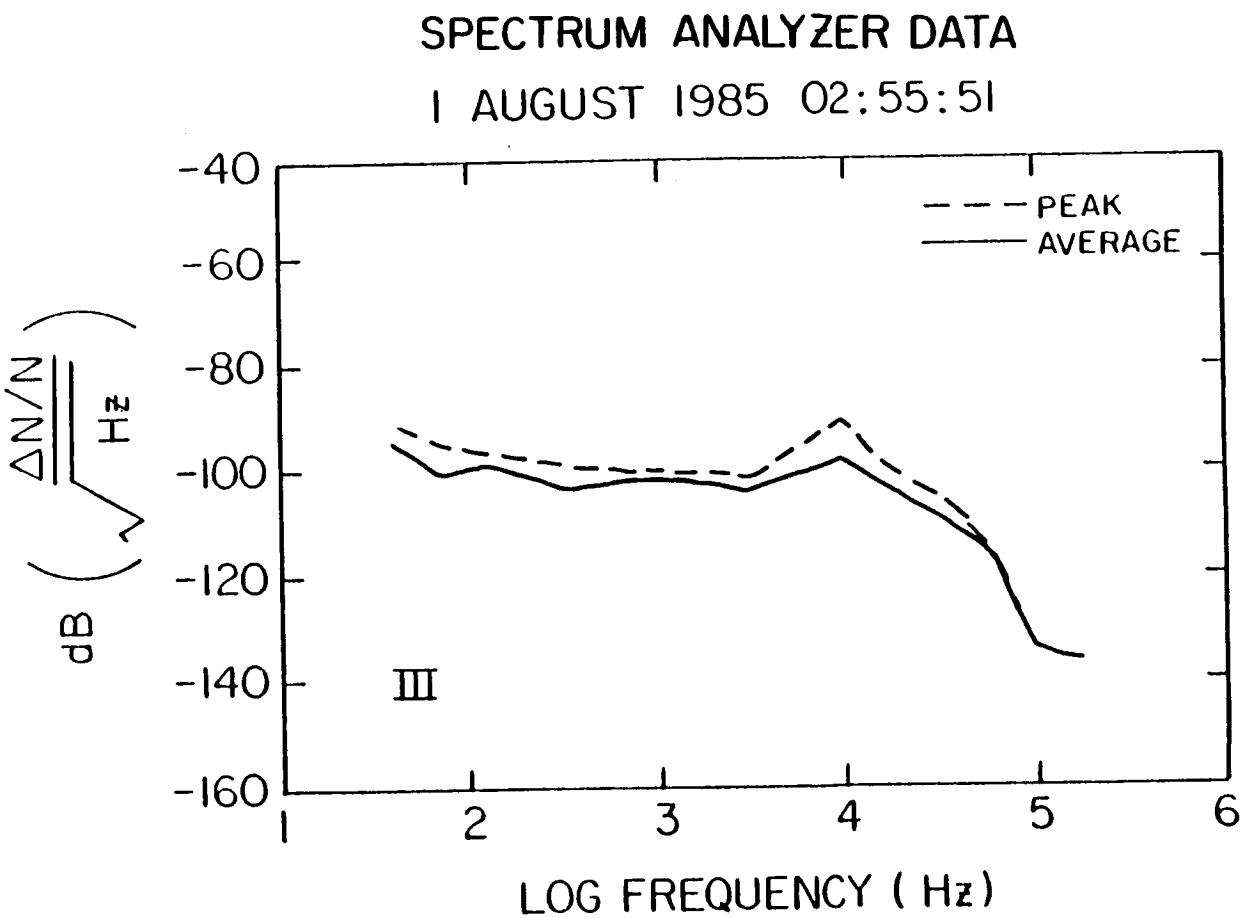

Figure 68. Spectral density of $\Delta N/N$ at location III.

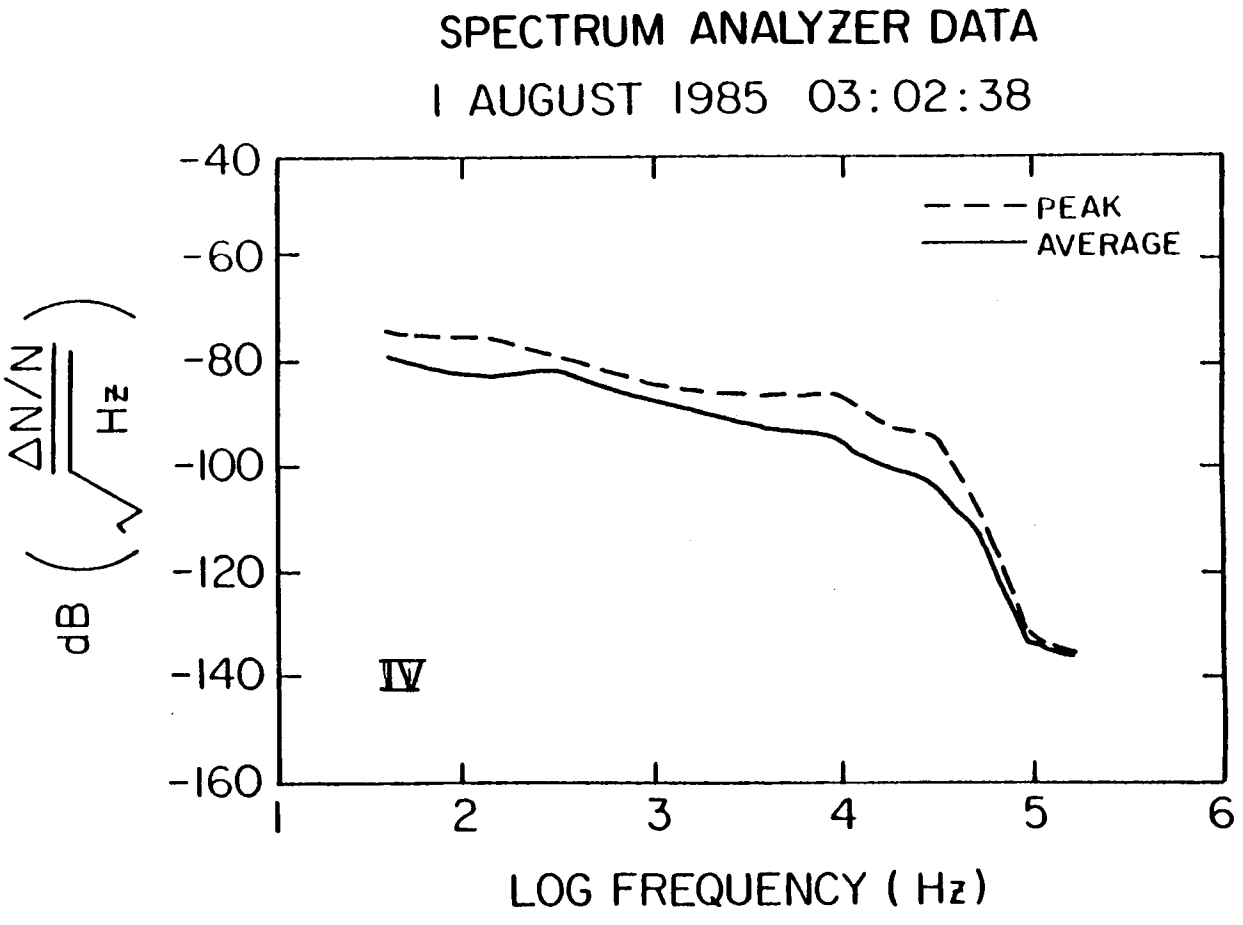

Figure 69. Spectral density of $\Delta N/N$ at location IV.

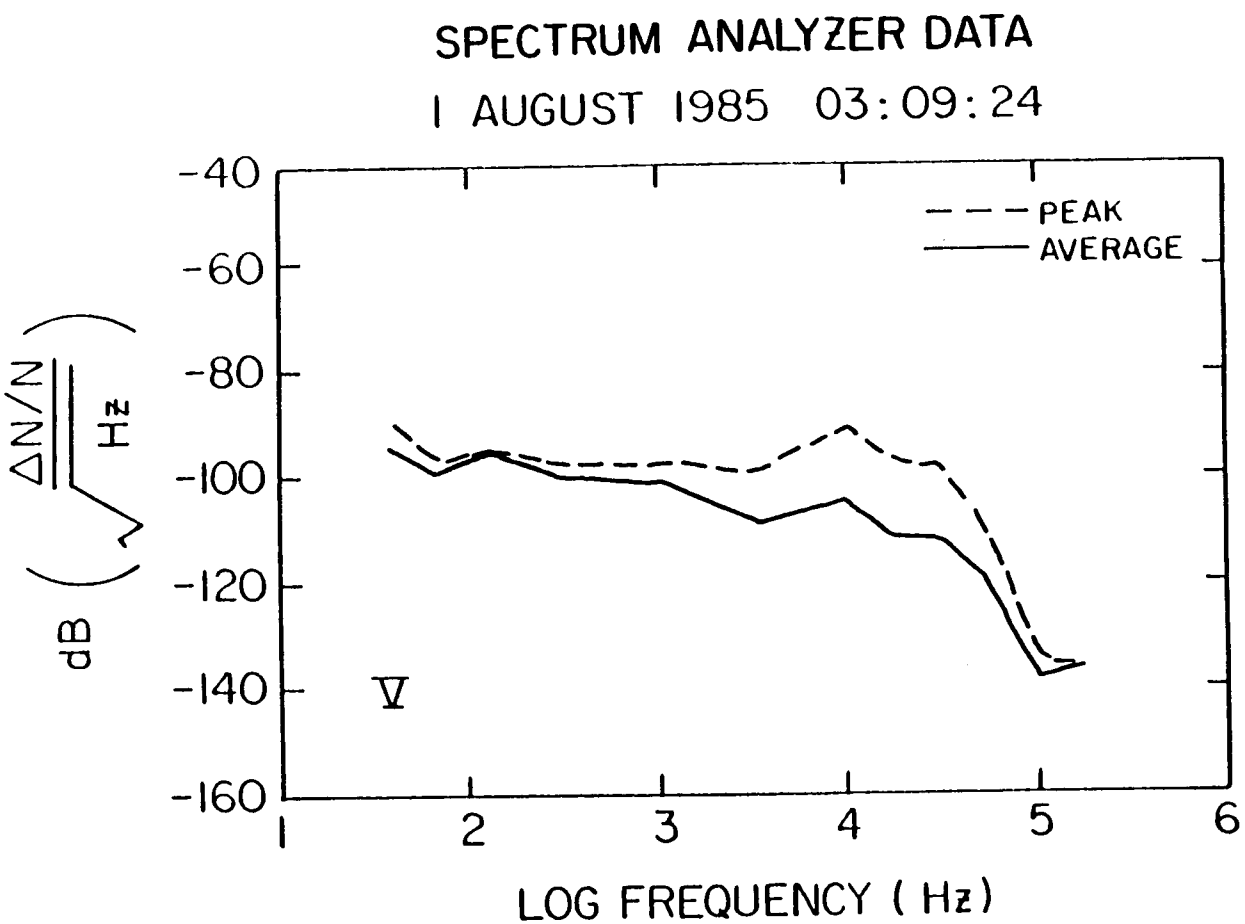

Figure 70. Spectral density of $\Delta N/N$ at location V.

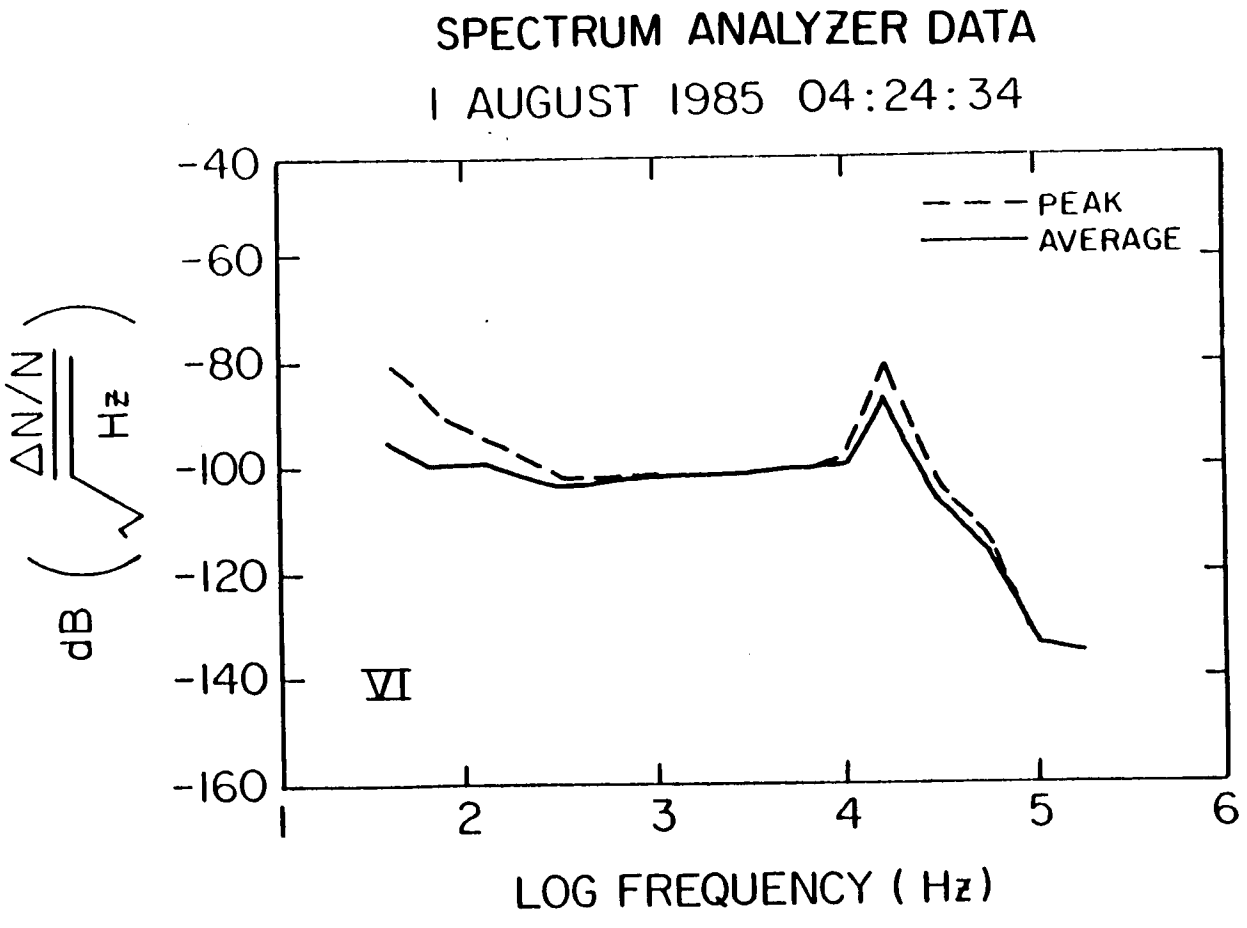

Figure 71. Spectral density of $\Delta N/N$ at location VI.

A-G88-157

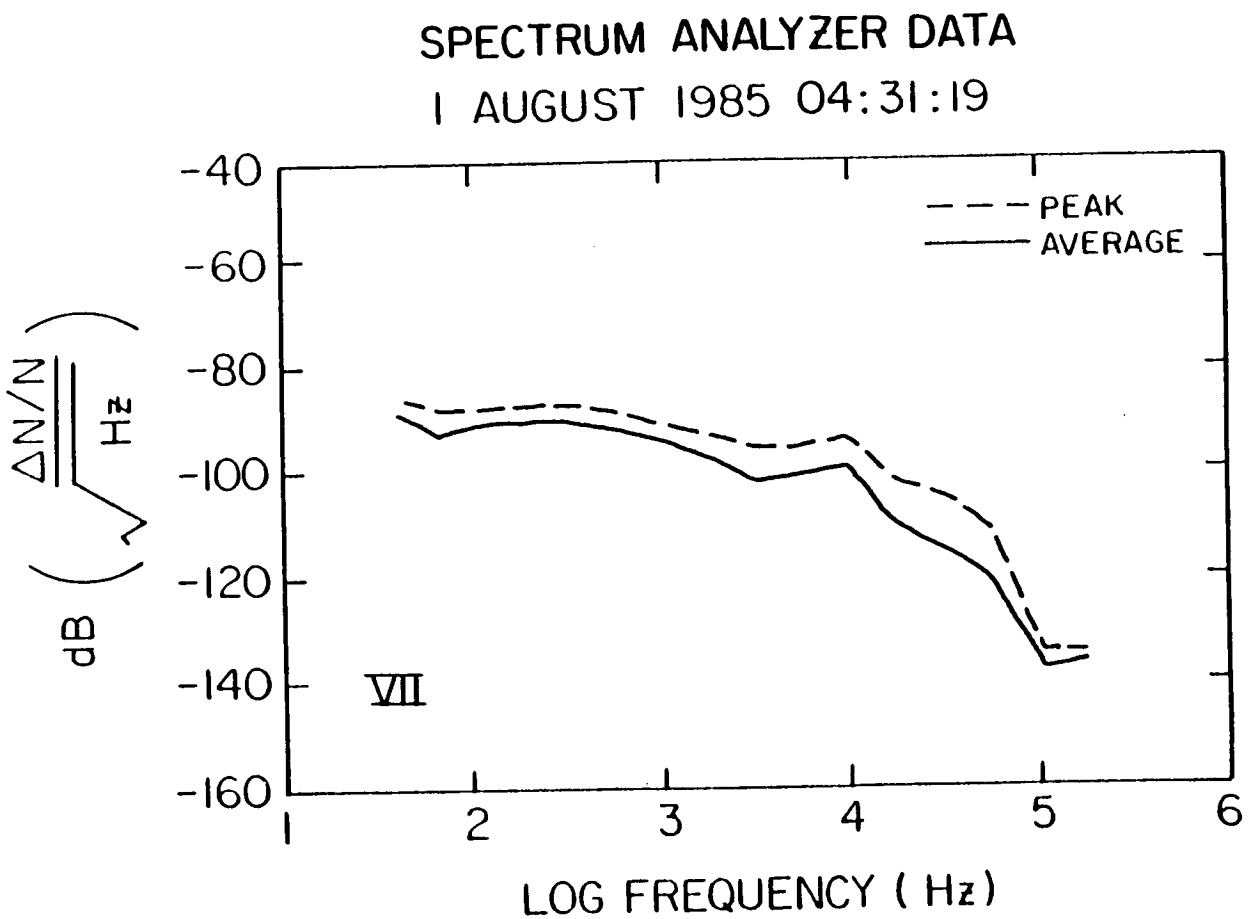

Figure 72. Spectral density of $\Delta N/N$ at location VII.

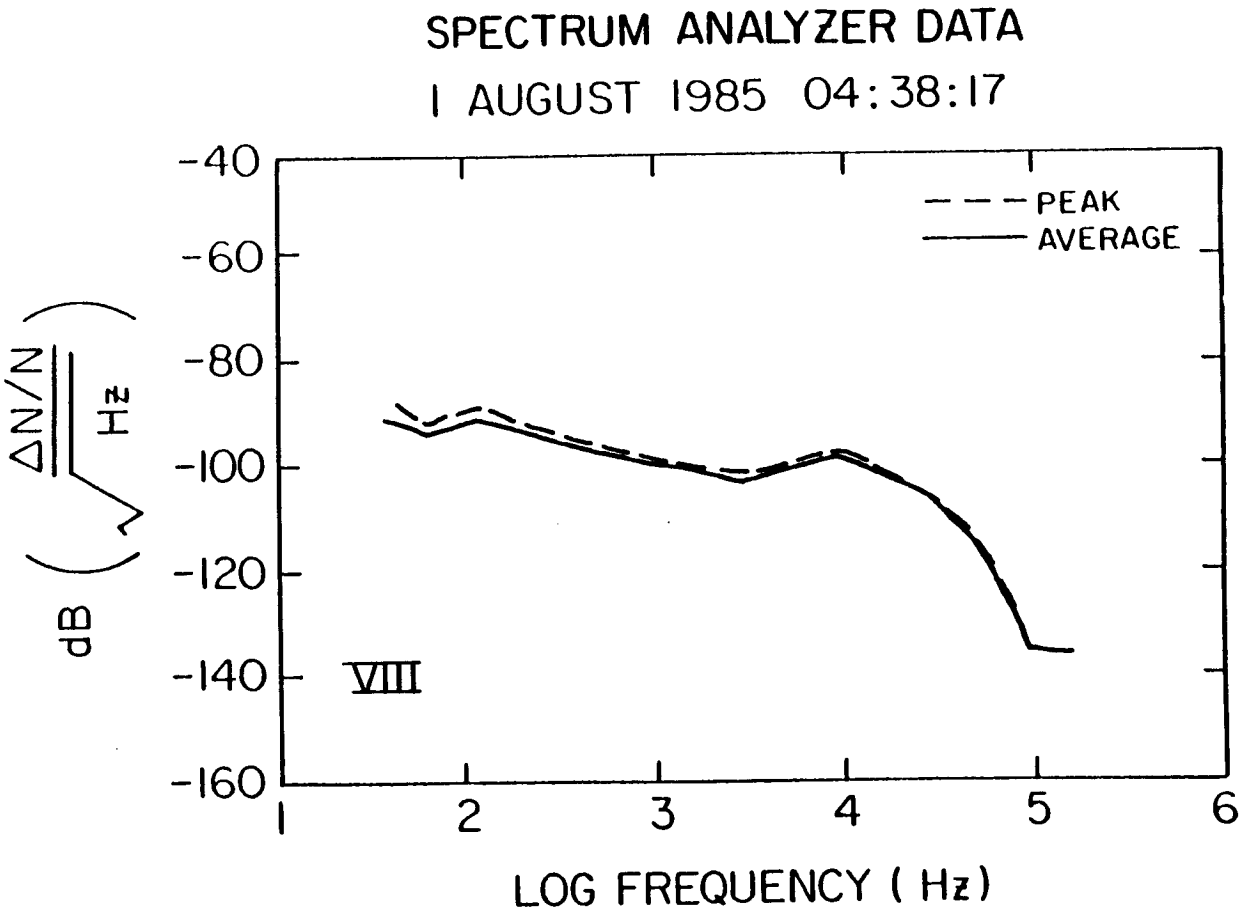

Figure 73. Spectral density of $\Delta N/N$ at location VIII.

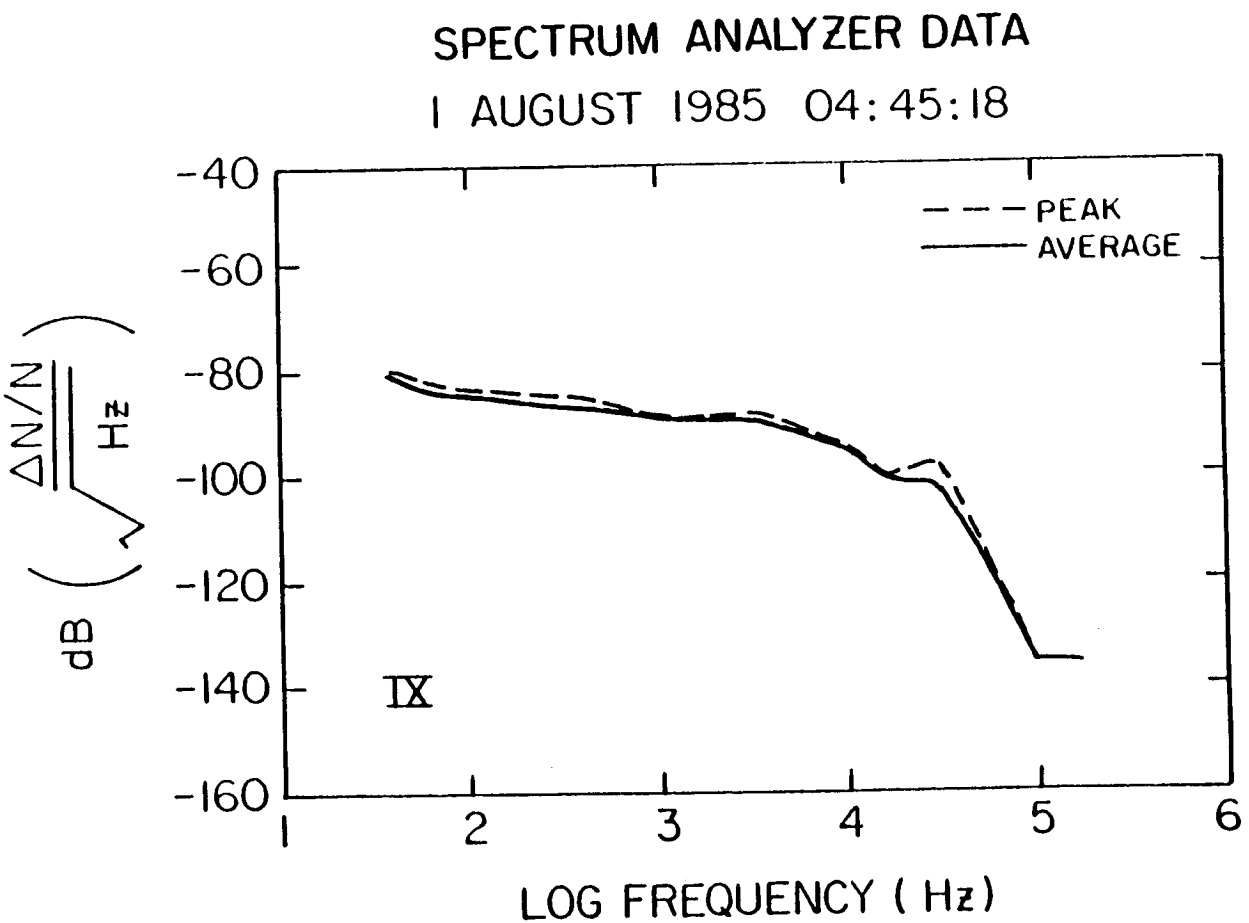

Figure 74. Spectral density of $\Delta N/N$ at location IX.

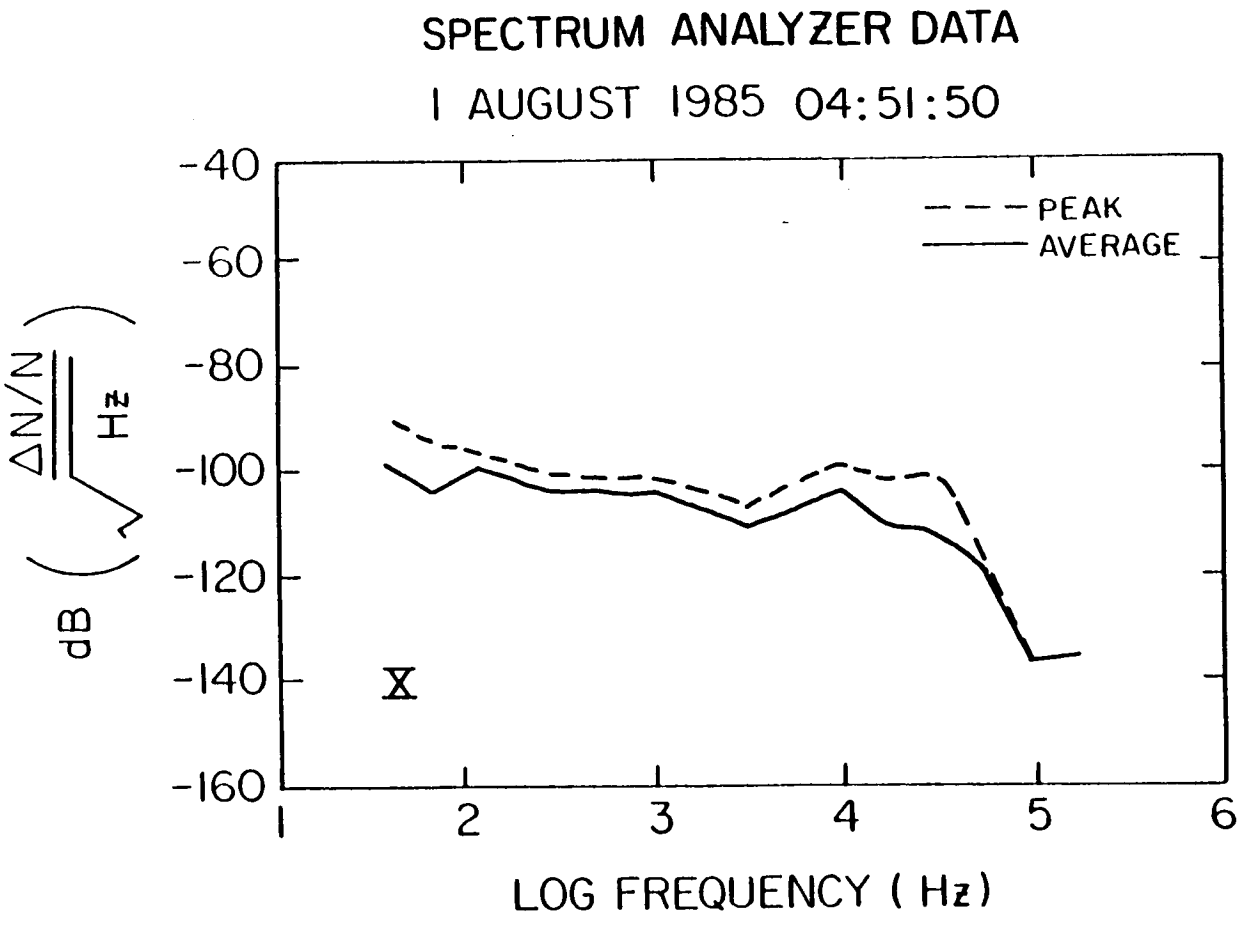

Figure 75. Spectral density of $\Delta N/N$ at location X.

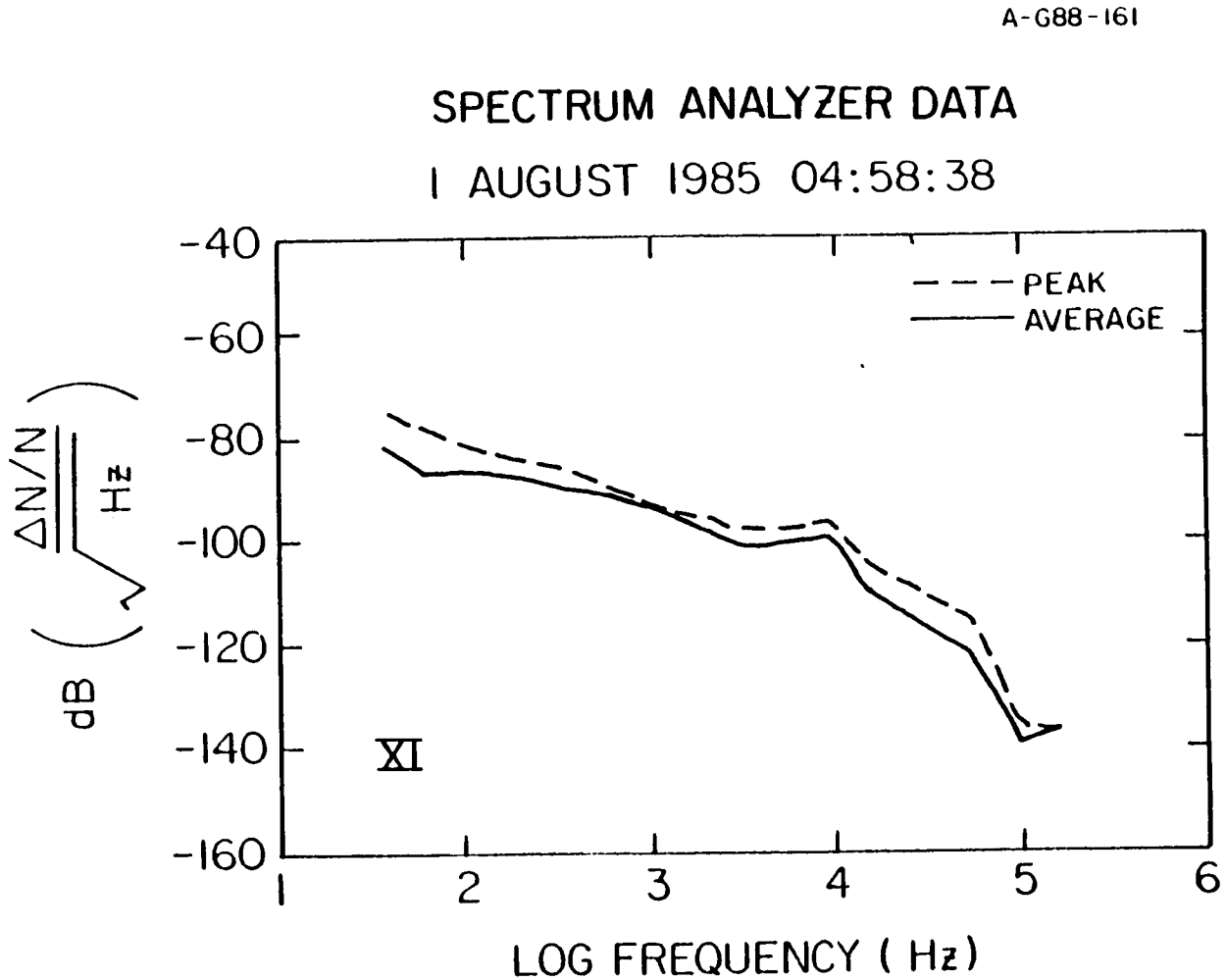

Figure 76. Spectral density of $\Delta N/N$ at location XI.

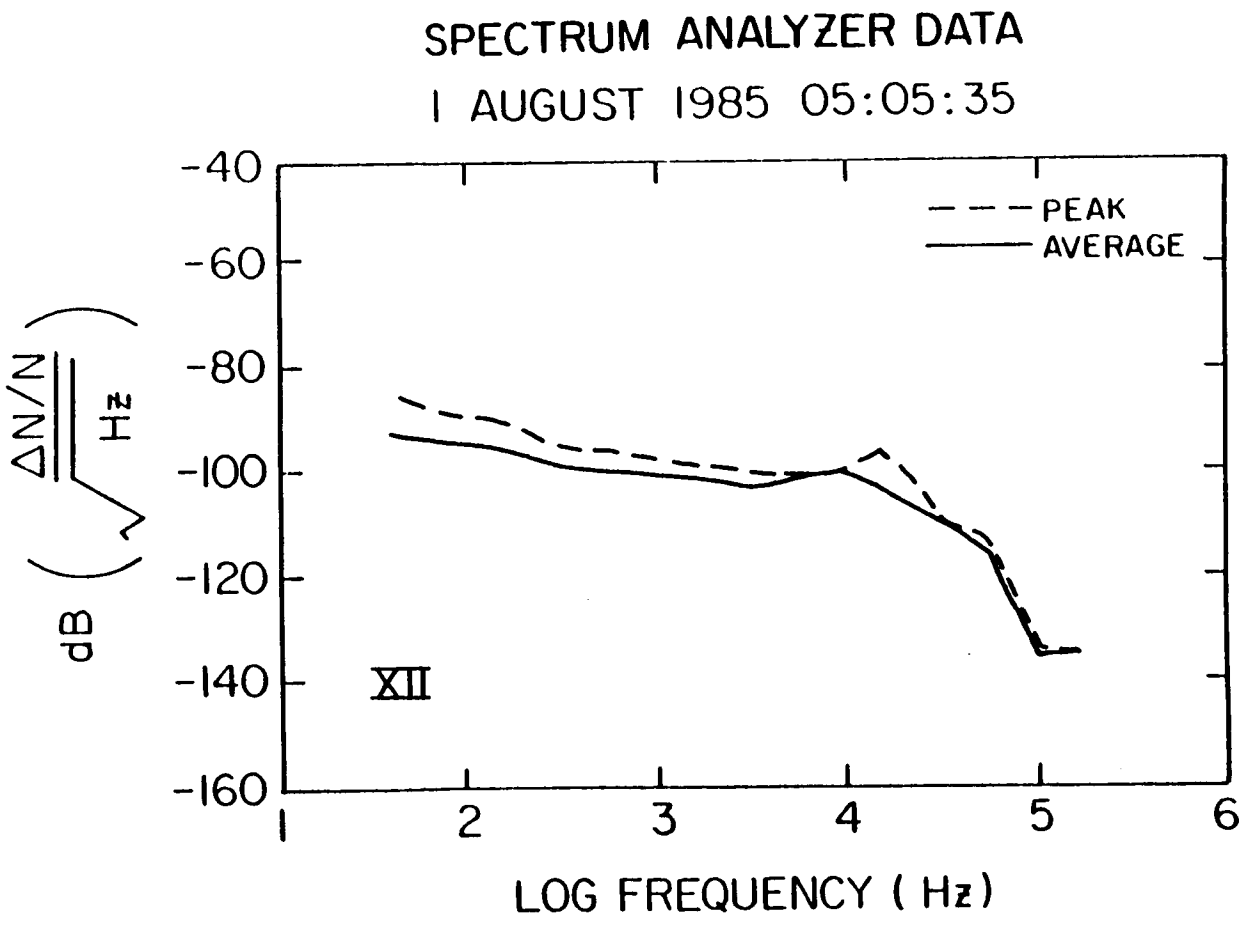

Figure 77. Spectral density of $\Delta N/N$ at location XII.

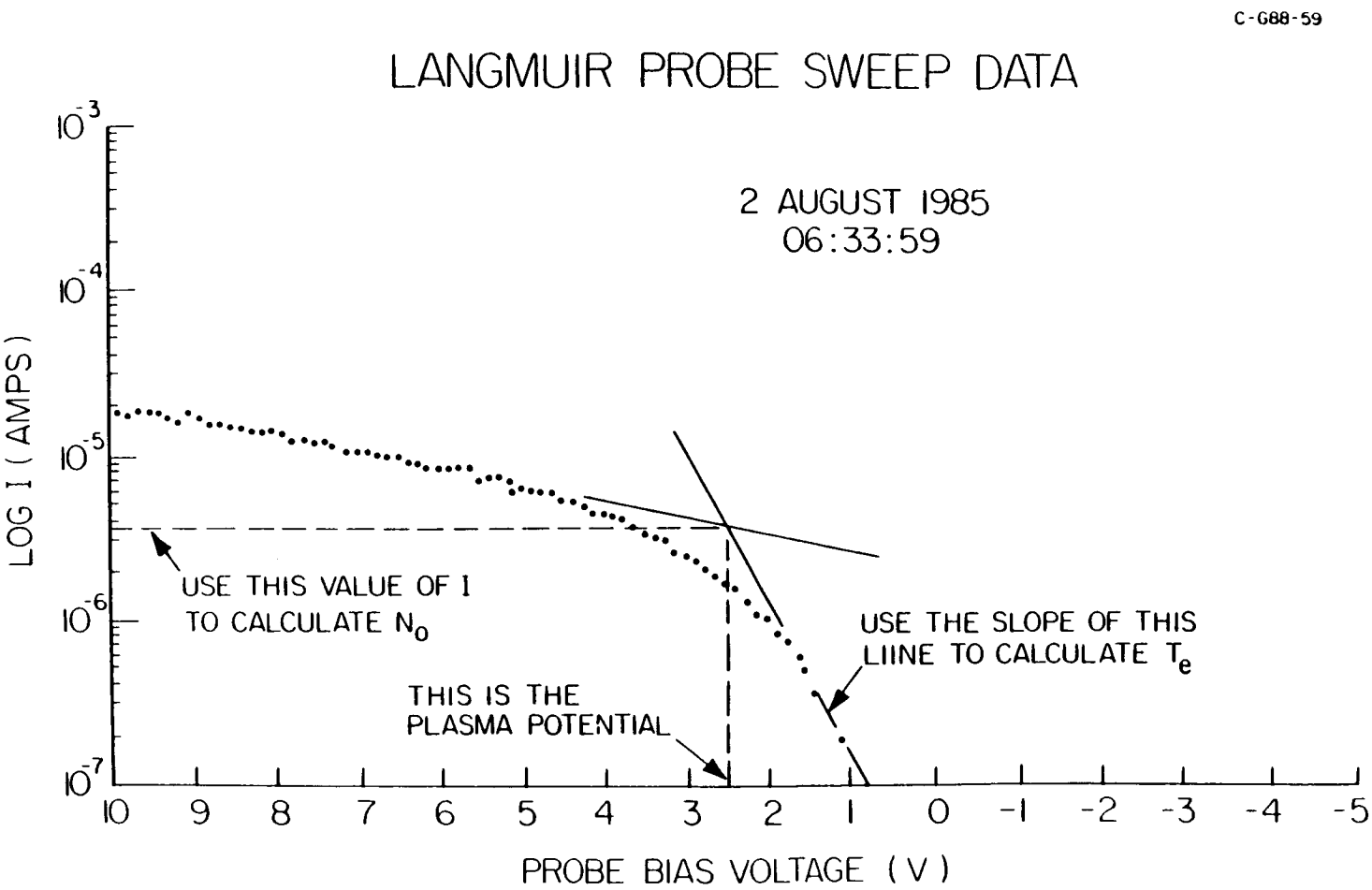

Figure 78. A typical Langmuir probe sweep showing the values of N_o, I, and 'slope' needed to calculate N_e, T_e, and V_p.

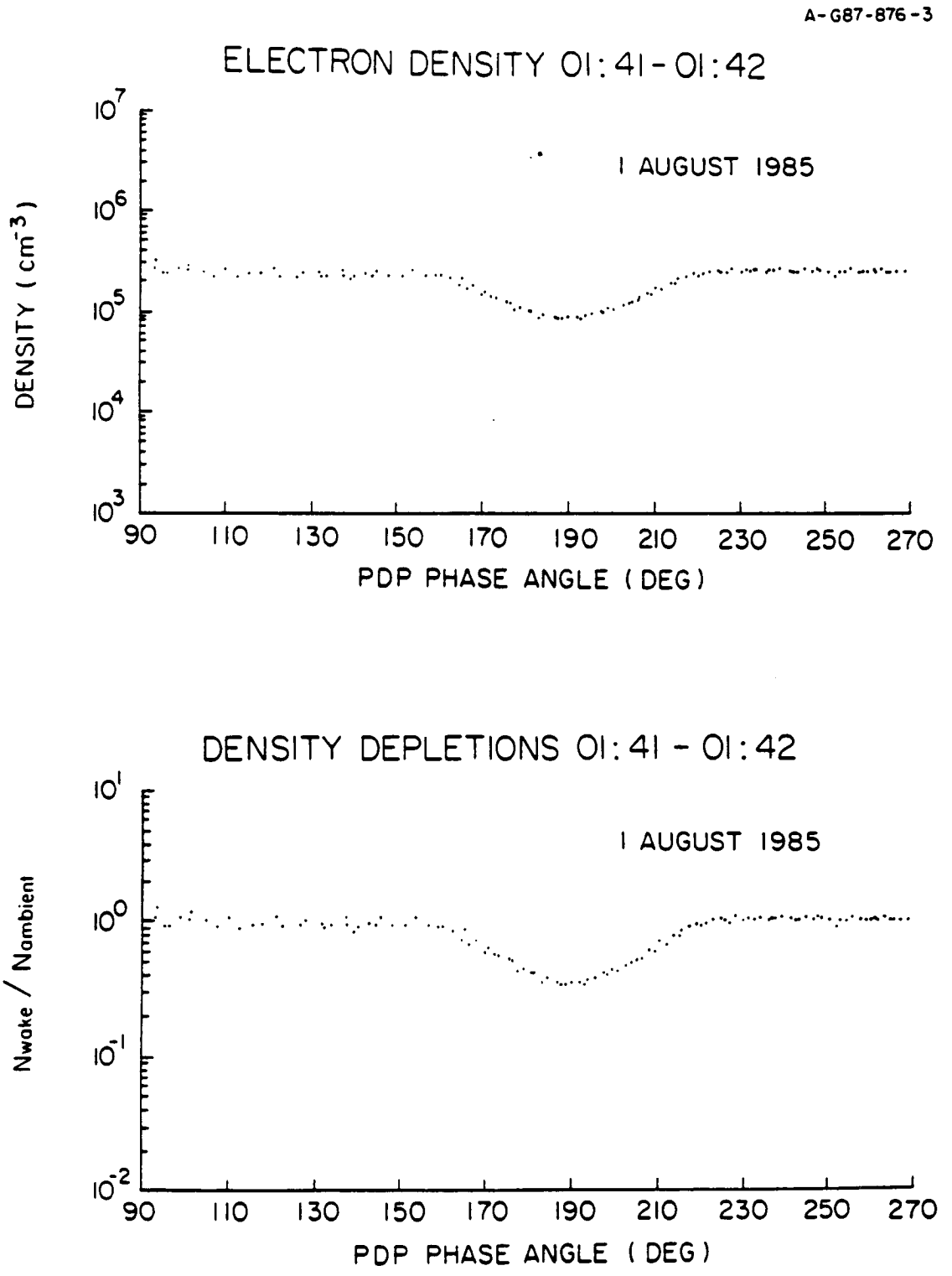

Figure 79. Electron density depletions in the wake of the PDP.

A-G87-877-3

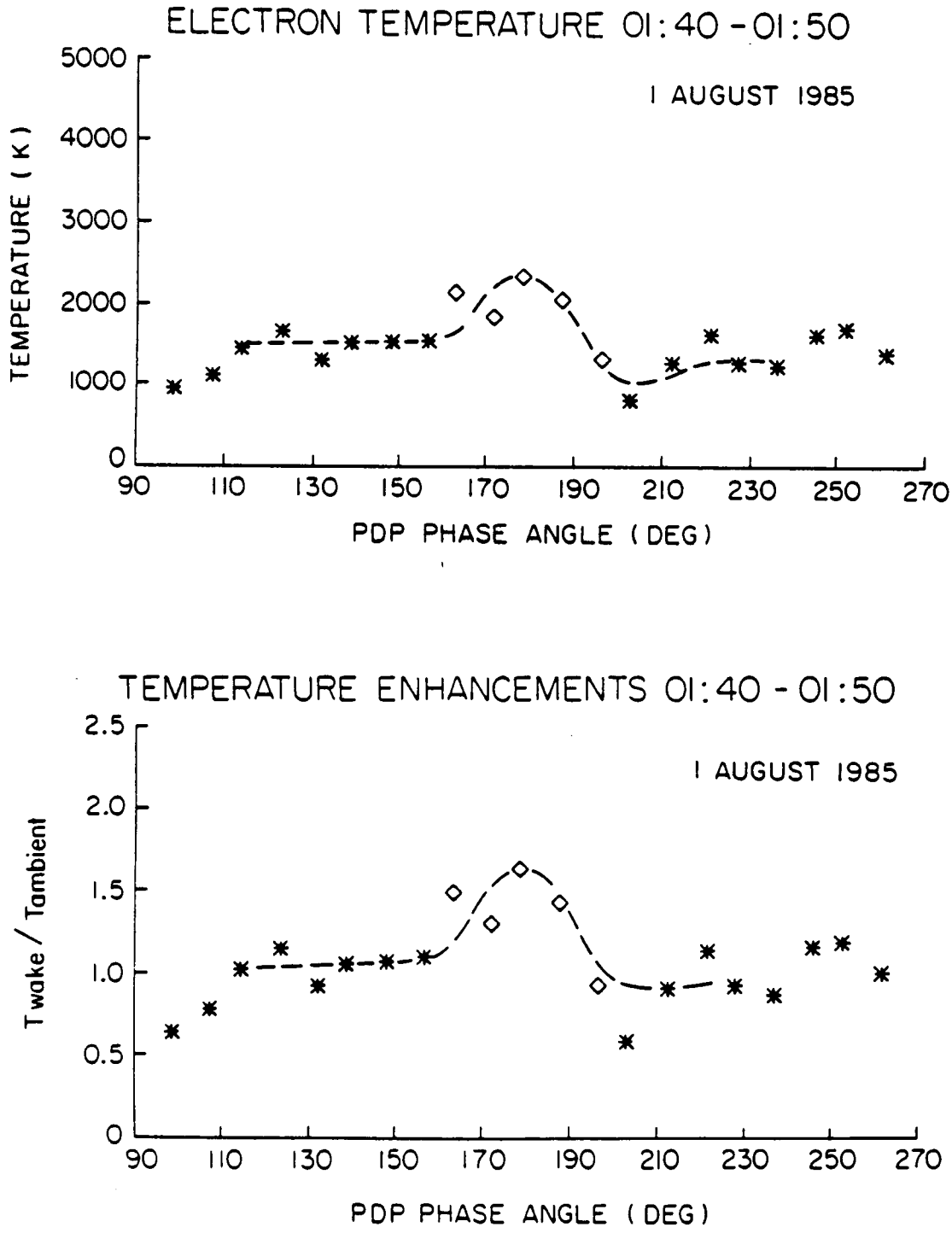

Figure 80. Electron temperature enhancements in the wake of the PDP.

REFERENCES

1. Martin, Anthony R., "Numerical Solutions to the Problem of Charged Particle Flow Around an Ionospheric Spacecraft," *Planet. Space Sci.*, Vol. 22, 121 (1974).

2. Samir, U., and G. L. Wrenn, "The Dependence of Charge and Potential Distribution Around a Spacecraft on Ionic Composition," *Planet. Space Sci.*, Vol. 17, 693 (1969).

3. Samir, U., and A. P. Willmore, "The Distribution of Charged Particles Near a Moving Spacecraft," *Planet. Space Sci.*, Vol. 13, 285 (1965).

4. Henderson, C. L., and U. Samir, "Observations of the Disturbed Region Around an Ionospheric Spacecraft," *Planet. Space Sci.*, Vol. 15, 1499 (1967).

5. Samir, Uri, "Bodies in Flowing Plasmas: Spacecraft Measurements," *Adv. Space Res.*, Vol. 1, 373 (1981).

6. Stone, N. H., and U. Samir, "Bodies in Flowing Plasmas: Laboratory Studies," *Adv. Space Res.*, Vol. 1, 361 (1981).

7. Murphy, G., J. Pickett, N. D'Angelo, and W. S. Kurth, "Measurements of Plasma Parameters in the Vicinity of the Space Shuttle," *Planet. Space Sci.*, Vol. 34, 993, 1986.

8. Raitt, W. J., D. E. Siskind, P. M. Banks, and P. R. Williamson, "Measurements of the Thermal Plasma Environment of the Space Shuttle," *Planet. Space Sci.*, Vol. 32, 457 (1984).

9. Tribble, A. C., N. D'Angelo, G. Murphy, J. Pickett, and J. Steinberg, "Exposed High-Voltage Source Effect on the Potential of an Ionospheric Satellite," *J. Spacecraft Rockets*, [in press].

10. M. A. Kasha, The Ionosphere and Its Interaction With Satellites, Gordon and Breach, Science Publishers, New York, 1965.

11. Samir, U., E. J. Maier, and B. E. Troy, Jr., "The Angular Distribution of Ion Flux Around an Ionospheric Satellite," *J. Atmos. Terres. Phys.*, Vol. 35, 513 (1973).

12. Samir, U., and G. L. Wrenn, "Experimental Evidence of an Electron Temperature Enhancement in the Wake of an Ionospheric Satellite," *Planet. Space Sci.,* Vol. 20, 899 (1972).

13. Illiano, J. M., and L. R. O. Storey, "Apparent Enhancement of Electron Temperature in the Wake of a Spherical Probe in a Flowing Plasma," *Planet. Space Sci.,* Vol. 22, 873 (1974).

14. Troy, B. E., Jr., E. J. Maier, and U. Samir, "Electron Temperatures in the Wake of an Ionospheric Satellite," *J. Geophys. Res.,* Vol. 80, 993 (1975).

15. Samir, U., L. H. Brace, and H. C. Brinton, "About the Influence of Electron Temperature and Relative Ionic Composition on Ion Depletion in the Wake of the AE-C Satellite," *Geophys. Res. Lett.,* Vol. 6, 101 (1979).

16. Morgan, M. A., C. Chan, and R. C. Allen, "A Laboratory Study of the Electron Temperature in the Near Wake of a Conducting Body," *Geophys. Res. Lett.,* Vol. 14, 1170 (1987).

17. Fournier, G., and D. Pigache, "Wakes in Collisionless Plasma," *Phys. Fluids,* Vol. 18, 1443 (1975).

18. J. C. Taylor, "Disturbance of a Rarefied Plasma by a Supersonic Body on the Basis of the Poisson-Vlasov Equations-I, The Heuristic Method," *Planet. Space Sci.,* Vol. 15 155 (1967).

19. J. C. Taylor, "Disturbance of a Rarefied Plasma by a Supersonic Body on the Basis of the Poisson-Vlasov Equations-II, Formal Method," *Planet. Space Sci.,* Vol. 15 463 (1967).

20. Skvortsov, V. V., and L. V. Nosachev, "The Structure of the Trail Behind a Spherical Model in a Stream of Rarefied Plasma," *Cosmic Res.,* Vol. 6, 191 (1968).

21. Skvortsov, V. V., and L. V. Nosachev, "Some Results on Disturbances Introduced by Extraneous Bodies into a Stream of Rarefied Plasma," *Cosmic Res.,* Vol. 6, 718 (1968).

22. J. P. M. Schmitt, "Wake Past an Obstacle in a Magnetized Plasma Flow," *J. Plasma Physics,* Vol. 15, 677 (1973).

23. Bogashchenko, I. A., A. V. Gurevich, R. A. Salimov, and Yu. I. Éĭdel'man, "Flow of Rarefied Plasma Around a Body," *Soviet Physics JETP,* Vol. 32, 841 (1971).

24. Stone, N. H., W. A. Oran, and U. Samir, "Collisionless Plasma Flow Over A Conducting Sphere," *Planet. Space Sci.,* Vol. 20, 1787 (1972).

25. Merlino, R. L., and N. D'Angelo, "The Interaction of a Conducting Object With a Supersonic Plasma Flow: Ion Deflection Near a Negatively Charged Obstacle," *J. Plasma Physics,* Vol. 37, 185 (1987).

26. Gurevich, A. V., L. V. Pariĭskaya, and L. P. Pitaevskiĭ, "Ion Acceleration Upon Expansion of a Rarefied Plasma," *Soviet Physics JETP,* Vol. 36, 274 (1973).

27. Singh, N., U. Samir, K. H. Wright, Jr., and N. H. Stone, "A Possible Explanation of the Electron Temperature Enhancement in the Wake of a Satellite," *J. Geophys. Res.,* Vol. 92, 6100 (1987).

28. Samir, U., K. H. Wright, Jr., and N. H. Stone, "The Expansion of a Plasma Into a Vacuum: Basic Phenomena and Processes and Applications to Space Plasma Physics," *Rev. Geophys. Space Phys.,* Vol. 21, 1631 (1983).

29. Oran, W. A., N. H. Stone, and U. Samir, "The Effects of Body Geometry on the Structure in the Near Wake Zone of Bodies in a Flowing Plasma," *J. Geophys. Res.,* Vol. 80, 207 (1975).

30. B. Könemann, "The Collisionless Flow of Unmagnetized Plasmas Around Bodies," *J. Plasma Physics,* Vol. 20, 17 (1978).

31. Bingham, G., et al., *Modern Techniques of Power Spectrum Estimation, IEEE Trans.*, AU-15 2, 56, 1967.

32. Murphy, G. B., D. L. Reasoner, A. Tribble, N. D'Angelo, J. S. Pickett, W. S. Kurth, "The Plasma Wake of the Shuttle Orbiter," *J. Geophys. Res.*, submitted December 1987.

33. Huddlestone, R. H., and S. L. Leonard (Eds.), Plasma Diagnostic Techniques, Academic Press, New York, 1965.

34. Parrot, M. J. M., L. R. O. Storey, L. W. Parker, and J. G. Laframboise, "Theory of Cylindrical and Spherical Langmuir Probes in the Limit of Vanishing Debye Number," *Phys. Fluids,* Vol. 25, 2388 (1982).

35. Rubinstein, J., and J. G. Laframboise, "Theory of a Spherical Probe in a Collisionless Magnetoplasma," *Phys. Fluids,* Vol. 25, 1174 (1982).

36. Szuszczewicz, E. P., and P. Z. Takacs, "Magnetosheath Effects on Cylindrical Langmuir Probes," *Phys. Fluids,* Vol. 22, 2424 (1979).

37. Makita, H., and K. Kuriki, "Current Collection by Spherical Langmuir Probes Drifting in a Collisionless Plasma," *Phys. Fluids,* Vol. 21, 1279 (1978).

QUASI-STATIC ELECTRIC FIELD MEASUREMENTS MADE WITH THE PLASMA DIAGNOSTICS PACKAGE IN FREE FLIGHT DURING SPACELAB-2

by

John Tyree Steinberg

An Abstract

Of a thesis submitted in partial fulfillment
of the requirements for the Doctor of
Philosophy degree in Physics
in the Graduate College of
The University of Iowa

May 1988

Thesis supervisor: Professor Donald A. Gurnett

ABSTRACT

As part of the Spacelab-2 mission the Plasma Diagnostics Package (PDP) was released from the shuttle as a free flying satellite. The shuttle performed maneuvers around the PDP in order that the ionospheric plasma around the shuttle might be studied. One objective of the PDP was to measure quasi-static electric fields in the vicinity of the shuttle. During most of the free flight, the measured electric field was comparable to the induced electric field due to the orbital motion of the spacecraft. The difference between the measured field and the motional field was typically on the order of the uncertainty of measurement. At certain times, when the shuttle thrusters were operating, decreases in the motional electric field by 10% to 20% were observed. The decreases are explained by the generation of an Alfvén wave from pickup current. An estimate of the electric field associated with Alfvén wave excitation agrees with the decreases observed at times of thruster firings. The Alfvén wave model predicts that large changes in the electric field should occur only at times of large neutral gas releases from the shuttle. The decreases in the electric field occur in the region of the thruster plume, as well as along the magnetic flux tubes passing through the plume.

During times when an electron beam was ejected from the shuttle, large signals were also recorded. These large signals were probably

not due to ambient electric fields, but can be attributed to three causes: differences in fluxes of streaming electrons to the two probes due to shadowing by the PDP chassis, depressions in the plasma density caused by the PDP wake, and spatial gradients in the fluxes of energetic electrons reaching the probes. Energetic electrons were found in a region 20 m wide and up to at least 170 m downstream from the electron beam. At 80 or more meters downstream from the beam, the energetic electrons had a preferential direction of motion opposite to the beam injection direction.

Abstract approved: David A. Gurnett
Thesis supervisor

Professor, Physics and Astronomy
Title and department

May 4, 1988
Date

QUASI-STATIC ELECTRIC FIELD MEASUREMENTS MADE WITH THE PLASMA DIAGNOSTICS PACKAGE IN FREE FLIGHT DURING SPACELAB-2

by

John Tyree Steinberg

A thesis submitted in partial fulfillment
of the requirements for the Doctor of
Philosophy degree in Physics
in the Graduate College of
The University of Iowa

May 1988

Thesis supervisor: Professor Donald A. Gurnett

Graduate College
The University of Iowa
Iowa City, Iowa

CERTIFICATE OF APPROVAL

PH.D. THESIS

This is to certify that the Ph.D. thesis of

John Tyree Steinberg

has been approved by the Examining Committee for the thesis requirement for the Doctor of Philosophy degree in Physics at the May 1988 graduation.

Thesis committee:

Thesis supervisor

Member

Member

Member

Member

ACKNOWLEDGEMENTS

I thank my graduate advisor, Dr. Donald A. Gurnett, for the support and guidance he has given me on this work. I also thank the following professors for their assistance: Dr. Nicola D'Angelo, Dr. Christoph K. Goertz, and Dr. Karl Lonngren. The following people, who have helped me on this work numerous times, have my gratitude: Terrance Averkamp, Scott Boardsen, William Farrell, Larry Granroth, Robert Lane, Gerald Murphy, William Paterson, Jolene Pickett, and Alan Tribble. Thanks also to John Birkbeck for his fine drafting. I am especially grateful to Kathy Kurth, and her able assistant, Tami Thompson, for taking the stacks of scrawled writings and the floppy disks I gave them, waving their magic wands over them, and transforming them into this thesis manuscript.

I thank my wife, Kati, for her constant faith in me. This thesis is dedicated to my father, the late Alvin Steinberg.

The research was supported by NASA though contract NAS8-32807 with Marshall Space Flight Center, contract NAG3-449 with NASA Lewis Research Center, and grant NGL 16-001-043 with NASA Headquarters.

ABSTRACT

As part of the Spacelab-2 mission the Plasma Diagnostics Package (PDP) was released from the shuttle as a free flying satellite. The shuttle performed maneuvers around the PDP in order that the ionospheric plasma around the shuttle might be studied. One objective of the PDP was to measure quasi-static electric fields in the vicinity of the shuttle. During most of the free flight, the measured electric field was comparable to the induced electric field due to the orbital motion of the spacecraft. The difference between the measured field and the motional field was typically on the order of the uncertainty of measurement. At certain times, when the shuttle thrusters were operating, decreases in the motional electric field by 10% to 20% were observed. The decreases are explained by the generation of an Alfvén wave from pickup current. An estimate of the electric field associated with Alfvén wave excitation agrees with the decreases observed at times of thruster firings. The Alfvén wave model predicts that large changes in the electric field should occur only at times of large neutral gas releases from the shuttle. The decreases in the electric field occur in the region of the thruster plume, as well as along the magnetic flux tubes passing through the plume.

During times when an electron beam was ejected from the shuttle, large signals were also recorded. These large signals were probably

C-7

not due to ambient electric fields, but can be attributed to three causes: differences in fluxes of streaming electrons to the two probes due to shadowing by the PDP chassis, depressions in the plasma density caused by the PDP wake, and spatial gradients in the fluxes of energetic electrons reaching the probes. Energetic electrons were found in a region 20 m wide and up to at least 170 m downstream from the electron beam. At 80 or more meters downstream from the beam, the energetic electrons had a preferential direction of motion opposite to the beam injection direction.

TABLE OF CONTENTS

LIST OF TABLES

LIST OF FIGURES

CHAPTER I

INTRODUCTION

As part of the Spacelab-2 mission, which was launched on July 29, 1985, a spacecraft called the Plasma Diagnostics Package (PDP) was released from the space shuttle to survey the plasma environment around the orbiter. The PDP, which consisted of a scientific instrument package containing 14 instruments, was designed and constructed at the University of Iowa, and is described by Shawhan et al. [1982]. The PDP was in free flight for roughly six hours, during which time the shuttle was maneuvered to performed two complete fly-arounds of the PDP. The fly-arounds allowed the PDP to make measurements both upstream and downstream from the shuttle at distances up to 400 meters. The fly-arounds also included four magnetic conjunctions during which the shuttle was targeted to pass through the magnetic field line passing through the PDP. At various times an electron beam was ejected from the shuttle so that the effects in the plasma might be studied. The electron beam generator, flown as part of the Vehicle Charging and Potential (VCAP) experiment provided by Stanford University and Utah State University, is described by Banks et al. [1987]. The PDP and the electron beam generator were previously flown on the STS-3 flight [Shawhan et al., 1984a]. The PDP carried instrumentation which made

differential voltage measurements between two floating probes in order to measure quasi-static electric fields. This thesis reports on efforts to measure the quasi-static electric fields in the plasma with the PDP during the free flight. The discussion is divided into two main topics: measurements of perturbations in the electric field associated with operation of the shuttle thrusters, and measurements of large differential voltages between the double probes at times of electron beam operations.

In situ measurements of the plasma environment around the space shuttle have shown that the plasma differs significantly from that expected for an ambient ionospheric plasma. Some of the plasma measurements which have been performed from the shuttle are reported in the papers by Stone et al. [1983], Raitt et al. [1984], Shawhan et al. [1984b], Pickett et al. [1985], Hunten and Calo [1985], Murphy et al. [1986], Reasoner et al. [1986], Stone et al. [1986], Grebowsky et al. [1987a], and Grebowsky et al. [1987b]. A review of the ion and neutral particle measurements on shuttle flights STS-2 through STS-4 is given by Green et al. [1985]. The plasma around the shuttle is characterized by the induced effects of neutral gases released from the orbiter. Neutral gases are released from the shuttle by outgassing of shuttle surfaces, orbiter water dumps, flash evaporator system releases, and thruster operations. Charge exchange reactions between the neutral particles of shuttle origin and the ambient plasma particles lead to the creation of molecular ions which are not naturally present at

shuttle altitudes, or that do not generally occur in the concentrations measured around the shuttle. The principal contaminant neutral species is H_2O, although the thruster emissions also include significant amounts N_2, H_2, and CO, plus lesser amounts of a few other species. The contaminant molecular ions identified in the region around the shuttle include H_2O^+, H_3O^+, NO^+, OH^+, N_2^+, N^+, and O_2^+. Some of the ions measured near the shuttle are found to have drift velocities with respect to the shuttle less than the orbital velocity [Hunten and Calo, 1985], thus suggesting that some plasma moves with the shuttle.

In this thesis, the effect of the interaction between shuttle derived neutrals and ambient plasma on the quasi-static electric field near the shuttle is considered. The motion of the orbiting shuttle through the earth's magnetic field $\vec{B}$ induces an electric field in the reference frame of the shuttle equal to $\vec{V} \times \vec{B}$, where $\vec{V}$ is the velocity vector of the shuttle relative to the ionospheric plasma, which is assumed to co-rotate with the earth. However, plasma processes may alter the electric field. Katz et al. [1984] point out that if a cloud of plasma drifts with the shuttle, the plasma cloud would polarize and partially or completely screen out the motional electric field. Pickett et al. [1985] suggest that if ions formed by charge exchange reactions do not drift with the shuttle, but rather are picked-up by the ionospheric plasma flow, then the motion of the pickup ions may cause partial screening out of the motional electric field. The effect

of pickup ions on the electric field will be considered further in a later section of this thesis.

Measurements of the electric field around the shuttle made using probes attached to the shuttle orbiter have previously been reported. Smiddy et al. [1983] measured electric fields by measuring the differential voltage between two spherical probes mounted 1.6 m apart in the bay of the orbiter. Their measurements showed no discernible changes in the motional $\vec{V} \times \vec{B}$ electric field during thruster firings or water dumps. Other indications of the electric field around the shuttle are given by the measurements of Shawhan et al. [1984b] and of Raitt et al. [1984]. Both groups measured the floating potential of a probe attached to the orbiter. Since the main engine nozzles are the only exposed conducting surfaces of the orbiter, the measurements were compared to $(\vec{V} \times \vec{B}) \cdot \vec{L}$, where $\vec{L}$ is the vector from the probe to the center of the main engine nozzles. Both groups claim that $(\vec{V} \times \vec{B}) \cdot \vec{L}$ provides a good first-order model of the data, indicating that the motional electric field is screened to only a small degree. However, the Shawhan et al. results show reductions in the measured potential at times of thruster operations (Figure 1). This suggests that at times of large gas releases such as those associated with thruster firings, the electric field may be partially screened.

Whereas the previous electric field measurements were made from probes attached to the orbiter, this thesis discusses measurements made with the PDP while it was released as a free-flying satellite. During

the free flight there were no water dumps, and no flash evaporator system operations were performed. The only chemical releases were the outgassing from the shuttle surfaces, and thruster firings. Except for perturbations related to electron beam operations, the only perturbations to the motional electric field detected with the PDP were associated with thruster firings.

In addition to study of the interaction of the ionospheric plasma with neutral gases released from the shuttle, the Spacelab-2 mission provided opportunity to study the interaction of an electron beam with the ionospheric plasma. Prior to shuttle flights, several electron beam experiments were performed in plasma chambers and from rockets. Some of these experiments included electric field measurements. Using the same PDP and electron beam generator later flown onboard Spacelab-2, quasi-static electric fields of the order of a few volts/m were measured within a few meters of the beam in a large plasma chamber at Johnson Space Flight Center [Shawhan, 1982]. Denig [1982] questioned the reliability of these measurements because of the possibility of differential charging on the measuring probes, and because the fields seemed too large to be sustained in the given apparatus. Kellogg et al. [1982] also reported measuring fields of a few volts/m in a similar chamber test. Measurements of the quasi-static electric fields have also been reported in association with electron beams emitted from rockets in the ionosphere. In the Polar 5 experiment, fields on the order of 0.1 volts/m were detected

over 100 meters away from the beam source [Jacobsen and Maynard, 1978]. During the Echo 6 experiment, Winckler and Erickson [1986] measured fields on the order of 0.2 volts/m at a distance of 40 meters from the flux tube on which the beam was expected to be centered. All the measurements mentioned here involved differential voltage measurements using floating probes. Considering the chamber and rocket experiments, on the Spacelab-2 mission we expected to detect fields on the order of 1 volt/m associated with the electron beam.

The electron beam generator was operated at various times throughout the free flight, both in a steady (DC) mode, and in a pulsed mode. During several of these times, signals on the order of 1 volt/m were detected by the quasi-static electric field instrument. In this thesis the large signals obtained in association with the electron beam firings are described and the origin of the signals is discussed.

Understanding the plasma environment around the shuttle is of interest for planning other scientific experiments to be performed from the shuttle, and for designing other large objects to be placed in low earth orbit. The interaction of the gas around the shuttle with the ambient plasma is also interesting because of its analogy to other important problems in space plasma physics, such as the interaction between comets and the solar wind, Io and the Jovian magnetosphere, or Titan and the Saturnian magnetosphere. Understanding beam plasma interactions is of interest as electron beam experiments continue to be performed in the ionosphere.

CHAPTER II

INSTRUMENTATION

Quasi-static electric field measurements were made on the PDP by measuring potentials using two conducting spheres, both at floating potential, mounted on insulated booms on opposite sides of the spacecraft. The sphere-to-sphere separation was 3.89 meters, and the diameter of the spheres was 10.2 cm. A diagram of the PDP, showing the dimensions of the main chassis and the locations of spherical probes, which are labeled sphere 1 and sphere 2, is presented in Figure 2. Two types of measurements were made: the differential voltage, V_{diff}, between the two probes was measured at both a high gain and a low gain, and the average voltage, V_{ave}, of the two probes relative to the PDP chassis was measured at a fixed gain. The following relations describe the two measurements:

$$V_{diff} = V_2 - V_1$$
$$V_{ave} = (V_2 + V_1)/2$$

where V_1 and V_2 are respectively the potentials of sphere 1 and sphere 2 relative to the PDP chassis. Typically the quantity V_{diff}/L, where L is the antenna length, is interpreted as a measurement of the electric

field. The basic instrument parameters and dynamic ranges are given in Table 1. Since the floating potential of an object in a plasma is dependent on the surface materials, it is also important to describe the surface properties of the spacecraft and spheres. The PDP chassis was covered with a teflon-coated fiberglass cloth which in turn was covered with an aluminum mesh to provide a uniform conducting surface. Potential measurements were referenced to the aluminum mesh. The spherical antenna probes were coated with a conducting graphite-epoxy paint.

After release from the shuttle, the PDP was made to spin by the action of an inertia wheel within the PDP. When spinning at its maximum rate, the spacecraft had a spin period of 13.1 seconds. The spin axis was oriented approximately perpendicular to the orbital plane. Thus, the spacecraft velocity vector lay approximately in the PDP spin plane.

The electron beam generator was mounted in the shuttle payload bay. A beam was produced by accelerating electrons emitted from a heated tungsten wire filament through a 1 kilovolt potential. The generator operated at beam currents of either 50 ma or 100 ma, and could produce either a steady or a pulsed beam. The beam was pulsed at frequencies up to 800 kHz.

CHAPTER III

DATA ANALYSIS

From the electric field signal (V_{diff}/L), one can obtain a measurement of the electric field in the spacecraft spin plane. The complete electric field vector was evaluated by first determining the electric field in the spin plane, and then using the assumption that $\vec{E}\cdot\vec{B} = 0$ to find the component of $\vec{E}$ along the spin axis. The magnetic field was determined from a multipole model of the earth's magnetic field. In the region of the ionosphere where the Spacelab-2 mission was flown, the parallel conductivity is generally much greater than the perpendicular conductivity, so the assumption that the parallel electric field is zero is reasonable. A discussion of the determination of the electric field in the spin plane follows.

Upon initial release from the shuttle, the PDP was not spinning. After release, the inertia wheel inside the PDP was activated and the PDP began to spin, attaining a spin period of 13.1 seconds after 73 minutes. The spin rate of the inertia wheel was gradually reduced starting at about 53 minutes before the end of the free flight, so that the PDP was not spinning when the spacecraft was retrieved. When the PDP was rotating, the potential difference between the spheres was expected to vary sinusoidally, with the spin period. A measurement of

the electric field vector in the spin plane, $\vec{E}_s$, was obtained by using a least square's fit method to fit a 13.1-second segment of the electric field signal to the function

$$F(t) = F_1 + F_2\cos(2\pi t/T - \Phi) \qquad (1)$$

where T is the spin period in seconds, and F_1, F_2, and Φ are parameters determined by the fit procedure. Measurements of the electric field were made for all times when the PDP spin period was 15 seconds or less. During these times the PDP was no closer than 50 meters from the shuttle.

As part of the fitting procedure, it was found to be necessary to remove certain contaminating signals. The contaminating signals were found to be related to the operation of the Low Energy Proton and Electron Differential Energy Analyzer (Lepedea) on the PDP. As Tribble et al. [1987] report, the operation of the Lepedea resulted in changes in the spacecraft potential. The Lepedea utilized a current collecting plate whose voltage jumped to +2 kilovolts every 1.6 seconds. The plate collected a large thermal electron current, and the PDP potential decreased by several volts, typically recovering its original value within 0.8 seconds. The average potential V_{ave} of the probes was sampled every 1.6 seconds and always 0.166 seconds after the voltage on the Lepedea current collecting plate jumped to 2 kilovolts. Thus, V_{ave} was sampled at a time when the PDP potential was lower than when

Lepedea was not collecting current. Or equivalently, the average potential of the probes relative to the PDP at the sample time was higher than when Lepedea was not collecting current. The degree of charging of the spacecraft was less when the Lepedea aperture faced the spacecraft wake, than when the aperture faced the ram direction. The V_{ave} potential signal was spin modulated because of this effect, as can be seen in Figure 3. For the V_{diff} measurement, a large negative potential on the PDP was equivalent to a large positive common mode signal on the probes. Because of limitations in the common mode rejection, the V_{diff} signal was contaminated whenever the PDP potential exceeded several volts negative. An example of the contaminating signal is shown in Figure 4. In order to remove this contaminating signal, 0.8 seconds of the signal was removed every 1.6 seconds. This process significantly degraded the accuracy and resolution of the electric field measurement, but was unavoidable due to the contaminating signal from the Lepedea.

In addition to the contamination from the Lepedea, times when one probe was in the PDP spacecraft wake were also removed from the signal. Examination of the electric field signal shows that during much of the free flight, the signal deviated from a sine wave whenever one of the probes passed through the PDP wake. An example is shown in Figure 4. In the spacecraft wake, the plasma density is lower than the ambient density, and the electron temperature is higher. Whenever the plasma environment differs between the two probes, differential voltage

measurements on floating probes do not give a reliable measure of the electric field. The antenna probe is typically within the Mach cone extending downstream from the PDP when the angle of the antenna to the velocity vector is less than 26^{o}. In order to be sure to remove the effects of the spacecraft wake, the electric field signal was removed if the angle between the antenna and the velocity vector was less than 35^{o}. This turns out to be a segment of the signal lasting 2.5 seconds. Figure 5 shows the signal remaining after the various known contaminating signals were removed.

Measurements of the electric field in the spin plane were made every 5 seconds, by sliding the 13.1-second sample of the signal used in the fit procedure along in 5-second intervals. That is, each measurement contains 8.1 seconds of the signal used in the previous measurement. In order to estimate the uncertainty of E_s for each measurement, the following goodness of fit parameter was calculated:

$$X = \left[\frac{\Sigma(F(t_i) - x_i)^2}{(N - 3)}\right]^{1/2}/F_2 \quad . \qquad (2)$$

The parameter X is derived from the chi square parameter normally used in statistical analysis, by scaling chi square to the sine wave magnitude F_2, so as to obtain a dimensionless parameter. Small values of X (less than about 0.1) indicate that fitted function F(t) represents the data well.

CHAPTER IV

GENERAL RESULTS

The magnitude of the measured electric field in the PDP spin plane was usually on the order of the component of $\vec{V} \times \vec{B}$ in the spin plane, which ranged from 0.04 volts/m to 0.16 volts/m. Exceptions occurred during the following five time intervals when the electron beam was operating, and V_{diff}/L signals from 0.5 volts/m to 2 volts/m were detected.

GMT 213 00:46:10 - 00:49:15

GMT 213 01:19:25 - 01:20:20

GMT 213 02:47:30 - 02:50:45

GMT 213 03:33:25 - 03:34:25

GMT 213 04:11:10 - 04:12:00

The signals during these intervals will be discussed in Section VI. Measured values of the electric field magnitude in the spin plane, for all times excluding the above five intervals, are shown in Figure 6. The line in the figure represents the spin plane component of $\vec{V} \times \vec{B}$. The magnitude of the measured field is generally within about 10% of the motional field. Figure 7 displays the uncertainty of measurement as determined from Equation 2.

After the electric field in the spin plane $\vec{E}_s$ was measured, the electric field vector $\vec{E}$ was determined as described in the previous section. The electric field vector was resolved into two components which lie in a plane perpendicular to the magnetic field. One component, E_v, is along the direction of the velocity vector projected into the plane perpendicular to the magnetic field. The other component, E_{VxB}, is along the direction of the motional field, $\vec{V} \times \vec{B}$. Figure 8 shows the measured values of E_v. Comparing Figures 7 and 8 one finds that the E_v component is of the order of magnitude of the uncertainty of measurement. Measured values of E_{VxB} are plotted as points in Figure 9. The line in the Figure 9 represents $|\vec{V} \times \vec{B}|$.

The measured values of E_{VxB} are considered further in Figure 10, where the ratio $E_{VxB}/|\vec{V} \times \vec{B}|$ is plotted. If $E_{VxB}/|\vec{V} \times \vec{B}|$ is 1, then only the motional field is measured. If $E_{VxB}/|\vec{V} \times \vec{B}|$ is less than 1, then the motional field is possibly being screened in the region near the shuttle. Values of $E_{VxB}/|\vec{V} \times \vec{B}|$ less than 1 were recorded during the free flight, although at no time was the magnitude of the measured electric field less than 0.5 times $|\vec{V} \times \vec{B}|$. Values of $E_{VxB}/|\vec{V} \times \vec{B}|$ greater than 1 were not expected, as they imply plasma flow past the spacecraft at speeds greater than the orbital speed. Yet values greater than 1 were recorded at times. Only during the five times listed at the beginning of this section, when operation of the electron beam generator on board the shuttle lead to large electric field signals, was $E_{VxB}/|\vec{V} \times \vec{B}|$ greater than 1.3. The measurements for these

five times, which are not included in Figure 10, will be discussed in Section VI. Figure 10 also shows that at other times the measured value of $E_{VxB}/|\vec{V} \times \vec{B}|$ was greater than 1. Possible reasons for this are considered next.

The times when $E_{VxB}/|\vec{V} \times \vec{B}|$ stayed consistently greater than 1 occurred primarily when the PDP was on the day side of the orbit. One can see this by comparing the times for dawn and dusk listed below to Figure 10.

Dawn	Dusk
GMT 212 23:49	GMT 213 00:44
GMT 213 01:20	GMT 213 02:15
GMT 213 02:50	GMT 213 03:45
GMT 213 04:21	GMT 213 05:16

At all times on the dayside of the orbit, the angle of the PDP spin plane to the Sun was such that one probe passed through the spacecraft shadow as the PDP rotated. A shadow on the probe can affect the electric field measurements in the following manner. While in the shadow, the probe does not emit photoelectrons, and thus the probe's floating potential is lower than if it were not in a shadow. The resulting effect on the measurement would be an apparent, but not real, electric field in the anti-Sunward direction. If $\vec{V} \times \vec{B}$ were also in the anti-Sunward direction, then the apparent electric field due to the photoelectric emission would add to the motional $\vec{V} \times \vec{B}$ field leading to values of $E_{VxB}/|\vec{V} \times \vec{B}|$ greater than one. However, on the day side of

the orbit, $\vec{V} \times \vec{B}$ as projected onto the spin plane was directed anti-Sunward at times and Sunward at other times. Thus, even though the values of $E_{VxB}/|\vec{V} \times \vec{B}|$ greater than 1 were recorded mainly on the day side of the orbit, the values are not explained by photoelectric emission from the probes.

Whereas the magnitude of the measured electric field in the spin plane varied between 0.03 volts/m and 0.16 volts/m, signals larger than 0.064 volts/m were out of the range of the high gain, as can be seen by referring to Table 1. The times when $E_{VxB}/|\vec{V} \times \vec{B}|$ stayed consistently greater than 1 occurred primarily when the electric field in the spin plane was greater than 0.064 volts/m, and the low gain was used. Thus, the values of $E_{VxB}/|\vec{V} \times \vec{B}|$ greater than 1 are probably related to the inaccuracy inherent the low gain data.

The resolution of the low gain circuitry (the size of one digitizing step) was 0.017 volts/m. Thus, the resolution of the low gain was on the order of 10% of $|\vec{V} \times \vec{B}|$. So, for those times when the electric field was out of the range of the high gain, the difference between the measured signal and $|\vec{V} \times \vec{B}|$ was typically on the order of the uncertainty of measurement. In order to measure precisely the small differences between the electric field in the plasma and the motional electric field, times when the measured signal in the spin plane was less than 0.064 volts/m were considered. At those times, the high gain can be used, and the resolution of the measurement is 0.51 millivolts/m. During the free flight, the measured signal was within

the range of the high gain for the following four time intervals.

(1) GMT 213 01:03:20 - 01:18:00

(2) GMT 213 02:30:00 - 02:47:00

(3) GMT 213 04:02:00 - 04:11:00

(4) GMT 213 04:12:25 - 04:19:56

The nature of the measured electric field during these time intervals will be discussed in Section V.

CHAPTER V

THRUSTER RELATED EFFECTS

A. Observations

The four time intervals when the measured signal was within the range of the high gain are listed in the previous section. In this section the nature of the measured signal during these intervals will be addressed. During interval 1, the PDP was located directly downstream from the shuttle, between 85 and 89 meters away. For interval 2, the PDP was located generally above the shuttle, between 212 and 256 meters away. During this interval, the PDP passed within 20 m of the magnetic flux tube passing through the shuttle, moving from upstream to downstream of the flux tube. During interval 3 the PDP was generally located above the shuttle, between 216 and 297 meters away. The PDP was upstream of the magnetic flux tube passing through the shuttle. At the end of this interval, the PDP approached to within 10 meters of the flux tube passing through the shuttle. During interval 4 the PDP was located above the shuttle, between 199 and 229 meters away. At that time the PDP was downstream from the magnetic flux tube passing through the shuttle.

In Figures 11, 12, and 13 the components E_v and E_{VxB} of the measured electric field are plotted. The motional field has been

subtracted from the measured electric field in these plots, so that a value of zero corresponds to a measured electric field equal to the motional field. Study of the measurements made during all four time intervals shows that deviations of the measured electric field from the predicted motional electric field occur primarily in the component E_{VxB}, and occur as decreases in the motional field. The ratio $E_{VxB}/|\vec{V} \times \vec{B}|$ during all four time intervals is shown in Figures 14, 15, and 16. These plots show that the motional field is reduced at times by 10% or more. Also shown in Figures 14, 15, and 16 is the total gas emission rate of all thrusters operating during the given interval. Inspection of these plots indicates a possible relation between the firing of the thrusters and the diminutions of E_{VxB}.

B. Discussion

In order to investigate the relationship between changes in E_{VxB} and thruster firings, the linear correlation coefficient between the ratio $E_{VxB}/|\vec{V} \times \vec{B}|$ and the thruster emission rate in grams/s was calculated. Because each measurement of the electric field uses 13.1 seconds of data, the thruster emissions were averaged over a comparable time period, 13.0 seconds, before evaluating the correlation coefficient. The correlation was evaluated using the total emission rate from all the 44 thrusters on the shuttle, and for the emission rate from a sum of those thrusters that should be more or less pointed at the PDP. Throughout the PDP free flight, except during a portion of interval 1, the shuttle was maintained in an orientation such that the

shuttle bay was pointed toward the PDP within about 10^{o}. Therefore the 9 thrusters which are directed "up," corresponding to the direction "up" out of the bay, were generally directed toward the PDP. A diagram showing the location and emission direction of the shuttle thrusters can be found in Murphy et al. [1983]. To aid in the interpretation of the correlation coefficients, we evaluated a second parameter: the probability of obtaining a correlation coefficient equal to or larger than the calculated coefficient, if the values are actually randomly distributed, given the size of the sample [Bevington, 1969]. The results are listed in Table 2. For time intervals 1, 2, and 4, the magnitude of the correlation between the ratio $E_{VxB}/|\vec{V} \times \vec{B}|$ and the sum of all thruster activity ranges from 0.30 to 0.44, and in each case is much larger than would be likely if the two quantities were randomly distributed. Thus, the ratio $E_{VxB}/|\vec{V} \times \vec{B}|$ appears to be anti-correlated to thruster activity.

The inverse relationship between the ratio $E_{VxB}/|\vec{V} \times \vec{B}|$ and thruster activity is indicated in Figure 17, where the measurements for all four time intervals are combined and plotted together. As in the determination of correlation coefficients, the thruster emissions are averaged over 13 seconds. In Figure 18 the measurements are separated into bins having similar numbers of measurements, and the average of the ratio $E_{VxB}/|\vec{V} \times \vec{B}|$ in each bin is plotted. The error bars indicate the standard deviation of the mean of each bin. Figure 18 indicates that $E_{VxB}/|\vec{V} \times \vec{B}|$ decreases as the average thruster emission rate

increases. It must be noted that during parts of the time intervals we are considering, the electron beam generator on board the shuttle was operating. During interval 2 the beam generator was turned on from 02:31:38 until 02:37:46. The beam generator was also turned for the period from 04:11:03 until 04:18:24, which overlaps intervals 3 and 4. In order to determine if the diminutions in the electric field are actually related only to the electron beam operation, and not to thruster operation, the ratio $E_{VxB}/|\vec{V} \times \vec{B}|$ was plotted versus thruster activity in Figure 19 for those times when there was no electron beam operation. In Figure 20 the measurements are separated into bins having similar numbers of measurements, and the average of the ratio $E_{VxB}/|\vec{V} \times \vec{B}|$ in each bin is plotted. Examination of the plot shows that, although, for thruster emission rates of less than 100 grams/sec the electric field is not significantly altered, for thruster emission rates greater than 100 grams/sec, the electric field is reduced.

In order to explain the relationship between the thruster firings and the electric field measurements, the thruster-induced effects which might reduce the validity of the measurements are considered. One such effect would be a large reduction in the plasma density. A large release on neutral gas can deplete the plasma density in a two-step process [Mendillo and Forbes, 1978]. First, the molecular neutral particles undergo charge exchange reactions with ionospheric O^+ ions. Then, the newly produced molecular ions recombine with electrons, doing so more readily than the ambient atomic ions. Recombination is more

favorable for molecular ions since only a two-body collision is required, whereas for atomic ions a three-body collision is necessary. If the plasma density becomes too low, then the probe sheath resistance becomes comparable to the input resistance of the differential voltage measurement circuitry. The measured signal is then less than the actual electric field. The probe sheath resistance can be estimated in the following manner. The potential of a probe in a plasma is given by [Kasha, 1969]

$$\Phi = -U_e \ln[(I - I_i)/I_e] \quad , \tag{3}$$

where U_e is the electron temperature in electron volts, I is the total current to the probe, I_i is the total ion current collected by the probe, and I_e is the electron current gathered by a probe at the plasma potential. The sheath resistance for a floating probe is given by

$$R_s = (d\Phi/dI)\Big|_{I=0} = \frac{U_e}{I_i} \quad . \tag{4}$$

Because the orbital velocity is greater than the ion thermal speed, the ion current is determined by the sweeping up of ions as the probe moves through the plasma. The expression for the ion current is

$$I_i = n_e A e V_{sc} \quad , \tag{5}$$

where n_e is the plasma density, A is the probe cross sectional area, and V_{sc} is the orbital velocity. With U_e = 0.2 volts, A = 82 cm^2, V_{sc} = 7.8 km/s, and $n_e = 10^2$ cm^{-3}, the sheath resistance is found to be 2.0×10^8 ohms. In contrast, the input resistance of the differential voltage measurement circuitry is greater than 10^{10} ohms. So for plasma densities greater than 10^2 cm^{-3}, the probe sheath resistance is not of concern. Although the Langmuir probe instrument on the PDP detected reductions in the plasma density at the times of the thruster firings studied in this paper, the measured density did not become as low as 10^2 cm^{-3} [personal communication, A.C. Tribble].

Another effect that might call into question the validity of the measurements is the possible deposition of thruster emission products on the probes. A deposit might form a resistive layer on a probe. If both probes are coated with deposit symmetrically, then the measurement will only be affected if the resistance of the layer is comparable to the instrument input resistance. If a deposit forms on the probes differentially, then the measured signal could be either larger or smaller than the actual electric field. The measured electric field is observed primarily to decrease at the times of thruster operations. The perturbations in the electric field do not last significantly longer than the thruster firing. Also the Langmuir probe measurements of the density depletions last only about as long as the thruster firing [personal communication, A.C. Tribble]. Thus, if deposits are formed on the probe, they apparently do not persist. However, if the

perturbations in the electric field are due to deposits on the probes, then the correlations calculated in Table 2 should be larger for the case where only thrusters directed toward the PDP are considered. For intervals 2 and 4, the correlation is in fact larger when all thrusters are considered. Thus, it seems to be unlikely that the decreases in measured electric field are due to deposits on the probe.

Having considered some possible sources of error in measurement, and argued that they are not important, changes in the plasma caused by the thruster operation are considered which would affect the electric field. The introduction of a large concentration of neutrals will alter the conductivity in the plasma by increasing the collision frequencies for ions and electrons. If the region of the thruster plume is a region of higher conductivity than the surrounding plasma, then it is possible that the motional electric field is screened out in the region of the plume. The collision frequencies, parallel conductivity, Pedersen conductivity, and Hall conductivity are calculated here from relations given by Hanson [1965]. The results are shown in Table 3. A reasonable value for the ambient neutral density is 3×10^{8} cm^{-3}. From a model of the thruster plume [Hoffman and Hetrick, 1982], it is estimated that the density of neutrals from the thruster 100 m away from the shuttle is approximately 10^{12} cm^{-3}. From Table 3 one can see that if the neutral density is increased from 3×10^{8} cm^{-3} to 10^{12} cm^{-3}, the Pedersen conductivity does not change by a very large amount. A larger change can be found in the Hall

conductivity, which becomes comparable to the Pedersen conductivity. However, a large Hall current leads to a polarization field with a component along the direction of $\vec{E} \times \vec{B}$, and this is not observed in the measured electric field.

The above evaluation of the conductivity does not consider an important source of current: the current due to the motion of the newly formed ions after a charge exchange reaction. The newly formed pickup ions move in such a way as to produce a current in the direction of the motional electric field [Goertz, 1980]. Consider a water molecule that is initially stationary with respect to the shuttle. If the H_2O molecule undergoes a charge exchange reaction, then an H_2O^+ ion is formed which is initially at rest with respect to the shuttle. In the frame of the H_2O^+ ion there is an electric field equal to $\vec{V} \times \vec{B}$. The ion will begin to move on a cycloid trajectory, drifting in the $\vec{E} \times \vec{B}$ direction. In addition, the guiding center of the ion is displaced in the direction of $\vec{V} \times \vec{B}$ by one cyclotron radius. The current is given by

$$\vec{J} = \Sigma\{q_s \frac{dn_s}{dt} r_{cs} \frac{E}{|\vec{E}|}\} - \Sigma\{\frac{dn_s}{dt} m_s \frac{\vec{E}}{|B|^2}\} \quad (6)$$

where q_s is the ion charge, n_s is the ion density, r_{cs} is the ion cyclotron radius, m_s is the ion mass, and the sum is over all product ion species. Even if the pickup ions undergo collisions at a rate greater than the cyclotron frequency, there will still be a pickup current, since the particles are still on average displaced in the direction of $\vec{V} \times \vec{B}$.

The thruster emissions are not initially stationary with respect to the shuttle. In fact, the exit velocity is about 3.5 km/s [Pickett et al., 1985]. Therefore, the trajectory of a pickup ion must be considered more carefully than previously stated. Consider the motion of a newly formed ion that has an initial velocity relative to the shuttle. The coordinates used here are represented in Figure 21. The shuttle velocity vector $\vec{V}$ is along the +y direction, the magnetic field is along the + z direction, and $\vec{V} \times \vec{B}$ is along the +x direction. At time t = 0, the ion is located at position x = 0 and y = 0, and has velocity V_{xo} and V_{yo}. Given the electric field $\vec{E} = \vec{V} \times \vec{B}$, the time averaged value of x is

$$\langle x \rangle = \frac{V_{yo} + E/B}{f_c} \quad . \tag{7}$$

Thus, the pickup ion will be displaced in the direction of $\vec{V} \times \vec{B}$, as long as $V_{yo} > -E/B$. The pickup ion may be displaced in the $-\vec{V} \times \vec{B}$ direction if the thrusters fire directly downstream, and E/B is less

than 3.5 km/s. For the observations presented here, E/B is always greater than 3.5 km/s, except from 04:02 until 04:08 during interval 3. During every other time considered here, pickup ions associated with thruster emissions should move in such a way as to produce a current.

With pickup current occurring within the thruster plume, the situation is that of a current source moving through a background plasma. In this situation, an Alfvén wave is generated. The topic was addressed originally by Drell et al. [1965] with application to conducting satellites in the ionosphere. The topic has also been treated with respect to Jupiter's moon, Io, by Goertz [1980] and Neubauer [1980], for example. The general picture is shown in Figures 22 and 23.

The Alfvén wave system shown in Figures 22 and 23 can be understood as follows. The current course causes a disturbance in the magnetic field, the electric field, and the plasma flow velocity. This disturbance propagates away from the current source along magnetic field lines as a shear Alfvén wave. The perpendicular current in the current source is closed by currents along the magnetic field lines, which in turn are closed by a polarization current in the propagating Alfvén wave front. The sheets of parallel current, which connect to each side of the current source, are referred to as Alfvén wings. Momentum is transferred from the moving current course to the plasma by the Alfvén wave. As the Alfvén wave front propagates along the field lines, the plasma behind the wave front, which is the plasma between

the Alfvén wings, is accelerated to convect with the current source. Because of the change in the plasma flow, the electric field in the region between the Alfvén wings (E_2 in Figures 22 and 23) is reduced from the motional electric field (E_1 in Figures 22 and 23). The electric field between the Alfvén wings is the same as the electric field within the current source region.

In order for an Alfvén wave, which is a magnetohydrodynamic wave, to be generated by the thruster plume, the plume must be much larger than the ion cyclotron radius. For a magnetic field of 0.25 gauss, atomic oxygen ions of energy 0.2 eV, a reasonable value for the thermal energy, will have larmor radius of 10 meters. The thruster plume extends over a comparably larger distance of a few hundred meters.

The plasma in the thruster plume convects with the current source as long as a current is driven through the source. If the thrusters are fired continuously, then the pickup current will be continuous. However, the thrusters firings are of finite duration. When a cloud of ionized gas is moving through a background plasma, momentum will be transferred from the cloud to the plasma by the Alfvén wave until the cloud comes to rest with respect to the background plasma. Scholer [1970] shows that the time scale for the cloud coming to rest with respect to the background plasma is given by

$$\tau = \frac{\mu_o \rho \Delta z V_a}{2B^2} \quad , \tag{8}$$

where ρ is the mass density of the ionized gas cloud, Δz is the thickness of the cloud in the $\vec{B}$ direction, and V_a is the Alfvén speed. The quantity τ is then the time for the Alfvén wave front to move over a volume of ambient plasma of mass comparable to the mass of the plasma cloud. Using the following representative values for the shuttle environment: $B = 0.25$ gauss, $\rho = 3.0 \times 10^{-15}$ kg/m^3, $V_a = 4 \times 10^5$ m/s, and $\Delta z = 100$ m, the time for the cloud to be picked up by the ambient flow is $\tau = 1.2 \times 10^{-4}$ sec. Because this time is so short, the perturbation in the electric field will only be present as long as the contaminating neutral gas is being released. When the source is removed, or when the thruster firing ends, the current source is turned off. The pickup ions formed are then immediately convected away with the ambient plasma.

An expression for the electric field in the perturbed region is obtained in the following manner. The force on the plasma in the region of the Alfvén wave front is expressed as

$$\vec{J}x\vec{B} = \rho \frac{d\vec{u}}{dt} \quad , \tag{9}$$

where ρ is the plasma mass density, and $\vec{u}$ is the plasma flow velocity. Using the coordinates shown in Figure 21, the relation becomes

$$J_{\perp} B_o = \rho \frac{dU_y}{dt} \quad . \tag{10}$$

Given that the Alfvén wave front propagates at speed V_a, the change in plasma flow velocity can be expressed as

$$\frac{dU_y}{dt} = V_a \frac{dU_y}{dz} \quad . \tag{11}$$

Combining equations 10 and 11, and noting that $U_y = E_x/B_o$, the current in the wave front $J_{\perp}$ can be expressed as

$$J_{\perp} = (\mu_o V_a)^{-1} \frac{dE_x}{dz} \quad . \tag{12}$$

The Alfvén conductance Σ_a is defined as $\Sigma_a = (\mu_o V_a)^{-1}$. For convenience, we integrate the current over the thickness of the Alfvén wave front, and write the relation in terms of the height integrated current $J_{\perp}'$

$$J_{\perp}' = \Sigma_a (E_1 - E_2) \quad , \tag{13}$$

where E_1 is the electric field in the undisturbed plasma, and E_2 is the field in the region of the current source and between the Alfvén wings. If the conductance within the region of pickup is called Σ_{pu}, then the current in that region can be written as

$$J_{\perp}' = \Sigma_{pu} E_2 \quad . \tag{14}$$

Equating Equations 13 and 14, one obtains a relation between the motional electric field and the perturbation electric field

$$E_2/E_1 = \Sigma_a/(\Sigma_a + \Sigma_{pu}) \quad . \tag{15}$$

To determine the change in the electric field, Σ_{pu} must be estimated. From Equation 6, the pickup conductivity is seen to be

$$\sigma_{pu} = \Sigma[\frac{dn_s}{dt} m_s]/B_o^2 \quad , \tag{16}$$

and thus the pickup conductance is

$$\Sigma_{pu} = \int \sigma_{pu} dz \quad . \tag{17}$$

The pickup ion production rate is expressed as

$$\frac{dn_s}{dt} = k_s[O^+][M_s] \tag{18}$$

where k_s is the reaction rate constant, and $[M_s]$ is the density of the molecular species. The electric field can now be determined from Equations 15, 16, 17, and 18.

First consider the prediction of this model for times when no thrusters are firing. Since significant screening of the motional field is observed mainly during thruster firings, the model should predict no change in the electric field. An approximation for Σ_{pu} during times of no thruster firings is needed. It is assumed that H_2O^+ is the only important contaminant ion. In assigning values to parameters in Equation 18, the highest expected values are chosen, so as to estimate the maximum change in electric field at times without thruster firings. The ambient plasma density, $[O^+]$, is estimated to be $10^6 cm^{-3}$, which is on the order of the upper range of densities measured by the Langmuir probe during the mission [personal communication A.C. Tribble]. During the STS-3 mission, the PDP detected neutral pressures in the near shuttle region on the order of 10^{-6} torr, which is an order of magnitude larger than the expected ambient pressure [Shawhan et al. 1984b]. Since 10^{-6} torr corresponds to approximately 10^{10} cm^{-3}, the water density, $[H_2O]$, is estimated to be 10^{10} cm^{-3}. The rate constant used is $k = 1.95 \times 10^{-9} cm^3/s$ [Turner and Rutherford, 1968]. A lower value of the rate constant, $k = 3.9 \times 10^{-10} cm^3/s$ was reported by Murad and Lai [1986]. For the present calculation, we want to find an upper limit to the electric field perturbation, so the larger value of the rate constant is used. Assuming a cloud with a diameter on the order of 200 m (a probable overestimate), the result is $\Sigma_{pu} = 0.19$ ohm^{-1}. Using $B = 0.25$ gauss, the Alfvén conductance is $\Sigma_a = 5.82$ ohm^{-1}. Thus,

from Equation 15, $E_2/E_1 = 0.97$; the estimated change in the electric field for this case is small, and the actual change in electric field is expected to be smaller.

Next, the electric field during a thruster firing is estimated. First, the pickup conductivity within the thruster plume must be determined. The thruster emissions include a number of molecular species which can undergo charge exchange reactions with O^+. However, here we consider only the following reactions:

$$H_2O + O^+ \rightarrow H_2O^+ + O \quad , \tag{19}$$

and

$$N_2 + O^+ \rightarrow NO^+ + N \quad . \tag{20}$$

The H_2O and N_2 make up 63% of the molecules in the thruster emission. Also, H_2O and NO have lower ionization potentials than O, making the above reactions favorable. The other molecules likely to undergo charge exchange reactions all have ionization potentials greater than O, making their reactions less likely. Inclusion of other charge exchange reactions between thruster molecules and ambient plasma particles would lead to a larger pickup conductivity. So, by considering only 2 reactions, we are underestimating the pickup current. However, the correct order of magnitude should be obtained.

The concentration of neutrals in the thruster plume is determined from the relation

$$[M_s] = \frac{f_s(6.02 \times 10^{23})Y}{M_{th} V_{th}} \quad , \tag{21}$$

where f_s is the mole fraction of the neutral molecule, M_{th} is the mass of one mole of thruster emission, V_{th} is the thruster emission speed, and Y is the mass flux of thruster emissions given by [Hoffman and Hetrick, 1982]

$$Y(r,\theta) = [1351.0/r^2][\cos(0.0126\theta)]^{10} \text{ g/cm}^2\text{/s} \quad [0^\circ \leq \theta \leq 64^\circ]$$

$$Y(r,\theta) = [35.0/r^2]e^{-0.084(\theta-64^\circ)} \text{ g/cm}^2\text{/s} \quad [64^\circ \leq \theta \; 180^\circ] \quad . \tag{22}$$

In the above expression, r is the distance from the thruster, and θ is the angle from the center line of the thruster nozzle. With Equations 16, 18, 21 and 22, Equation 17 is integrated numerically over the thruster plume.

Some values for the pickup conductance, obtained by integrating Equation 17, and the corresponding values of $E_{V\times B}/|\vec{V} \times \vec{B}|$, are shown in Tables 4 and 5. The calculations are performed using both values of the rate constant given earlier for Equation 19. The higher value of the rate constant is used for Table 4, and the lower value is used for

Table 5. The rate constant used for Equation 20 is $k = 3 \times 10^{-10}$ cm^3/s [McFarland et al., 1973]. For the cases presented, the integration is performed along a magnetic field line which intersects the centerline of the thruster nozzle at a distance of 100m from the nozzle. Results are shown for thruster injections at various angles to the magnetic field. Also, calculation results are shown for different values of the magnetic field strength and ambient plasma density. The magnetic field strengths and plasma densities used are typical of the F-region of the ionosphere. The model results in Tables 4 and 5 for the electric field values are of the same order of magnitude as the measured values shown in Figures 11-16. For example, given the representative values $n_e = 10^5$ cm^{-3} and B = 0.5 gauss, the computed value of $E_{V\times B}/|\vec{V}\times\vec{B}|$ in Table 5 varies from 0.96 for a thruster injection angle of 90°, to 0.47 for a thruster injection angle of 2°. Thus the model can account for the measured values.

The results in Tables 4 and 5 indicate that the electric field screening is stronger for higher ambient plasma densities, for weaker magnetic field strengths, and for smaller thruster injection angles to the magnetic field. These dependences are understood simply as follows. If the ambient plasma density is higher, the rate of pickup ion production is greater, so the pickup current is larger. For weaker magnetic fields, the Larmor radius of the pickup ion is larger; thus, the pickup ion is displaced a greater distance and the pickup current is larger. If the thruster injection angle is small, (injection is

along the magnetic field) then the integrated pickup current along the magnetic flux tube will be much larger than if the thruster injection angle is large (injection is perpendicular to the magnetic field).

The electric field at the PDP is reduced under either one of the following conditions: 1.) the PDP is within the thruster plume where the pickup process is taking place; or 2.) the PDP is on a magnetic field line which passes through the region of the thruster plume where the pickup process is taking place. The thrusters do not have to be firing directly toward the PDP. Thus, it is not surprising that the correlation coefficient did not improve when we considered only thrusters firing generally toward the PDP, instead of all the thrusters [see Table 2]. However, by including all thrusters, we included thruster firings which do not satisfy either of the above conditions, and thus are not related to changes in the electric field.

The screening of electric field will last only for the duration of the thruster operation, which can be a very short time; the thrusters have a minimum on-time of about 80 milliseconds. Further, recall that each measurement of the electric field requires 13.1 seconds. Thus, a change in the electric field will only be noticed during times when thrusters are fired continuously over a period of more than a second. Recall that in Figures 18 and 20, the average thruster emission rate for 13.0 seconds was plotted. The actual thruster emission rate for the primary thrusters is 1419 grams/second/engine. A 13.0-second averaged thruster emission rate of 100 grams/sec could correspond to a

single thruster firing lasting 0.92 seconds. Thus, the ratio $E_{VxB}/|\vec{V} \times \vec{B}|$ in Figures 18 and 20 should be lower mainly for thruster emission rates above 100 grams/sec. If the electric field was screened for only a few seconds, then the measured reduction in the field will be less than the actual reduction, because the measurement is an average value of the field over 13.1 seconds. Also, recall that in the data reduction, certain segments of the measured signal up to 2.5 seconds long were removed. Thus, for a thruster firing lasting less than 2.5 seconds, its effect on the electric field may be completely missed in the measurement. Given the above considerations, it is not surprising that the thruster firings and the electric field measurements do not appear to be perfectly correlated.

As mentioned earlier in this section, the observations considered have included time periods when the electron beam generator on the shuttle was operating. The relationship of the electron beam to screening of the electric field has not yet been discussed. When the beam is emitted from the shuttle, there is a return current to the shuttle. A perpendicular current is then driven through the shuttle, and the possibility that this current generates an Alfvén wave should be considered. Alfvén wings might form on opposite sides of the shuttle vehicle. For the Alfvén wave model to be an appropriate description, the separation of the Alfvén wings should be greater than two ion Larmor radii for typical ions. A thermal O^+ ion has a Larmor radius on the order of 10m. The largest shuttle dimension is the nose

to tail length of 37m. So the condition that the Alfvén wings be separated by more than two Larmor radii might only barely be met. The thruster plume, in contrast, spreads out over several hundred meters. We point out also that the predicted total current associated with the pickup ions at the time of a thruster firing is typically several times larger than the beam current. The electron beam generator normally operated at 100ma. The total current associated with the pickup ions is estimated as follows. The height integrated current density, $J_\perp'$ in Equation 13 is approximated by

$$J_\perp' = I/L \tag{23}$$

where I is the total current and L is the size of the thruster cloud along the direction of the velocity flow. Equation 13 becomes

$$I = L\,\Sigma_a(E_1 - E_2) \quad . \tag{24}$$

Reasonable approximations for L and $(E_1 - E_2)$ are L = 100m and $(E_1 - E_2) = 0.01$ volts/m. Values for the Alfvén conductance Σ_a range from 0.3 mhos to 7.3 mhos, which yields total currents ranging from 290 ma to 7.3 amps. Thus, the pickup current may be more important than the beam current. Under certain conditions, the beam current may enhance the current associated with the pickup ions. The beam will also have other important affects on the plasma which will complicate the

physical picture. For example, the electron beam will cause ionization through impacts, which can produce pickup ions. Plasma heating will occur in regions disturbed by the electron beam. A complete physical description of the case when thrusters operate and the electron beam generator is operating is quite complicated, and will require a more detailed analysis than attempted here. However, for electric field screening, the thruster effects are more important than the beam effects.

The measurements have several other features which are not fully explained. For example, in Figures 14, 15 and 16 the measurements appear to have a periodicity of about 1 minute. This periodicity has been investigated, but no cause for variation of the signal at this frequency has been determined. Also, in some cases the measured reductions in the motional electric field are not simultaneous with thruster firings as the model suggests they will be. Instead, the reduction is found up to one minute after a thruster firing. Additionally, note that the discussion thus far has emphasized the reduction in the electric field in the region between the Alfvén wings, but in the region immediately outside the Alfvén wings the electric field will be enhanced. Although reductions in the electric field associated with thruster firings are observed, significant enhancements of the field are not observed. Failure to observe enhanced electric fields indicates that the PDP was never outside the Alfvén wings. The measurements presented were made at distances up to 300 meters away

from the shuttle, so the region of plasma influenced by the thruster plume likely extends to 300 meters. Typically, several thrusters pointing in different directions are fired at once, so that pickup current is produced in an extended region of several overlapping plumes. Thus, the region of space influenced by the thruster plumes is known to be quite large, but a complete understanding of the extent of the thruster plume requires further study.

In summary the following conclusions are drawn from analysis of the time intervals where the measured signal was within the range of the high gain. Partial screening of the motional electric field was observed at distances over 200 meters away from the shuttle. The screening of the field, which was on the order of 10% to 20%, occurred primarily when the shuttle thrusters were operating. The changes in the electric field are explained by the generation of an Alfvén wave from pickup current, as suggested by Pickett et al. [1985]. An estimate of the electric field associated with an Alfvén wave is in agreement with the measurements at times of thruster firings. Further, the model predicts that the pickup current is sufficient to produce a large change in the electric field only at times of large releases of neutral gas from the shuttle. The effect occurs in the region of the thruster plume, as well as along the magnetic flux tubes passing through the plume. Thus, perturbations in the electric field can be detected far from the shuttle. The screening of the field lasts only for the duration of the thruster firing, and thus was not detectable

with the PDP unless many thruster firings occurred over a period of several seconds.

CHAPTER VI

ELECTRON BEAM RELATED EFFECTS

A. Observations

At five times during the free flight when the electron beam generator was operating, electric field signals were recorded that were significantly larger than $|\vec{V}x\vec{B}|$. The five time intervals are listed in section IV. The cause of these large signals is discussed in this section.

The signals for the five events are shown in Figure 24, and the events are numbered 1 through 5. At no other times during the PDP free flight were signals this large recorded. Of these five events, the beam was operated in a steady mode for three events, and in a pulsed mode for two events. The beam injection pitch angle varied widely among these events. Table 6 lists the beam operation mode, injection pitch angle, beam current, and several other important parameters.

In addition to the basic periodicity due to the spinning of the spacecraft, the V_{diff} signals in Figure 24 have a number of unusual features. During event 1 the instrument saturates. Thus, the difference voltage on the probes is greater than 8 volts, which corresponds to an inferred electric field strength in the spin plane greater than 2 volts/m. Event 2 has a "spiky" character, and events 3,

4, and 5 all show a "double peak" character. At the end of event 3 (around 00:49), there is an apparent higher frequency structure to the signal. This structure is associated with the pulsing of the electron beam. Note that as long as the beam pulse frequency is much greater than the V_{diff} sample rate, then no effect of the pulsing should be apparent in the V_{diff} signal. Such is the case for event 2, where the beam was pulsed at 1.2 kHz. However, during event 3 the beam pulse frequency was lowered in steps from 600 Hz down to frequencies near the V_{diff} sample frequency of 20 Hz. The apparent higher frequency structure is the result of a beating effect that occurs between the beam pulse rate and the V_{diff} sample rate.

In order to understand the origin of the large signals, the phase angle of the spinning PDP was investigated. Arrows are plotted in Figure 24 at the top of the graph to indicate times when the electric antenna was aligned with the spacecraft velocity vector. Recall that the velocity vector lay approximately in the PDP spin plane. Arrows are plotted in Figure 24 at the bottom of the graph to indicate times when the antenna was aligned with the magnetic field projected onto the spin plane. In general, the magnetic field vector did not lie exactly in the spin plane, but made an angle of between 10^{o} and 24^{o} with the spin plane. The angle for each event is given in Table 6. Inspection of Figure 24 reveals that for cases 2, 3, 4, and 5 a voltage peak occurs when the antenna is aligned with the spacecraft velocity vector,

and for cases 3, 4, and 5 a second peak occurs when the antenna is aligned parallel to the magnetic field projected onto the spin plane.

Figure 25 shows the trajectory of the PDP in a plane perpendicular to the magnetic field during all times that the electron beam generator was operating. The direction $V_{\perp}$ indicated in the figure is along the component of the velocity perpendicular to $\vec{B}$. The origin represents the position of the magnetic field line on which the electron beam should be centered. The beam is assumed to lie on a magnetic field line which intersects the electron beam generator, and the field is determined from a multipole model of the Earth's magnetic field. Although the beam is shown in Figure 25 only as a point, the beam electrons will have a cyclotron motion about the magnetic field. The injection pitch angles are listed in Table 6. The pitch angles are relatively small (less than 10^{o}) for events 1 and 2 and large (greater than 30^{o}) for events 3, 4, and 5. The beam also has some spreading due to beam divergence, space charge repulsion of the beam electrons, and beam instability. The actual width of the beam is unknown; however, previous beam experiments indicate that the cyclotron radius of a beam electron with pitch angle 90^{o} is a reasonable approximation for the beam radius. For a 1 keV electron in a magnetic field of 0.25 - 0.5 gauss, the cyclotron radius is approximately 2-4 meters.

The trajectories during the five large events are shown in Figure 25 as solid segments, and the trajectories during times when the beam generator was operating but the measured differential voltages as small

(i.e., approximately equal to $|(\vec{V}x\vec{B})\cdot\vec{L}|$, are shown by the dashed lines. During events 1 and 2, the length of time the electron beam generator was turned on was longer than the length of time large signals were recorded, indicating that the spatial region over which large signals occur is limited. For each of events 3, 4, and 5, large signals were recorded for the entire period the beam generator was on. Note that events 1 through 5 occur at times when the PDP was in a region downstream of the flux tube carrying the electron beam. Except briefly during event 1, the perpendicular distance from the PDP to the flux tube of the electron beam was much greater than the 2 to 4 meter predicted beam radius, so that the PDP was well outside of the region of the primary beam. Events 1 and 2 occur when the PDP was closest to the flux tube of the electron beam, and are the largest in magnitude.

The average potential V_{ave} measurements for events 1 through 5 are shown in Figure 26. The largest changes in the average potential measurements associated with the electron beam are seen during events 1 and 2, where the average potential measurements of the probes goes from positive values of +2 to +4 volts to negative values of -2 to -4 volts. The spin period variation of the signal discussed in Section III can be seen in the graphs for events 1 and 2 during the times before and after the large negative excursions of the signal. During events 3, 4, and 5, the average potential does not change by a large amount, but the smooth spin period variation of the signal is disrupted.

B. Discussion

Because the determination of the quasi-static electric field with the PDP is based on measurements of the differential voltage between two floating probes, the results can be affected by energetic beam electrons striking the probes. It is easily shown that a small flux of energetic electrons may alter the floating potential of the probes by a large amount [Fahleson, 1967]. Arnoldy and Winckler [1981] reported a population of energetic electrons in the region around an electron beam, causing the floating potential of the Echo 3 rocket to become several volts negative. A similar observation was made on Echo 6 [Winckler et al. 1984]. Thus we expect to find that the PDP potential is affected by energetic electrons around the beam. In fact, during each of events 1 through 5 discussed here, the Lepedea on the PDP detected energetic electrons at energies nearly up to the beam energy [W. R. Paterson, personal communication, 1987]. Further, data from the PDP Langmuir probe seems to indicate that the PDP charged to at least -4.3 volts during event 2, and to at least -7.6 volts during event 1 [A. C. Tribble, personal communication, 1987]. Therefore there is reason to suspect that the probes also charged. If the charging is different for the two probes, then V_{diff}/L cannot be safely interpreted as a good measure of the electric field.

To determine the possible effect on our measurements, a simple calculation of the floating potential is performed. This is done by considering the balance of currents to the object of concern (see for

example Kasha, 1969). The possible current sources are: (1) thermal (background) electrons, (2) thermal (background) ions swept up by the motion of the spacecraft, (3) energetic electrons (energies >> kT_e), (4) energetic ions (energies >> 5.0 eV, the ramming energy), (5) secondary electron emission, and (6) photoelectron emission. Measurements made with the Lepedea indicate that the current from energetic ions is much less than that from the ramming ions [W. R. Paterson, personal communication, 1987], so this current can be neglected. The maximum secondary electron yields for aluminum (PDP surface material) and graphite (probe surface material), are 1.0 secondaries/primary for 300 eV primaries [Whetten, 1985]. Thus, secondary production would reduce the negative charging effect of the energetic electrons by some fraction. Photoemission would also reduce the negative charging. But since we wish to obtain a worst case estimate of the spacecraft potential, both secondary production and photoemission are neglected. Consider then the following current balance equation for an object at potential $V < 0$

$$A_x n_e u_{sc}(1 - eV/E_i) - A_s n_e (kT_e/2\pi m_e)^{1/2} \exp(eV/kT_e) - A_s J_b = 0 \quad . \quad (25)$$

The first term in the above equation includes the ion current due to the sweeping up of the ionospheric ions by the spacecraft motion plus some effect of the attraction of ions to the negatively charged object. The second term is the electron current from the thermal electrons.

The third term is the current to the object due to energetic electrons. The variables in the Equation 25 are identified in Table 7. Note that Equation 25 differs from the expression for probe potential used in Section IV (Equation 3), in which the energetic electron current and the attraction of ions to the negatively charged object were neglected.

Using the representative parameters given in Table 7, Equation 25 was solved numerically for various values of J_b and n_e. The floating potential was determined from Equation 25 for both the spherical probes and for the PDP chassis. The current collecting area of the PDP was taken to be its surface area. Unfortunately, the current collecting properties of the spacecraft body are complicated, and this estimate is to be taken only as a rough approximation. The solution for the floating potential as a function of the energetic electron current density is plotted in Figure 27. Measurements from the Lepedea during beam event 1 indicate J_b was as high as 4×10^{-4} amp/m^2 [W. R. Paterson and L. A. Frank, personal communication, 1987]. The Langmuir probe measurements indicate that during event 1, n_e was of the order of 10^{11} m^{-3} [A. C. Tribble, personal communication, 1987]. From Figure 27 one can see that under the conditions of event 1 the PDP floating potential could easily be lower than -10 volts. This is consistent with the Langmuir probe observation mentioned previously which show that the PDP charged to at least -7.6 volts during event 1. More importantly for the V_{diff} measurements, under the conditions of event 1 differences in J_b on the order of 10^{-5} amp/m^2 lead to floating

potential differences on the probes of several volts. During events 2, 3, 4, and 5 the Langmuir probe measurements indicate that n_e was on the order of 10^{10} m^{-3} [A. C. Tribble, personal communication, 1987]. For this lower ambient density, Figure 27 shows that differences in J_b on the order of 10^{-6} amp/m^2 lead to floating potential differences on the probes of several volts. Figure 27 also shows that for a fixed value of J_b, small differences in the ambient plasma density lead to floating potential differences of several volts.

Using the differential voltage between the probes to infer electric field values can produce erroneous results if the two antenna probes receive different amounts of current from any of the various current sources. Current differences can occur if one of the probes is shielded by the PDP chassis from a current source, or if the plasma environment is nonuniform over the length of the antenna. During events 2, 3, 4, and 5 the peaks in the electric field data are associated with special orientations of the antenna, and therefore can be primarily attributed to shadowing of one probe. A shadowing effect was observed by Winckler et al. [1984] during the Echo 6 experiment. In that experiment, large signals at the payload spin frequency were attributed to shadowing of one probe from a magnetic field aligned plasma flow. At the time, the electric probes were stowed in the payload body. During events 3, 4, and 5 the "double peak" character of the signals indicates that two different shadowing effects are occurring. Each effect is discussed separately below.

For events 3, 4, and 5 one finds a voltage peak, and therefore a probable shadowing of one probe, when the antenna is aligned with the magnetic field. Because the local ion larmor radius is much larger than the PDP, a shadowing along field lines suggests a shadowing of electrons. We explain the signal peak in the following manner. For events 3, 4, and 5 the beam was injected in the direction of $\vec{B}$. At the time when the antenna was aligned with $\vec{B}$, the probe on the boom pointing in the direction of $\vec{B}$ was at a lower potential than the probe on the boom pointing in the direction of $-\vec{B}$. Thus, we conclude that some energetic electrons are moving in the direction of $-\vec{B}$, and one probe is shielded from them. So, for the three events when the PDP is 80 or more meters from the beam, the energetic electrons have a preferred direction, which is opposite to the injection direction. This explanation is consistent with the report by the Lepedea group of a secondary electron beam in the shuttle wake [Frank et al., 1987]. The shadowing of one probe from electrons moving down the field lines is pictured in Figure 28. Consideration of Figure 29. shows that if the angle θ of the magnetic field to the spacecraft spin plane is too large, then shadowing along the field lines will not occur. The range of angles where shadowing is possible is $\theta < 20.4^{\circ}$. Referring to the values of θ listed in Table 6, one finds that shadowing along field lines is possible for events 2, 3, 4, and 5.

The energetic electrons moving down the field lines and charging the probes in events 3, 4, and 5, may be attributed to reflection of

beam electrons by collisions with atmospheric neutrals, or to a beam plasma interaction. First, consider reflection of electrons by collisions. Given the distance of the PDP downstream from the beam for these events, and the spacecraft velocity, one can determine the time of flight for the energetic electrons to be around 10 to 20 msec. For 1 keV electrons, the corresponding total distance traveled is about 200 to 400 km. For comparison, the mean free path of electrons for collisions with oxygen atoms can be roughly estimated by $\lambda = 1/(n_n \sigma)$, where n_n is the atomic oxgen density and σ is the collision cross section. We use a value for σ of 7×10^{-16} cm^2, the total scattering cross section for 100 eV electrons measured by Sunshine et al. [1967]. At an altitude of 300 km, n_n is approximately 10^8 cm^{-3} [Johnson, 1965], which yields a mean free path $\lambda \approx 140$ km. Because the atomic oxygen density is larger at lower altitude, λ will become shorter at lower altitudes. Thus, for events 1 and 3 where the beam was injected downward, it is quite reasonable that electrons reflected by collisions with neutrals could reach the PDP. Since the atomic oxygen density is smaller at higher altitudes, λ becomes longer at higher altitudes. At an altitude of 400 km, n_n is approximately 10^7 cm^{-3}, which yields $\lambda \approx 1400$ km. For events 2, 4, and 5 where the beam was injected upward, it may seem unlikely that the PDP could be affected by reflected electrons. However, it is not necessary that most of the beam particles be reflected. The solution of Equation 25 showed that the measured signals are explained by differential energetic electron

currents of the order of 10^{-6} amp/m^2, and this current can result from only a small percentage of beam particles being reflected. An alternative explanation is considered by Wilhelm et al. [1985]. In the SCEX experiment, Wilhelm et al. measured energetic electrons in the region downstream of an electron beam. They discuss the possibility that the energetic electrons are the product of a beam plasma interaction. Both explanations are possible, and without a further, more detailed analysis we cannot say which is correct.

A different shadowing effect occurs for events 2, 3, 4, and 5 when the antenna is aligned with the velocity vector. Because the local ion thermal speed is less than the spacecraft velocity, ions are swept up by the spacecraft motion. The electron thermal velocity is much greater than spacecraft velocity, so the electrons are not swept up. However, because quasineutrality must be maintained, both the ion and the electron densities are reduced behind the spacecraft, forming a plasma wake. The sweeping of the antenna through the wake as the PDP spins is indicated in Figure 28. Because the velocity vector lay in the PDP spin plane as shown, the antenna always passed through the wake region. In order to estimate the plasma density in the wake at the location of the antenna probe, we use the self-similar solution for the expansion of a plasma into a vacuum as shown by Samir et al. [1983] and Singh and Schunk [1982]. In the standard treatment one assumes initially a plasma of density N_o for the region $x < 0$, and a vacuum for the region $x > 0$. At time $t = 0$ the plasma is allowed to expand into

the vacuum region. The solution for the density at later times is given by

$$N = N_o \exp[-(x/(S_o t) + 1)] \qquad (26)$$

where S_o is the ion sound speed. To obtain from Equation 24 an estimate of the density at the probe when the probe is in the wake, we take for x the radius of the PDP, x = 0.53 m, and for t the time for the ionospheric plasma to flow a distance of half of the antenna length relative to the PDP, $t = 2.5 \times 10^{-4}$ sec. Assuming an electron temperature of 0.2 eV, and assuming ions are atomic oxygen, the ion sound speed is estimated to be about 1.4×10^3 m/s, yielding a wake density

$$N = 0.08\ N_o \quad . \qquad (27)$$

This solution corresponds to the expansion of the plasma in one direction only. The wake fills in from all directions, so we expect the density in the wake at the location of the antenna probe to be greater than $0.08\ N_o$, but less than N_o. Examination of Figure 27 shows that if both probes receive the same amount of energetic electron current, but one probe is in the wake where the density is lower, then the probe in the wake will be several volts lower in potential than the

probe upstream. This explanation is consistent with the observed signals.

Event 1 does not lend itself to explanation in terms of probe shadowing, as the other events do. The angle θ between the magnetic field and the spin plane (see Table 6) is greater than 20.4^{o}, so that probes are not shadowed along field lines. Figure 24 shows that the peaks in voltage are not consistently centered about the times the antenna is aligned with the velocity vector or the magnetic field. The peaks are also broader than expected if due only to a shielding effect. Thus the signal is due either to only a gradient in the fluxes of energetic electrons reaching the probes, or both a gradient in fluxes of energetic electrons and an electric field. We cannot rule out the possibility that we have measured the electric field. However, because the entire region where energetic electrons are observed is only 20 meters wide (refer to Figure 25), gradients over the antenna length are expected. As will be discussed below, we consider it likely that the electric field measurement in event 1 is caused mainly by a gradient in energetic electron fluxes.

In order to investigate the possible interpretation of the large signals associated with event 1, the V_{diff} signals were analyzed as follows. Due to the spacecraft rotation, the V_{diff} signal varies sinusoidally with the PDP spin period of 13.1 seconds, and it is assumed that V_{diff} attains peak value when the antenna is aligned with the direction of strongest gradient in the energetic electron flux.

The direction and relative magnitude of the gradient is then obtained by using a least squares method to fit a 13.1-second segment of the V_{diff} signal to the function F(t) defined in Equation 1 in Section III. If the signal is interpreted as a measure of the gradient of the energetic electron flux, then the constant F_2 gives the magnitude of the gradient and ϕ gives the direction of the gradient in the spin plane. It is not expected that the energetic electron flux varies much along the direction of $\vec{B}$, so it is assumed that the gradient lies in the plane perpendicular to $\vec{B}$ and that the component of the gradient projected onto the PDP spin plane has been measured. Using this assumption, the magnitude of the gradient vector in the plane perpendicular to $\vec{B}$ was determined. In order to establish a "goodness of fit" of the curve performed for each measurement, the test variable X, defined in Equation 2 in Section III was calculated. Measurements were retained if $X < 0.25$, corresponding roughly to 25% error.

The vectors obtained by the above analysis are shown in Figure 30. The vectors are plotted along the trajectory of the PDP relative to the electron beam where the coordinate directions are the same as in Figure 25. The V_{diff} signals first become larger than $|(\vec{V} \times \vec{B}) \cdot \vec{L}|$, and the gradient in the energetic electron flux first becomes significant when the PDP is about 10 meters away from a line extending directly downstream from the center of the beam. The V_{diff} signal, and thus the gradient in the electron flux, becomes larger as the PDP gets closer to this line. The gradient vectors tend to point toward the line. The

indicated picture is that of a region of energetic electrons downstream from the primary electron beam. The region is not homogeneous but rather the electron flux increases as the PDP approaches the line extending directly downstream from the primary beam.

The presence of a gradient in energetic electron flux can account for the large magnitude (larger than 8 volts) of the V_{diff} signals during event 1. If the magnitude of the gradient in J_b is estimated from the Lepedea measurements, then the V_{diff} signal that would result from such a gradient can be estimated. As stated previously, the Lepedea measured a peak value of J_b of about 4×10^{-4} amp/m^2. We assume that the flux of energetic electrons is peaked on a line extending directly downstream from the center of the beam, and is symmetric about that line. Since the region where large signals are detected is about 20 meters wide, the spatial gradient $\Delta J_b/\Delta x$ is approximately $(4 \times 10^{-4}$ amp/m$^2)/(10\text{m}) = 4 \times 10^{-5}$ amp/m. The resulting V_{diff} can be estimated by

$$V_{diff} = (\Delta J_b/\Delta x)(\Delta V/\Delta J_b)(L\sin\theta) \qquad (28)$$

where the quantity $\Delta V/\Delta J_b$ must be determined from Figure 27, L is the antenna length, and θ is the angle of $\vec{B}$ to the spin plane. For $n_e = 10^{11}$ m^{-3} and $J_b > 4 \times 10^{-5}$ amp/m^2, $\Delta V/\Delta J_b$ is -1.6×10^5 volts/amp/m^2. The antenna length is 3.89m (see Table 1) and θ is about 23° (see Table 6). Using Equation 28 with the given values, we obtain

$V_{diff} \approx 9.7$ volts. Thus, a gradient in the energetic electron flux of the magnitude indicated by the Lepedea measurements could possibly produce the V_{diff} signals recorded during event 1.

Even though the energetic electron flux is expected to be symmetric about the line extending directly downstream from the electron beam, the electric field signals during event 1 do not indicate a reversal of the gradient as this line is crossed. The reason for a lack of a reversal is not completely understood. However, at the time the PDP crossed the line extending directly downstream from the expected beam center, the PDP was within about 3 meters of the beam center. The electron beam width is expected to be on the order of about 3 meters. Thus, the PDP was possibly in a region containing both backscattered beam electrons and primary beam electrons. Within such close proximity of the beam center, the description of the plasma becomes more complicated than further away from the beam center. The failure to detect a reversal in the electric field signal is probably due to effects of the primary beam, given the small distance between the PDP and the primary beam at the time the PDP crossed the line extending directly downstream from the beam center.

Analysis of all five events suggests that energetic electrons are found in a region about 20 meters wide extending up to 170 meters downstream from the injected electron beam. Consideration of event 1 indicates that very close to the beam, there is a large spatial gradient in the energetic electron flux: the flux increases as one

approaches the line extending directly downstream from the center of the beam. For events 3, 4, and 5, in which the PDP was 80 or more meters away from the beam, the signals are explained by the presence of energetic electrons having a preferential direction of motion along the magnetic field line, but in a direction opposite to the beam injection.

Although the main features of the electric field signals during events 1 through 5 are understood in terms of the discussion given above, some features remain unexplained. For example, the voltage peaks during event 4 are bumps on a signal that is otherwise sinusoidal. The peaks in event 4 are explained by alignment of the antenna with the magnetic field or with the velocity vector in the presence of energetic electrons. However, the electric field signal for event 4 shown in Figure 24 would also provide a reasonably good fit to the function in Equation 1. Yet, since the shadowing effects are apparent in the measurements, a fit of the signal to Equation 1 would be difficult to interpret. It is not clear why event 4 has a more sinusoidal character than events 3 or 5. Similarly, the large peaks in the signal during event 2 can be attributed to alignment of the antenna with the velocity vector in the presence of energetic electrons, but the signal remains $> |(\vec{V}x\vec{B})\cdot\vec{L}|$ when the probes are not in the spacecraft wake.

Finally, the average potential measurements are considered. The measurements show that during periods of no beam operation, the average probe floating potential was several volts higher than the PDP chassis

floating potential. The solution of Equation 25 (see Figure 27) indicates that the probes should float to a potential which is much less than a volt higher than the PDP potential. During events 1 and 2 the average probe floating potential became lower than the PDP potential. The solution of Equation 25 indicates that the average probe floating potential should always be higher than the PDP chassis potential. The reasons for these discrepancies are not clear. However, it is probable that explanation involves the properties of the PDP surface materials. In solving Equation 25 for the PDP potential, it was assumed that the PDP had a uniformly conducting surface. However the potential of the aluminum mesh on the PDP surface may be influenced by the fiberglass cloth which underlies it. The fiberglass cloth may have charged to a different potential than the aluminum mesh. Katz and Davis [1987] analyzed some of the effects of the fiberglass cloth-aluminum mesh arrangement for the case of the PDP attached to the shuttle. The ultimate effect on the mesh potential when the PDP was in free flight is uncertain.

In summary, analysis of the large signals seen at times of electron beam operations leads to the following conclusions. The large signals measured by the PDP quasi-static electric field instrument during electron beam operation can primarily be attributed to three causes. First, at times when the electric antenna is aligned with the projection of the magnetic field into the spin plane, the spacecraft body shields one probe from energetic electrons moving along the

magnetic field lines. The two probes receive different amounts of electron current, thereby causing large signals. Second, at times when energetic electrons are reaching both probes, but one probe is in the PDP wake, the wake produces asymmetries in the plasma density at the two probes, thereby causing large signals. Finally, spatial gradients in the energetic electron current to the two probes, thereby causing large signals. When the electron beam generator is operating, energetic electrons are found in a region about 20 meters wide and up to 170 meters downstream from the injected electron beam. Because the region is so narrow, the spatial gradients are significant even over the length of the PDP antenna. For events 80 or more meters away from the beam, the electric field results are explained by the presence of energetic electrons having a preferential motion back down the magnetic field line on which the beam was injected.

CHAPTER VII

CONCLUSION

The electric field measured with the PDP in free flight during the Spacelab-2 mission was generally on the order of the motional field $\vec{V} \times \vec{B}$. Much of the time, the difference between the measured field and the motional field was within the measurement uncertainty. At a few times when the signal was within the range of the instrument high gain, partial screening of the motional field was observed. The screening of the field during these times was associated with operation of the shuttle thrusters. Signals much larger than $\vec{V} \times \vec{B}$ were observed five times when the electron beam generator on board the shuttle was operating.

Partial screening of the motional electric field associated with thruster operations can be explained by the generation of an Alfvén wave from pickup current, as suggested by Pickett et al. [1985]. An estimate of the electric field associated with an Alfvén wave is in agreement with the measurements at times of thruster firings. This model predicts that that the pickup current is sufficient to produce a large change in the electric field only at times of large releases of neutral gas from the shuttle. Though the shuttle is constantly

outgassing, screening of the electric field is not significant except during a large gas release.

The large signals detected at times of electron beam operation are not representative of ambient electric fields. Rather they can be attributed to three causes: differences in fluxes of energetic electrons to the two probes due to shadowing by the PDP chassis, depressions in the plasma density caused by the PDP wake, and spatial gradients in the fluxes of energetic electrons reaching the measurement probes.

On the Spacelab-2 mission, it was demonstrated that it is possible to carry out detailed studies of electron beam effects from the shuttle. Further, it should be possible to obtain a good map of the electric field near an electron beam. However, our experience indicates that double probe floating potential measurements are not reliable in the region near the beam. The floating potential of an object in a region of energetic electrons can be many times kT_e/e more negative than the plasma potential. A small difference in energetic electron current collected by each probe of a double probe system can then lead to differential voltages much higher than those due to any electric field in the plasma. Reliable potential measurements near a beam probably require biased probes, such as described by Fahleson [1965], or emissive probes such as described by Bettinger [1965]. These active potential measurements are not as sensitive to energetic electrons. An example of a biased probe system is found on the ISEE-1

spacecraft [Mozer et al., 1978]. In general, though, active potential measurements have not been used much because of the appealing simplicity of floating potential measurements. However, for future spacecraft electron beam experiments, active instead of passive potential measurements will have to be considered.

Table 1. Instrument parameters and dynamic ranges

Electric field high gain range	± 0.064 volts/m
Electric field high gain precision	± 0.51 millivolts/m
Electric field low gain range	± 2.0 volts/m
Electric field low gain precision	± 0.017 volts/m
Electric field sample rate	20.0 samples/second
Average potential range	± 8.0 volts
Average potential sample interval	1.6 seconds/sample
Spherical probe separation	3.89 meters
Spherical probe diameter	10.2 cm

Table 2. Correlation coefficient between $|E_{VxB}|/|\vec{V}x\vec{B}|$ and the emission rate of thrusters, and the probability of obtaining a correlation coefficient greater than or equal to the value calculated if the measurements are randomly distributed

time interval GMT	213 01:03:20 - 01:18:00	213 02:30:00 - 02:47:00	213 04:02:00 - 04:11:00	213 04:12:25 - 04:19:56
correlation coefficient, all thrusters	-0.31633	-0.37168	0.05206	-0.44041
probability of correlation, all thrusters	2.98×10^{-5}	2.17×10^{-6}	0.593	1.63×10^{-5}
correlation coefficient, thrusters directed toward PDP		-0.29937	0.13804	-0.43155
probability of correlation, thrusters directed toward PDP		1.87×10^{-5}	0.154	2.40×10^{-5}

Table 3. Parallel conductivity $\sigma_{\parallel}$, Pedersen conductivity σ_p, and Hall conductivity σ_h for different neutral densities n_n, assuming an ambient plasma density $n_e = 10^5$ cm^{-3} and magnetic field B = 0.25 gauss

n_n(cm^{-3})	f_e(Hz)	f_i(Hz)	$\sigma_{\parallel}$(Ω^{-1}m^{-1})	σ_p(Ω^{-1}m^{-1})	σ_h(Ω^{-1}m^{-1})
3×10^8	57.8	3.1	50.0	1.3×10^{-5}	-2.8×10^{-7}
10^{11}	2.6×10^3	10^3	1.1	9.4×10^{-5}	-6.3×10^{-4}
10^{12}	2.6×10^4	10^4	0.11	1.3×10^{-5}	-6.3×10^{-4}
10^{13}	2.6×10^5	10^5	1.1×10^{-2}	3.9×10^{-5}	-6.4×10^{-4}
10^{14}	2.6×10^6	10^6	1.1×10^{-3}	2.8×10^{-4}	-4.7×10^{-4}

Table 4. Electric field screening determined from Alfvén wave model. Reaction rate constant used for $H_2O + O^+$ reaction was 1.95×10^{-9} cm^3/s

thruster injection angle degrees	plasma density cm^{-3}	B field gauss	Σ_{pu} $ohms^{-1}$	Σ_a $ohms^{-1}$	$E_{VxB}/IV \times BI$
2.0	1.0x104	0.25	1.3340	0.5812	0.3035
2.0	1.0x105	0.25	13.3400	1.8379	0.1211
2.0	1.0x106	0.25	133.3999	5.8119	0.0417
2.0	1.0x104	0.50	0.3335	0.2906	0.4656
2.0	1.0x105	0.50	3.3350	0.9189	0.2160
2.0	1.0x106	0.50	33.3500	2.9059	0.0802
45.0	1.0x104	0.25	0.0655	0.5812	0.8987
45.0	1.0x105	0.25	0.6554	1.8379	0.7371
45.0	1.0x106	0.25	6.5545	5.8119	0.4700
45.0	1.0x104	0.50	0.0164	0.2906	0.9466
45.0	1.0x105	0.50	0.1639	0.9189	0.8487
45.0	1.0x106	0.50	1.6386	2.9059	0.6394
90.0	1.0x104	0.25	0.0467	0.5812	0.9256
90.0	1.0x105	0.25	0.4672	1.8379	0.7973
90.0	1.0x106	0.25	4.6723	5.8119	0.5543
90.0	1.0x104	0.50	0.0117	0.2906	0.9614
90.0	1.0x105	0.50	0.1168	0.9189	0.8872
90.0	1.0x106	0.50	1.1681	2.9059	0.7133

Table 5. Electric field screening determined from Alfvén wave model. Reaction rate constant used for $H_2O + O^+$ reaction was 3.9×10^{-10} cm^3/s

thruster injection angle degrees	plasma density cm^{-3}	B field gauss	Σ_{pu} ohms-1	Σ_a ohms-1	$E_{VxB}/\|V \times B\|$
2.0	1.0x104	0.25	0.4728	0.5812	0.5514
2.0	1.0x105	0.25	4.7281	1.8379	0.2799
2.0	1.0x106	0.25	47.2807	5.8119	0.1095
2.0	1.0x104	0.50	0.1182	0.2906	0.7109
2.0	1.0x105	0.50	1.1820	0.9189	0.4374
2.0	1.0x106	0.50	11.8202	2.9059	0.1973
45.0	1.0x104	0.25	0.0232	0.5812	0.9616
45.0	1.0x105	0.25	0.2323	1.8379	0.8878
45.0	1.0x106	0.25	2.3231	5.8119	0.7144
45.0	1.0x104	0.50	0.0058	0.2906	0.9804
45.0	1.0x105	0.50	0.0581	0.9189	0.9406
45.0	1.0x106	0.50	0.5808	2.9059	0.8334
90.0	1.0x104	0.25	0.0166	0.5812	0.9723
90.0	1.0x105	0.25	0.1656	1.8379	0.9173
90.0	1.0x106	0.25	1.6560	5.8119	0.7782
90.0	1.0x104	0.50	0.0041	0.2906	0.9860
90.0	1.0x105	0.50	0.0414	0.9189	0.9569
90.0	1.0x106	0.50	0.4140	2.9059	0.8753

Table 6. Beam parameters, Sunlight conditions, PDP orientation

Event	1	2	3	4	5
Distance from PDP to shuttle	206m	218m	93m	90m	235m
Distance from PDP to Flux Tube of Beam	26-3m	9-40m	87m	84m	143m
θ - Angle of B to Spin Plane	22.9^{o} -23.6^{o}	15.4^{o} -15.7^{o}	15.1^{o} -19.4^{o}	10.8^{o} -12.1^{o}	15.4^{o} -16.6^{o}
Day/Night	day	night	night	night -sunrise	night -sunrise
Beam Current	50 ma	100 ma	100 ma	100 ma	100 ma
Beam Injection Direction	down	down	down	up	up
Beam Injection Pitch Angle	$<7.5^{o}$	2.4^{o}-10^{o}	54^{o}-70^{o}	68^{o}-69^{o}	38^{o}-45^{o}
Beam Mode	DC	1.2 kHz	54s DC 115s pulsed 600 Hz stepped down to 10 Hz	DC	DC

Table 7. Parameters used in evaluation of Equation 25

U_{sc} spacecraft velocity		7.8×10^{3} km/s
Ax cross sectional area for ion collection:	PDP	0.869 m^2
	probe	8.11×10^{-3} m^2
As total surface area:	PDP	4.52 m^2
	probe	3.24×10^{-2} m^2
Ei ion energy in spacecraft reference frame		5.08 eV
T_e electron temperature		0.2 eV
n_e plasma density		5.0×10^{11} m^{-3}
J_b current density of energetic electrons		0-5.5×10^{-4} amp/m^2

Figure 1. Measurements made with the PDP during the STS-3 mission. The plot labeled -SC POT is the average potential of the electric probes of the PDP relative to the shuttle potential. The potential changes at times of thruster operations [Shawhan et al., 1984].

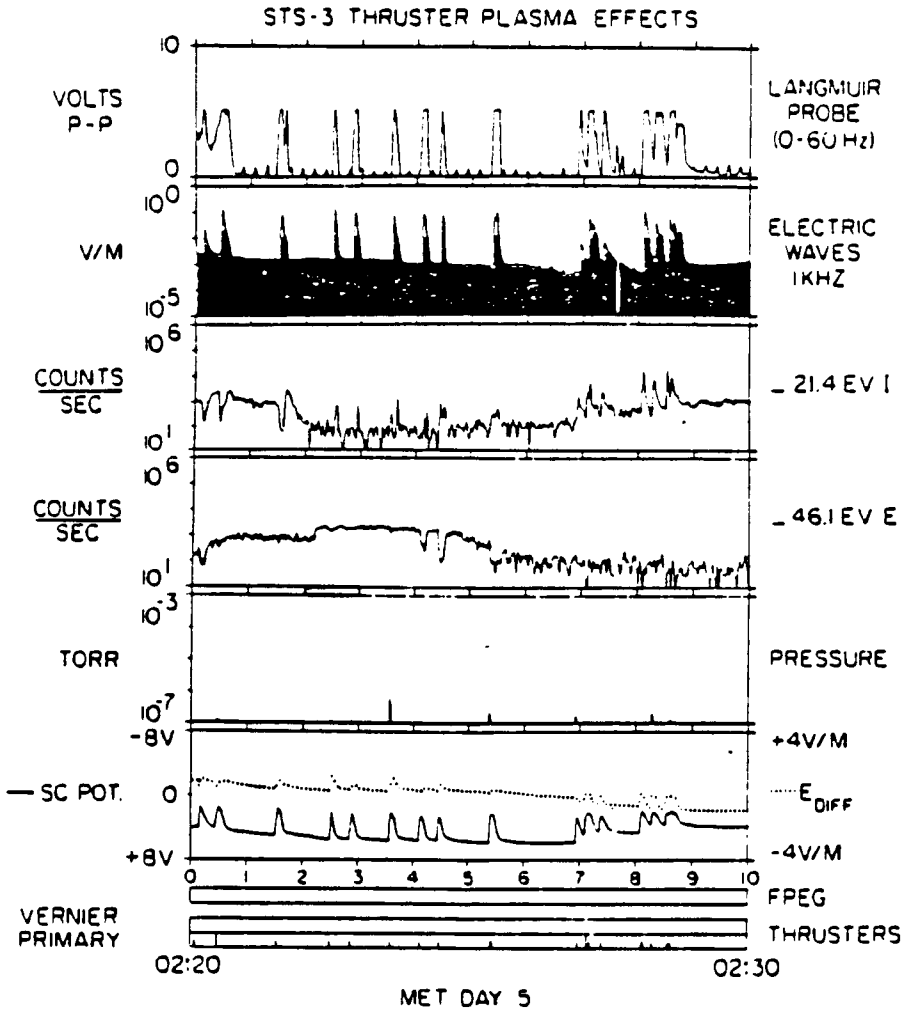
STS-3 THRUSTER PLASMA EFFECTS
VOLTS P-P
10
0
LANGMUIR PROBE (0-60 Hz)
V/M
10^0
10^{-5}
ELECTRIC WAVES 1KHZ
COUNTS SEC
10^6
10^1
- 21.4 EV I
COUNTS SEC
10^6
10^1
- 46.1 EV E
TORR
10^{-3}
10^{-7}
PRESSURE
-8V
+4V/M
— SC POT.
0
E_{DIFF}
+8V
-4V/M
0 1 2 3 4 5 6 7 8 9 10
VERNIER PRIMARY
FPEG THRUSTERS
02:20
02:30
MET DAY 5

Figure 2. The Plasma Diagnostics Package. Dimensions are given in meters.

C-087-683-1

PDP CONFIGURATION

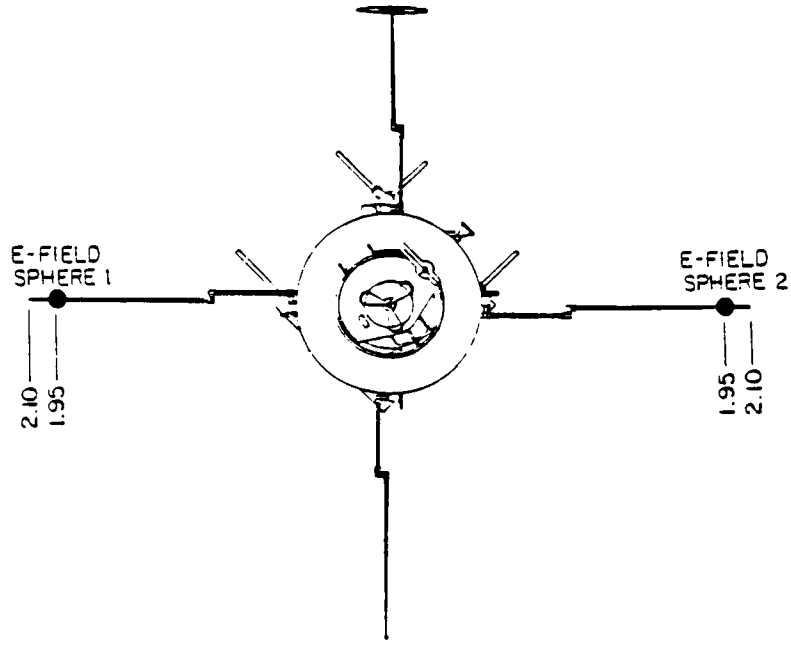

TOP VIEW

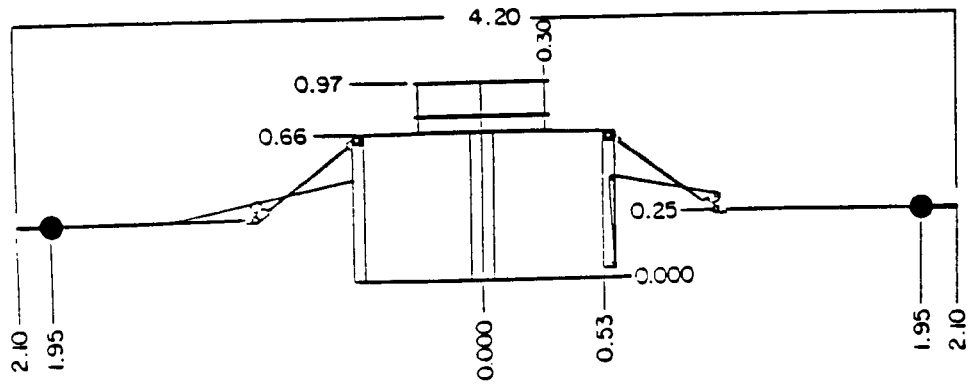

SIDE VIEW

Figure 3. Average potential measurements showing a variation at the spacecraft spin period. Arrows indicate the times when the aperature of the Lepedea faced directly into the ram direction.

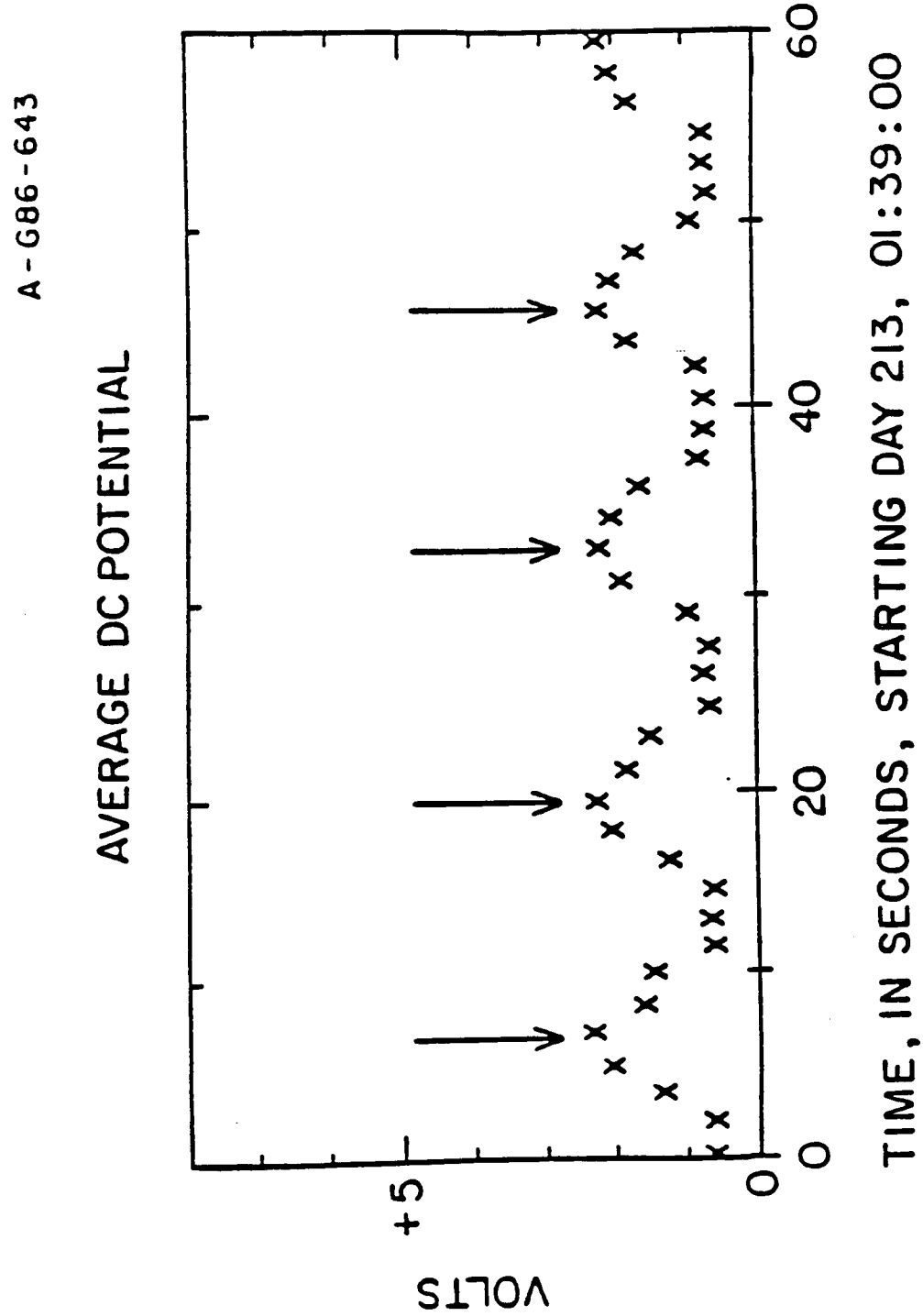
A-686-643
AVERAGE DC POTENTIAL
VOLTS
+5
0
0
20
40
60
TIME, IN SECONDS, STARTING DAY 213, 01:39:00

Figure 4. A segment of the electric field signal showing the contamination of the signal by a common mode signal related to the operation of the Lepedea, and the passage of the probes through the spacecraft wake.

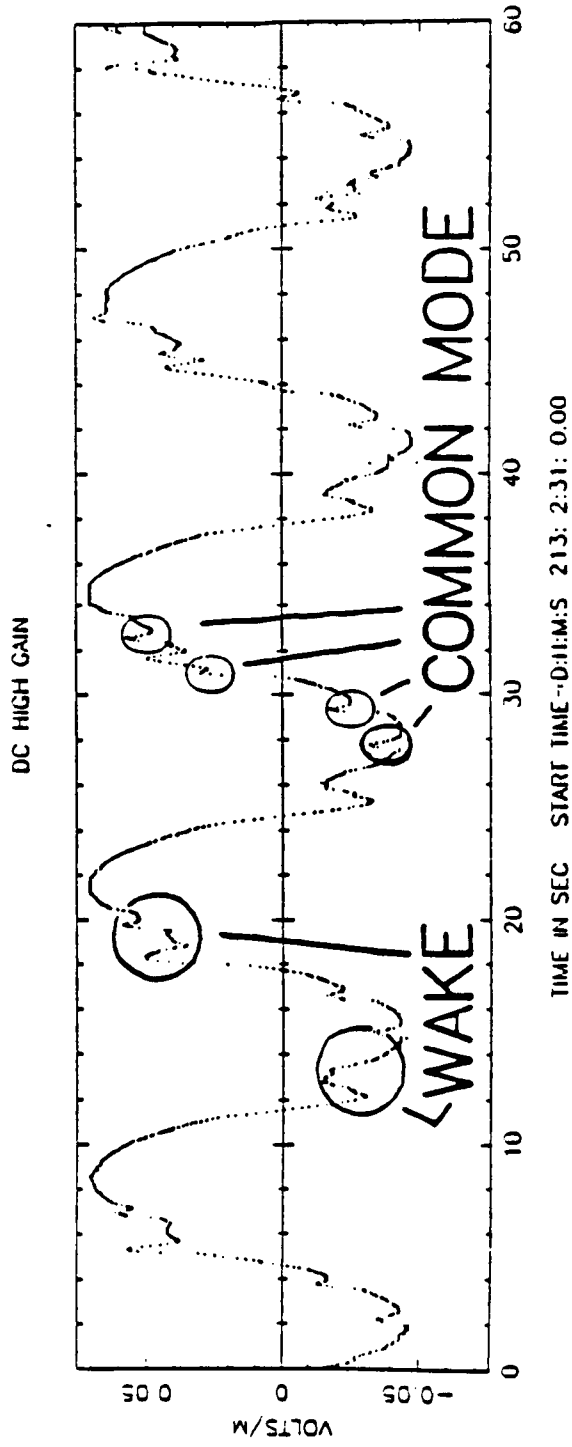
DC HIGH GAIN
VOLTS/M
0.05
0
-0.05
0
10
20
30
40
50
60
TIME IN SEC
START TIME--D:H:M:S 213: 2:31: 0.00
WAKE
COMMON MODE

Figure 5. The portion of the electric field signal remaining after segments of the signal known to be contaminated are removed.

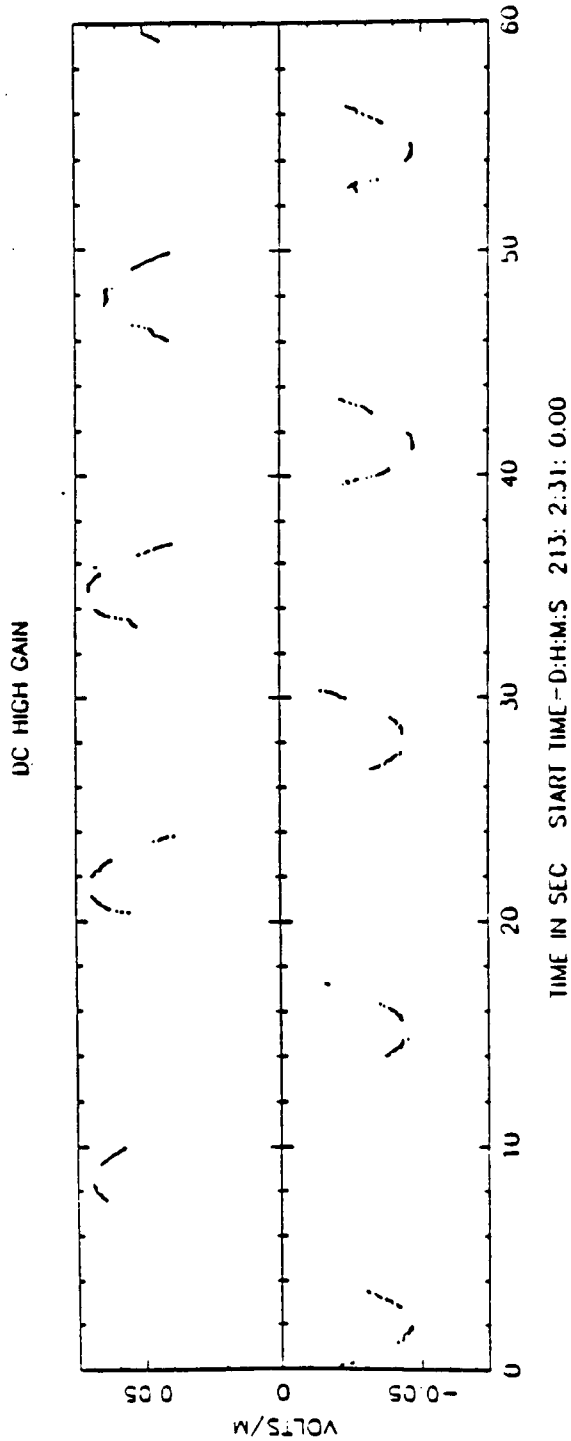
DC HIGH GAIN
VOLTS/M
0.05
0
-0.05
0
10
20
30
40
50
60
TIME IN SEC START TIME-D:H:M:S 213: 2:31: 0.00

Figure 6. Dots indicate measurements of the magnitude of the electric field in the spacecraft spin plane. The solid line indicates the projection of $\vec{V} \times \vec{B}$ in the spin plane.

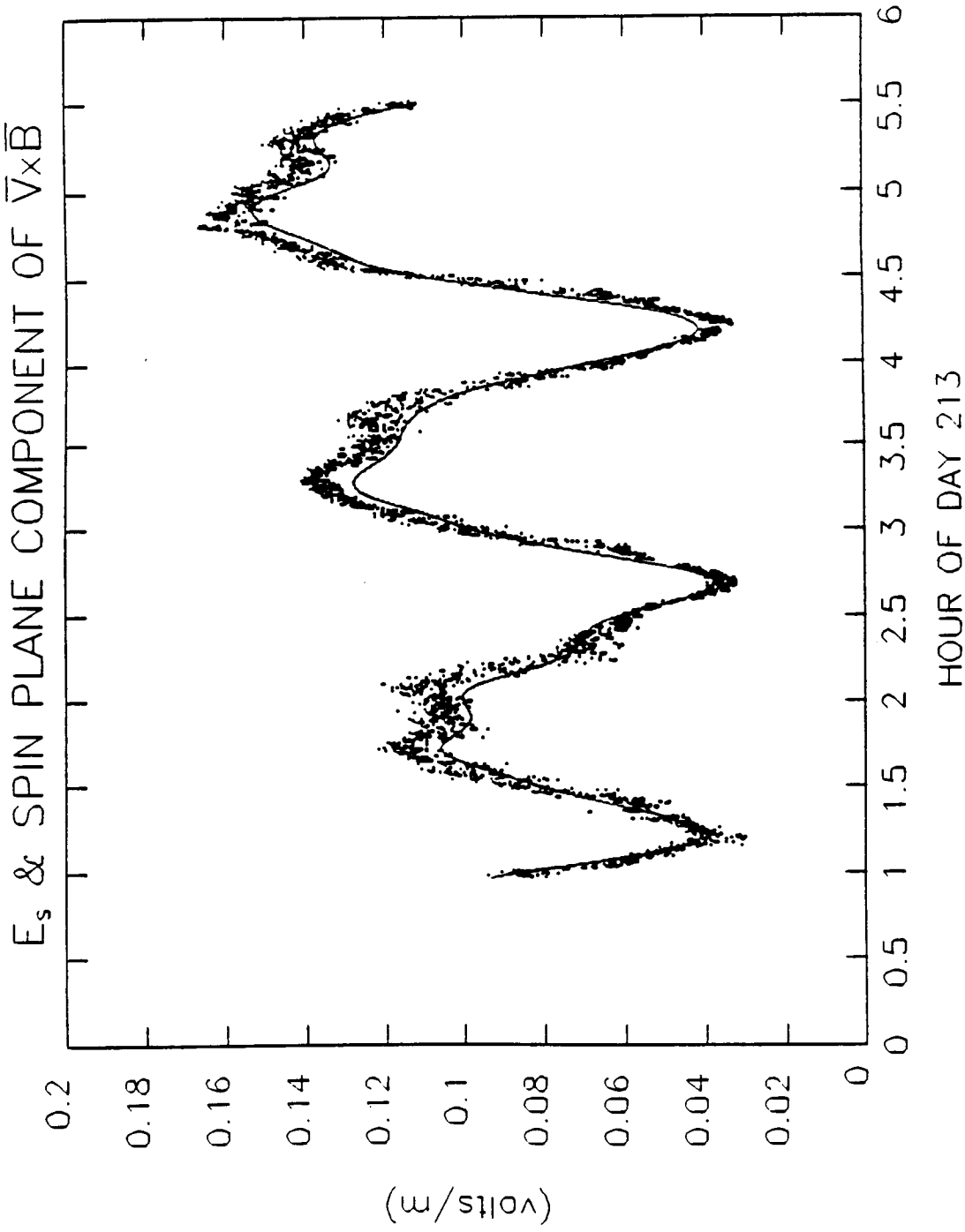
E_s & SPIN PLANE COMPONENT OF $\overline{V}\times\overline{B}$
(volts/m)
0.2
0.18
0.16
0.14
0.12
0.1
0.08
0.06
0.04
0.02
0
0
0.5
1
1.5
2
2.5
3
3.5
4
4.5
5
5.5
6
HOUR OF DAY 213

Figure 7. The RMS error of the sampled electric field values with respect to the least square's fit to a sinusoidal function.

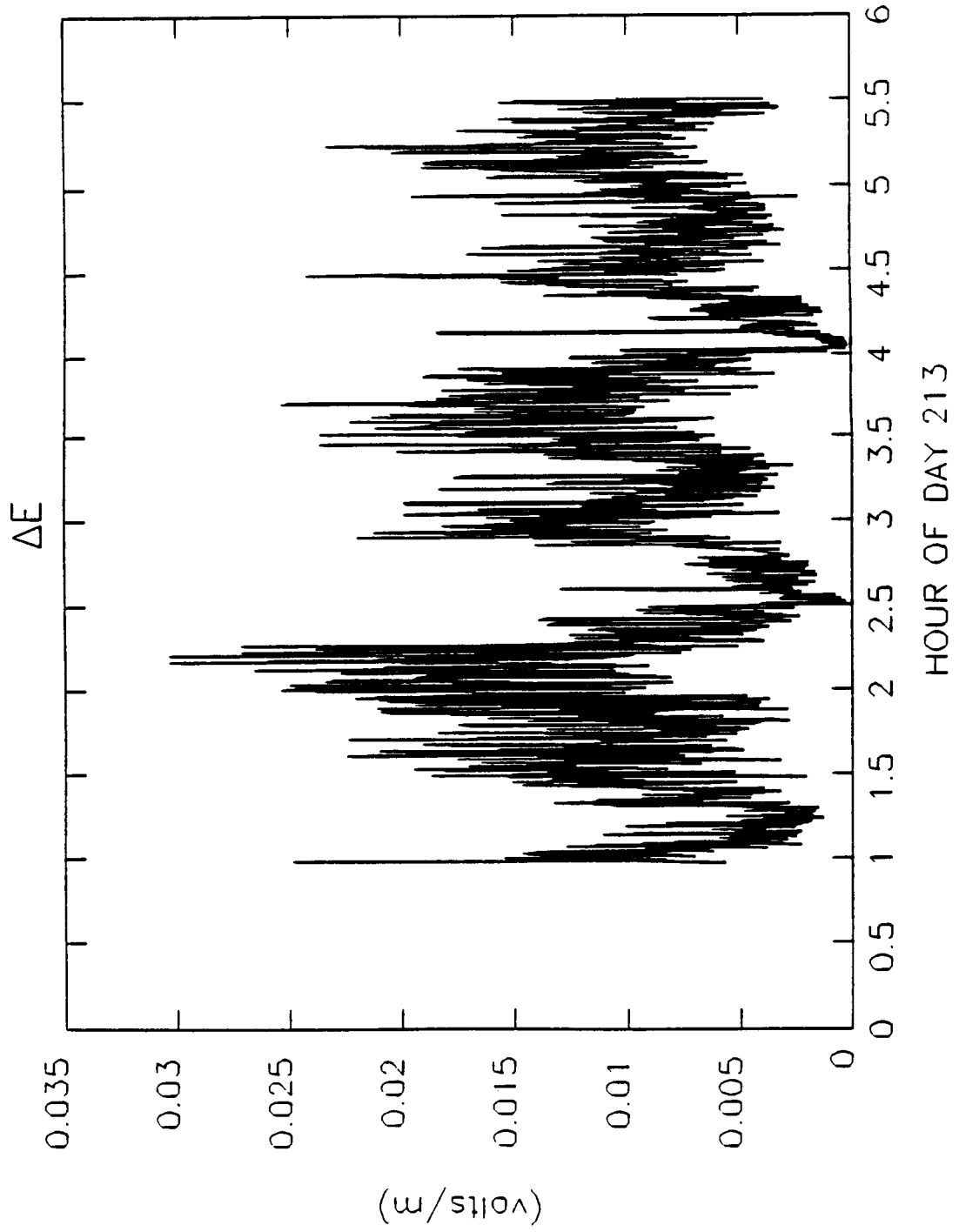
ΔE
(volts/m)
0.035
0.03
0.025
0.02
0.015
0.01
0.005
0
0
0.5
1
1.5
2
2.5
3
3.5
4
4.5
5
5.5
6
HOUR OF DAY 213

Figure 8. The component of the electric field along the direction of the velocity vector projected into a plane perpendicular to the magnetic field.

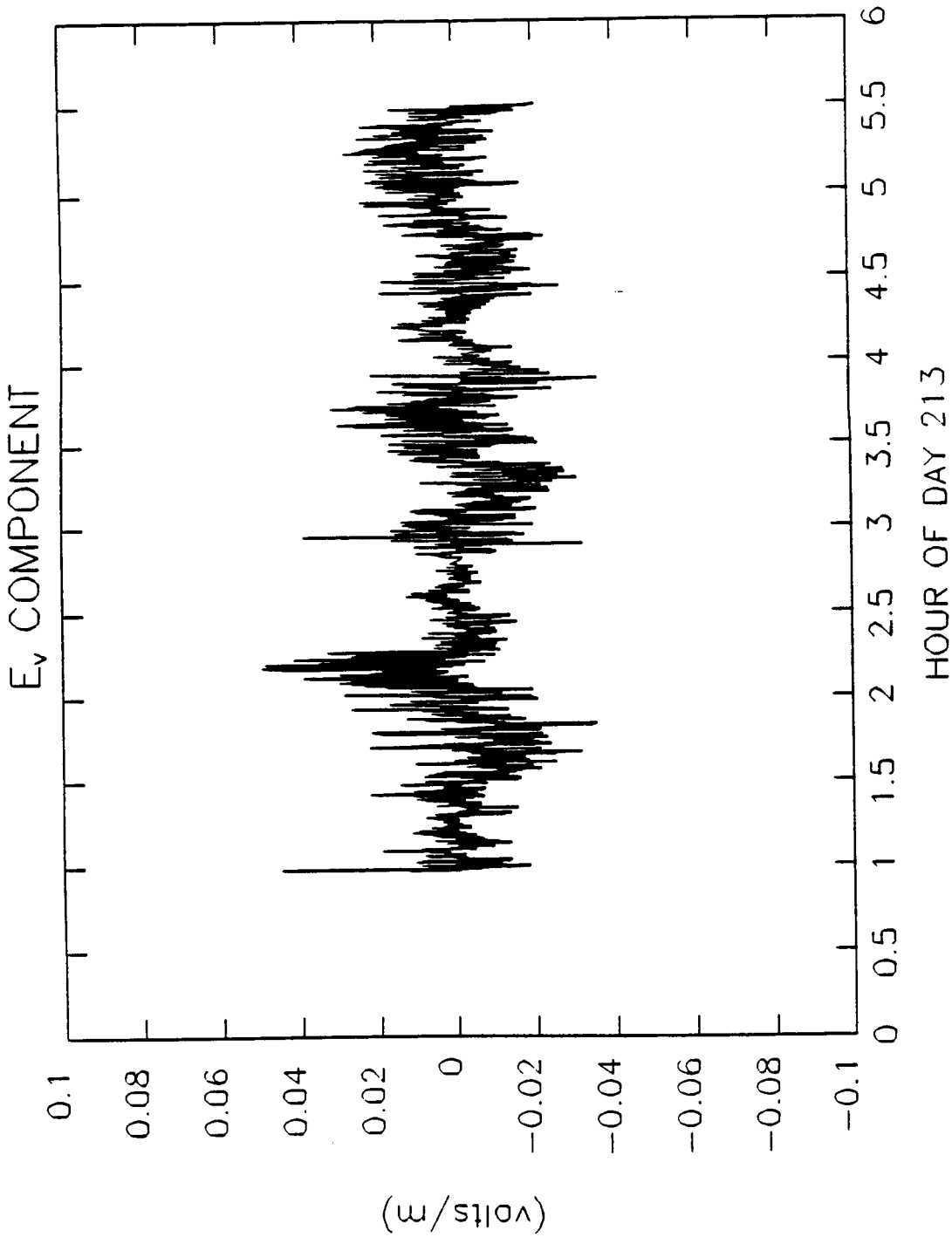
E_v COMPONENT
(volts/m)
0.1
0.08
0.06
0.04
0.02
0
−0.02
−0.04
−0.06
−0.08
−0.1
0
0.5
1
1.5
2
2.5
3
3.5
4
4.5
5
5.5
6
HOUR OF DAY 213

Figure 9. Dots indicate measurements of the component of the electric field along the direction of $\vec{V} \times \vec{B}$. The solid line indicates $\vec{V} \times \vec{B}$.

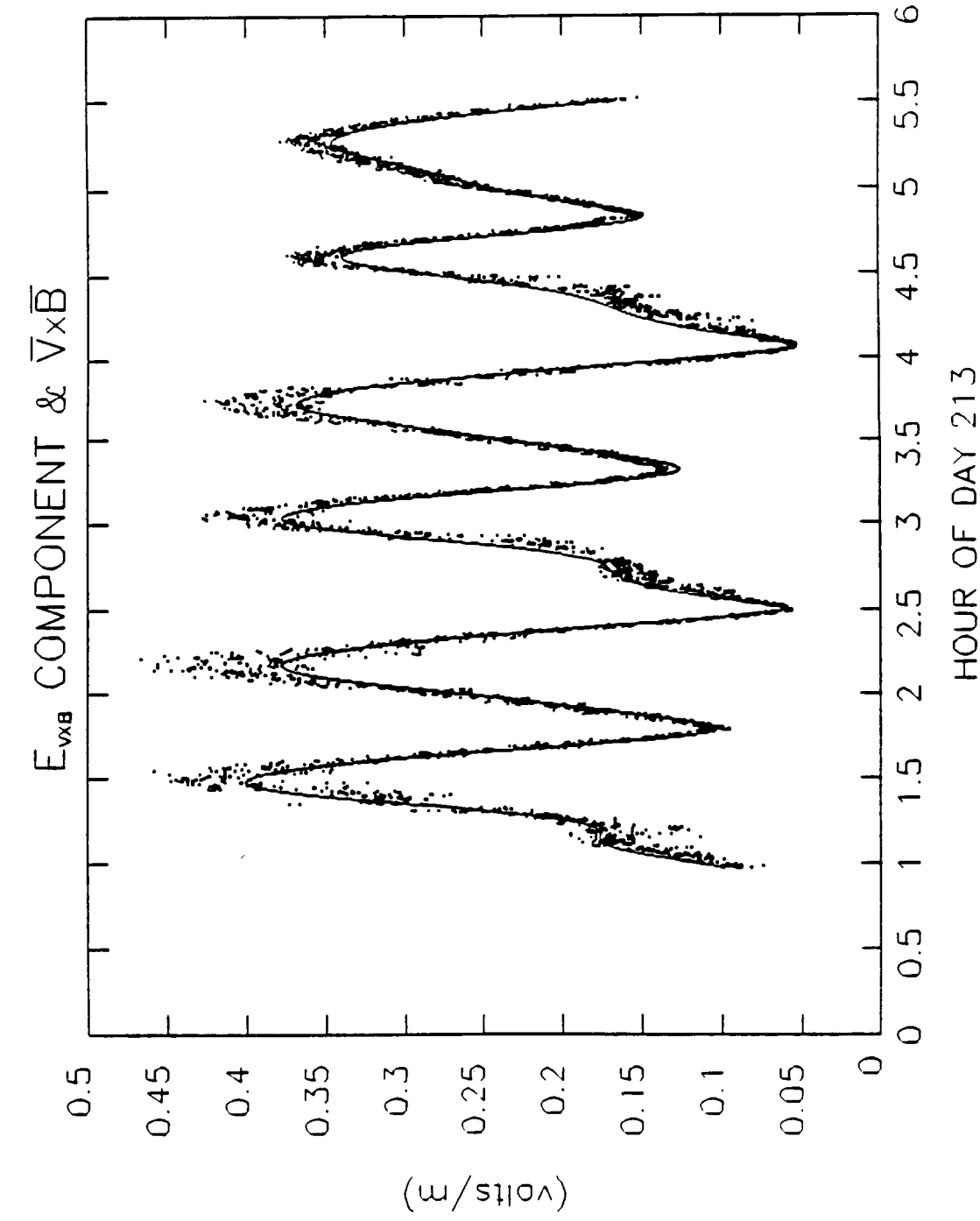
$E_{V\times B}$ COMPONENT & $\overline{V}\times\overline{B}$
(volts/m)
0.5
0.45
0.4
0.35
0.3
0.25
0.2
0.15
0.1
0.05
0
0 0.5 1 1.5 2 2.5 3 3.5 4 4.5 5 5.5 6
HOUR OF DAY 213

C-8

Figure 10. The ratio of the component of the electric field along the direction of $\vec{V} \times \vec{B}$ to the magnitude of $\vec{V} \times \vec{B}$.

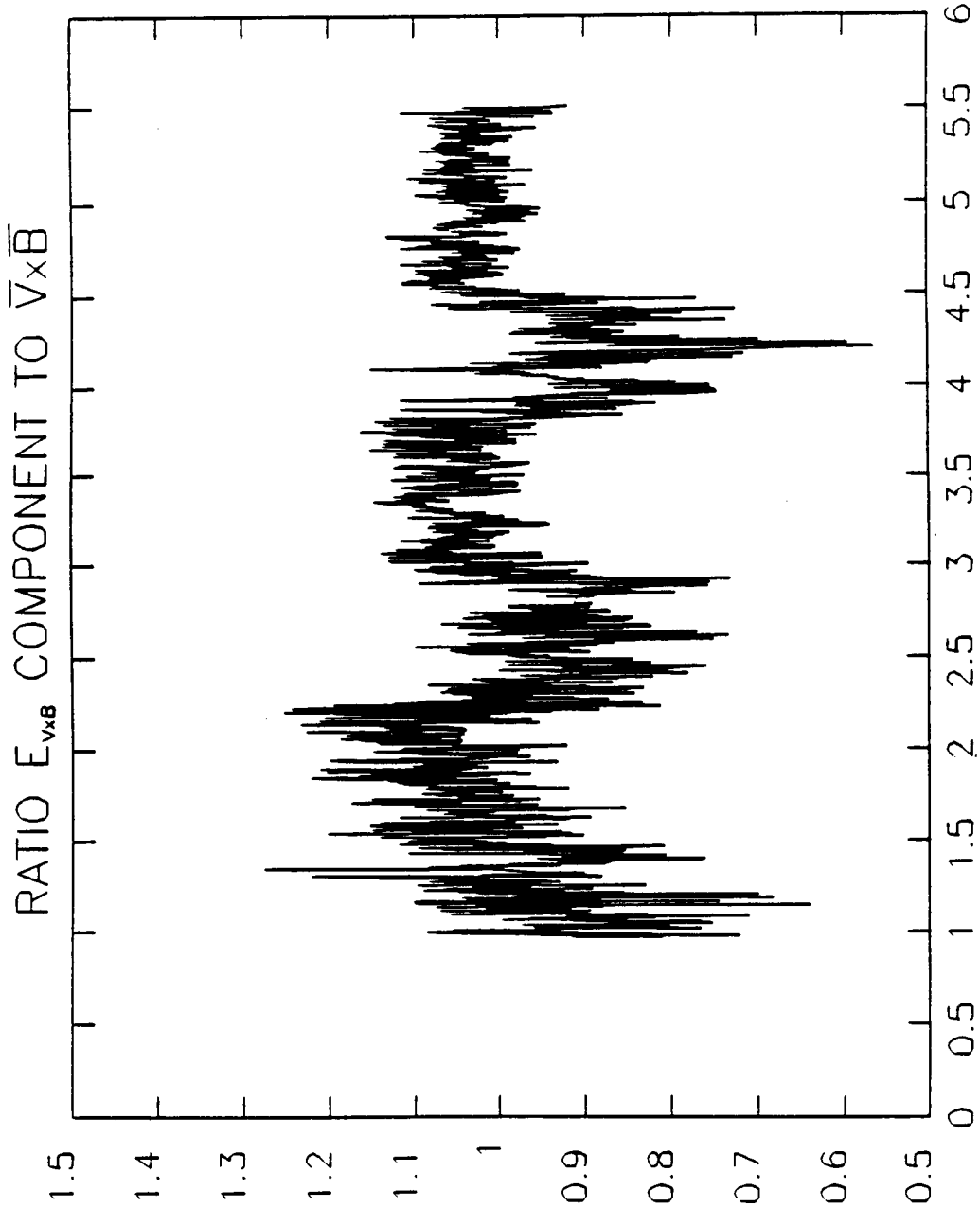
RATIO $E_{v\times B}$ COMPONENT TO $\overline{V}\times\overline{B}$
1.5
1.4
1.3
1.2
1.1
1
0.9
0.8
0.7
0.6
0.5
0
0.5
1
1.5
2
2.5
3
3.5
4
4.5
5
5.5
6
HOUR OF DAY 213

Figure 11. Electric field measurements during interval 1 when the high gain was not saturated. Dotted line is the component in the direction of $\vec{V} \times \vec{B}$. The motional field $\vec{V} \times \vec{B}$ has been subtracted from the measured field. Solid line is the component in the direction of $V_{\perp}$, the velocity projected into the plane perpendicular to the magnetic field.

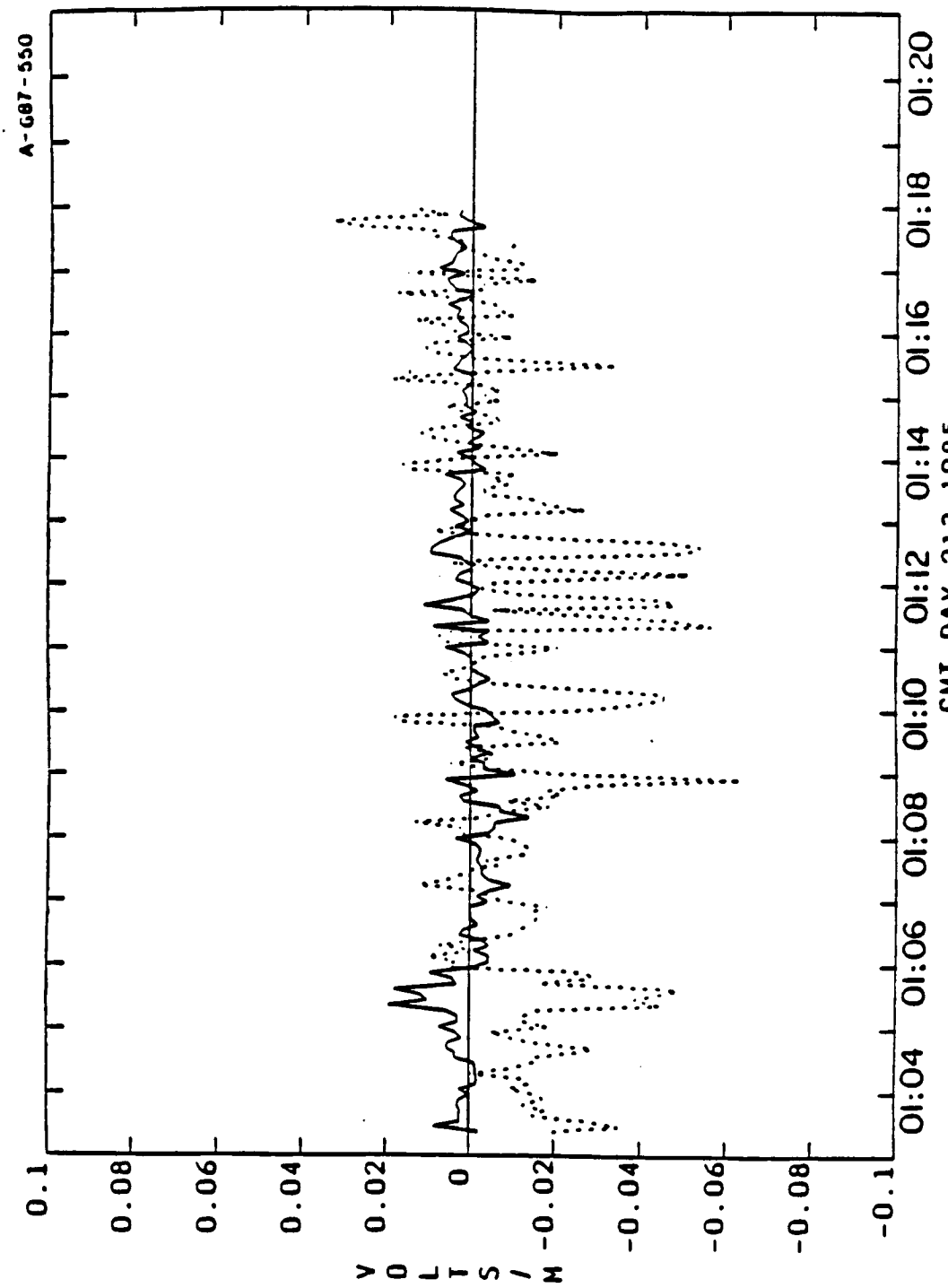
A-687-550
0.1
0.08
0.06
0.04
0.02
0
-0.02
-0.04
-0.06
-0.08
-0.1
VOLTS/M
01:04
01:06
01:08
01:10
01:12
01:14
01:16
01:18
01:20
GMT DAY 213 1985

Figure 12. Electric field measurements during interval 2 when the high gain was not saturated. Dotted line is the component in the direction of $\vec{V} \times \vec{B}$. The motional field $\vec{V} \times \vec{B}$ has been subtracted from the measured field. Solid line is the component in the direction of $V_{\perp}$, the velocity projected into the plane perpendicular to the magnetic field.

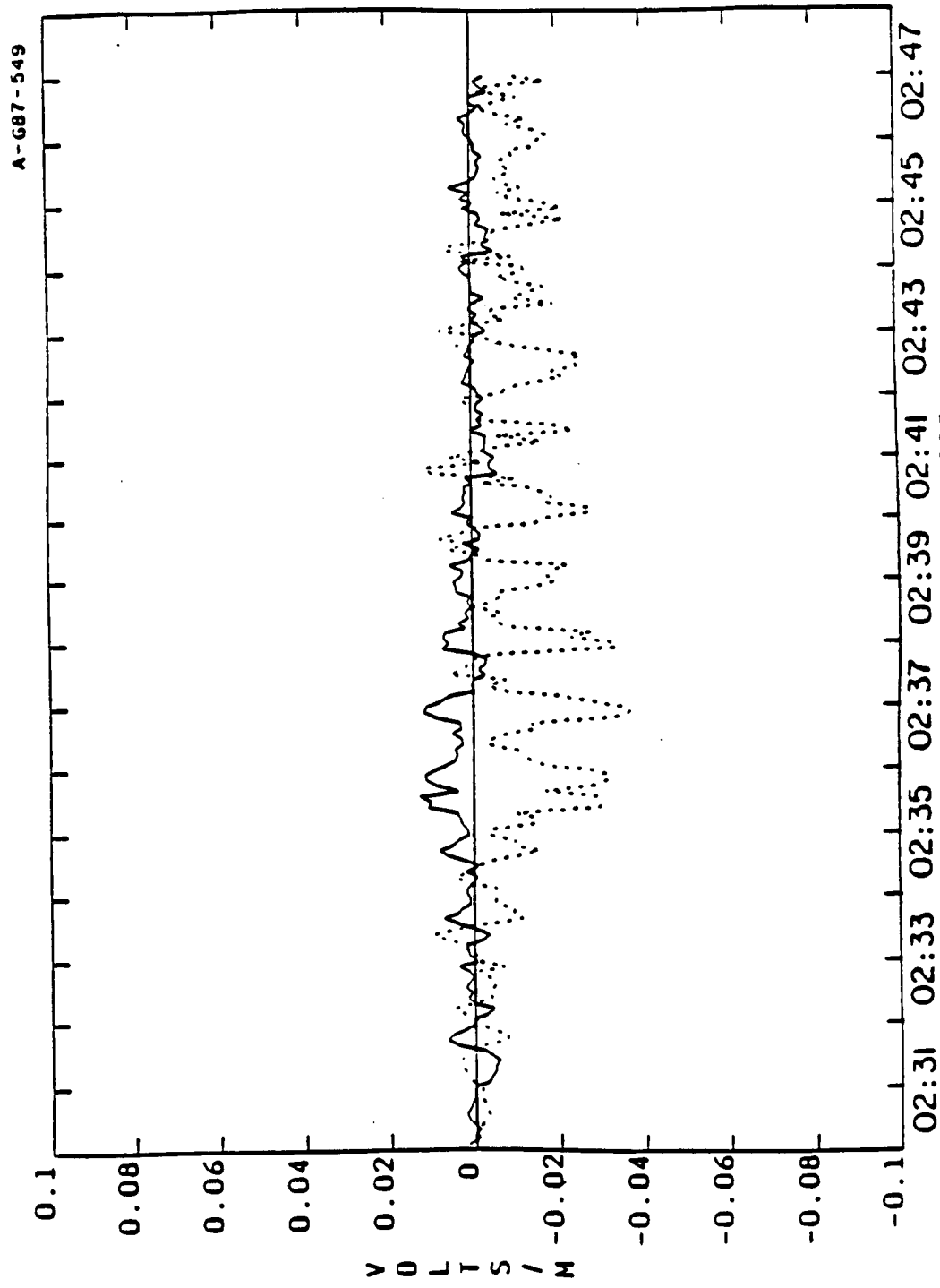
A-687-549
0.1
0.08
0.06
0.04
0.02
0
-0.02
-0.04
-0.06
-0.08
-0.1
VOLTS/M
02:31
02:33
02:35
02:37
02:39
02:41
02:43
02:45
02:47
GMT DAY 213 1985

Figure 13. Electric field measurements during intervals 3 and 4 when the high gain was not saturated. Dotted line is the component in the direction of $\vec{V} \times \vec{B}$. The motional field $\vec{V} \times \vec{B}$ has been subtracted from the measured field. Solid line is the component in the direction of $V_{\perp}$, the velocity projected into the plane perpendicular to the magnetic field.

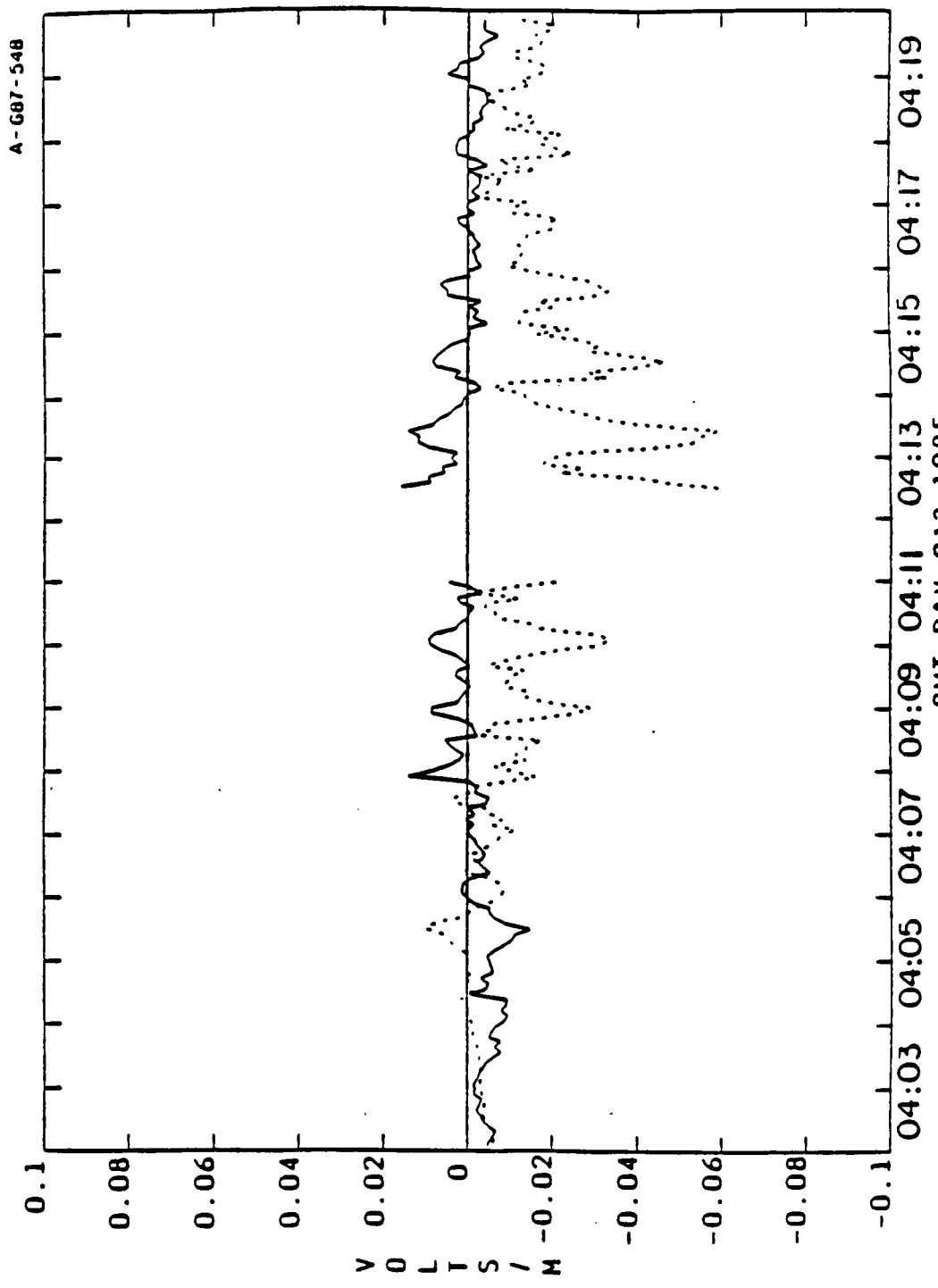
A-G87-548
0.1
0.08
0.06
0.04
0.02
0
-0.02
-0.04
-0.06
-0.08
-0.1
VOLTS/M
04:03
04:05
04:07
04:09
04:11
04:13
04:15
04:17
04:19
GMT DAY 213 1985

Figure 14. Upper plot shows the ratio $E_{VxB}/|\vec{V}x\vec{B}|$. Lower plot shows the thruster emission rate.

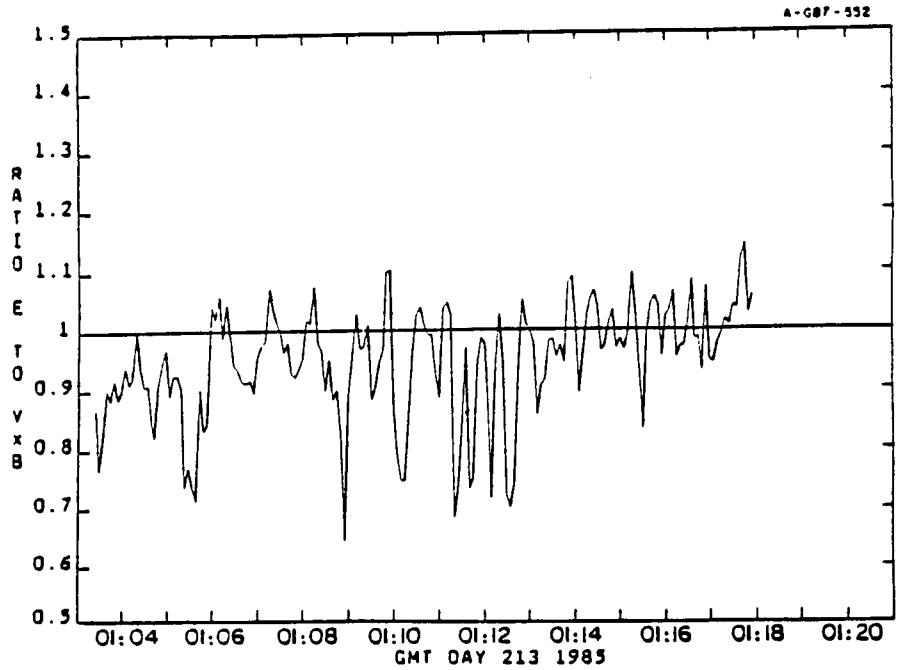
A-G87-552
RATIO E TO vxB
1.5
1.4
1.3
1.2
1.1
1
0.9
0.8
0.7
0.6
0.5
01:04
01:06
01:08
01:10
01:12
01:14
01:16
01:18
01:20
GMT DAY 213 1985

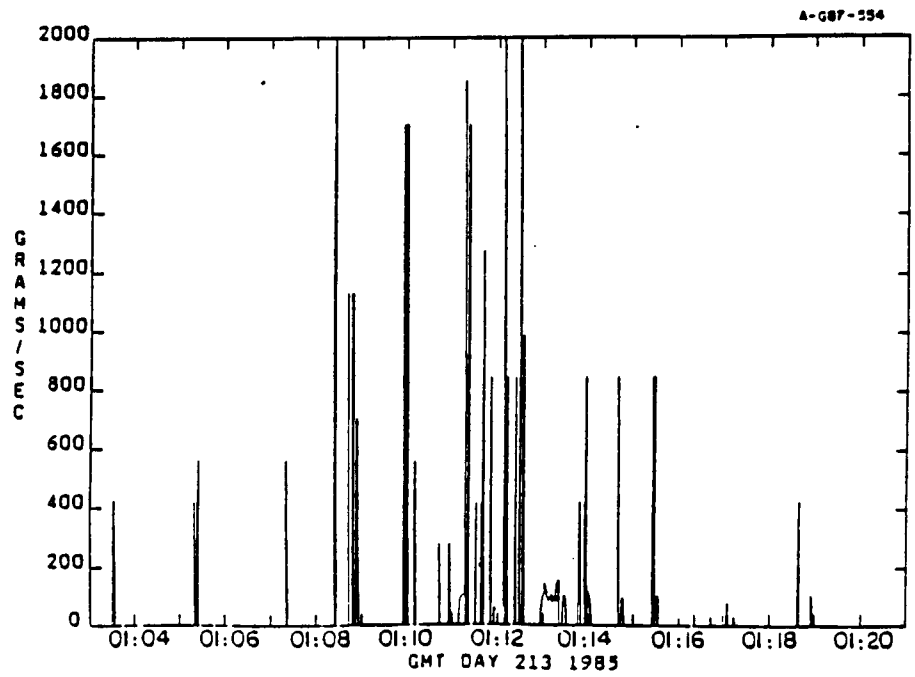
A-G87-554
GRAMS/SEC
2000
1800
1600
1400
1200
1000
800
600
400
200
0
01:04
01:06
01:08
01:10
01:12
01:14
01:16
01:18
01:20
GMT DAY 213 1985

Figure 15. Upper plot shows the ratio $E_{VxB}/|\vec{V}x\vec{B}|$. Lower plot shows the thruster emission rate.

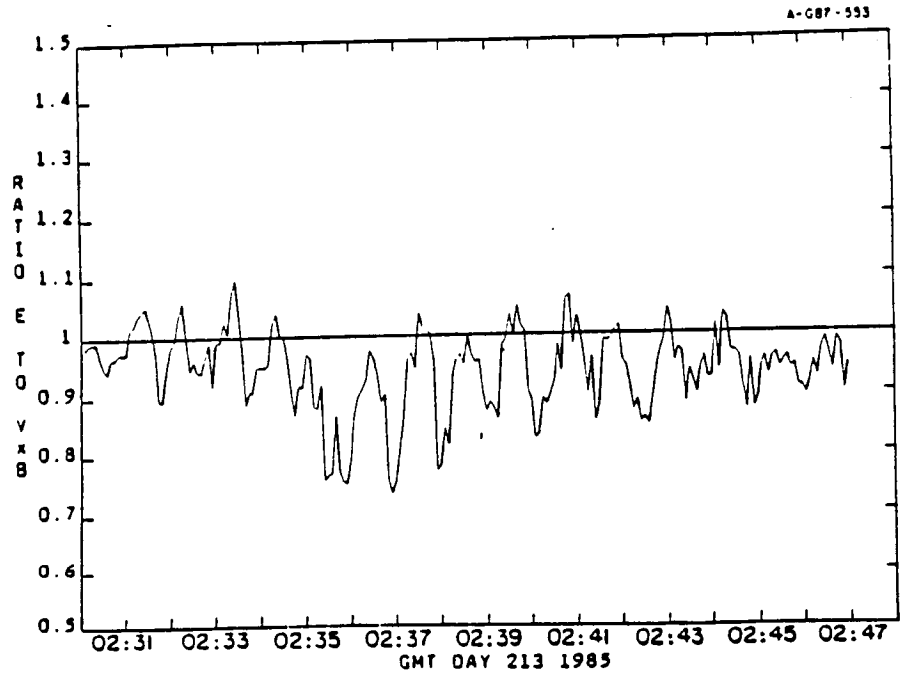
A-G87-553
RATIO E TO VxB
1.5
1.4
1.3
1.2
1.1
1
0.9
0.8
0.7
0.6
0.5
02:31 02:33 02:35 02:37 02:39 02:41 02:43 02:45 02:47
GMT DAY 213 1985

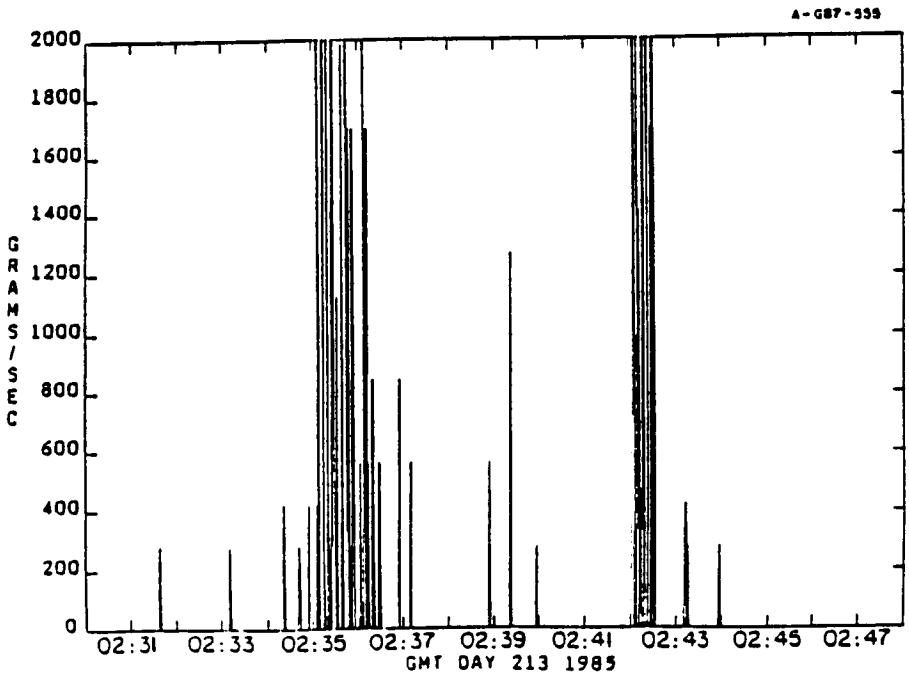
A-G87-559
GRAMS/SEC
2000
1800
1600
1400
1200
1000
800
600
400
200
0
02:31 02:33 02:35 02:37 02:39 02:41 02:43 02:45 02:47
GMT DAY 213 1985

Figure 16. Upper plot shows the ratio $E_{VxB}/|\vec{V}x\vec{B}|$. Lower plot shows the thruster emission rate.

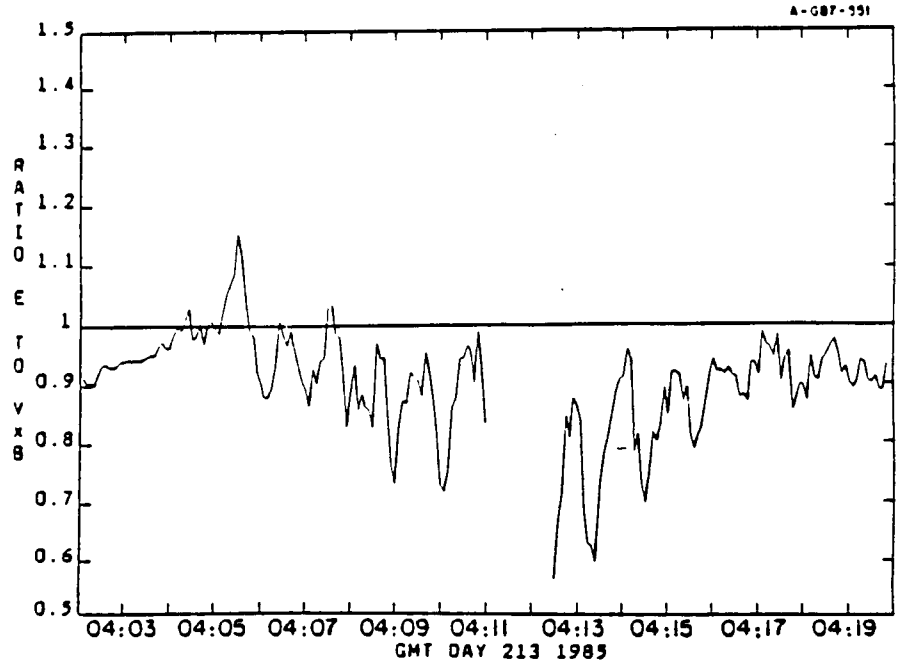
A-G87-551
RATIO E TO VxB
1.5
1.4
1.3
1.2
1.1
1
0.9
0.8
0.7
0.6
0.5
04:03 04:05 04:07 04:09 04:11 04:13 04:15 04:17 04:19
GMT DAY 213 1985

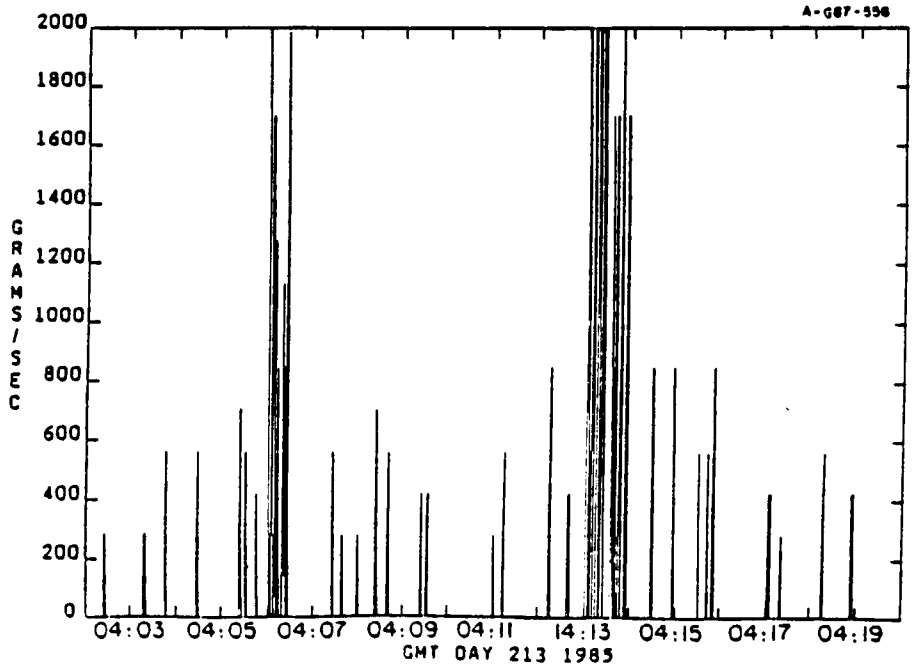
A-G87-556
GRAMS/SEC
2000
1800
1600
1400
1200
1000
800
600
400
200
0
04:03 04:05 04:07 04:09 04:11 14:13 04:15 04:17 04:19
GMT DAY 213 1985

Figure 17. The ratio $E_{VxB}/|\vec{V}x\vec{B}|$ versus the thruster emission rate averaged over 13 seconds. Points from all 4 time intervals are included.

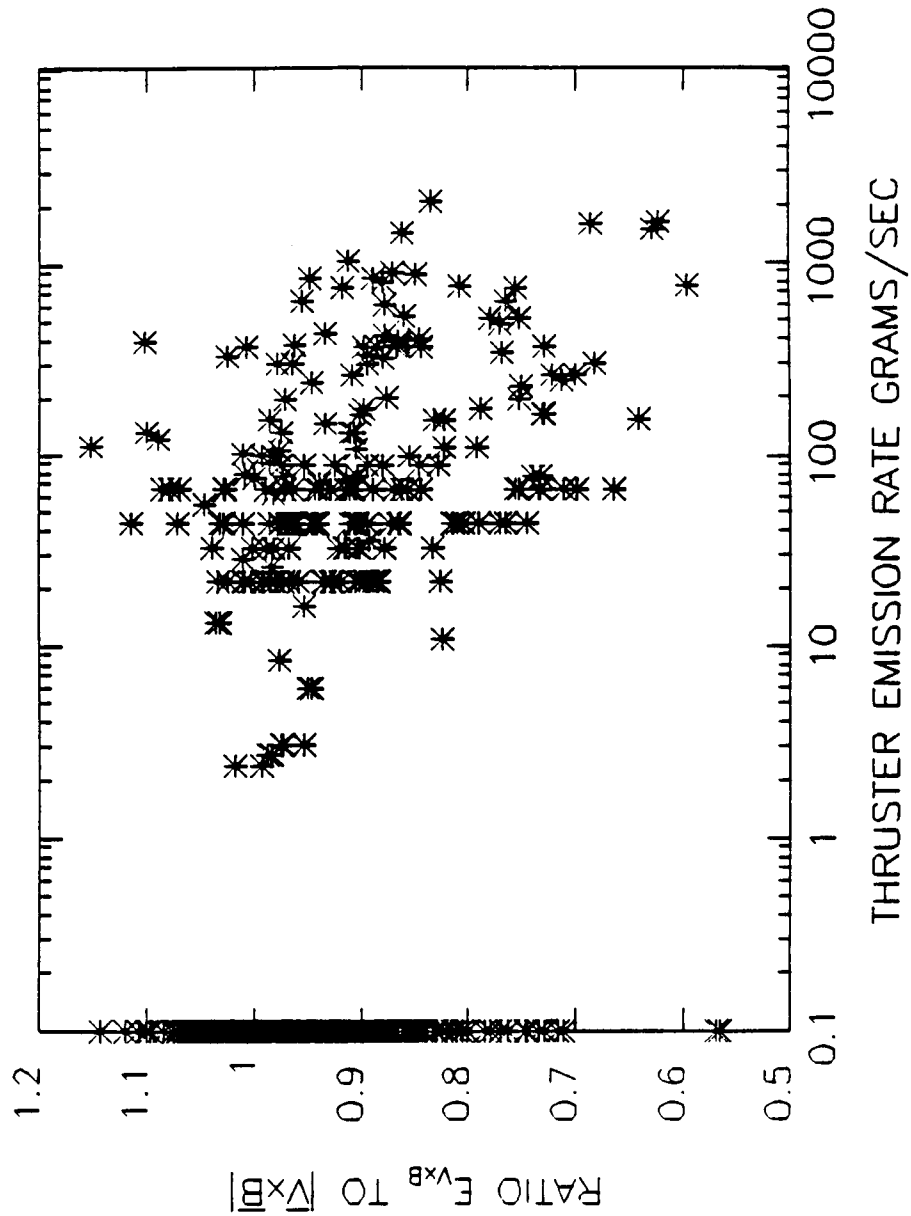
RATIO $E_{v\times B}$ TO $|\bar{V}\times\bar{B}|$
1.2
1.1
1
0.9
0.8
0.7
0.6
0.5
0.1
1
10
100
1000
10000
THRUSTER EMISSION RATE GRAMS/SEC

Figure 18. Measurements of $E_{VxB}/|\vec{V}x\vec{B}|$ are segregated into bins having comparable numbers of measurements, and averaged. The vertical lines show the boundaries of each bin. The error bars indicate the standard deviation of the mean in each bin.

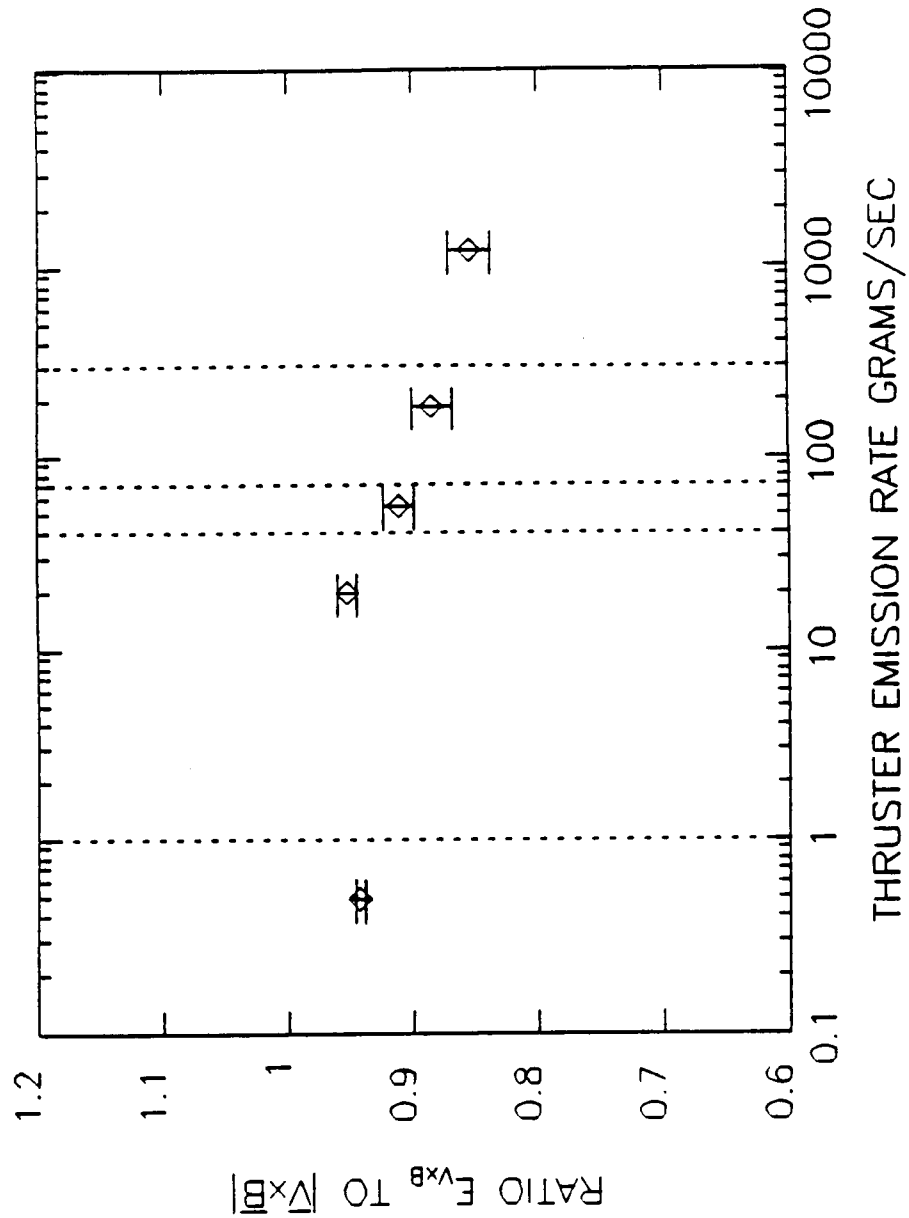
RATIO E_{vxB} TO $|\bar{V}x\bar{B}|$
1.2
1.1
1
0.9
0.8
0.7
0.6
0.1
1
10
100
1000
10000
THRUSTER EMISSION RATE GRAMS/SEC

Figure 19. The ratio $E_{VxB}/|\vec{V}x\vec{B}|$ versus the thruster emission rate averaged over 13 seconds. Points from all four time intervals are included. Times when the electron beam generator was operating are excluded.

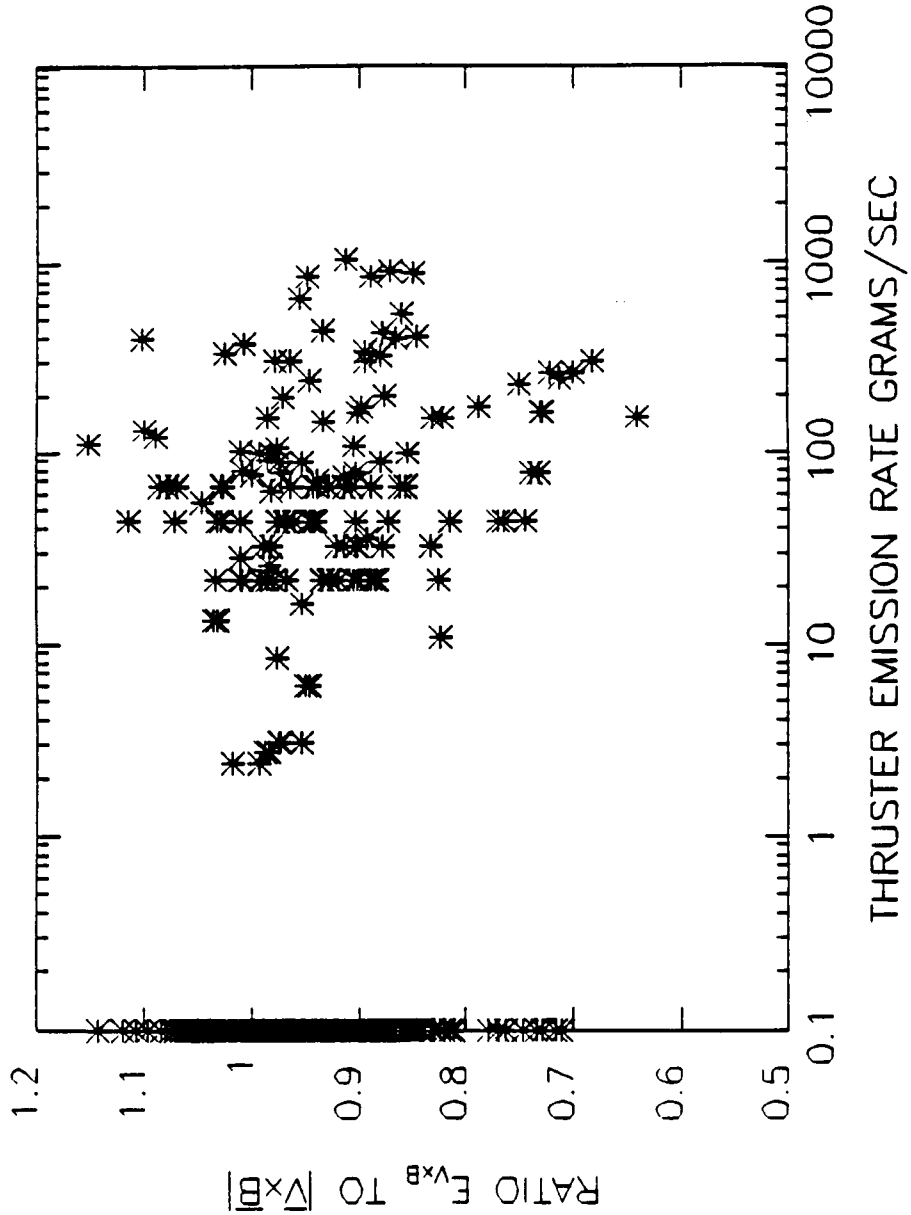
RATIO $E_{v\times B}$ TO $|\bar{V}\times\bar{B}|$
1.2
1.1
1
0.9
0.8
0.7
0.6
0.5
0.1
1
10
100
1000
10000
THRUSTER EMISSION RATE GRAMS/SEC

Figure 20. Measurements of $E_{VxB}/|\vec{V}x\vec{B}|$ are segregated into bins having comparable numbers of measurements, and averaged. The vertical lines show the boundaries of each bin. The error bars indicate the standard deviation of the mean in each bin. Times when the electron beam generator was operating are excluded.

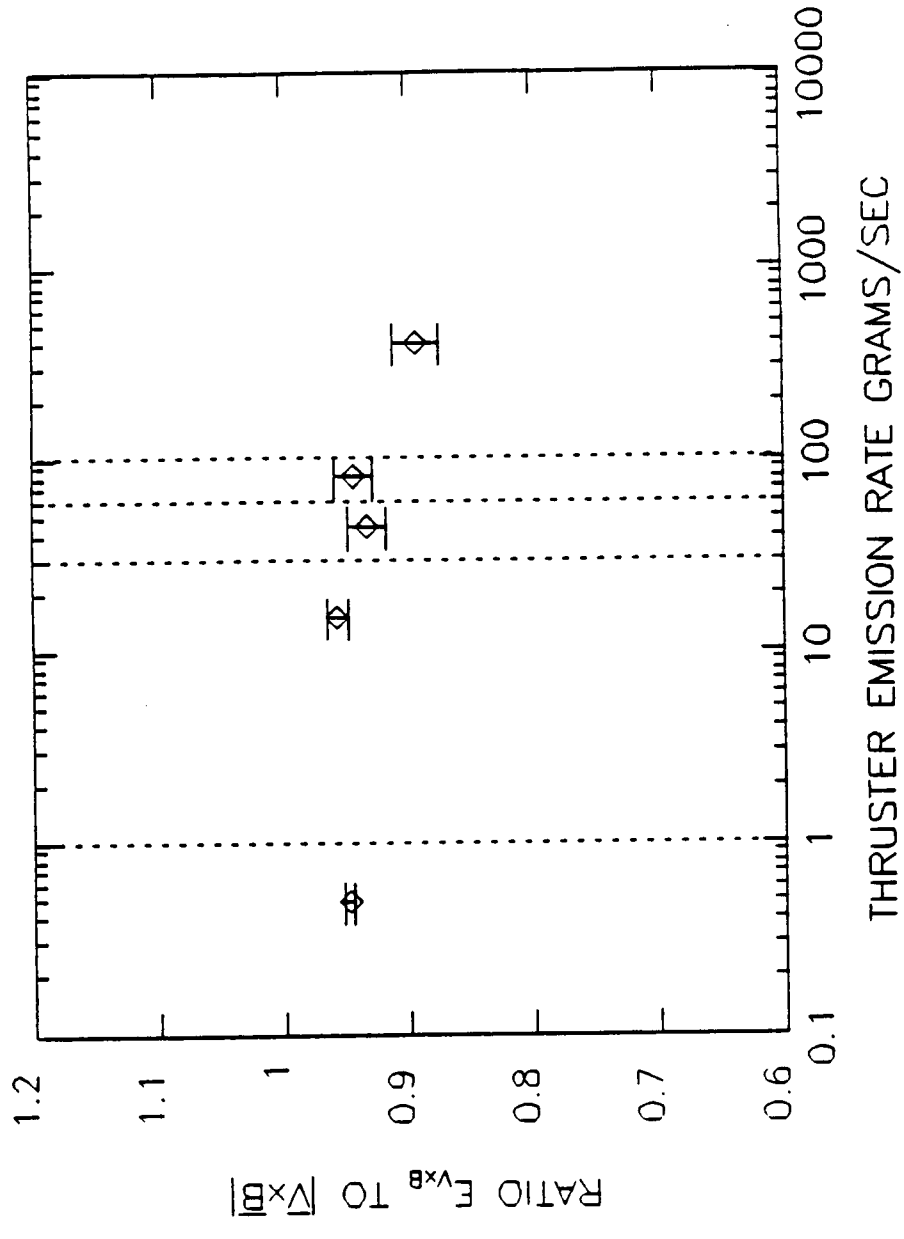
RATIO $E_{v\times B}$ TO $|V\times B|$
1.2
1.1
1
0.9
0.8
0.7
0.6
0.1
1
10
100
1000
10000
THRUSTER EMISSION RATE GRAMS/SEC

Figure 21. Directions of x, y, z coordinates.

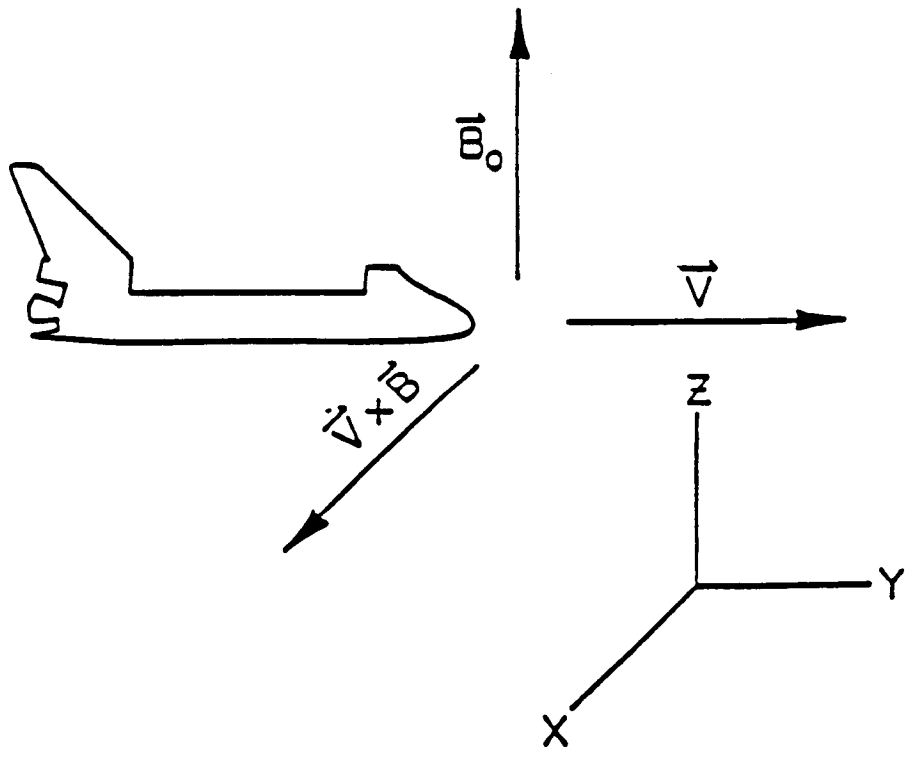
B-G87-558
$\vec{B}_o$
$\vec{V}$
$\vec{V}\times\vec{B}$
Z
Y
X

Figure 22. Alfvén wave disturbance generated by a current source moving through a magnetized plasma. The electric field E_2 between the current wings is of lower magnitude than the motional field $E_1 = \vec{V} \times \vec{B}$.

B-G87-325

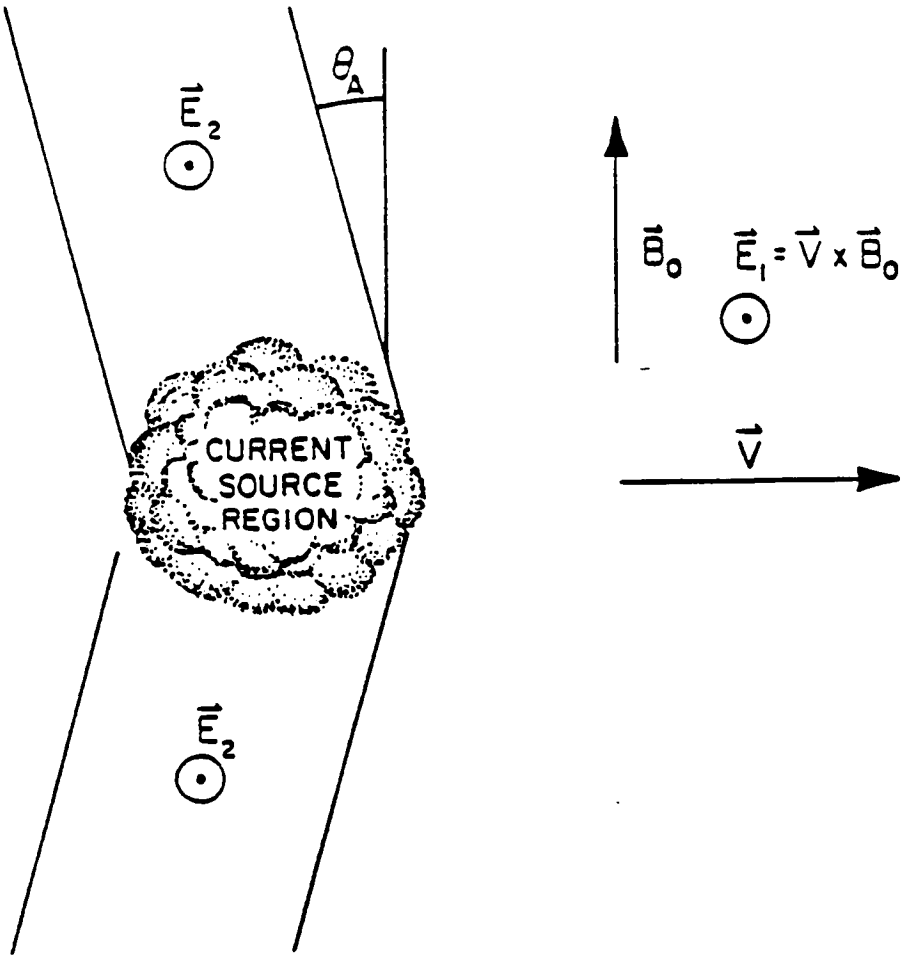
θ_A
$\vec{E}_2$
CURRENT SOURCE REGION
$\vec{E}_2$
$\vec{B}_0$
$\vec{E}_1 = \vec{V} \times \vec{B}_0$
$\vec{V}$

Figure 23. Alfvén wave disturbance generated by a current source moving through a magnetized plasma. The electric field E_2 between the current wings is of lower magnitude than the motional field $E_1 = \vec{V} \times \vec{B}$.

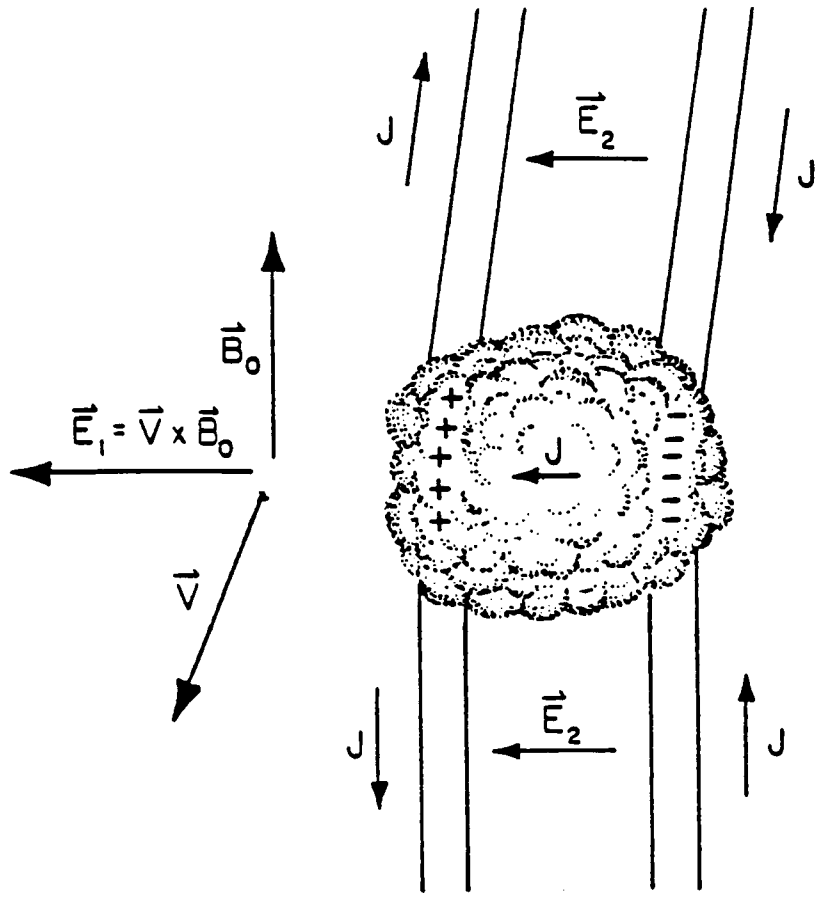
J
$\vec{E}_2$
J
$\vec{B}_o$
$\vec{E}_1 = \vec{V} \times \vec{B}_o$
J
$\vec{V}$
J
$\vec{E}_2$
J

Figure 24. Large differential voltage signals associated with times of the electron beam generator operation.

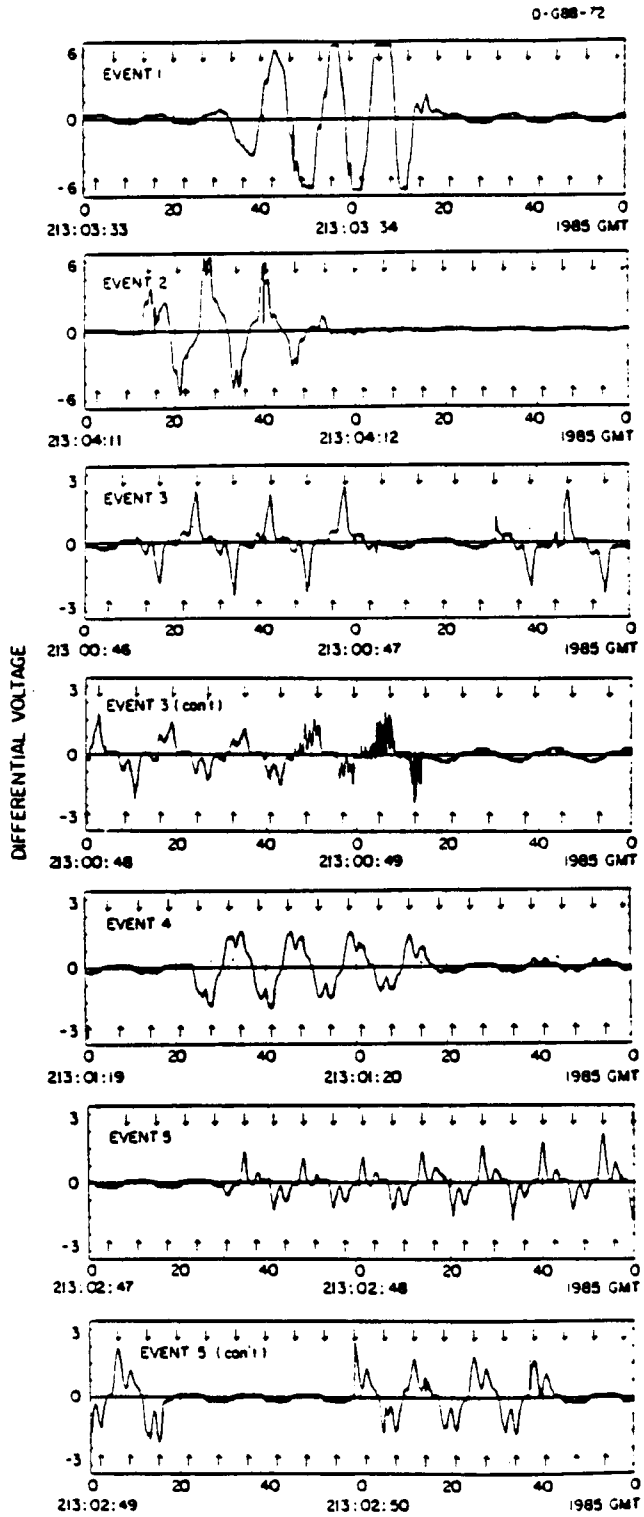
0-688-72
EVENT 1
213:03:33
213:03:34
1985 GMT
EVENT 2
213:04:11
213:04:12
1985 GMT
EVENT 3
213:00:46
213:00:47
1985 GMT
EVENT 3 (con't)
213:00:48
213:00:49
1985 GMT
EVENT 4
213:01:19
213:01:20
1985 GMT
EVENT 5
213:02:47
213:02:48
1985 GMT
EVENT 5 (con't)
213:02:49
213:02:50
1985 GMT
DIFFERENTIAL VOLTAGE

Figure 25. Dashed lines indicate the trajectory of PDP in the plane perpendicular to $\vec{B}$ during times of electron beam generator operation. The trajectories for events 1 through 5 are shown as solid segments. The origin represents the position of the magnetic field line on which the beam lies. $V_{\perp}$ is the component of velocity perpendicular to $\vec{B}$.

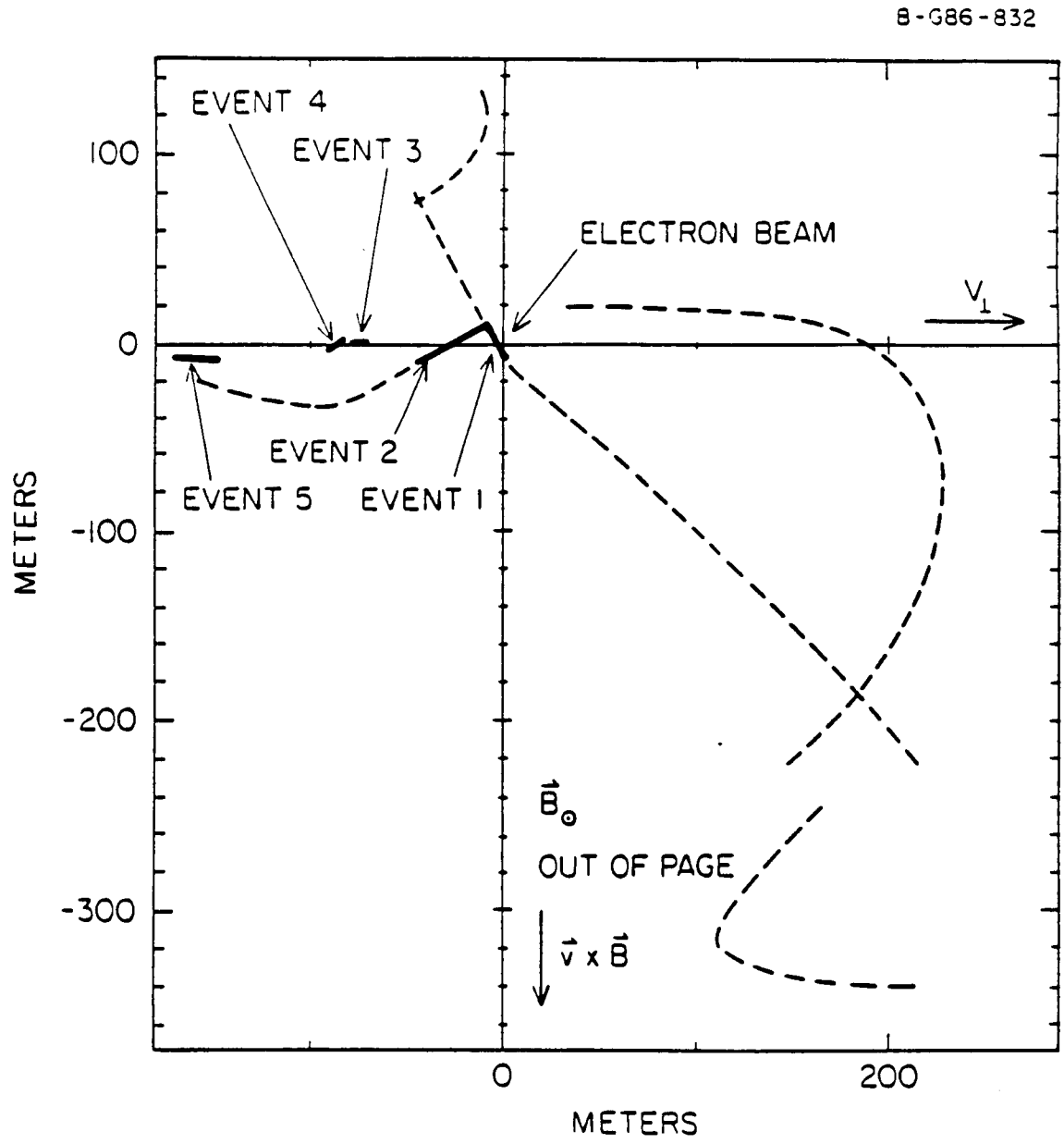
8-G86-832
EVENT 4
EVENT 3
ELECTRON BEAM
$V_\perp$
EVENT 2
EVENT 5
EVENT 1
$\vec{B}_\odot$
OUT OF PAGE
$\vec{v} \times \vec{B}$
100
0
-100
-200
-300
METERS
0
200
METERS

Figure 26. Average potential measurements during times when large electric field signals were detected.

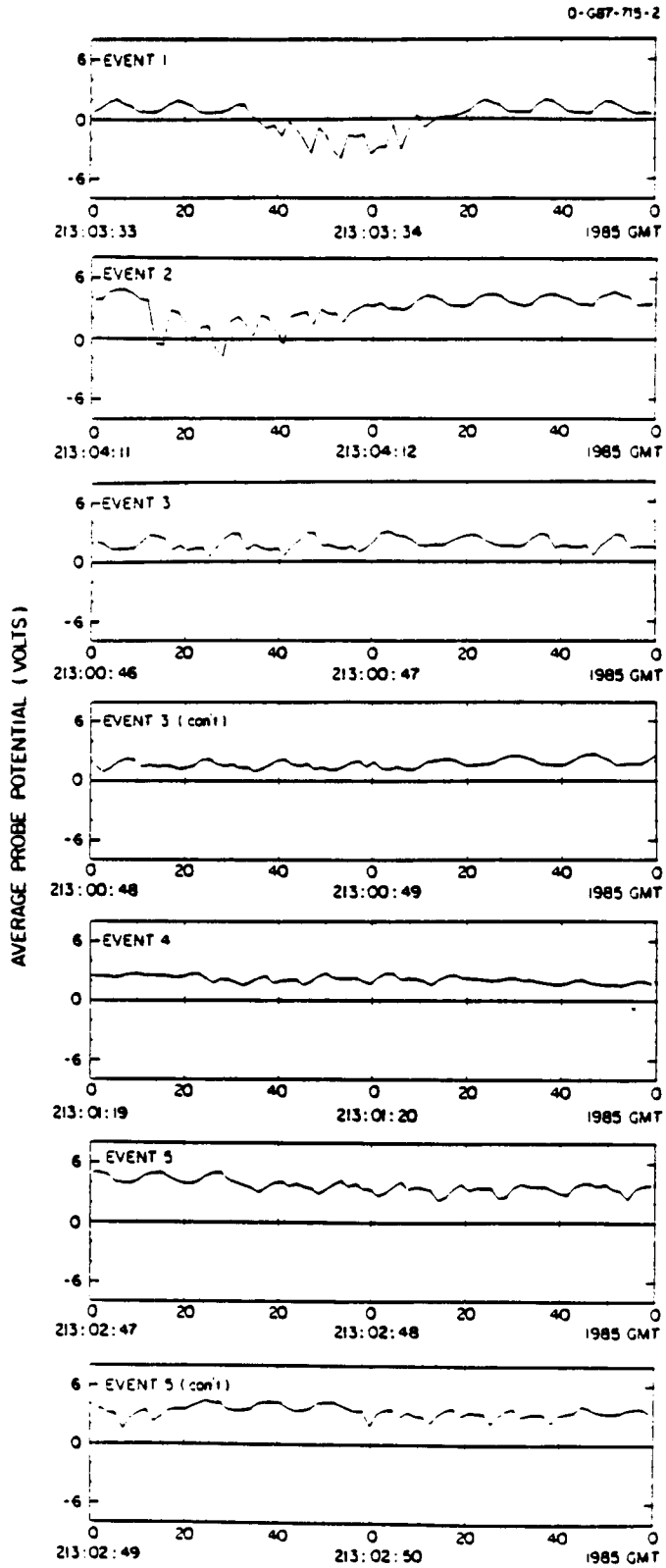
0-687-715-2
AVERAGE PROBE POTENTIAL (VOLTS)
EVENT 1
6
0
-6
0 20 40 0 20 40 0
213:03:33
213:03:34
1985 GMT
EVENT 2
213:04:11
213:04:12
EVENT 3
213:00:46
213:00:47
EVENT 3 (cont)
213:00:48
213:00:49
EVENT 4
213:01:19
213:01:20
EVENT 5
213:02:47
213:02:48
EVENT 5 (cont)
213:02:49
213:02:50

Figure 27. Solution of Equation 25 using values from Table 6. Model of floating potential as a function of energetic electron current. Antenna probe and PDP chassis have different floating potentials because of their different current collecting surface areas.

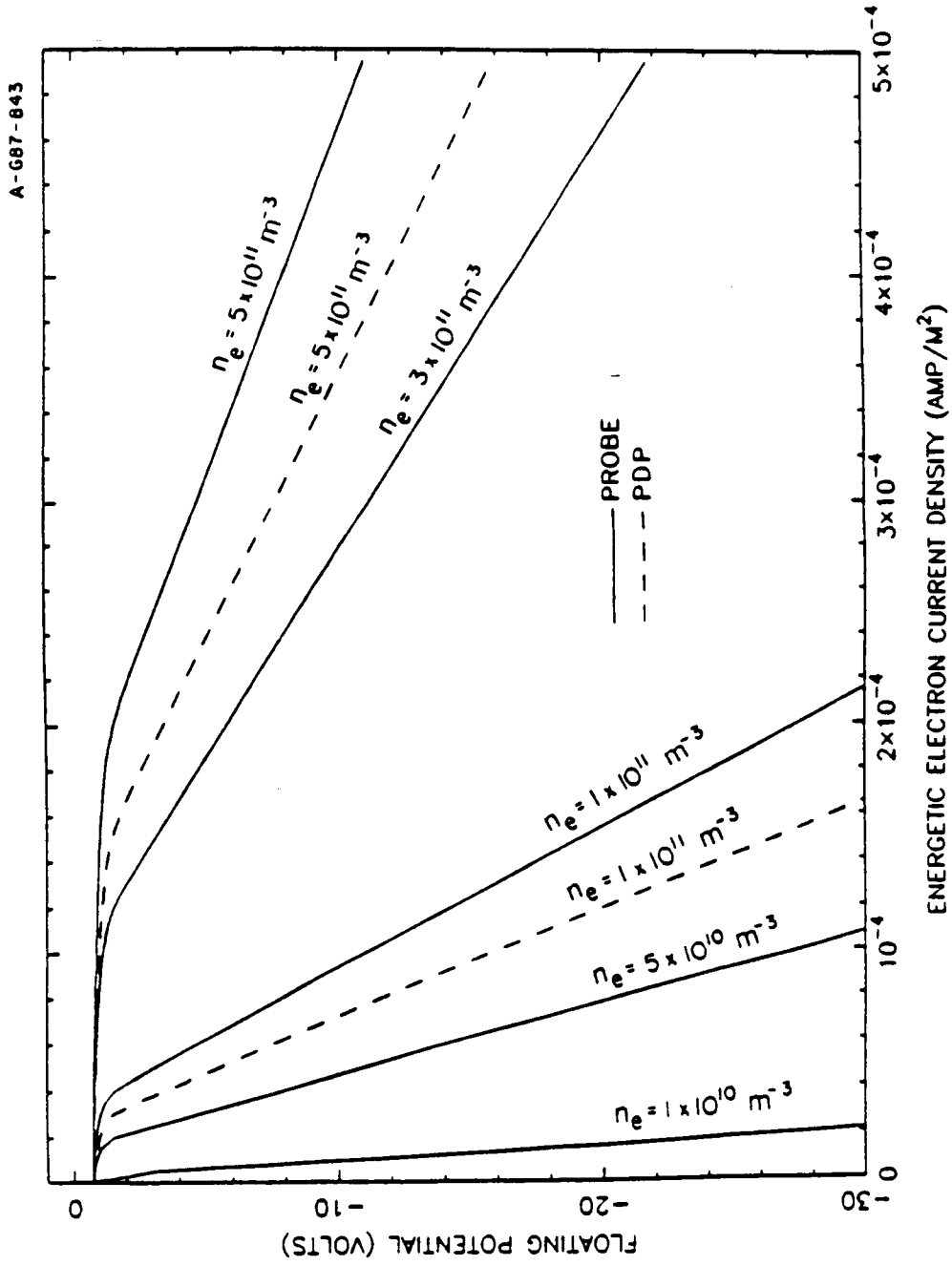
A-G87-843
$n_e = 5 \times 10^{11}\ m^{-3}$
$n_e = 5 \times 10^{11}\ m^{-3}$
$n_e = 3 \times 10^{11}\ m^{-3}$
PROBE
PDP
$n_e = 1 \times 10^{11}\ m^{-3}$
$n_e = 1 \times 10^{11}\ m^{-3}$
$n_e = 5 \times 10^{10}\ m^{-3}$
$n_e = 1 \times 10^{10}\ m^{-3}$
0
10^{-4}
2×10^{-4}
3×10^{-4}
4×10^{-4}
5×10^{-4}
ENERGETIC ELECTRON CURRENT DENSITY (AMP/M^2)
0
−10
−20
−30
FLOATING POTENTIAL (VOLTS)

Figure 28. The PDP with the spin plane corresponding to the plane of the page. Energetic electrons move along the field lines. As the PDP spins, the antenna periodically becomes aligned with the magnetic field, and one probe is shielded from the electron flux. The probe also passes through the PDP wake.

A-G87-681

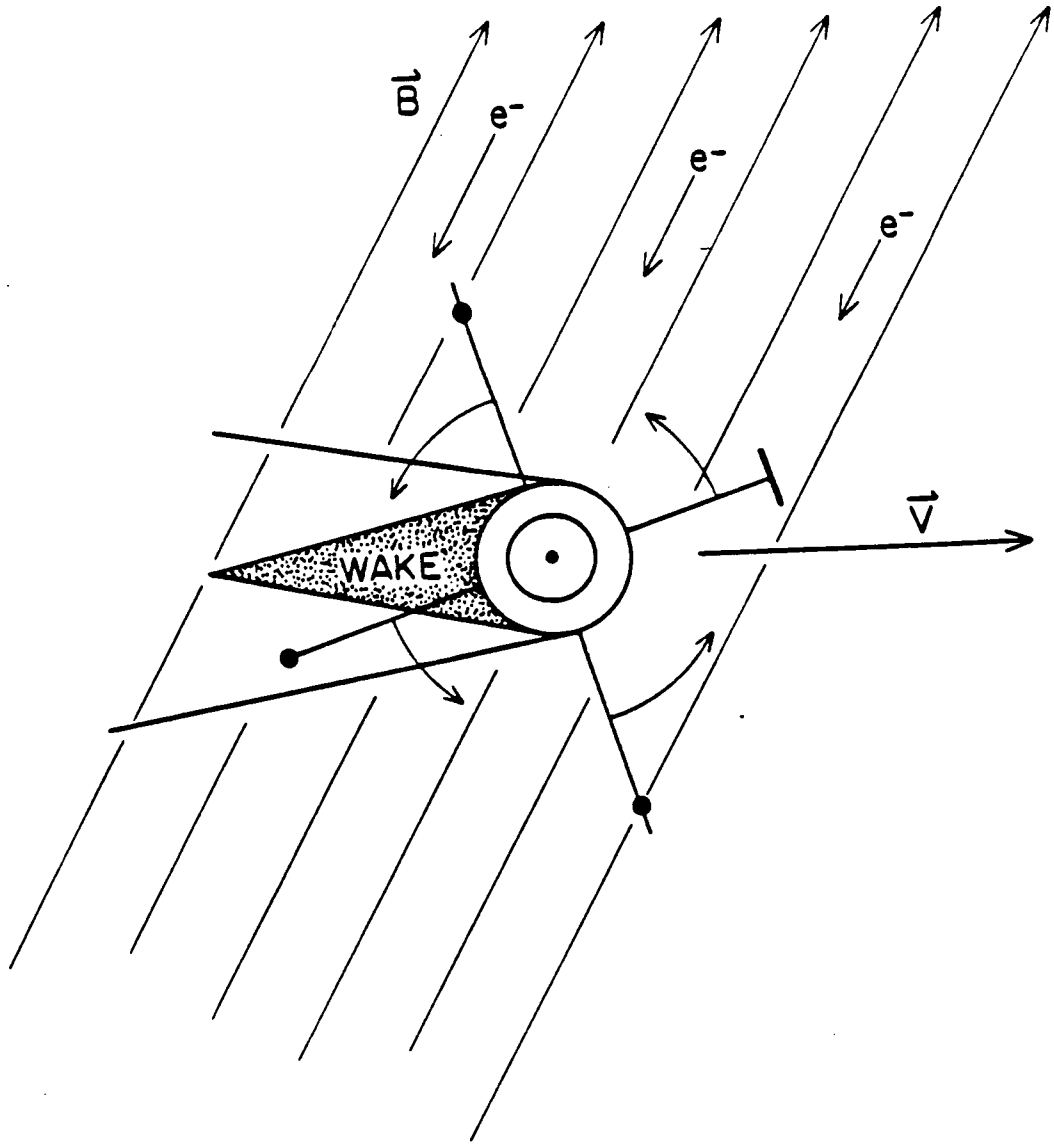

Figure 29. The PDP viewed with the spin axis in the plane of the page. The angle θ of the magnetic field to the spin plane is shown. If θ is small, then particles moving along field lines can be shadowed from one probe.

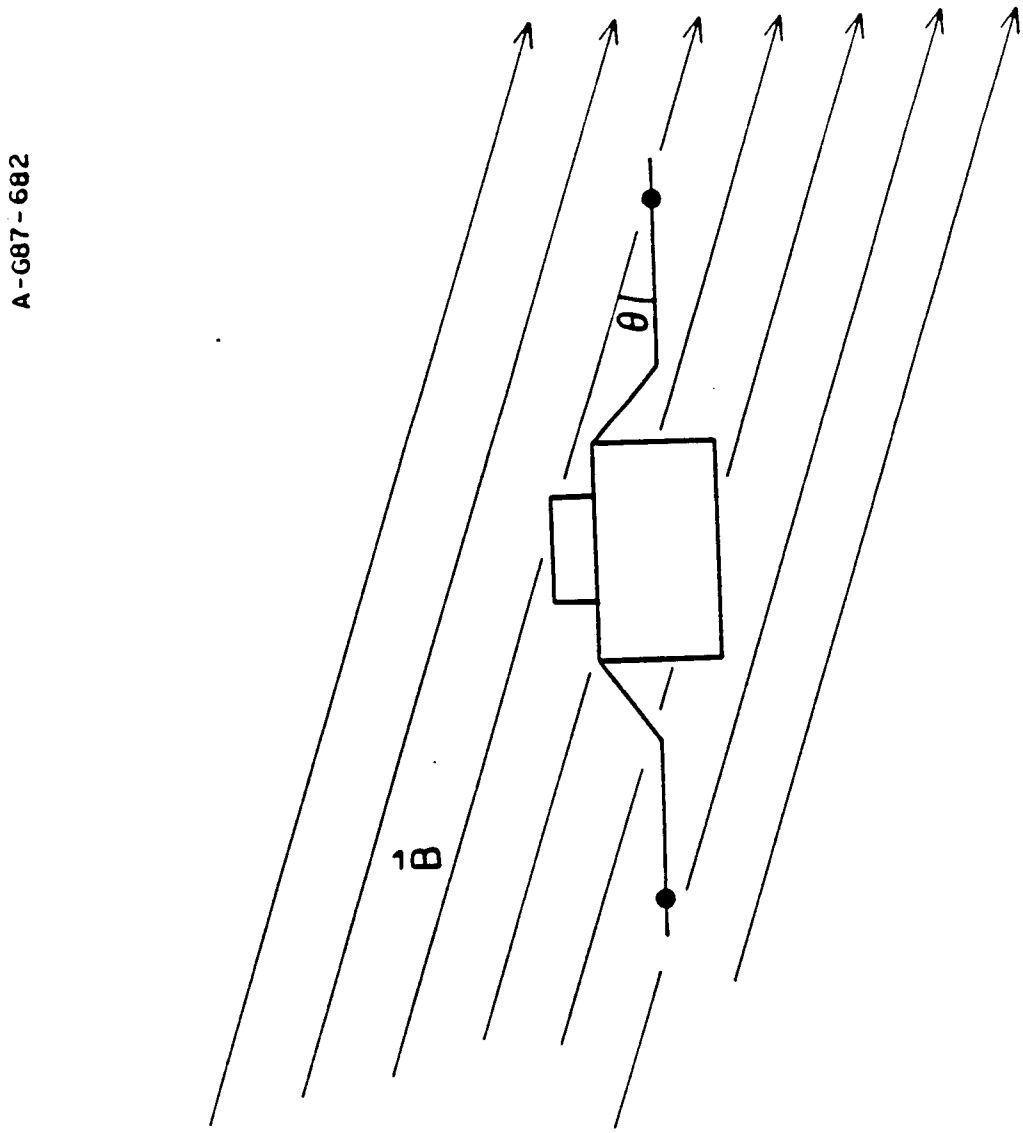
A-G87-682
θ
1B

Figure 30. Vectors showing the gradient in energetic electron flux along the trajectory of the PDP. Note that the beam will have a finite width, and the location of the beam center shown is accurate only to within a few meters.

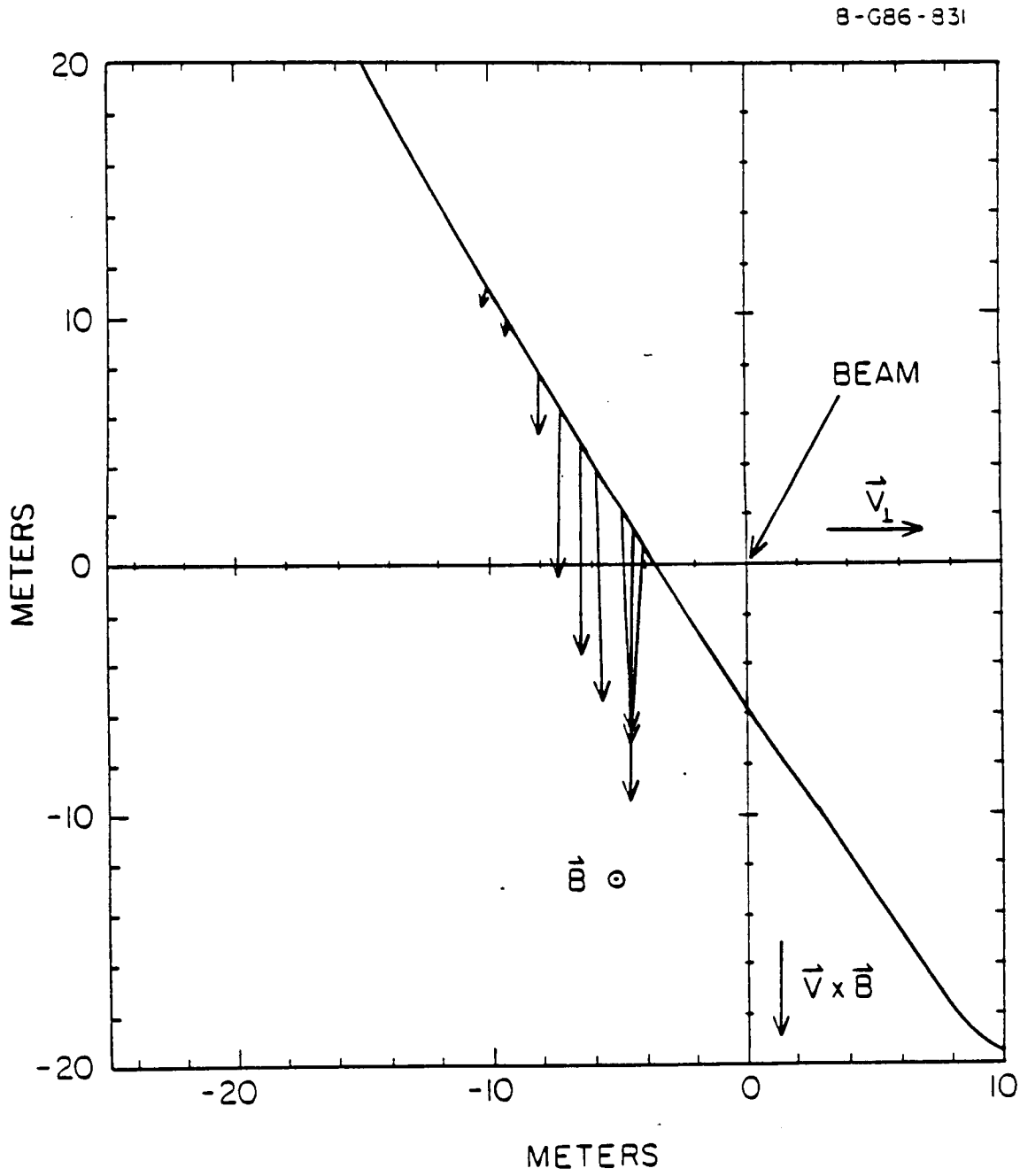
8-G86-831
20
10
0
-10
-20
METERS
-20
-10
0
10
METERS
BEAM
$\vec{V}_\perp$
$\vec{B}$ ⊙
$\vec{V} \times \vec{B}$

REFERENCES

Arnoldy, Roger L., and John R. Winckler, The hot plasma environment and floating potentials of an electron beam-emitting rocket in the ionosphere, J. Geophys. Res., 86, 575-584, 1981.

Banks, P. M., W. J. Raitt, A. B. White, R. I. Bush, and P. R. Williamson, Results from the Vehicle Charging and Potential Experiment on STS-3, J. Spacecraft and Rockets, 28, 138-149, 1987.

Bettinger, Richard T., An in situ probe system for measurement of ionospheric parameters, in Interactions of Space Vehicles With an Ionized Atmosphere, ed. S. F. Singer, 163-270, Pergamon Press, New York, 1965.

Bevington, Philip R., Data Reduction and Error Analysis for the Physical Sciences, McGraw-Hill Book Company, New York, 1969.

Denig, W. F., Wave and particle observations associated with the beam plasma discharge in a space simulation chamber, Ph.D. Thesis, Utah State University, 1982.

Drell, S. D., Foley, H. M., Ruderman, M. A., Drag and propulsion of large satellites in the ionosphere: An Alfvén propulsion engine in space, J. Geophys. Res., 70, 3131-3145, 1965.

Fahleson, U., Theory of electric field measurements conducted in the magnetosphere with electric probes, Space Science Reviews, 7, 238-262, 1967.

Frank, L. A., D. A. Gurnett, M. Ashour-Abdalla, W. R. Paterson, W. S. Kurth, N. Omidi, P. M. Banks, and W. J. Raitt, The secondary electron beams and plasma waves associated with electron beam injection in space (abstract), Bulletin American Physical Society, 32, 1823, 1987.

Goertz, C. K., Io's interaction with the plasma torus, J. Geophys. Res., 85, 2949-2956, 1980.

Grebowsky, J. M., H. A. Taylor, and W. M. Pharo III, Thermal ion perturbations in the vicinity of the space shuttle, Planet. Space Sci., 35, 501-513, 1987a.

Grebowsky, J. M., H. A. Taylor, and W. M. Pharo III, Thermal ion complexities observed within the Spacelab 2 bay, Planet. Space Sci., 35, 1463-1469, 1987b.

Green, B. D., G. E. Caledonia, and T. D. Wilkerson, The shuttle environment: Gases, particles, and glow, J. Spacecraft and Rockets, 22, 500-511, 1985.

Hanson, W.B., Structure of the ionosphere, in Satellite Environment Handbook, Second Edition, ed. Francis S. Johnson, Stanford University Press, Stanford, California, 1965.

Hoffman, R. J., and M. A. Hetreck, Jr., Plume contamination effects prediction: Contam III Computer Program, Tech. Rep. AFRPL TR82-033, Air Force Rocket Propul. Lab., Edwards AFB, Calif., 1982.

Hunten, D.E., and J. M. Calo, Low energy ions in the shuttle environment: Evidence for strong ambient-containment interactions, Planet. and Space Sci., 33, 945-951, 1985.

Jacobsen, T. A., and N. C. Maynard, Polar 5 - An electron accelerator experiment within an aurora. 3. Evidence for significant spacecraft charging by an electron accelerator at ionospheric altitude, Planet. Space Sci., 28, 291-307, 1978.

Johnson, Francis S., Structure of the upper atmosphere, in Satellite Environment Handbook, Second Edition, ed. Francis S. Johnson, 3-20, Stanford University Press, Stanford, California, 1965.

Kasha, Michael A., The Ionosphere and Its Interaction With Satellites, Gordon and Breach, Science Publishers, New York, 1969.

Katz, I., D. E. Parks, D. L. Cooke, and J. A. Lilley, Jr., Polarization of spacecraft generated plasma clouds, Geophys. Res. Lett., 11, 1115-1116, 1984.

Katz, I., and V. A. Davis, Ram ion scattering caused by space shuttle VxB induced differential charging, J. Geophys. Res., 92, 8787-8791, 1987.

Kellogg, P. J., H. R. Anderson, W. Bernstein, T. J. Hallinan, R. H. Holzworth, R. J. Jost, H. Leinbach, and E. P. Szuszczewicz, Laboratory simulation of injection particle beams in the ionosphere, in Artificial Particle Beams in Space Plasma Studies, ed. by B. Grandel, pg. 289, Plenum Press, New York, 1982.

McFarland, M., D. L. Albritton, F. C. Fehsenfeld, E. E. Ferguson, and A. L. Schmeltekopf, Flow-drift technique for ion mobility and ion-molecule reaction rate constant measurements, II, Positive ion reactions of N^+, O^+, and H_2^+ with O_2 and O^+ with N_2 from thermal to ~2eV, J. Chem. Phys., 59, 6620, 1973.

Mendillo, Michael, and Jeffrey M. Forbes, Artificially created holes in the ionosphere, J. Geophys. Res., 83, 151-162, 1978.

Mozer, F. S., R. B. Torbert, U. V. Fahleson, C. G. Falthammer, A. Gonfalalone, and A. Pedersen, Measurements of quasistatic and low-frequency electric fields with spherical double probes on the ISEE-1 spacecraft, IEEE Trans. Geosci. Elect., GE-16, 258-261, 1978.

Murad, Edmond, and S. T. F. Lai, Some charge exchange reactions involving H_2O, Chem. Phys. Lett., 126, 427-429, 1986.

Murphy, G., J. Pickett, N. D'Angelo, and W. S. Kurth, Measurement of plasma parameters in the vicinity of the space shuttle, Planet. Space Sci., 34, 993-1004, 1986.

Murphy, Gerald B., Stanley D. Shawhan, and Jolene S. Pickett, Perturbations to the plasma environment induced by the orbiter's maneuvering thrusters, AIAA 83-2599, 1983, AIAA Shuttle Environment and Operations Meeting, Oct. 31 - Nov. 2, 1983, Washington D.C.

Neubauer, F. M., Nonlinear standing Alfvén current system at Io: Theory, J. Geophys. Res., 85, 1171-1178, 1980.

Pickett, J. S., G. B. Murphy, W. S. Kurth, C. K. Goertz, S. D. Shawhan, Effects of chemical releases by the STS-3 orbiter in the ionosphere, J. Geophys. Res., 90, 3487-3497, 1985.

Raitt, W. J., D. E. Siskind, P. M. Banks, P. R. Williamson, Measurements of the thermal plasma environment of the space shuttle, Planet. Space Sci., 32, 447-467, 1984

Reasoner, David L., Stanley D. Shawhan, and Gerald Murphy, Plasma Diagnostics Package measurements of ionospheric ions and shuttle induced perturbations, J. Geophys. Res., 91, 13,463-13,471, 1986.

Samir, U., K. H. Wright, Jr., and N. H. Stone, The expansion of a plasma into a vacuum: Basic phenomena and processes and application to space plasma physics, Rev. Geophys. and Space Phys., 21, 1631, 1983.

Scholer, M., On the motion of artificial ion clouds in the magnetosphere, Planet. Space Sci., 18, 977-1004, 1970.

Shawhan, S.D., Description of the Plasma Diagnostics Package (PDP) for the OSS-1 shuttle mission and JSC chamber test in conjunction with the Fast Pulse Electron Gun (FPEG), Artificial Particle Beams In Space Studies, ed. by B. Grandel, 419-430, Plenum, N. York, 1982.

Shawhan, S. D., G. B. Murphy, P. M. Banks, P. R. Williamson and W. J. Raitt, Wave emissions from dc and modulated electron beams on STS-3, Radio Science, 19, 471-486, 1984a.

Shawhan, S. D., G. B. Murphy, and J. S. Pickett, Plasma Diagnostics Package initial assessment of the shuttle orbiter plasma environment, J. Spacecraft and Rockets, 21, 387-391, 1984b.

Singh, N., and R. W. Schunk, Numerical calculations relevant to the initial expansion of the polar wind, J. Geophys. Res., 87, 9154, 1982.

Smiddy, M., W. P. Sullivan, D. Girouard, and P. J. Anderson, Observation of electric fields, electron densities and temperature from the space shuttle, AIAA 83-2625, 1983, AIAA Shuttle Environment and Operations Meeting 1983, Washington D.C.

Steinberg, J. T., D. A. Gurnett, P. M. Banks, and W. J. Raitt, Quasi-static electric field measurements near the electron beam on Spacelab-2, submitted to J. Geophys. Res., 1987.

Stone, N. H., U. Samir, K. H. Wright, Jr., D. L. Reasoner, and S. D. Shawhan, Multiple ion streams in the near vicinity of the space shuttle, Geophys. Res. Lett., 10, 1215-1218, 1983.

Stone, N. H., K. H. Wright, Jr., K. S. Hwang, U. Samir, G. B. Murphy, and S. D. Shawhan, Further observations of space shuttle plasma-electrodynamic effects from OSS-1/STS-3, Geophys. Res. Lett., 13, 217-220, 1986.

Sunshine, Gabriel, Bertand B. Aubrey, and Benjamin Bederson, Absolute measurements of total cross sections for the scattering of low-energy electrons by atomic and molecular oxygen, Phys. Res., 154, 1-8, 1967.

Tribble, A. C., N. D'Angelo, G. Murphy, J. Pickett, and J. T. Steinberg, Effect of an exposed High-Voltage Source on the potential of an ionospheric satellite released from the shuttle orbiter, to be submitted to J. Spacecraft and Rockets, 1986.

Turner, B. R., and J. A. Rutherford, Charge transfer and Ion-atom interchange reactions of water vapor ions, J. Geophys. Res., 73, 6751-6758, 1968.

Whetten, N. R., Secondary electron emission, in CRC Handbook of Chemistry and Physics, 65th Edition CRC Press, Inc., Boca Raton, Florida, 1985.

Wilhelm, Klaus, Willian Bernstein, Paul J. Kellog, and Brian A. Whalen, Fast magnetospheric echoes of energetic electron beams, J. Geophys. Res., 90, 491-504, 1985.

Winckler, J. R., J. E. Steffen, P. R. Malcolm, K. N. Erickson, Y. Abe, and R. L. Swanson, Ion resonances and ELF wave production by an electron beam injected into the ionosphere: Echo 6, J. Geophys. Res., 89, 7565-7571, 1984.

Winckler, J. R., and K. N. Erickson, Plasma heating, plasma flow and wave production around an electron beam injected into the ionosphere, JPL Symposium on Space Technology Plasma Issues in 2001, ed. by Henry Garrett, Joan Feynman, Stephen Gabriel, pg. 295-306, JPL Publication 86-49, Oct. 1, 1986.